Transactions of the ASME

EDITORIAL STAFF
Director, Technical Publishing,
JOS. SANSONE
Managing Editor,
CORNELIA MONAHAN
Production Editor,
JACK RUMMEL
Editorial Production Asst.
BETH DARCHI
Associate Editors
Air Pollution Control
R. E. HALL
Diesel and Gas Engine Power
W. R. TABER, Jr.
Gas Turbine
G. K. SEROVY
Power
N. T. NEFF
Advanced Energy Systems
J. SNELL
Fuels
J. PAPAMARCOS
Nuclear Engineering
B. D. ZIELS

BOARD ON COMMUNICATIONS
Chairman and Vice-President
M. J. RABINS

Members-at-Large
W. BEGELL
J. CALLAHAN
M. HELMICH
D. KOENIG
M. KUTZ
F. LANDIS
J. W. LOCKE
J. E. ORTLOFF
C. PHILLIPS
K. REID

Business Staff
345 E. 47th St.
New York, N.Y. 10017
(212) 644-7789
Mng. Dir., Publ., J. J. FREY

OFFICERS OF THE ASME
President, ROBERT B. GAITHER
Exec. Dir. & Sec'y
BURKE E. NELSON
Treasurer, ROBERT A. BENNETT

Journal of Engineering for Power (ISSN 0022-0825) is edited and published quarterly at the offices of The American Society of Mechanical Engineers, United Engineering Center, 345 E. 47th St., New York, N. Y. 10017. ASME-TWX No. 710-581-5267, New York. Second Class postage paid at New York, N.Y., and at additional mailing offices.
CHANGES OF ADDRESS must be received at Society headquarters seven weeks before they are to be effective. Please send old label and new address.
PRICES: To members, $30.00, annually; to nonmembers, $60.00. Single copies, $20.00 each. Add $5.00 for postage to countries outside the United States and Canada.
STATEMENT from By-Laws. The Society shall not be responsible for statements or opinions advanced in papers or ... printed in its publications (B 7.1, para. 3).
COPYRIGHT © 1982 by the American Society of Mechanical Engineers. Reprints from this publication may be made on condition that full credit be given the TRANSACTIONS OF THE ASME – JOURNAL OF ENGINEERING FOR POWER, and the author, and date of publication be stated.
INDEXED by the Engineering Index, Inc.

Journal of Engineering for Power

Published Quarterly by The American Society of Mechanical Engineers
VOLUME 104 • NUMBER 2 • APRIL 1982

TECHNICAL PAPERS

255 A Modular Optimizing Calculation Method of Power Station Energy Balance and Plant Efficiency (81-GT-22)
H. Sonnenschein

260 *Dust and Sand Protection for Marine Gas Turbines* (81-GT-74)
M. R. Caskey

268 Heat-Transfer Coefficients for Staggered Arrays of Short Pin Fins (81-GT-75)
G. J. Van Fossen

275 Cooling Air Flow Characteristics in Gas Turbine Components (81-GT-76)
H. F. Jen and J. B. Sobanik

281 Inverse or Design Calculations for Nonpotential Flow in Turbomachinery Blade Passages (81-GT-78)
W. T. Thompkins, Jr. and Siu Shing Tong

286 *Interactive Multimode Blade Impact Analysis* (81-GT-79)
A. Alexander

296 Rotating Blade Vibration Analysis Using Shells (81-GT-80)
A. W. Leissa, J. K. Lee, and A. J. Wang

303 Low NO_x and Fuel Flexible Gas Turbine Combustors (81-GT-99)
H. G. Lew, S. M. DeCorso, G. Vermes, D. Carl, W. J. Havener, J. Schwab, and J. Notardonato

314 Establishing Cruise-Engine Cycle Payoffs for a Supersonic VSTOL Aircraft (81-GT-100)
J. D. Cyrus, P. F. Piscopo, and R. T. Lazarick

320 *Design of a Turbomachine Set for a Fluid Catalytic Cracking Plant and Its Shop-Testing* Under Full-Load Conditions (81-GT-101)
L. Turanskyi and G. U. Woelk

330 Combined Gas and Steam Cycle for a Gas-Cooled Solar Tower Plant (81-GT-102)
B. Becker, H. H. Finckh, and R. Meyer-Pittroff

341 Modified Brayton Cycles Utilizing Alcohol Fuels (81-GT-103)
M. F. Bardon

349 Effect of Temperature Dependent Mechanical Properties on Thermal Stress in Cooled Turbine Blades (81-GT-105)
J. M. Allen

354 Nonlinear Damage Cumulation in Solution-Treated and Aged Titanium 6Al-4V (81-GT-106)
J. H. Adams

360 Flow Transition Phenomena and Heat Transfer Over the Pressure Surfaces of Gas Turbine Blades (81-GT-107)
A. Brown and B. W. Martin

368 Design and Preliminary Results of a Fuel Flexible Industrial Gas Turbine Combustor (81-GT-108)
A. S. Novick, D. L. Troth, and H. G. Yacobucci

377 Low NO_x Combustion Systems for Burning Heavy Residual Fuels and High-Fuel-Bound Nitrogen Fuels (81-GT-109)
D. J. White, A. Batakis, R. T. LeCren, and H. G. Yacobucci

386 An Aeorthermodynamic Analysis of Transonic Compressor Rotors Containing Three-Dimensional Shocks (81-GT-120)
Xu Jian-zhong, Jiang Zuo-ren, Yang Jin-sheng, Zhang Ying, and Du Shuan-she

394 Computation of Three-Dimensional Flow Fields Through Rotating Blade Rows and Comparison With Experiment (81-GT-121)
K. P. Sarathy

403 Evaluation of Methods for the Treatment of Mean Stress Effects on Low-Cycle Fatigue (81-GT-122)
M. Doner, K. R. Bain, and J. H. Adams

412 Time-Variant Aerodynamics of High Turning Blade Elements (81-GT-123)
M. D. Rothrock, R. L. Jay, and R. E. Riffel

420 Application of a Fast Pseudo-Unsteady Method to Steady Transonic Flows in Turbine Cascades (81-GT-124)
J. A. Essers and F. Kafyeke

(Contents continued on p. 302)

Downloaded 03 Jun 2010 to 171.66.16.159. Redistribution subject to ASME license or copyright; see http://www.asme.org/terms/Terms_Use.cfm

(Contents Continued)

429 Evaluation of Advanced Combustors for Dry NO_x Suppression With Nitrogen Bearing Fuels *in Utility and Industrial Gas Turbines* (81-GT-125)
M. B. Cutrone, M. B. Hilt, A. Goyal, E. E. Ekstedt, and J. Notardonato

439 A Quasi-Three-Dimensional Blade Surface Boundary Layer Analysis for Rotating Blade Rows (81-GT-126)
W. T. Thompkins, Jr. and W. J. Usab, Jr.

450 A Baseload Gas Turbine to Meet Utility Requirements for Reliability and Availability (81-GT-127)
P. E. Grevstad, M. J. Smith, and R. L. Duncan

458 New Correlations of the Two-Dimensional Turbine Cascade Aerodynamic Performance (81-GT-128)
K. F. Qiang and N. X. Chen

467 Interaction of Compressor Rotor Blade Wake With Wall Boundary Layer/Vortex in the End-Wall Region (81-Gr/GT-1)
B. Lakshminarayana and A. Ravindranath

479 Measurement and Analysis of Total-Pressure Unsteadiness Data From an Axial-Flow Compressor Stage (81-Gr/GT-2)
W. C. Zierke and T. H. Okiishi

489 Nonequilibrium Streamline Curvature Throughflow Calculations in Wet Steam Turbines (81-Gr/GT-3)
C. C. Yeoh and J. B. Young

497 Study of Secondary Flows in Blade Cascades of Turbomachines (81-Gr/GT-4)
F. Bario, F. Leboeuf, and K. D. Papailiou

510 A Computation and Comparison With Measurements of Transonic Flow in an Axial Compressor Stage With Shock and Boundary Layer Interaction (81-Gr/GT-5)
U. K. Singh

516 Development of Screening Criteria for Selecting Long-Distance Heat Transmission Fluids
S. Szepe and J. M. Calm

DISCUSSION

522 Discussion of a previously published paper by
A. R. Wadia and T. C. Booth

522 Discussion of a previously published paper by
B. Beacher, W. Tabakoff, and A. Hamed

ANNOUNCEMENTS

274 Change of address form for subscribers

280 *Mandatory excess-page charge notice*

524 Information for authors

Downloaded 03 Jun 2010 to 171.66.16.159. Redistribution subject to ASME license or copyright; see http://www.asme.org/terms/Terms_Use.cfm

A Modular Optimizing Calculation Method of Power Station Energy Balance and Plant Efficiency

H. Sonnenschein
Deutsche Babcock AG,
D-4200 Oberhausen, West Germany

A project engineer employed in the field of power plants needs an effective instrument for designing and comparing of energy-cycle concepts when planning new stations or when modifying the flow concept of existing plants. The offered method is considered as such an instrument. Its special feature is based on its consequent modulating which allows adaptation to every cycle concept. The hierarchical structure, the dependence of program modules when operating with one another and the possibility of enlarging the scope of modules are shown by an example. Finally, a typical application of the method will be demonstrated by means of a combined gas-steam turbine power plant.

1 Introduction

In planning a power station today it is necessary to calculate the energy cycle thermodynamically with a very high degree of accuracy. The reason for this is that the owner usually sharply defines the guarantee conditions. Moreover, the energy market situation increasingly requires the conservation of energy and better utilization of available energy sources. Therefore efforts must be made to achieve as high an efficiency as possible for power station cycles.

To facilitate finding the conditions for an optimum efficiency, a numeric calculation method was developed which is fast and easy to handle. A special feature of power station cycles is the wide variety of possible arrangements. It is true, however, in the final analysis they are invariably composed of the same assemblies, such as boiler, turbine, condenser, pumps, preheaters, etc. This results in the necessity of using a calculation method which covers the wide variety of cycles but always draws on identical calculation modules.

2 Program Structure

The modular technique with the use of the Electronic Data Processing (EDP) is customary today, not a novelty. It is used where complex varying systems are to be dealt with. Its use in technical calculations in the field of power stations was introduced for the first time by Dittmar [1]. The idea of modular calculation offers considerable advantages over closed calculation models, indeed, it is in the last analysis the only possible and reasonable method as, due to the wide variety of cycles, it is impossible to develop a closed model for each power station concept. In the modular calculation concept these difficulties are not encountered, however, this concept requires a very precise analysis of the cycle if a good reproduction is to be obtained. An example may illustrate how such a calculation method [2] can be used for power station arrangements.

2.1 Geometric Modules

2.1.1 Division of a Cycle Into Plant Modules. A modern power station cycle consists of a large number of components, such as condenser, boiler, turbine, pumps, preheaters of various types, flasch evaporators for process or heating steam, shut-off devices and others.

As an example, a combination plant of medium capacity (150 MW) as shown in Fig. 1 is considered. The condensate is heated up in a preheater section consisting of three L.P. heaters, a deaerator, two H.P. heaters and a downstream flue gas heated feedwater heater and supplies to the boiler. The superheated steam is passed to the H.P. stage of the steam turbine. After a single superheater stage it flows through the intermediate and low pressure stage of the turbine and is subsequently condensed in the condenser. An open gas turbine of a capacity of 30 MW supplies part of its exhaust gas to the boiler as supply air, the remaining portion of the exhaust gas of the gas turbine is passed together with the boiler waste gas through two flue gas heated feedwater heaters, only a partial flow is admitted to the last one which is arranged in parallel to the steam-heated L.P. heaters.

Modular program technique does not only mean taking into account the varying demands and operating conditions of the owners, but also being able to handle highly varying cycle configurations. This is achieved by dividing the cycle into its essential plant items. The components marked in Fig. 1 represent the essential assemblies. All arrangements which are common practice in power station construction are invariably composed of these basic elements, they are the basis modules from which the large number of possible schematics can be arranged. Figure 2 shows a complete survey of those power station modules on which the method [2] is based.

As it turned out, type and number suffice for a satisfactory

Contributed by the Gas Turbine Division and presented at the International Gas Turbine Conference and Exhibit, Houston, Texas, March 8–19, 1981, of THE AMERICAN SOCIETY OF MECHANICAL ENGINEERS. Manuscript received at ASME Headquarters December 5, 1980. Paper No. 81-GT-22.

Copyright © 1982 by ASME
Downloaded 01 Jun 2010 to 171.66.16.62. Redistribution subject to ASME license or copyright; see http://www.asme.org/terms/Terms_Use.cfm

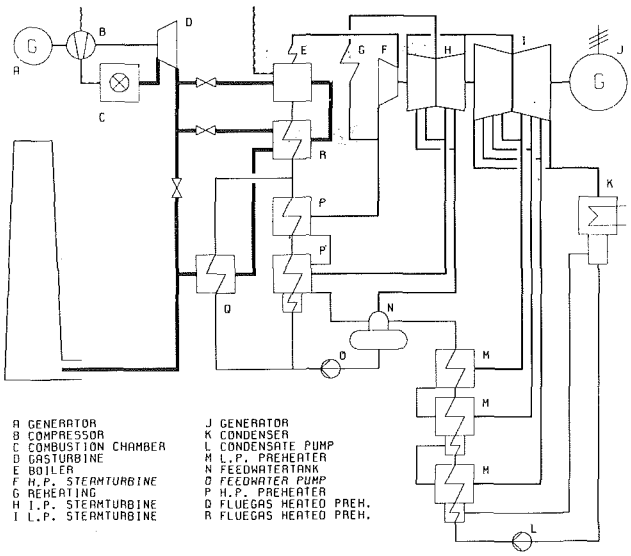

Fig. 1 Representation of the composition of the cycle of a power station of the plant modules

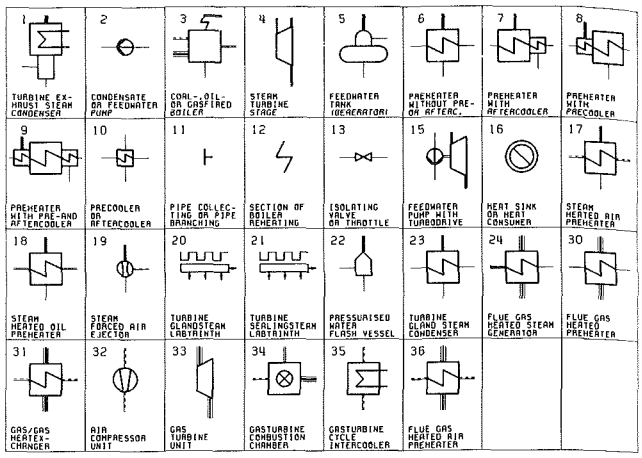

Fig. 2 List of cycle modules for preparing digital calculation models according to [2]

description of usual power station cycles. However, there are no limitations, so that components of other power station cycles which have not been covered or are novel, merely supplement this list but do not make the principle of the module technique dubious. This is the considerable advantage already mentioned of the modular method, i.e. it is open to further developments.

2.1.2 Structure of Modular Networks. For each module there is an EDP program whose function is to reproduce the component in its physical behaviour as accurately as possible without entering into constructional details. A cycle - Fig. 3 shows a simple example - is composed of these modules as of building blocks. The fact that the calculation engineer is forced to carry out a detailed analysis is demonstrated by the turbine which is not considered as one whole module, but is dealt with separately from extraction point to extraction point, divided into sections.

In order to obtain a coherent system from the modules listed side by side without relation to one another - in Fig. 3 represented by a control space shown in broken lines - the necessary connections between the modules are to be provided which correspond to the run of the lines. Each module is furnished with its index according to the module list (Fig. 2) and each line between the module with a number, the positive sign describing the supply flow and the negative sign the discharge flow from a module. For example, the fourth row of digits "2, +202, −203" represents a pump (index 2, Fig. 2) to which the fluid is supplied through the line with number 202 and from which the fluid is discharged through the line 203.

In addition, the calculation engineer may make arrangements which divide the line numbers into certain categories to identify the type of the flowing medium. In the mentioned example, all line numbers consist of three digits, i.e. with the digit 1 in the first place for the identification of steam, 2 for condensate and 3 for cooling water as a medium. The line category is at the same time criterion for the selection of the fluid data to be used. As both the type of categories and their number are not subjected to any limitations it is also possible to define other categories which allow the use of fluid types other than those of water and steam. In combination cycles, for example, the line category with digit 0 in the first place denotes air-and/or exhaust gas lines.

Here, too, the advantage of modular structure is again demonstrated. In principle, the catalogue of the fluid data may be a compilation of a wide variety of fluids whose use is fixed by the selection of the line number and the category assigned to it.

Accordingly, the set of digits sufficiently describes the interaction of the components of the simple cycle given as an example. In this case, only seven components are involved. Larger cycles easily include a number of approximately 100 modules which are interconnected. The principle of linking is however invariably the same. It is quite obvious that for a more precise consideration of the cycle modular characteristics, such as characteristic curves, heat transfer properties and the like have to be defined. However, in this context, this is not to be considered in further detail.

2.2 Thermodynamic Modules

2.2.1 Program Executing Control by Option Routines. Figure 4 shows the hierarchic nature of the program structure. At the highest level there are routines for controlling the program flow. Three options are given, namely "check calculation, optimizing and part load". Each of the operation options uses the calculation module assigned to it in structure level 2 which contains the iteration conditions.

The term "check calculation" means on the one hand to design a power station cycle so that the given technical data of individual components are adhered to. This is always the case when the components cannot be freely selected due to type series. On the other hand, "check calculation" also means being able to design a cycle completely free of given variables. Not matter how this term is to be understood it always means that calculation is carried out at 100 percent load. Here, either the required terminal output of the generator or the live steam flow at boiler outlet may be given. In the iterative cycle calculation procedure it is used as a desired variable and all calculations are repeated until this variable has been fulfilled with sufficient selectable accuracy.

The second option of the program flow control, "optimizing" of a cycle, does not start from fixed technical data but seeks the point of optimum interaction of the selected components. Optimizing is effected in two stages. In the first one, the planned full heating-up range for the cycle considered is distributed to the preheaters so that the efficiency is an optimum. In the second stage the full heating-up range is optimized, retaining the optimum distribution found previously in the preheater chain. This methodology is taken from the Gauss-Seidel strategy [3] which finds the optimum by calculating a relative optimum first by altering one variable

Downloaded 01 Jun 2010 to 171.66.16.62. Redistribution subject to ASME license or copyright; see http://www.asme.org/terms/Terms_Use.cfm

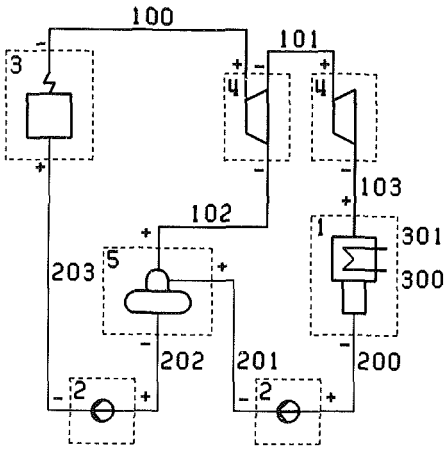


```
1,103,-200,300,-301,
2,200,-201,
5,201,-202,102,
2,202,-203,
3,203,-100,
4,100,-101,-102,
4,101,-103,
```

Fig. 3 Example of a cycle convenient for EDP according to [2]

of influence which is subsequently improved by successive variation of the other parameters.

The third aspect in the option of the program operation is the "part load". To a check or optimizing calculation one or several calculations for altered operating conditions may be connected. This also includes the bypass or shut-down of individual components or component groups. Examination of bypasses of assemblies by calculation is of interest when individual components have failed, are to be shut down or replaced by new ones. In combination cycles the gas and steam turbine sections may separately or jointly subjected to altered operating conditions.

2.2.2 Thermodynamic Interaction. The calculation modules or interaction routines of structure level 2 use the geometric modules of level 3 which includes those routines which describe the physical behavior of components. These can be divided into groups for which the same or similar aspects hold for the calculation:

(*a*) heat-exchanging units
(*b*) pumps, compressors and turbines
(*c*) throttling devices, shut-off devices, heat sinks and sources, auxiliary units (steam ejector, flash evaporator etc.)
(*d*) boiler, furnace chamber
(*e*) condenser

Apart from the operating pressure and pressure drop, a heat exchanging unit is characterized by four characteristic quantities which are: upper and lower terminal temperature difference, heating-up range and steam demand. A preheater is sufficiently described when two of the four quantities are given, the two unknown ones can be determined. With these combination possibilities highly differing requirements on the physical calculation of the preheater can be met.

The second group of components with similar basic physical laws comprises the fluid flow engines. They are characterized by their expansion and compression lines. The pressures are fixed by the type of turboengine used. This is the essential advantage of the method, namely to be able to start

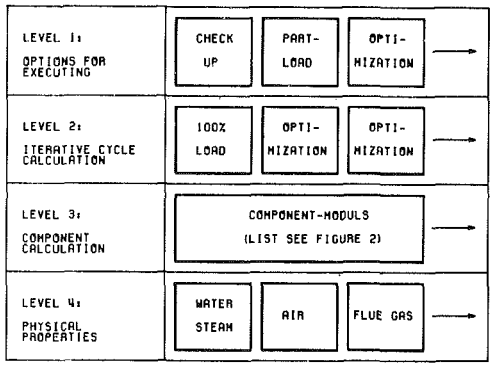

Fig. 4 Program structure, representation of the hierarchic levels and indication of the extension possibilities

from fixed technical data of a turboengine so that certain type sizes can be considered. If, however, no certain type is to be verified, efficiency and expansion pressures can be freely chosen or determined from empirical values depending on the size. In the case of steam turbines, leakage and gland steam flow can be considered, and in the case of wet steam stages, drains.

With the components of the third group pressure drops and heat supply and abstraction on certain components can be dealt with. These include shut-off devices and valves, process steam utilizing plants, auxiliary units etc. All characteristic quantities should be given.

The boiler as heat source of the cycle is characterized by inlet pressure, outlet pressure, and temperature as well as by its efficiency. The appropriate method for dealing with the combustion of the fuel to be fired is the statistical combustion calculation [4]. It gives the required fuel and air flows, flue gas composition and thus also the basis for the calculation of the thermodynamic variables of state of the flue gas. Within the framework of this approach it is not necessary to consider the structural design of the boiler proper.

Largely analogously to the boiler the combustion chambers of gas turbines can be dealt with. A special feature is, however, that the separation of primary combustion air and secondary cooling air is to be considered. As governing factor of the cycle, the condenser plays as important a part as the boiler. The gradient reduced in the turbo set is decisively determined by it as it fixes the expansion pressure. It is left to the discretion of the user of the calculation program either to give the condenser pressure directly or to determine the cooling water outlet temperature via the terminal temperature difference.

In the part load range some characteristic data of the components change according to the certain physical relations. In particular, these are for heat exchanging units the terminal temperature differences, for the condenser with constant cooling water flow the pressure as well as all pressure drops. If the part load behaviour of the units is not fixed by certain characteristic curves given, the following theoretical or empirical functions are used. Changes in the terminal temperature differences of the heat exchangers can be calculated in the case of condensation by the exponential function according to Schröder [5], in the case of gas-gas heat exchangers by that according to Bammert [6]. For the characteristic curves of turbines the improved steam cone law of Flügel [7] has proved satisfactory.

2.2.3 Fluid Values. The last level of the program structure according to Fig. 4 contains the fluid modules. At present, it is possible to calculate the thermodynamic values of water and steam as well as of air and flue gas. The values of water and steam are represented by the well-known IFC polynomials as

Downloaded 01 Jun 2010 to 171.66.16.62. Redistribution subject to ASME license or copyright; see http://www.asme.org/terms/Terms_Use.cfm

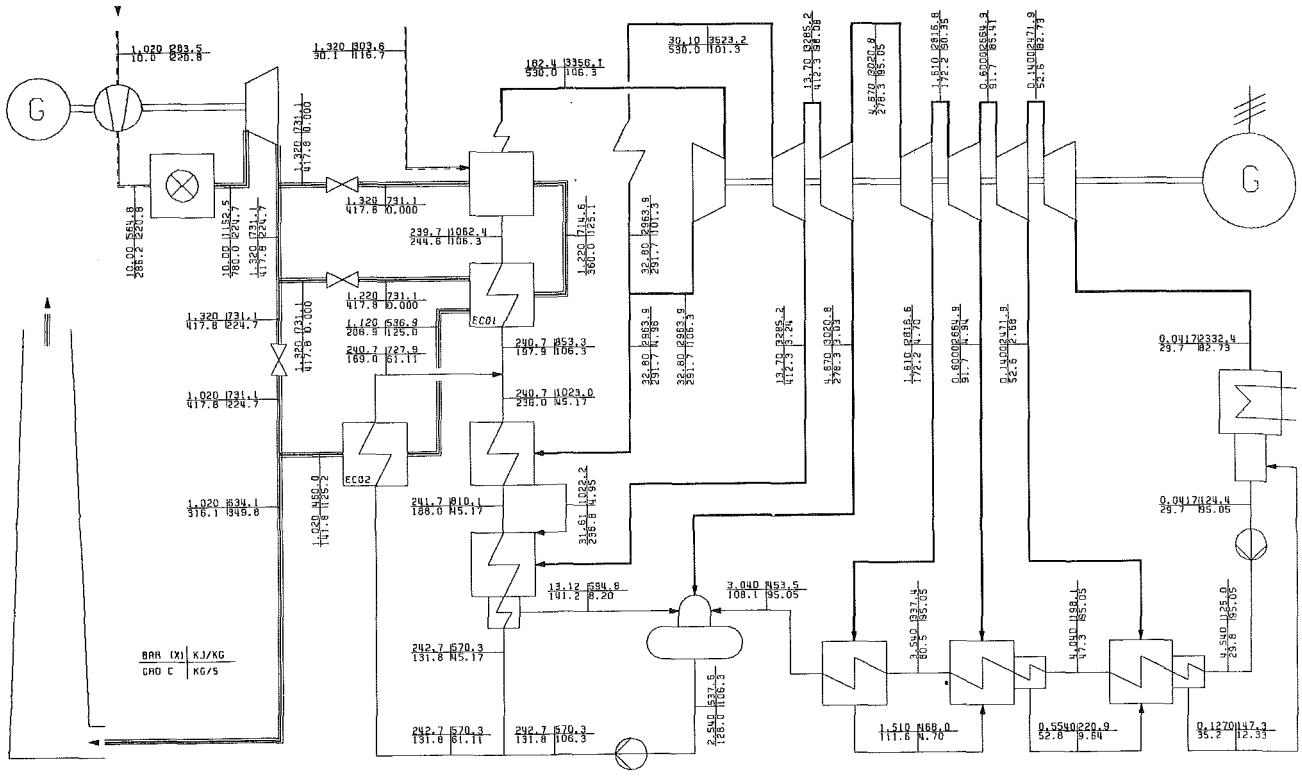

Fig. 5 Results of the calculation of a combined gas-steam turbine *power station with decoupled gas turbine*

they are represented in [8] on an international basis for water/steam and described in the form of ASME papers under the aspect of programming technique in [9] and [10]. This method has the advantage of being recognized internationally and of being free from inaccuracies inherent to interpolating methods. For air the polynominals according to Baehr/Schwier [11] are used which take into account the real behaviour of air. As in the gas turbines used in combination cycles maximum pressures of about 10 bar occur, the equations indicated in the *FDBR Manual* [4] may be applied for calculating the thermodynamic values of flue gas.

The type of overall structure clearly shows that each program level can be extended in a way corresponding to the requirements without affecting the basic concept of the system. This is the essential advantage of the modular structure which allows adjustment to the altered requirements without any problems. For example, it is possible to increase the number of components at level 3 or also to add further fluids, such as helium, argon, freon, or others, to level 4.

3 Typical Calculation with Variation

3.1 Combined Gas/Steam Turbine Plant with Decoupled Gas Turbine

In conclusion, an example may serve to illustrate how the described calculation method can be used. Figure 1 shows a power station cycle as a combination plant (150-MW steam section, 30-MW gas turbine). The steam is generated in the boiler and expanded in the H.P. turbine. In a reheater energy is again imparted to it which is converted in an I.P. and L.P. turbine. The condensate is heated in three L.P. heaters before it is passed into the feedwater tank. After the tank the temperature is increased further in two steam-heated H.P. heaters. The boiler waste gas is used to heat up the feed water to its final temperature in a last preheater (economiser 1) before it is supplied to the boiler. Parallel to the two steam-heated H.P. heaters a partial flow of the feed water can be extracted after the feed pump and heated up in a downstream flue gas heated preheater (economiser 2). A gas turbine with single-stage compression without intermediate cooler may supply part of its exhaust gas to the boiler as supply air and deliver another partial flow to economiser 1 to which the boiler waste gases are admited. In Fig. 5 it is assumed that the boiler is not supplied with turbine exhaust gas and additional flue gas is not led to economiser 1, either, i.e. that the gas turbine is to be considered as decoupled, separated from the steam section. This means for the boiler that its total air demand has to be supplied as primary air. Figure 5 shows the thermodynamic states at all relevant cycle points. The graph was prepared with the plot routines of the method [2]. It gives the planner and designer a clear general view of the cycle. It is obvious that the turbine is decoupled as no gas is supplied either to the boiler or to economizer 1. The specific heat comsumption of the steam cycle is 7450 kJ/kWh, that of the gas cycle 15245 kJ/kWh, the mixed value is 9580 kJ/kWh.

3.2 Variation of the Cyclic Course by Coupling the Gas Turbine

At this point of the studies at the latest the planner and designer will have the wish to learn by variation of some cycle data in how far the cycle can be improved, e.g. whether a cycle improvement is achieved by lowering the final flue gas temperature to a further degree by increasing the flow extracted after the feedwater pump. However, in this context this question is not to be studied, it is only one possible investigation using the presented calculation method, but the objective is to show the effect coupling of the gas turbine will have. Figure 6 illustrates the calculation results. The boiler does not require any additional primary air as it is supplied with hot turbine exhaust gas as supply air. Additional waste gas is likewise admitted to economiser 1 so that the feedwater inlet temperature to the boiler is considerably raised. This results in an appreciable improvement of the steam section as

Downloaded 01 Jun 2010 to 171.66.16.62. Redistribution subject to ASME license or copyright; see http://www.asme.org/terms/Terms_Use.cfm

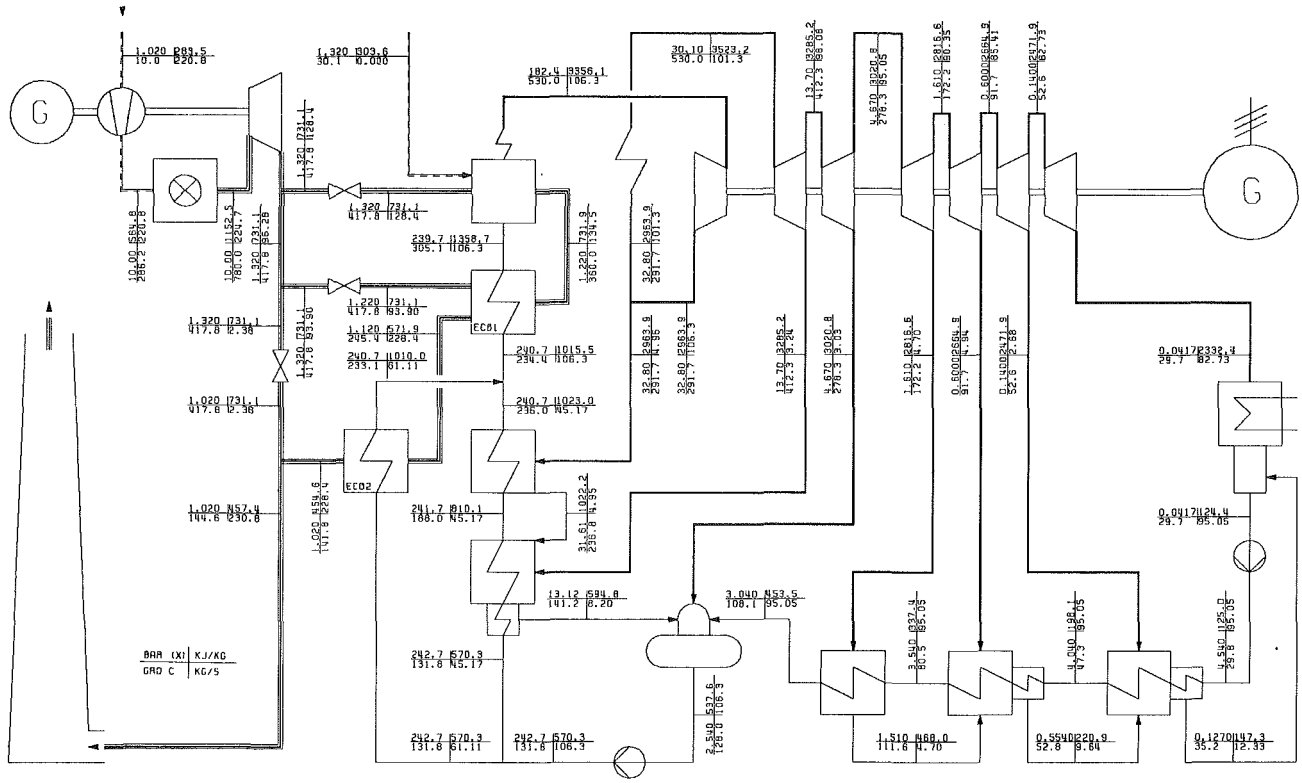

Fig. 6 Variation example: Effect of an altered cyclic course on the overall efficiency with coupled gas turbine

now the boiler requires less energy in the form of fuel to produce the final live steam temperature. The specific heat consumption of the steam section is now 6670 kJ/kWh and the mixed value is improved to 7790 kJ/kWh. It is not a new finding that the combination cycle offers advantages, the novelty is perhaps the methodology of the calculation procedure which rendered this result fixable within seconds. Purely theoretically it takes such a short period of time to improve cycles. It has always been, and will be increasingly in the future, the duty of all engineers in the field of power station construction to put such cycle improvements into practice. The means of calculation methodology are provided and are rapidly available by means of efficient EDP.

Acknowledgment

The development of the calculation procedure including all improvements required a work effort of five man-years. Today is has reached a degree of sophistication ensuring unproblematic, rational use of it for power station calculations. The basic conception of the procedure was worked out at the Institute for Fluid Mechanics of the University of Hanover under the leadership of Prof. Dr. Bammert; the completion of a first version was carried out by Dr. H. Zwahr (former assistant of Prof. Bammert, now employee of Hamburger Elektrizitätswerke). Deutsche Babcock acquired the procedure and developed it to its present level in close contact with practical cases of application and with the excess support of Dr. Bitterlich, Executive Vice President of Babcock AG. Without the personal involvement of all concerned, the successful conclusion of the work would not have been possible. Therefore the author's particular thanks are due both to Prof. Bammert, his former teacher, for the numerous suggestions, and also to Dr. Zwahr for his hard work and in particular to Dr. Bitterlich for his encouragement and support for the development of the procedure.

References

1 Dittmar, H., "Einsatz eines Programmsystems zur Berechnung von thermodynamischen Kreisprozessen bei den VEW," VGB Kraftwerkstechnik 53, No. 2, 1973, pp. 71-77.

2 Sonnenschein, H., and H. Zwahr, "Ein Verfahren zur Berechnung von Kreislaufprozessen in Kraftwerken Atomkernenergie (ATKE), Vol. 32, 1978, Lfg. 4.

3 Rechenberg, I., *Evolutionsstrategie,* Stuttgart-Bad Cannstatt, Frommann publishers, 1975.

4 *FDBR-Manual,* Fachverband Dampfkessel-, Behälterund Rohrleitungsbau e.V., Essen, Vulkan publishers, 1975.

5 Schröder, K., *Grosse Dampfkraftwerke,* third volume, Part A, Die Kraftwerksausrüstung, Berlin/Heidelberg/New York, Springer publishers, 1966.

6 Bammert, K., and Twardziok, W., "Das stationäre Betriebsverhalten von konventionell-und nuklearbeheizten Gasturbinen," *Atomkernenergie,* Vol. 11, No. 5/6, 1966, pp. 185-204.

7 Flügel, G., "Die Dampfturbine bei grossen Änderungen des Betriebszustandes," *VDI Journal,* Vol. 93, 1951, p. 721.

8 Schmidt, E., *Properties of Water and Steam in SI-Units,* Berlin/Heidelberg/New York, Springer Publishers, Munich, R. Oldenbourg, 1969.

9 McClintok, R.B., and Silvestri, G.J., "Formulations and Iterative Procedures for the Calculation of Properties of Steam," ASME (1968).

10 McClintok, R.B., and Silvestri, G.J., "Some Improved Steam Property Calculation Procedures," ASME JOURNAL OF ENGINEERING FOR POWER, 1970, pp. 123-128.

11 Baehr, H.D. and Schwier, K., *Die thermodynamischen Eigenschaften der Luft,* Berlin/Göttingen/Heidelberg: Springer Publishers, 1961.

12 Adrian F., and Sonnenschein, H., "Kreisprozessbetrachtungen für kombinierte Gas-und Dampfturbinenanlagen," *Jahrbuch der Dampferzeugertechnik,* 4th edition, 1980, Vulkan Publishers Essen.

Downloaded 01 Jun 2010 to 171.66.16.62. Redistribution subject to ASME license or copyright; see http://www.asme.org/terms/Terms_Use.cfm

Dust and Sand Protection for Marine Gas Turbines

M. R. Caskey

Manager, Ship Systems,
Ingalls Shipbuilding Division,
Pascagoula, Miss. 39567

The newest ship class to enter the U.S. Navy (USN) fleet is the DDG-993 KIDD Class guided missile destroyer. The lead ship of the Class, delivered March 1981, incorporates the main features of the DD 963 Class hull and main propulsion system designs. Originally ordered by the Imperial Iranian Navy (IIN), the ship design also incorporates unique features for protection from dust and sand. The ventilation ducting, deck machinery, and gas turbine combustion air all required modifications to protect against damage due to the expected Persian Gulf environment. This paper will outline the hardware changes considered necessary to meet the requirements for satisfactory IIN performance for the propulsion and electrical generator gas turbines.

Introduction

The newest class of combatant ship to enter the USN completed for delivery in January 1982. It is the DDG-993 KIDD Class guided missile destroyer. The basic design combines the hull and propulsion plant of the DD 963 Spruance Class destroyer and the fire-control/missile system of the CGN 38 Virginia Class.

The genesis of this potent addition to the fleet was the desire of the IIN to have a modern flagship based on the successful DD 963 Class. Study contracts were awarded by Fiscal Year 1975 to fund levels of effort (LOE) by various agencies to determine the desired characteristics of the new IIN ship. The USN Naval Sea Systems Command acted as procurement activity for the IIN.

One of the considerations outside the sphere of experience of many U.S. naval ship designers was the dust haze and sand storm conditions to be expected in the Persian Gulf. As part of one LOE contract, the ship designer, Ingalls Shipbuilding Division of Litton Industries, developed probable dust/sand conditions.

The separation of dust is not new to the marine designer. Bulk carriers designed in the early 1960s required protection from the ever-present dust during grain loading operations. Stationary power facilities used for oil production in arid areas have long had dust/sand protection for combustion air. Helicopers have also utilized separators for gas turbine (GT) air inlets. The challenge facing the designer was thus simplified by related experience in unrelated fields.

The IIN DD 993 design evolved from the basic DD 963 Class, fully incorporating the changes dictated by the harsh Persian Gulf environment. Higher ambient temperatures and dust/sand protection were among the factors used to determine system designs. The completed design became a reality when construction began at Ingalls on October 24, 1977, with the cutting of steel for the first of four hulls. The kneel was laid on June 26, 1978, the ship launched August 11, 1979, and Builder's Trial (BT) held August 19, 1980. Figure 1 shows the KIDD at sea on Builder's Trial.

In February, 1979 the government of Iran fell. The incoming government indicated the IIN DD 993 Class was no longer desired. Construction was well advanced on the first two ships and had also begun on the remaining ships. As a result, four new guided missile destroyers became available for the USN. Some of the ships' features were not of the usual design, particularly oversize seawater heat exchangers and extensive dust/sand protection. The class designation was changed from IIN DD 993 to DDG-993 in August, 1979.

Background

Detailed studies were conducted under LOE contracts to determine the necessary design parameters for the IIN DD 993 Class. These were forwarded to the USN, compiled, and incorporated into the ship design specification. Table 1 provides a comparison between the DDG-993 and the DD 963 requirements [1,2].

The higher seawater temperature resulted in all seawater heat exchangers being physically sized upward to keep the same heat transfer capability. This included the two lube oil and the air coolers for the ship service gas turbine generators (SSGTGs).

In a study of dust/sand conditions, it was determined that dust haze can reduce visibility to 2 miles (3.2 km) and dust/sand storms to less than 100 yards (91.4 m). These conditions are more extreme in the Persian Gulf than in the Gulf of Oman or Arabian Sea. Dust/sand conditions vary significantly over the year, with May to July being the most severe months. Table 2 provides a summary of the average number of days with dust/sand conditions at representative locations [3].

The DDG-993 Class utilizes the same basic propulsion and electric plants as the DD 963 Class, with four General Electric LM 2500, 21,500 horsepower main propulsion gas turbine (GTM) engines. Three 2000 kw ship service electrical generators are each driven by a Detroit Diesel Allison 501-K17

Contributed by the Gas Turbine Division of THE AMERICAN SOCIETY OF MECHANICAL ENGINEERS and presented at the International Gas Turbine Conference, Houston, Texas, March 8-12, 1980. Manuscript received at ASME Headquarters December 11, 1980. Paper No. 81-GT-74.

Copyright © 1982 by ASME

Downloaded 01 Jun 2010 to 171.66.16.62. Redistribution subject to ASME license or copyright; see http://www.asme.org/terms/Terms_Use.cfm

Fig. 1 KIDD DDG-993 at sea during builder's trial, August 19, 1980

Table 1 Environmental comparison

Parameter	DDG 993	DD 963	Notes
Machinery plant design			
Air temperature, minimum	0°F (−17.8°C)	−40°F (−40°C)	
Air temperature, maximum	120°F (48.9°C)	100°F (37.8°C)	1
Relative humidity	0-100%	0-100%	
Seawater temperature			
Minimum	28°F (−2.2°C)	28°F (−2.2°C)	2
Maximum	95°F (35°C)	85°F (29.4°C)	3

Notes:
(1) The DD 963 requires air temperature, maximum, of 100°F for full capability, with reduced capability but not availability from 100°F to 120°F.
(2) Seawater density is not specified as a design requirement. However, DD 963 class was designed for 1.0256 gm/cm^3; IIN/DD 993 was expected to be 1.0245 to 1.0300 gm/cm^3.
(3) The DD 963 requires sea temperature, maximum, of 85°F for full capacity, with reduced capability but not availability from 85° to 95° F.

gas turbine (GTG). The DD 963 Class propulsion and electrical plants have been previously described [4]. The basic GTG/GTM performance requirements remain the same as achieved for DD 963 [5].

Gas Turbine Combustion Air

The deleterious effects of contaminants on GT combustion air have been previously discussed in the literature [6]. Both salt from sea spray and dust can cause serious compressor blade erosion. Helicopters in Southeast Asia used an inertial separator to combat sand [7]. Protection against foreign object damage (FOD) is essential for successful GT operation.

A series of studies were conducted to determine which type separator would be most effective to combat the dust/sand conditions of Table 2. These conditions were simulated by tests using the parameters of Table 3. The parameters were used to judge the efficiency of the units and acceptability for GT operation.

Four types of filters were evaluated for use in the IIN DD 993. Table 4 shows the relative merits of viscous impingement (Navy standard), dry roll, and high-efficiency filters, and inertial separators [8]. Commercial units of each type are readily available for marine applications. Militarized versions could be readily adapted. High efficiency with low pressure drop in a restricted space required some type of inertial separator.

Selection of Cleaner Type. A series of tests were then performed. Figure 2 shows three types of inertial separators: vane, vortex, and ballistic. Testing was conducted to determine the optimum scavenge air flow for two of the three types. Figure 3 shows the efficiency of separation for the inertial vane and inertial vortex type separators. Both coarse and fine dust were tested. A pressure drop of 2 in. (5.1 cm) of water was allowed across the separator. It can be seen there is little improvement in efficiency when scavenge flow is increased above approximately 10 percent, regardless of the type dust or separator.

Downloaded 01 Jun 2010 to 171.66.16.62. Redistribution subject to ASME license or copyright; see http://www.asme.org/terms/Terms_Use.cfm

Table 2 Airborne contaminants

Region	Hour (Local)	Monthly Range (2)	Total Days (3)
	Mean Number of Days with Dust Haze, Per Year (1)		
Abadan	0600	0 – 4	22
	1200	2 – 12	74
	1500	1 – 13	74
Bandar-E-Bushehr	0600	0 – 3	10
	1200	0 – 3	11
	1500	0 – 3	13

Region	Monthly Range (2)	Total Days (3)
	Mean Number of Days with Sand Storms, Per Year (4)	
Bandar-E-Bushehr	0 – 3	13
Chah Bahar	0 – 1	7
Hangam – Jadid	0 – 2	14
Jask – E Kohneh	0 – 3	13

Notes:
(1) Visibilty < 7 miles (11.3 km) at hour indicated
(2) Monthly range is fewest and greatest days per month for condition indicated
(3) Data were recorded over 3-7 years for location/time
(4) Visibility ≤ 1,000 yards (914.4 m) and wind speed ≥ 13 miles per hour (20.9 km per hour)

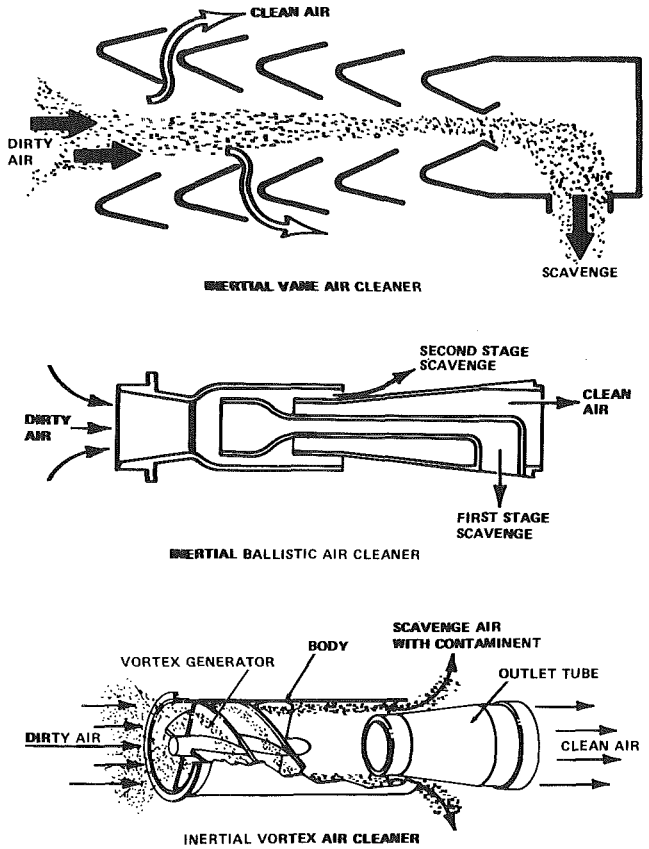

Fig. 2 Inertial cleaner types

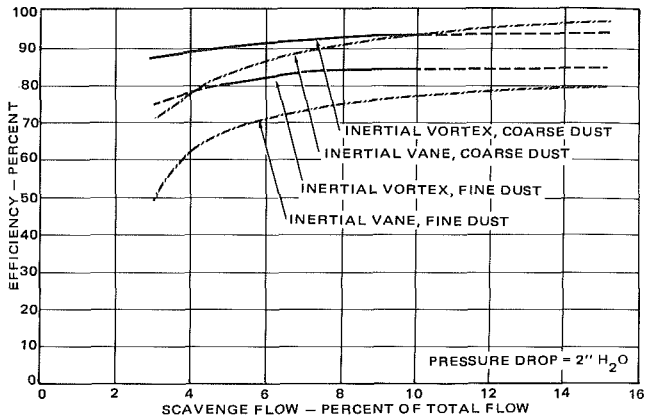

Fig. 3 Separation efficiency versus scavenge flow

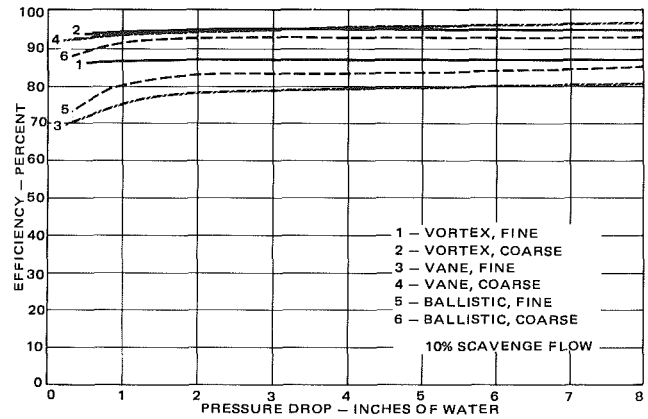

Fig. 4 Separation efficiency versus pressure drop

Figure 4 shows a comparison of all three types of inertial cleaners with coarse and fine dust. Separation efficiencies raised very little when the ΔP across the separator was raised above 2 in. (5.1 cm) of water, using 10 percent scavenge flow.

The inertial vortex type was selected because its efficiency was greater at smaller particle sizes, as shown by Fig. 5, thus reducing the total weight of contaminants per year passed by the separator. Table 5 shows the results of this testing for the vortex separator with 10 percent scavenge flow and a 2-in. water pressure drop. The contamination level shown is for the GTM. The GTM would experience a significantly reduced level of contamination, proportional to the reduced air flow requirement.

The selection of the inertial vortex separator was followed by selection of a scavenge air prime mover. Table 6 compares three types of prime movers. The vane axial fan was selected,

Downloaded 01 Jun 2010 to 171.66.16.62. Redistribution subject to ASME license or copyright; see http://www.asme.org/terms/Terms_Use.cfm

Table 3 Imposed conditions

Condition	Contaminant Level, mg/ft^3	Avg. Contam. Level, mg/ft^3	Particle Size, Microns	Frequency of Occurence	
				Days/yr	Hrs/day
Sand storm	0.1 – 4.0	2.0	5 – 15	5.8	11.0
Dust haze	0.005 – 0.1	0.05	1 – 3	122	14.0
Clean air	0.005	0.0005	0 – 1	All remaining time	

Table 4 Evaluation of filter types

Type	Advantages	Disadvantages
Viscous impingement, Navy standard filter	1. Effective for coarse dust 2. Small space to install 3. Low procurement cost 4. Low ΔP 5. Permanent type medium	1. Not effective for fine dust 2. Requires frequent removal for maintenance (clean/oil) 3. At 300-600 FPM, agglomerates of collected dust can reenter air stream
Dry roll type filter	1. Effective for coarse and fine dust 2. Low ΔP 3. Can operate automatically to replace medium 4. Higher efficiency than impingement type	1. Large space to install 2. Requires stowage area for spare rolls 3. Must operate at low air velocity (<500 FPM) 4. Complex to install and maintain
Inertial separators	1. Moderate space to install 2. Low maintenance, self-cleaning 3. Can operate at high air velocity	1. Not effective for fine dust 2. High ΔP 3. Requires large air intake opening 4. Requires added scavenge air fan
High efficiency filters	1. Remove 95% of dust	1. Requires large stowage area for spares 2. High ΔP 3. High life cycle cost 4. Low capacity 5. Requires prefilters

Table 5 Dust/sand passed by inertial separator

Particle Size Microns	Total Exposure Hours/Year	Average Efficiency Percent	Contamination to Engine Pounds (KG)/Year
<1	3000	20 (EST)	11.8 (5.35)
1 – 3	918	60	176 (79.8)
5 – 10	64	96	29.3(13.3)
10 – 15	64	99	4.9 (2.2)
>15	64	100 (EST)	0
			222 (100.7)

NOTES:
1. Assumes 3000 hours of operation per year at 20 knots with one GTM per shaft
2. Assumes 10% scavenge air flow with ΔP of 2″ H_2O

Table 6 Scavenge air prime movers

Type	Eductor Ratio	Primary Flow/ Speed	Power to Operate (Note 1)	Weight
GT bleed air eductor (Note 2)	70:1	1.42 lb/sec (0.644 kg/sec)	109 hp	143 lb (64.9 kg)
Blower eductor	12:1	4.5 lb/sec (2.04 kb/sec)	27 hp	900 lb (408 kg)
Vane-axial fan	NA	3450 rpm	20 hp	560 lb (254 kg)

NOTES:
1. Assumes 12 lb/sec (5.44 kg/sec) scavenge air flow against 5.0″ (12.7 cm) H_2O head at GTM cruise speed.
2. Bleed air poses the added problems of hot surfaces (450°F (232°C)) and reduced availability at high ambient air temperatures and/or high GT power output. Bleed air is also used for prairie/masker.

Downloaded 01 Jun 2010 to 171.66.16.62. Redistribution subject to ASME license or copyright; see http://www.asme.org/terms/Terms_Use.cfm

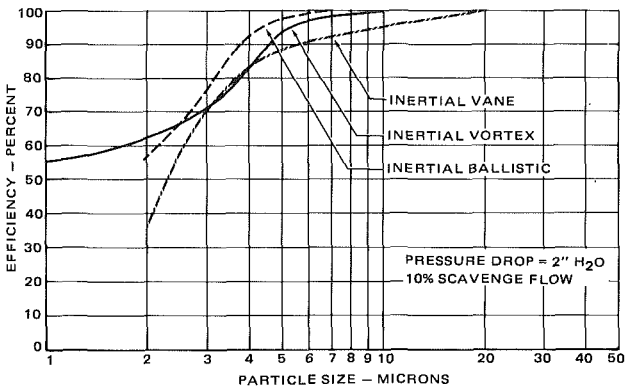

Fig. 5 Separation efficiency versus particle size

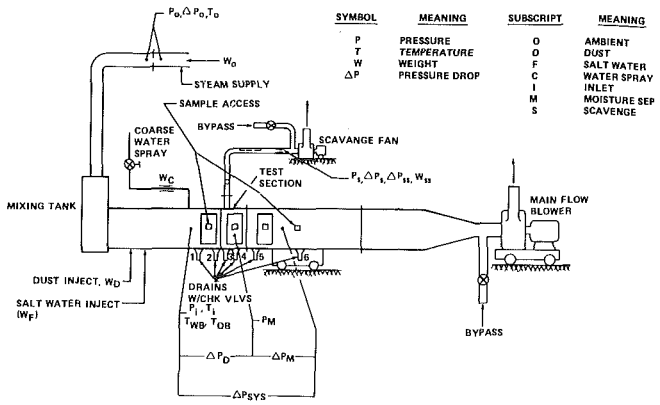

Fig. 6 Moisture/sand separator test setup

being more fuel effective than eductors and ligher than the blower eductor.

It was determined the two-stage, fixed filter moisture separator modules identical to those used in the DD 963 Class would remain the primary method of removing water (and salt) from the combustion air. The coalescers and collectors are made of modacrylic fiber matt. The acrylonitrile polymer fiber is an irregular-shaped cross-section, 24 denier in weight. It is blended with plastisized polyvinyl chloride (PVC) cold adhesive and a flame retardant. The fiber is stitched between PVC-coated mild steel wire screen. The coalescer is wave-shaped, while the collectors are chevrons. The moisture separator provides protection from dust particles of under 5 microns which pass through the vortex units. One of the primary concerns in this selection was commonality with the DD 963 Class, and the logistics support thus available.

The combination of dust/sand separators and moisture separators in series, with blow-in doors to bypass both in cases of emergency, is used for both the GTMs and GTGs.

Main Propulsion Gas Turbine Protection. The GTM has the following requirements.

1. Air flow of 25 lb/s (11.3 Kg) at idle
2. Air flow of 91 lb/s (41.3 Kg) at 20-Knot cruise
3. Air flow of 140 lb/s (63.5 Kg) at full power
4. Air flow for the module cooling fan is 20 lb/s (9.1 Kg)
5. Inlet air must not contain particles exceeding 0.2 grains (0.013 g) per 1000 cu/ft (28.32 m^2)
6. Particle size/density distribution must be such that not more than 5 percent by weight of solid particles are 10 microns or larger.

An inlet air ΔP of 2.5 in. (6.35 cm) H_2O will increase specific fuel consumption (SFC) 0.22 percent at cruise. This results in a ship range loss of 0.26 percent to 0.35 percent over the operating range of LM 2500. Therefore, the ΔP across the moisture/sand separator was held to a minimum to avoid serious impact on cruising radius.

Gas Turbine Generator Protection. The GTG has the following requirements (constant speed 13,820 rpm).

1. Air flow of 37.2 lb/s (16.9 Kg) at 0 deg F (– 17.8 deg C)
2. Air flow of 33.2 lb/s (15.1 Kg) at 60 deg F (15.6 deg C)
3. Air flow of 29 lb/s (13.2 Kg) at 120 deg F (48.9 deg C)
4. Air flow for the module cooling fan is 4.73 lb/s (2.1 Kg)
5. Inlet air/particle size the same as for GTMs.

The total ΔP on the GTG inlet and exhaust must not exceed 20 inches (50.8 cm) H_2O. This allows for GT bleed air to be extracted for the vital ship services.

GT Module Cooling. A module cooling vane-axial fan on the DD 963 Class operated on a thermostatic control whenever module temperature exceeded 180 deg F (82.2 deg C). The fan cools the gas turbine portion of the module. Air is educted from the module by the GT exhaust. When the fan is not operating, the air is drawn from the combustion air duct. The fan is rated at 12.5 horsepower, 5,000 CFM (141.6 m^3/min), with 10 in. (25.4 cm) H_2O pressure rise.

Bleed air from the GTGs is used to start other GTGs or the GTMs. Bleed air is also used to supplement GTM bleed air for Prairie/Masker. Therefore, it is necessary to maintain bleed air availability under both 2000 kW loads and 120°F (48.9°C) temperatures however, not simultaneously.

The added ΔP due to the moisture/sand separator and the higher ambient air temperature resulted in the decision to provide a constantly running module cooling fan of 25 horsepower, 4000 CFM (113.3 m^3/min), and pressure rise of 20 in. (50.8 cm) H_2O. A parallel fan was added with controls to insure one fan is always in operation for cooling when the associated GT is operating.

Moisture/Sand Separator Development

The proposed moisture/sand separator required tests to verify dust, sand, and salt removal performance over time. The tests were conducted by the Hamilton-Standard Division of United Technologies. A test stand was used to run one section of the inertial vortex separator and a moisture separator module wall. It was estimated each GTM would require 11 sections minimum, which was increased to two rows of six each; and each GTG would require four sections, which was designed as two rows of two each.

A single section of sand separator wall is 49 in. high, 28 in. wide, and 5 in. deep (124.5 cm × 71.1 cm × 12.7 cm) and contains 380 vortex tubes. Each tube has an outside diameter of 1.375 in. (3.5 cm) and is 5 in. (12.7 cm) long. A section of moisture separator wall for the GTM has a frame 54.33 in. high, 28.31 in. wide and 14.65 in. deep (138 cm × 71.9 cm × 37.2 cm). The GTG's frame is 42.21 in. high and 32.21 in. wide (107.21 cm × 81.8 cm). Each GTM section has 178.5 sq in. (1151.6 cm^2) greater cross-sectional area to the air flow than a GTG's. Both types of moisture separator frames contain two vertically mounted coalescer and collector assemblies.

Scale Model Test Stand. The scale model test setup and instrumentation are shown in Fig. 6. Air flow was simulated by the main flow blower drawing suction through the sand and moisture separator walls in the test section. Appropriate engine power levels were simulated by varying the amount of bypass air. Scavenge air flow rates were also tested with bypass air to the scavenge fan. Relative humidity was varied by injecting steam into the air supply.

Coarse water was injected by hydraulic spray nozzles to test moisture separation. Salt water was injected at a measured

Downloaded 01 Jun 2010 to 171.66.16.62. Redistribution subject to ASME license or copyright; see http://www.asme.org/terms/Terms_Use.cfm

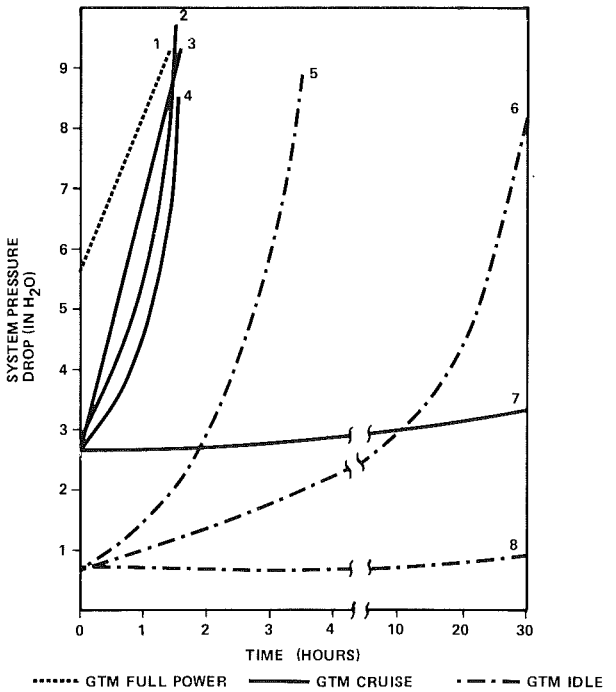

CURVE NO.	ENGINE INLET AIR FLOW LB/MIN (KG/MIN)	SCAVENGE AIR FLOW LB/MIN (KG/MIN)	INLET DUST CONCENTRATION MG/FT^3 (MG/M^3)	INLET MOISTURE CONCENTRATION PPM
1	800 (363)	60 (27.2)	2.25 (79.5)	0.5
2	555 (252)	75 (34.0)	3.4 (120.1)	5.0
3	555 (252)	75 (34.0)	3.4 (120.1)	0.5
4	555 (252)	75 (34.0)	3.3 (116.5)	...
5	225 (102)	85 (38.6)	2.47 (87.2)	0.5
6	225 (102)	–	1.96 (69.2)	...
7	555 (252)	–	0.05 (1.8)	...
8	225 (102)	–	0.05 (1.8)	...

Fig. 7 System pressure drop versus time

concentration. A Cassela Cascade Impactor was used downstream of the moisture separator to determine the effectiveness of moisture separation.

Standard fine Arizona road dust was injected by a Vibrascrew at a measured rate. Matched pairs of Millipore filters were used to filter samples drawn both up and downstream of the sand separator and downstream of the moisture separator. A Gravimetric analysis was used to determine the weight of dust drawn through the filters over a measured peirod of time.

Separate tests were conducted for moisture and sand. Then tests were conducted on the combined elements, up to heavy dust and coarse spray conditions.

GTM sand and moisture separator sections were used to conduct the test, with data extrapolated for both the full scale GTM unit at varying engine rates and the full scale GTG units.

Test Results. Table 7 shows results of the test, as extrapolated. It was concluded from the efficiencies realized by the test that the design was adequate to protect GT combustion air for an indefinite period of time in the Persian Gulf environment.

The test results of Fig. 7 show the growth in system ΔP over time for varying GT air flows. The curves show various combinations of dust/sand and moisture loading. The blow-in doors open at 8.5 in. (21.6 cm) H_2O. Therefore, it is desirable to take corrective action whenever ΔP reaches 8.0 in. (20.3 cm) H_2O.

These results show the moisture/sand separators will

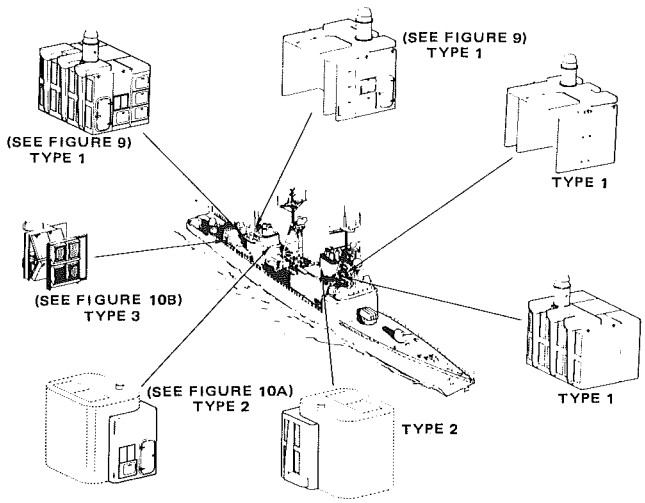

Fig. 8 GT inlet moisture/sand separators

operate efficiently for a reasonable operating period prior to reaching 8.0 in. H_2O ΔP. When this limit has been reached, two courses of action are possible, light off another GT to replace the unit in operation or, for the GTM, lower power output while cleaning the moisture separator. Remote alarms indicate 8 inches ΔP on the GTM, 7 in. on the GTG.

Fixed nozzles are installed to spray directly on the moisture separator coalescer pads. A water wash flow of 0.25 gpm (0.95 liters) through each nozzle (2 nozzles per moisture separator section), washing with the GT secured (the prescribed method) produces the following results. With the GTM combustion air flow rate at 111 lb/s (50.3 Kg) before and after wash, ΔP's are as shown.

System ΔP (in. H_2O)

Wash Time	Before Wash	After 1st Wash	After 2nd Wash	Clean
10 minutes	7.0	3.65	3.55	2.64
30 minutes	10.0+	3.21	---	2.45

If the water wash is conducted with a GTM at idle drawing air through the coalescer pads, the system ΔP can be restored to a near-clean condition.

From these data, it can be seen that the GTMs could be rotated at full power and maintain two engines on the line at all times in the most severe conditions.

Production Hardware

The test results proved the design performance of the Type I (GTM), Type II (engine room GTG), and Type III (aft GTG) units. Production proceeded with seven units per ship as shown by Fig. 8. Figure 9 shows a typical pair of GTM units, and Fig. 10 shows the two types of GTG units.

All three types of units were heavyweight (barge), shock-tested in accordance with MIL-S-901C using a minimum 50 Hz resonant frequency deck simulator. The Types II and III units were vibration tested (4-15 Hz) in accordance with MIL-STD-167B. The vibration test was exempted for the Type I unit, which could not be tested due to its size, weight, and location of center of gravity. Both categories of testing were successful with only minor anomalies noted. The Types I and II units are essentially ship structure. Therefore, nuclear air blast resistance was included in the aluminum bulkhead and overhead using standard design methods [9].

The entire assembly for each type unit was built by the subcontractor, Hamilton-Standard. They were transported to Ingalls in as few pieces as possible. The Type I units were landed on the 04 level just prior to ship launch; the Type II

Downloaded 01 Jun 2010 to 171.66.16.62. Redistribution subject to ASME license or copyright; see http://www.asme.org/terms/Terms_Use.cfm

Table 7 Moisture/sand separator model tests

Flow PPS	Scavenge PPS (%)	Dust Concentration MG Per Ft^3 Inlet	Dust Concentration MG Per Ft^3 Outlet	Dust Removal Efficiency	Salt at Inlet PPM	Salt Efficiency Particle Size 1.7-5μ	Salt Efficiency Particle Size 5μ
45	8.4 (16)	1.16	0.057	95.0%	0.44	84.65%	92.67%
45	8.4 (16)	5.5	0.146	97.3%	13.7	80.55%	99.72%
111	12 (10)	4.5	0.096	97.8%	12.7	97.43%	99.90%
160	12 (7)	1.126	0.070	94.3%	11.6	99.48%	99.93%

NOTES:
1. Data are reduced to a standard 80°F (26.7°C), 29.92″ hg (76 cm hg) abs., and 50% relative humidity
2. 45 pounds per second (PPS) simulates GTG at 0°F ambient air or GTM at idle
   111 PPS simulates GTM at cruise
   160 PPS simulates GTM at full power
3. Data for sand and moisture separation efficiencies shown here were collected on separate runs. Simultaneous loading with sand and moisture confirmed these data are representative of the combined conditions.

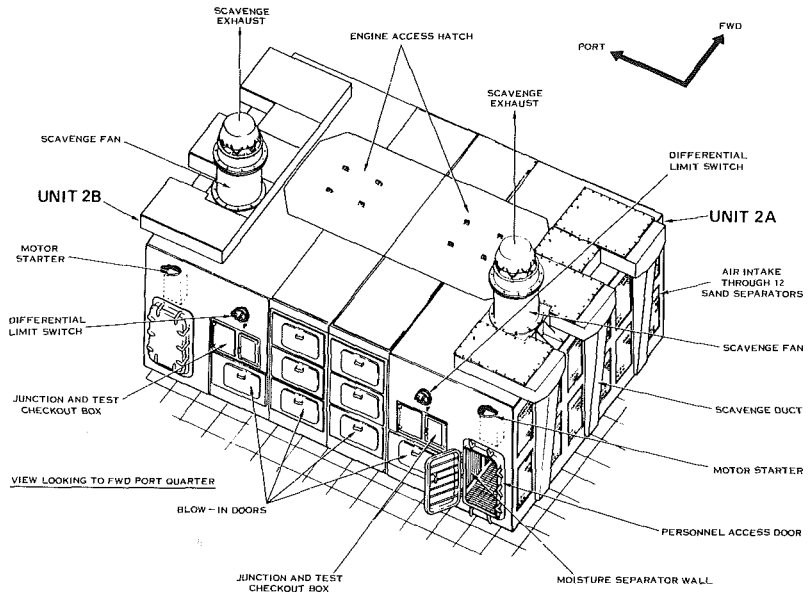

Fig. 9 GTM moisture/sand separators

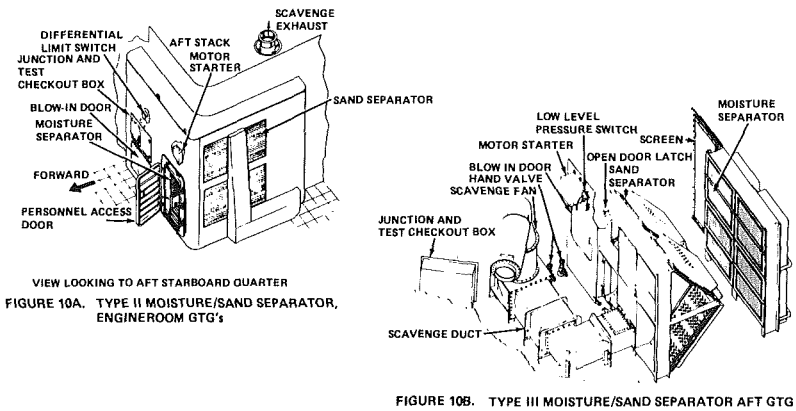

Fig. 10 GTG moisture/sand separator

units erected with the stacks late in integration; and the Type III units assembled in the main deck compartment early in the erection sequence.

The need for added protection against icing became evident when the ships were changed from the IIN to the USN. A design was developed to allow removal of the vortex separator panels. Electrically heated louvers similar to those of the DD 963 Class were installed immediately upstream of the moisture separator module. This provides protection for the GTM inlets in freezing conditions.

Downloaded 01 Jun 2010 to 171.66.16.62. Redistribution subject to ASME license or copyright; see http://www.asme.org/terms/Terms_Use.cfm

The DDG 993 builders trials were first held on August 25, 1980. The change from IIN to USN required several revisions to the basic design [10]. These were incorporated and the ship was delivered on May 4, 1981. The fourth and final ship of the class was delivered on January 18, 1982, with commissioning, March 13, 1982.

These ships have not yet deployed. Both DDG 993 and DDG 994 have reentered the shipyard for planned post-shakedown availabilities. They will deploy upon completion of these industrial periods. GT operating experience with the moisture/sand separator is therefore limited. These trials will not produce the specific atmospheric conditions the new units are designed to protect against. The real value will not be demonstrated until the ship is deployed to such a hostile weather location.

Summary and Conclusions

Close examination of the DD 963 Class design for the ability to withstand the adverse heat, dust, and sand conditions to be expected in the Persian Gulf revealed the need to upgrade several systems. The GT combustion air intake design, as employed on USN ships, is highly vulnerable to ingestion of dust which will ultimately foul the various components of the system.

The GT engine is particularly susceptible to FOD. Operation of ships with GT propulsion or generators in sand/dust environments significantly shortens compressor life. The adequate protection of GTs is readily available within the state of the art as demonstrated in the DDG-993 Class design.

The following conclusions may be drawn from the development of the DDG-993 Class.

(*a*) The present USN ship design requirements are not adequate for sustained operations in the Mid-East.

(*b*) Adequate protection is feasible if the need is identified at the beginning of the ship design effort.

(*c*) The vital interests of the United States, which will apparently continue over the foreseeable future, indicate the need for a capability to project a viable Naval presence in the Indian Ocean, Persian Gulf, and Red Sea areas. Providing this capability requires an upgrading of ship design requirements to compensate for the atmospheric conditions to be expected in these areas.

References

1 The "Specifications for Building Imperial Iranian Destroyer DD 993 Class" NAVSEA 0902-00-030-2010, superseded by NAVSEA 0902-00-030-2030, Sections 070d and 200c define the requirements for the machinery environment.

2 The "System Specifications for DD 963 Class Ship (U)" SY9310000, pp 36b-37 and 107/108 define the requirements for the machinery plant operational environment.

3 Anonymous, *IIN DD 993 Iranian Environmental Baseline Study,* CDRL A00C, Contract N00024-75-C-7044, Task No. 6-6140, Pascagoula, MS; Ingalls Shipbuilding, Feb. 7, 1975, pp. 8-9.

4 Rains, Dean A., "DD 963 Power Plant," *Marine Technology,* Vol. 12, No. 1, Jan. 1975.

5 Rains, Dr. Dean A.; Beyer, CAPT Kenneth M., USN (Ret); Keene, W. P.; Lindgren, J. R., Jr.; Mogil, E.; Page, T. E.; Untershine, J.; and Youngworth, J. F., "Design Appraisal - DD-963," *Naval Engineers Journal,* Vol. 88, No. 5, Oct. 1976, pp. 45-46, 48-50.

6 Hill, D. G. T., "Gas Turbine Intake Systems in Unusual Environments," ASME Publications 73-GT-38, Gas Turbine Conference & Products Show, Washington, D.C., Apr. 8-12, 1973.

7 Stephenson, C. D., "CH-54A Engine Air Particle Separator - 3 1/2 Years of Successful Operation," ASME Publication 70-GT-97, Gas Turbine Conference & Products Show, Brussels, Belgium, May 24-28, 1970.

8 Development work was performed by Ingalls Shipbuilding under U.S. Navy contract N00024-75-C-7044, and by the Hamilton-Standard Division of United Technologies under subcontract to Ingalls.

9 Dye, L. C., and Lankford, B. W., Jr., "A Simplified Method of Designing Ship Structure for Air Blast," *Naval Engineers Journal,* Vol. 78, No. 4, Aug. 1966.

10 Caskey, Maurice R., "DDG 993 and DD 997, Today's Variants of the Versatile DD 963 Class," presented to American Society of Naval Engineers, Pascagoula Section, June 19, 1980.

Downloaded 01 Jun 2010 to 171.66.16.62. Redistribution subject to ASME license or copyright; see http://www.asme.org/terms/Terms_Use.cfm

Heat-Transfer Coefficients for Staggered Arrays of Short Pin Fins

G. J. VanFossen
National Aeronautics and Space Administration,
Lewis Research Center,
Cleveland, Ohio

Short pin fins are often used to increase the heat transfer to the coolant in the trailing edge of a turbine blade. Due primarily to limits of casting technology, it is not possible to manufacture pins of optimum length for heat-transfer purposes in the trailing edge region. In many cases the pins are so short that they actually decrease the total heat-transfer surface area compared to a plain wall. A heat-transfer data base for these short pins is not available in the literature. Heat-transfer coefficients on pin and endwall surfaces were measured for several staggered arrays of short pin fins. The measured Nusselt numbers when plotted versus Reynolds numbers were found to fall on a single curve for all surfaces tested. The heat-transfer coefficients for the short pin fins (length to diameter ratios of 1/2 and 2) were found to be about a factor of two lower than data from the literature for longer pin arrays (length to diameter ratios of about 8).

Introduction

In designing the cooling configuration for a turbine blade, many heat transfer augmentation schemes are available; film cooling, internal impingement, boundary layer trip strips, and various types of fins are a few of the popular ones. In the trailing edge region, however, aerodynamic considerations demand a small wedge angle for the blade profile. As a result the internal passages become so narrow that the choice of cooling scheme is limited. Pin fins are one augmentation device that can be used to increase heat transfer in this region. Pin fins at the trailing edge also serve a structural purpose by holding the suction and pressure surfaces of the blade together. The pin fins of interest here are circular cylinders that span the distance between the suction and pressure surfaces which form the endwalls of the cooling passage. Heat from the hot gas stream passes through the endwalls and is conducted along the pins and convected to the cooling air. Heat is also convected to the cooling air from the endwalls between the pins.

Due mainly to limits in casting technology, pin fins cannot be reliably made much smaller than about 1 mm (0.04 in.) in diameter. This means that in the narrow trailing edge of most turbine blades the pins may be relatively "short" (less than about four diameters in length). In some cases, the addition of pins to the cooling passage may actually cover up more wall surface area than they add in pin surface area; thus, the terms fin or extended surface do not really apply in the literal sense. One of the main functions of the pins in the turbine cooling application is to increase the level of turbulence in the cooling flow rather than add heat transfer surface area.

There are no data for short pin fins of the type used in turbine blade cooling available in the literature. Data for both in-line and staggered arrays of pin fins are given in references [1] to [5]. The data in these references were taken by people interested in high-efficiency, compact heat exchangers. To keep heat-transfer effectiveness high, the configurations they tested all contained relatively long pins; the shortest were four diameters in length. These pins are long compared to those used in many cooled turbine blades. In references [4] and [5], both staggered and in-line arrays of pin fins were investigated but the pins did not extend entirely across the passage.

Heat exchangers usually contain many rows of pins in the streamwise direction. The flow and heat transfer are said to be "fully developed" for more than about eight rows of pins; that is, the heat transfer coefficient changes rapidly in the first few rows and then remains relatively constant in the downstream direction. Thus the average heat-transfer coefficient for the case of only a few rows will be different than that for "fully developed" flow. Due to the limited space available, the turbine blade cooling application does not allow a large number of rows to be used, and again one can see that another type of data is required by the turbine blade designer.

Another possible source of heat-transfer data is the extensive literature on heat transfer to tube banks. Examples of these are found in references [1, 6] and [7]. Tube banks resemble long pin fins. There are two major differences, however, between the pin fins of interest here and tube banks. One difference is that no endwalls are present for tube banks; a large portion of the heat transfer is known to be through the endwalls for the turbine cooling application. The other difference is in the boundary conditions. For the turbine application or for compact heat exchanger application, heat is conducted along the pin and is convected from both endwall and pin surfaces; this results in a significant temperature gradient along the pin. Tube banks usually have fluid flowing in the tubes; heat is conducted through the tube wall and is

Contributed by the Gas Turbine Division of THE AMERICAN SOCIETY OF MECHANICAL ENGINEERS and presented at the Gas Turbine Conference and Products Show, March 9-12, 1981, Houston, Texas. Manuscript received at ASME Headquarters December 11, 1980. Paper No. 81-GT-75.

Copyright © 1982 by ASME

Downloaded 01 Jun 2010 to 171.66.16.62. Redistribution subject to ASME license or copyright; see http://www.asme.org/terms/Terms_Use.cfm

then convected from the tube surface. The tube walls are thus nearly isothermal in the direction of the tube axis. The application of tube bank data to turbine blade cooling is therefore questionable.

The objective of this study was to obtain heat transfer data for staggered arrays of short pin fins in order to determine if data available in the literature can be applied to turbine blade cooling. Heat transfer coefficients on both the pins and the endwalls were obtained for four pin fin surfaces. Two different model geometries were used in the present study. The larger model had 0.635-cm (0.25-in.) dia pins which were spaced four diameters apart in an equilateral triangular array. The pins for this model were two diameters long. Three variations of this model were tested; one had copper pins that were perpendicular to the endwalls, another had wooden pins that were perpendicular to the endwalls and the third had copper pins that were inclined to the endwalls. The smaller test section had copper pins that were 0.3175 cm (0.125 in.) in diameter and spaced two diameters apart; the pin height of the smaller model was 0.5 dia. All pin fin configurations tested had four rows of pins in the flow direction. Two plain channel (no pin fins) configurations were also tested to check the accuracy of the data by comparing the heat transfer results with an accepted correlation for flow in a duct. Reynolds numbers ranged from 300 to nearly 60,000 which is sufficient to cover the range of interest for the turbine cooling application. Heat-transfer data are presented as Nusselt number versus Reynolds number. The wooden pins were used to determine the ratio of heat convected from the pins to heat convected from the endwalls. The inclined pins were tested to determine if they would increase the heat-transfer rate over that of perpendicular pins. The pin fin heat-transfer data from the present study were compared to data for longer pins and an existing correlation that contains terms to account for the range of pin lengths and pin spacings of interest in turbine cooling.

Apparatus

A layout of the rig used in the pin fin experiments is shown in Fig. 1. Room air enters the test section through a constant acceleration inlet, passes through one of two turbine flow meters, through the flow control valves and exits to the building altitude exhaust system. Temperatures were measured with Chromel-Alumel thermocouples referenced to a 339 K (150° F) oven. Pressures were measured with a microprocessor-controlled pressure scanning system similar to the one described in reference [8]. Volumetric flow rates were measured with turbine-type flow meters; mass flows were calculated by multiplying volumetric flow rates by the density of the air at the exit of the turbine meter. Density was calculated from the perfect gas law for air using the measured temperature and pressure at the turbine meter exit. All data were converted to engineering units and recorded with the laboratory data acquisition system [9].

Figure 2 shows the test section assembly used for the large plain channel and large pin fin models. The inlet bellmouth was covered with 150 grit silicon carbide sandpaper and had a 0.519-cm (0.0625-in.) dia trip wire to insure turbulent flow in the test section. Immediately downstream of the inlet there were three thermocouples to read the inlet air total temperature. Three thermocouples measured the outlet total temperature. During the tests, the whole assembly was wrapped with a thick blanket of fiberglass insulation to minimize heat loss.

Test Specimens

Figure 3 shows the geometry for the perpendicular pin fin test sections. The dimensions and pin spacings are given in Table 1. Figure 4 shows the construction of the flow channel for the large pin fin model. The endwalls that formed the top and bottom of the flow channel were constructed of 0.635- cm (0.25-in.) copper plate. The pins were inserted into holes drilled in each plate and soft soldered in place. The solder formed very small fillets between the plate and pins. Pins cast into a turbine blade will probably have much larger fillets. No attempt was made to simulate these larger fillets. The sides of the flow channel were machined from a cloth-reinforced phenolic plastic. The sides were held in place by bolts which extended through the copper plates and phenolic material. The assembly was sealed from air leakage with a silicone rubber sealant.

Nomenclature

$\bar{A}$ = average flow area in test section, V/L
A_p = cross sectional area of a pin, $\pi D_0^2/4$
A_w = endwall area defined by equation (11)
D' = characteristic length of test section
D_0 = pin diameter
H = height of plain channel
$\bar{h}$ = average heat transfer coefficient in pin fin test section
h_{eff} = effective heat transfer coefficient as defined by equation (6)
$\bar{h}_p$ = average heat transfer coefficient on pin surface
$\bar{h}_w$ = average heat transfer coefficient on endwall surface
k_a = thermal conductivity of air evaluated at T_r
k_p = thermal conductivity of pin material
L = length of heated portion of test section in flow direction
ℓ = pin half length used in equation (9)
m = fin parameter defined by equation (13)
N_L = number of pin rows in flow direction
N_T = number of pins in a row transverse to flow direction
Nu = Nusselt number, $\bar{h}D'/k_a$
P = pin perimeter, πD_0
Pr = Prandtl number of air
Q = heat dissipated in electric heater
Q_{loss} = heat lost to surroundings from test section
r = recovery factor
Re = Reynolds number, $(\dot{w}/\bar{A})D'/\mu$
S = total heat transfer surface area
S_h = surface area of heaters
T_a = ambient air temperature
T_{aw} = adiabatic wall temperature
T_r = reference temperature defined by equation (5)
T_s = air static temperature
T_w = endwall temperature
U = overall heat transfer coefficient for heat loss from test section to surroundings
V = open volume in test section
W = width of plain channel
$\dot{w}$ = mass flow rate
X = ratio of heat transfer coefficient on pin surface to that on the endwall, $\bar{h}_p/\bar{h}_w$
x_s = ratio of pin height to pin diameter
x_T = ratio of pin spacing to pin diameter
θ = pin angle of inclination measured from normal to endwall
μ = viscosity of air

Downloaded 01 Jun 2010 to 171.66.16.62. Redistribution subject to ASME license or copyright; see http://www.asme.org/terms/Terms_Use.cfm

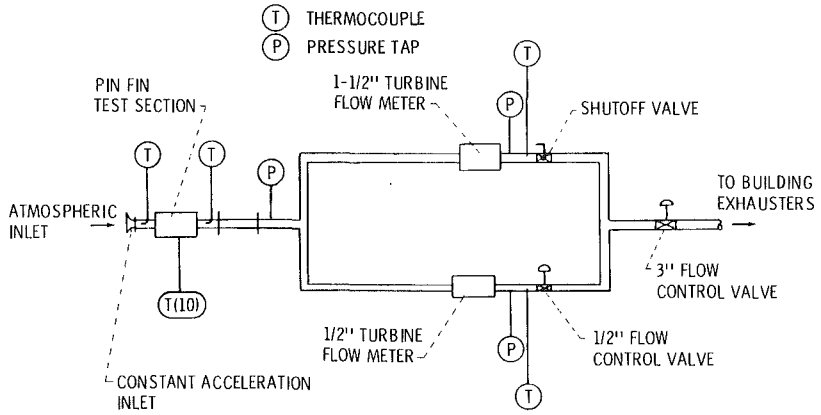

Fig. 1 Schematic of pin fin heat transfer rig

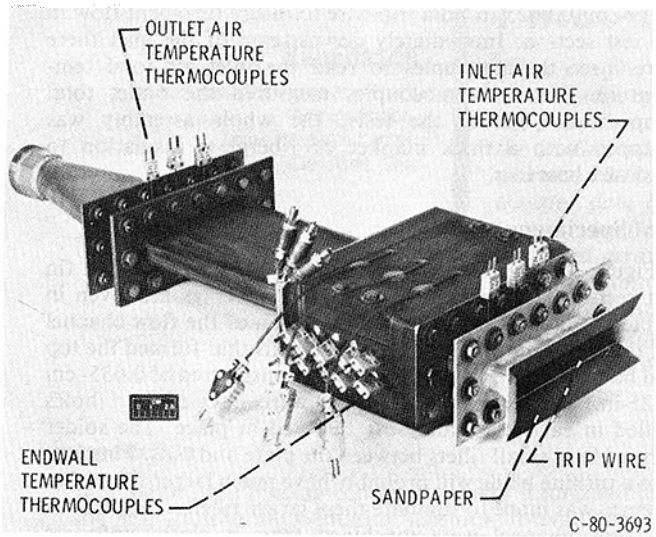

Fig. 2 Pin fin test section assembly

Table 1 Pin fin nominal geometries

Plotting system	D_0, cm	X_T	X_S	N_T	N_L	θ, deg	Pin material
P	0.635	4	2	5	4	0	Copper
W	0.635	4	2	5	4	0	Wood
R	0.635	4	2	5	4	30	Copper
S	0.3175	2	0.5	5	4	0	Copper

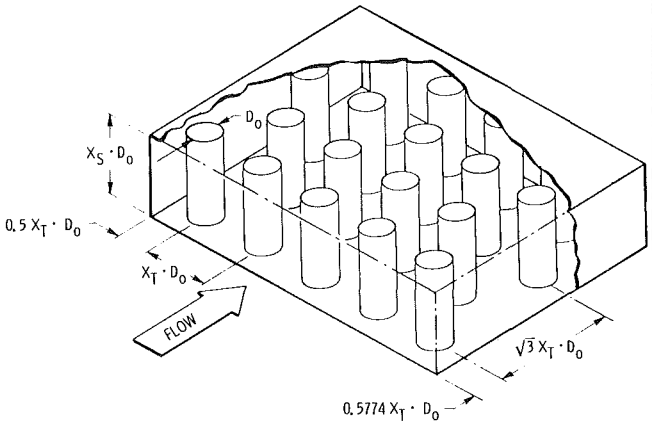

Fig. 3 Perpendicular pin fin channel geometry

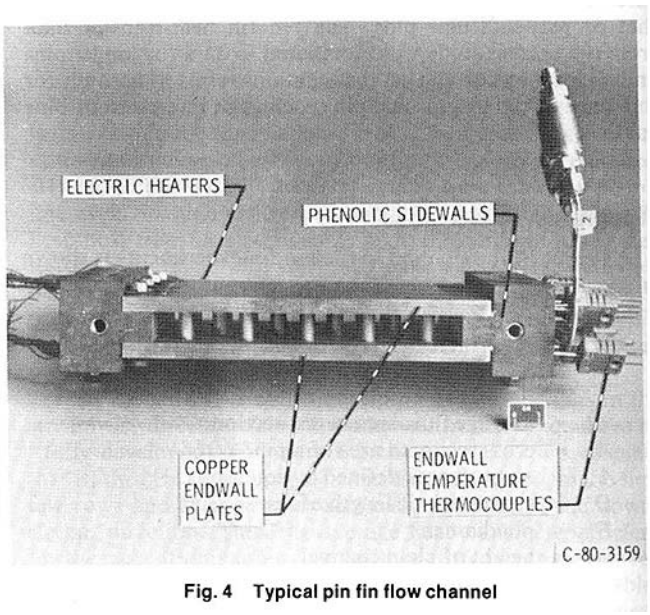

Fig. 4 Typical pin fin flow channel

Thermocouples to measure the endwall temperature were inserted into holes drilled in the edge of each plate. The thermocouples can be seen at the right of Fig. 4. Five thermocouples were used in each plate. Commercially available metal foil electric heaters encased in a polymide base film were attached to the endwalls with a pressure sensitive adhesive. The heater leads can be seen at the left side of Fig. 4.

The test section with wooden pins was made with 0.635-cm (0.25-in.) copper plates as endwalls with birch dowels epoxied between the endwalls to form the pins. The endwalls were not drilled to accommodate the wooden pins. A slightly larger fillet was formed between the pins and the endwalls by the epoxy than was formed by the solder used on the copper pins.

The inclined pin fin test section was constructed in a fashion similar to that of the other models with copper pins but the pins were inclined to the endwalls. The angle of inclination was arbitrarily selected as 30 deg from a normal to the surface of the endwalls. This angle is measured in a plane perpendicular to the flow direction and alternates between positive and negative with successive rows in the streamwise direction. Figure 5 is a photograph of the inclined pin test section. The pins were set in a staggered array at the endwalls (not an equilateral triangular array) but because successive rows cross at mid-span they give the appearance of an in-line array when viewed in the streamwise direction.

Downloaded 01 Jun 2010 to 171.66.16.62. Redistribution subject to ASME license or copyright; see http://www.asme.org/terms/Terms_Use.cfm

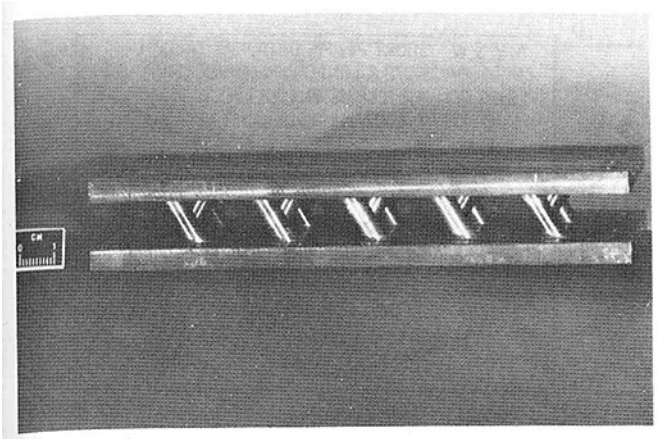

Fig. 5 Inclined pin fin flow channel

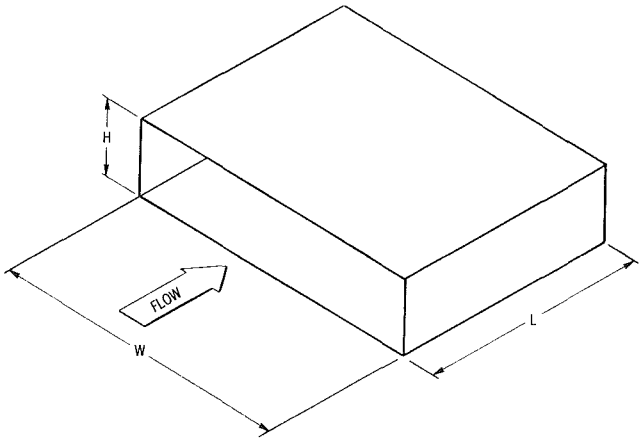

Fig. 6 Plain channel geometry

The small pin fin test section was constructed in a fashion similar to the large test section with the exception of the pin spacing and pin lengths. Dimensions for this test section are also given in Table 1. Only one thermocouple was installed in each top and bottom endwall plates due to size limitation.

In both the large and small pin fin test sections there were four rows of pins in the streamwise direction. In both models the number of pins in each of the four rows alternated between four and five. The first row contained five, the second four, and so on.

Figure 6 shows the geometry of the plain channel test specimens. Two different size plain channels (corresponding to the two sizes of pin fin test sections) were tested. The dimensions of the plain channels are given in Table 2. Construction was the same as the pin fin models but the pins were left out.

Test Procedure

Heat Loss Calibration. Before any heat-transfer data could be analyzed, the heat loss to the surroundings had to be measured. To accomplish this, a series of calibration runs were made with no airflow through the test section. The flow channel was sealed off to minimize natural convection during these tests. Heater power was set at a level that would produce approximately the plate temperature of interest. The rig was then allowed to come to equilibrium which usually took 12 to 14 hr. When a steady plate temperature was reached, power level, plate temperature and ambient air temperature were measured so that an overall loss heat-transfer coefficient could be calculated.

Table 2 Plain channel

NOMINAL GEOMETRIES

Plotting symbol	L, cm	W, cm	H, cm
L	9.576	12.70	1.270
M	2.469	3.175	0.1588

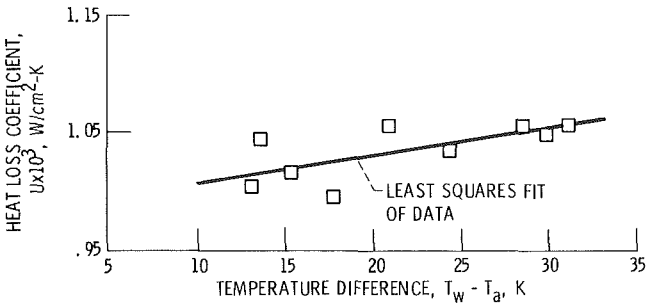

Fig. 7 Typical heat loss calibration curve

Data Runs. Before a data run was made, the electric heaters were used to bring the endwall plate temperature up to the desired value with no airflow through the test section. Plate temperatures were set at an average 21 K (38° F) above ambient air temperature. This value was high enough to allow good accuracy in the measured temperature difference between plate and air and low enough to minimize thermal property variations in the test section. Once the insulation reached approximate equilibrium, the air flow was set to the desired value. Heater power was then adjusted to maintain the plate temperature. When it was certain that equilibrium was attained, five samples of all the data channels were recorded for processing.

Data Analysis

This section describes how the heat-transfer and flow data were reduced to dimensionless form.

Heat Loss. The overall loss heat-transfer coefficient U is defined as

$$U = \frac{Q_{\text{loss}}}{S_h (T_w - T_a)} \tag{1}$$

This overall loss coefficient was calculated for a range of endwall plate to air temperature differences. A typical plot of the loss coefficient versus endwall plate-to-air temperature difference is shown in Fig. 7. The loss coefficient is a weak function of temperature difference. Once the plate and air temperature are known, Fig. 7 and equation (1) can be used to calculate the heat loss from the test section for the purpose of data analysis.

Reynolds Number. The Reynolds number for all test sections was calculated from the following equation:

$$\text{Re} = \frac{(\dot{w}/\tilde{A})D'}{\mu} \tag{2}$$

The characteristic length D' was defined as

$$D' = \frac{4V}{S} \tag{3}$$

Note that for the plain channel this reduces to the classical definition of hydraulic diameter for a closed channel. The average flow area is defined by

Downloaded 01 Jun 2010 to 171.66.16.62. Redistribution subject to ASME license or copyright; see http://www.asme.org/terms/Terms_Use.cfm

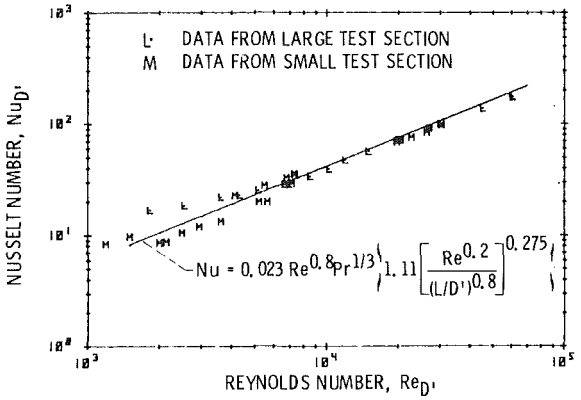

Fig. 8 Plain channel data compared to modified duct flow correlation

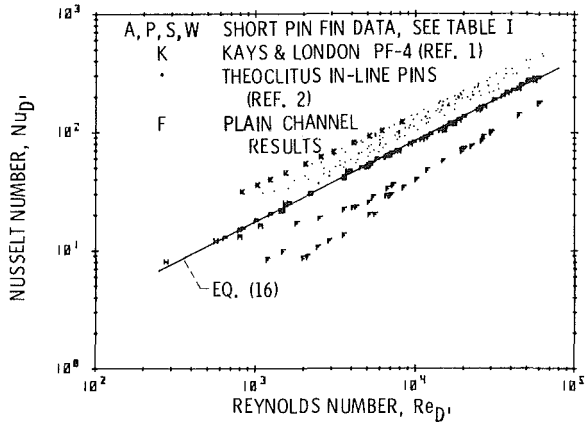

Fig. 9 Comparison of short pin fin data with long pin data and plain channel data

$$\bar{A} = \frac{V}{L} \tag{4}$$

The viscosity was evaluated at the Eckert reference temperature [10]

$$T_r = 0.5\,T_w + 0.28\,T_s + 0.22\,T_{aw} \tag{5}$$

Heat-Transfer Coefficients. The effective heat-transfer coefficient for all test sections was calculated from

$$h_{\text{eff}} = \frac{Q - Q_{\text{loss}}}{S_h(T_w - T_{aw})} \tag{6}$$

The adiabatic wall temperatures used in equations (5) and (6) were calculated from the following equation:

$$T_{aw} = T_s + r(T_t - T_s) \tag{7}$$

where r is the recovery factor. The total and static temperatures, T_t and T_s, respectively, were determined by solving the one-dimensional momentum and energy equations for the pressures and temperatures in the channel. From tests conducted with no heat flow at high test section Mach numbers it was determined that the best value of recovery factor was

$$r = \sqrt{\text{Pr}} \tag{8}$$

The cross-sectional area used for the pin fin portion of the flow model was the minimum free flow area. This value gave the best adiabatic wall temperature and pressure drop results.

Equation (6) gives the heat-transfer coefficient which includes the effects of pin efficiency. To find the average heat-transfer coefficients on the pin and endwall surface, the heat lost by a plain surface with a heat-transfer coefficient of h_{eff} was equated to the heat lost by the pin finned surface. The resulting transcendental equation is then

$$h_w\left(1 - \frac{A_p}{A_w \cos\theta}\right) + \frac{\sqrt{PX\bar{h}_w k_p A_p}}{A_w}\tanh\left(\frac{m\ell}{\cos\theta}\right) - h_{\text{eff}} = 0 \tag{9}$$

For each h_{eff} measured, equation (9) was solved for the root h_w by the Newton-Raphson iteration technique. In equation (9), A_p is the cross-sectional area of a pin defined by

$$A_p = \frac{\pi}{4} D_0^2 \tag{10}$$

A_w is the area of the endwall associated with one half pin

$$A_w = \frac{\sqrt{3}}{2}(x_T D_0)^2 \tag{11}$$

P is the perimeter of the pin

$$P = \pi D_0 \tag{12}$$

The fin parameter m is given by

$$m = \sqrt{\frac{X\bar{h}_w P}{k_p A_p}} \tag{13}$$

where X is the ratio of heat-transfer coefficient on the pin surface to that on the endwall surface.

Nusselt Number. The Nusselt number was calculated from the average heat-transfer coefficient as

$$\text{Nu} = \frac{\bar{h}D'}{k_a} \tag{14}$$

where $\bar{h}$ is the heat-transfer coefficient on the pin and endwall surfaces ($X = 1.0$ in equation (9)). The thermal conductivity of air was evaluated at the reference temperature defined by equation (5).

Thermal Properties. The viscosity and thermal conductivity of air were determined from curve fits of data given in reference [11]. The thermal conductivity of the copper used was 3.46 W/cm•K (200 Btu/hr•ft•°F). The thermal conductivity used for the wooden pins was 0.0035 W/cm•K (0.2 Btu/hr•ft•°F).

Results and Discussion

Figure 8 is a comparison of both the large and small plain channel heat-transfer results with a correlation for turbulent heat transfer in a duct. The correlation has been modified for entrance length effects. The correlation is from reference [12] and the entrance length correction was taken from reference [13]. The modified correlation used was

$$\text{Nu} = 0.023\,\text{Re}^{0.8}\text{Pr}^{1/3}\left\{1.11\left[\frac{\text{Re}^{0.2}}{(L/D')^{0.8}}\right]^{0.275}\right\} \tag{15}$$

For Reynolds numbers above 6000, the agreement between the modified correlation and the experimental data is very good. This good agreement gave confidence that the measurement technique and the data analysis were working well. Below Reynolds numbers of 6000, the agreement is not good. Data for the large and small models are not consistent. This disagreement is thought to be due to differences in the inlets of the two models. The large model had sandpaper and a trip wire at the inlet while the small model did not. In any case, only data in the turbulent range is of interest here because, with pin fins in place, the flow in the test section cannot be laminar and, therefore, inlet treatment is not thought to be important.

It should be noted that two levels of maximum Mach number were obtained in the tests. In the large models (both plain channel and pin fin) the highest Mach number reached was about 0.3, while in the small models the flow was choked at the highest Reynolds number. From Fig. 8 the agreement at high Reynolds numbers for both models indicates that Mach

Downloaded 01 Jun 2010 to 171.66.16.62. Redistribution subject to ASME license or copyright; see http://www.asme.org/terms/Terms_Use.cfm

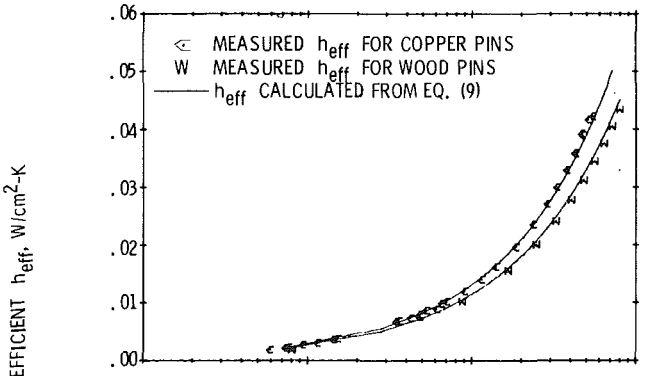

Fig. 10(*a*) Comparison of measured and calculated h_{eff} for $X = 1.0$

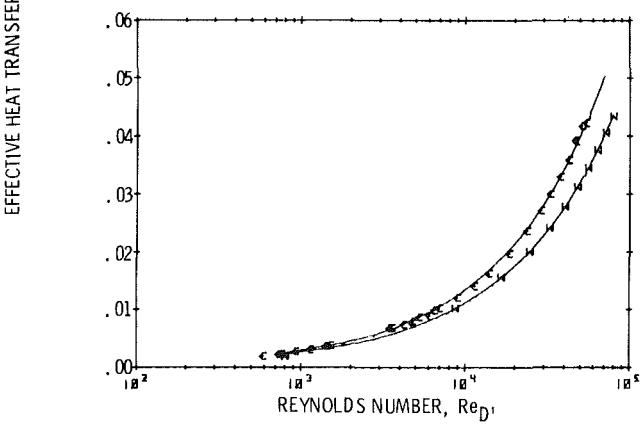

Fig. 10(*b*) Comparison of measured and calculated h_{eff} for $X = 1.345$

Fig. 10

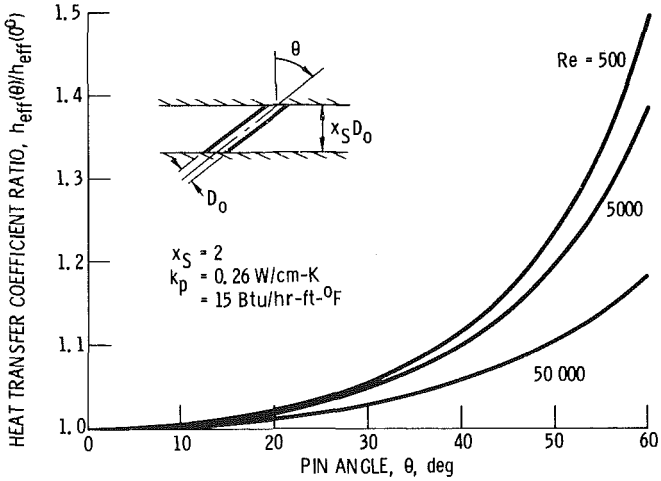

Fig. 11 Calculated increase in effective heat transfer coefficient as a function of pin angle

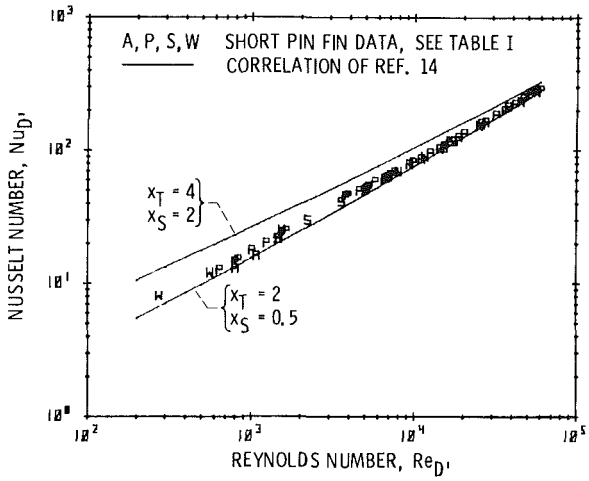

Fig. 12 Comparison of pin fin heat transfer correlation from reference [14] with short pin fin data

number is not a significant parameter if the data are analyzed as indicated in the previous section.

Figure 9 is a plot of the short pin fin heat transfer results along with those from other pin fin references. The plain channel data are also replotted on this figure for comparison purposes. The meaning of the letters used for plotting symbols can be found in Table 1. When examining the figure, three things become obvious; one is that data from all four configurations tested fall on a single correlating line when the Reynolds and Nusselt numbers are defined as explained in the Data Analysis Section. A least-squares curve fit of all the short pin fin data is

$$\mathrm{Nu} = 0.153\ \mathrm{Re}^{0.685} \tag{16}$$

The reader is cautioned that this good correlation of data may be fortuitous as only two different geometries were tested. Another conclusion that can be drawn from the figure is that the heat transfer data for short pins are lower than for data found in the literature for longer pins. The third conclusion is that short pin fin heat transfer is about a factor of two higher than that for a plain channel with no fins.

The results shown in Fig. 9 were all obtained using equation (9) with X set equal to 1 to determine $\bar{h}$, the average heat-transfer coefficient on the pin and endwall surface. This was done to facilitate comparison with data from the literature where it was assumed that $X = 1$. Data from the test section with wooden pins were used to obtain an estimate of the actual value of X. If equation (9) is applied to the large copper and wooden pin test sections, two independent equations result. The geometries of these two test sections were the same; the only difference was the thermal conductivity of the pins. Experimental data for h_{eff} from both the large copper and the wood pin test sections were curve fit as a function of Reynolds number. At any given Reynolds number the heat-transfer coefficient $\bar{h}_w$ was assumed to be the same for both copper and wood test sections because their geometry was identical. For each of a series of Reynolds numbers that covered the range of data, the best value of $\bar{h}_w$ was found by minimizing the difference between the curve fit of experimental data and the value of h_{eff} calculated from equation (9) for both copper and wooden pins. Figure 10(*a*) shows a comparison of calculated and measured h_{eff} using $X = 1.0$ for both the copper and wooden pin test sections. From this figure it can be concluded that $X = 1.0$ is not the correct value.

The best value of X for the range of Reynolds numbers of interest was estimated using the method of least squares. Figure 10(*b*) shows the comparison between measured and calculated values of h_{eff} using the best estimate $X = 1.345$. Agreement between calculated and measured values is much better. It can be concluded from this analysis that the average heat transfer coefficient on the pin surface is about 35 percent larger than that on the endwalls.

In an effort to increase the average heat transfer coefficient on the pin surface, the inclined pins described previously were tested. It was hoped that the wake shed from a row of inclined pins would be stretched across the next downstream row of pins inclined at the opposite angle and thus be intensified. Inclined pins were found, instead, to give the same average heat transfer coefficient as the perpendicular pins. However, the effective heat transfer can be increased by inclining the

Downloaded 01 Jun 2010 to 171.66.16.62. Redistribution subject to ASME license or copyright; see http://www.asme.org/terms/Terms_Use.cfm

pins because of the added pin surface area. Figure 11 shows the calculated benefit of inclining the pins. The ordinate is the ratio of calculated effective heat-transfer coefficient for inclined pins to that for pins perpendicular to the endwalls. The effective heat-transfer coefficients were obtained from equation (9) using equations (14) and (16) to find the average heat transfer coefficient $\bar{h}$. For these calculations X was set equal to unity. Pin thermal conductivity was set to 0.26 W/cm•K (15 Btu/hr•ft•°F); this value is representative of the thermal conductivity of the nickel-based superalloys used in turbine blades. Pin spacing was four pin diameters and the distance between the endwalls was two diameters. Effective heat-transfer coefficient is seen to increase with pin angle and the increase is greater at the low Reynolds numbers. At a Reynolds number of 500 the effective heat transfer for pins angled at 60 deg is nearly 50 percent greater than that for perpendicular pins.

A correlation of pin fin heat-transfer data that was derived from data available in the literature for pin fins and tube banks is presented in reference [14]. The correlation contains terms to account for pin length and spacing. Figure 12 is a comparison of the heat transfer data from this study with this correlation. It can be concluded from the figure that the correlation does not adequately represent the data for short pin fins.

Summary of Results

The results of this experimental investigation into the heat transfer characteristics of short, staggered pin fin arrays over a Reynolds number range from 300 to nearly 60,000 can be summarized as follows:

1 Heat transfer for short pin fins was found to be lower than data available in the literature for longer pins.

2 Heat-transfer data for both pin fin configurations tested in this study fell on a single correlating line.

3 Heat-transfer coefficients on the pin surface were estimated to be about 35 percent higher than those on the endwalls.

4 Inclined pins had the same average heat transfer coefficient as the pins that were perpendicular to the endwalls. It was shown analytically that increasing the pin surface area by inclining the pins can be used to increase the effective heat transfer. This increase was the greatest at the low Reynolds numbers.

5 Short pin fin heat transfer coefficients were significantly higher than those for a plain channel with no pins.

6 An existing correlation for pin fin heat transfer which contains terms to account for the effect of pin length does not adequately represent heat transfer data for short pins.

References

1 Kays, W. M., and London, A. L., *Compact Heat Exchangers,* National Press, Palo Alto, Calif., 1955.

2 Theoclitus, G., "Heat-Transfer and Flow Friction Characteristics of Nine Pin-Fin Surfaces," ASME *Journal of Heat Transfer,* Vol. 88, Nov. 1966, pp. 385-390.

3 Norris, R. H., and Spofford, W. A., "High Performance Fins for Heat Transfer," *Trans. ASME,* Vol. 64, 1942, pp. 489-496.

4 Sparrow, E. M., and Ramsey, J. W., "Heat Transfer and Pressure Drop for a Staggered Wall-Attached Array of Cylinders with Tip Clearance," *International Journal of Heat and Mass Transfer,* Vol. 21, 1978, pp. 1369-1377.

5 Sparrow, E. M., Ramsey, J. W., and Altemani, C. A. C., "Experiments on In-Line Pin-Fin Arrays and Performance Comparisons with Staggered Arrays," ASME *Journal of Heat Transfer,* Vol. 102, No. 1, Feb. 1980, pp. 44-50.

6 Pierson, O. L., "Experimental Investigation of the Influence of Tube Arrangement on Convection Heat Transfer and Flow Resistance in Cross Flow of Gases over Tube Banks, *Trans. ASME,* Vol. 59, 1937, pp. 563-572.

7 Huge, E. C., "Experimental Investigation of Effects of Equipment Size on Heat Convection Transfer and Flow Resistance in Cross Flow of Gases over Tube Banks," *Trans. ASME,* Vol. 59, 1937, pp. 573-581.

8 Anderson, R. C., A Microprocessor Controlled Pressure Scanning System," NASA TM X-71886, May 1976.

9 Miller, R. L., "ESCORT: A Data Acquisition and Display System to Support Research Testing," NASA TM-78909, May 1978.

10 Eckert, E. R. G., and Drake, R. M., *Heat and Mass Transfer,* 2nd. Edition, McGraw-Hill, New York, 1959, p. 270.

11 Hilsenrath, J., et al. *Tables of Thermal Properties of Gases,* NBS-Circ-564, 1955.

12 Dittus, F. W., and Boelter, L. M. K., "Heat Transfer in Automobile Radiators of the Tubular Type," University of California, Berkley, *Publications in Engineering,* Vol. 2, No. 13, 1930, pp. 443-461.

13 McAdams, W. H., *Heat Transmission,* 3rd. ed., McGraw-Hill, New York, 1954, p. 225.

14 Faulkner, F. E., "Analytical Investigation of Chord Size and Cooling Methods on Turbine Blade Cooling Requirements," AiResearch Mfg. Co., Torrance, Calif., AIRESEARCH-71-7487-BK-1, Aug. 1971, Appendix D, p. 189.

Downloaded 01 Jun 2010 to 171.66.16.62. Redistribution subject to ASME license or copyright; see http://www.asme.org/terms/Terms_Use.cfm

Cooling Air Flow Characteristics in Gas Turbine Components

H. F. Jen
Mem. ASME

J. B. Sobanik
Avco Lycoming Division,
Stratford, Conn.
Mem. ASME

An analytical model for the prediction of cooling air flow characteristics (mass flow rate and internal pressure distribution) in gas turbine components is discussed. The model addresses a number of basic flow elements typical to gas turbine components such as orifices, frictional passages, labyrinth seals, etc. Static bench test measurements of the flow characteristics were in good agreement with the analysis. For the turbine blade, the concept of equivalent pressure ratio is introduced and shown to be useful for predicting (i) the cooling air flow rate through the rotor blade at engine conditions from the static rig and (ii) cooling air leakage rate at the rotor serration at engine conditions. This method shows excellent agreement with a detailed analytical model at various rotor speeds. A flow calibration procedure preserving flow similarity for blades and rotor assemblies is recommended.

Introduction

With today's level of fuel prices and anticipated fossil fuel shortages in the future, turbine engineers face a challenge to improve the efficiency of the engine. One of the methods for improving the turbine efficiency is to increase the turbine inlet temperature. However, higher gas temperatures will require more sophisticated cooling schemes for achieving acceptable component life with the same material. To achieve the goal, accurate estimates of both local gas side and coolant side heat flux loads are essential during the component design phase. Much emphasis has been on the gas side heat transfer characteristics. As the cooling scheme becomes more complex, a better understanding of the internal pressure distribution and heat transfer coefficient is necessary to yield accurate predictions of hot section metal temperature, especially when the gas side heat transfer coefficient depends on the cooling air injection rate into the main gas stream. For a turbine blade, the effect of turbine rotation on the cooling air complicates the prediction. It would be convenient to develop a simple technique for determing the cooling air flow rate of turbine blades at engine conditions from the static rig flow without using detailed computer simulation on each turbine blade. This paper presents (*a*) an analytical model for predicting the cooling airflow characteristics (e.g., mass flow rate, internal pressure and temperature distributions) in gas turbine hardware, (*b*) the concept of equivalent pressure ratio to account for the centrifugal effect in a rotating condition, and (*c*) recommended flow calibration procedures for turbine blades and blade/disc assembly.

The analytical model lends itself to an effective numerical technique to yield the solution for the flow characteristics because the gas turbine flow network is modeled as a variety of passage elements. Otherwise, nonlinearity of the basic governing equations will consume a lot of computation time when the size of the flow network becomes big. Bench tests were done to measure blade flow characteristics. The comparison of data with analytical results is presented. The theory and application of equivalent pressure ratio are discussed in detail. The paper concludes with recommended flow calibration procedures for gas turbine components to accurately estimate the cooling air flow rate at engine conditions.

Contributed by the Gas Turbine Division of THE AMERICAN SOCIETY OF MECHANICAL ENGINEERS and presented at the Gas Turbine Conference and Products Show, March 9-12, 1981, Houston, Texas. Manuscript received at ASME Headquarters December 11, 1980. Paper No. 81-GT-76.

Analytical Model

Basic Equation. The static pressure loss of a flow passage shown in Fig. 1 can be expressed one dimensionally as:

$$\frac{p_2 - p_1}{\rho} = K_r \frac{V^2}{2g_c} + K_1 \frac{V^2}{2g_c} + \Delta p_b \tag{1}$$

The first term on the right hand side is the pressure change due to the flow area variation from the upstream to the downstream, a reversible quantity. The second term is the pressure loss associated with the wall friction and flow separation, both irreversible processes in the passage. The third term is the increase of the body force on the flow passage assuming the exit of the passage at a larger radius then the entrance.

The parameters K_r and K_1 depend on a number of flow characteristics of the passage, such as equivalent cross-sectional area, passage length, hydraulic diameter, passage configuration, surface roughness, entrance configuration, Reynolds number etc.

The present day turbine stator and blade are cooled by both convective and surface film cooling. The cooling air is supplied by a high pressure source and discharged to one or a number of locations on the airfoil surfaces with different exit pressures. The intricate cooling scheme can be decomposed into a number of basic flow elements with proper correction factors to account for their interaction. The correction factors can be developed by comparing the analytical and experimental results.

The constants K_r, K_1 in equation (1) for a number of flow

Copyright © 1982 by ASME
Downloaded 01 Jun 2010 to 171.66.16.62. Redistribution subject to ASME license or copyright; see http://www.asme.org/terms/Terms_Use.cfm

Table 1 Basic flow elements suitable to equation (1)

Flow Elements	K_r	K_l	Flow Area	Comments
Abrupt contraction	$(1-\sigma^2)$	K_c	Minimum Area	K_c = Loss Coefficient see references [1,2,3]
Abrupt Expansion	$(1-\sigma^2)$	K_e	Minimum Area	K_e = Loss Coefficient see references [1,2,3]
Frictional Passage	$(\sigma_d^2-\sigma^2)$	$4f\frac{L}{D_h}$	Average Area of Passage	see references [1,4,5]
Bending Loss	0	K_b	Minimum Bend Area	K_b = Bend Loss Coefficient see references [7]

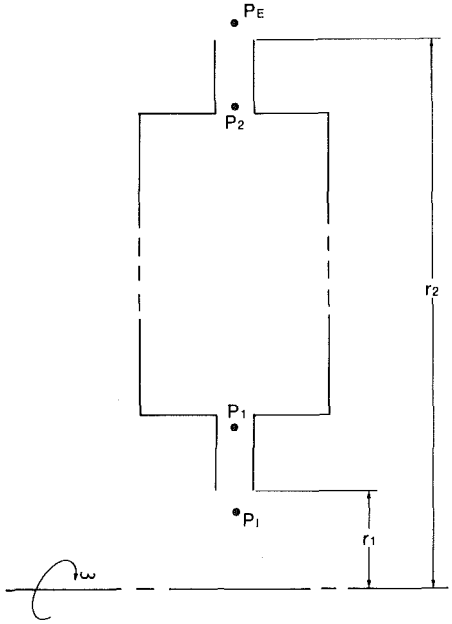

Fig. 1 Model of rotational flow passage

elements frequently used in the flow simulation are shown in Table 1. There are flow configurations in which the flow and pressure relationship is directly expressed in the form of:

$$w=\frac{Cp_0A}{(R_nT_0)^{1/2}} \tag{2}$$

where C is a function of pressure ratio. It is more convenient to keep this form during the numerical analysis. Examples of the constant C are shown in Table No. 2.

Numerical Method. The cooling air passage in gas turbine components can be subdivided into a number of flow passage elements connected in series or parallel to establish a flow network with one or more sources and sinks. To facilitate the numerical analysis, points (nodes) are located at the entrance and the exit of each element and are assigned with reference numbers. The number of nodal points would depend on the magnitude of each flow element pressure drop and the desired accuracy of simulating the flow characteristics in the passage. If necessary the flow parameters of each element could be properly adjusted to account for the effects of the upstream flow configuration.

After completing the subdivision of the flow system, the flow parameter $K_{ij} = (K_r + K_l)$ between two-end nodes, i and j, can be calculated. The coolant flow rate, w_{ij} from nodes i to j is

$$w_{ij}=A_{ij}\left(\frac{g_c}{K_{ij}R_nT_0}\right)^{1/2}(p_i^2-p_j^2)^{1/2} \tag{3}$$

if the body force is excluded temporarily for the convenience of discussion. Equation (3) indicates that the coolant mass flow w_{ij} of each element depends nonlinearly on its upstream and downstream pressures (p_i and p_j). The coolant mass flow balance for any internal node i must satisfy the flow continuity condition, i.e.

$$\sum_{j=1}^{N} w_{ij}=0 \tag{4}$$

The internal pressures of all nodes cannot be readily obtained by the substitution of equations (3) into (4) due to nonlinearity. Any attempt to linearize equation (4) will not be successful because of the impossibility to provide a reasonably good guess on all internal pressures to approximately satisfy

Nomenclature

A = area, m^2
A = matrix A
B = matrix B
C = constant in equation (2)
C^m = constant in equation (5)
C_D = discharge coefficient
D_h = hydraulic diameter, m
f = frictional loss coefficient
G = flow stream mass velocity, (W/A), Kg/m^2 s
g_c = proportionality factor in Newton's second law
K_r = pressure change coefficient due to area variation
K_l = pressure loss coefficient
K_f = constant defined in equations (8, 9) and (12)
K = flow loss constant
L = flow element length, m
N = number of knives in labyrinth,
p = static pressure, Pa
P^m = pressure matrix
P_r = pressure ratio
Δp_b = pressure due to centrifugal force, P_a
ΔP = pressure increase matrix iteration, P_a
Q = volumetric flow rate, m^3/s
R_n = air gas constant
$\bar{r}$ = average exit radius, m
r = radius, m
T = temperature, K
V = velocity, m/s
w = mass flow rate, Kg/s
ν = kinematic viscosity
ω = rotation speed, radian/s
σ = ratio of free-flow area to frontal area
γ = thermal capacity ratio
ρ = density
μ = dynamic viscosity

Subscripts

0 = total, equivalent
1 = location 1
2 = location 2
b = flow bend, disk bore
d = downstream
E = exit
i = node i, disk rim
I = inlet
j = node j
u = upstream
eq = equivalent
in = inlet

Superscripts

m = iteration index

Downloaded 01 Jun 2010 to 171.66.16.62. Redistribution subject to ASME license or copyright; see http://www.asme.org/terms/Terms_Use.cfm

Table 2 Basic flow elements suitable to equation (2)

Flow Element	C	Comments
Labyrinth Seal	$5.68\,K\left[\dfrac{1-\left(\frac{P_2}{P_{01}}\right)^2}{N-\ln\left(\frac{P_2}{P_{01}}\right)}\right]^{1/2}$	Seal Equation after reference [6]
Flow Orifice	$C_D\left[2g_c\dfrac{\gamma}{\gamma-1}\left[\left(\frac{P_2}{P_{01}}\right)^{2/\gamma}-\left(\frac{P_2}{P_{01}}\right)^{\gamma+1/\gamma}\right]\right]^{1/2}$	Isenstropic Orifice Equation

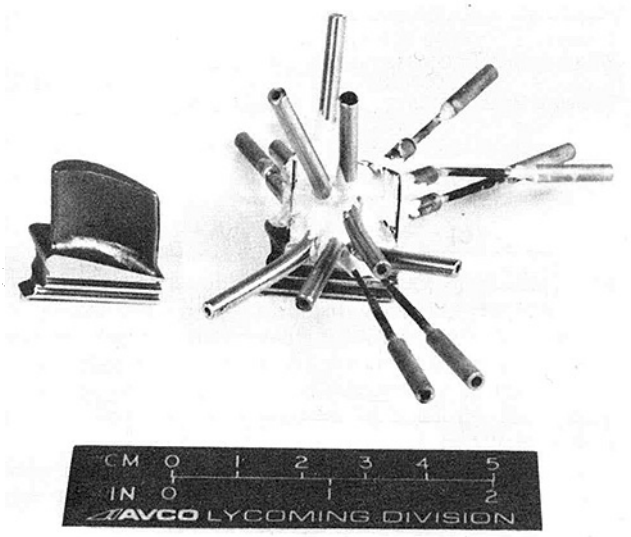

Fig. 2 Lycoming H.P. blade instrumented with pressure taps

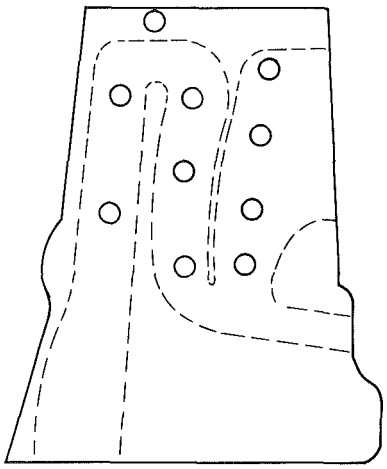

Fig. 3 Location of pressure taps

the continuity equation. The best alternative for the problem is using the iteration method. When the iteration method is employed to determine the internal pressures and the mass flows rates, an initial guess on these quantities will result in mass flow inbalances at all internal nodes. The objective then becomes the determination of internal pressure increase/decrease at each iteration such that the mass inbalances are reduced gradually at internal nodes. That is, for i^{th} node:

$$C^m\sum_{j=1}^{N}w_{ij}+\left(\sum_{j=1}^{N}\frac{dw_{ij}}{dp_i}\right)\Delta p_i^m+\sum_{\substack{j=1\\ j\neq i}}^{N}\left(\frac{dw_{ij}}{dp_j}\Delta p_j^m\right)=0 \tag{5}$$

where m is indexed with each iteration and is not an exponent. The constant C^m on the first term will be adjusted internally during each iteration such that the numerical instability is avoided and a faster convergency is achieved. Equation (5) can be rewritten into a matrix form as

$$A\bullet\Delta P^m=B \tag{6}$$

The elements in A and B are computed on the basis of the pressure P^{m-1} of the previous iteration, and subsequently,

$$P^m=P^{m-1}+\Delta P^m \tag{7}$$

The above operation will continue until the convergence criterion on the mass inbalance is reached.

Body Forces. The body force on the cooling air of a turbine blade/disk is the centrifugal force generated due to the turbine rotation. The governing equation of a forced vortex pumping is:

$$\frac{\gamma}{\gamma-1}\left(1-\left(\frac{p_i}{p_0}\right)^{\frac{\gamma-1}{\gamma}}\right)=\frac{\omega^2}{T_0}\,\frac{(r_0^2-r_i^2)}{2g_cR_n}K_f^2 \tag{8}$$

where $K_f = 1.0$ for a turbine blade, because the cooling air in the blade flows at the same local tangential velocity as the turbine.

The average velocity of cooling air between a turbine disc and sealing plate is a fraction of the local tangential velocity of the disc because the air is not adjacent to the disk and cannot achieve the same velocity as the disk by viscous shear forces. Daily et al. [8] developed an empirical relationship, equation (9), for the core rotation. The radial pressure depends on the centrifugal forces of core rotation and the radial diffuser effect on the radial flow of cooling air. The contribution of the radial diffusion is negligible. Therefore, the pressure change, induced by the rotation, in the flow passage of a turbine blade and disk becomes independent of passage geometry, the frictional characteristics, and the coolant mass flow. As a result the pressure can be calculated and accounted for in equation (1) prior to computing equation (3). The effect of body forces is significant for gas turbines.

$$K_f=\frac{0.5}{12.75\left(\frac{Q}{\omega r_0^3}\right)\left(\frac{\omega r_0^2}{\nu}\right)^{.2}\left(\frac{r_0}{r_i}\right)^{2.6}+1} \tag{9}$$

Heat Transfer. Heat transfer effects on the flow characteristics should also be included in the computation. A number of heat transfer coefficient formulas available in the literature can be incorporated into a computerized numerical analysis. The temperature increase at each element is calculated from the computed heat transfer coefficient and the assumed wall temperature. The effects of a preswirl nozzle on the upstream pressure and the relative total temperature can be included in the analysis. The rotation of the turbine

Downloaded 01 Jun 2010 to 171.66.16.62. Redistribution subject to ASME license or copyright; see http://www.asme.org/terms/Terms_Use.cfm

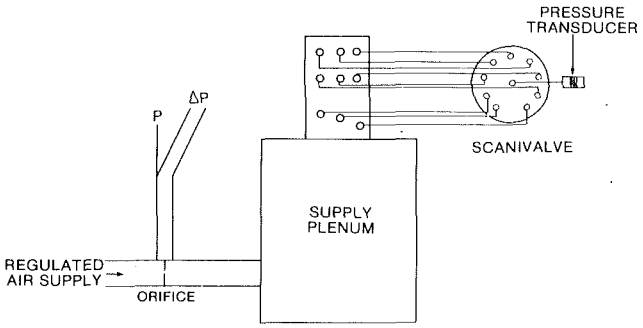

Fig. 4 Schematic of test rig

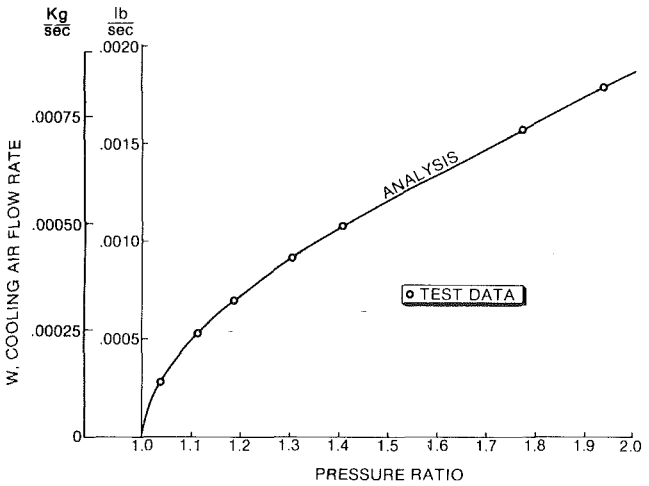

Fig. 5 Comparison of analytical and experimental mass flow versus pressure ratio results

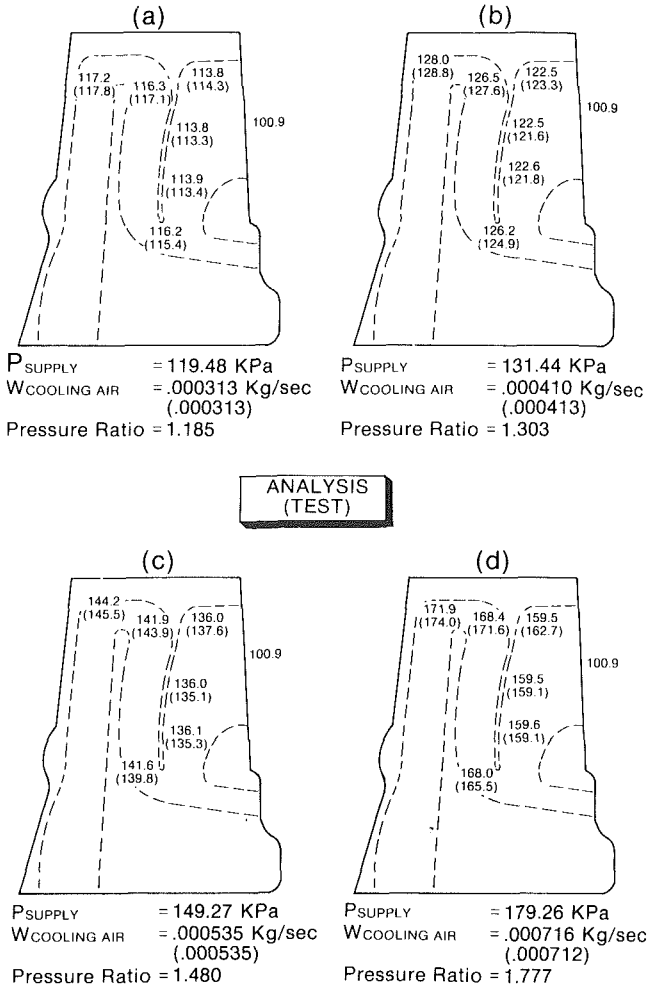

Fig. 6 Comparison of analytical and experimental flow characteristics at four pressure ratios

blade will incur a temperature change on the coolant because of the work done on and by the coolant. Euler's turbine equation is used to compute temperature increase and decrease.

Experimental Verification

To enhance the understanding of flow behavior in the gas turbine cooled component and to improve its prediction accuracy, a number of Lycoming turbine hardware were instrumented with pressure taps along the cooling flow passage and bench flowed at a series of pressure ratios to generate static pressure distribution and mass flow rate data. Figure 2 shows a typical instrumented blade. Figure 3 shows a schematic of the test blade and approximate pressure tap location. Figure 4 shows a schematic of the test rig. All pressure taps were adapted to the data system scanivalve and read by a single transducer during the test scans to assure consistency in the readings. A scan was taken when the regulated plenum pressure became stabilized. Test data of air flow rate versus pressure ratio is presented in Fig. 5. There is an excellent correlation in flow rate between the experiment and the analysis. Data displaying internal pressure distribution are presented in Figure 6 as compared with analytical results. The test internal pressures shown are the average of pressure and suction sides. The discrepancy in the static pressure is relatively small compared to the total pressure drop in the blade.

Equivalent Pressure Ratio

A turbine blade is normally flow calibrated in a static rig for reasons of cost saving, convenience and quickness in the calibration. An estimation of the cooling airflow rate at engine conditions is then required from the data of the rig flow calibration. During the estimation the effect of turbine rotation must be included in conjunction with the correction on pressure and temperature. This section presents a simple concept and technique for considering all three parameters simultaneously during the estimation.

Turbine rotation introduces centrifugal forces on the cooling air and results in higher cooling airflow. The magnitude of increase depends on the rotor speed and geometric factors. As a result the cooling airflow of a turbine blade at part power condition differs from those at full power. When analyzing the engine performance at various powers, one could rely on the analytical simulation of the blade at the static rig condition and then extend the model to include the centrifugal force effect. However, at the various engine conditions the mass flow rate of an actual blade will differ from the design mass flow rate because of the manufacturing tolerance. The extrapolation process becomes more complicated and costly in computation if a computer simulation method is employed for every batch of manufactured blades. The simplified method of assuming a constant ratio between mass flow rates at all engine conditions and the static rig condition is not correct because the ratio varies with the rotor speed. Furthermore, the coolant leakage through the blade platform and serration is under different magnitude of centrifugal and shear pumping. The simplified constant ratio assumption for the cooling air flow rate of an turbine blade to static rig conditions is definitly not applicable

Downloaded 01 Jun 2010 to 171.66.16.62. Redistribution subject to ASME license or copyright; see http://www.asme.org/terms/Terms_Use.cfm

to leakage conditions. The leakage calibrated at the static condition does not relate to the leakage at the engine condition in a consistent pattern since the flow geometry associated with the leakage has altered at the blade attachment due to turbine rotation. Therefore, it is desirable to have an algebraic formula to account for the turbine rotation in the engine performance analysis. The concept of equivalent pressure ratio is developed to provide an effective and accurate technique of estimating the cooling airflow rate from the static rig flow calibration.

Simplified Equation. For a simple flow passage shown in Figure 1 with $\omega=0$, the governing equation for the system under the static mode is

$$p_I - p_E = (K_r + K_1)\frac{G_1^2}{2\rho_1 g_c} \tag{10}$$

on the basis of equation (1). For the same flow configuration under the rotating mode, the governing equation becomes

$$p_I - p_E + \Delta p_b = (K_r + K_1)\frac{G_2^2}{2\rho_2 g_c} \tag{11}$$

By comparing equation (10) with (11), one notes that if the downstream pressure is assumed constant, the effect of centrifugal force on the coolant mass flow rate is equivalent to an additional entrance (supply) pressure in the static mode because the centrifugal force is independent of the passage characteristics. The net pressure induced by the forced pumping on a blade/disc can be derived by conducting a binominal expansion on the left hand side of equation (8) and neglecting higher order terms. That is:

$$\frac{\Delta p_b}{p_i} = \frac{\omega^2}{T}\frac{(r_0^2 - r_i^2)K_f^2}{2g_c R_n} \tag{12}$$

It indicates that the pumping depends on the upstream pressure, rotational speed and radial locations of the entrance and the exit. For a turbine blade with a slot exit, the overall effective pumping can be determined by analytical integration on equation (12) across the slot height. The integration yields an equation similar to (12) for the overall pumping effect, but with an equivalent outer radius of

$$\bar{r}_0^2 = \frac{1}{3}\frac{r_2^3 - r_1^3}{r_2 - r_1} \tag{13}$$

The above equation can also apply for a blade with evenly spaced exit holes.

Applying equations (11) and (12), the equivalent supply pressure for a turbine blade becomes

$$p_{eg} = p_{in}\left(1 + \frac{\omega^2}{T}\frac{\bar{r}_0{}^2 - r_i{}^2}{2g_c R_n}\right) \tag{14}$$

The same principle also applies to the turbine blade/disc assembly. For a turbine blade/disk assembly, the equivalent inlet pressure at the disc inner location becomes:

$$p_{eg} = p_{in}\left(1 + K_f\frac{\omega^2}{T}\frac{r_i^2 - r_b^2}{2g_c R_n}\right)\left(1 + \frac{\omega^2}{T}\frac{\bar{r}_0^2 - r_i^2}{2g_c R_n}\right) \tag{15}$$

To verify the above concept, the following two steps were taken:

1 Conduct flow experiments on turbine blades to measure the airflow and internal pressure distribution in a static rig at a number of pressure ratios and develop an analytical model for the blades to correlate with measured results.

2 Apply the analytical model to the engine condition because the centrifugal force is independent of the passage characteristics. A number of turbine rotating speeds were considered, including "zero" rotation.

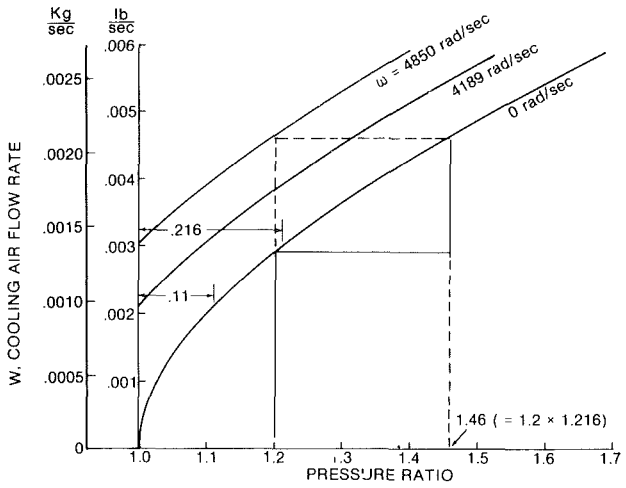

Fig. 7 Graph demonstrating equivalent pressure ratio

A typical result is presented hereafter to demonstrate the technique of utilizing equivalent pressure ratio for the cooling airflow prediction of turbine blades.

The cooling airflow rates of the turbine blade shown in Fig. 5 are presented in Fig. 7 for the engine condition. The curve of zero rotation speed determined from Fig. 5 by assuming $w\sqrt{T_0}/p_0$ is constant at each pressure ratio. $w\sqrt{T_0}/p_0$ can be treated as constant since the Reynolds number effect on the pressure drop is very small compared to the total pressure loss in the blade. Substitution of geometric values, turbine rotation speed and mean air temperature into equation (14) yields

$$p_{eq} = p_{actual} \times 1.216 \text{ for } \omega = 4850 \text{ rad/s}$$
$$p_{eq} = p_{actual} \times 1.11 \text{ for } \omega = 4180 \text{ rad/s}$$

This means that the equivalent pressure ratio, p_{eq}/p_{inlet}, is 1.216. This is the pressure ratio which would result in the same mass flow as if there were just rotational pumping (ω = 4850 rad/s) (i.e., no static pressure ratio across the blade). For a static pressure ratio of 1.2 across the blade, the cooling airflow rate at w = 4850 rad/sec is equal to the flow rate at the equivalent pressure ratio of 1.2 × 1.216 1.46 and ω = 0. The same procedure applied to a rotational speed of ω = 4189 rad/s and static pressure ratio of 1.2 yields an equivalent pressure ratio of 1.33.

Flow Calibration Procedure for a Turbine

It is clear from the concept of equivalent pressure that the cooling air flow through a gas turbine blade depends on the turbine rotating speed. To properly account for this variation, the following calibration procedures for a turbine blade similar to Fig. 2 are recommended.

1 Select cooling air temperature and discharge (exit) pressure such that Reynolds number and pressure coefficient of the rig condition is equal to those of the engine condition. The similarity condition is:

$$\left(\frac{p}{\mu T^{1/2}}\right)_{engine} = \left(\frac{p}{\mu T^{1/2}}\right)_{rig} \tag{16}$$

This step can be ignored when the pressure drops in flow passages dependent on Reynolds number are very small compared to the overall pressure drop.

2 Calibrate the blade at three supply pressure ratios: the actual ratio, the equivalent pressure ratio of;

Downloaded 01 Jun 2010 to 171.66.16.62. Redistribution subject to ASME license or copyright; see http://www.asme.org/terms/Terms_Use.cfm

$$P_{r_{eq}} = P_r\left(1 + \frac{\omega}{T}\frac{\bar{r}_0^2 - r_i^2}{2g_c R_n}\right) \tag{17}$$

and mean ratio between the actual and the equivalent. Should the interest be on the maximum cooling airflow rate, only the equivalent pressure ratio is chosen.

3 Compute the cooling airflow at the engine condition based on the equation:

$$\left(\frac{wT^{1/2}}{p}\right)_{\text{engine}} = \left(\frac{wT^{1/2}}{p}\right)_{\text{rig}} \tag{18}$$

Then a formula can be developed to specify the cooling airflow as a function of turbine speed. The air leakage of a turbine blade/disc assembly cannot be calibrated in a static rig. Therefore, either of the following calibration procedures must be used to determine the cooling airflow rate at engine condition:

1 Flow calibrate all blades following the above procedure prior to assembling except at an equivalent pressure of equation (15) and then sum up with the analytical leakage computed from the serration and platform leakage areas in which a lower equivalent pressure must be used to account for the smaller pumping effect.

2 Flow calibrate all blades as in procedure 1 to determine the cooling airflow rate in terms of pressure ratio or turbine speed, and then calibrate the assembly in a dynamic mode (at a much lower rotation speed than the engine) similar to the blade. Subsequently, the leakage rate can be determined with measured data. The superposition method can then be used to determine the total cooling airflow as a function of engine rotating speed.

Conclusions

An analytical model has been developed to simulate cooling flow networks of gas turbine cooled components. The matrix solution scheme and the iteration method have resulted in an accurate convergence on the internal pressure distribution, flow rate, and temperature distribution. Analytical results of internal pressure distribution and airflow rate have correlated very well with the measurements in static rig experiments on turbine hardware. It indicates that published flow characteristics on the basic elements such as friction factor, entrance and expansion losses, etc. can be employed directly to accurately predict the cooling airflow rate and internal pressure distribution. Therefore, the study of the coolant side flow characteristics can concentrate on the basic flow elements instead of each new design configuration.

The concept of equivalent pressure ratio to include the centrifugal effect on the cooling air in a rotating component has been shown useful to quickly and accurately predict the cooling airflow at engine conditions from the static rig calibration. Flow calibration procedures for the gas turbine components are recommended to satisfy the similarity condition to accurately estimate the cooling airflow rate at engine conditions.

References

1 Kays, W., and London, A. L., *Compact Heat Exchangers*, Second Edition, McGraw Hill, New York, 1955, pp. 92–97.

2 Benedict, R. P., Carlucci, N. A., and Swetz, S. D., "Flow Losses in Abrupt Enlargements and Contractions," ASME JOURNAL OF ENGINEERING FOR POWER, Jan., 1966, pp. 73.

3 Benedict, R. P., and Carlucci, N. A., *Handbook of Specific Losses in Flow Systems*, 1966.

4 Peng, Y., and Ederer, J., "Experimental Evaluation of Turbine Blade Internal Pin Fin Cooling Configuration," Avco Lycoming Report No. 3195.2.20, Mar. 1970.

5 Churchill, S. W. "Friction - Factor Equation Spans all Fluid-Flow Regimes," *Chemical Engineering*, Nov. 7, 1977, p. 91.

6 Vermes, G., "A Fluid Mechanics Approach to the Labyrinth Seal Leakage Problem," ASME JOURNAL OF ENGINEERING FOR POWER. Vol. 83, Apr. 1961, pp. 161–169.

7 Miller, D. S., *Internal Flow Systems*, BHRA Fluid Engineering Series.

8 Daily, J. W., Ernest, W. D., and Asbedian, V. V., "Enclosed Rotating Disks with Superposed Through-flow, Mean Study and Periodic Unsteady Characteristics of Induced Flow," MIT Hydrodynamic Lab, Report No. 64, 1964.

Downloaded 01 Jun 2010 to 171.66.16.62. Redistribution subject to ASME license or copyright; see http://www.asme.org/terms/Terms_Use.cfm

Inverse or Design Calculations for Nonpotential Flow in Turbomachinery Blade Passages

W. T. Thompkins, Jr.
Associate Professor.

Siu Shing Tong
Research Assistant.

Department of Aeronautics and Astronautics,
Massachusetts Institute of Technology,
Cambridge, Mass. 02139

A new inverse or design calculation procedure has been devised for nonpotential flow fields and has been applied to turbomachinery blade row design. This technique uses as input quantities the surface pressure distribution and geometric constraints and may be used for two- or three-dimensional flows as well as inviscid or viscous flows. If a geometry satisfying both the constraints and the pressure distribution cannot be found, a solution satisfying the constraints and a relaxed pressure distribution is found. Calculational examples are presented for inviscid supersonic compressor cascade designs and the extension to three-dimensional flows discussed.

Introduction

A successful and complete design system for turbomachinery blade rows would, at a minimum, provide a calculational tool by which blade row geometry could be computed from "suitable" design input, demonstrate what type of design input (such as blade surface pressure) is required to generate an acceptable blade geometry, illustrate the constraints design input must satisfy if any aerodynamic or geometric constraints are to be satisfied, and provide a mechanism by which optimum geometries may be defined and determined. Before any real progress can be made toward the final goal of determining optimum blade geometries the fundamental question of whether any inverse technique applicable to Euler or Navier-Stokes flow simulations be devised must be answered at least in principle. Enough progress has been made on efforts to develop a blade design system to report that an inverse scheme based on specification of blade surface pressures plus geometric constraints is feasible, but many unanswered questions exist about uniqueness and existance of the flow solutions and the optimization process.

Design or inverse techniques for turbomachinery blade rows already exist for the special cases of two-dimensional, shock-free flow [1], and two-dimensional potential flows with weak shock waves [2]. These schemes appear satisfactory for stator design problems [3], but are not satisfactory for high approach Mach number rotor designs or for three-dimensional designs. In addition, geometric constraints such as closed trailing edge conditions are difficult to enforce. Considerable progress for inlet diffuser or duct flow problems has been made by Zannetti [4] in which some geometric constraints are satisfied directly, but no scheme suitable for more complex internal flow problems now exists.

Direct or analysis techniques, for which the geometry is always specified, now exist which consider, at least in an approximate manner, all of the characteristic features of high Mach number turbomachinery flows: mixed subsonic and supersonic zones, approach Mach numbers of 1.5 and above, strong shock waves, and a high degree of geometric complexity. Such computer codes are nearly always shock-capturing, time-marching schemes [see [5] and [6] as examples], and it is natural to ask if these solvers can be used as the basis of an inverse calculation scheme without the need for numerical optimization techniques or a cut and try approach. This paper proposes a theoretical framework in which various time-marching direct solvers may be used as inverse solvers, solves some two-dimensional, inviscid transonic cascade problems, and discusses the extension of these techniques to three-dimensional designs.

Analysis

The first step in the development of a complete blade row design system is to demonstrate that at least one inverse technique applicable to Euler or Navier-Stokes simulations exists and to determine what general design input is required to construct a solution. The inverse technique used as a demonstration procedure is fundamentally a sequence of direct calculations on a time dependent geometry. This technique will be developed as applied to two-dimensional, inviscid, transonic cascade design and some simple examples computed. The most important information gained from the procedure is not the particular new cascade designs illustrated, but rather, the knowledge that new designs can be constructed using this process.

Flow Equations for Two-Dimensional Inviscid Example. The inverse technique presented in this paper uses the strong conservation law form of the Euler or Navier-Stokes equations expressed in a form suitable for use with time-dependent, body-fitted coordinate systems [see [7] or [6]].For two-dimensional, inviscid flow, these equations written in vector form for Cartesian coordinates are:

$$\partial_t \bar{q} + \partial_x \bar{F} + \partial_y \bar{G} = 0 \qquad (1)$$

Contributed by the Gas Turbine Division of THE AMERICAN SOCIETY OF MECHANICAL ENGINEERS and presented at the Gas Turbine Conference and Products Show, March 9-12, 1981, Houston, Texas. Manuscript received at ASME Headquarters December 11, 1980. Paper No. 81-GT-78.

Copyright © 1982 by ASME

Downloaded 01 Jun 2010 to 171.66.16.62. Redistribution subject to ASME license or copyright; see http://www.asme.org/terms/Terms_Use.cfm

where

$$\bar{q}=\begin{bmatrix}\rho\\ \rho u\\ \rho v\end{bmatrix}\quad F=\begin{bmatrix}\rho u\\ \rho u^2+P\\ \rho uv\end{bmatrix}\quad G=\begin{bmatrix}\rho v\\ \rho uv\\ \rho v^2+P\end{bmatrix}$$

These equations express conservation of mass and momentum. In inverse code applications where only steady-state solutions are required, the energy equation may be replaced with the assumption of isoenergetic flow, or the assumption that the stagnation enthalpy (h_0) is constant everywhere. This assumption provides a simple algebraic relation between the pressure, density, and velocity components.

$$P=\rho\frac{(\gamma-1)}{\gamma}\left[h_0-\frac{(u^2+v^2)}{2}\right] \tag{2}$$

These equations can seldom be solved for realistic geometries without transforming from a Cartesian system (t, x, y as independent variables) to a more general computational system (t, ξ, η as independent variables). The transformed equations are most useful when the new coordinate system is at least a body-fitted system. In a body-fitted coordinate system, flow boundary surfaces such as blade profile shapes become coordinate lines in the computational space. A simple body-fitted coordinate mapping is illustrated in Fig. 1, and a more complex one is illustrated in Fig. 2.

Following Viviand [8], a coordinate mapping may be defined as

$$\xi=\xi(x,y,t)\qquad \eta=\eta(x,y,t)\qquad t=t \tag{3}$$

where ξ and η are general mapping functions that may depend on time. Subject to such a mapping, the flow equations may be written as

$$\partial_t\hat{\bar{q}}+\partial_\xi\hat{\bar{F}}+\partial_\eta\hat{\bar{G}}=0 \tag{4}$$

where

$$\hat{\bar{q}}=\bar{q}/J\qquad \hat{\bar{F}}=[(\partial_t\xi)\bar{q}+(\partial_x\xi)\bar{F}+(\partial_y\xi)\bar{G}]/J$$
$$\hat{\bar{G}}=[(\partial_t\eta)\bar{q}+(\partial_x\eta)\bar{F}+(\partial_y\eta)\bar{G}]/J$$

Here J is the transformation Jacobian

$$J=(\partial_x\xi)(\partial_y\eta)-(\partial_y\xi)(\partial_x\eta) \tag{5}$$

These equations have a particularly instructive form when the contravariant velocities along coordinate lines are introduced:

Normal to the ξ coordinate line

$$U=\partial_t\xi+(\partial_x\xi)u+(\partial_y\xi)v \tag{6}$$

and normal to the η coordinate line:

$$V=\partial_t\eta+(\partial_x\eta)u+(\partial_y\eta)v \tag{7}$$

With these definitions, the flux vectors $\hat{\bar{F}}$ and $\hat{\bar{G}}$ may be rewritten as:

$$J\hat{\bar{F}}=\begin{bmatrix}\rho U\\ \rho uU+(\partial_x\xi)P\\ \rho vU+(\partial_y\xi)P\end{bmatrix},\quad J\hat{\bar{G}}=\begin{bmatrix}\rho V\\ \rho uV+(\partial_x\eta)P\\ \rho vV+(\partial_y\eta)P\end{bmatrix} \tag{8}$$

Along the body surface, $\eta = 0$ and $\eta = 1$ in Fig. 1, the flow tangency boundary condition is simply expressed as $V = 0$. The wall pressure is usually found from a compatability condition derived from the momentum equation such as:

$$\partial_n P=\frac{\rho U_p^2}{R_s} \tag{9}$$

where n indicates the direction normal to the surface,
U_p is the velocity parallel to the surface, and
R_s is the radius of curvature of the surface.

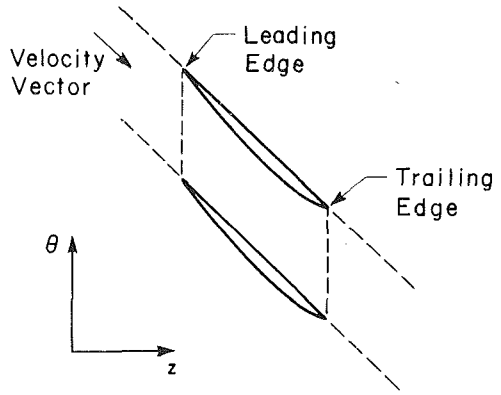

Fig. 1(a) Typical blade to blade view, physical space

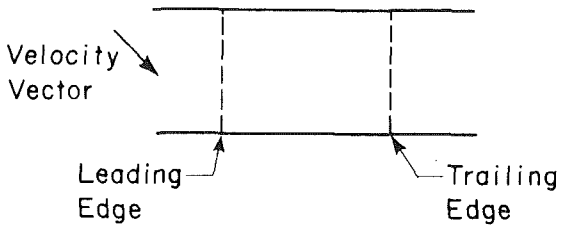

Mapping Function

$$\eta=\frac{\theta-\theta_{ps}}{\theta_{ss}-\theta_{ps}}$$

Fig. 1(b) Blade to blade view, computational space

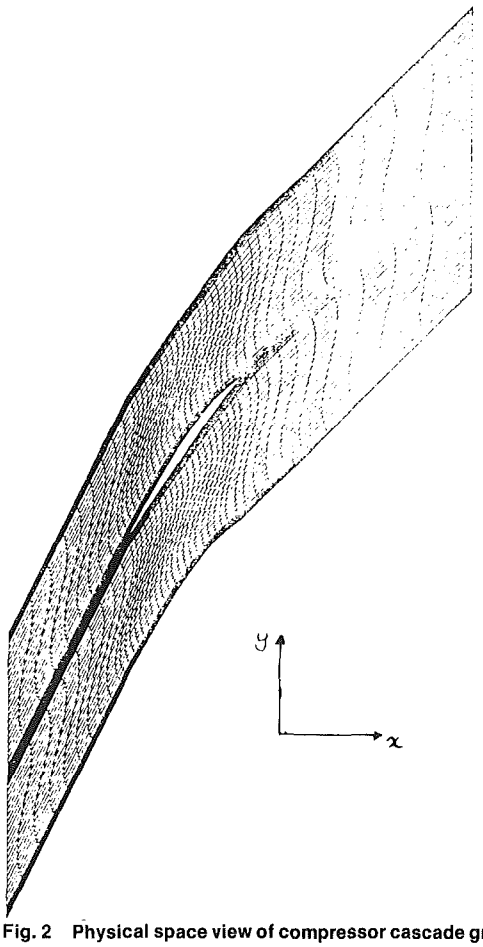

Fig. 2 Physical space view of compressor cascade grid

Downloaded 01 Jun 2010 to 171.66.16.62. Redistribution subject to ASME license or copyright; see http://www.asme.org/terms/Terms_Use.cfm

Inverse Technique. An inverse calculation procedure which is fundamentally a sequence of direct calculations for a time-dependent geometry can be constructed using the observation that the flow equations (4) may be integrated at all interior points using only a specified wall pressure. To illustrate this point consider the simplest time-marching scheme (forward time-centered space differencing) applied at grid node points near a solid wall (see Fig. 3 for grid illustration). This differencing applied to equation (4) yields:

$$\frac{\hat{q}^{n+1}_{i,1} - \hat{q}^{n}_{i,1}}{\Delta t} = -\left[\frac{\hat{\bar{F}}^{\eta}_{i+1,1} - \hat{\bar{F}}^{\eta}_{i-1,1}}{\Delta \xi}\right] - \left[\frac{\hat{\bar{G}}^{\eta}_{i,2} - \hat{\bar{G}}^{\eta}_{i,0}}{\Delta \eta}\right] \tag{10}$$

The flux vectors at interior node points ($\hat{\bar{F}}^{\eta}_{i+1,1}$, $\hat{\bar{F}}^{\eta}_{i-1,1}$ and $\hat{\bar{G}}^{\eta}_{i,2}$) pose no difficulties, but the wall flux vector ($\hat{\bar{G}}^{\eta}_{i,0}$) must incorporate the solid wall boundary conditions. This flux vector may be written in a form containing only the wall pressure since the relative normal flow velocity ($V_{i,0}$) is always zero. This form is

$$\bar{G}^{n}_{i,0} = \begin{bmatrix} \rho V \\ \rho u V + (\partial_x \eta) P \\ \rho v V + (\partial_y \eta) P \end{bmatrix}^{n}_{i,0} = \begin{bmatrix} 0 \\ (\partial_x \eta) P \\ (\partial_x \eta) P \end{bmatrix}^{n}_{i,0} \tag{11}$$

The geometry construction technique proceeds by first assuming a trial geometry, coordinate system, and Jacobian members. The flow equations are then integrated at all interior points using a pressure derived from the compatability equation (9). A new wall pressure consistent with the current flow field is computed and the difference between the design pressure and the computed pressure is used to predict a corrected wall shape. When a new wall shape has been predicted, a new coordinate system is computed and the flow solution is updated at each interior node point. For convenience during the present exploratory phase, the direct solver used has been an explicit method by MacCormack [8]. Nearly any other explicit scheme could have been used as well as implicit schemes like that of Beam and Warming [9].

A key element in this procedure is the scheme by which the wall shape corrections are derived from the wall pressure error. The local blade shape correction is determined by setting the difference between the design wall flux vector and transient wall flux vector to zero. This difference is defined as:

$$\hat{\bar{G}}^{n}_{i,0} - \hat{\bar{G}}^{d}_{i,0} = \begin{bmatrix} 0 \\ \rho u V^{s} + (\partial_x \eta) P \\ \rho v V^{s} + (\partial_\eta \eta) P \end{bmatrix}^{n}_{i,0} - \begin{bmatrix} 0 \\ (\partial_x \eta) P \\ (\partial_y \eta) P \end{bmatrix}^{d}_{i,0} = 0 \tag{12}$$

where

$$V^{s} = (\partial_x \eta) u^{s} + (\partial_y \eta) v^{s}$$

For a steady-state solution, ($V^{s}_{i,0}$) would be zero, and ($\hat{\bar{G}}^{n}_{i,10}$) would equal to ($\hat{\bar{G}}^{d}_{i,0}$). This flux vector error term consists of two equations which may be solved for the steady-state flow velocities at the wall, ($u^{s}_{i,0}$), ($v^{s}_{i,0}$):

$$[(\rho u)^{s}[(\partial_x \eta) u^{s} + (\partial_y \eta) V^{s}]]_{i,0} = (\partial_x \eta)(P^{d}_{i,0} - P^{n}_{i,0}) \tag{13}$$

$$[(\rho v)^{s}[(\partial_x \eta) u^{s} + (\partial_y \eta) V^{s}]]_{i,0} = (\partial_y \eta)(P^{d}_{i,0} - P^{n}_{i,0}) \tag{14}$$

where ($P^{d}_{i,0}$) is the specified wall pressure, ($P^{n}_{i,0}$) is the wall pressure found from the wall compatability equation, and ρ is the wall density. However, the true value of ($V^{n}_{i,0}$) is always zero, and this may now be used to find the time derivative of η (x, y, t).

$$(\partial_t \eta)^{n}_{i,0} = -V^{s}_{i,0} \tag{15}$$

The wall velocity is proportional to $(\partial_t \eta)^{n}_{i,0}$, and the new wall positions are found by time integration of the wall velocities. It was found to be computationally efficient to under-relax the wall movement calculation with an under-relaxation factor of 0.010 and to update the wall movement only every 50 time steps of the direct solver.

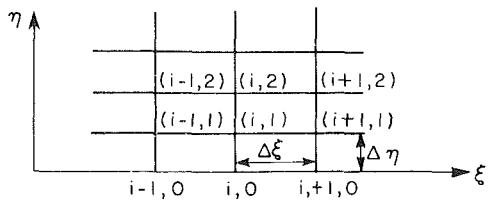

Fig. 3 Computational space grid definition

Constraints. In an axial compressor design, the blade profile shapes are nearly the last design element to be specified. The blade shapes must then satisfy several geometric and nongeometric constraints. Typically the blade chord, the number of blades, the blade row inflow angle, and the desired static pressure rise will be specified before blade shapes are decided. In addition, geometric constraints like trailing edge closure, maximum or minimum blade thickness or prescribed leading edge radius or wedge angle must also be satisfied.

The proposed inverse technique allows these types of constraints to be satisfied with little difficulty. Most nongeometric constraints are satisfied through selection of far-field boundary conditions or control of the grid generation process. Specific geometric constraints are satisfied by using the wall compatability pressure rather than a design pressure when either a section of the blade shape is to be specified or the computed blade shape would violate the constraint. For example, the blade trailing edge is always specified to be closed, and thus the pressure at this point may not be specified.

Special Boundary Conditions. The two-dimensional cascade problem requires far-field boundary conditions, flow periodicity conditions, and a Kutta condition as well as the hard wall boundary conditions. The far-field inflow condition maintains a specified value of stagnation pressure, stagnation temperature, and inlet flow angle. The inlet velocity is calculated using a method of characteristics analysis similar to that of Gopalakrishnan [10]. The far-field exit velocity is calculated using a similar model but with the exit static pressure specified. A Kutta condition is imposed by requiring that the static pressure at the last grid point on the blades be equal on the suction and pressure surfaces. Periodic flow conditions are specified upstream and downstream of the blade row.

Results and Discussion

Direct Solver Test Case. The inverse technique requires an accurate direct solution procedure to be available and the scheme chosen for development calculations is that of MacCormack [8]. This scheme is an explicit, second-order accurate, time-marching scheme of shock capturing type. The cascade geometries chosen for development testing were sharp leading blade sections typical for moderately supersonic inflow, M_{in} approximately 1.55. A typical flow solution calculated for a row static pressure ratio of 2.5 is shown in Fig. 4 in terms of Mach number contour levels. Of special note here is the upstream extent of the bow wave shock system and the strong passage shock. The flow is subsonic behind the passage shock. Static pressure profiles on the suction surface and pressure surface are shown in Fig. 5. The passage shock on the suction surface is resolved over 5 to 6 mesh points.

Inverse Technique Example Solution. In order to verify that the inverse technique can be used to construct a blade row

Downloaded 01 Jun 2010 to 171.66.16.62. Redistribution subject to ASME license or copyright; see http://www.asme.org/terms/Terms_Use.cfm

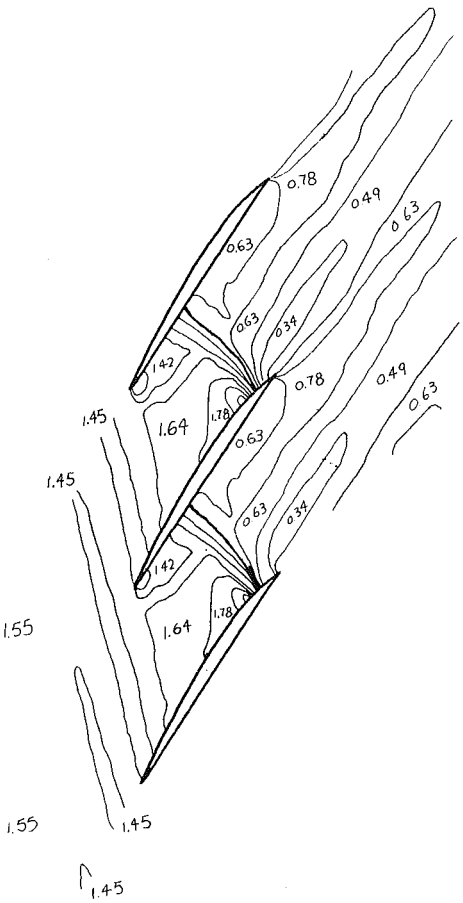

Fig. 4 Typical compressor cascade Mach number distribution

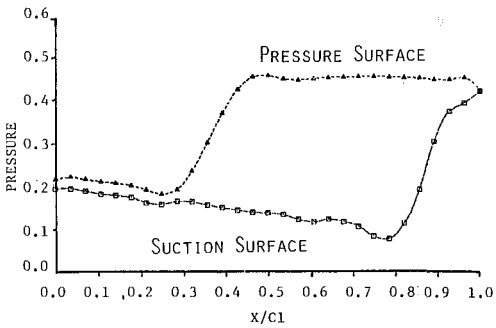

Fig. 5 Typical blade pressure distribution for inlet Mach number of 1.55

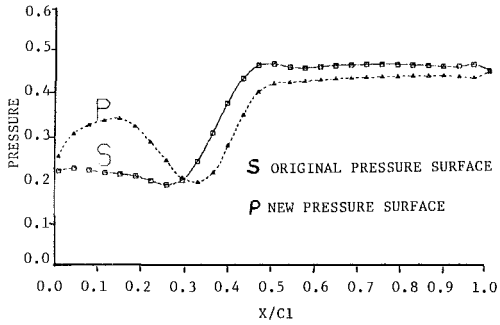

Fig. 6 Improved blade pressure distribution to reduce suction surface Mach number

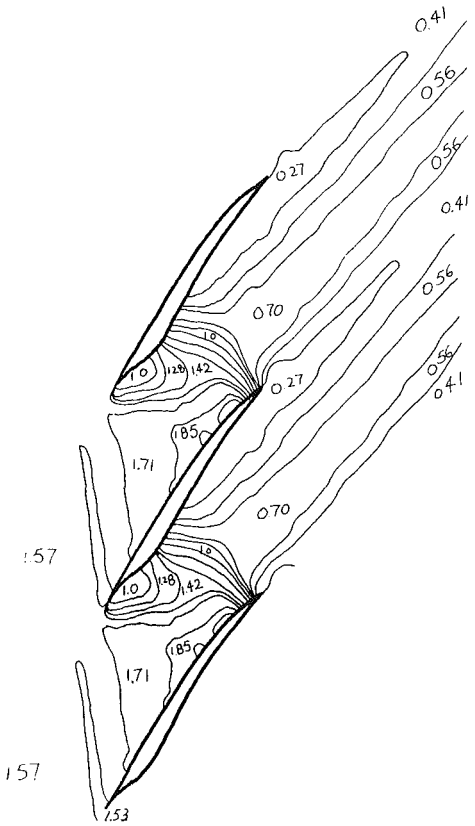

Fig. 7 Mach number distribution and blade shape as predicted by inverse technique

geometry, at least under the best conditions, the direct solver pressure distribution illustrated in Fig. 5 was used as design input. The technique should accurately reproduce the original geometry from a variety of assumed initial geometries. Solutions were found to converge as long as the calculation was begun from a converged direct solver flow solution for the initial geometry. Convergence for this special test case proves little of a general nature, but on the other hand, the instability to recompute the original geometry would be a disastrous failure.

A more interesting test example would be to construct a new blade geometry which has for approximately the same inflow and outflow conditions a different surface pressure distribution. Examination of Figs. 4 and 5 illustrates that such a problem statement occurs naturally in blade row design as the maximum suction surface Mach number in front of the passage shock is well above the upstream Mach number, nearly 1.8 for an inlet value of 1.55. In order to make the comparison of the inverse solution and the original solution as direct as possible, the far-upstream flow angle and the downstream static pressure of the direct solver example were retained. If the far-upstream Mach number is also to remain nearly the same, the suction surface geometry up to the first captured Mach wave must remain the same. For simplicity, the entire original suction surface geometry was retained. Intuitively, it was felt that an increased leading edge wedge angle would reduce the maximum suction surface Mach number, and a new pressure distribution on the blade pressure surface consistent with this assumption was selected. The new and old pressure distributions are shown in Fig. 6.

Figure 7 illustrates the computed blade geometry and Mach number contours, while Fig. 8 shows the new blade pressure distribution. The maximum suction surface Mach number was reduced from 2.06 to 1.94, while the far-upstream Mach number was increased from 1.52 to 1.57. The flow turning for the new design is 11.3 deg and is 8.0 deg for the old solution. The blade row total pressure ratio is decreased from 0.59 to 0.55. The new blade shape produces higher total pressure loss for the same static pressure rise by combining a stronger

Downloaded 01 Jun 2010 to 171.66.16.62. Redistribution subject to ASME license or copyright; see http://www.asme.org/terms/Terms_Use.cfm

initial compression with a weaker passage shock, but with larger turning.

This blade shape calculation illustrates that an inverse technique for inviscid, compressible flows can be developed. The present inverse scheme is primarily designed to demonstrate that blade geometries and flow solutions can be constructed from specifications of blade surface pressures plus geometric constraints. While the present technique was not originally intended to be used as a blade design system, it can be used in its present form as a method to refine blade row designs. If, for example, a blade row or blade section has been designed, then blade chord lengths, blade spacings, and desired flow angles are already known as well as an initial geometry guess. If the computed blade pressures (using the direct solver available) are not satisfactory, this inverse technique may be used as in the previous example to compute new blade geometries with improved pressure distributions.

This mode is not likely to be the most useful mode for inverse schemes to operate in, nor is this the only mode in which the present scheme may operate. If inverse schemes have any practical utility, it is in the belief that specification of blade pressure distributions is a more general way to describe blade row families than mean camber line families plus thickness distributions. The geometric constraints imposed or relied on in the inverse scheme (chord length and blade spacing) become parameters to be varied. Thus inverse techniques can be viewed as a tool to generalize the search for optimum configurations rather than as just a tool to refine existing designs.

An important feature of this inverse formulation is the possible extension to three-dimensional flow fields. This extension is one goal of the present research effort, since a two-dimensional technique is felt to be of marginal utility. The extension is based on the fact that the Strong Conservation Law Form of the three-dimensional, Navier-Stokes or Euler equations is identical to the two-dimensional forms. The three-dimensional form is:

$$\partial_t \hat{\bar{q}} + \partial_\xi \hat{\bar{F}} + \partial_\eta \hat{\bar{G}} + \partial_\zeta \hat{\bar{H}} = 0 \tag{16}$$

where

$$\hat{\bar{q}} = \bar{q}/J$$

$$\hat{\bar{F}} = [(\partial_t \xi)\bar{q} + (\partial_x \xi)\bar{F} + (\partial_y \xi)\bar{G} + (\partial_Z \xi)\bar{H}]/J$$

$$\hat{\bar{G}} = [(\partial_t \eta)\bar{q} + (\partial_x \eta)\bar{F} + (\partial_y \eta)\bar{G} + (\partial_X \xi)\bar{H}]/J$$

$$\hat{\bar{H}} = [(\partial_t \zeta)\bar{q} + (\partial_x \zeta)\bar{F} + (\partial_y \zeta)\bar{G} + (\partial_Z \zeta)\bar{H}]/J$$

J is the Jacobian of the transformation

$$\xi = \xi(x,y,z,t) \quad , \quad \eta = \eta(x,y,z,t) \quad ,$$
$$\zeta = \zeta(x,y,z,t) \quad , \quad t = t \tag{17}$$

The flux vectors retain the same general form:

$$\bar{G} = \begin{bmatrix} \rho V \\ \rho u V + (\partial_x \eta) P \\ \rho v V + (\partial_y \eta) P \\ \rho w V + (\partial_Z \eta) P \end{bmatrix} \tag{18}$$

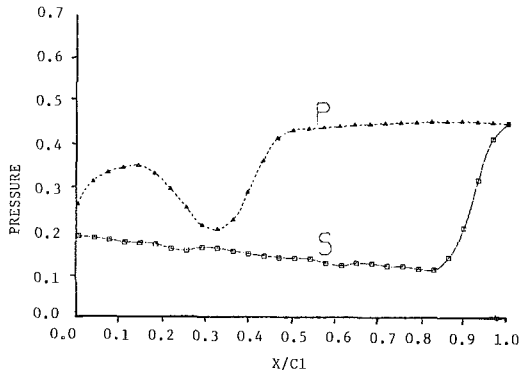

Fig. 8 Blade pressure distribution using predicted blade shape as input to direct solver

where

$$V = (\partial_t \eta) + (\partial_x \eta)u + (\partial_y \eta)v + (\partial_Z \eta)w$$

The flow tangency condition is still $V = 0$, and the same general analysis of the interior node calculation problem will apply.

A three-dimensional inverse technique would be expected to require the same type of wall pressure information and follow closely the development of the two-dimensional version. General experience with three-dimensional solvers suggests that the practical extension to a three-dimensional inverse solver will not be a simple process.

Acknowledgments

This research was supported by Air Force Office of Scientific Research under contract number F49620-78-C-0084, supervised by James D. Wilson.

References

1 Bauer, F., Garabedian, P., and Korn, D., "Supercritical Wing Section III," *Lecture Notes in Economics and Mathematical Systems*, Vol. 150, Springer-Verlage, New York, 1977.

2 Ives, D. C. and Liutermozu, J. L., "Analysis of Transonic Cascade Flow Using Conformal Mapping and Relaxation Technique," *AIAA Journal*, Vol. 15, May 1977, pp. 647-752.

3 Stephens, H. E., "Supercritical Airfoil Technology in Compressor Cascades: Comparison of Theoretical and Experimental Results," *AIAA Journal*, Vol. 17, June 1979, pp. 594-600.

4 Zannetti, L., "Time-Dependent Method to Solve the Inverse Problem for Internal Flows," *AIAA Journal*, Vol. 18, July 1980, pp. 754-758.

5 Haymann-Haber, G. and Thompkins, W. T., "Comparison of Experimental and Computation Shock Structure in a Transonic Compressor Rotor," ASME paper No. 80-GT-81 (to appear in ASME JOURNAL OF ENGINEERING FOR POWER).

6 Steger, J. L., "Implicit Finite-Difference Simulation of Flow about Arbitrary Two-Dimensional Geometries," *AIAA Journal*, Vol. 16, July 1978, pp. 679-686.

7 Viviand, H., "Conservative Forms of Gas Dynamic Equations," *La Recherche Aerospatiale*, No. 1, Jan.-Feb. 1974, pp. 65-68.

8 MacCormack, R. W., "Computational Efficiency Achieved by Time Splitting of Finite Difference Operators," AIAA Paper No. 72-154.

9 Beam, R. M. and Warming, R. F., "An Implicit Factor Scheme for the Compressible Navier-Stokes Equation," *AIAA Journal*, Vol. 16, April 1978, pp. 393-402.

10 Gopalakrishnan, S. and Bozzola, R., "Numerical Representation of Inlet and Exit Boundary Conditions in Transient Cascade Flow," ASME Paper No. 73-GT-55, 1973.

Downloaded 01 Jun 2010 to 171.66.16.62. Redistribution subject to ASME license or copyright; see http://www.asme.org/terms/Terms_Use.cfm

Interactive Multimode Blade Impact Analysis

A. Alexander
Staff Engineer,
Hercules Incorporated,
Allegany Ballistics Laboratory,
Cumberland, Md.

This paper describes the theoretical methodology used in developing an analysis for the response of turbine engine fan blades subjected to soft body (bird) impacts and the computer program that was developed using this methodology as its basis. This computer program is an outgrowth of two programs that were previously developed for the purpose of studying problems of a similar nature (a three-mode beam impact analysis and a multimode beam impact analysis). The present program utilizes an improved missile model that is interactively coupled with blade motion which is more consistent with actual observations. It takes into account local deformation at the impact area, blade camber effects, and the spreading of the impacted missile mass on the blade surface. In addition, it accommodates plate-type mode shapes. The analysis capability in this computer program represents a significant improvement in the development of the methodology for evaluating potential fan blade materials and designs with regard to foreign object impact resistance.

Introduction

The availability of an accurate and reliable method for the impact analysis of aircraft engine fan blades can play a major part in designing these blades for foreign object damage (FOD) resistance and in assessing new materials for blade applications. The Multimode Blade Impact (MMBI) computer program [1] described below provides the designer with a tool that enables him to study the transient effects of soft body impacts on blades exhibiting characteristic coupled modes of vibration. The major features include a consistent missile model; the ability to account for the spreading impacted missile mass with respect to time; and the calculation of deformations, pressure distribution, and stresses at the impact region of the blade, as well as over the entire blade.

The analysis is based upon a theoretical and experimental analysis of incident two-dimensional and three-dimensional fluid jets combined with the methods of modal response analysis. Included in the methodology are the initial and ending effects of the missile forward and aft shape, the pressure variations due to the blade surface curvature, and the local perturbations on the relative impact angle and velocity due to blade response. The solution for the blade response during each time step interval is obtained from a closed form solution of the uncoupled modal equations of the system, the results of the previous time step being used as initial conditions.

Missile and Blade Geometry

Two geometric reference systems are used to develop the problem geometry. In mapping the distributed impacted missile mass on the blade face, the three-dimensional surface of the face is developed onto a flat plane (Fig. 1). During each time step, the center of impact and stagnation pressure point are located on this planform representation of the blade face, and the spreading missile mass is mapped out relative to these two points.

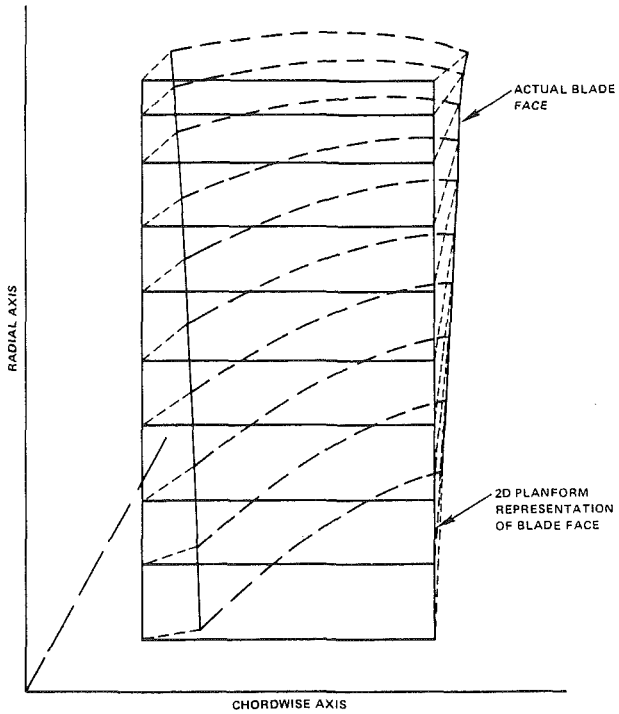

Fig. 1 Blade face mapped out on planform plane

Contributed by the Gas Turbine Division of THE AMERICAN SOCIETY OF MECHANICAL ENGINEERS and presented at the Gas Turbine Conference and Products Show, March 9-12, 1981, Houston, Texas. Manuscript received at ASME Headquarters December 11, 1980. Paper No. 81-GT-79.

Copyright © 1982 by ASME

Downloaded 01 Jun 2010 to 171.66.16.62. Redistribution subject to ASME license or copyright; see http://www.asme.org/terms/Terms_Use.cfm

The chordwise contour of the blade face at the impact radial station is represented in a reference system which lies in a plane whose normal is parallel to the blade axis and such that the blade axis of rotation lies parallel to the ordinate axis and the plane of rotation lies parallel to the absissa (Fig. 2). Within this in-plane/out-of-plane (IP/OOP) system, with instantaneous positions of missile and blade, the location, angle and velocity of impact, and the length of unimpacted missile remaining at any instant during the impact event are determined.

Missile Model

A general conceptualization of the missile model is illustrated in Figs. 3 and 4. In essence, the missile is conceived as built-up of a number of two-dimensional and three-dimensional fluid jet layers which approximate the general shape of the body. During impact, the pressure distribution and deflected thickness distribution on the blade face are calculated for each layer separately, with the central portion having a stream form representative of a two-dimensional jet (Fig. 5) and the outer extremities being treated as half of a three-dimensional jet (Fig. 6).

The governing equations used in calculating the pressure, velocity and deflected thickness distributions are based on the work of Von W. Schach [2, 3] pertaining to the study of the two-dimensional oblique impacting jet and the three-dimensional cylindrical oblique impacting jet. From this work, approximate analyses were developed which agreed well with the available test data.

Figure 7 summarizes Schach's expressions for calculating the pressure and velocity distribution, and the locations of center of force and stagnation pressure for a two-dimensional jet missile. For very small impingement angles α_0, which are

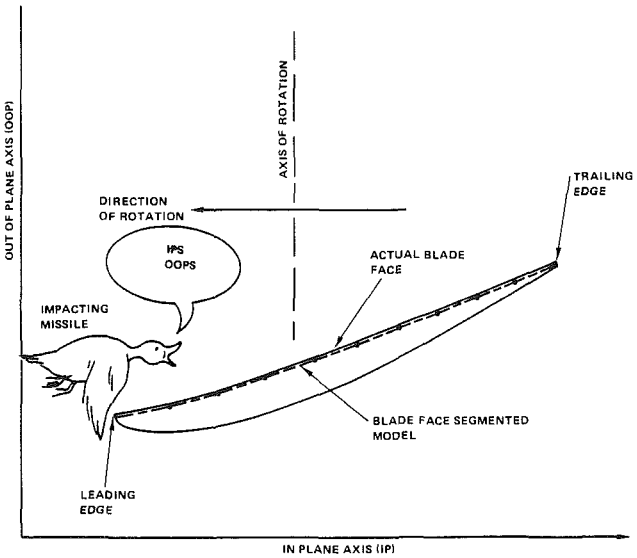

Fig. 2 Blade cross section in IP/OOP frame

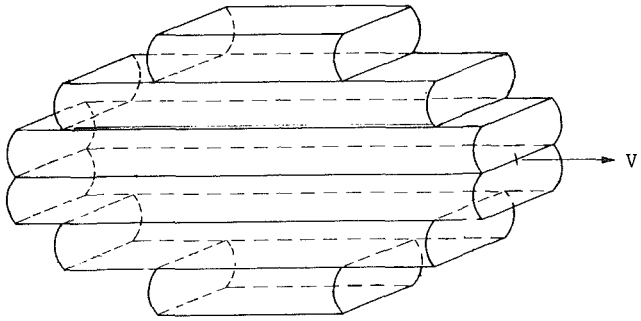

Fig. 3 Missile definition

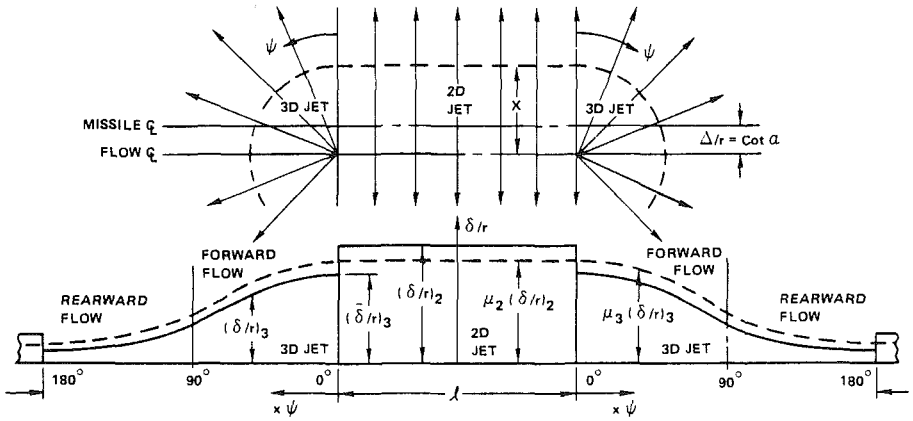

Fig. 4 General, symmetrical jet missile

Nomenclature

L = total impact force
V = missile and flow velocity
V_0 = initial impact velocity
P = pressure
P_i = generalized forcing function for the ith mode
P_0 = stagnation pressure
a = thickness of missile
e = location of force from jet centerline
f = location of stagnation pressure from force
g = location of stagnation pressure from jet centerline
m_i = ith modal mass
q_i = ith generalized modal coordinate
x,r = distance from flow center measured in direction of flow
α = impact angle
α_0 = initial impact angle
β_i = critical damping constant for the ith mode
δ = deflected missile thickness
λ = pressure decay constant
ρ = mass density of missile
ω = damped natural frequency
ω_i = characteristic natural frequency of the ith mode

Downloaded 01 Jun 2010 to 171.66.16.62. Redistribution subject to ASME license or copyright; see http://www.asme.org/terms/Terms_Use.cfm

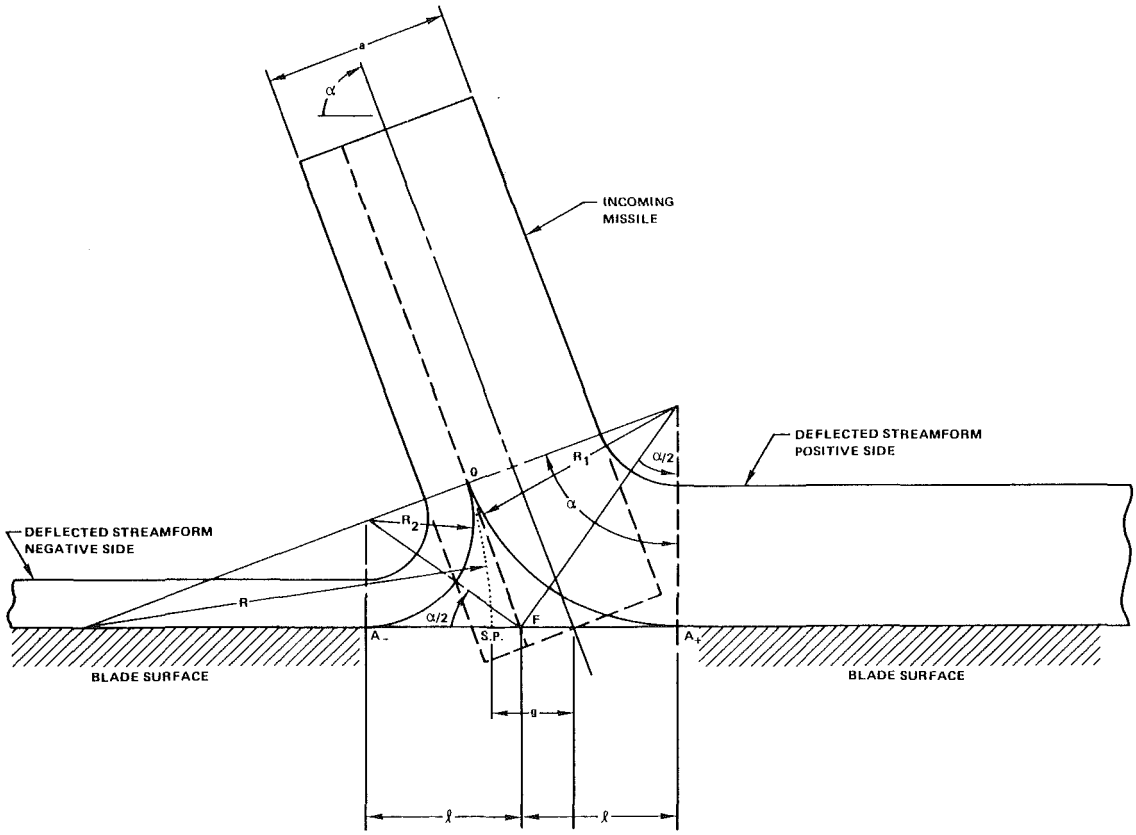

Fig. 5 Two-dimensional jet missile

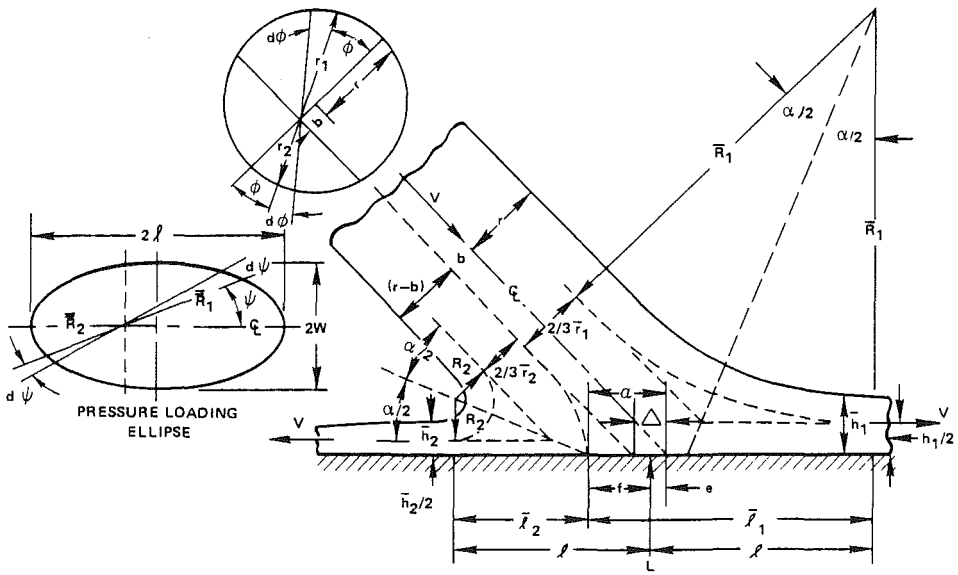

Fig. 6 Three-dimensional jet missile

of prime importance, Schach's solution places the location of the stagnation pressure point outside of the jet envelope. Because of this apparent deficiency, an approximate model was developed, which satisfied all the hydrodynamic load and moment criteria, but placed the stagnation pressure location at the edge of the jet for small impingement angles. The basis of the approximation lies in the assumption that the velocity distribution can be represented by the expression

$$V/V_0 = 1 - e^{-x/\lambda}, \tag{1}$$

where λ is a decay coefficient determined by evaluating the force and its position on the impacted surface, recognizing that the pressure distributions are based on the stagnation point. Since the pressure along the impacted surface is

$$P/P_0 = [1 - (V/V_0)^2], \tag{2}$$

the resulting pressure distribution will have the form

$$P/P_0 = e^{-x/\lambda}(2 - e^{-x/\lambda}) \tag{3}$$

Using this expression for calculating the total impact force and its location relative to the stagnation pressure results in expressions for the decay coefficients in the forward and

Downloaded 01 Jun 2010 to 171.66.16.62. Redistribution subject to ASME license or copyright; see http://www.asme.org/terms/Terms_Use.cfm

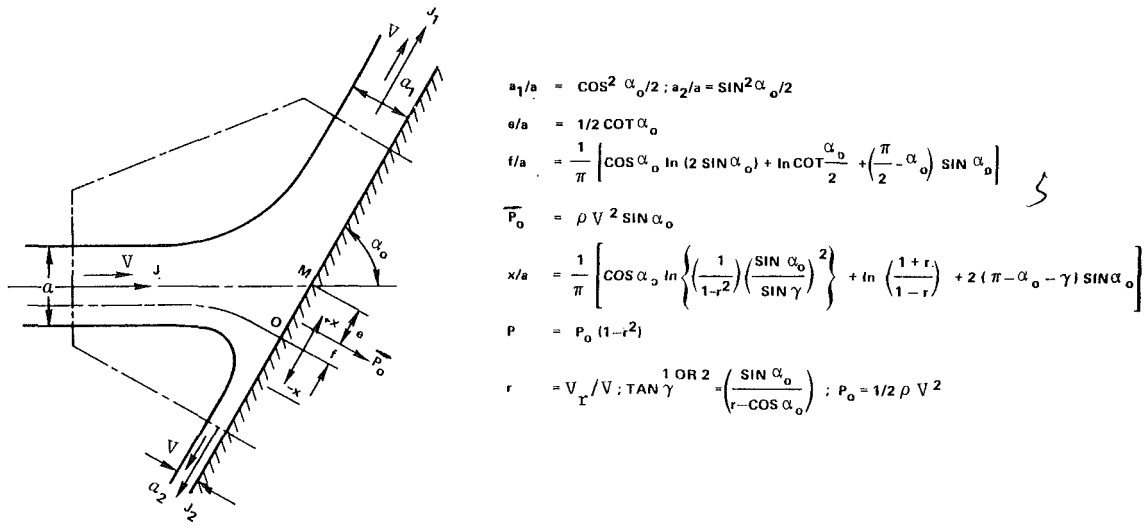

Fig. 7 Two-dimensional jet missile - Schach

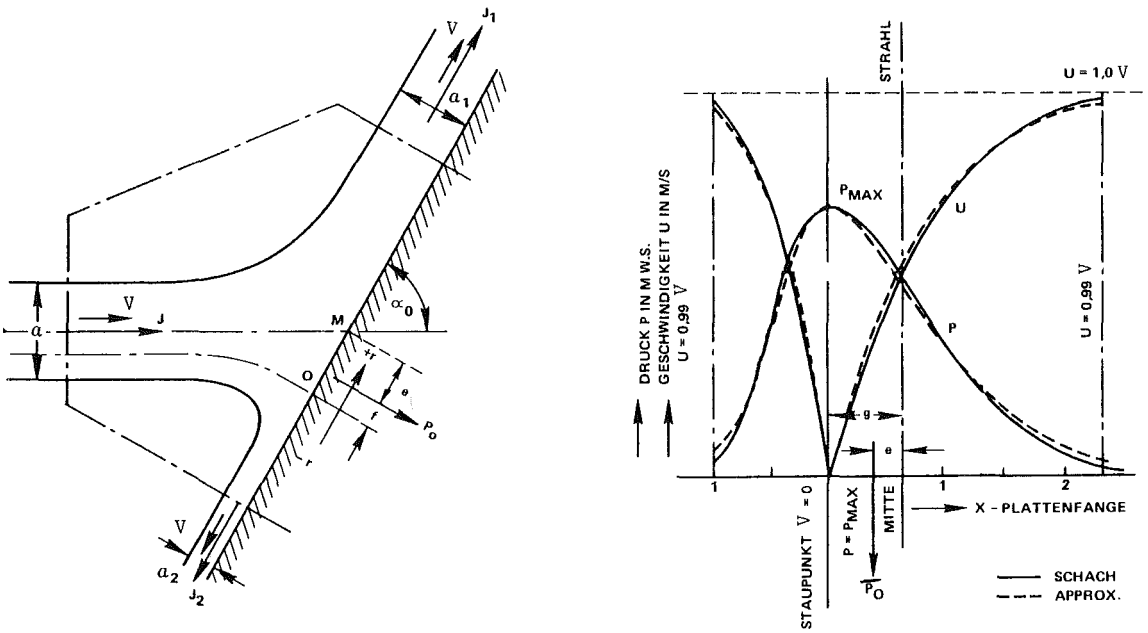

Fig. 8 Pressure and velocity distributions for 60 deg impingement of two-dimensional jet - Schach and approximation

rearward sides of the flow split respectively, i.e.

$$\lambda_1 = \frac{2a}{3}\sin\alpha + \frac{3}{7}f \tag{4}$$

and

$$\lambda_2 = \frac{2a}{3}\sin\alpha - \frac{3}{7}f \tag{5}$$

From evaluation of the test and analysis results in reference [3], it was found that f, the location of the center of force relative to the stagnation pressure, can be approximated with sufficient accuracy from

$$f/a = \frac{14}{9}\left(1 - \frac{2\alpha}{\pi}\right)\sin\alpha \tag{6}$$

This results in the following expressions for the decay coefficients

$$\lambda_1 = \frac{4}{3}\left(1 - \frac{\alpha}{\pi}\right)\sin\alpha \tag{7}$$

and

$$\lambda_2 = \frac{4}{3}\left(\frac{\alpha}{\pi}\right)\sin\alpha \tag{8}$$

Figures 8 and 9 compare the pressure and velocity distributions given by Schach's solution and the exponential approximation for 60 deg and 15 deg impingement angles, respectively. At the higher impact angle, the correlation is excellent while for the lower angle there is reasonable correlation except for the location of stagnation pressure.

As there appeared to be no general solution for a three-dimensional cylindrical oblique impacting jet, an approximate analysis for the general case of a cylindrical jet obliquely impinging on a flat plate was developed on the basis of the concepts and test results reported by Schach and on his solution for a 90 deg impingement of a cylindrical missile. The approximate analysis assumes that the fluid in the impacting jet is split into and remains in radial sectors after being deflected by the plate. This was found to correlate very well with test results [2].

Downloaded 01 Jun 2010 to 171.66.16.62. Redistribution subject to ASME license or copyright; see http://www.asme.org/terms/Terms_Use.cfm

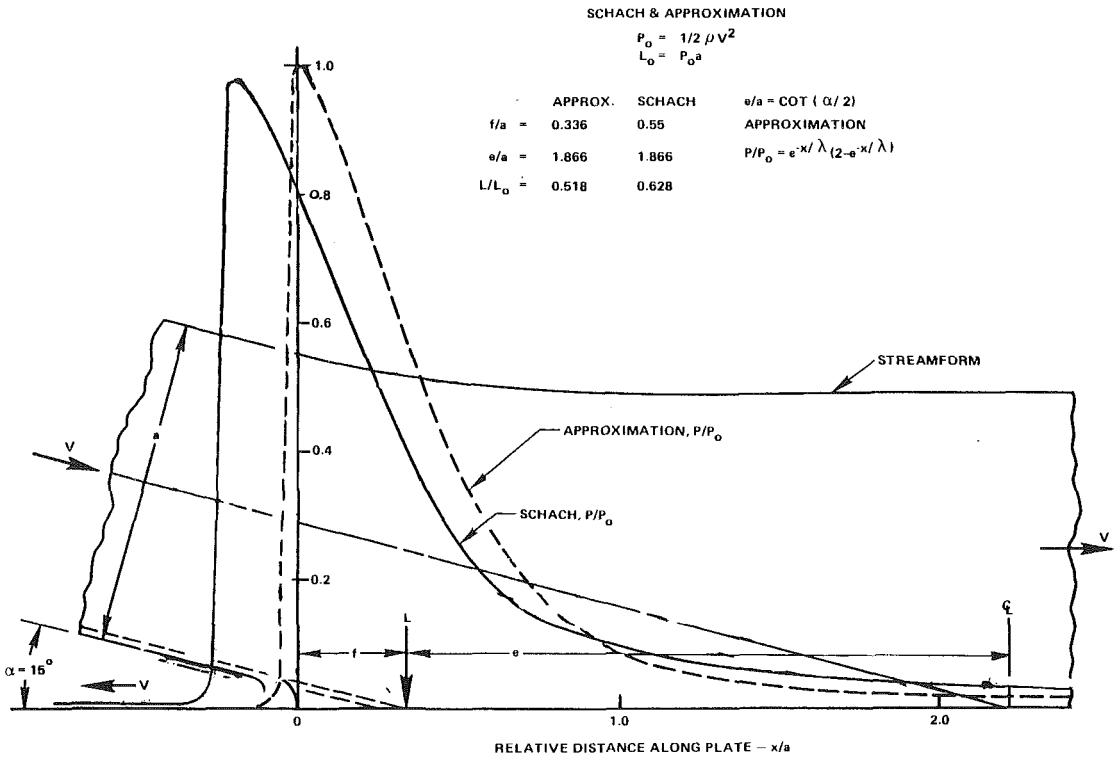

Fig. 9 Pressure distributions for 15 deg, two-dimensional jet - Schach and Approximation

It was further assumed that the velocity distribution can be represented by the expression

$$V/V_0 = [1 - e^{-(x/\lambda)^2}] \tag{9}$$

where x is the radial distance from the stagnation point and λ is a decay parameter that is a function of $\cos\psi$; see Fig. 6. The resulting pressure distribution is given by the expression [1]

$$P/P_0 = 1 - (V/V_0)^2 = e^{-(x/\lambda)^2}[2 - e^{-(x/\lambda)^2}] \tag{10}$$

These expressions were found to fit the experimental data quite well, as illustrated in Fig. 10, reprinted from reference [2], and Fig. 11.

The expressions for the decay parameter, λ, and the location of the center of force were determined by imposing constraints for the normal force and the moment equilibrium on the plate. The results, which are derived in reference [1], are for the decay parameter

$$\lambda^2 = \frac{4}{3} x^2 \sin^3\alpha \sqrt{\frac{(1+\cos\psi\cos\alpha)}{(1-\cos\psi\cos\alpha)^3}} \tag{11}$$

and for the positions of the load from the stagnation point and jet centerline

$$g/r = \frac{8\cot\alpha}{3\pi} \text{ and } e/r = \frac{(8\cot(\alpha))/3\pi}{1+\sqrt{\sin\alpha}} \tag{12}$$

These expressions for g/r and e/r were found to correlate with test data very well; see Fig. 12. The value of f/r is obtained from

$$f/r = g/r - e/r \tag{13}$$

Although missiles impacting blades are of arbitrary shape, they can be usually depicted approximatley as either an ellipsoid or cylinder. However, because of the impacting angle, the finite length, and the orientation of the missile with respect to the impacted airfoil surface of the blade, the simple three-dimensional jet model given above cannot be used directly to represent the missile. Instead the missile must be approximated by a combination of a two-dimensional jet and a three-dimensional jet. For the MMBI analysis, the impacting section of the missile is assumed to consist of a two-dimensional jet in the center bounded by halves of a three-dimensional jet; see Fig. 13. As the front of the missile progressively impinges on the airfoil, the impacting area and shape progressively changes. For a cylindrical missile, the approximation given in Fig. 13 degenerates to a cylinder once the end effect is passed.

The location of the impact force and stagnation centers are assumed to be the weighted average of those for the two-dimensional and three-dimensional jets making up the particular cross sections. The resulting pressure loading and squashing thickness distributions are modified values of the corresponding two-dimensional and three-dimensional jet results, so that there is no discontinuity between the two. The former is done on an incremental load basis, whereas the latter is done on an incremental fluid area basis. Table 1 summarizes the expressions for defining the general jet missile based on those for the two-dimensional and three-dimensional jet missiles [1].

The spreading of the missile mass upon the blade surface is modeled as the expanding oval shown in Fig. 4. As the missile continues to impact upon the blade, the oval expands at a rate equal to the impact velocity. When the aft end of the missile reaches the impacted surface, a void appears and the mass subsequently spreads as an oval ring [1].

Modal Response of the Blade

To calculate the response of the blade during the impact event, a discrete point model of the blade surface is used, with associated characteristic mode shapes, ϕ_i, modal frequencies, ω_i, and modal masses, m_i. By determining the pressure distributions over the blade surface at a particular instant

Downloaded 01 Jun 2010 to 171.66.16.62. Redistribution subject to ASME license or copyright; see http://www.asme.org/terms/Terms_Use.cfm

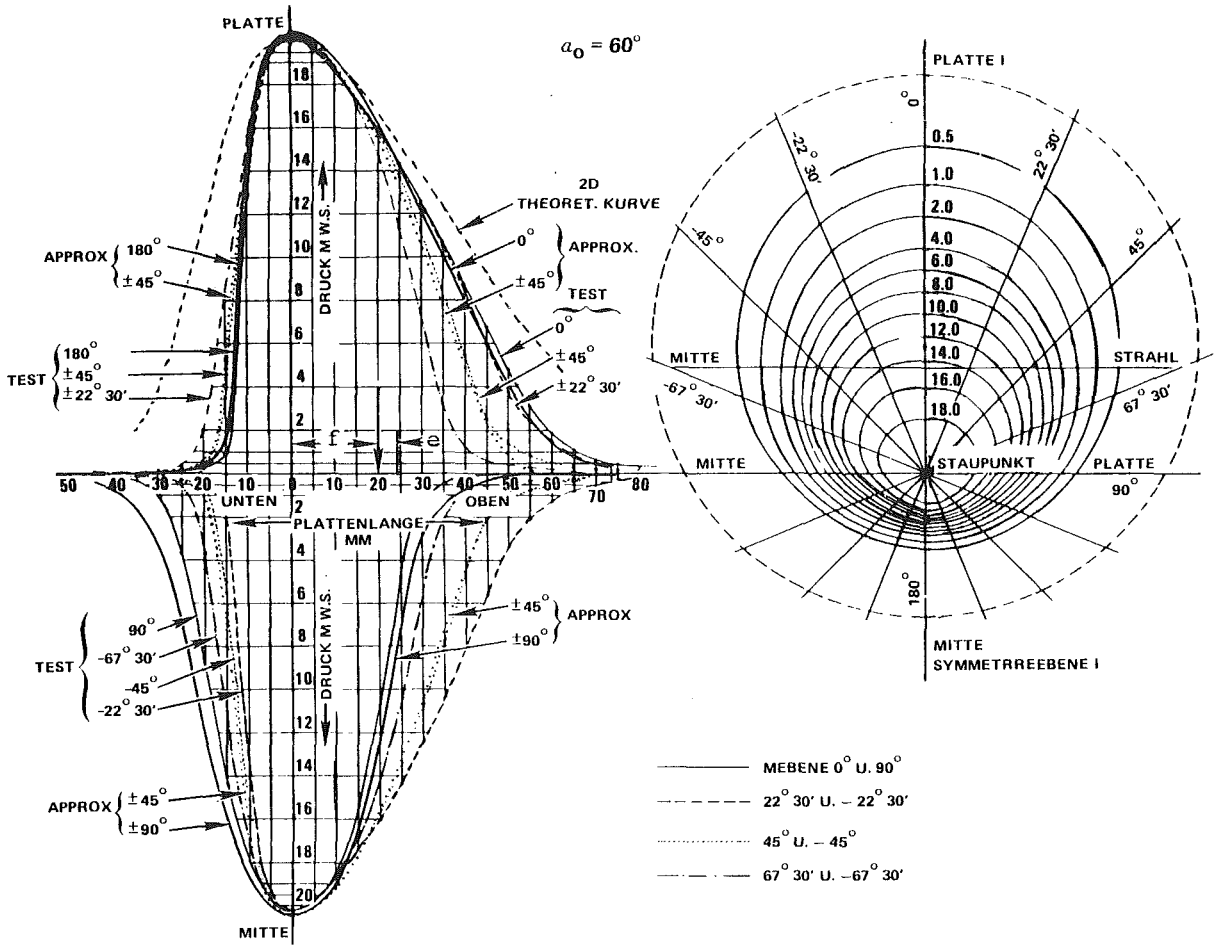

Fig. 10 Pressure distribution for 60 deg, three-dimensional jet - Schach, Approximation and Test

during the impact event, and integrating around the discrete area associated with each physical point, the generalized force, P_i, associated with each mode is calculated and used in the uncoupled modal equations of motion as

$$\ddot{q}_i + 2\beta_i \dot{q}_i + \omega_i{}^2 q_i = \frac{1}{m_i} P_i \tag{14}$$

where q_i, $\dot{q}_i$ and $\ddot{q}_i$ are respectively, the generalized coordinate, velocity and acceleration of the ith mode. Also

$$\beta_i = \frac{b_i}{2m_i} \text{ and } \omega_i = \frac{k_i}{m_i} \tag{15}$$

with b_i being the ith modal damping coefficient and k_i being the ith modal stiffness. Assuming that over a small number of short discrete time intervals during the impact event the general force P_i can be considered as linearly varying in time, and that during a particular time interval the load is constant, the solution for the generalized coordinate and velocity at the end of the time interval is

$$q_{i,(n+1)} = F_{q_{i,n}} + G\dot{q}_{i,n} + \bar{A}P_{i,n} \tag{16}$$

and

$$\dot{q}_{i,(n+1)} = F' q_{i,n} + G' \dot{q}_{i,n} + \bar{B}P_{i,n} \tag{17}$$

where

$$F = e^{-\beta_i \tau}[\cos\omega\tau + (\beta_i/\omega)\sin\omega\tau] \tag{18}$$

$$G = \frac{1}{\omega} e^{-\beta_i \tau} \sin\omega\tau \tag{19}$$

$$F' = \frac{\omega_i{}^2}{\omega} e^{-\beta_i \tau} \sin\omega\tau \tag{20}$$

$$G' = e^{-\beta_i \tau}[\cos\omega\tau - (\beta_i/\omega)\sin\omega\tau] \tag{21}$$

$$\bar{A} = \frac{-1}{k_i \omega_i}[e^{-\beta_i \tau}(\beta_i \sin\omega\tau - \omega\cos\omega\tau) + \omega] \tag{22}$$

$$\bar{B} = \frac{1}{k_i \omega} e^{-\beta_i \tau}(\omega_i{}^2 \sin\omega\tau) \tag{23}$$

$$\omega^2 = \omega_i{}^2 - \beta_i{}^2 \tag{24}$$

where τ is the length of the time interval. Also, the generalized coordinate and velocity at the beginning of the time interval are given by

$$q_{i,n} = \bar{A}P_{i,n} \text{ and } \dot{q}_i = \bar{B}P_{i,n} \tag{25}$$

where $P_{i,n}$ is the value of the forcing function at the beginning of the time interval

The above solution is repeated in the MMBI analysis for each time step interval with the results of the previous time step interval as initial conditions. Thus, if at the start of a time interval the in-plane and out-of-plane coordinates of the points describing the blade are contained in the $2N$ vector

$$\{X_0\} = \begin{Bmatrix} X_1 X_2 X_3 \ldots\ldots X_N \\ Y_1 Y_2 Y_3 \ldots\ldots Y_N \end{Bmatrix} \tag{26}$$

then the coordinates at the end of the time period are given by

Downloaded 01 Jun 2010 to 171.66.16.62. Redistribution subject to ASME license or copyright; see http://www.asme.org/terms/Terms_Use.cfm

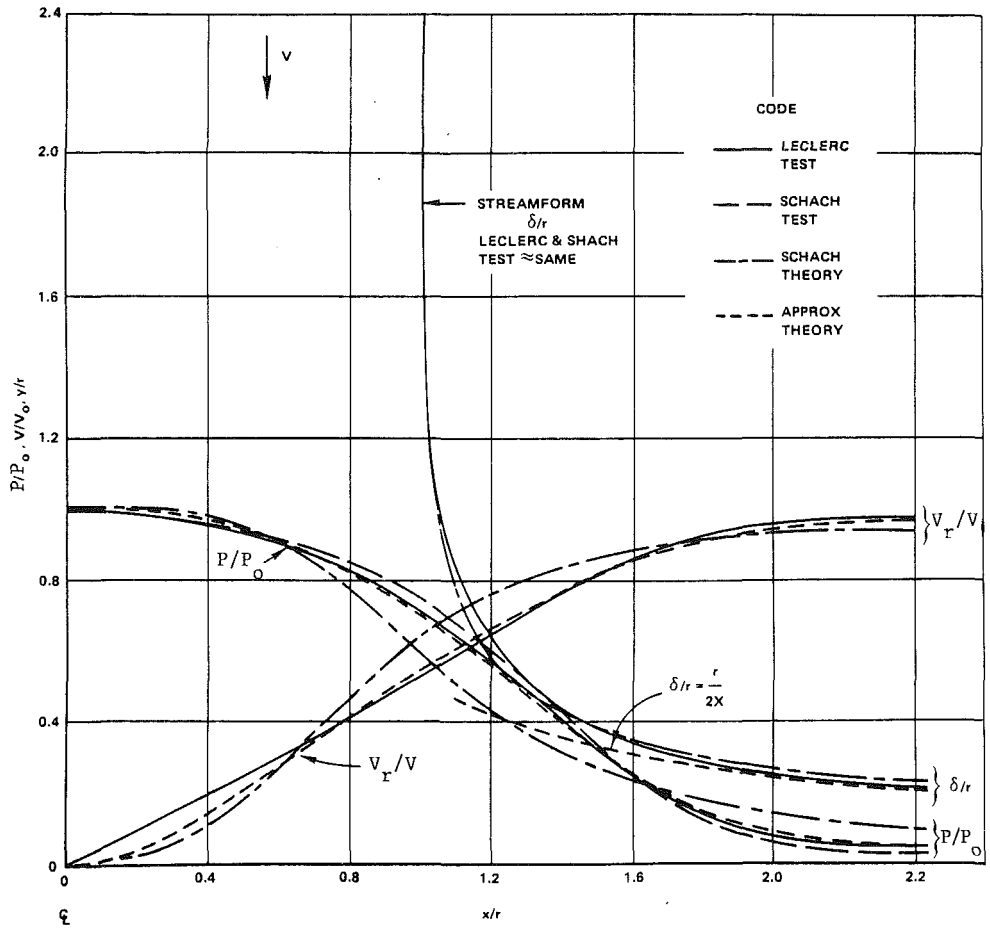

Fig. 11 Normal impingement of three-dimensional jet pressure, streamform and velocity distributions—theory and test

$$\{X\} = \{X_0\} + \sum_i q_{i,n} \{\theta\}_i \tag{27}$$

Throughout the duration of the impact analysis, the MMBI program determines the time step size such that continuity of the impact event and convergence to a solution are assured. The outputs available at the end of each time step include the instantaneous pressure distribution, gross blade displacements and stresses and local deformations and stresses on the blade surface at the impact area.

Application

Figures 14 and 15 present the calculated pressure distributions for impacts of cylindrically shaped missiles on flat rigid plates at incident angles of 45 deg and 90 deg, respectively. The calculated values are compared with measured data obtained from reference [4]. Generally, the measured data indicate a 0.75 in. shift toward the stagnation pressure point which is due to apparent misalignment of the center of impact on the target. The shape of the distributions, however, correlated quite well.

Presented in Fig. 16 is a plot of the calculated flatwise displacement response and the corresponding measured data for the impact on a test blade of a 3.75 in. dia, 1 lb gelatin sphere at a 30 deg incident angle with a velocity of 600 ft/s [1]. The blade consists of a rigid steel plate bolted onto a titanium spar between the 26-in. and 33.75-in. radial stations; see Fig. 17. The impact was at the 30-in. radius of the blade at a chordwise distance of 0.6 in. from the twist axis. Due to the lack of a good finite element plate model for the test blade, it was necessary to extrapolate the modal data from a beam analysis eigenvalue solution, using the first five modes. Since the plate is relatively rigid, it was felt that this approximation would not impose any gross errors in the displacement response of the blade.

The test data in Fig. 16 indicate the presence of higher mode contributions to the response of the blade; however, these contributions are minimal. With respect to the duration of the response and the general shape of the curve, the correlation between calculated and test results is very good. The peak displacement predicted by the MMBI program is within 6.7 percent of the test results.

Summary and Conclusions

In its present form, the MMBI analysis combines the effects of coupled modal response with the nonlinear loading developed by an impacting soft body missile. The calculations of pressure distribution, spreading of the impacted missile mass on the blade surface, and the general response of the blade are performed within acceptable accuracy. The program provides the designer with an efficient method for analyzing the response of blades subjected to soft body impacts at minimal cost. It, therefore, offers itself as a good tool for studying the resistance of aircraft engine fan to blades foreign object impact and in assessing new materials for blade applications.

Downloaded 01 Jun 2010 to 171.66.16.62. Redistribution subject to ASME license or copyright; see http://www.asme.org/terms/Terms_Use.cfm

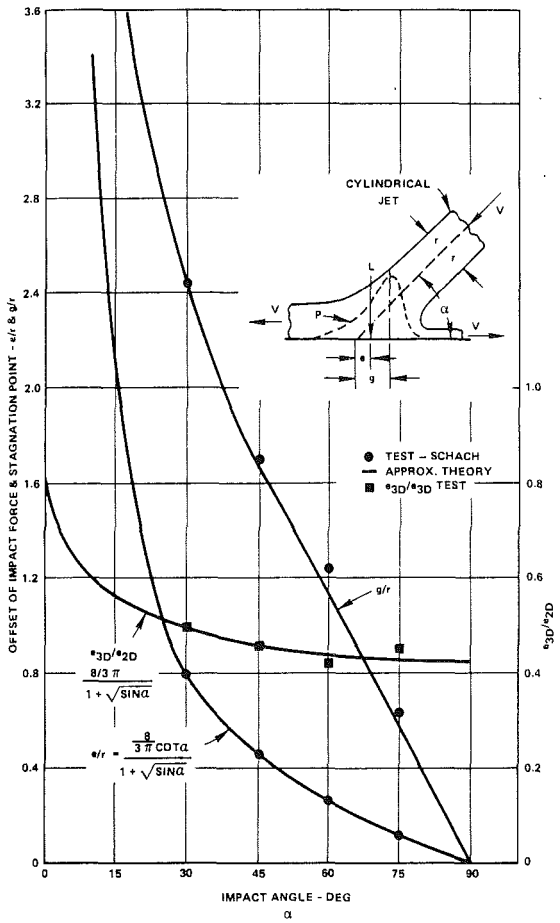

Fig. 12 Three-dimensional jet locations of impact force and stagnation point e/r and g/r

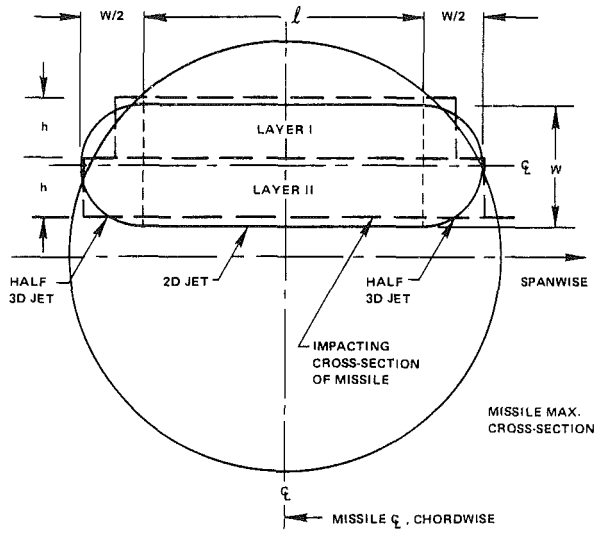

$W = 2h \text{ OR } mh_m$

$A_{sect} = A_3 + A_2 = \sum_{Impact} A_{Layers}$

$A_3 = \frac{\pi}{4} W^2$

$A_2 = \ell W$

m = NUMBER OF RECTANGULAR LAYERS h THICK SIMULATING MISSILE

Fig. 13 Approximation of general shaped missile from two-dimensional and three-dimensional jets

Table 1 Relationships for two-dimensional, three-dimensional and general symmetrical missile models

1. FORWARD FLOW AREA	$A^F_2 = \frac{wa}{2}(1+\cos\alpha)$	$A^F_3 = \frac{\pi a^2}{4}(1-\frac{\alpha}{\pi}+\frac{\sin 2\alpha}{2\pi})$	$\bar{A}^F = A^F_2 + A^F_3$
2. PRESSURE DISTRIBUTION $P_o = \frac{1}{2}\rho V_o^2$	$(P/P_o) = e^{-(x/\lambda)}\,[2-e^{-(x/\lambda)}]$	$(P/P_o)_3 = e^{-(x/\lambda)^2}\,[2-e^{-(x/\lambda)^2}]$	$\overline{P/P_o} = r_3\,(P/P_o)_3 + r_2\,(P/P_o)_2$ *
3. DECAY COEFFICIENTS	$\lambda_1/a = \frac{1}{3}(1-\frac{\alpha}{\pi})\sin\alpha$ $\lambda_2/a = \frac{\alpha}{3\pi}\sin\alpha$	$(\lambda/a)^2 = \frac{4}{3}\frac{\sin^3\alpha}{(1-\cos\psi\cos\alpha)^2}\sqrt{1-(\cos\psi\cos\alpha)^2}$	———
4. DEFLECTED THICKNESS	$(\delta/a)_2 = \frac{1}{2}(1\pm\cos\alpha)$	$(\delta/a)_3 = \frac{a}{2X}\left(\frac{\sin\alpha}{1-\cos\psi\cos\alpha}\right)^2\sin\alpha$	$(\bar{\delta}/a) = \mu_3\,(\delta/a)_3 + \mu_2\,(\delta/a)_2$ +
5. FORCE FROM JET ℄	$(e/a)_2 = \frac{1}{2}\cot\alpha$	$(e/a)_3 = \frac{4\cot\alpha}{3\pi(1+\sqrt{\sin\alpha})}$	$(\bar{e}/a) = \frac{A_2(e/a)_2 + A_3(e/a)_3}{A_2+A_3}$
6. STAG. PRESSURE FROM FORCE	$(f/a)_2 = \frac{14}{9}(1-\frac{2\alpha}{\pi})\sin\alpha$	$(f/a)_3 = \frac{2.3}{2}(1-\frac{2\alpha}{\pi})\,[1-(1-\frac{2\alpha}{\pi})^{27}] + \frac{0.1\sin 2\alpha}{2}$	———
7. STAG. PRESSURE FROM JET ℄	$(g/a)_2 = \frac{1}{2}[\cot\alpha + \frac{28}{9}(1-\frac{2\alpha}{\pi})\sin\alpha]$	$(g/a)_3 = (e/a)_3 + (f/a)_3$	$(\bar{g}/a) = \frac{(g/a)_3 A_3 + (g/a)_2 A_2}{A_3+A_2}$

* $r_2 = \frac{1+[wP_2/(dL/dX)_3]}{(P_2/P_3)+[wP_3/(dL/dX)_3]}$; $r_3 = \frac{1+[(dL/dX)_3/wP_2]}{(P_3/P_2)+[(dL/dX)_3/wP_2]}$

+ $\mu_2 = \frac{1+A_2/A_3}{[(\bar{\delta}/a)_2/(\bar{\delta}/a)_3]+A_2/A_3}$; $\mu_3 = \frac{1+A_3/A_2}{[(\bar{\delta}/a)_3/(\delta/a)_2]+A_3/A_2}$

NOTE: $\bar{P}_3$ & $\bar{\delta}_3$ ARE VALUES FOR $\psi = 0$

$(dL/dX)_3 \approx 2\int_0^{\pi/2} \times P_3\,d\,\psi$

Downloaded 01 Jun 2010 to 171.66.16.62. Redistribution subject to ASME license or copyright; see http://www.asme.org/terms/Terms_Use.cfm

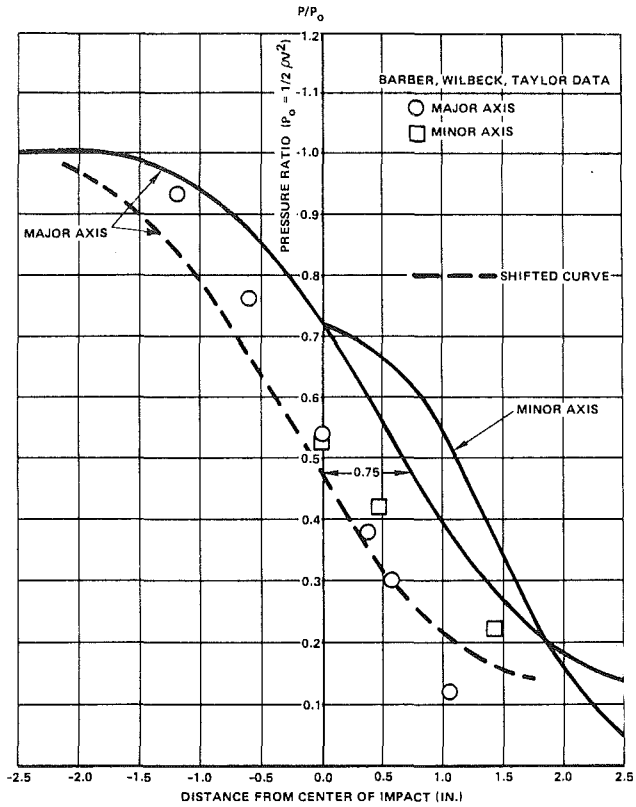

Fig. 14 Forty-five deg impact on rigid plate

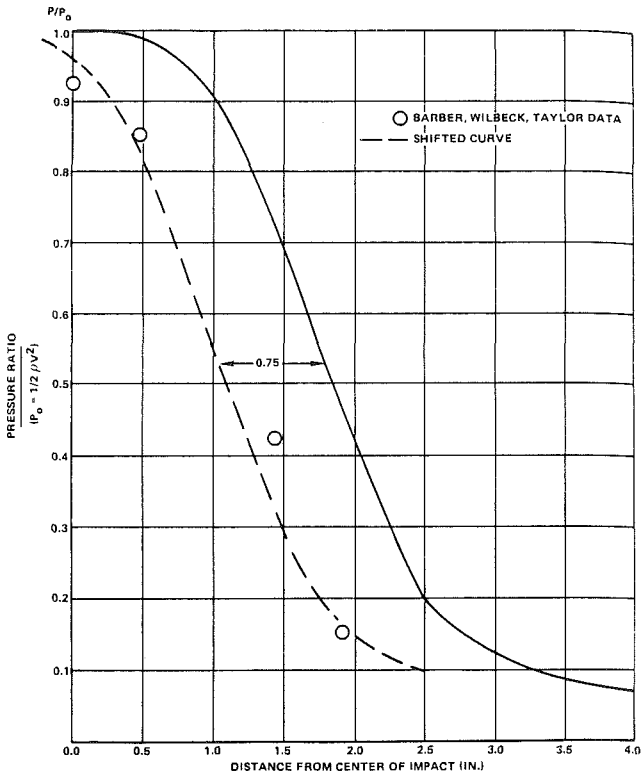

Fig. 15 Ninety deg impact on rigid plate

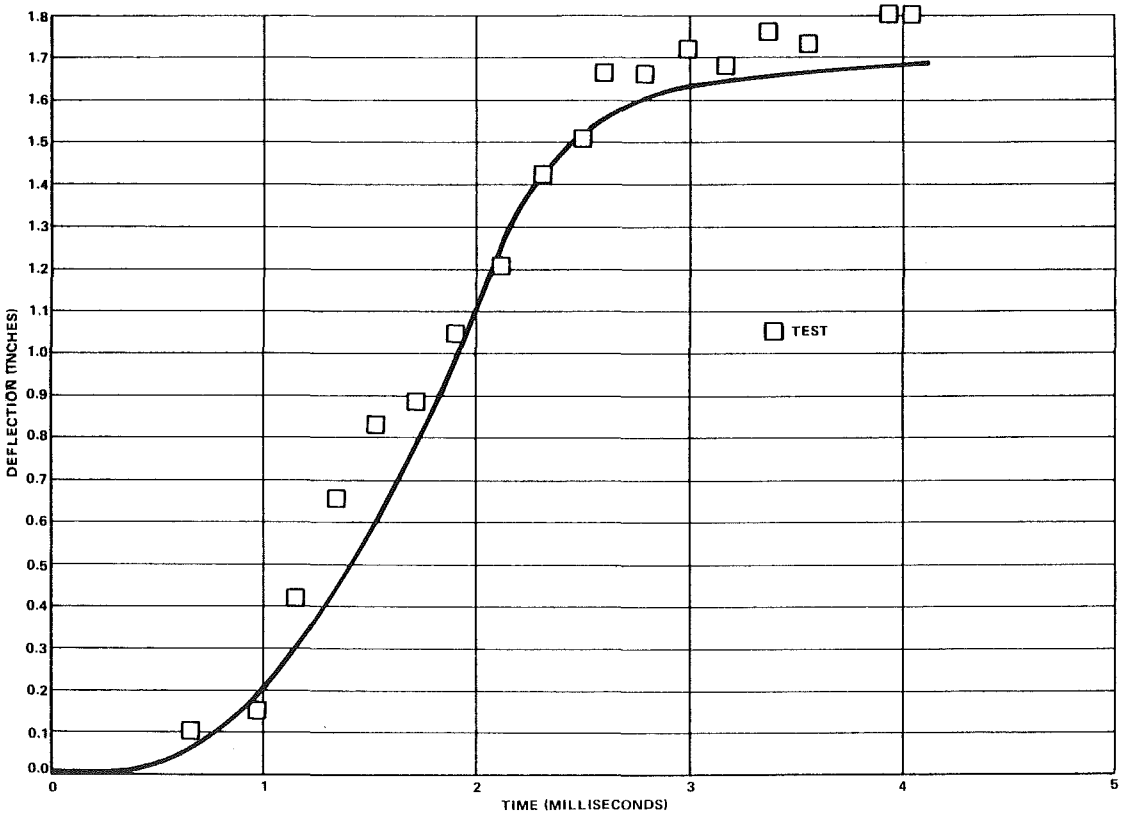

Fig. 16 Flatwise displacement response of simulated Q-fan blade subjected to a 30 deg impact of a 1 lb sphere at 600 ft/s

Downloaded 01 Jun 2010 to 171.66.16.62. Redistribution subject to ASME license or copyright; see http://www.asme.org/terms/Terms_Use.cfm

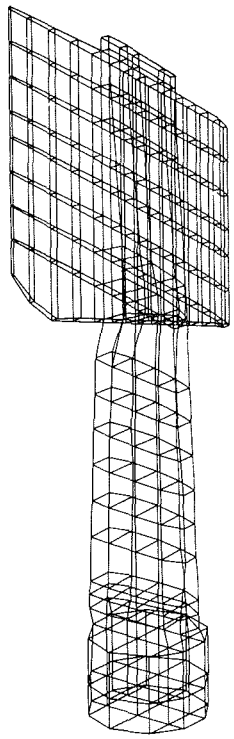

Fig. 17 Simulated Q-fan blade model

Acknowledgments

This program is an outgrowth of two analyses that were previously developed at Hamilton Standard, Division of United Technologies Corporation, Windsor Locks, Connecticut: a three-mode beam impact analysis and a multimode beam impact analysis. The work for the present program was also conducted at Hamilton Standard under NASA Lewis Research Center Contract No. NAS3-20091. The development of the equations used for the missile models based on studies of two-dimensional and three-dimensional fluid jets, was carried out by Dr. R. W. Cornell. Dr. C. C. Chamis of NASA Lewis Research Center monitored the contract.

References

1 Alexander, A., Cornell, R. W., "Interactive Multi-Mode Blade Impact Analysis," NASA CR-159462, August 1978.

2 Von W. Schach, "Umlenkung eines frien Flüssigheitsstrahles an einer ebenen Platte," *Ingenieur-Archiv*; V. Band, 4 Heft; 1934; pp. 245–265.

3 Von W. Schach, "Umlenkung eines Kreisförmigen Flüssigheitsstrahles an einer ebenen Platte senkrecht zur Stromungsrichtung," *Ingenieur-Archiv*; VI Band, 1935; pp. 51–59.

4 Barber, J. P., Wilbeck, J. S., and Taylor, H. R., "Bird Impact Forces and Pressures on Rigid and Compliant Targets," Univeristy of Dayton Research Institute Final Contract Report UDRI-TR-77-17, Contract F33615-76-C-3103, Mar. 1977.

Downloaded 01 Jun 2010 to 171.66.16.62. Redistribution subject to ASME license or copyright; see http://www.asme.org/terms/Terms_Use.cfm

A. W. Leissa
Professor.

J. K. Lee
Assistant Professor.

A. J. Wang
Graduate Student.

Department of Engineering Mechanics,
Ohio State University,
Columbus, Ohio

Rotating Blade Vibration Analysis Using Shells

Shallow shell theory and Ritz method are employed to determine the frequencies and mode shapes of turbomachinery blades having both camber and twist, rotating with non-zero angles of attack. Frequencies obtained for different degrees of shallowness and thickness are compared with results available in the literature, obtained from finite element analyses of nonrotating blades. Frequencies are also determined for a rotating blade, showing the effects of changing the (1) angular velocity of rotation (2) disk radius and (3) angle of attack, as well as the significance of the most important body force terms.

Introduction

Hundreds of references can be found which relate directly to the turbine engine blade vibration problem (cf., [1-3]). However, the vast majority treat the blades as beams; that is, the problem is characterized as a one-dimensional one, with a single coordinate measured along the beam axis. Such a representation is highly inaccurate if (*a*) the blade has a small aspect ratio, (*b*) the blade is thin, or (*c*) more than the first two or three frequencies and mode shapes are needed. A few works have also attempted to model a blade as a rotating plate, but the important stiffening effect of chordwise camber cannot be represented by this model.

A number of references are available which analyze blades, treating them as shells having camber and/or twist, as summarized in a current survey article [4]. The vast majority of these studies utilize various forms of finite elements (e.g., triangular or quadrilateral, plate or shell, conforming or nonconforming). Very few of them consider centrifugal force effects.

Figure 1 depicts a considerably simplified, first model of a turbine engine blade. The blade is represented as a thin, shallow, cylindrical shell having one edge ($x=0$) rigidly clamped and the other three completely free. The planform is rectangular, having length "*a*" and width "*b*" and the shell thickness is denoted by "*h*." Displacements of the shell are completely characterized by its two-dimensional middle surface which, in turn, can be related to the *xy* reference plane. The three orthogonal components of displacement are *u* (parallel to the *xy*-plane) and *v*, tangent to the shell mid-surface, and *w*, normal to it.

As depicted the blade rotates with angular velocity Ω about an axis located at some distance r_0 from the blade root. The figure is drawn for zero angle of attack; that is, the *xy* plane is perpendicular to the rotation axis. In general, the attack angle can vary between (at least) zero and 90 deg.

In general, of course, the geometry of the mid-surface of a blade is considerably more complicated than that depicted in Fig. 1. Rather than having curvature in only one direction,

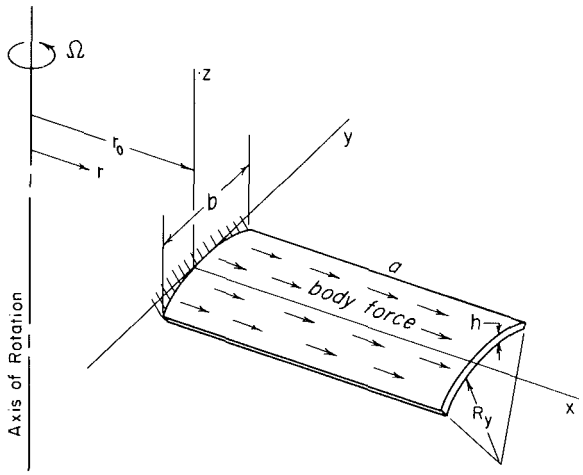

Fig. 1 Simplified model of a rotating blade

measured by the radius R_y shown, it has two components of curvature and one of twist, requiring three coefficients R_x, R_y and R_{xy} to define. While curvature in the *x*-direction is typically small, the twist is usually considerable. Furthermore, R_x, R_y and R_{xy} are not constants, but vary along the blade.

Rotation of the blade causes centrifugal body forces within the shell. At a typical point, the body force has three components, one normal and two tangent to the shell surface, which can be either stabilizing (frequency increasing) or destabilizing (frequency decreasing).

The present analysis is based upon the Ritz method and determines free vibration frequencies and mode shapes of rotating blades accurately. Low aspect ratio, thin blades and large angular velocities are adequately accounted for. Variable blade thickness can be straightforwardly accommodated.

Free Vibration Analysis: Ritz Method

For a shallow shell having radii of curvature and twist, R_x, R_y and R_{xy} the maximum strain energy (which occurs at

Contributed by the Gas Turbine Division of THE AMERICAN SOCIETY OF MECHANICAL ENGINEERS and presented at the Gas Turbine Conference and Products Show, March 9-12, 1981, Houston, Texas. Manuscript received at ASME Headquarters December 11, 1980. Paper No. 81-GT-80.

Copyright © 1982 by ASME

Downloaded 01 Jun 2010 to 171.66.16.62. Redistribution subject to ASME license or copyright; see http://www.asme.org/terms/Terms_Use.cfm

maximum displacement) is given by (cf., [5-7])

$$V_{max} = V_1 + V_2 + V_3 \tag{1}$$

where V_1 represents the membrane effects due to stretching of the middle surface of the shell,

$$V_1 = \frac{Eh}{2(1-\nu^2)} \int_{-b/2}^{b/2} \int_0^a \left\{ (\epsilon_x + \epsilon_y)^2 - 2(1-\nu)\left(\epsilon_x \epsilon_y - \frac{\gamma_{xy}^2}{4}\right)\right\} dxdy \tag{2}$$

V_2 represents the bending strain energy,

$$V_2 = \frac{Eh^3}{24(1-\nu^2)} \int_{-b/2}^{b/2} \int_0^a \left\{ (\nabla^2 w)^2 - 2(1-\nu)\left[\frac{\partial^2 w}{\partial x^2}\frac{\partial^2 w}{\partial y^2} - \left(\frac{\partial^2 w}{\partial x \partial y}\right)^2\right]\right\} dxdy \tag{3}$$

and V_3 is the strain energy developed during vibrational deformation due to the presence of initial stress resultants, N_x^0, N_y^0 and N_{xy}^0 (i.e., forces per unit length), which are caused by rotational body forces,

$$V_3 = \frac{1}{2} \int_{-b/2}^{b/2} \int_0^a \left\{ N_x^0 \left(\frac{\partial w}{\partial x}\right)^2 + N_y^0 \left(\frac{\partial w}{\partial y}\right)^2 + 2N_{xy}^0 \frac{\partial w}{\partial x}\frac{\partial w}{\partial y}\right\} dxdy \tag{4}$$

For free vibration the three components of displacement of the shell midsurface are expressed as

$$\begin{aligned} u(x,y,t) &= U(x,y)\ \sin\omega t \\ v(x,y,t) &= V(x,y)\ \sin\omega t \\ w(x,y,t) &= W(x,y)\ \sin\omega t \end{aligned} \tag{5}$$

The membrane strains are related to the displacements by

$$\begin{aligned} \epsilon_x &= \frac{\partial U}{\partial x} + \frac{W}{R_x} \\ \epsilon_y &= \frac{\partial V}{\partial y} + \frac{W}{R_y} \\ \gamma_{xy} &= \left(\frac{\partial V}{\partial x} + \frac{\partial U}{\partial y}\right) + 2\frac{W}{R_{xy}} \end{aligned} \tag{6}$$

E is Young's modulus, h is the shell thickness and ν is Poisson's ratio.

The maximum kinetic energy (which occurs at zero displacement, and maximum velocity) is

$$T_{max} = \frac{\rho h \omega^2}{2} \int_{-b/2}^{b/2} \int_0^a (U^2 + V^2 + W^2) dxdy \tag{7}$$

where ρ is the mass density per unit volume.

In the foregoing representation of a rotating, vibrating shell, several simplifications have been made to arrive at a first model of the problem, namely:

1 A rectangular planform (having dimensions $a \times b$) is assumed. More general types of planforms would require more general integration.

2 The material is isotropic and homogeneous (E, ν and ρ are constant), and the thickness is constant.

3 The initial stress is constant with respect to time (but not with respect to x or y).

4 Displacement-dependent centrifugal body forces are not included. These will be discussed later. Coriolis effects are also neglected.

5 Displacements are small, permitting the use of linear strain-displacements and stress-strain equations.

Displacement functions are assumed to be algebraic polynomials in the form

$$U(\xi,\eta) = \sum_{i=1}^{I} \sum_{j=0}^{J} A_{ij} \xi^i \eta^j \tag{8a}$$

$$V(\xi,\eta) = \sum_{k=1}^{K} \sum_{l=0}^{L} B_{kl} \xi^k \eta^l \tag{8b}$$

$$W(\xi,\eta) = \sum_{m=2}^{M} \sum_{n=0}^{N} C_{mn} \xi^m \eta^n \tag{8c}$$

(where $\xi = x/a$ and $\eta = 2y/b$) which satisfy the clamped edge conditions exactly; that is,

$$U(0,\eta) = V(0,\eta) = W(0,\eta) = \frac{\partial W}{\partial \xi}(0,\eta) = 0 \tag{9}$$

The Ritz method requires minimization of the functional $T_{max} - V_{max}$. This is accomplished by setting

$$\frac{\partial (T_{max} - V_{max})}{\partial A_{ij}} = 0 \ (i = 1, \ldots I;\ j = 0, \ldots, J) \tag{10a}$$

$$\frac{\partial (T_{max} - V_{max})}{\partial B_{kl}} = 0 \ (k = 1, \ldots, K;\ l = 0, \ldots, L) \tag{10b}$$

$$\frac{\partial (T_{max} - V_{max})}{\partial C_{mn}} = 0 \ (m = 2, \ldots, M;\ n = 0, \ldots, N) \tag{10c}$$

which yields a total of $I(J+1) + K(L+1) + (M+1)(N+1)$ simultaneous, linear, characteristic equations in an equal number of unknowns A_{ij}, B_{kl} and C_{mn}. For a non-trivial solution, the determinant of the coefficient matrix is set equal to zero. The zeros of the determinant are the eigenvalues (nondimensional frequency parameters). Substituting each eigenvalue back into the original set of equations, yields the corresponding eigenvector (amplitude ratio) in the usual manner.

For shell vibration problems the tangential inertia is often neglected, thereby eliminating the higher frequency modes which are principally associated with tangential displacements, and often allowing considerable simplification in the problem [8,9], and even closed form formulas for the frequencies, in some cases. Tangential inertia can be neglected in the present problem by dropping U^2 and V^2 from equation (7). By a proper matrix elimination procedure, one can then reduce the size of the eigenvalue determinant considerably, to the order $(M-1)(N+1)$.

Example: Nonrotating Cambered Blades

The method of analysis described in the preceding section will first be demonstrated on a cambered blade for which considerable numerical results are already available in the literature.

In an excellent, relatively early paper dealing with the application of finite element methods to shell problems, Olson and Lindberg [10] applied their procedure to a model of turbofan blade having dimensions R_y = 61.0 cm(24.0 in), h = 0.305 cm(0.120 in), a = b = 30.5 cm(12.0 in). These dimensions yield a shell which is relatively shallow, thin and small aspect ratio. A nonconforming, cylindrical shell element of rectangular planform was used, having 28 deg of freedom. Numerical results for frequencies and corresponding mode shapes were derived for mathematical models composed of 1, 4, 9 and 16 finite elements, and were compared with results obtained from an experimental model made from sheet steel. Experimental frequencies, as well as the analytical results for the three most accurate finite element models, are reproduced in Table 1 for the first eight modes. In the calculations tangential inertia was neglected in order to reduce the size of the resulting eigenvalue problems.

Downloaded 01 Jun 2010 to 171.66.16.62. Redistribution subject to ASME license or copyright; see http://www.asme.org/terms/Terms_Use.cfm

Table 1 Comparison of frequencies (Hz) obtained from experiments, three finite element solutions and the present method for a steel fan blade; R_y = 61.0 cm(24.0 in), h = 0.305 cm(0.120 in), $a = b$ = 30.5 cm(12.0 in)

Ref.	Description	Symmetric modes				Antisymmetric modes			
		1	2	3	4	1	2	3	4
[10]	Experiment	135.5	258.9	395.2	751.2	86.6	350.6	531.1	743.2
[11]	Experiment	134.5	259.	395.	751.	85.6	351.	531.	743.
[10]	2x2 grid (42 d.o.f.)	179.7	278.7	495.8	*	122.24	485.0	608.0	*
	3x3 grid (84 d.o.f.)	155.1	260.9	452.9	820.4	100.71	430.0	535.0	798.3
	4x4 grid (140 d.o.f.)	147.6	255.1	423.5	792.2	93.47	393.1	534.3	781.5
[11]	2x2 grid (78 d.o.f.)	144.9	264.8	461.2	*	95.74	413.4	583.8	*
	3x3 grid (152 d.o.f.)	139.8	253.3	406.7	783.2	87.53	359.1	540.8	756.1
	4x4 grid (250 d.o.f.)	139.2	251.3	393.4	746.4	86.60	348.6	533.4	752.1
[12]	2x2 grid (63 d.o.f.)	147.1	270.1	494.4	*	102.3	454.4	610.3	*
	3x3 grid (124 d.o.f.)	140.9	252.6	423.2	765.1	88.6	371.5	540.9	802.1
	4x4 grid (205 d.o.f.)	139.6	249.0	398.5	761.4	86.6	351.0	534.5	749.0
Present method	3x(4x4) = 48 d.o.f.	154.8	285.6	503.2	773.9	88.08	362.3	913.3	1572.4
	3x(5x5) = 75 d.o.f.	141.4	258.9	401.8	742.2	87.09	358.8	751.8	807.1
	3x(6x6) = 108 d.o.f.	138.5	249.9	392.4	736.7	86.02	345.0	578.5	742.2
	3x(8x5) = 120 d.o.f.	141.3	258.8	401.0	737.8	87.04	358.0	748.4	798.7
	3x(5x8) = 120 d.o.f.	137.8	248.6	387.4	736.3	85.94	342.9	531.9	738.4

* Results not given in references.

A subsequent paper by the same authors [11] utilized a conforming, doubly-curved shallow shell element of triangular shape to analyze the same problem. Each element had 38 deg of freedom. The rectangular grids used in [10] were further divided by diagonals to yield right triangular elements, and finite element models resulted having considerably more degrees of freedom than those used in the earlier analysis [10]. Tangential inertia was once more elminated in the analytical solutions. Experimental results were obtained again for the same shell. Relevant data from this reference are included in Table 1.

The problem was also among several examples used by Walker [12] to demonstrate a finite element approach using doubly curved, right helicoidal shell elements, each having 40 deg of freedom. Again, frequencies and nodal patterns were obtained using the same finite element grids of [10,11], and comparison for the first eight modes can be seen in Table 1. Tangential inertia was included in the calculations.

The three types of finite element approaches thus provide an excellent set of results against which the present method can be compared. Let displacement functions be taken in equations (8) using four, five, and six terms in both ζ and η directions for each of the displacement components. This yields 48, 75, and 108 deg of freedom, respectively, for the blade, and frequency determinants of corresponding size. Resulting vibration frequencies from the various solutions are listed in Table 1. Additional solutions using eight terms in the x-direction and five in the y-direction (8×5), and conversely, were also obtained to demonstrate the relative importance of the directions in choosing displacement polynomials.

Before comparing the results in Table 1 among the various methods of solution, it is important to discuss first their convergence characteristics. It is well known that the Ritz method yields upper bounds on the vibration frequencies. Furthermore, if a *complete* set of displacement functions is used as a basis for the sequence of approximating functions, the sequence will converge, in the limit, to the exact solution of the problem (cf. [13–15]). The algebraic polynomials used in equations (8) do form complete sets when the upper limits on the summations become infinite. Thus by the present method, as additional terms are taken, the frequencies converge monotonically towards the exact values.

The finite elements utilized in [11,12] are conforming, and therefore will exhibit the same type of monotonic convergence. The results of [10], however, are based upon nonconforming elements, and therefore oscillating convergence could result, even though the convergence exhibited by this method in Table 1 does appear to be monotonic.

The number of degrees of freedom ascribed to each solution in Table 1 is based on the assumptions that:

1 Tangential inertia is not neglected.
2 No advantage of symmetry is taken.

Tangential inertia can be eliminated in all of the methods used in Table 1. The effect is to reduce the number of degrees of freedom considerably at the cost of:

1 slight inaccuracies in the frequencies of the low frequency flexural modes, and
2 complete loss of the "in-plane" modes; that is, the modes involving significant u and/or v displacements.

Both effects are insignificant for practical purposes if the shell is sufficiently shallow.

Careful consideration of the symmetry in the present problem permits uncoupling of the symmetric vibration modes from the antisymmetric ones, and reduction of an eigenvalue determinant to two of smaller order. This procedure can be followed in all the analytical solutions.

Comparing the values in Table 1, it would seem that the results of the present method using 108 deg of freedom are generally better than those of [10] using 140 d.o.f., and at least as good as those of [11] and [12], using 250 and 205 deg of freedom, respectively. Further improvement in the frequencies is seen to occur in Table 1, if more terms are taken in the y-direction (viz, 5×8 solution). The 6×6 solution is seen to yield more accurate results than the best solutions of [10–12], except for two of the eight modes, while the 5×8 solution is more accurate for all the modes. A glance at the mode shapes, given in [10–12] shows that only the first two modes (torsion and bending) are predictable by one-dimensional beam-rod theory.

The turbofan blade in the preceding example can be characterized as a thin, shallow shell. In [12] numerical results, both theoretical and experimental, were also obtained for three other blades made of sheet steel, having the same planform dimensions ($a = b$ = 30.5 cm(12.0 in), with b

Downloaded 01 Jun 2010 to 171.66.16.62. Redistribution subject to ASME license or copyright; see http://www.asme.org/terms/Terms_Use.cfm

Table 2 Comparison of frequencies (*Hz*) among three fan blades; $a = b = 30.5$ cm(12.0 in), steel

Blade description R_y (cm), h (cm)	Source of results	Degrees of freedom	Symmetric modes				Antisymmetric modes			
			1	2	3	4	1	2	3	4
Deep, thin	[12]	Exper.	196	360	486	*	128	494	566	932
		124	196.2	379.6	550.3	*	128.1	561.7	603.1	1018.2
30.5, 0.318		205	189.9	374.3	497.3	*	123.6	500.6	573.7	964.7
	Present method	108	187.8	373.7	474.9	955.9	121.9	496.2	667.8	959.0
		120	185.9	373.7	468.3	922.8	121.5	474.7	571.4	935.9
Shallow, thick	[12]	Exper.	190	856	930	1800	292	1050	*	2120
		124	196.3	867.8	989.8	1896.0	293.0	1086.3	1806.0	2182.5
61.0, 1.27		205	195.7	861.8	982.4	1878.8	291.9	1076.5	1793.7	2181.0
	Present method	108	194.4	865.3	984.1	1899.0	291.9	1072.9	1754.2	2237.5
		120	194.4	860.5	978.7	1874.8	291.9	1072.8	1754.2	2174.6
Deep, thick	[12]	Exper.	286	878	1184	1876	294	1068	*	2136
		124	324.5	899.3	1319.4	2054.3	306.4	1179.2	1806.7	2175.3
30.5, 1.27		205	322.8	892.1	1290.5	2028.4	303.5	1153.6	1794.2	2169.2
	Present method	108	316.0	913.9	1274.4	2051.8	303.7	1144.9	1755.2	2272.6
		120	315.8	906.0	1266.7	2034.1	303.6	1144.3	1755.1	2177.8

* Result not given in [12]

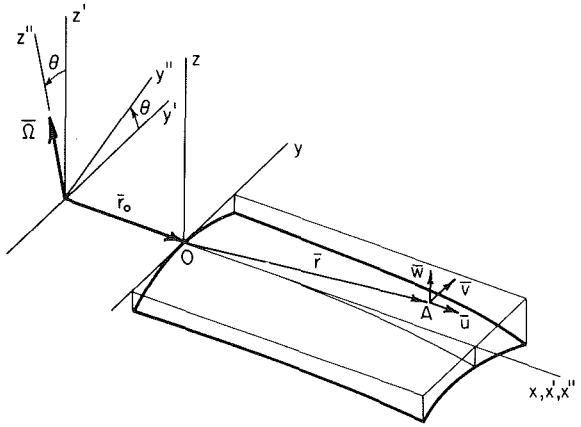

Fig. 2 Rotating shallow shell

measured along the circumference). These shells were made less shallow (i.e., deeper) as a result of a smaller R_y, and/or thicker. The resulting deeper shells are at the limits of application of shallow shell theory, whereas the deep/thick model also is at the limits of thin shell theory ($R_y/h = 24$).

Numerical results from [12], as well as 6×6 (108 d.o.f.) and 5×8 (120 d.o.f.) solutions by the present method, are displayed in Table 2. On the whole the best solutions obtained by both methods agree quite closely. Significant differences do occur between three of the seven frequencies obtained by the finite element method and the present method in the case of the deep, thin model, indicating slow convergence of the former approach when the membrane effects are dominant.

Body Forces and Initial Stresses Due to Rotation

Figure 2 shows a blade represented by the middle surface of a shallow shell. In general, the equation of the middle surface is given by

$$z(x,y) = \sum_{i,j} a_{ij} x^i y^j \tag{11}$$

Choosing the coordinates so that the xy-plane is tangent to the shell surface at the clamped edge, as depicted in Fig. 2, then

$$z(0,0) = \frac{\partial z}{\partial x}(0,0) = \frac{\partial z}{\partial y}(0,0) = 0 \tag{12}$$

whence, the rigid body orientation constants a_{00}, a_{10} and a_{01} are zero. The theory of shallow shells is based on the assumption that the squares and products of $\partial z/\partial x$ and $\partial z/\partial y$ are small in comparison to unity [6,7]. That is

$$\left(\frac{\partial z}{\partial z}\right)^2 << 1 \quad \frac{\partial z}{\partial x}\frac{\partial z}{\partial y} << 1, \quad \left(\frac{\partial z}{\partial y}\right)^2 << 1 \tag{13}$$

Then the curvatures $1/R_x$ and $1/R_y$, and the twist $1/R_{xy}$, of the surface reduce to

$$\frac{1}{R_x} = -\frac{\partial^2 z}{\partial x^2}, \quad \frac{1}{R_y} = -\frac{\partial^2 z}{\partial y^2}, \quad \frac{1}{R_{xy}} = -\frac{\partial^2 z}{\partial x \partial y} \tag{14}$$

And for the case of constant curvatures and twist, equation (11) reduces to

$$z = -\frac{1}{2}\left(\frac{x^2}{R_x} + 2\frac{xy}{R_{xy}} + \frac{y^2}{R_y}\right) \tag{15}$$

Figure 2 is drawn with R_x, R_y and R_{xy} all taken as positive quantities.

The blade is rotating with an angular speed Ω about an axis which, in general, is not perpendicular to the xy-plane. The angle between the vector $\bar{\Omega}$ and the z (or z') axis is denoted by θ as shown. The vector $\bar{r}_0$ is drawn from the axis of rotation to the origin (0) of the xyz coordinate system.

Consider a typical point A located on the blade middle surface by a position vector $\bar{r}$ drawn from 0. Assuming $\bar{\Omega}$ is constant, and neglecting Coriolis effects, the acceleration of A is given by:

$$\bar{a}_A = \bar{a}_0 + \bar{\Omega} \times [\bar{\Omega} \times (\bar{r} + \bar{\Delta})] + \bar{a}_{\text{rel}} \tag{16}$$

where $\bar{a}_0$ is the centripetal acceleration of the origin, given by

$$\bar{a}_0 = \bar{\Omega} \times (\bar{\Omega} \times \bar{r}_0) = -\Omega^2 r_0 \bar{i}_x \tag{17}$$

where multiplication signs denote vector cross products, and where $\bar{i}_x$, $\bar{i}_y$ and $\bar{i}_z$ are used to denote unit vectors in the x, y and z directions, respectively. Further, $\bar{\Delta}$ denotes the vector

Downloaded 01 Jun 2010 to 171.66.16.62. Redistribution subject to ASME license or copyright; see http://www.asme.org/terms/Terms_Use.cfm

displacement of point A from the equilibrium position of the shell, which can be written as

$$\bar{\Delta} = u\bar{i} + v\bar{j} + w\bar{k} \tag{18}$$

in terms of unit vectors tangent and normal to the middle surface. Displacements are assumed to be sufficiently small, that the directions of latter three unit vectors are not significantly changed by the displacements themselves. Finally,

$$\bar{\Omega} = -\Omega \sin\theta \bar{i}_y + \Omega \cos\theta \bar{i}_z \tag{19a}$$

$$\bar{r}_0 = r_0 \bar{i}_x \tag{19b}$$

$$\bar{r}_0 = x\bar{i}_x + y\bar{i}_y + z\bar{i}_z \tag{19c}$$

$$\bar{a}_{\text{rel}} = \ddot{u}\bar{i} + \ddot{v}\bar{j} + \ddot{w}\bar{k} \tag{19d}$$

Considering the shallow shell assumptions (13), $\bar{i}_x$, $\bar{i}_y$ and $\bar{i}_z$ can be expressed in terms of $\bar{i}$, $\bar{j}$, and $\bar{k}$ as

$$\bar{i}_x = \bar{i} - \frac{\partial z}{\partial x}\bar{k}$$

$$\bar{i}_y = \bar{j} - \frac{\partial z}{\partial y}\bar{k}$$

$$\bar{i}_z = \frac{\partial z}{\partial x}\bar{i} + \frac{\partial z}{\partial y}\bar{j} + \bar{k} \tag{20}$$

For the case of constant curvature and twist, substituting equation (15) into (20) yields

$$\bar{i}_x = \bar{i} + \left(\frac{x}{R_x} + \frac{y}{R_{xy}}\right)\bar{k}$$

$$\bar{i}_y = \bar{j} + \left(\frac{x}{R_{xy}} + \frac{y}{R_y}\right)\bar{k} \tag{21}$$

$$\bar{i}_z = -\left(\frac{x}{R_x} + \frac{y}{R_{xy}}\right)\bar{i} - \left(\frac{x}{R_{xy}} + \frac{y}{R_y}\right)\bar{j} + \bar{k}$$

and

$$\bar{r} = x\bar{i}_x + y\bar{i}_y - \left(\frac{1}{2}\frac{x^2}{R_x} + \frac{xy}{R_{xy}} + \frac{1}{2}\frac{y^2}{R_y}\right)\bar{i}_z \tag{22}$$

Substituting equations (17) through (22) into (16), and using D'Alembert's principle, the centrifugal body forces per unit volume are found to take the forms:

$$F_u = \rho\Omega^2(f_1 + g_{11}u + g_{12}v + g_{13}w)$$

$$F_v = \rho\Omega^2(f_2 + g_{21}u + g_{22}v + g_{23}w) \tag{23}$$

$$F_w = \rho\Omega^2(f_3 + g_{31}u + g_{32}v + g_{33}w)$$

where the f_i and the g_{ij} are functions of x and y.

The initial stress resultants N_x^0, N_y^0, and N_{xy}^0 can be determined by the Ritz method, utilizing algebraic polynomials of the same form given previously in equations (8), and minimizing the total potential of the rotating (but nonvibrating blade). In this static analysis the body forces in equations (23) which are proportional to u, v and w are treated as if they arise from springs, the spring constants being either positive or negative, corresponding to the signs of the g_{ij}.

For a flat plate, $R_x = R_y = R_{xy} = \infty$, and calculation of the body forces is considerally simplified. In this case equations (23) become

$$F_u = \rho\Omega^2(r_0 + x)$$
$$F_v = \rho\Omega^2 y\cos^2\theta \tag{24}$$
$$F_w = -\rho\Omega^2 \sin^2\theta w$$

That is, all but f_1, f_2, and g_{33} are zero in equations (23). An accurate determination of the initial stress resultants, which are caused by F_u and F_v requires solution of a mixed boundary value problem in plane elasticity. But, a reasonably close first approximation using strength of materials type assumptions gives

$$N_x^0 = \frac{\rho h\Omega^2}{2}[(r_0 + a)^2 - (r_0 + x)^2]$$

$$N_y^0 = \frac{\rho h\Omega^2}{2}\cos^2\theta\left[\left(\frac{b}{2}\right)^2 - y^2\right] \tag{25}$$

$$N_{xy}^0 = 0$$

These terms may be used in the expression for the potential function for V_3, given by equation (4). The presence of the displacement-dependent body force F_w requires the addition of another potential function, V_4, to the right-hand side of equation (1), which for the case given by the third of equations (24) becomes

$$V_4 = -\frac{\rho h\Omega^2}{2}\sin^2\theta\int_{-b/2}^{b/2}\int_0^a w^2\,dxdy \tag{26}$$

The negative sign indicates that F_w embodies a destabilizing (i.e., frequency reducing) component of body force.

For a shell of sufficient shallowness, the body force effects can be reasonably well accounted for by using equations (24-26).

Example: A Rotating Cambered Blade

To demonstrate rotational effects upon the vibration frequencies of cambered turbomachine blades, the same blade is taken which was used to obtain the nonrotating results of Table 1. Numerical results for frequencies of the first four modes of each symmetry class are given in Table 3 for the case when the axis or rotation is the clamped edge of the blade (i.e., $r_0/a = 0$), and when the ratio of the rotational frequency to the fundamental (i.e., lowest) natural frequency (ω_0) is one. It is seen that the effect of rotation is to increase all of the frequencies, primarily because of the body force component F_u and, to a lesser extent, F_v. The effect of changing the angle of attack (θ) is also demonstrated by Table 3. For a fixed rotational speed, increasing θ yields decreasing values of all of the frequencies, mainly due to negatively increasing F_w. One also observes that greater change in the frequencies occurs as θ increases from zero to 45 deg, than in increasing from 45 to 90 deg.

To show the separate effects of the body force components F_u, F_v and F_w upon the frequencies, Table 4 is included, which presents frequencies for the case when $r_0/a = 0$, $\Omega/\omega_0 = 1$ and $\theta = 45$ deg. The first set of results corresponds to Table 3, with all body force components included. The second set gives the frequencies which would result if only the largest body force component F_u were considered. The third set demonstrates the additional stiffening effect obtained by adding F_v to F_u. The effect would be less significant for a larger aspect ratio blade. The fourth set shows the destabilizing effect of adding the F_w component to F_u; it is

Downloaded 01 Jun 2010 to 171.66.16.62. Redistribution subject to ASME license or copyright; see http://www.asme.org/terms/Terms_Use.cfm

Table 3 The effects of rotational speed (Ω) and angle of attack (θ) upon frequencies; $a/b = 1$, $a/R_y = 0.5$, $a/h = 100$, $\nu = 0.3$, $r_0/a = 0$

$\frac{\Omega}{\omega_0}$	θ (deg)	Mode Number	Frequencies (Hz) Symmetric	Antisymm.
0	all	1	138.46	86.020
		2	249.95	345.00
		3	392.38	578.54
		4	736.72	742.15
1	0	1	170.28	150.98
		2	301.94	418.24
		3	463.48	623.35
		4	789.09	829.04
1	45	1	150.22	110.23
		2	266.56	404.90
		3	448.12	592.37
		4	780.63	819.63
1	90	1	147.84	105.10
		2	262.69	403.48
		3	446.48	589.06
		4	779.76	818.58

Table 4 The effects of body force terms upon frequencies (same blade as for Table 3, with $\Omega/a_0 = 1$, $\theta = 45$ deg)

Body force terms F_u	F_v	F_w	Mode Number	Frequencies (Hz) Symmetric	Antisymm.
yes	yes	yes	1	150.22	110.23
			2	266.56	404.90
			3	448.12	592.37
			4	780.63	819.63
yes	no	no	1	164.90	124.27
			2	266.23	408.76
			3	450.29	586.45
			4	782.09	852.87
yes	yes	no	1	166.85	132.18
			2	276.28	411.42
			3	454.03	596.85
			4	784.00	822.87
yes	no	yes	1	148.03	100.61
			2	256.13	402.20
			3	444.33	581.89
			4	778.72	816.98

seen to be particularly important for the low frequency symmetric modes.

Table 5 shows the effects of increasing Ω/ω_0 and/or r_0/a. Frequencies are given for $\theta = 45$ deg. Angular velocity and disk radius are seen to have profound effects upon all the modes, especially the lower frequency ones.

All numerical results presented in Tables 3, 4 and 5 were obtained using displacement polynomials having six terms in each direction (i.e., 6×6), or 108 degrees of freedom.

Table 5 The effects of rotational speed (Ω) and disk radius (r_0) upon frequencies (same blade as for Table 3, except r_0/a variable and $\theta = 45$ deg)

$\frac{\Omega}{\omega_0}$	$\frac{r_0}{a}$	Mode Number	Frequencies (Hz) Symmetric	Antisymm.
1	0	1	150.22	110.23
		2	266.56	404.90
		3	448.12	592.37
		4	780.63	819.63
2	0	1	177.55	160.37
		2	309.90	541.88
		3	580.82	631.59
		4	868.30	962.14
1	1	1	183.17	152.46
		2	287.53	476.92
		3	515.60	603.36
		4	826.43	899.54
2	1	1	273.27	263.62
		2	374.81	659.11
		3	741.13	764.17
		4	1005.7	1098.2

Discussion and Conclusions

In the foregoing work it is demonstrated how the classical Ritz method can be employed to determine the free vibration frequencies and mode shapes of simplified representations of turbomachinery blades. The method is capable of considerable generalizations beyond the description given above, as will be demonstrated in future papers by the present authors. Among the numerous tractable generalizations are:

1 elastic constraints at the root, representing the translational and rotational stiffness components of the support disk,
2 attached shrouds having both translational and rotational mass and stiffness,
3 thick shell theory, to include shear deformation and rotary inertia of relatively thick blades,
4 deep shell theory, to accommodate blades having severe curvature,
5 inclusion of Coriolis effects,
6 variable thickness and curvature,
7 nonrectangular blade planforms,
8 anisotropic and/or homogeneous materials, such as composites,
9 determination of initial, non-vibrational stresses and displacements to sufficient accuracy,
10 inclusion of structural damping or layered damping treatments.

The present method is not intended to take the place of the widely-used finite element method, but rather to complement it. The finite element method is very good for representing bodies of irregular shape, such as actual turbine blade designs. However, the present method is well suited for changes of parameters such as thickness ratio, shallowness ratio, and aspect ratio in simplified blade representations for purposes of preliminary design and for physical understanding of the rotating blade problem.

Acknowledgment

This work was carried out with the support of the National Aeronautics and Space Administration, Lewis Research Center, under Grant No. NAG 3-36.

References

1 Rao, J.S., "Natural Frequencies of Turbine Blading - A Survey," *Shock and Vibration Digest,* Vol. 5, No. 10, 1973, pp. 3-16.

2 Rao, J.S., "Turbine Blading Excitation and Vibration," *Shock and Vibration Digest,* Vol. 9, No. 3, 1977, pp. 15-22.

3 Rao, J.S., "Turbomachine Blade Vibration," *Shock and Vibration Digest,* Vol. 12, No. 2, 1980, pp. 19-26.

4 Leissa, A.W., "Vibrations of Turbine Engine Blades by Shell Analysis," *Shock and Vibration Digest,* Vol. 12, No. 11, 1980.

Downloaded 01 Jun 2010 to 171.66.16.62. Redistribution subject to ASME license or copyright; see http://www.asme.org/terms/Terms_Use.cfm

5 Novozhilov, N.V., *The Theory of Thin Shells* (English translation), P. Noordhoff, Groningen, The Netherlands, 1959.

6 Nazarov, A.A., *On the Theory of Thin Shallow Shells* (English translation), NACA Tech. Memo. 1426, 1956.

7 Leissa, A.W. and Kadi, A.S., "Analysis of Shallow Shells by the Method of Point Matching," Air Force Flight Dynamics Lab Rept. TR-69-71, 1969.

8 Leissa, A.W. and Kadi, A.S., "Curvature Effects on Shallow Shell Vibrations," *Journal of Sound and Vibration,* Vol. 16, No. 2, 1971, pp. 173–187.

9 Leissa, A.W., *Vibration of Shells,* NASA SP-288, U.S. Govt. Printing Office, 1973.

10 Olson, M.D. and Lindberg, G.M., "Vibration Analysis of Cantilevered Curved Plates Using a New Cylindrical Shell Finite Element," Proc. 2nd Conf. Matrix Meth. Struct. Mech., Wright-Patterson Air Force Base, Ohio, AFFDL-TR-68-150, pp. 247–270.

11 Olson, M.D. and Lindberg, G.M., "Dynamic Analysis of Shallow Shells with a Doubly-Curved Triangular Element," *Journal of Sound and Vibration,* Vol. 19, 1971, pp. 283–293.

12 Walker, K.P., "Vibrations of Cambered Helicoidal Fan Blades," *Journal of Sound and Vibration,* Vol. 59, No. 1, 1978, pp. 35–57.

13 Kantorovich, L.V. and Krylov, V.I., *Approximate Methods of Higher Analysis* (English translation), P. Noordhoff, Groningen, The Netherlands, 1958.

14 Mikhlin, S.G., *Variational Methods in Mathematical Physics* (English translation), MacMillan, New York, 1964.

15 Hopper, A.T., Leissa, A.W., Hulbert, L.E. and Clausen, W.E., "Numerical Analysis of Equilibrium and Eigenvalue Problems," Air Force Flight Dynamics Lab Rept. TR-67-121, 1967.

Downloaded 01 Jun 2010 to 171.66.16.62. Redistribution subject to ASME license or copyright; see http://www.asme.org/terms/Terms_Use.cfm

H. G. Lew
Mem. ASME

S. M. DeCorso
Mem. ASME

G. Vermes
Mem. ASME

D. Carl
Mem. ASME

Westinghouse Electric Co.,
Concordville, Pa.

W. J. Havener
Westinghouse Electric Co.,
Madison, Pa.

J. Schwab
Westinghouse Electric Co.,
Pittsburgh, Pa.

J. Notardonato
NASA Lewis Research Center,
Cleveland, Ohio

Low NO_x and Fuel Flexible Gas Turbine Combustors

The work described in this paper is a part of the DOE/LeRC "Advanced Conversion Technology Project" (ACT). The program is a multiple contract effort with funding provided by the Department of Energy and technical program management provided by NASA LeRC. Testing has been done burning a petroleum distillate fuel (ERBS fuel), a coal derived fuel (SRC II middle distillate), a petroleum residual fuel, and various blends of these fuels. Measurements are made of NO_x CO, and UHC emissions, and other measurements are made to evaluate combustor performance. Results to date indicate that rich-lean diffusion flames, with low fuel bound nitrogen conversion, are achievable with very high combustion efficiencies.

Introduction

Westinghouse, under Contract DEN 3-146, is participating in Phase I of the DOE/NASA Low NO_x Heavy Fuel Combustor Concept Program which has been described by Lister, et al., in reference [1]. The objective of this work is to develop low emission combustors for application to utility and industrial gas turbine systems which will meet EPA Standards of Performance for Stationary Sources utilizing minimally processed petroleum residual and synthetic liquid fuels. Emphasis is placed on low NO_x performance with the wide range of fuel bound nitrogen contained in these fuels. The combustors to be developed in this program will meet these requirements without the use of conventional water and steam injection techniques for NO_x suppression, since these techniques are costly, often have an adverse effect on thermal efficiency, and have limited effectiveness in avoiding the conversion of fuel bound nitrogen to NO_x emission.

The low NO_x combustor program makes fundamental changes in the way that fuels are burned in combustion turbines. The program goals reflect the environmental guidelines established by EPA and the practical real-world constraints of operability (over the load range), durability, maintainability and retrofitability, while maintaining high standards of performance in terms of combustion efficiency, pressure loss, and uniformity of exit temperature profile. These goals and objectives are outlined in Table 1.

A secondary goal for this program is achievement of "ultra-low" NO_x emissions capability (defined by NASA as 50 percent of the EPA limit) when operating on conventional petroleum distillate fuels. This objective is especially important in areas with high ambient air concentration of NO_x. EPA emissions offset requirements may be satisfied by means of retrofit installations of combustors at existing sites, in order to permit the construction of new fuel burning installations for utility, industrial or cogeneration purposes. This paper reports the work performed to develop low emission fuel flexible gas turbine combustors under these conditions.

The development work reported in this paper encompasses four primary areas:

- Conceptualization of advanced combustors
- Design of advanced combustors
- Fabrication of the combustion rig and combustors
- Demonstration of combustor viability by testing at full

Contributed by the Gas Turbine Division of THE AMERICAN SOCIETY OF MECHANICAL ENGINEERS and presented at the Gas Turbine Conference and Products Show, March 9–12, 1981, Houston, Texas. Manuscript received at ASME Headquarters December 11, 1980. Paper No. 81-GT-99.

Copyright © 1982 by ASME

Downloaded 01 Jun 2010 to 171.66.16.62. Redistribution subject to ASME license or copyright; see http://www.asme.org/terms/Terms_Use.cfm

Table 1 Low NO_x heavy fuels combustor concept program summary of goals and objectives

A. Emissions Limits (All Operating Conditions)	
1. Oxides of nitrogen	– 75 ppm at 15 percent 0_2
2. Sulfur dioxide	– 150 ppm at 15 percent 0_2
3. Smoke	– S.A.E. No. = 20
B. Performance Specifications	
1. Combustion efficiency	>99 percent (at all operating conditions)
2. Total pressure loss	<6 percent (at base load power)
3. Outlet temperature Pattern factor	<0.25 (at base load and peak load power)
4. Combustor exit Temperature radial profile	– Equivalent to typical production engine combustor values
C. General	
1. Retrofitable to current production and field engines	
2. Highly durable	
3. Maintainable	
4. Fuel flexible-capable of meeting emissions and performance specification on liquid fuels including petroleum distillates and residuals and synfuels from coal and shale.	

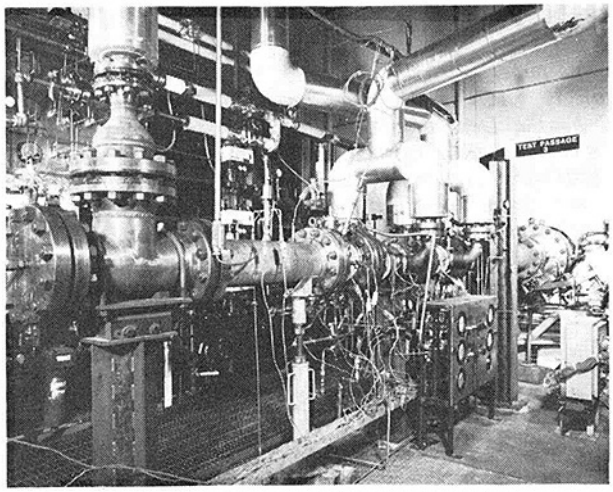

Fig. 1 High pressure combustor test passage

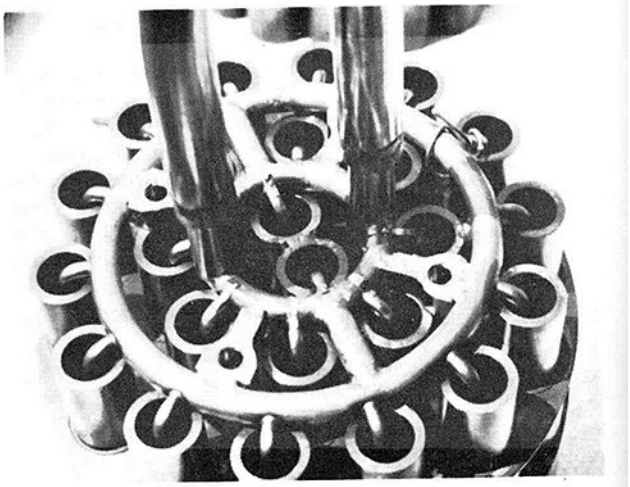

Fig. 2 Fuel injector for prevaporized and premixed configurations after NASA

temperature and pressure conditions [(2100°F/12 atm) (1149°C/1.216 MPa)].

Minimally processed fuels, such as coal derived liquids, contain bound nitrogen, which leads to an increase of NO_x emissions above those that result from its production thermally. This conversion of fuel bound nitrogen is high during normal engine combustion conditions as demonstrated in test results [2, 3]. For that reason, the goal of the advanced combustor designs is to minimize this conversion of fuel bound nitrogen to NO_x and to minimize the NO_x produced thermally.

Combustor configurations selected for development and design involved staged combustion (rich-lean) utilizing diffusion flames, rich-lean prevaporized/premix flames, and staged catalytic combustion. The configurations have been fabricated and tested at full pressure and temperature. The test rig, designed and constructed for this program involves a modular construction for staged combustion. It consists of a rich burner module, a quench module, and a lean combustion module. The features of this test rig include on-line fuel blending control and nonvitiated compressed air supply at each state point of the rich-lean process: the rich burner module, the quench module, and the lean combustion module.

Test results have been obtained for the combustor configurations while burning three fuels: petroleum distillate fuel, a coal derived liquid (SRC-II middle distillate), and a petroleum residual fuel. Other results have been obtained using various blends of these fuels. Emission measurements and operational performance data have been obtained for the evaluation of these combustor configurations. Analyses and evaluations of combustor performance will be the basis for demonstrating the feasibility of the various low emission gas turbine combustor configurations.

Test Rig

Test Rig Description. The test rig utilized in this program is shown in Fig. 1. The rig pressure boundary is formed by flanged sections of 8 in. Schedule 80 304 stainless steel pipe designed for 300 psig (2.07 MPa) at a 1000°F (538°C) surface temperature. The rig is comprised of three major parts: inlet section, combustor section, and pressure control/exhaust section. The inlet section consists of the valve and piping arrangement that directs unvitiated primary combustion air (preheated to approximately 700°F/371°C) to the combustor section.

The vaporizer portion of the inlet section is a smooth-walled duct. Flow perturbations are minimized in this section to avoid flashback and auto-ignition problems. When prevaporized/premixed concepts are being tested, fuel is sprayed into the primary air stream to allow vaporization

Downloaded 01 Jun 2010 to 171.66.16.62. Redistribution subject to ASME license or copyright; see http://www.asme.org/terms/Terms_Use.cfm

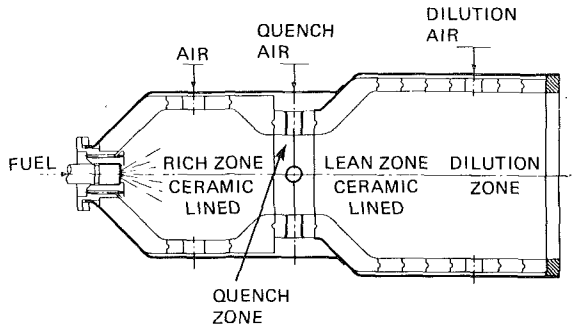

Fig. 3 Rich-lean diffusion flame venturi quench configuration

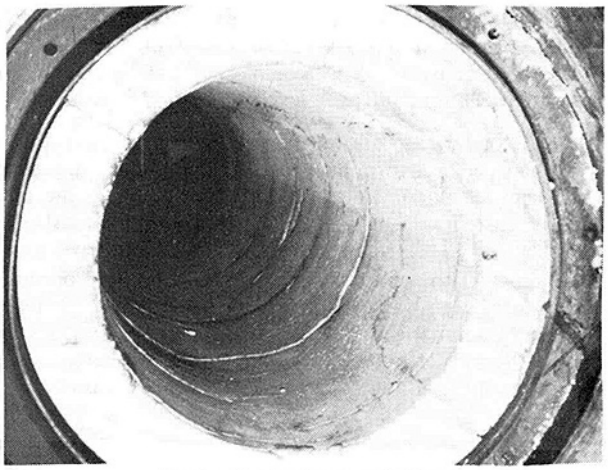

Fig. 4 Combustor ceramic liner

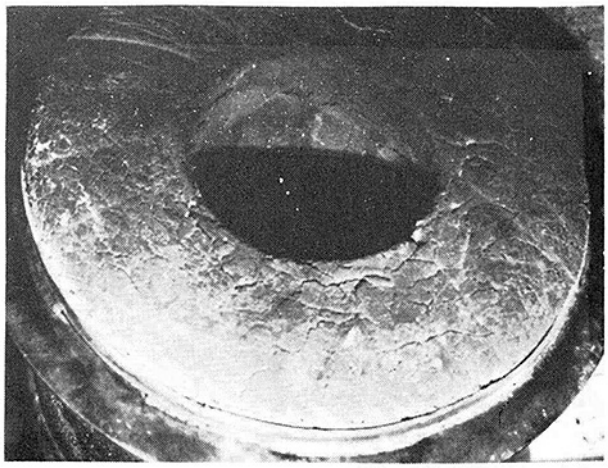

Fig. 5 Combustor ceramic liner after combustion

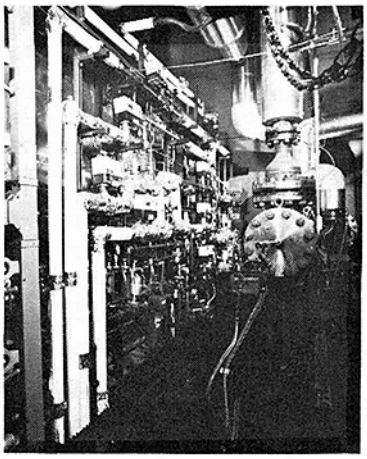

Fig. 6 Fuel blending system

prior to combustion. Figure 2 shows the fuel injector used in this arrangement.

The combustor section is made up of three subsections: rich burner, quench, and lean burner. Exit gas from this section simulates nominal turbine inlet conditions of 2100°F (1149°C) and 180 psig (1.24 MPa) ("near-term" 12-to-1 pressure ratio engine).

Figure 3 shows the test passage, configured in the ceramic lined rich burner, opposing jet quench and lean burner mode. Figures 4 and 5 show some of the ceramic linings used in the various sections of the passages.

The basic design approach is to standardize flame tube geometry and change internal details to yield different configurations. While a particular setup is being tested, another can be modified with the "plug in" components for subsequent testing. The subsections can be independently removed and replaced as necessary to change internal configurations.

Fuel System. The petroleum distillate fuel is stored in a 10,000 gal underground tank and transferred to 500 gal day tanks in the Fuel Blending Building, which are connected to the combustion test passage.

Petroleum residual fuel oil is stored in a 5000 gal heated storage tank and is piped to a 1000 gal heated and insulated day tank in the Fuel Blending Building. It is then pumped to the test passage through heated and insulated piping.

SRC-II coal derived liquid fuel is stored in an underground 5000 gal tank and transferred to a 500 gal day tank in the Fuel Blending Building. The day tank is connected to the combustion test passage.

Pyridine is stored in a 55 gal drum and pumped by a separate metering pump to the combustion test passage.

The fuels are blended and mixed on line and their flow ratio is controlled automatically. Figure 6 shows the piping arrangement of the fuel blending system.

Instrumentation. Instrumentation is provided for monitoring of rig inputs and determination of rig section and overall performance. Flow rate, temperature and pressure are measured for fuels, pyridine, primary air, secondary air, atomizing air and cooling air. Atomizing air and fuel pressure drops are measured across the fuel nozzles. Inlet air humidity is also determined in the compressor exit.

Test rig performance is determined by instrumentation stations as shown in Fig. 7. Each station consists of a water cooled 5 in. (127 mm) unit housed in an 8 in. (203 mm) flange. Multiple penetrations provide for thermocouples for temperature profile determination, water cooled sampling probes for emission analysis, and a static pressure tap. One of these flanged instrumentation stations is provided at the rich burner outlet, the quench module outlet, and the lean burner outlet. This arrangement allows evaluation of each combustor component rather than only overall rig performance. Rig duct metal surface and ceramic internal temperature measurements reduce burnout possibilities and give indications of both

Downloaded 01 Jun 2010 to 171.66.16.62. Redistribution subject to ASME license or copyright; see http://www.asme.org/terms/Terms_Use.cfm

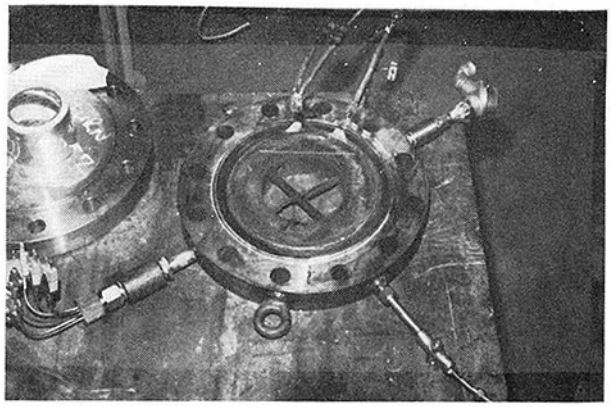

Fig. 7 Instrumentation flange showing temperature rake and emission sampling probe

radial and axial temperature profiles. Metal surface temperature measurement was accomplished with surface mounted thermocouples.

Continuous monitoring of all parameters previously mentioned is provided. Selected variables are recorded on strip chart recorders and trend recorders. All data are fed to the data acquisition system.

Figure 8 shows the relative location of the foregoing instrumentation in the various sections of the test rig.

On-line continuous monitoring of the combustion rig emission is accomplished with a Beckman designed gas analysis system. The system includes a heated sample line, a smoke meter with detached densitometer and the instruments in the following list.

Analyzer	Method	Type
NO/NO_x	Chemiluminescence	Beckman 951 H
CO	Infrared	Beckman 865
CO_2	Infrared	Beckman 865
H_2O	Infrared	Beckman 865
O_2	Magnetic susceptibility	Beckman
Hydrocarbons	Flame Ionization	Beckman 402
NO_x	Electrochemical	Dynasciences
Smoke	SAE	

All parameters, except smoke, are recorded locally and are transmitted to the data acquisition system and put on magnetic tape. Sample flow to any instrument can be interrupted for on-line calibration checks and all calibrations are checked prior to and following each test period.

Data Acquisition System. A PDP 11/34 computer system supports the data acquisition activity. This system includes 128K words of MOS memory, 7.5 million bytes of mass storage (disk) capacity, magnetic tape drive, video CRT, hard copy terminal, a line printer and an interface to process instrumentation via A/D converters with multiplexers and digital sensor inputs.

Raw data are collected at regular intervals and analyzed for high/low limits to generate appropriate alarms and are reduced on line to generate various flows, averages, and fuel/air ratios. Raw data and reduced data, including all process constants needed for data reduction, are stored on magnetic tape for permanent off-line data retrieval and further data reduction.

The CRT display and printer provide continuous monitoring of the system during a test.

Combustor Designs

To meet the objectives of a low NO_x burner, advanced

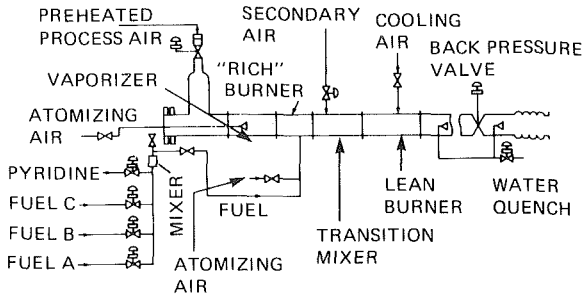

Fig. 8 Process flow diagram

combustor designs with fuel flexibility fall into two major categories:

- Staged combustion to effectively control the fuel nitrogen conversion to NO_x of nitrogen bearing fuels
- Lean combustion for petroleum distillates or fuels with moderate fuel bound nitrogen levels.

Staged combustion allows the fuel nitrogen conversion to N_2 in the rich stage (primary) with a minimum of conversion in the lean (secondary) stage. The temperature in the latter stage is sufficiently low that thermal NO_x formation is minimized.

For most of the combustors tested, a modular concept of combustor design was used in which burner components can be readily interchanged. As discussed in the previous section, each of the burner modules is housed in a pressure chamber and connected via flanges. The modules are as follows:

- Rich burner module made of conventional head end diffusion flame or a premixed flame with an ignition source
- Quench module where additional air is added to reduce the gas temperature and chemical reaction
- Lean burner module where the combustion process is completed

The turbine inlet temperature condition is attained by dilution with air at the end of the lean burner module. The potential of rich-lean system in minimizing NO_x emissions from fuel bound nitrogen is further discussed in reference [4].

In addition to the modular burners, this program contains two combustors in which the individual aerodynamic and combustion processes are performed in more integrated fashion.

The combustor configurations designed and built are given in the following list:

Direct Injection – Rich-Lean

1 Direct injection, venturi quench
2 Direct injection, vortex quench
3 Direct injection, vortex quench, perforated plate
4 Direct injection, vortex quench, catalyst
9 Multiannular swirl burner
11 Rolls-Royce combustor

Premix Rich-Lean

5 Recirculating counter swirl, venturi quench
10 Perforated plate, venturi quench

Rich Primary Catalytic – Lean Staged Combustion

7 Catalyst A, venturi quench
8 Catalyst B, venturi quench

Rich Hybrid Premix/Direct Injection

6 Hybrid piloted rich burner, venturi quench

Downloaded 01 Jun 2010 to 171.66.16.62. Redistribution subject to ASME license or copyright; see http://www.asme.org/terms/Terms_Use.cfm

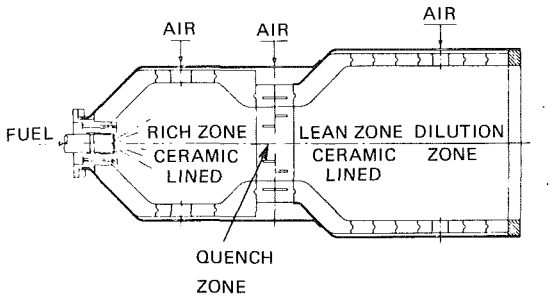

Fig. 9 Staged combustion with opposing swirl quench

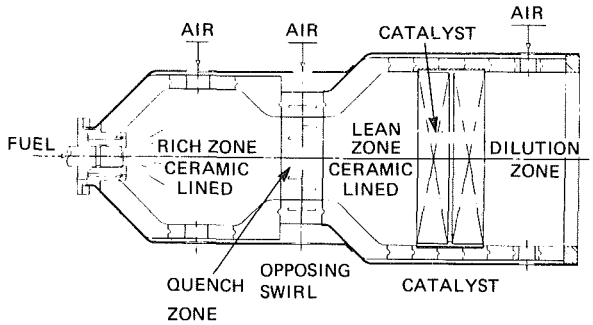

Fig. 10 Staged combustion with lean burn catalyst module

Lean Catalytic

12 Catalytic

Lean Hybrid Premix/Direct Injection

13 Hybrid piloted lean burner

Rich-Lean Direct Injection Staged Combustors. The modular rich-lean direct injection combustor utilizes a modification of a Westinghouse B-4 standard combustor for the rich burn module. An air-assist pressure atomizing nozzle is used in this burner. The inner walls of the combustor are lined with a high alumina ramming type ceramic. This type of hot wall construction enhances the combustion process for the rich mixture. The ceramic liner lies inside a metal sleeve with an external air sleeve. Primary air for combustion cools the ceramic containing sleeve, then returns and passes through ports into the combustion region (Fig. 3). The total primary hole area and spacing and diameter/length corresponds approximately to the standard B-4 design. Adjustment of the primary for any test may be easily made by plugging the holes (Fig. 3). The ignitor is placed in the plane of the first row of holes.

There are two quench module designs for this rich-lean configuration. In the venturi jet quench (Fig. 3), four quench holes inject air radially to rapidly cool the hot mixture of combustion products passing through the venturi section of the tube. The number and size of the quench zone holes were determined from a jet penetration correlation.

A second rich/lean configuration uses a vortex mixer quench in place of a venturi jet quench. In the vortex mixer quench, which uses opposing swirls to achieve the mixing, there are two consecutive vortex admissions – the second counteracting the swirl from the first. Figure 9 shows the construction features of this quench section with the arrangement of the vortex disks in series in the venturi throat. These disks can have eight slots, which may inject in a tangential or secantial direction. Combinations of these injections provide different qualities of penetration and mixing. For example, the tangential slots have better mixing than penetration, whereas the secantial slots have both qualities. Both systems have been tested in this program.

The lean burner portion of the system (shown in Fig. 3) completes the combustion after quenching had been accomplished. Of several lean burners considered, one is a ceramic-lined flame tube with the capability of a pilot flame to relight. A second lean burner, which uses a catalytic module, is shown in Fig. 10. The design selected for this burner is the Engelhard DXE-442 catalyst (Pd/stabilized alumina). The length of the element is 4 in. (101.6 mm) with 60 channels per square inch (9.3/cm^3) and is made of DuPont Torvex α-Al_2O_3. Typical expected operating conditions at full pressure are catalyst inlet and outlet temperatures of about 1480°F (804°C) and 2100°F (1140°C), respectively.

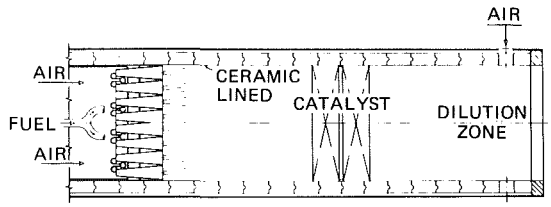

Fig. 11 Lean catalytic combustor for ultra-low NO_x emission burning petroleum distillate

The composition of the gas entering the catalyst is typical of that of a low Btu gas.

Three of the possible configurations using the combination of rich burner modules have been tested and are discussed later in this paper.

Lean Catalytic Combustor. The lean catalytic combustor uses a fuel lean mixture to obtain ultra-low NO_x emission with petroleum distillate [5, 6]. It is expected that the conversion of fuel bound nitrogen of synthetic fuels by this combustor to NO_x is still acceptable because of low thermal NO_x. This configuration is shown in Fig. 11.

Since only lean combustion is considered, the quench module is not needed in this configuration. This configuration uses the fuel preparation module (Figs. 2 and 11) ahead of the catalyst which supplies a premixed, prevaporized lean fuel mixture.

The catalytic combustor has been shown to be a low NO_x device [5, 7]. The catalytic element is a honeycomb device with a catalyst coating on a ceramic substrate, which burns fuel efficiently with very low emissions of NO_x, UHC, CO and smoke. With a temperature rise in the catalytic element, gas phase reactions will occur simultaneously with the catalytic reactions within the catalyst channels. Eventually, all portions of the gas attain a temperature that is sufficient to support homogeneous reaction. This effect is known as CATATHERMAL[1] combustion (a catalytically-supported thermal combustion). With this combustion system, NO_x formation is minimal, combustion is stable, and exit temperature patterns are uniform.

The catalyst outlet temperature of 2200°F (1204°C) and a reference velocity of about 80 ft/s (24.4 M/s) are conditions appropriate for this design as lean combustor module. The catalyst is a multicell, multisegment configuration that reduces pressure losses. The upstream segment is 2 in. (50.8 mm) of Engelhard DXE-442 catalyst (Pd/stabilized alumina) with 256 channels per sq in. and is made of Zircon composite, followed by 4 in. length (101.6 mm) of DXE-442 catalyst (Pd/stabilized alumina) with 60 channels per sq in. (9.3 channels/cm^2) of DuPont Torvex α-Al_2O_3. The total length is 6 in. (152.4 mm).

[1] CATATHERMAL is a registered trademark of Engelhard Industries Division.

Downloaded 01 Jun 2010 to 171.66.16.62. Redistribution subject to ASME license or copyright; see http://www.asme.org/terms/Terms_Use.cfm

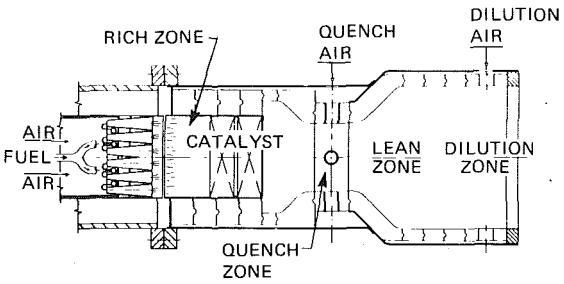

Fig. 12 Catalytic rich-lean combustor

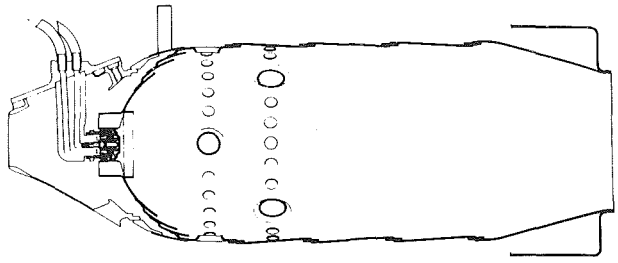

Fig. 13 Rolls-Royce low NO_x combustor

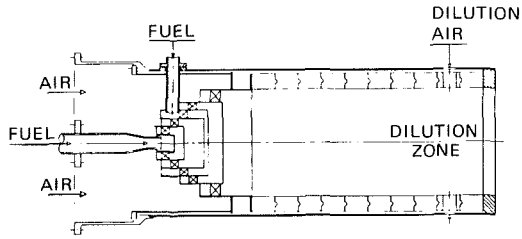

Fig. 14 Multiannular swirl burner (after Beér [9])

Rich-Lean Premixed/Catalytic. For fuels with bound nitrogen, rich-lean combustion via a catalytic combustor is a viable alternative to the conventional head end. Configurations with catalytic combustion of rich fuel-air mixtures are shown in Fig. 12. In this arrangement, the quench module is operating as in the other rich-lean combustors, using the better of the two quench modules and the better of the two lean burner modules.

Two types of catalyst elements, designed for rich operation, will be used in this concept.

The two types of catalysts will differ in maximum operation temperatures. It is expected that the rich catalyst element will permit operation of the rich burner with reduced soot formation at higher equivalence ratios.

The designs of the catalyst are based on an air inlet temperature of 700°F (371°C) with an outlet temperature range between 2200°F (1204°C) and 2600°F (1427°C). At the lower temperature, an Engelhard DXE-442 catalyst (Pd/stabilized alumina) on 4 in. of 60 channels per sq in. made of DuPont Torvex α-$A1_20_3$ has been selected based on Engelhard data. At the higher outlet temperature of 2600°F (1427°C), the precious metal catalyst is modified with base metal to provide a higher operating, adiabatic flame temperature capability.

Rich-Lean Direct Injection Integral Combustor. The requirements of low NO_x emission coupled with those for acceptable concentrations of CO, hydrocarbons and soot in the flue gas represent a challenge for the design of single burner combustors where the fuel rich pyrolysis of fuel bound nitrogen, the fast quench of the rich mixture and the burn-out of the residual combustible matter has to be achieved entirely by the management of the flow and mixing pattern and not by the physical separation of rich and lean combustors.

Rolls-Royce Combustor. The Rolls-Royce burner [8] is based on a modified scaled version of an existing in-service combustor. This burner performs the functions of the various modules of the previous configurations (rich module, quench, lean module, dilution zone) in one device. Low emission is achieved by utilizing a localized rich-lean mode of combustion near the nozzle.

The burner (Fig. 13) consists of three zones, each of which controls a phase of the total combustion process. Air entering the combustor primary zone is assumed to react in two initial zones: a recirculation zone, which deals with fuel preparation, and ignition; and an initial "rich burn" flame propagation zone. The combustion process proceeds downstream to enter a post-secondary burnout zone consisting of a less stired section in which combustion is completed. It assists in the burnout of hydrocarbons and free carbon carried over from the rich recirculation zone. Final admission of dilution air and quench air insures that no further reaction occurs, and conditions the gas stream for entry to the turbine.

The fuel rich primary zone features a swirler cuff, which is a short cylindrical unit containing an axial swirler aligned with the combustor centerline in the head end. In conjunction with the high penetration secondary air ports of the combustor, the cuff swirler provides vigorous stirring for the primary reaction zone. Strong recirculation is provided by sufficient ventilation due to the low blockage of the secondary air holes.

By virtue of the vigorous nature of the primary recirculation zone and its excellent fuel/air preparation, it is possible to run on the rich side of stoichiometric without producing excessive amounts of carbon. The design fuel/air equivalence ratio of the primary zone is ϕ_F = 1.3-1.4. (ϕ_F is defined by $(F/A)/(F/A)_{stoic}$; fuel rich conditions occur for $\phi_F > 1$.) NO_x production will be reduced by running at this condition.

The secondary reaction zone operates at a design ϕ_F = 0.65, which insures completion of the reaction at low temperature, and helps avoid excessive thermal NO_x production while still permitting consumption of primary zone carbon and unburned materials. Residence time within this zone is critical and is a compromise between NO_x production and hydrocarbon burnout. Therefore, the axial positioning of the third and final zone is very important.

Rapid quench is achieved by introduction of quench air downstream of the secondary reaction. Air injection is accomplished by four high penetration jets, which insures that quench air reaches the center of the combustor where most of the secondary reaction takes place. In this design, air distribution is such that the rapid quench zone becomes the dilution section.

The Rolls-Royce burner design endeavors to perform all the functions necessary for the successful operation of a low-NO_x burner running on nitrogen-containing fuels.

Multiannular Swirl Burner (MASB). The multiannular swirl burner achieves the tasks outlined for the rich-lean, direct injection, integral combustors by subdividing a single combustion chamber into concentric annuli. This arrangement permits tight control of the axial and swirl velocity distribution in the burner (Fig. 14).

The burner, based on Beér's design [9], consists of a system of axially displaced concentric rings. Each pair of radially adjacent rings forms an annulus. The axial displacement of the annular rings is such that the envelope of the ring tips forms a divergent passage.

The annuli of the MASB have the combustion air (or air-fuel mixture) enter each annulus axially. The desired tangential velocity distribution is produced by the flow passing through blade rows in the individual annuli. One

Downloaded 01 Jun 2010 to 171.66.16.62. Redistribution subject to ASME license or copyright; see http://www.asme.org/terms/Terms_Use.cfm

Table 2 Fuel Properties

	ERBS	Petroleum Residual	SRC-II-Middle Distillate
Gravity, °API (15.6°C)	38.2	–	13.3
Specific Gravity	0.8338 at 15.6°C	0.9533 (at 22°C)	0.9772
Hydrogen, wt percent	12.55	11.43	9.19
Nitrogen, wt percent	0.008	0.22	0.79 – 0.8
Sulfur, wt percent	0.09	0.48	0.25
Ash, wt percent	<0.0002	0.03	0.0015
Pour Point, °C (°F)	– 45.6 (– 50)	23.9 (+ 75)	– 59.4 (– 75)
Viscosity, cst at 37.8°C (100°F)	1.87	>835 (furol s)	4.03
Distillation Temp. °C (°F)			
IBP	126.(259)	180 (356)	110 (230)
10 percent	180 (356)	250 (482)	190 (374)
50 percent	224 (435)	358 (676)	242 (486)
90 percent	330 (620)	445 (833)	295 (563)
FBP	408 (776)	490 (914)	370 (698)
Net Heat of Combustion Btu/lb	18,343	17,609	16,674

consequence of the controlled swirl velocity distribution is the strong radial transfer of the angular momentum in the flow resulting in high intensity turbulence; the mixing is intensive between the adjacent annular flows due to the formation of concentric layers in which the turbulent shear stresses are maintained high [10].

Another feature of the burner is that, as a result of the combination of swirling flow and the divergent passage formed by the concentric nozzles, a toroidal recirculation zone is formed in the central region of the burner; the size and strength of this recirculation zone is dependent, for a given divergent passage geometry, upon the axial and swirl velocity distribution in the burner.

When operated in the staged combustion mode as a low NO_x burner, the central nozzle will run locally fuel rich, with the fuel rich zone forming a well stirred recirculation zone in front of the central nozzle. The fuel rich fuel gases will be intensively mixed with cold air entering through radially and axially displaced annuli along the boundaries of the recirculation zone; this provides fast reduction of the mixture temperature to below the limit of "thermal NO_x" formation. Following this fast "quench," the air from the outer annuli is admixed to form the lean second stage of the burner in which the combustion is completed in a temperature range high enough for the burn-out of soot and combustible gases, but sufficiently low to minimize the formation of thermal NO_x.

The hot recirculating gases in the central, toroidal vortex also provide flame holding and permit stable burner operation over a wide range of turn-down without the need for bluff body stabilizers or refractory surfaces directly exposed to the flame.

The burner is recuperatively cooled by the combustion air flowing through the annular rings, and there is, therefore, no need for film cooling air; as a consequence, the total amount of the combustion air is available for the management of the flow and mixing pattern in the burner.

Fuel with chemically bound nitrogen is expected to burn in this swirl combustor with low emission of NO_x. Axial staging of fuel and/or air can be accomplished easily with this design, permitting another degree of freedom in tailoring the rich burner section to the task of reducing NO_x. Another advantage of the MASB is that the turbulence intensity is uniformly high throughout the combustion volume. The high turbulence intensity and strong back mixing are conducive to the suppression of carbon formation: the onset of smoke formation shifts to a lower O/C (oxygen/carbon) atomic ratio of a premixed hydrocarbon/air mixture when the reactor volume is strongly stirred.

Fuel is injected through a central nozzle (Fig. 14) and through three nozzles into the third annulus. Air atomizing nozzles are used to achieve the desired drop size.

Hybrid Premix – Direct Injection Combustor. This combustor uses both a diffusion and a premix prevaporized flame. It operates through a hybrid mode of splitting the fuel and air flows into non-premixed and premixed streams. There are two distinct configurations since the combustors can be operated in two modes. When only lean combustion is considered, ultra-low NO_x emission is expected for petroleum distillate. Rich-lean staged combustion may also be implemented by this combustor by the addition of the quench and lean burner modules; in this rich-lean mode of operation, it is a modular design. Previous work in the lean mode is given in reference [11] where the NO_x performance over load range has been found adequate.

The configuration uses the Westinghouse B-4 headend for the pilot flame (Fig. 3). The pilot burner only uses a relatively small fraction of the primary fuel and air. This B-4 headend pilot burner precedes the premixed headend, which injects the balance of the fuel for the primary zone. This premixed prevaporized fuel and air mixture enters the flame tube by means of a bypass pipe protected from droplet deposition by a coaxial inner tube built from sintered material. Air seeping through the pipe wall performs this function. The premixed mixture enters the flame tube via a swirler system, combines with the B-4 headend flow, and then proceeds in an axial direction. The quench and lean burner modules follow the rich headend.

Fuel Characteristics

Three fuels are used in the test programs: petroleum distillate, petroleum residual, and a coal derived liquid. The petroleum distillate has been selected as the NASA research test fuel known as an Experimental Referee Broadened Specification (ERBS) aviation turbine fuel [12]. This fuel mixture is a blend of about 65 percent kerosine and 35 percent hydrotreated catalytic gas oil. The exact blend composition is determined by the hydrogen content required; the bound nitrogen content is low. The SRC-II coal liquid (middle distillate) is a representative synthetic fuel with reduced hydrogen content and higher fuel bound nitrogen. The measured values of the properties of these fuels and the petroleum residual fuel are given in Table 2.

Emission Goals

The emission goals of this program are contained in the EPA NO_x Emission Standards and are given in Tables 1 and 3. In addition to these goals, the objective of the program was to limit the smoke to SAE number of 20 and to achieve combustion efficiencies greater than 99 percent at all operating conditions. In addition to the NO_x emissions, CO,

Downloaded 01 Jun 2010 to 171.66.16.62. Redistribution subject to ASME license or copyright; see http://www.asme.org/terms/Terms_Use.cfm

Table 3 EPA NO_x emission standards with 15 percent oxygen in exhaust as a function of cycle efficiency

Cycle Efficiency, percent	Metropolitan Area		Non-metropolitan Area*	
	Maximum without FBN	Maximum with FBN**	Maximum without FBN	Maximum with FBN**
25	75ppm	125 ppm	150 ppm	200 ppm
30	90	140	180	230
35	105	155	210	260
40	120	170	240	290
45	135	185	270	320

*Gas or oil transportation and production only

**Assumes Fuel Bound Nitrogen (FBN) content equals or exceeds 0.25 percent.

CO_2, O_2, and UHC also were monitored during the test program.

Combustion Test Results

Staged Combustion/Rich-Lean Direct Injection.

Venturi Jet Quench. The configurations first tested were the staged combustion concepts. The first test series was intended to optimize the quench modules and the lean burn modules using the B-4 burner to produce a rich diffusion flame. In this B-4 burner, air is admitted through rows of radial holes leading to a recirculation of hot gases and a subsequent axial flow of rich combustion products toward the quench modules.

The venturi jet, with varying values of air flows, constitutes the quench module. The lean burner is a ceramic lined pipe. The nominal test conditions for these test runs are burner outlet pressure and temperature at 165 psia (1.14 MPa) and 1950°F (1066°C). The burner inlet temperature is set at 600°F (316°C) with a total air flow of 4.1 lb/s (1.86 kg/s). Primary equivalence ratio values were varied from 1.5 to 2 to determine the value for minimum NO_x emission.

Secondary equivalence ratios are effectively changed by the air entering the quench module. This ratio also was varied to determine the effect on the minimum NO_x emission.

A set of results of NO_x emissions for this combustor is shown in Fig. 15. Three levels of the quench flow, i.e., the secondary equivalence ratio for ERBS fuel are shown. Minimum NO_x values of 68–70 ppm were obtained for the ERBS fuel at a primary equivalence ratio of approximately 1.8. Combustion efficiencies greater than 99 percent were obtained for these test runs (between 99.88 and 99.93 percent, based on the exhaust oxygen content).

The test of this configuration with SRC II fuel oil shows similar behavior of the NO_x emission, but at a higher level. The NO_x emissions are shown in Fig. 15 as a function of the quench air flow. The difference in NO_x values between this SRC II fuel oil and ERBS fuel is approximately 70 ppm.

Smoke measurements on this configuration for the ERBS fuel show that the SAE smoke numbers were 20 and 26 for the primary equivalence ratio of 1.6. The smoke numbers were higher for the SRC-II fuel oil. Examples of these numbers were SAE numbers of 27.5 and 29 for the primary equivalence ratios of 1.89 and 1.62.

Vortex Mixer. The quench module with the vortex mixer was tested under similar conditions. The system uses two vortex admissions, the second counteracting the swirl from the first and producing axial flow. The results given here are for the cases where slots on the disks are such that tangential flow occurs through the first admission and secantial flow in the second admission. Thus the two disks in the swirler create a vortex to promote mixing of the quench air with the hot axial flow from the rich burner module.

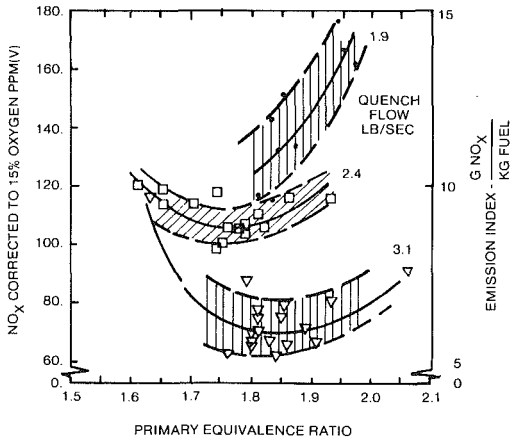

R/L MODULAR (CONFIGURATION 1) NO_X FOR ERBS FUEL

Fig. 15 NO_x emissions for rich-lean combustion of ERBS fuel with venturi jet quench

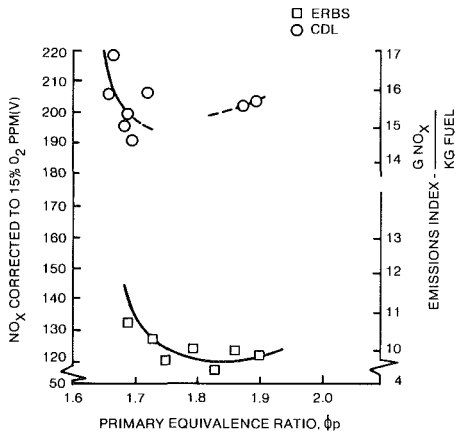

R/L MODULAR (CONFIGURATION 2) NO_X FOR ERBS, CDL FUELS

Fig. 16 NO_x emissions of rich-lean combustor with opposing swirl quench and lean burner pipe at inlet pressure of 185 psia normalized to 15 percent oxygen

The emissions results using this quench module are shown in Fig. 16 for the ERBS fuel and SRC-II fuel oil with a ΔNO_x of 80 ppm between the results of ERBS and SRC-II fuels.

Catalytic Lean Burner. The configuration with staged combustion using the vortex mixer and the catalytic lean burner was tested with both ERBS and SRC-II fuel oils. These results are shown in Fig. 17. The NO_x emissions do not change appreciably over the range of equivalence ratios considered. The difference between the NO_x results for the two fuels is about 70 ppmv. Fuel-bound nitrogen conversion

Downloaded 01 Jun 2010 to 171.66.16.62. Redistribution subject to ASME license or copyright; see http://www.asme.org/terms/Terms_Use.cfm

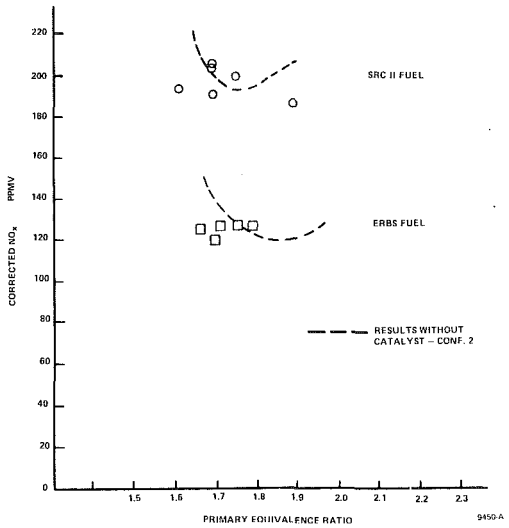

Fig. 17 NO_x emissions of rich-lean combustor with opposing swirl catalytic lean burner at inlet pressure of 185 psia normalized to 15 percent oxygen

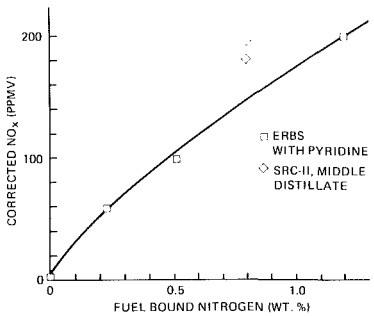

Fig. 18 NO_x corrected to 15 percent oxygen versus fuel bound nitrogen for lean premixed prevaporized catalytic combustor at 720°F (650K) and 180 psia (1.2 MPa)

of the SRC II coal liquid is about 23 percent in this rich-lean combustor with a catalytic reactor in the lean burner.

Lean Catalytic Burner. This configuration features a catalyst for lean combustion. A fuel preparation module is utilized to create the premixed and prevaporized mixture. Test results were obtained for the ERBS and SRC II fuel oil. In addition, pyridine was also used to simulate the fuel bound nitrogen in the ERBS fuel. The combustor inlet pressure was kept at 180 psia (1.24 MPa) with an air inlet temperature of 720°F (382°C). With the fuel air ratio of 0.021, the adiabatic flame temperature of the combustor is 2080°F (1138°C) on ERBS fuel. For the test runs with ERBS fuel, the NO_x emission is 2 ppm. Addition of pyridine increases the NO_x emissions and these results are shown in Fig. 18 for various values of the fuel bound nitrogen. Combustion efficiencies greater than 99 percent were obtained for all the ERBS test runs. The conversion efficiencies of the fuel bound nitrogen using pyridine in ERBS are shown in Fig. 19. As expected, there is a decrease in conversion with increase of FBN.

SRC-II fuel was also burned in this combustor (Fig. 18). The conversion efficiency of fuel bound nitrogen from SRC-II in the lean catalytic combustor is about 50 percent (See Fig. 19). This is a conversion level appreciably lower than that previously reported in the literature.

Rolls-Royce Combustor. The results for this combustor, burning ERBS fuel, confirm the fact that it is a low NO_x burner and is a considerable improvement over the state-of-the-art. For this combustor, the test peak condition for pressure and air flow were 163 psia (1.13 MPa) and 7.6 lb/s (3.45 kg/s). In addition, conditions corresponding to the load range were also simulated in the test program. The NO_x

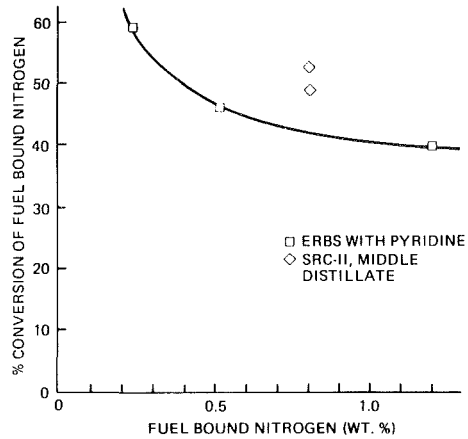

Fig. 19 Conversion of fuel bound nitrogen to NO_x versus fuel bound nitrogen for lean premixed prevaporized catalytic combustor at 720°F (650K) and 180 psia (1.2 MPa)

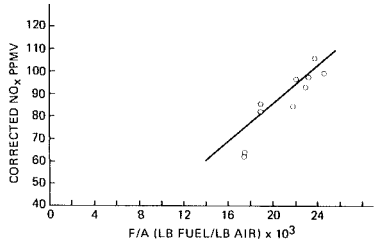

Fig. 20 NO_x emissions for Rolls-Royce combustor (ERSB Fuel) normalized to inlet conditions of 162.7 psia, 632°F and air flow of 7.6 lb/s

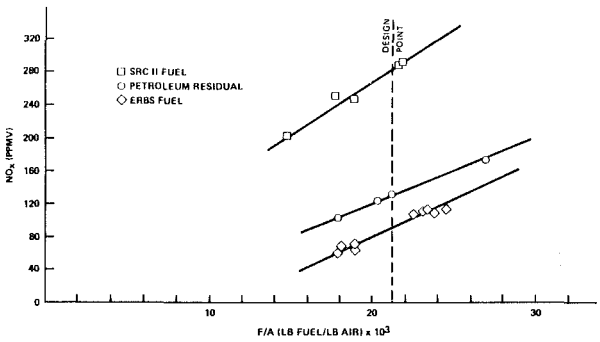

Fig. 21 Measured NO_x emissions (ppmv) for Rolls-Royce combustor versus fuel-air ratio for all fuels

emissions given in Fig. 20 for ERBS fuel show that the NO_x value is 91 ppm at the peak design condition. These data have been adjusted for the various test inlet conditions of the burner. The linear correlation of the data is evident. The combustion efficiencies are higher than 99.9 percent. At the peak design condition, the CO and UHC emissions are 8 and 2 ppmv, respectively. Two smoke numbers, SAE = 5 and 11, were obtained. The quality of the sample for SAE = 11 is suspect and this number is likely to be very pesimistic.

The combustor design tested on the SRC II fuel oil (0.8 wt,. percent FBN) converted about 40 percent of the bound nitrogen. The measured NO_x emissions are given in Fig. 21. At the design point, for instance, the NO_x emission is 280 ppmv. A straight line variation exists for the points measured. A smoke number of 7 (SAE) was observed for a CDL run with CO varying between 16–37 ppmv and UHC of 2 ppmv.

Additional tests were run for ERBS fuel and for petroleum residual fuel (Fig. 21). The NO_x emissions for the three fuels are ordered corresponding to increasing values of the fuel bound nitrogen. The conversion rates of the fuel bound nitrogen in the tests with residual fuel vary between 30–40 percent and as in the SRC II fuel oil are comparable to those

Downloaded 01 Jun 2010 to 171.66.16.62. Redistribution subject to ASME license or copyright; see http://www.asme.org/terms/Terms_Use.cfm

Table 4 Multiannular swirl burner preliminary results

Test Run	Fuel	Temperature, °F (°C)	NO_x ppmv	Remarks
20	ERBS	2035 (1113)	86	Central nozzle only
40	CDL	1948 (1064)	165	Central and radial nozzles
43	Residual	1995 (1091)	127	Central and radial nozzles

found in conventional combustors. These results indicate that fuel rich zones have not been sufficiently established in the combustor to alleviate the conversion of fuel bound nitrogen to NO_x. The primary equivalence ratios of this combustor about the design point are estimated to be 1.3, below the value of 1.6 which has been found to be optimum for minimum FBN conversion. It should be noted, however, that the exact definition of the primary zone is difficult in the case of an integral design combustor and it is possible that the effective air flow into the headend is less than calculated.

One test to determine the weak extinction limit of the burner was done and the extinction occurred at an AFR of 1100:1.

The combustion efficiencies were high on all the test runs (greater than 99 percent and in most cases greater than 99.9 percent).

Multiannular Swirl Burner. The multiannular swirl burner was operated in the rich-lean mode for optimum conversion of the fuel bound nitrogen. Maximum primary equivalence ratios were estimated to be about 1.5 with overall equivalence ratios of 0.2 - 0.25. These conditions were sufficient for the burner to achieve a low NO_x performance.

Test conditions for some of the preliminary results discussed in this paper are inlet pressure and temperature of 11.2 atmos (1.19 MPa) and 638°F (338°C) with a mass flow of 5.2 lb/s (2.36 kg/s). The results are shown in Table 4.

The NO_x results using SRC II fuel oil and residual oil in Table 4 show an increment in NO_x as compared with the results using ERBS fuel. This increment is consistent with the results observed in the operation of the rich-lean combustor discussed in the previous section. It appears that the percentage of FBN conversion (20 percent at 0.8 percent FBN) is significantly lower than that of a conventional burner.

Comparison of Test Results

Test results show that staged combustion (rich-lean) with the venturi jet quench has the best performance in terms of minimum NO_x emission for both the ERBS and SRC II fuel oils (except for lean catalytic combustion). The lowest value of NO_x is 70 ppmv for the ERBS fuel. This value occurs at the primary equivalence ratio of 1.8. For SRC II fuel oil, the NO_x increased for most combustors by an increment of 50 - 80 ppmv. For the rich-lean, venturi jet configuration, the increment is 70 ppmv. Quench module performance in rapidly quenching the NO_x forming reactions is critical to the amount of thermal NO_x formed. Of the two quench modules tested, the venturi jet is more efficient than the vortex mixer, if the NO_x formation is used as the criterion.

Two types of lean burner were tested: a ceramic lined section and a catalyst element. Results show that the ceramic lined section is adequate to complete combustion in all cases. However, the minimum NO_x becomes independent of the primary equivalence ratio in the presence of the catalytic reactor in the lean burner. This fact is of practical significance since smoke becomes a problem at higher equivalence ratios.

The catalytic combustor in the lean mode forms the lowest NO_x with ERBS fuel. Conversion rates in the range of 40-50 percent for SRC II fuel oil with fuel bound nitrogen at the 0.8 percent level were observed.

The Rolls-Royce combustor achieved a low NO_x emission at the design condition for the ERBS fuel. This value is comparable with that obtained from the multiannular swirl burner. However, the Rolls-Royce combustor primary zone is not sufficiently rich to prevent the conversion of the fuel bound nitrogen, which leads to conversion values on the order of 50 percent. The NO_x from the combustion of SRC II is the highest of the combustors tested.

With the coal-derived liquid SRC II (0.8 percent FBN), the multiannular swirl burner adds an increment of NO_x to the ERBS result which is on the order of the increment found in modular burners. The conversion efficiency of the MASB for SRC-II fuel is low.

Conclusions

This program to develop fuel flexible combustors with low emissions to meet the EPA regulation has been successful in meeting its objectives to date. The following combustors have been designed and tested at full pressure and temperature and have been found adequate and promising for further development:

1 The NO_x emissions of the burner with the rich-lean diffusion flame venturi quench and ceramic lined pipe lean burner meet the EPA limit for the ERBS fuel and close to meeting the limit for the SRC II coal derived liquid for a 30 percent cycle efficiency.

2 The primary equivalence ratio for minimum conversion of NO_x for this rich-lean configuration is between 1.6 and 1.63.

3 The multiannular swirl burner also meets the EPA limit for the ERBS and residual fuels. It appears that the NO_x level performance can be further lowered to that of (1) aforesaid.

4 The Rolls-Royce combustor meets the EPA regulation for ERBS fuel for a cycle efficiency of 30 percent.

5 The lean catalytic combustor meets the ultra low NO_x limit (one-half of the EPA limit) for ERBS fuel (#2 distillate).

6 There is a difference in NO_x results between pyridine doped fuel and real fuels with fuel bound nitrogen. This difference may arise from two sources. One is that the conversion efficiency of pyridine doped fuel is different from that of coal derived liquid fuel. The second is due to the inaccuracy in the fuel analysis techniques in determining the fuel bound nitrogen in coal derived liquid fuels.

7 It has been shown that staged combustion with diffusion flame is successful in creating rich-lean conditions for minimum NO_x production.

8 This diffusion flame advantage allows heavy residual fuel to be effectively burned without the requirement of prevaporization.

9 The use of a ceramic lined wall in the combustor modules has been shown to be effective in the enhancement of combustion processes and in handling the heat transferred from the hot gases to the wall.

Acknowledgments

The work described in this paper is a part of the DOE/LeRC "Advanced Conversion Technology Project"

Downloaded 01 Jun 2010 to 171.66.16.62. Redistribution subject to ASME license or copyright; see http://www.asme.org/terms/Terms_Use.cfm

(ACT). The program is a multiple contract effort with funding provided by the Department of Energy and technical program management provided by NASA LeRC. The DOE Program Manager is Mr. Warren Bunker of the Heat Energy and Heat Recovery Division of the Office of Coal Utilization.

This work has been carried out at Westinghouse and has active support from D. Protheroe, of the Industrial and Marine Division of Rolls-Royce, Ltd., on the Rolls-Royce combustor; I. Osgerby, of Engelhard Minerals and Chemical Corporation, on the catalytic configurations; and Prof. J. Beér, MIT, on the multiannular swirl burner. The authors wish to thank these participants in the program.

In the Westinghouse R&D Center, Dr. William E. Young and Dr. E. A. DeZubay made valuable contributions to the project.

References

1 Lister, E., Niedzwiecki, R. W., and Nichols, L., "Low NO_x Heavy Fuel Combustor Program," ASME Paper No. 80-GT-69, Mar. 1980.

2 Pillsbury, P. W., et al., "Fuel Effects in Recent Combustion Turbine Burner Tests of Six Coal Liquids," ASME Paper No. 79-GT-137, Mar. 1979.

3 Cohn, A., et al., "Combustion Effects of Coal Liquid and Other Synthetic Fuels in Gas Turbine Combustors — Part I, Fuels Used and Subscale Combustion Results," ASME Paper No. 80-GT-67, Mar. 1980.

4 DeZubay, E., "Low NO_x Burner Systems for Gas Turbines," American Power Conference Proceedings, Apr. 21-23, 1980, Chicago.

5 DeCorso, S. M., et al., "Catalysts for Gas Turbine Combustors Experimental Test Results," ASME Paper No. 76-GT-4, Mar. 1976.

6 Carrubba, R. V., et al., "Catalytically-Supported Thermal Combustion for Emission Control," *Proceedings of the NO_x Control Technology Seminar,* EPRI SR-39, Feb. 1976.

7 Lew, H. G., et al., "Experimentally Determined Catalytic Reactor Behavior and Analysis for Gas Turbine Combustors," ASME Paper No. 79-GT-150.

8 McKnight, D., "Development of a Compact Gas Turbine Combustor to give Extended Life and Acceptable Exhaust Emissions," ASME Paper No. 78-GT-146, 1978.

9 Beér, J. M., "Improvements in or Relating to Burners for Pulverized Coal or like Solid Fuel or for Liquid or Gaseous Fuel," British Patent No. 45652, 1968, U.S. Pat. appl. for 238668, 1981.

10 Gupta, A. K., Beér, J. M., and Swithenbank, J., "Concentric Multiannular Swirl Burner: Stability Limits and Emission Characteristics," *Sixteenth (International) Symposium on Combustion,* The Combustion Institute, 1976.

11 Mumford, S. E., et al., "A Potential Low NO_x Emission Combustor for Gas Turbines Using the Concept of Hybrid Combustion," ASME Paper No. 76-WA/GT-15, 1976.

12 Prock, G. M., and Seng, G. T., "Initial Characterization of an Experimental Referee Broadened Specification ERBS Aviation Turbine Fuel," NASA TM 81440, Jan. 1980.

Downloaded 01 Jun 2010 to 171.66.16.62. Redistribution subject to ASME license or copyright; see http://www.asme.org/terms/Terms_Use.cfm

Establishing Cruise-Engine Cycle Payoffs for a Supersonic VSTOL Aircraft

J. D. Cyrus
Naval Air Development Center,
Warminster, Pa.
Mem. ASME

P. F. Piscopo

R. T. Lazarick
Naval Air Propulsion Center,
Trenton, N.J.

Engine-aircraft mission studies have been conducted by the Navy to establish changes in the weight and performance of supersonic VSTOL aircraft resulting from changes in the main cruise engine configuration, cycle characteristics, and complexity. The effects of engine component efficiency variations were quantified by a sensitivity analysis which identified performance changes on four different missions for a single engine aircraft. Studies of a twin engine aircraft with four different propulsion system configurations established the impact of changes in various cycle parameters on aircraft takeoff gross weight for the same three missions and identified thermodynamic and physical constraints for the cycles.

Introduction

For the last three years the Naval Air Development Center (NADC) and the Naval Air Propulsion Center (NAPC) have been conducting joint in-house studies for the Naval Air Systems Command to quantify the sensitivity of Navy-designed supersonic Vertical/Short Takeoff and Landing (VSTOL) aircraft to changes in cruise engine configuration and component efficiency. In-house engine simulations at both NADC and NAPC were used and constant technology levels were maintained throughout the study. While the studies are of a conceptual nature, the engine modeling was conducted at a level of detail which defined the number of compressor and turbine stages, turbine cooling flow requirements, compressor and turbine loading, and materials technology. The investigations were limited in scope to the main lift/cruise engines and did not include an investigation into lift system technology.

Background

Because supersonic VSTOL aircraft consume fuel in significant amounts on each of several mission segments and because aircraft mission performance is strongly affected by propulsion system weight and size, thrust and specific fuel consumption considerations for a single mission segment cannot adequately indicate an engine's impact upon an aircraft. Therefore, engine-aircraft-mission studies were utilized to gain an understanding of the impact of changes in the propulsion system design and performance; aircraft takeoff gross weight (TOGW), range, and time-on-station (TOS) were used as figures-of-merit.

This study was conducted in two phases. In the first phase, an investigation of the effect of component efficiency variations upon aircraft performance was conducted on a model of a lift/lift-cruise VSTOL configuration utilizing a single turbofan engine and two turbojet lift engines. This configuration, shown in Fig. 1, was based on the design in Reference 1. It was chosen because it was a reasonable configuration with which to evaluate changes and because a computer simulation of the aircraft was available and operational at NADC. In the second phase of the study, the effects of engine configuration variations were investigated utilizing a three-poster airframe design shown in Fig. 2 (described in reference [2]). It employed two lift/cruise engines and a lift system consisting of either lift engines or a Remote Augmentor Lift Systems (RALS). These lift devices were of similar shape and could conceivably by installed in a single aircraft configuration. This configuration also rovided space within the fuselage to contain the ducting for the RALS.

In the parametric component sensitivity analysis the effect of component efficiency variations were established for four different engine parameters on three different missions. In the configuration/cycle studies, the effects of cycle variations on mission performance and aircraft takeoff gross weight (TOGW) were established for configurations utilizing single spool turbojets, twin spool turbojets, fixed cycle turbofans, and variable cycle turbofans. The engine configurations investigated during this study were selected because they span the spectrum of engine complexity. The mission profiles, ground rules, and engine/aircraft configurations used in this study were arbitrarily selected for study purposes only and do not reflect official Navy policy. It is recognized that other lift systems and/or aircraft configurations could be effectively utilized in a supersonic VSTOL aircraft.

Method of Analysis

In both the component efficiency and engine configuration studies, NAPC defined the component technology levels, calculated the design point uninstalled engine performance data using in-house engine performance codes, and computed the bare engine weights and dimensions using the Boeing Weight Code (WATE) (reference [3]). This data was transmitted to NADC where the engines were modeled and inlet

Contributed by the Gas Turbine Division of THE AMERICAN SOCIETY OF MECHANICAL ENGINEERS and presented at the Gas Turbine Conference and Products Show, March 9-12, 1981, Houston, Texas. Manuscript received at ASME Headquarters December 11, 1980. Paper No. 81-GT-100.

Copyright © 1982 by ASME
Downloaded 01 Jun 2010 to 171.66.16.62. Redistribution subject to ASME license or copyright; see http://www.asme.org/terms/Terms_Use.cfm

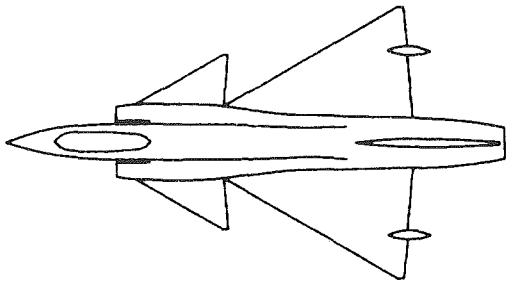

Fig. 1 Configuration for component efficiency investigations

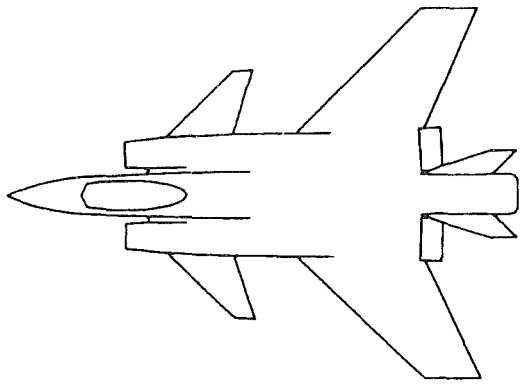

Fig. 2 Configuration for cycle parameter investigation

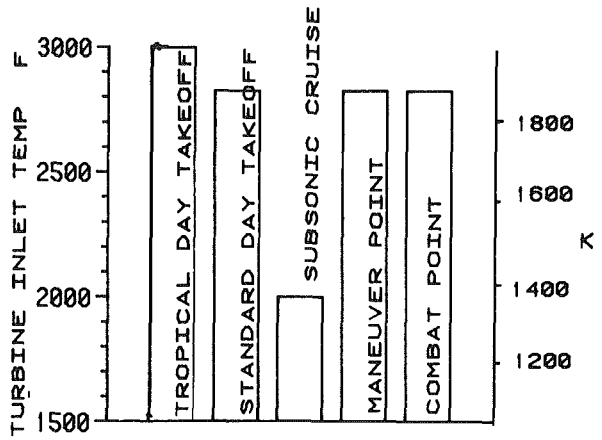

Fig. 3 Turbine inlet temperature limits

and nozzle installation effects were added using the NEPCOMP engine performance code (reference [4]). Installed engine data decks were then generated for use with NADC's aircraft synthesis code, HIPERAC. The baseline vehicle's geometry was adjusted to accommodate the engine and, the vehicle was sized to meet NAVAIR study design ground rules as specified in reference [2]. Mission performance data were generated and TOGWs were computed for the baseline engine and then for each of the varient engines within the same category. Comparisons between the baseline engines and the varients were made in terms of the resulting difference in aircraft range, TOGW, or TOS for the respective vehicles. With the exception of single and twin-spool turbojets, comparisons were not made between aircraft with different engine configurations.

Airframe Technology Ground Rules. The airframes considered in the two phases of this study were designed for the Deck Launched Intercept (DLI) mission. The propulsion system was flat rated to provide a tropical day takeoff capability while accounting for suckdown and reingestion losses as well as providing a vertical acceleration margin of five percent. To achieve this, the aircraft were designed with a vertical takeoff thrust-to-weight ratio of 1.22.

The airframes in the two phases of the study were markedly different in several respects. The single cruise engine aircraft used in the parametric sensitivity analysis was an all-metal aircraft with a thrust split of 0.64/0.36 (64 percent of the aircraft's takeoff thrust comes from the forward nozzle and 36 percent comes from the aft nozzle). The twin engine configuration (Fig. 2) used in the configuration/cycle study was designed with a thrust split of 0.37/0.63. It employed significant amounts of composite material which were projected to produce weight savings in the major components which varied from 17 percent in the landing gear to 32 percent in the tail. The weight savings from the composites and the relatively large size of its cruise engine gave it significantly greater specific excess power and maneuvering capability than the single engine aircraft.

Propulsion System Technology Ground Rules. A consistent set of engine material and component performance technologies were used throughout both study phases. The technology levels are representative of an aircraft with an initial operating capability of 1995. To maintain a consistent set of material technologies the turbine blade and vane bulk metal temperatures were limited to the same level for all systems. The cooling flows were therefore sized by this constraint. Consequently, changes in the engine thrust-to-weight ratio were caused by cycle variations and not by material technology improvements. All engines were flat rated for a 90°F (305.3 K) tropical day by increasing the turbine inlet temperature above the sea level static day operating level; the turbine cooling bleed flows were sized for a 30 min rating by the tropical day condition. The maximum turbine inlet temperature for all of the turbofan engines was utilized only during tropical day takeoff. At other operating conditions the turbine inlet temperatures were lower so the blades and vanes had excess cooling flow available; this enabled the engine to operate at these conditions without time-limited ratings. Figure 3 shows the typical turbine rotor inlet temperature (TRIT) usage at a variety of aircraft flight conditions. A detailed discussion of the engines and the propulsion system technologies used in these studies is provided in reference [5].

Propulsion System Sizing. In these studies the engine size was determined by mission constraints, the thrust split between the lift device and the lift/cruise engine (which was dictated by the aircraft configuration and balance requirements) and the aircraft control scheme (which dictated the bleed flow requirements from the engine). Initial estimates of engine weight and size were generated at NAPC based on the aircraft size and the tropical day takeoff thrust split. Engine-aircraft-mission analysis was then used to check the engine's ability to meet mission requirements for maximum sustained maneuver load factor (Nz) and specific excess power (Ps). Subsequent changes in the engine size were handled in the aircraft synthesis code by simple scaling laws.

Installed Engine Performance. In both the parametric sensitivity study and the configuration/cycle study, the aircraft designs used two-dimensional two-ramp inlets. The parametric sensitivity aircraft employed an axisymmetric three bearing swivel nozzle while the configuration/cycle study aircraft employed two dimensional vectoring nozzles. The uninstalled engine data was adjusted as shown in Fig. 4 for losses in inlet total pressure, and drags resulting from inlet spillage and nacelle boattail. The inlet pressure recovery (RF) was assumed to vary as a function of Mach number with no

Downloaded 01 Jun 2010 to 171.66.16.62. Redistribution subject to ASME license or copyright; see http://www.asme.org/terms/Terms_Use.cfm

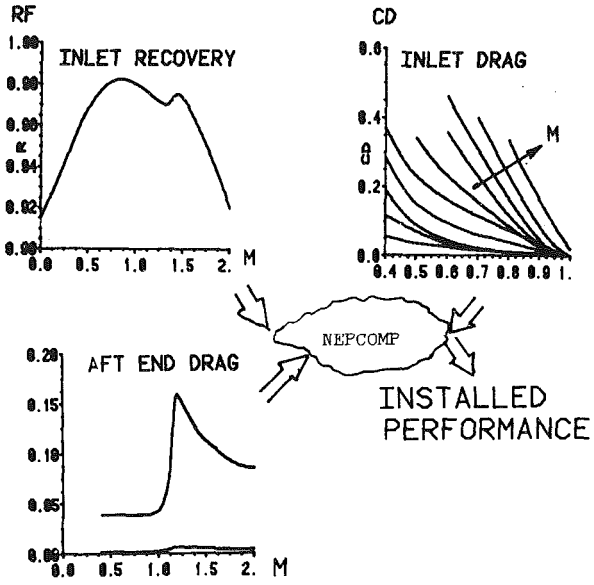

Fig. 4 Installation effects

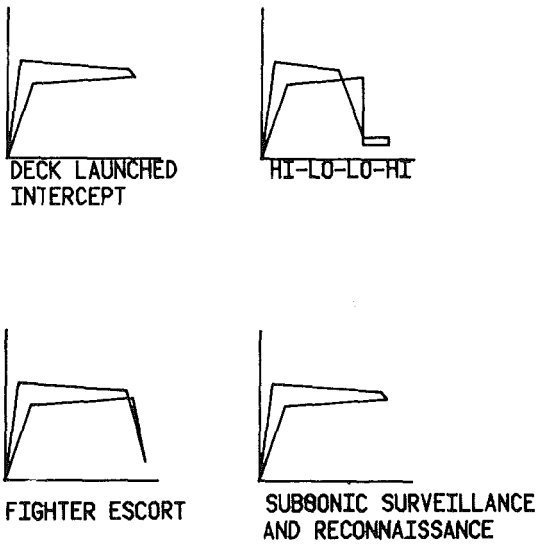

Fig. 5 Mission profiles

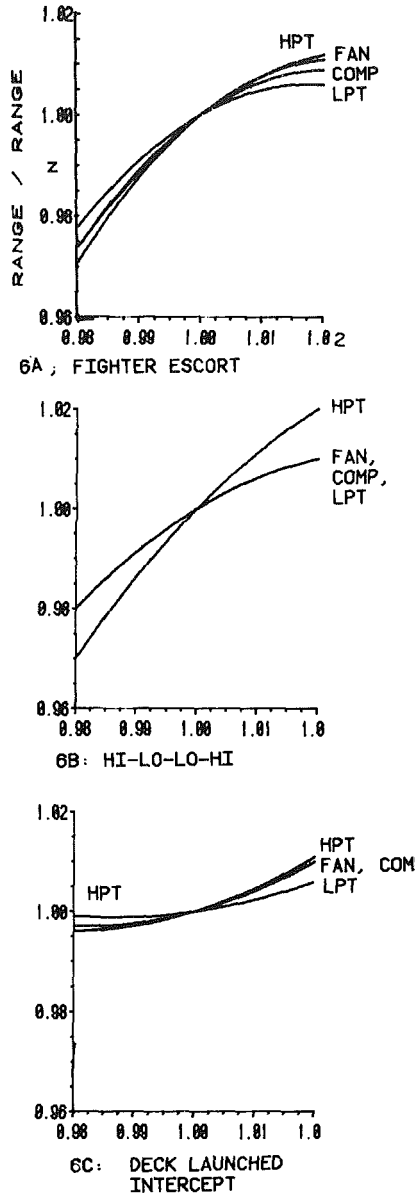

Fig. 6 Effect of efficiency variations on range

dependence upon airflow. The inlet spillage drag was calculated as a function of mass flow ratio and Mach number. The inlet capture area was established for each of the parametric engines by calculating the free stream airflow demand of the engine at 36,000 ft (10,973 m) for a Mach numbers of 2.0, and adding three percent to this value to insure that the inlet would not choke. The throttle dependent boattail drag for the propulsion system was calculated as a function of Mach number and nacelle geometry.

Installed engine performance data were calculated for a matrix of altitudes, Mach numbers and power settings. Power settings varied from 20 percent of intermediate to maximum afterburning; altitudes varied from sea level to 50,000 ft (15,240 m); and Mach numbers varied from 0.0 to 2.0. Approximately 300 data points were generated for each engine.

Description of Missions. Four missions were considered at various stages of the study: a Deck Launched Intercept (DLI) mission, A Fighter Escort (FE) mission, an Interdiction (Hi-Lo-Lo-Hi) mission, and a subsonic surveillance and reconnaissance mission. These are depicted schematically in Fig. 5.

Parametric Component Sensitivity Analysis

Aircraft System Description. The aircraft design used in this portion of the study is a delta-wing/canard configuration powered by a single lift/cruise turbofan engine and two turbojet lift engines. The lift/cruise engine is supplied by two inlets, described earlier, which are mounted on either side of the fuselage. Vectoring of the lift/cruise engine for vertical takeoff was accomplished through a three bearing swivel nozzle. It was assumed that the control requirements of the aircraft would be met by bleeding the lift engines; consequently, no control penalties were assessed to the lift/cruise engine.

A mixed flow turbofan configuration was used for the parametric sensitivity study. Baseline engine cycle characteristics for the engine are shown in Table 1.

Parametric Sensitivity Study Results. In the sensitivity study the baseline engine was varied parametrically to establish the effect on the aircraft of two percent variations in fan efficiency, compressor efficiency, high pressure turbine efficiency, and low pressure turbine efficiency on DLI, Hi-

Downloaded 01 Jun 2010 to 171.66.16.62. Redistribution subject to ASME license or copyright; see http://www.asme.org/terms/Terms_Use.cfm

Table 1 Parametric sensitivity baseline engine cycle characteristics

Parameter	Design Point
Bypass Ratio	1.0
Fan Pressure Ratio	3.6
Fan Efficiency	0.83
Compressor Pressure Ratio	6.8
Compressor Efficiency	0.85
Burner Efficiency	0.99
Burner Pressure Drop	0.06
Turbine Rotor Inlet Temperature	3000°F (1922 K)
Allowable Turbine Metal Temp	1800°F (1255 K)
HP Turbine Efficiency	0.845
LP Turbine Efficiency	0.88
Afterburner Pressure Drop	0.05
Afterburner Max Temperature	3200°F (2033 K)
Afterburner Efficiency	0.89
Nozzle Thrust Coefficient	0.98

Lo-Lo-Hi, and FE missions. Installed engine decks were prepared for each of the parameters at levels above and below the baseline values. Combinations of component perturbations were not considered.

The effect of the efficiency variations varied from component to component and from mission to mission as shown in Figs. 6(*a*, *b*) and (*c*). The FE mission was the most sensitive to efficiency changes, with a two percent efficiency loss causing nearly a three percent loss in range. The Hi-Lo-Lo-Hi mission was the next most sensitive, and the Deck Launched Intercept mission was the least sensitive. For the DLI mission, a two percent change in efficiency caused, at most, a one percent change in mission radius. In general, the aircraft's range was affected by changes in high pressure turbine efficiency, fan efficiency, compressor efficiency, and low pressure turbine efficiency in that order. Changes in high pressure turbine efficiency had nearly twice the impact of changes in low pressure turbine efficiency.

Configuration/Cycle Study

Aircraft System Description. The aircraft design used in the configuration/cycle study is a three-poster arrangement with two lift/cruise engines located outboard of the fuselage and lift engines or remote augmentor lift systems located in the fuselage behind the cockpit. The aircraft utilizing single-spool turbojets and twin spool turbojets employed lift engines while remote augmentor lift systems were utilized with the fixed and variable cycle turbofans. Each lift/cruise engine is fed by a separate inlet. Vectoring of the cruise engine thrust for vertical takeoff operations was accomplished with an Augmented Deflector Exhaust Nozzle (ADEN).

When a RALS was used in conjunction with a lift/cruise engine, air is ducted from the lift/cruise engine forward through the fuselage to the RALS.

The control technique varied with the lift device. Nose-up pitch control for the aircraft employing lift engines was obtained by increasing the thrust of the lift engines while nose-down pitch was achieved by increasing the exhaust gas temperature of the lift/cruise engines. Roll and yaw control for this aircraft were achieved from reaction control jets supplied by bleed flow from the direct lift and lift/cruise engines. For the aircraft which utilized remote augmentor lift systems, nose-up pitch control was obtained by modulating the RALS burner temperature while nose down control was obtained by modulating the lift/cruise engine exhaust gas temperature. Roll control was obtained from puffer pipes fed by fan air taken from the RALS duct. Yaw control was obtained by gimballing the RALS nozzle.

During the configuration/cycle study single-spool turbojet, twin-spool turbojet, fixed cycle turbofan, and variable cycle turbofan configurations were examined. The cycle parameters considered varied with the configuration. Tables 2 and 3 provide a list of the engine cycle characteristics for the turbojet and turbofan systems, respectively. A summary of the engine configuration—cycle parameter matrix is shown in Table 4.

Table 2 Configuration/cycle study turbojet system design parameters

Parameter	Design Point
Overall Compressor Ratio	10-25
HP Compressor Efficiency	0.83-.87
Burner Efficiency	0.99
Burner Pressure Drop	0.05-.06
Turbine Rotor Inlet Temperature	2200-3000° F (1478-19 22 K)
Allowable Turbine Metal Temp	1800°F (1255 K)
HP Turbine Efficiency	0.858-.87
LP Turbine Efficiency	0.88
Afterburner Pressure Drop	0.05
Afterburner Max Temperature	2800-3200°F (1811-2033 K)
Afterburner Efficiency	0.96
Nozzle Thrust Coefficient	0.96

Table 3 Configuration/cycle study turbofan engine system design parameters

Parameter	Design Point
Bypass Ratio	1.0
Fan Pressure Ratio	3.6
Fan Efficiency	0.83
Compressor Pressure Ratio	6.8
Compressor Efficiency	0.85
Burner Efficiency	0.99
Burner Pressure Drop	0.06
Turbine Rotor Inlet Temperature	2800-3200°F (1810-2033 K)
Allowable Turbine Metal Temp	1800°F (1255 K)
HP Turbine Efficiency	0.845
LP Turbine Efficiency	0.893
Afterburner Pressure Drop	0.05
Afterburner Max Temperature	3400°F (2144 K)
Afterburner VTO Temperature	2800°F (1810 K)
Afterburner Efficiency	0.89
Nozzle Thrust Coefficient	0.98

Turbojet Results. In the configuration/cycle turbojet studies, the effects of control bleed flow level, TRIT, and overall cycle pressure ratio variations on aircraft TOGW were defined. Control bleed flow was examined at 0, 7.5, and 15 percent levels; TRIT was examined at 2200, 2600, and 3000°F (1477, 1500, 1921 K); and overall pressure was examined at 20:2 and at 25:1.

The effect of increasing the control bleed from the lift/cruise, single-spool turbojet engine was to increase TOGW. Figure 7 shows that for up to 7.5 percent control bleed, the increase in takeoff gross weight was modest; the change in gross weight from the baseline aircraft's level (with zero bleed) was only three percent at 7.5 percent bleed. Beyond 7.5 percent, additional increments in bleed flow caused the takeoff gross weight to increase rapidly. At 15 percent control bleed the change in TOGW was 35 percent.

The relationship of aircraft TOGW to TRIT is shown in Fig. 8. Increasing TRIT from 2200 to 2600°F (1366 to 1699 K) reduced aircraft TOGW 7 percent. As the TRIT is increased above 2600°F (1699 K), the cooling flow requirements of the turbine and afterburner liner increasingly penalized engine SFC and caused engine thrust-to-weight ratio improvements to diminish. This can be seen in Fig. 9. Since the bulk of the fuel used by the aircraft is consumed during subsonic

Downloaded 01 Jun 2010 to 171.66.16.62. Redistribution subject to ASME license or copyright; see http://www.asme.org/terms/Terms_Use.cfm

Table 4 Summary of engine configuration—cycle parameter matrix

TRIT	One-Spool turbojet	Two-Spool turbojet	RALS/VCE turbofan	RAL/FCE turbofan
2200	0/13*			
2600	0/13*			
	7.5/11*			
	15.0/10*			
	5/20*	5/25*		
2800			1.0/24.3**	
				1.0/24.3**
				1.2/24.3**
3000	0/13*		1.0/24.3**	
				1.0/24.3**
				1.2/24.3**
3200			1.0/24.3**	
				1.0/24.3**
				1.2/24.3**

Note: * percent bleed/OPR
**BPR/OPR

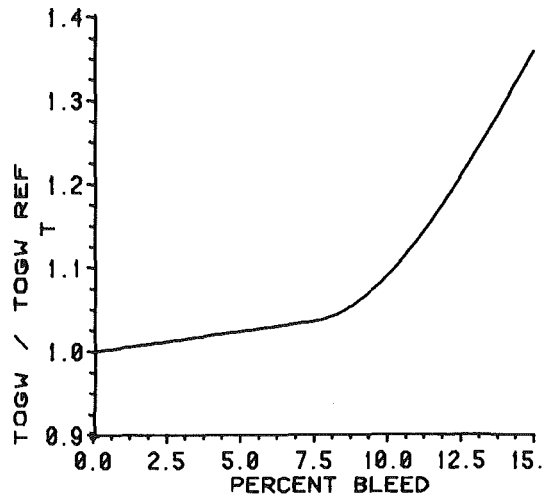

Fig. 7 Effect of bleed flow on TOGW

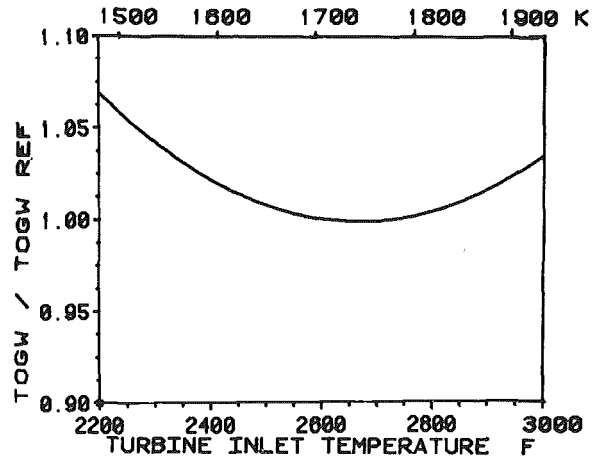

Fig. 8 Effect of T4 variations on TOGW

operation (see Fig. 10), the penalties due to increased SFC more than offset the improvements from a slightly better thrust-to-weight ratio. The net result was to increase aircraft TOGW as TRIT increased from 2600 to 3000°F (1699 to 1921 K).

Two different turbojet configurations were used to examine the overall pressure ratio effects. A 20:1 system was configured with a single spool compressor driven by a two stage turbine; a 25:1 system was configured as a two spool turbojet with single stage high and low pressure turbines. Control bleed and TRIT were held constant at 0 percent and 2600°F

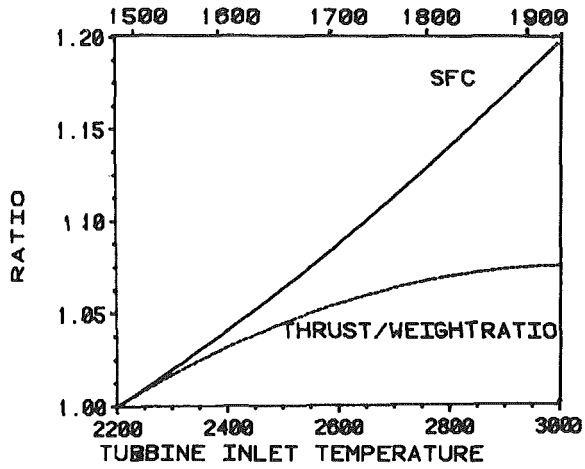

Fig. 9 Effect of T4 on SFC and thrust/weight ratio

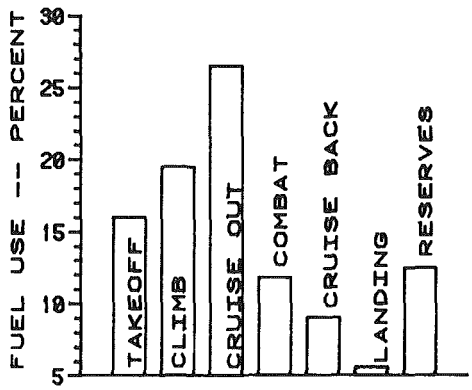

Fig. 10 Fuel use on a DLI mission

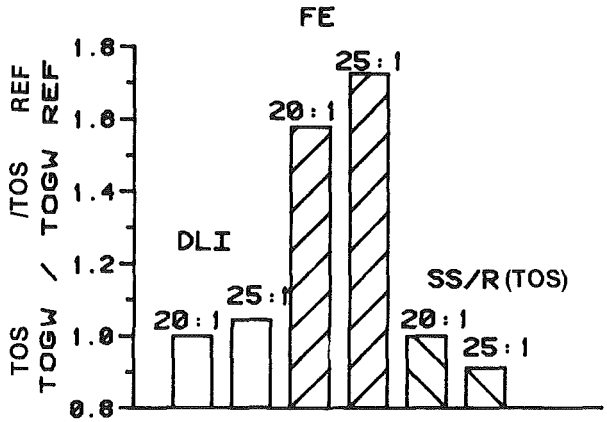

Fig. 11 Effect of OPR on TOGW for turbojets

(1699 K) respectively. The 20:1 single-spool turbojet powered aircraft has a slight advantage over an aircraft with a 25:1 twin-spool turbojet (see Fig. 11); the takeoff gross weight required to perform a Deck Launched Intercept mission is four percent less with the single-spool engine; the takeoff gross weight required to perform a fighter escort mission is nine percent less; and the time on station with the single-spool turbojet is ten percent greater. This finding does not imply that all twin-spool turbojets produce poorer aircraft than a good single-spool engine. Higher pressure ratio twin-spool engines may be competitive with the single-spool turbojets.

Fixed Cycle RALS Turbofan. In the configuration/cycle fixed cycle RALS turbofan studies, the effects of TRIT and bypass ratio (BPR) on aircraft TOGW and time-on-station were assessed. TRIT was varied from 2800 to 3200°F (1811 to

Downloaded 01 Jun 2010 to 171.66.16.62. Redistribution subject to ASME license or copyright; see http://www.asme.org/terms/Terms_Use.cfm

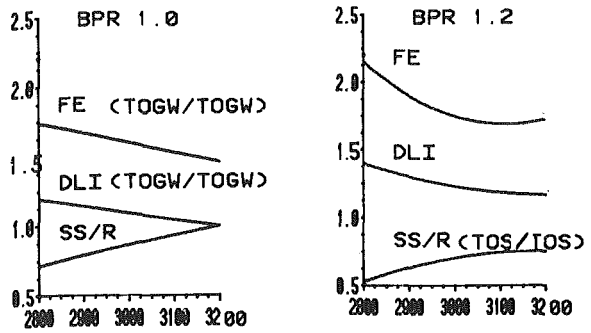

Fig. 12 Effects of BPR and T4 on mission performance

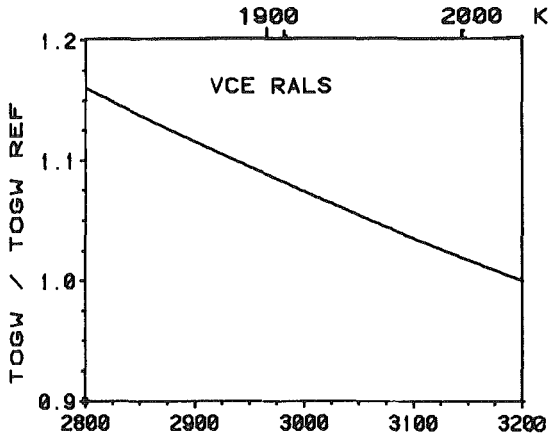

Fig. 13 Effect of T4 on TOGW

2033 K) while BPR was investigated at two levels, 1.0 and 1.2.

Figures 12 (*a*) and (*b*) show the impact of TRIT on TOGW and TOS for the BPR 1.0 and 1.2 engines, respectively. In both cases, increases in TRIT resulted in a reduction in aircraft TOGW and an increase in TOS.

An increase in BPR from 1.0 to 1.2 reduced TOS and increased TOGW. This was due to a combination of factors. The lower pressure ratio associated with the BPR 1.2 engines caused the RALS ducting to grow. This in turn caused the fuselage width, fuselage weight, and aircraft drag to increase. Finally, the core exhaust gas temperatures of the 1.0 and 1.2 BPR engines were arbitrarily limited to the same temperature, 2938°F (1888 K), to maintain the same "technology level" and control margin capability. This latter choice, in effect, required an increase in airflow (and engine weight) for the BPR 1.2 engines. Approximately one third of the total difference between the aircraft gross weights arises from this choice.

Variable Cycle RALS Turbofan. In the RALS/variable cycle turbofan studies, the effects of TRIT and engine exhaust gas temperatures (EGT) on aircraft TOGW were assessed on a DLI mission.

Turbine inlet temperature was found, as in the fixed cycle turbofan systems, to have a significant impact upon aircraft TOGW. It can be seen in Fig. 13 that a decrease in turbine inlet temperature from 3200°F (2033 K) to 2800°F (1811 K) will cause the aircraft takeoff gross weight to grow approximately fifteen percent.

In Fig. 14 it can be seen that there is a weight advantage to RALS with hot gas temperatures, or conversely there is a substantial penalty to be paid if the RALS exhaust temperatures must be reduced to comply with a deck temperature limitation. At constant TRIT, the TOGW of the aircraft will increase eighteen percent as the RALS exhaust temperature is reduced from 2800°F (1811 K) to 2200°F (1478 K). In contrast, the exhaust temperature of the turbojet/lift engine

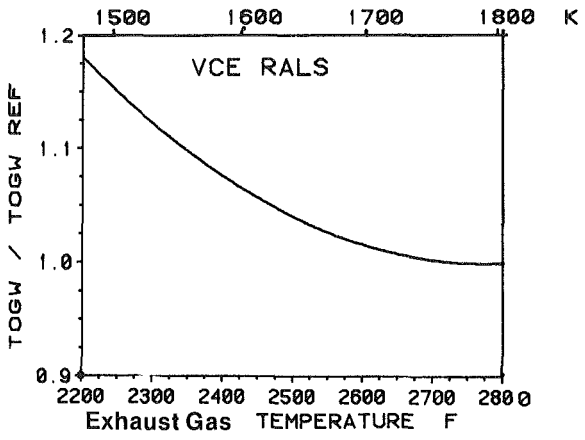

Fig. 14 Effect of EGT on TOGW

system is only 2000°F (1428 K), which is the exhaust temperature of the lift engine.

Conclusions

During this study a wide range of cruise engine configurations were considered, from single-spool turbojets to variable cycle turbofans. The single most significant conclusion of this study was that all of these configurations can produce competitive aircraft designs. However, certain items were identified which can have a marked impact on the weight of the vehicle. As a result of this study the following observations are made:

1 Aircraft takeoff gross weight and mission performance are strongly impacted by reaction bleed flow requirements, particularly at bleed flow values above 7.5 percent.

2 Aircraft TOGW is strongly affected by EGT or deck temperature limitations.

3 For aircraft with RALS, aircraft TOGW is quite sensitive to changes in RALS duct pressure.

4 In general, there is a beneficial effect obtained from increasing TRIT with both the fixed and variable cycle turbofans.

5 Increasing turbine inlet temperature for a single-spool turbojet was beneficial up to approximately 2600°F (1700 K). At higher temperatures, cycle considerations, such as turbine cooling bleed and turbine loading limitations, held the potential engine weight payoff down while fuel consumption characteristics deteriorated; the combined impact of these trends caused aircraft gross weight to increase.

6 Because of vehicle thrust requirements, maximum turbine rotor inlet temperatures were needed only for tropical day takeoff. Therefore, the life of these engines is extended in comparison to those engines that utilize the maximum turbine inlet temperature capability at a variety of points in the mission.

7 The impact of small perturbations in engine component efficiencies are not a strong driver on aircraft range.

References

1 "Aircraft/Engine and Performance Tradeoff Analysis of a V/STOL Delta Canard Lift Plus Lift-Cruise Aircraft," General Dynamics Report GDCA-DHG73-005, 2 July 1973.

2 Becker, W.E., Et al, "Impact of Technologies on Potential V/STOL B Aircraft," NADC Report NADC-80007-60, 21 Jan 1980.

3 Caddy, Michael J., and Shapiro, Stanley R., "NEPCOMP—The Navy Engine Performance Computer Program, Version I," NADC Report NADC-74045-30, 15 April 1975.

4 Pera, R.J., Et Al, "A Method to Estimate Weight and Dimensions of Aircraft Gas Turbine Engines," NASA CR135171, May 1977.

5 Piscopo, P.F., "Effects of Turbine Rotor Inlet Temperature, Bypass Ratio, and Reaction Control Bleed Flow on Supersonic VSTOL Propulsion Systems," ASME Paper No. 80-XXX.

Downloaded 01 Jun 2010 to 171.66.16.62. Redistribution subject to ASME license or copyright; see http://www.asme.org/terms/Terms_Use.cfm

Design of a Turbomachine Set for a Fluid Catalytic Cracking Plant and Its Shop-Testing Under Full-Load Conditions

L. Turanskyj

G.-U. Woelk

M.A.N. Maschinenfabrik,
Augsburg-Nürnberg,
Aktiengesellschaft,
Division GHH STERKRADE,
Oberhausen/Rhld., West Germany

In fluid catalytic cracking plants, heavy hydrocarbons are converted into low-boiling point products. The highly developed technology of this process makes it particularly suitable for the handling of heavy fractions and thus for energy economy in the future. Starting from a concise description of the energy recovery system, this paper details the design features of a turbo machine set for an FCC plant, with the emphasis on the design of the four-stage 12,000 kW process gas expander. Since this expander incorporates new design features, an extensive test programme was carried out at a large turbomachinery test facility, where, in addition to testing the individual machine units under full-load conditions, a string test of the complete turbomachine set was performed under hot-gas conditions.

Introduction

Despite higher oil prices worldwide, there is still an increasing demand for light hydrocarbons. This is due to the continuing increase in motorized transport and the concentration of the process industry upon the use of these oil-based feedstocks for the production of plastics, synthetic fibre, etc.. It can be assumed that this development will be continuing in the coming years.

However, the increasing demand for light hydrocarbons can no longer be covered by simple distillation of the crude oil, but it is increasingly necessary to introduce additional cracking operations to split heavy hydrocarbons into low-boiling fractions. These processes are also attractive from an economic point of view, as the cheaper heavier ends were difficult to sell in the past. The fluid catalytic cracking process (FCC) has been introduced as a reliable method for feedstock conversion.

In the course of several decades, this particular process has been steadily refined [1, 2], making it possible today to handle virtually all crudes in FCC plants with good efficiency and at acceptable costs, particularly since in the design stage, or during subsequent reconstruction, the plant can be adapted to the respective feedstock.

A major portion of the energy still contained in the waste gases obtained can be recovered by means of process gas expanders with series-connected waste heat boilers. This particular application is becoming more and more important in the face of rising energy costs. The operator of any FCC plant will try to achieve minimum operating costs by demanding a maximum of energy recovery for the given cracking process. Any R + D work concentrating on improving the energy utilization is therefore aimed at sophisticating the process technology proper as well as the plant components used. These tasks must be solved in collaboration between the process licensers, operators, and component suppliers.

Based on many years of experience in the manufacture of turbomachine sets with hot-gas expanders, including those for application in nitric acid plants or in closed-cycle gas turbine systems, machine sets for advanced FCC plants have been designed which generally consist of axial-flow or centrifugal compressor for the compression of atmospheric air as well as steam turbine and process gas expander, motor/generator, and often gearing.

For 12,000 kW process gas expander to be used in an FCC plant at Rotterdam, the Netherlands, new design developments were made in line with the particular operating conditions of the machinery concerned. In view of the fact that this was one of the first multistage process gas expanders, an extensive test program was carried out on the complete machine set under full-load conditions in a large capacity test facility in order to demonstrate the full operational reliability of the turbo set before delivery to site. The present paper deals with design details of the machine units built for this FCC plant, as well as with the implementation of the test program and with the test results.

Energy Recovery System

The task to be performed by an FCC plant is the catalytic conversion of heavy hydrocarbons into low-boiling products. The catalyst is a fine-grained powder consisting of Al_2o_3 and Sio_2 which together with the feedstock continuously flows through a vertical reactor (Fig. 1). During the cracking

Contributed by the Gas Turbine Division of THE AMERICAN SOCIETY OF MECHANICAL ENGINEERS and presented at the Gas Turbine Conference and Products Show, March 9-12, 1981, Houston, Texas. Manuscript received at ASME Headquarters December 11, 1980. Paper No. 81-GT-101.

Copyright © 1982 by ASME

Downloaded 01 Jun 2010 to 171.66.16.62. Redistribution subject to ASME license or copyright; see http://www.asme.org/terms/Terms_Use.cfm

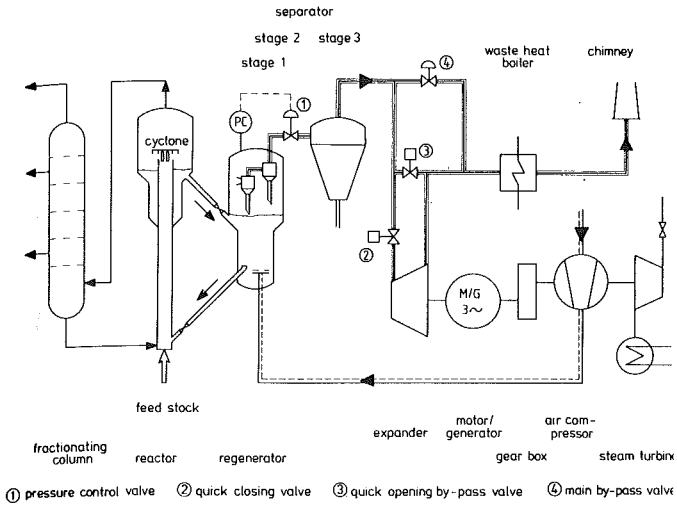

Fig. 1 Flow sheet of FCC process with energy recovery system

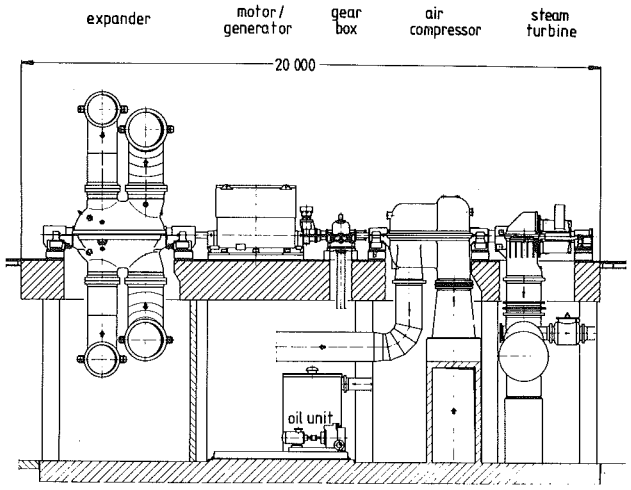

Fig. 2 Machine set for an FCC plant

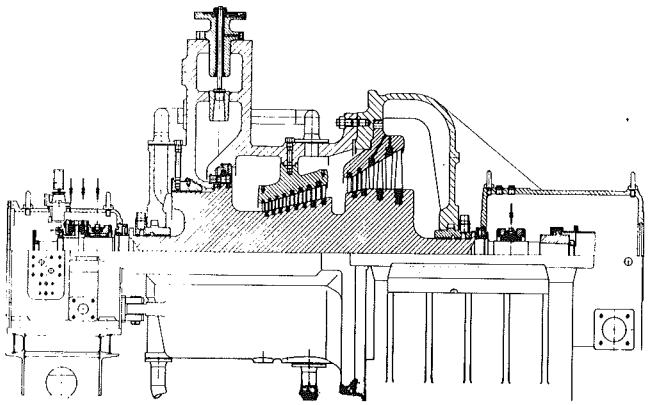

Fig. 3 Start-up steam turbine

process, carbon is deposited on the catalyst particles in the form of coke. In addition, traces of heavy metals and sulphur are also deposited, thus making the catalyst ineffective. Through connecting pipework the catalyst is returned to a regenerator located at a lower level, where the deposited coke is burnt off. The regenerated catalyst is then resupplied to the reactor, thus closing the catalyst loop.

The waste gas generated when burning the coke reaches a temperature of 700 to 760°C in modern FCC plants, at a pressure of approximately 3 bar. The energy still contained in the gas is utilized by means of a recovery system mainly consisting of a process gas expander with subsequent waste heat recovery boiler.

In the process gas expander (Fig. 1) the waste gas is expanded to about atmospheric pressure. The power output is primarily absorbed by the air compressor which keeps the catalyst in the regenerator in a fluidized phase and supplies the air required for burning the deposited coke. Depending upon the gas inlet temperature, the expander can provide up to 120 percent of the required drive input power of the compressor. Today, the machine train in such a plant would typically consist of the following components:

- process gas expander
- motor/generator
- gearbox
- air compressor
- steam turbine.

The "excess" mechanical power developed in the process gas expander is converted into electric power by the asynchronous motor/generator which would under these conditions be generating.

The steam turbine is used during the start-up phase of the machine set. When the process gas expander is not producing energy, the full power required by the air compressor can be jointly provided by the asynchronous M-G machine (operating as a motor), and by the steam turbine.

The pressure in the regenerator is adjusted by means of a control valve (Fig. 1, item 1); in cases of maloperation, the process gas expander is protected by a trip butterfly valve (Fig. 1, item 2) included in the machine set supply. To prevent the turbo set from being accelerated in the event of load release by the generator, a bypass valve (Fig. 1, item 3) is provided which opens very quickly to dump a portion of the flue gas flow, thus reducing the expander power output. If there is serious trouble, all the flue gas can be directed past the expander through a bypass (Fig. 1, item 4).

Figure 2 shows the turbomachine train of the FCC plant which was previously tested in exactly the same arrangement at a works test facility for large turbomachinery, including requisite hot-gas piping and trip butterfly valve. At a gas inlet temperature of 727°C and an inlet pressure of 2.91 bar, the process gas expander has a power output of 12,000 kW, with a gas mass flow of 200,000 kg/h. About 80 percent of this power is absorbed by the axial-flow air compressor while some 5 percent covers the losses of the gearing and the windmilled condensing steam turbine. The remaining 15 percent is converted into electric power.

The process gas expander and the motor/generator operate at 3000 rpm; air compressor and steam turbine are coupled via a gearbox and for optimum aerodynamic design, run at a speed of 5180 rpm.

Under design operating conditions, with live-steam at 27.6 bar and 343°C, the 13-stage condensing steam turbine represented in Fig. 3 gives a power output of 6500 kW. To permit the air compressor - which has a maximum power requirement of approximately 11,000 kW - to be initially tested for its performance without the motor or process gas expander, the steam turbine was designed so as to supply the necessary power using the steam available at the test stand (i.e., 40 bar and 400°C).

The air compressor of the machine train (Fig. 4) has ten axial-flow stages, of which the first four stages incorporate adjustable stator blades, as well as a centrifugal end stage, which is a characteristic feature of this particular design. At a power input of 9500 kW the machine compresses 186,000 m^3/h of atmospheric air to 3.7 bar. The air compressor can be adapted to off-design load conditions at constant speed by adjustment of the variable stator blades. The wide operating range required of the compressor is insured by suitable blade selection, whose degree of reaction continuously rises from

Downloaded 01 Jun 2010 to 171.66.16.62. Redistribution subject to ASME license or copyright; see http://www.asme.org/terms/Terms_Use.cfm

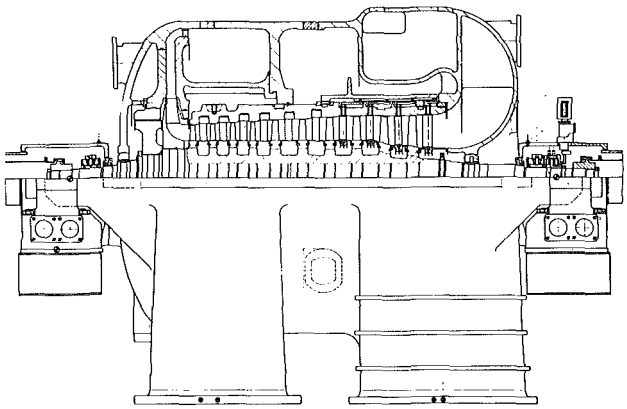

Fig. 4 Air compressor

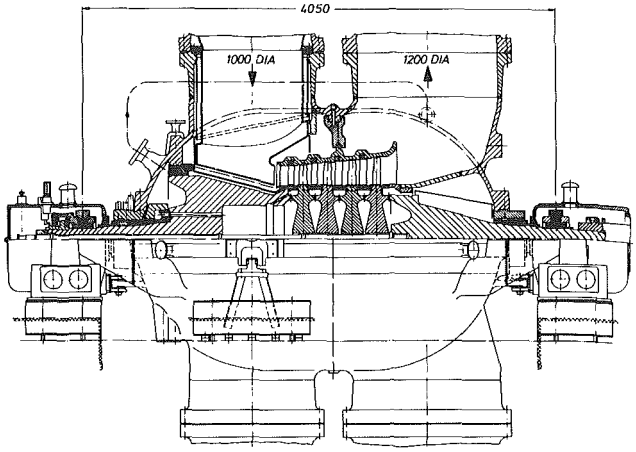

Fig. 5 Multistage process gas expander for an FCC plant

approximately 85 percent in the first stage to 100 percent in the final stages, with the final centrifugal stage giving a stabilizing effect in this regard. The single helical gearbox arranged between the air compressor and the motor/generator (Fig. 2) is designed for a maximum power transmission capacity of 11,000 kW. Mounted on the gearbox is a motorised barring gear capable of turning the complete turbo machine set. The 10-kV motor/generator has a maximum power output of 3750 kW as a motor to drive the air compressor, or as a generator to the electrical grid.

Design Measures to Avoid Erosion in the Process Gas Expander

Despite extensive cleaning operations in three separator stages, the waste gas still contains a residual amount of catalyst particles which may cause erosion in the expander and the control valves. In order to reduce this erosive effect to an acceptable degree, the flow velocities must be as low as possible and the flow channels must be so designed as to minimize local dust concentrations.

In previous applications the enthalpy difference available to process gas expanders in FCC plants was "spoilt" to allow the use of single-stage machines [3,4]. With rising inlet pressures and temperatures in line with modern process technology, the flow velocities in these expanders would, however, be too high for an acceptable blade service life.

Therefore, advanced process gas expanders for FCC plants are designed as multistage machines (Fig. 5). The flow velocities are about half those of single-stage machines of a comparable power rating, thus reducing the kinetic energy of the dust particles to roughly a quarter. Since, as a first approximation, the erosive effect of the dust particles can be considered directly proportional to their kinetic energy, this measure considerably increases the service life of the blading. Furthermore, the multistage design involves a relatively low aerodynamic stage load with small flow deflection angles in the stator and rotor blade channels. This also accordingly lessens the effect of the centrifugal forces acting upon the dust particles during the process of deflection in the blade cascade. As a result, the erosive effect which is bound to be stronger on the pressure side of the blades towards the trailing edge, is mitigated. Thus, switching to a multistage design reduces erosion in two respects.

The effect of erosion is not uniformly distributed over the blade height, but is more pronounced in areas which have a distinct secondary flow pattern. To prevent inadmissible local dust concentrations in the area of the blade roots, armoured deflection edges are arranged upstream each row of blades (Fig. 6). These edges are fitted to the hub upstream the stage row and to the stator blade carrier upstream the stator blade

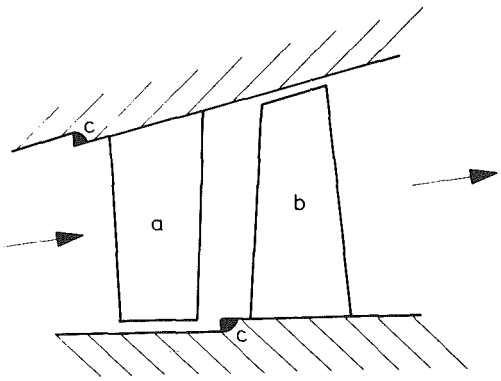

Fig. 6 Stellited/explosion-clad dust deflection edges (*a*) stator blade (*b*) rotor blade (*c*) dust deflection edge

rim. Their effect is that the flow near the wall and the dust particles entrained in it are deflected towards the middle of the flow channel, thus reducing the dust concentration at the channel wall. This eliminates the risk of vibration failure occurring in the blade root area through erosion of the blade cross-sections.

The resistance against erosion of the deflection edge surfaces is increased by stelliting or by explosion cladding with chromium carbide. An FCC process gas expander equipped with such deflection edges has been operating for about 40,000 hr. So far, there have been no major signs of erosion on the blades, with only a minor decrease in the turbine efficiency [5].

Increasing the axial spacing of the individual rows of blades is another design measure to achieve a uniform distribution of the dust particles over the blade height. This particular measure can be easily implemented in process gas expanders where the rotor is located between the bearings. On the machine in question the axial spacing of the stator and rotor blades was increased to approximately 1.5 times the normal distance used on expanders handling dust-free gases.

Experience has shown that the effect of erosion becomes more pronounced towards the trailing edge of the blade, in particular in the outer area of the rotor blades. To increase the blading service life, the trailing edges are therefore made about twice as thick as the blades in gas turbines which have a relatively low dust load. The effect of the design measures described above upon the internal efficiency of the expander blading could not be precisely calculated and it was agreed to define this efficiency during the test by way of experiments under hot-gas conditions. Initially, the thermodynamic rating was therefore based on conventional assumptions.

Downloaded 01 Jun 2010 to 171.66.16.62. Redistribution subject to ASME license or copyright; see http://www.asme.org/terms/Terms_Use.cfm

Table 1 Materials of expander

part	material-no. and DIN-specification		equivalent U.S.-specification
outer casing and stator blade carrier	1.4581	G-X7 Cr Ni Mo Nb 18 10	ACI-CF-8C (+ 2% Mo)
inlet casing	1.4981	X8 Cr Ni Mo Nb 16 16	AISI 347 (with 16% Ni + 1.8% Mo)
rotor disks	1.4980	X5 Ni Cr Ti 26 15	ASTM A 638 Grade 660 (A 286)
rotor blades	2.4969	Ni Cr 20 Co 18 Ti (Nimonic 90)	Nimonic 90
stator blades	1.4981	X8 Cr Ni Mo Nb 16 16	AISI 347 (with 16% Ni + 1.8% Mo)

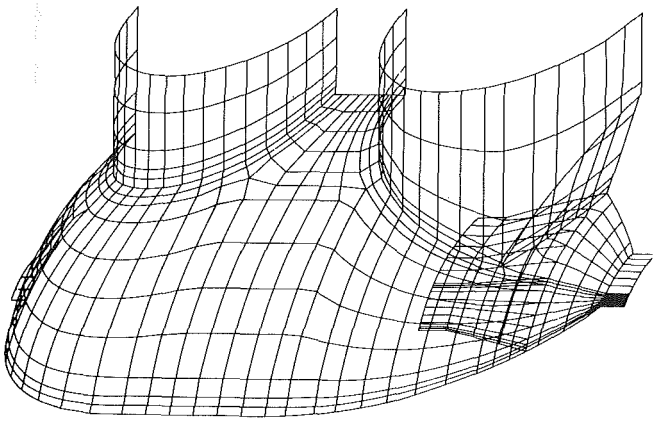

Fig. 7 Finite-element structure for calculation of the expander casing

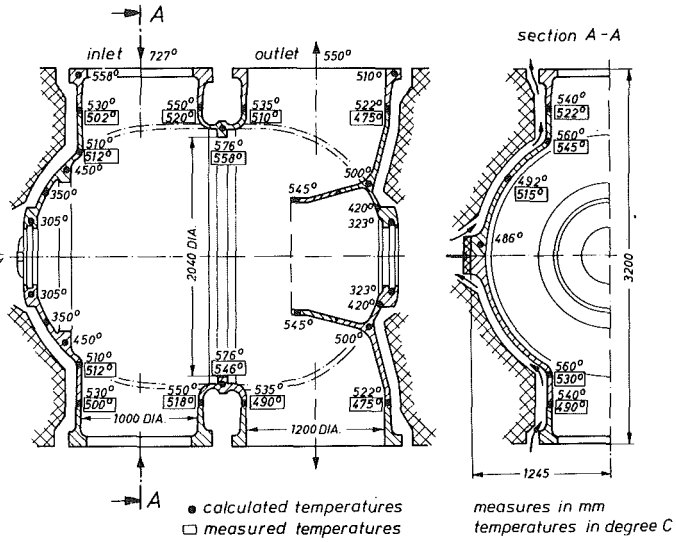

Fig. 8 Temperature distribution at expander casing

FCC Process Gas Expander Design

The process gas expander for energy recovery in FCC plants represented in Fig. 5 incorporates the antierosion design features previously described. The maximum permissible dust concentration downstream the third separator stage was 160 ppm, with 95 percent of the particles to be less than 10 microns in size. Based on a flue gas throughput of 200,000 kg/h, this means a dust weight of 32 kg passing through the expander every hour.

The large volumetric flow rate resulting from the low pressure and high temperature at the expander inlet is handled in this case by two inlet and two outlet connections. This provides a casing which is symmetrical about the horizontal joint, and likewise gives symmetrical distribution of both temperatures and stresses. The thin-walled expander casing is a casting of high temperature resistant austenitic steel (Table 1). On large machines where casing diameters of 2 m and above are employed, the nozzles, the outlet cone and the casing support brackets are cast separately and welded to the casing. This particular method of manufacture insures that the high casting quality demanded is achieved in all areas of the casing.

Finite element methods were used to calculate the highly stressed components of the process gas expander. In Fig. 7 we see, for example, the element structure for the outer casing. These sophisticated calculations were necessary because the casing does not have any internal insulation. The model is a cut-away view of the top part of the symmetrical casing. Deformations and stresses were calculated in consideration of local temperatures and pressure differentials for when the expander was stationary and also in transient operation, i.e., with due regard to the starting and run-down phases.

The calculations showed that the loads on the casing were mainly caused by temperature gradients which arise not only in transient operation but partly also under stationary conditions (Fig. 8). In order to achieve a uniform temperature distribution in large areas of the outer casing while reducing the temperature level, the expander was equipped with a "chimney" cooling arrangement. For this purpose the expander insulation above and below the partition joint flanges was installed at a distance of 100 mm from the casing wall. As shown in the right-hand part of Fig. 8, ambient air flows through the chimney are due to natural convection. In the area of the inlet nozzle this cooling arrangement causes the temperature to drop by approximately 150 K below the values achieved by the conventional insulation.

To protect the outer casing from excessive gas inlet temperatures, two fabricated inner casings (one for each casing half) are mounted in the expander inlet sections, which direct the gas from the inlet nozzles to the blading. Additional heat radiation shields are provided in the inlet section of the expander (Fig. 5). The rotor is of disk type with the disks and shaft ends centered relative to one another by suitable curvic tooth couplings and located by means of central tie-rod.

The rotor was provided with an internal and external cooling system. To prevent residual quantities of unburnt gases from being burnt subsequently in the expander, superheated steam was used as the cooling fluid. One cooling-steam route runs through the shaft in the area of the rotor blade roots from one rotor disk to the next, and the exhaust after the last blade row is mixed with the waste gas flow.

Downloaded 01 Jun 2010 to 171.66.16.62. Redistribution subject to ASME license or copyright; see http://www.asme.org/terms/Terms_Use.cfm

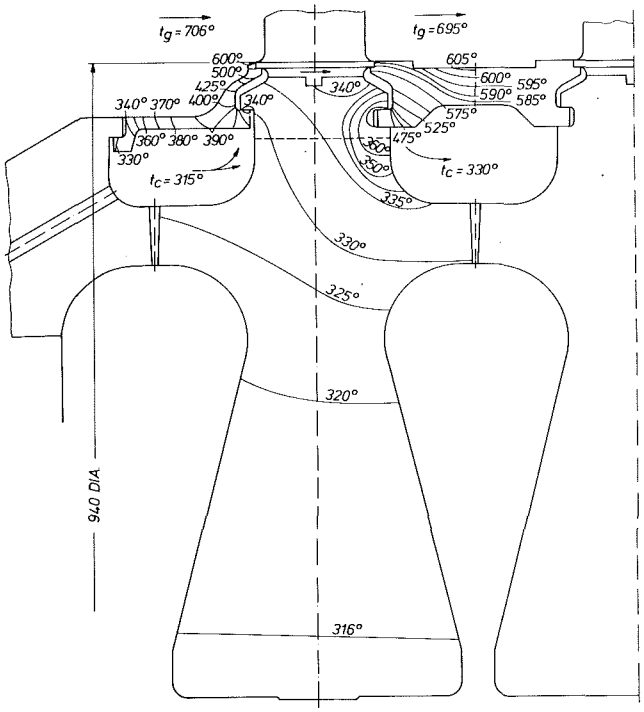

Fig. 9 Stationary temperature distribution in the first-stage rotor disk: t_g = gas temperature; t_c = cooling-steam temperature; dimensions in mm; temperature in °C

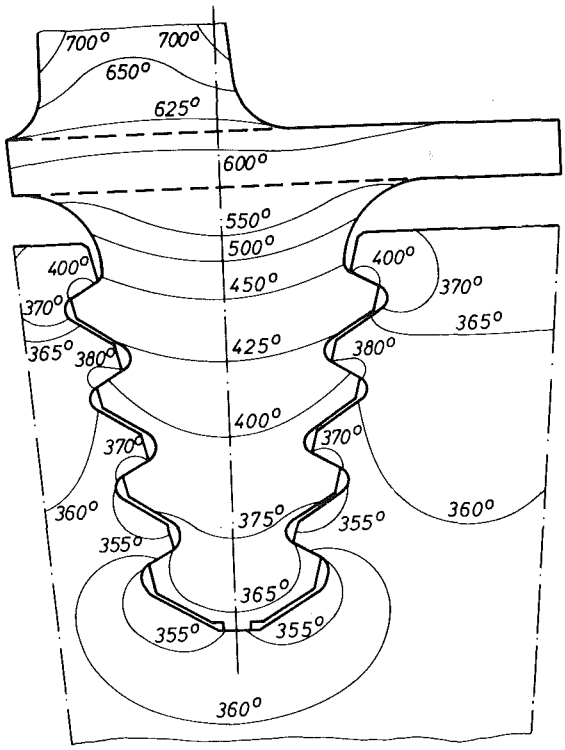

Fig. 10 Stationary temperature distribution in first-stage rotor-blade root; temperature in °C

Another steam cooling stream flows via the balancing drum which is thus protected against the heat radiated from the inlet section. This cooling stream enters the main flow channel downstream the first row of stator blades. Extensive calculations were performed to determine the stress distribution pattern inside the rotor disks and blade roots in consideration of the cooling effect. Figure 9 shows the theoretical temperature distribution in the first rotor disk and in the rotor heat shields (positioned between the blade rows) of the cooling-steam channels upstream and downstream the first disk. The temperature values given in the graph apply to the design point, with a gas inlet temperature of 727°C and a theoretical cooling-steam temperature of 315°C. The heat shield upstream of the first rotor disk is cooled by the two steam flows from the inside and outside and thus has a relatively low temperature level. Therefore, this ring is not split. Maximum temperatures arise in the rotor heat shields between the individual disks of the four-stage machine subjected to gas flow on the outside and the cooling-steam flow on the inside. These rings are therefore split into four quadrants to reduce the stresses.

The resulting spatial temperature distribution in the rotor blade roots and the rotor disk of the first stage under stationary operating conditions is represented in Fig. 10. Similar temperature conditions were also calculated for the blade roots of the following stages. Due to the increasing temperature of the cooling steam, the temperature level rises by approximately 50 K until the fourth stage.

The blading was designed in line with the free vortex law with a reaction of 50 percent in the middle section. The cylindrical stator blades and twisted rotor blades were precision-forged from 16/16 CrNi steel and Nimonic 90, respectively. The rotor blades are fixed in axial grooves by a fir-tree root. The rotor disks were forged from 15/26 CrNi steel A 286, and finish-machined (Table 1). Figure 11 shows the bladed rotor while being placed in the expander casing.

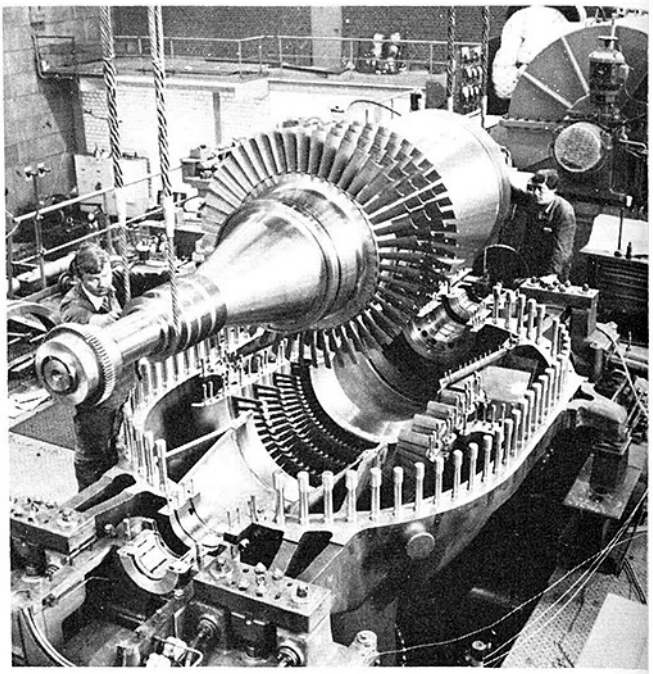

Fig. 11 Process gas expander rotor

Hot-Gas Piping

The hot-gas piping (DN 1200 mm/48 in.) is split at a fixed point tee section, into two pipe loops (DN 1000 mm/40 in.) which run above and below the table foundation to the two inlet nozzles of the expander. Another two pipe loops (DN 1200 mm/48 in.) extend from the two expander outlet nozzles above and below the table foundation to another tee section which provides the connection to the outlet header (DN 1800 mm/72 in.). The trip butterfly valve designed to protect the expander is located upstream of the tee in the inlet main.

Downloaded 01 Jun 2010 to 171.66.16.62. Redistribution subject to ASME license or copyright; see http://www.asme.org/terms/Terms_Use.cfm

Table 2 Materials of hot-gas piping and hot-gas butterfly valve

part	material	remarks
hot-gas piping	ASTM A 240, type 304 H	Mo max. 0.3% C = 0.04 to 0.08%
expansion joints	INCOLOY 800 H	
valve body	ASTM A 240 type 304H	C = 0.04 to 0.08%
disk	Manaurite 900 (20 Cr 33 Ni)	cast INCOLOY 800 without Ti, Al
shaft	INCONEL X 750	

The piping systems between the tees and the expander nozzles as well as the trip butterfly valve were included within the scope of supply.

Thermal expansion of the hot-gas piping was compensated by the installation of bellows in the horizontal and vertical pipe sections. The horizontal bellows are steam-flushed to avoid with absolute certainty any possibility of the bellows expansion being impeded by catalyst dust depositing in the corrugations. The forces and moments resulting at the expander nozzles from the pipework and compensation arrangement are less than half the values permissible according to NEMA SM-23.

The piping material is ASTM A 240, type 304 H, with a restricted analysis (molybdenum content max. 0.3 percent, carbon content 0.04 to 0.08 percent), while Incoloy 800 H was used for the bellows (Table 2).

During testing of the machine set, wall-temperature measurements were performed at critical points of the hot-gas piping system in order to confirm the assumptions made for the calculations.

Trip Butterfly Valve

The trip butterfly valve which is designed to protect the expander in the event of potential failures – such as lack of oil, axial displacement of the rotor, lack of cooling steam, or overspeed – is mounted directly upstream the tee of the inlet main and as such has a nominal diameter of 1200 mm/48 in. The butterfly disk has no sealing effect. At room temperature, the theoretical leakage rate is approximately 0.3 percent, while at the design temperature of 760°C it is a maximum of 2.5 percent of the rated throughput. To provide protection from erosion, the inside surface of the valve body as well as the edge of the disk are stellited. The single piece shaft that passes through the disk is supported by external roller bearings which are not in contact with the medium. Additional support is provided by internal journal bushings. A high-temperature-resistant graphite packing is used for sealing the shaft to the atmosphere. Prevention of the catalyst dust penetrating the internal bushings or the packings is achieved by a steam sealing arrangement on the shaft. The materials of the main components are listed in Table 2.

The butterfly valve is operated pneumatically, with the working air being drawn from the air supply system of the FCC plant via a non-return and shutoff valve at a gauge pressure of 6 bar.

Should the air supply system fail, an adequate air quantity for two closing and opening operations is available from two storage tanks which are directly connected to the air system of the butterfly valve (i.e., without any isolating valves). A further safeguard is provided by two easily exchangeable high-pressure nitrogen cylinders, each of which is linked to the air system through a pressure-reducing/shutoff valve which is only closed when one of the cylinders is to be exchanged. The operating pressure of the reducing valves is slightly below the pressure normally prevailing in the system.

While the machine set is in operation, the trip butterfly valve—which is not a control device—is not affected by fluctuations in the process sequence and thus normally stays in its "open" limit position. To be able to check the operational reliability of the valve at regular intervals, a test connection is incorporated by means of which the valve disk can be moved in the closing direction and back through a maximum of 10 percent of the total closing angle through the effect of a simulated emergency trip action.

The closing time of the butterfly valve was so defined that even a potential "coupling breakage" failure can be safely mastered. The closing time is 1.5 s, including all dead times which may arise in the electric or pneumatic part of the control system. On the assumption that the toothed coupling between the process gas expander and the motor/generator breaks under full-load conditions, calculations with this closing time produced a maximum overspeed of the expander of approximately 30 percent. The closing time of the butterfly valve was determined in cold state and under hot-gas conditions in the general context of the tests conducted with the turbo set.

Shop-Testing of Machine Set under Full-Load Conditions

The past years have witnessed an ever increasing tendency of testing individual machines and complete turbo machine trains at the supplier's works. The main reasons for this were the requirement to test prototype sets for new technological processes as well as greater dimensions of the machinery, more stringent guarantee requirements, complex control/safety systems and oil units, and quicker erection and commissioning of the machine at site.

To satisfy the requirements inherent in this development, a new test facility was set up for both individual machines and complete turbo sets, where a maximum steam-turbine drive power of 18,000 kW is available [6]. A steam supply system with a capacity of 60 *t/h* at a pressure of 55 bar and a temperature of 560°C permits turbocompressors with large power consumptions to be driven by a test-stand turbine, as well as the testing of turbomachine sets with their contract turbines—either supplied by the main contractor or by others—and of process gas expanders. In the latter case either steam can be used instead of process gas or—as in the present case—oil-fired combustion chambers are employed for hot-gas generation with a maximum output of 20,000 kW.

The mechanical and thermodynamic testing of all machine set components, including oil unit and the control and safety equipment, was part of the supply contract concluded for this turbo set. In detail, the following individual test sequences were performed:

(*a*) Common mechanical running test of the main and

Downloaded 01 Jun 2010 to 171.66.16.62. Redistribution subject to ASME license or copyright; see http://www.asme.org/terms/Terms_Use.cfm

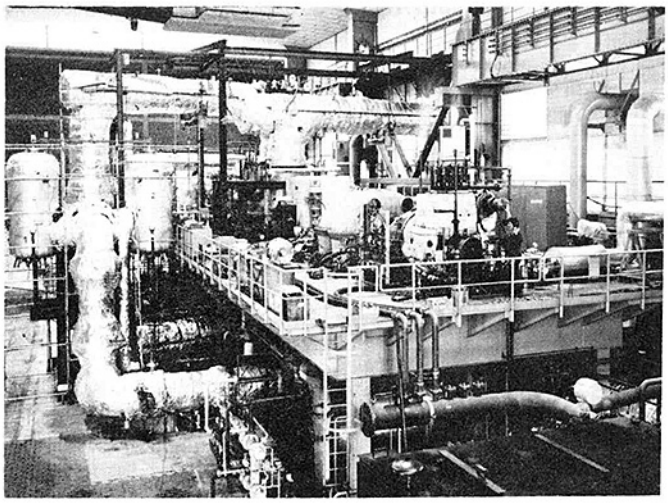

Fig. 12 Works testing of machine set

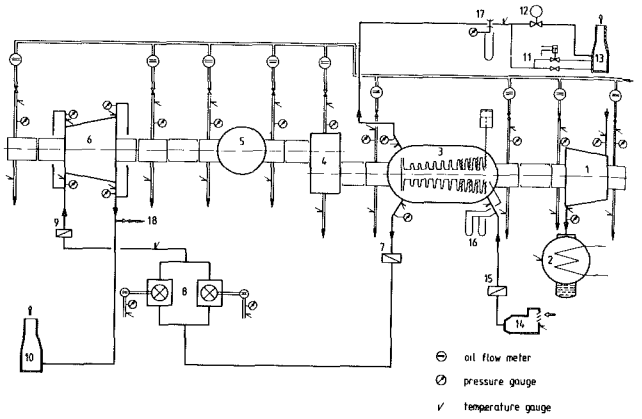

Fig. 13 Measuring-point location chart for testing the turbomachine set: 1 steam turbine, 2 condenser, 3 air compressor, 4 gearbox, 5 motor/generator, 6 expander, 7 throttle flap, 8 combustion chambers, 9 hot-gas butterfly valve, 10 hot-gas chimney, 11 blow-off valves, 12 throttle valve, 13 chimney, 14 air inlet duct, 15 throttle flap, 16 flow measurement, 17 orifice, 18 gas analyser

spare rotors of steam turbine and axial-flow compressor, including gearbox.

(*b*) Performance test of air compressor under full-load conditions.

(*c*) Common mechanical running test of steam turbine, axial-flow compressor, gearbox and motor/generator.

(*d*) Electric testing of motor/generator and testing of the load distribution controller.

(*e*) Windmilling test of steam turbine.

(*f*) Common mechanical running test of steam turbine, axial-flow compressor, gearing, motor/generator, and process gas expander in cold state.

(*g*) "Ten day (10 hour/day) test" of process gas expander at varying start and load conditions, with a simultaneous performance test of the expander, including demonstration of the closing time of the hot-gas trip butterfly valve under hot-gas conditions.

Testing was performed in agreement with internationally recognized rules and codes (API 612, API 614, API 617, VDI 2045, VDI 2056, DIN 1952) and in line with the customer's specifications. The power figures during performance testing of the axial-flow compressor and process gas expander were determined from the mass flow rate and the changes of enthalpy. The gas required for hot-gas testing was produced in two oil-fired combustion chambers (KWU design) arranged in parallel and was fed to the expander through the contract hot-gas pipework. From the expander outlet the gas was again vented to atmosphere through the contract pipework and a sound insulated hot-gas stack. The necessary combustion air was provided by the axial-flow compressor. The set-up of the machine set on the test stand was the same as it is at site (Fig. 12).

The test program was carried out according to the sequence detailed below under (*a*) to (*g*):

(*a*) The common mechanical running test of the main and spare rotors of steam turbine, axial-flow compressor and gearbox using also the contract condenser and condensate plant. Testing was performed in line with API 612, API 617, and VDI 2056. To evaluate the operating response, the machine set's own shaft vibration measuring equipment of Bently-Nevada type was used, as well as the test stand's vibration monitoring equipment which measured the vibration velocities horizontally and vertically at the bearing pedestals.

(*b*) The mechanical running tests were followed by a performance test of the axial-flow compressor, where adherence to two guarantee points, the surge-limit curve, and operation in a minimum duty point were to be demonstrated. The location of the measuring points is given in Fig. 13. The pressures and temperatures upstream and downstream the compressor were measured in straight pipe sections according to ASME-PTC 10-1965.

For taking the flow measurements a standard orifice in accordance with DIN 1952 was used in the discharge pipe. At the same time flow measurements were carried out in the compressor suction nozzle using differential pressure measurements at two cross-sections in the inlet; these readings were then calibrated to the values attained on the discharge side. Speed measurements were made by an electronic speed transmitter. To define the mechanical power loss the lube-oil flow rates were measured by oil flow meters as well as the oil inlet and outlet temperatures. The measuring equipment used was tested and verified with regard to the expected accuracy and the data acquisition methods prior to starting the test procedure.

Evaluation of the test results was performed in an electronic data processing plant immediately following the measurements. All pressures and pressure differences were fed to the data logging system by means of electronic transmitters. The most important pressure values were measured at the same time by direct-reading equipment (manometers or precision pressure gauges). All temperatures were determined by calibrated thermocouples and directly processed by the EDP system.

Details of the test results are given in Fig. 14. For the purpose of comparison, the theoretical performance curves and the duty points ascertained by testing are both plotted in the graph. All guarantee requirements were fully satisfied.

(*c*) Upon completion of the performance test the motor/generator was coupled to the machine set and was initially tested mechanically under no-load conditions. Following this it was connected to the works 10-kV-mains at synchronous speed. The test phases following then were designed to check the reliable functioning of the load distribution controller which is required to keep the speed of the machine system constant in the event of fluctuations in the power distribution between the steam turbine and the motor/generator. The power input to the motor/generator was increased step by step to the maximum value of 3750 kW by setpoint-value presetting at the power controller.

The power output of the steam turbine was varied by re-adjusting the positions of the axial-flow compressor stator blades.

Downloaded 01 Jun 2010 to 171.66.16.62. Redistribution subject to ASME license or copyright; see http://www.asme.org/terms/Terms_Use.cfm

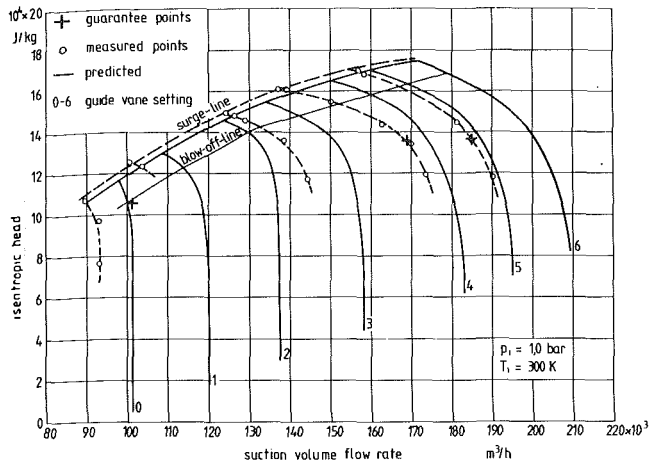

Fig. 14 Performance map of axial-flow compressor with theoretical and measured values

Return of the machine set speed to synchronous speed was demonstrated by repeatedly shutting down the motor/generator from different load conditions. Another parameter that was demonstrated was speed constancy at predetermined motor power and changes in the power input to the axial-flow compressor, conditioned by the stator blades being continuously opened or closed. Towards the end of the test series the asynchronous machine was tested in the generator operating mode at a power output of 1000 kW. The additional power required by the axial compressor was supplied by the steam turbine. Data required for monitoring the future operation of the machine set, such as winding temperatures, cooling-water flow rates, and shaft vibration levels, were recorded during all phases of testing.

(*d*) During actual site operation of the machine, in the normal event the steam turbine will only have a start-up function and will then "windmill" while the set is on-line. In this regard it will be necessary to direct a minimum steam flow rate through the turbine for cooling purposes. In continuous operation, the exhaust-steam temperature downstream the turbine blading should not exceed 120°C. The tests conducted in the following were designed to define a particular valve opening for the steam turbine at which this condition is just being fulfilled. For this purpose the motor/generator was subjected to an input load of 3750 kW while the steam turbine was adjusted to "zero power". Using the start-up ejectors, an exhaust-steam temperature of 115°C was adjusted in continuous operation. The valve position thus ascertained was firmly set by means of shims to limit the valve lift, in order to ensure passage of the required minimum steam flow rate.

(*e*) Following coupling of the FCC expander to the train, an auxiliary piping system was used for the cold mechanical running test of the first expander rotor (spare rotor). This permitted part of the air supplied by the axial-flow compressor to be used for cooling of the expander. The tests were not only designed to demonstrate the mechanical running of the expander rotor, but were further intended to coordinate the trip actions of the steam turbine and expander in the cold state.

(*f*) Before testing was continued, the air supply system to the hot-gas expander was changed as shown in Fig. 13. An additional butterfly valve was installed downstream the axial-flow compressor to permit the necessary ignition pressure to be adjusted for ignition of the dual combustion chambers. Through a special pipe the combustion air supplied by the axial compressor was directed to the two parallel combustion chambers (Fig. 13), in which light fuel oil was burnt. The original hot-gas butterfly valve with a diameter of 1200 mm was connected directly downstream this pipe. The hot-gas piping extending from the valve to the expander inlet and from the expander outlet to the hot-gas stack had the original dimensions. With the hot-gas butterfly valve in closed position, the axial-flow compressor discharged the air through the opened blow-off valves to the atmosphere. During testing, the complete machine set was connected to the contract oil unit which had previously been tested according to API 614. All other auxiliary systems, such as the rotor steam cooling system, were also operated with the original instrumentation and pipe work.

(*g*) Testing was conducted in three main phases. Before the performance of the mechanical running test under hot-gas conditions of 727°C the optimum rotor cooling-steam temperature and the necessary steam flow rate were determined by way of experiments. The optimum cooling-steam temperature was defined as 200°C, at a steam flow rate of 3 percent of the hot-gas throughput. Upon ignition of the combustion chambers, the temperature upstream the expander immediately rose to approximately 380°C. Similar conditions are to be expected after process ignition at site. When the rated speed had been reached, the expander inlet temperature was increased to 727°C at a rate of 60 K/h. After this and all further tests, the machinery was shut down by trip action. Trip-induced shut-down of steam turbine and expander under hot-gas conditions also formed part of the detailed test programme.

Then, testing of the complete machine set was started for various operating conditions. These tests were designed to verify that the turbo set could operate reliably during a ten day test period. This period was used to simulate load conditions such as may arise in continuous operation of the machine set as well as possible upset conditions. The first test case (temperature cycle A) was characterized by a rapid decrease of the temperature by 50 or 100 K, starting from 727°C. The expander inlet temperature was reduced at a rate of approximately 6 K/min; it was then maintained at steady-state conditions for 30 min and finally raised to 727°C at the same rate. Following steady-state conditions, this cycle was repeated, upon which the machine set was shut down by emergency tripping and then kept at idling speed using the barring gear.

Figure 15 shows the temperature cycle A as a function of time. In cycle B the machine set was caused to operate at steady-state temperature conditions in the same way as detailed above. The tests which then followed were designed to demonstrate the machine set's ability to be quickly started after an emergency trip, after a short machine downtime, and 30 min of rotation at barring speed, the expander was quickly re-started to 727°C. The operating chart for this process is depicted in Fig. 16. The cycle was tested on a total of five days, each time being reproduced in respect of the associated boundary conditions.

As part of this test series, the hot-gas expander was also subjected to performance testing. It was agreed to define the measured variables for a specific test point at approximately 80 percent of the rated mass flow and to convert these to the guarantee conditions.

The measuring points were arranged according to the chart indicated in Fig. 13. Upstream and downstream the gas expander, the pressures were measured in the casing top and bottom parts at four points located on the connecting pipes, while the temperatures in the top and bottom inlet and outlet pipes were measured by two thermocouples arranged in series in the center of the pipe section. The measuring point used for gas analysis was located immediately upstream the waste-gas stack inlet. The speed and the mechanical losses of the shaft system were measured in the same way as described for the

Downloaded 01 Jun 2010 to 171.66.16.62. Redistribution subject to ASME license or copyright; see http://www.asme.org/terms/Terms_Use.cfm

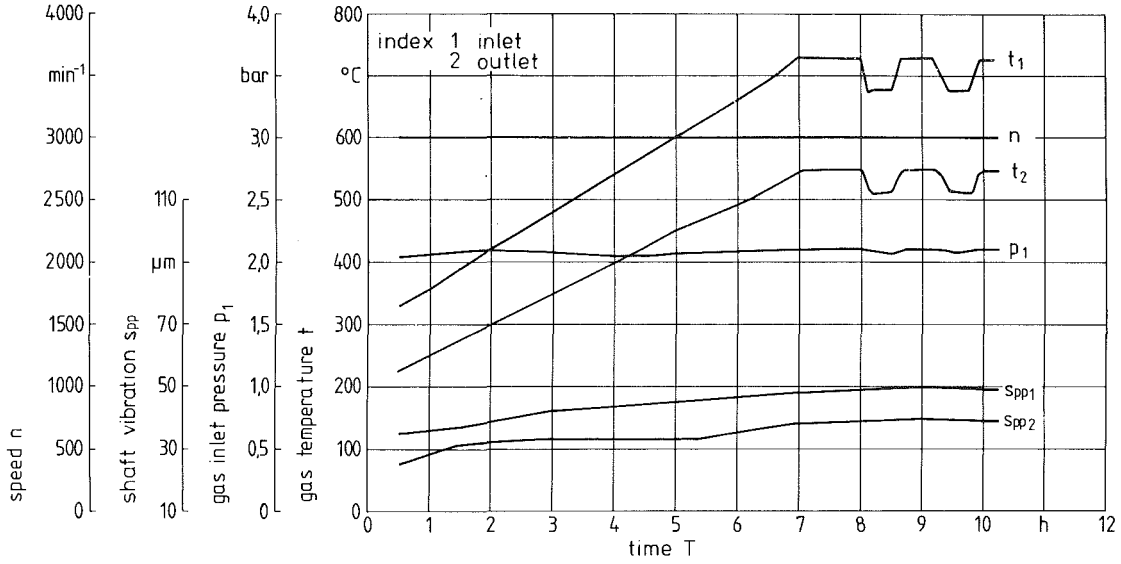

Fig. 15 Test cycle A

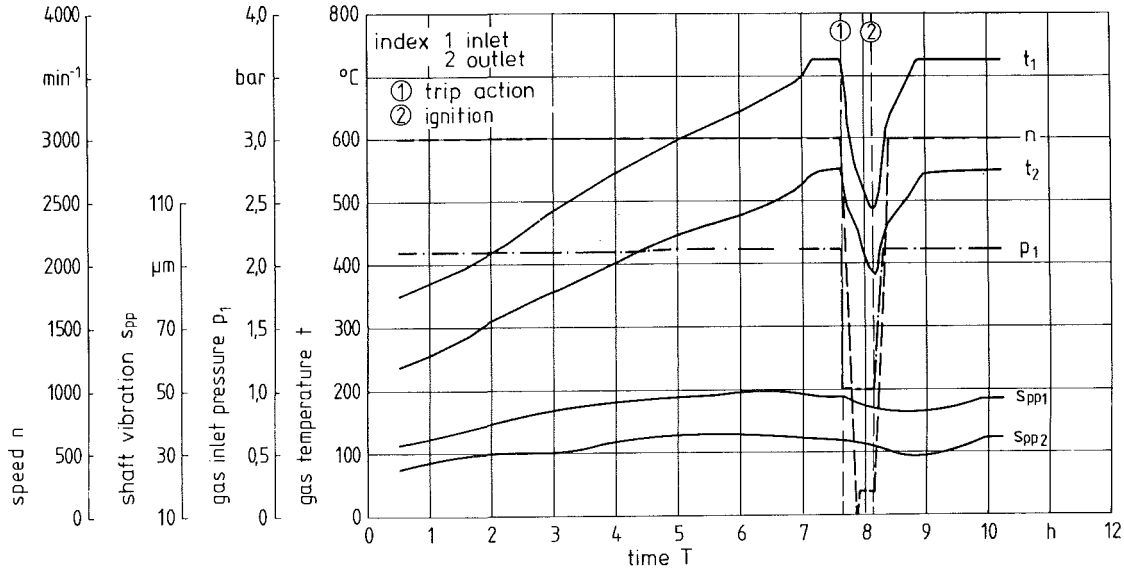

Fig. 16 Test cycle B

axial-flow compressor. The mass was determined from the calibrated differential pressure measurements taken at the compressor inlet.

Further factors to be included in the heat balance were the enthalpy of the cooling-steam and the cooling-steam flow rate. The internal isentropic total efficiency of the process gas expander blading was determined as amounting to 87.4 percent. Conversion to guarantee conditions showed that the power actually supplied by the expander at its coupling, i.e., 10,650 kW, deviated from the guaranteed power by a mere 0.35 percent. Testing of the machine set was concluded when this result had been established.

During the tests conducted under hot-gas conditions, continuous recordings were made of the temperatures prevailing at various points of the process gas expander casing. Temperature measurement was performed by means of 53 NiCr-Ni thermocouples with an asbestos insulation, which were fixed to the casing by precision spot welding. The measured temperatures were used to check the theoretical values. Fig. 8 is a comparison of the calculated temperatures

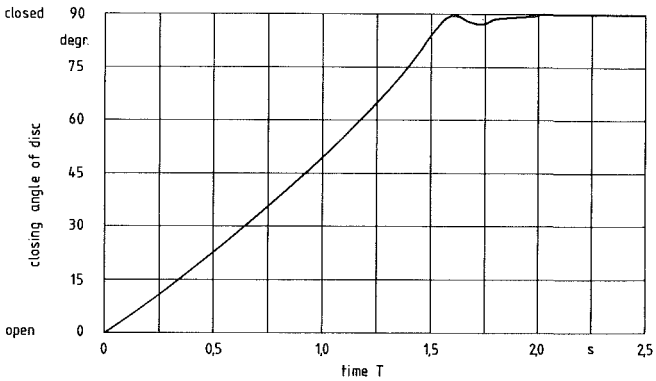

Fig. 17 Closing time of hot-gas butterfly valve under hot-gas conditions

and the measured temperature values for the same casing locations. The deviations observed are mainly due to the

Downloaded 01 Jun 2010 to 171.66.16.62. Redistribution subject to ASME license or copyright; see http://www.asme.org/terms/Terms_Use.cfm

boundary conditions employed for the calculations. A striking feature is the symmetry of the measured values.

Another important functional test under hot-gas conditions was concerned with the closing action of the hot-gas butterfly valve. The closing time of this valve had been guaranteed to be 1.5 s under hot-gas conditions. In a number of shutdown series the valve closing mechanism was adjusted to the guaranteed closing time. Fig. 17 indicates the measured closing-angle pattern as a function of time, demonstrating adherence to the guaranteed conditions.

Summary

In view of rising temperatures and pressures in FCC plants it has become necessary to make the step from single-stage to multistage process gas expanders in order to make use of the available enthalpy and to increase the blading service life. While it is possible to build the components of the turbo set for an FCC plant, viz. steam turbine, air compressor, motor/generator, and gearbox according to conventional design practices, special designs are required for the process gas expander so as to prevent erosion by the catalyst dust entrained in the fluid. Major design features and measures to avoid damage by erosion are described in this paper by reference to a four-stage process gas expander.

As this was the first multi-stage FCC expander of this size, an extensive test programme was carried out at the works test facility, where the individual machine units were tested under full-load conditions. All mechanical and thermo-dynamic guartantee data were fully demonstrated for the various machines. The operating response of the complete turbo set was examined in great detail with regard to simulated trip conditions such as may arise during operation at site.

References

1 Strother, C.W., Vermillion, W. L., and Conner, A. J., "Riser Cracking Gives Advantages," *Hydrocarbon Processing*, Vol. 51, No. 5, 1972, pp. 89–92.

2 Magee, J. S., Ritter, R. E., and Rheaume, L., "A Look at FCC Catalyst Advances," *Hydrocarbon Processing*, Vol. 58, No. 9, 1979, pp. 123–130.

3 Stettenbenz, L. M., "The Power Recovery Gas Expander in the Fluid-Bed Catalytic Cracking Cycle," *Proceedings of the 47th annual meeting of the Western Gas Processors and Oil Refiners Association*, Newport Beach, Calif., Oct. 5, 1972.

4 Dziewulski, T. A., and Bews, J. H., "Recover Power from FCC Units," *Hydrocarbon Processing*, Vol. 57, No. 12, 1978, pp. 131–135.

5 Jericha, H., "Einsatz von Abgasturbinen zur Energierueckgewinnung bei catalytischen Crackanlagen," *ELIN-Zeitschrift*, Vol. 24, No. 2, 1972, pp. 1–7.

6 Turanskyj, L., "Ueber die Entwicklung und Erprobung von Axialverdichtern grosser Leistungsaufnahme fuer den Anlagenbau," *Atomkernenergie* (ATKE), Vol. 32, No. 4, 1978, pp. 273–278.

Downloaded 01 Jun 2010 to 171.66.16.62. Redistribution subject to ASME license or copyright; see http://www.asme.org/terms/Terms_Use.cfm

Combined Gas and Steam Cycle for a Gas-Cooled Solar Tower Power Plant

B. Becker
Manager,
Gas Turbine Technology.

H. H. Finckh
Assistant Advisor,
Energy Technology Development.
Mem. ASME

R. Meyer-Pittroff
Manager,
Systems Technology.

Kraftwerk Union AG,
Erlangen - Mulheim, West Germany

In gas-cooled solar power plants the radiant energy of the sun is transferred to the cycle fluid in a cavity type solar receiver and converted into electric energy by means of a combined gas and steam turbine cycle incorporating a waste heat steam generator. The design and optimization of the energy conversion system in accordance with solar-specific considerations are described with particular regard to the gas turbine. In designing the energy conversion system several variants on the combined cycle with waste heat steam generator are investigated and special measures for the improvement of the cycle efficiency, such as the refinement of the steam process through the addition of pressure stages are introduced. It is demonstrated that the solar power plant meets the requirements both for straight solar and constant load operation with fossil fuel substitution. In order to establish the possibilities of attaining high part-load efficiencies in straight solar operation, two modes, variable and constant speed of the gas turbine, are compared with one another.

Introduction

In a gas-cooled solar tower power plant the radiant energy of the sun is concentrated by means of a heliostat field, transferred to the cycle fluid in a solar receiver and converted into mechanical and electric energy with the aid of a gas cycle. The particular requirements relating to the design and operation of a solar power plant are summarized in [1] and call for special adaptation of the gas turbine plant.

Studies on the economics of solar power plants [2], have concluded that the heliostat field and receiver constitute the most expensive systems of all.

As regards the energy chain of the solar power plant, the capital investment for these systems, in particular, can be reduced if the energy conversion system is of high thermodynamic quality.

In this context, the following problem complexes that serve as a basis for establishing the reference concept are dealt with in their relation to the energy conversion system:

- The cycle concept is to be carefully selected on the basis of the criteria of potential attainable efficiency and feasibility.
- Given the predetermined upper process temperature, the thermodynamic cycle is to be optimized to obtain maximum efficiency.
- A high power yield is to be achieved even at reduced insolation, which presupposes efficient part-load operation. This, however, is to be considered in conjunction with the part-load characteristic of the solar receiver which functions as an interface.
- Measures for the installation of a supplementary fossil combustion facility for periods of reduced or no insolation are also to be taken into account.

Cycle Design Assumptions

The design data (shown in Table 1) that underlie the analysis of cycle variants relate to a hypothetical site.

The datum point is taken as 12.00 h solar time on June 21. At this instant the thermal output of the solar receiver to the working medium is to be 60 MW. The temperature of the working medium at the receiver outlet is restricted to 800°C, which is roughly the upper feasibility limit for a receiver with metallic tubing.

Since a site for the solar power plant has not yet been named the ambient data have been selected to enable design of the power plant for extreme conditions. Accordingly the air temperature at ground level is taken to be 50°C at an air pressure of 1 bar and relative humidity of 20 percent.

A cooling water temperature of 35°C is postulated for the design point.

It is assumed that an existing, stable power grid is available for the solar power plant.

Selection of the Basic Cycle

The gas-cooled solar tower power plant can incorporate a gas turbine cycle of either the closed or open type. Efficiencies of similar magnitude can be achieved by means of both cycles given appropriate cycle arrangement and identical design data, such as the maximum and minimum process temperatures.

It is, however, the objective of this study exclusively to

Contributed by the Gas Turbine Division of THE AMERICAN SOCIETY OF MECHANICAL ENGINEERS and presented at the Gas Turbine Conference and Products Show, March 9-12, 1981, Houston, Texas. Manuscript received at ASME Headquarters December 11, 1980. Paper No. 81-GT-102.

Copyright © 1982 by ASME

Downloaded 01 Jun 2010 to 171.66.16.62. Redistribution subject to ASME license or copyright; see http://www.asme.org/terms/Terms_Use.cfm

Table 1 Cycle design assumptions. Design point: June 21, 12.00 h solar time

Thermal power from receiver to cycle fluid	60 MW
Receiver outlet temperature	800°C
Air temperature	50°C
Humidity of air	20 %
Air pressure	1 bar
Cooling water temperature	35°C

investigate the possibilities of the utilization of the open-gas cycle.

The special features in favor of the open cycle are:

- The high temperature and hence efficiency potential afforded by largely existing gas turbine technology.
- The resultant possibility of raising temperatures in the further development of solar receivers for high thermal flux densities.
- The relatively low expense involved in the adaptation of conventional gas turbines for solar applications.
- Substitution of direct fossil heat input to the cycle fluid in the absence of insolation by means of a combustion chamber.

As was mentioned in the introduction only processes that are capable of fulfilling the precondition of high thermodynamic efficiency come into question in the selection of an energy converter.

Essentially two basic variants that satisfy the above requirement can be derived from the elementary open-cycle gas turbine process which, when adapted for installation in a solar tower power plant, comprises the components, compressor, solar receiver and turbine. They are:

- The open-cycle gas turbine process with a recuperative heat exchanger and two compressor stages with intercooler and
- The combined gas and steam cycle incorporating a waste heat steam generator (CGS cycle).

The cycle configuration and associated temperature-entropy diagram of a gas turbine process with one intercooler and recuperative heat exchanger are shown in Fig. 1(*a*) and Fig. 1(*b*), respectively. The numbers in Fig. 1(*a*) are identical to those on the T,S-diagram in Fig. 1(*b*).

The intake air from the atmosphere drawn into the low-pressure compressor a (1, 2) is recooled in the intercooler b (2, 3) and brought up to maximum process pressure in the high-pressure compressor c (3, 4).

In the recuperative heat exchanger d the compressed air is preheated to the receiver inlet temperature by means of heat transferred from the hot exhaust gas of the turbine (4, 5). In the receiver e the maximum process temperature is reached through solar heat input (5, 6). A tailing combustion chamber f can substitute fossil fuel energy for reduced or absent insolation. The air expands in the turbine (6, 7) thereby releasing mechanical energy to drive the compressor and the electric generator g. From the turbine exhaust the gas passes to the low-pressure section of the recuperator (7, 8) and transfers heat to the high-pressure side (4, 5). The residual waste heat is released to the atmosphere via the vent stack.

Figure 2(*a*) shows the schematic of an open CGS plant with a tailing waste heat steam generator with two pressure stages, and Fig. 2(*b*) depicts the associated temperature-entropy diagram. The numbers in Fig. 2(*a*) are again identical to those on the T,S-diagram in Fig. 2(*b*).

The intake air from the atmosphere is brought up to the peak process pressure of the gas cycle in the compressor a (1, 2). In the receiver b the incident solar heat is transferred to the cycle fluid [3] which is raised to the peak process temperature (2, 3). During periods of reduced or no insolation a fossil-fueled combustion chamber c provides the heat input to the cycle. The air expands in the turbine d (3, 4) thereby generating mechanical energy that drives both the compressor a mounted on the same shaft and the electric generator e.

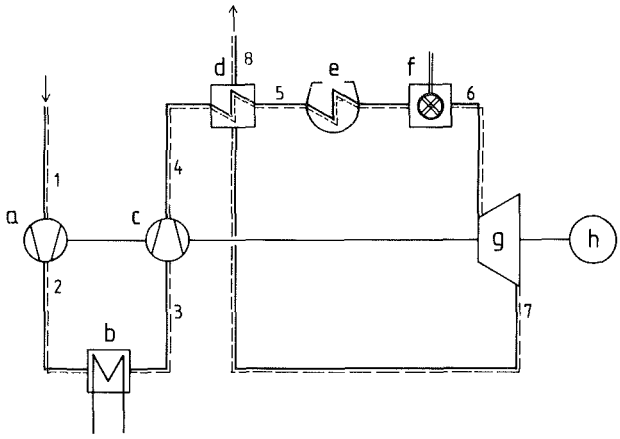

Fig. 1(*a*) Schematic diagram of open-cycle gas turbine process with recuperative heat exchanger and intercooler: a = LP compressor; b = intercooler; c = HP compressor; d = recuperative heat exchanger; e = solar receiver; f = combustion chamber; g = turbine; h = generator

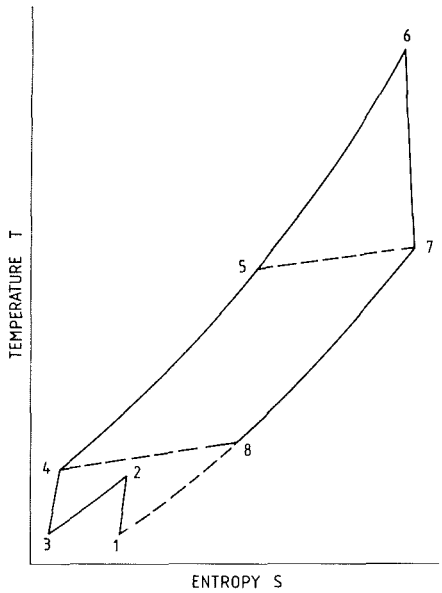

Fig. 1(*b*) Temperature-entropy diagram of process in Fig. 1(*a*)

The hot exhaust gas at the gas turbine outlet transfers a large proportion of its thermal energy in the waste heat steam generator to the water/steam cycle (4, 5) before leaving the plant via the vent stack.

In the presented water/steam cycle – in this instance with two pressure stages – the condensate is brought up to the pressure of the first stage of the steam generator by means of the boiler feed pump g and heated to saturation temperature in the economizer of the waste heat steam generator f (6, 7). A part of the feedwater flow is bled off in the boiler drum at this pressure, evaporated (7, 8) and superheated (8, 9). The pressure of the main feedwater flow is boosted to the high-pressure stage, preheated to the corresponding saturation temperature (10, 11), evaporated (11, 12) and superheated (12, 13). In the steam turbine h, the steam from the high-

Downloaded 01 Jun 2010 to 171.66.16.62. Redistribution subject to ASME license or copyright; see http://www.asme.org/terms/Terms_Use.cfm

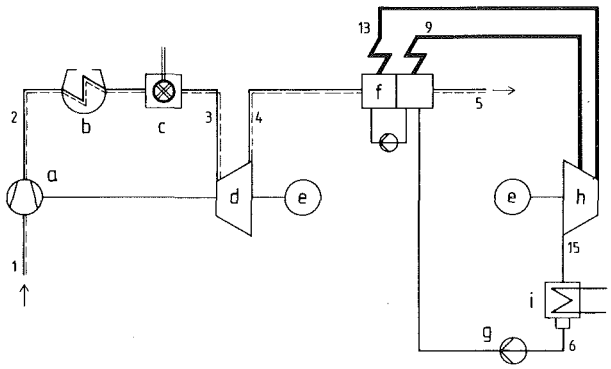

Fig. 2(*a*) Schematic diagram of combined gas and steam (CGS) cycle with waste heat steam generator: a = compressor; b = receiver; c = combustion chamber; d = gas turbine; e = generator; f = waste heat steam generator with two pressure stages; g = boiler feed pump; h = steam turbine; i = condenser

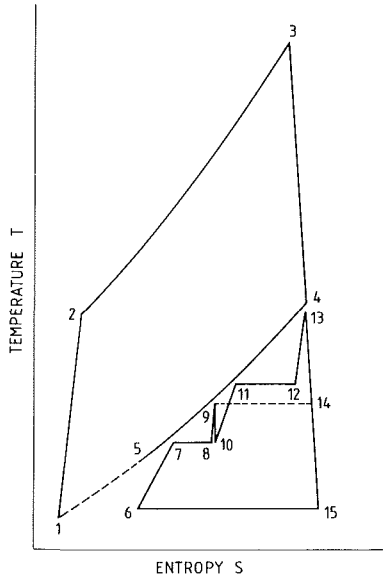

Fig. 2(*b*) Temperature-entropy diagram of CGS cycle in Fig. 2(*a*)

pressure stage first expands to the pressure of the lower pressure stage thereby releasing mechanical energy (13, 14). Subsequently the steam from the lower pressure stage is admixed and both expand in the low-pressure section of the turbine (14, 15). Finally the exhaust steam of the steam turbine is precipitated in the condenser i (15,6) where the waste heat is removed by means of an open-loop water cooling system.

As shown in references [4] and [5], optimized design pressure ratios for gas turbine processes with recuperative heat exchangers are substantially lower than those for elementary gas turbine processes. This holds true regardless of the absolute pressure level and cycle fluid. In the open-cycle recuperative process, air is taken in at atmospheric pressure which permits low peak process pressures and working medium densities. Furthermore the temperature rise of the working medium is lower than in the elementary gas turbine or the CGS cycle, which in turn calls for a higher mass flow to achieve the same input heat flux. Both factors necessitate greater volume flows and, hence, considerably larger components than in the CGS cycle. This disadvantage of the recuperative process and the fact that a new gas turbine would have to be developed for the purpose, while the CGS process relies on proven technology, are the reasons in favor of selection of a CGS cycle.

Thermodynamic Optimization at the Design Point

The CGS cycle and its components are to be designed with the objective of stipulating the thermodynamic parameters such that maximum efficiency is reached at the design point (12.00 h, June 21).

The optimization problem can be represented by means of the simple correlation:

$$\eta_C = \frac{P_{GT} + P_{ST}}{\dot{Q}_C} = \max \tag{1}$$

where

P_{GT} = the electric terminal output of the gas turbine,
P_{ST} = the electric terminal output of the steam turbine, and
$\dot{Q}_C$ = the thermal input to the cycle

Since the thermal input into the cycle $\dot{Q}_C$ is known, only the maximum electric output is open to optimization, hence

$$P_{el} = P_{ST} + P_{DT} = \max \tag{2}$$

In addition to the assumptions relating to the fictive site empirical values are stated for cycle-specific variables, such as:

- machine efficiencies of the gas and steam turbines,
- relative cooling air flow rate of the gas turbine,
- pressure losses in the gas and water/steam cycles, and
- temperature differences in the waste heat steam generator between the exhaust gas and water/steam side in the individual pressure stages.

The variables that remain to be investigated for the purposes of design and optimization are therefore:

- mass flow in the compressor $\dot{m}_v$,
- pressure ratio π_v in the compressor,
- live steam qualities generated by the individual pressure stages (p_{nF}, ϑ_{nF}), and
- live steam flow rates $\dot{m}_{nF}$ in the individual steam lines to the turbine.

If the gas turbine electric output in equation (2) is stated in greater detail as the difference between the turbine and compressor outputs taking into account the enthalpy drop and efficiencies, the following is obtained:

$$\begin{aligned} P_{GT} &= \eta_G \eta_m (P_{iT} - P_{iV}) \\ &= \eta_G \eta_m \dot{m}_v \left(\eta_{TS} \Delta h_{TS} - \frac{1}{\eta_{vs}} \Delta h_{VS} \right) \end{aligned} \tag{3}$$

where

η_G = generator efficiency
η_m = mechanical efficiency
η_{TS} = isentropic turbine efficiency
η_{VS} = isentropic compressor efficiency
Δh_{TS} = isentropic enthalpy drop of turbine
Δh_{VS} = isentropic enthalpy increase of compressor
P_{iT} = internal work of turbine per unit time
P_{iV} = internal work of compressor per unit time

Under the assumptions made above it can be easily demonstrated that the individual terms $\dot{m}_V$, h_{TS}, h_{VS} in equation (3) are exclusively functions of the pressure ratio in the compressor π_v. Equation (3) is then as follows:

$$P_{GT} = \eta_G \eta_m \dot{m}_v(\pi_v) \left[\eta_{TS} \Delta h_{TS}(\pi_v) - \frac{1}{\eta_{vs}} \Delta h_{VS}(\pi_v) \right] = P_{GT}(\pi_v) \tag{4}$$

In this instance the pressure ratio in the turbine is linked with the pressure ratio of the compressor via the given pressure loss $\Delta p/p$ between the compressor outlet and turbine inlet:

Downloaded 01 Jun 2010 to 171.66.16.62. Redistribution subject to ASME license or copyright; see http://www.asme.org/terms/Terms_Use.cfm

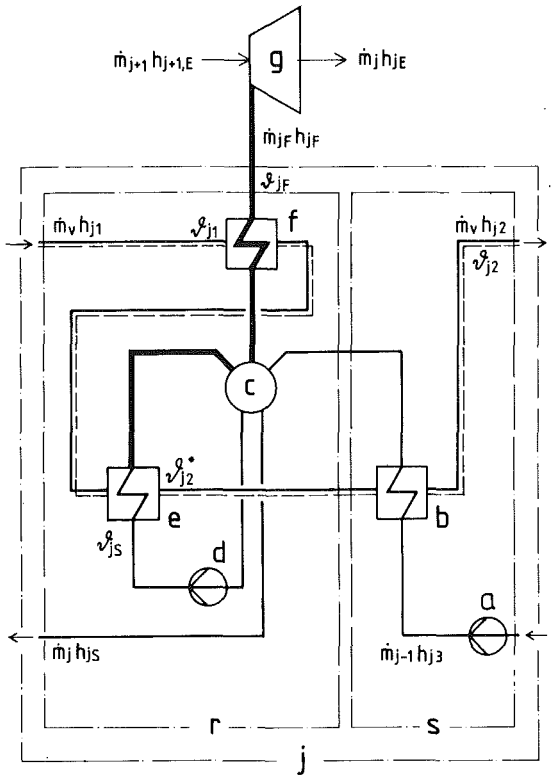

Fig. 3 Schematic of pressure stage section j of waste heat steam generator with the associated blading section of the steam turbine: a = feedwater pump; b = economizer; c = boiler drum; d = circulating pump; e = evaporator; f = superheater; g = blading section j of steam turbine; r = subsection of pressure stage j consisting of evaporator and superheater; s = subsection including economizer of pressure stage j

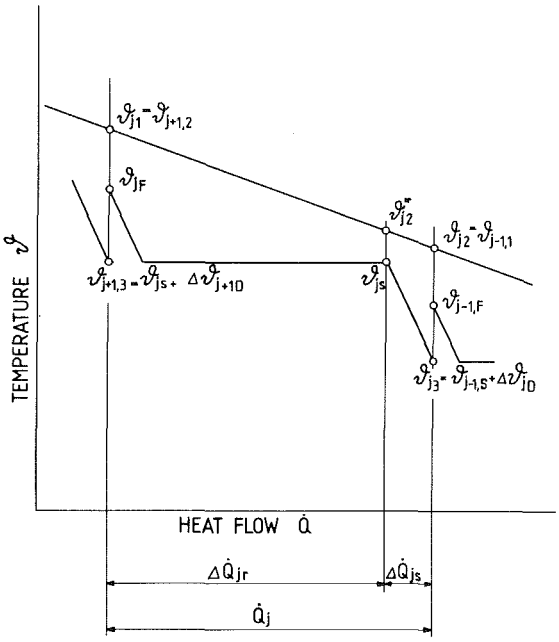

Fig. 4 Temperature-heat flow diagram for pressure stage j of the waste heat steam generator

$$\pi_T = \pi_v \left(1 - \frac{\Delta p}{p}\right) = \pi_T(\pi_v) \tag{5}$$

The turbine exhaust gas temperature ϑ_4 is to be stated since it is an important boundary condition in the design of the tailing water/steam process. For a known turbine inlet temperature and polytropic expansion in the gas turbine and with the correlation in equation (5) the turbine exhaust gas temperature is likewise a function of the pressure ratio of the compressor:

$$\vartheta_4 = \vartheta_4(\pi_v) \tag{6}$$

The useful heat flow in the waste gas $\dot{Q}_S$ of the gas turbine is a link variable for the gas turbine and steam turbine processes and is transferred to the water/steam cycle by way of the individual pressure stages of the waste heat steam generator which comprise the preheater, evaporator and superheater, respectively.

The total useful heat for a waste heat steam generator with j pressure stages is:

$$\dot{Q}_S = \sum_{j=1}^{n} \dot{Q}_{jS} \tag{7}$$

A random pressure stage section j of the waste heat steam generator is shown in Fig. 3 with its associated blading section in the steam turbine. In the selected configuration the feedwater flow from the preceding stage $\dot{m}_{j-1}$ is heated in the economizer b to the boiling point of the boiler drum c after its pressure has been boosted by pump a. A part flow of the feedwater $\dot{m}_{jF}$ is bled off in the boiler drum to which it is returned after circulation through an evaporator e by means of pump d. After superheating in f this part flow is piped as main steam $\dot{m}_{jF}$ to the jth blading section of the steam turbine g. The remaining feedwater flow $\dot{m}_j$ is passed to the next higher pressure stage of the waste heat boiler. The energy balance, subdivided as below into parts r and s on the basis of the pinch point in accordance with Fig. 4, applies to the transferred heat flow in section j:

$$\dot{Q}_{js} = \Delta\dot{Q}_{jr} + \Delta\dot{Q}_{js} \tag{8}$$

where

$$\begin{aligned} \Delta\dot{Q}_{jr} &= \dot{m}_v c_{pj}(\vartheta_{j1} - \vartheta^*_{j2}) \\ &= \dot{m}_{jF}(h_{jF} - h_{jS}) \end{aligned} \tag{9}$$

$$\begin{aligned} \Delta\dot{Q}_{js} &= \dot{m}_v c_{pj}(\vartheta^*_{j2} - \vartheta_{j2}) \\ &= \dot{m}_{j-1}(h_{jS} - h_{j3}) \end{aligned} \tag{10}$$

In the above equations:

c_{pj} = specific heat
ϑ_{j1} = exhaust gas temperature at admission of superheater
ϑ^*_{j2} = exhaust gas temperature at pinch point
ϑ_{j2} = exhaust gas temperature at economizer exit
h_{jF} = enthalpy of live steam
h_{jS} = enthalpy of feedwater at boiling point
h_{j3} = enthalpy of feedwater at economizer inlet

The temperature differences between the flue gas and boiling point at the pinch point

$$\Delta\vartheta_{jP} = \vartheta^*_{j2} - \vartheta_{jS} \tag{11}$$

and between the flue gas inlet and main steam temperature

$$\Delta\vartheta_j = \vartheta_{j1} - \vartheta_{jF} \tag{12}$$

as the characteristic of the heat transfer capacity of the individual stages in the waste heat steam generator are taken as given. The live steam mass flow $\dot{m}_{jF}$ is obtained from the part energy balance of equation (9) the lower flue gas temperature in stage section ϑ_{j2} from equation (10).

Each pressure stage in the waste heat steam generator shown in Fig. 3 is provided with one live steam line to the steam turbine and is assigned to one blading section.

The internal steam turbine output is determined as the sum of the outputs of the individual sections and is as follows:

Downloaded 01 Jun 2010 to 171.66.16.62. Redistribution subject to ASME license or copyright; see http://www.asme.org/terms/Terms_Use.cfm

$$P_{iST} = \sum_{j=1}^{n} P_{ij} = \sum_{j=1}^{n} \eta_{jT} \dot{m}_{jT} (h_j - h_{jE}) \tag{13}$$

where the mass flow $\dot{m}_{jT}$ of the jth blading section is obtained from the mass balance in the steam turbine and h_j as the enthalpy of the flow mixture from the energy balance at the same point. Furthermore η_{jT} and h_{jE} denote the isentropic efficiency and the enthalpy of the expansion line endpoint, respectively.

Taking into consideration the mechanical and generator losses as well, the steam turbine terminal output is obtained as

$$P_{ST} = \eta_G \eta_m \sum_{j=i}^{n} P_{ij} \tag{14}$$

The main steam pressures from the individual pressure stages of the waste heat steam generator p_{jF} (for $1 \leq j \leq n$) are taken as variable parameters for the purposes of optimizing the cycle. With the boundary conditions at the interface between the gas turbine exhaust duct and the nth stage of the waste heat steam generator on the one hand as

$$\vartheta_{n1} = \vartheta_4(\pi_v) \tag{15}$$

$$\vartheta_{nF} = \vartheta_4(\pi_v) - \Delta\vartheta_n = \vartheta_{nF}(\pi_v) \tag{16}$$

and the predetermined condenser pressure at the cold end of the first stage on the other as

$$p_{j-1,F} = p_{\text{kond}} \quad \text{for } j = 1$$

it can be demonstrated by means of equation (9) to (13) that the steam turbine output can be represented as an exclusive function of the pressure ratio of the compressor and the live steam pressures. Thus equation (14) becomes:

$$P_{ST} = P_{ST}(\pi_v; p_{nF}; p_{n-1,F} \ldots p_{1F},) \tag{17}$$

Given the variables of equations (4) and (17), the optimized electric terminal output at the design point may be formulated as follows:

$$P_{el} = P_{GT}(\pi_v) + P_{ST}(\pi_v; p_{nF}; p_{n-1,F}; \ldots p_{1F}) \tag{18}$$

The maximum outputs are to be determined numerically for various cycle arrangements by means of equation (18) in a data processing system.

Results

Given the preconditions described in the design assumptions the optimum cycle efficiency for various cycle arrangements is determined by means of equations (18) and (1). Beginning with the most simple CGS cycle with only one pressure stage the possibilities of thermodynamic improvement by incorporating several pressure stages are demonstrated.

In Fig. 5 the cycle efficiency of a single-pressure stage CGS process is shown as a function of the compressor pressure ratio π_v. Curve a shows the efficiency of the gas turbine cycle only which, given a receiver outlet temperature of 800°C, reaches its peak at $\pi_v = 10.5$. The component of the tailing steam process in curve *b* is represented by its relative power output $P_{ST}/\dot{Q}_C$ and decreases as the pressure ratio rises. This is to be attributed to the decrease in turbine exhaust gas temperature and the accompanying reduction in live steam temperature with which it is linked by means of the terminal temperature difference of the superheater. The overall efficiency of the cycle is shown in curve c as the sum of curves a + b and its maximum value amounts to $\eta_C = 39.1$ percent. The optimum pressure ratio of the combined-cycle process compared with that of the straight gas turbine cycle shifts to a lower value of $\pi_v = 7$. The pattern of the efficiency curve around the maximum is flat and relatively insensitive to a variation of the pressure ratio. The optimum live steam pressure for each pressure ratio is represented as a second variable by curve d.

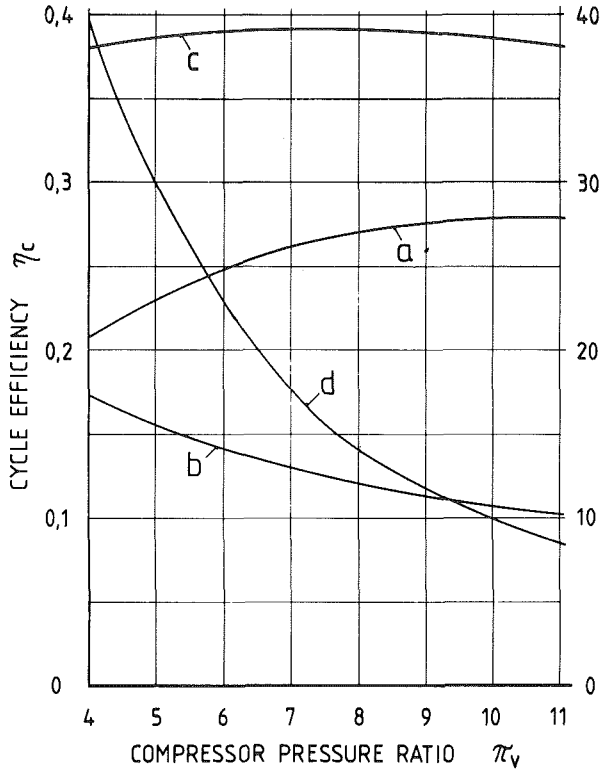

Fig. 5 Efficiencies of the CGS cycle with single pressure stage as a function of compressor pressure ratio: a = efficiency of gas turbine cycle η_{GT}; b = relative power of steam turbine referred to cycle heat flow $P_{ST}/\dot{Q}_C$; c = overall cycle efficiency η_C; d = optimum live steam pressure p_F

Owing to the incorporation of a second pressure stage in the waste heat steam generator the temperature differences between the exhaust gas to be cooled and the feedwater to be heated and evaporated is reduced. This also enables cooling of the exhaust gas to lower temperatures.

Generally speaking the trend of the efficiency patterns of the two-pressure process depicted in Figure 6 is the same as that of the single-pressure process. Although the efficiency of the gas turbine process (curve a) is somewhat lower than in the single-pressure process (curve b) because of the greater pressure losses in the waste heat steam generator the share of the steam turbine process can be increased by about 15% (curve c as opposed to curve d). The peak cycle efficiency is $\eta_C = 40.5\%$, again at $\pi_v = 7$ (curve e) which represents an efficiency increase of $\Delta\eta_C = 1.5\%$ points (curve f) over the single-pressure process.

The corresponding optimum live steam pressures of the two pressure stages are $p_{1F} \approx 5$ bar and $p_{2F} \approx 35$ bar.

Improvement of Efficiency at the Design Point

If a CGS plant is installed in a solar power plant further improvement of the thermodynamic cycle at additional expense is of considerable benefit. If, for instance, the cycle efficiency is raised while the terminal output remains constant the heat input to the cycle can be lowered and the high-investment heliostat field reduced in size. The individual measures that can be taken and their effects, expressed as an increase in efficiency, are presented below:

1 The waste heat of the gas turbine exhaust gas can be used more efficiently if a third pressure stage is added. This serves to increase the steam turbine output.

Downloaded 01 Jun 2010 to 171.66.16.62. Redistribution subject to ASME license or copyright; see http://www.asme.org/terms/Terms_Use.cfm

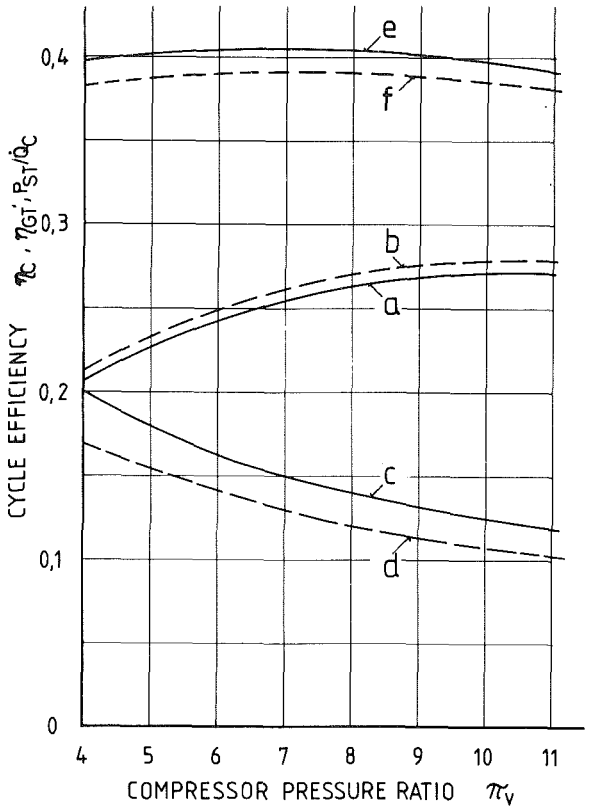

Fig. 6 Comparison of cycle efficiencies of single pressure and two pressure stage CGS cycle plotted versus compressor pressure ratio: a, b = efficiency η_{GT} of gas turbine cycle only in connection with a single pressure and a two pressure stage waste heat steam generator (WHSC), respectively; c, d = power of steam turbine with respect to cycle heat flow $P_{ST}/\dot{Q}_C$ of single pressure stage and two pressure stage WHSG, respectively; e, f = overall cycle efficiency η_C of single pressure and two pressure stage WHSG, respectively

2 By enlarging the heating surfaces of the waste heat steam generator the temperature differences between the exhaust gas and water/steam are reduced. In particular the pinch point margin is reduced and the live steam is superheated to an even higher temperature.

3 By injecting water into the intake air flow ahead of the compressor the consequent temperature drop can be utilized as far as the limits given by the saturation point permit. Under the specified ambient conditions this enables considerable cooling of the intake air at least during the summer months.

The results that can be achieved by means of these three measures are presented in Fig. 7. The cycle efficiency of the three-pressure process is plotted against the specific output in $P_{el}/\dot{m}_v$ with the pressure ratio as a parameter in curve *a*. The optimum efficiency is $\eta_C = 42.5$ percent at $\pi_v = 7$.

For comparison the single and two pressure stage processes are plotted as curves b and c respectively. The improvements afforded by the three pressure stage process are reflected in the considerable gain of 2.4 percent over the two pressure stage process. To round off the comparison between the various cycles the recuperative process with intercooling as represented in Fig. 1 is also shown as curve d. It is evident that, at its best, this process certainly features high efficiencies but the specific power is considerably less than that of the CGS process because of the high mass flow involved. The optimum pressure ratio of $\pi_v \approx 4$ is low by comparison with the $\pi_v = 7$ of the CGS process which gives rise to very large volumetric flows on the high-pressure side. This would necessitate high construction costs for the components, gas turbine and receiver.

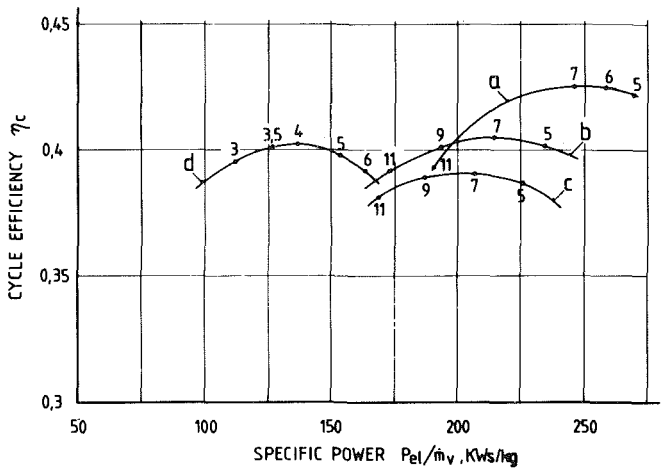

Fig. 7 Comparison between cycle efficiencies of CGS cycle variants and recuperative cycle plotted as functions of specific power. Numbers *on curves indicate compressor pressure ratio: a = three pressure stage* CGS process; b = two pressure stage CGS process; c = single pressure stage CGS process; d = recuperative gas turbine cycle with intercooler and two compressor stages

Compatibility of Cycle and Receiver

The design data for a compatible cycle and receiver process are selected not only on the basis of thermodynamic considerations. The flat optimum curve a in Fig. 7 gives a certain degree of flexibility in the selection of the pressure ratio. The determining factor in specifying the pressure ratio is the need to create favorable design conditions for the two principal components of the cycle, the receiver and gas turbine. In view of the optimum receiver design, which can be varied within justifiable limits with respect to its size and efficiency, the pressure ratio is about $\pi_v = 9$. As regards the gas turbine type to be installed the selected pressure ratio for the envisaged capacity constitutes a feasible value. The cycle efficiency amounts to 42.1 percent and is located a little to the right of the optimum. The optimized live steam pressures of the individual pressure stages of the waste heat steam generator are 45/10/2 bar.

The effect on the cycle efficiency of any change to the essential design parameters at this design point is to be seen from Table 2. From left to right the columns contain the layout parameters under consideration and their reference value x, their variation Δx and the last column gives the efficiency variation $\Delta\eta_C$.

Part-Load Characteristics

The daily and annual fluctuations in solar intensity do not allow for constant power output in straight solar operation. Even at times of reduced insolation the plant is to operate with a high effective power yield which necessitates good efficiency at part-load of both the thermodynamic cycle and the receiver.

In this context two different modes of operation for the three pressure stage CGS process are contrasted with one another:

1 The gas turbine generator set is run at constant speed which, at constant compressor inlet temperature, gives rise to an almost constant mass flow. Under conditions of reduced heat input to the cycle fluid the temperature decreases proportionately. The peak process temperature and cycle efficiency decrease accordingly.

2 *Variable Speed Operation.* To utilize better the variable heat flow to the cycle the gas turbine generator set is operated at variable speed by means of a frequency converter. As a result the air mass flow developed by the compressor is

Downloaded 01 Jun 2010 to 171.66.16.62. Redistribution subject to ASME license or copyright; see http://www.asme.org/terms/Terms_Use.cfm

Table 2 Effect of variation of design parameters on cycle efficiency

Varied parameter	x	Δx	$\Delta\eta_C$
Receiver outlet temperature	800°C	± 10 K	± 0.35
Compressor inlet temperature	50°C	± 10 K	∓ 0.21
Efficiency (isentropic)			
– Compressor	89.3 %	± 1 %	± 0.45
– Turbine	92.0 %	± 1 %	± 0.46
Cooling air flow	4.0 %	± 1 %	∓ 0.22
Pressure drop	11.7 %	± 1 %	∓ 0.23
Pinch-point	7 K	± 5 K	∓ 0.31
Condenser pressure	0.12 bar	± 0.1 bar	∓ 1.12

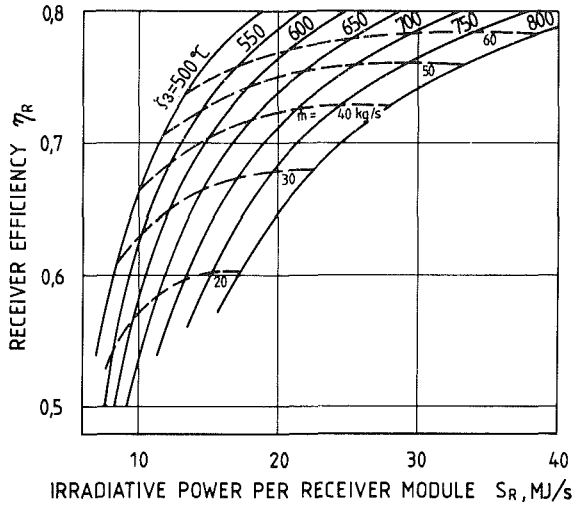

Fig. 9 Receiver characteristic lines for CGS cycle: Receiver efficiency as a function of irradiative power. Reference data: ambient temperature ϑ_a = 50°C, receiver inlet temperature ϑ_2 = 350°C, design point 76,1 MJ/s: Parameters on curves: $\dot{m}$ = receiver mass flow; ϑ_3 = receiver outlet temperature; (By courtesy of MAN, [6])

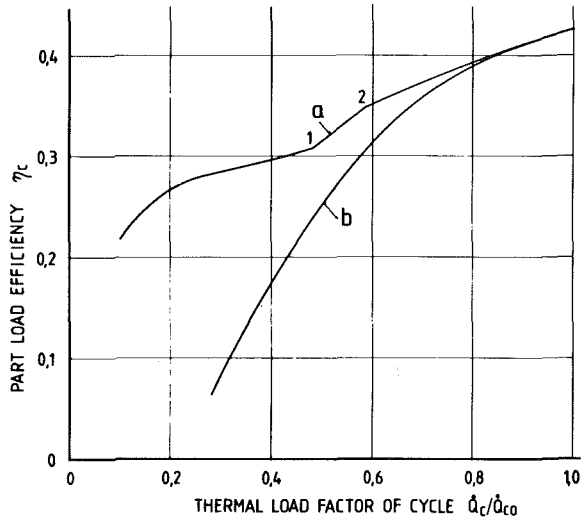

Fig. 8 Part load efficiencies of three pressure stage CGS process versus thermal load factor of cycle at variable and constant speed of gas turbine in straight solar operation (Reference thermal input: $\dot{Q}_{CO}$ = 60 MJ/s to working medium): a = variable speed of gas turboset; b = constant speed of gas turboset

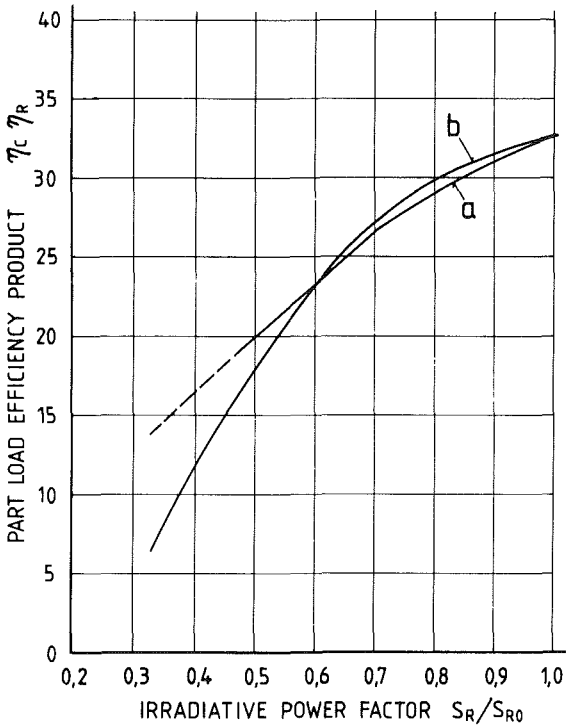

Fig. 10 Total part load efficiency of the CGS cycle including the receiver as a function of the irradiative power for variable and constant gas turbine speed in straight solar operation. Reference irradiative power input from heliostat field S_R = 76,1 MJ/s: a = variable speed of gas turboset; b = constant speed of gas turboset

matched to the respective insolation such that the receiver outlet temperature of 800°C is maintained at a constant level. While the presssure ratio and turbine generator efficiencies drop and consequently the gas turbine process deteriorates thermodynamically the turbine exhaust gas temperature is raised. Since the exhaust gas entering the waste heat steam generator is hotter the live steam quality is higher than at the design point; this enhances the steam process in the upper power range.

In Fig. 8 the part-load efficiencies of the cycle are plotted against the cycle's thermal input for both procedures.

In the variable speed mode (curve a) the speed of the gas turbine generator set is raised gradually in the lower power range to point 1 such that the receiver outlet temperature reaches its peak value of 800°C at about 1/3 load. The bleed valves are kept open during this phase to prevent pumping of the axial compressor at raised turbine inlet temperatures. Closure of the bleeds commences at point 1 and is completed at 2; the speed remains constant during this phase. In the upper power range the speed is raised to rated value as the receiver outlet temperature remains constant and the cycle output increases. It is evident that with a variable speed procedure (curve a) a considerably better part-load cycle efficiency can be achieved than in the constant speed mode (curve b). In a fossil CGS power plant the mode represented by curve a would be of real advantage since heat in the form of fuel is transferred directly and practically without loss to the cycle fluid.

In the solar power plant, however, the irradiation power S_R

Downloaded 01 Jun 2010 to 171.66.16.62. Redistribution subject to ASME license or copyright; see http://www.asme.org/terms/Terms_Use.cfm

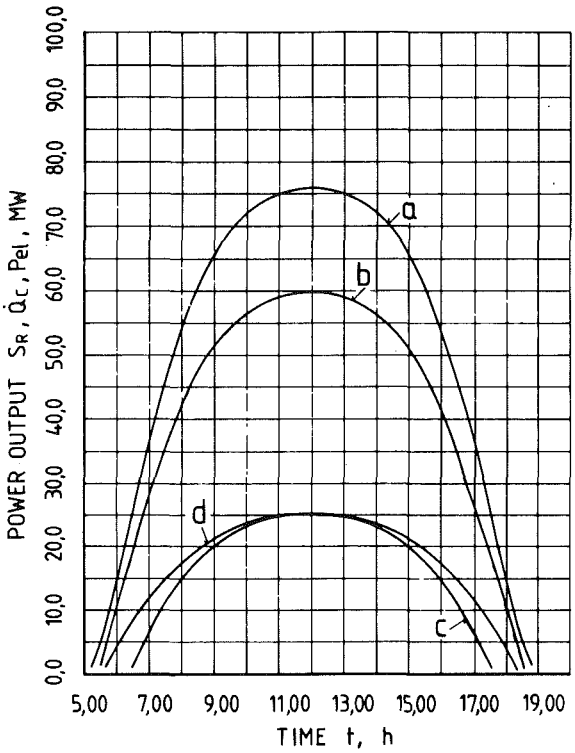

Fig. 11 Output curves for straight solar and constant load operation plotted against time of day on June 21st: a = irradiative power input into receiver from heliostats; b = thermal power input into CGS cycle fluid; c = electric power output at constant speed and straight solar operation; d = solar-generated portion of electrical output at constant load (solar and fossil) operation

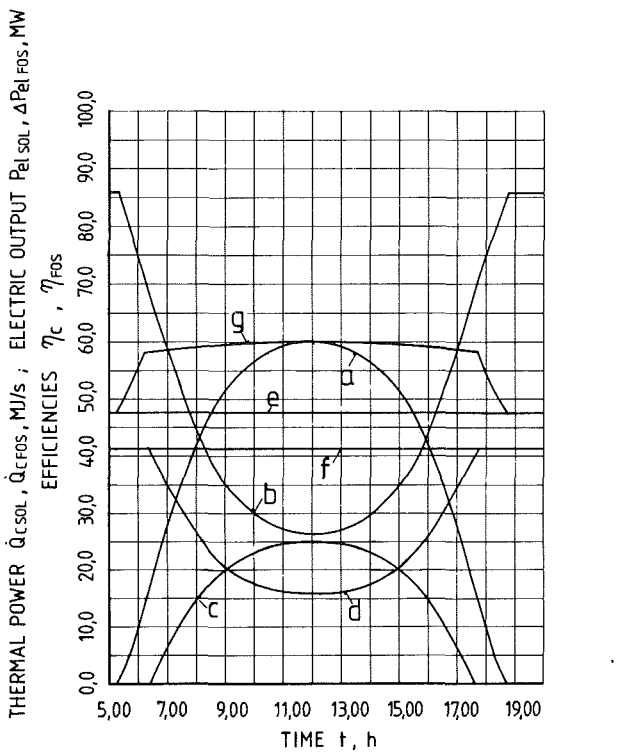

Fig. 12 Output and efficiencies of constant load hybrid operation of CGS cycle when the combustion chamber outlet temperature is raised from 800 to 1 000°C on June 21st: a = thermal solar power into cycle fluid; b = fossil fuel power into cycle fluid; c = electric power output in straight solar operation (800°C); d = electric power generated by fossil fuel substitution; e = total cycle efficiency; f = total electric power output in hybrid operation (1 000°C); g = degree of fuel utilization

is transferred to the cycle fluid via the receiver which acts as an interface. The electric terminal output is obtained from the irradiative power input into the receiver diminished by the chain of efficiencies as

$$P_{el} = \eta_C \eta_R S_R \tag{19}$$

where the receiver efficiency η_R, as given by its characteristic, depends on the irradiative power S_R and the operating mode of the cycle [6]. Figure 9 represents the receiver characteristics as a function of S_R with the receiver outlet temperature and mass flow rate as parameters.

The efficiency of the receiver deteriorates severely when the mass flow decreases at reduced speed. In the constant speed mode, however, that is at constant mass flow and reduced receiver outlet temperature, the efficiency decreases only slightly.

In Fig. 10 the product of $\eta_C \eta_R$ is plotted against the irradiative power S_R into the receiver. In view of the above it is understandable why the two curves a and b for the two modes of operation run close to each other. In the upper insolation range, 60 percent $\leq S_R/S_{RO} \leq$ 100 percent marginally better results are achieved with the constant speed mode than with variable speed. In the load range $S_R/S_{RO} \leq$ 60 percent variable speed operation (curve a) would theoretically give better results, but the absolute yield of electric energy is very low since this range represents operation at points on the steep slopes of the daily insolation curve.

Solar and Hybrid Operation

- In straight solar operation electric energy is only generated during the hours of daylight along the sun's insolation curve; the gas turbine generator set is run at constant speed.
- At constant load operation however, the missing solar energy input to the cycle is substituted by means of fossil fuel in the combustion chamber.

As a criterion for the generation of electrical work from solar energy the integral of the annual work can be used for the purpose of comparing the two operating modes:

$$E = \int_0^{1a} P_{sol}\,dt = \int_0^{1a} S\ \eta_F \eta_A \eta_R \eta_C\ dt \tag{20}$$

Both the insolation S and the individual efficiencies are time dependent variables.

As a numerical example the above-mentioned integral is evaluated for the two modes, straight solar operation and constant load, with the aid of the predetermined insolation curve for June 21 employing the optimum three pressure stage process. The individual output curves are plotted as follows in Fig. 11.

The solar irradiation into the receiver (curve a) and the thermal input transmitted by the receiver to the gas cycle (curve b) are identical in both operating modes, since the receiver heats the same mass flow under otherwise unchanged insolation conditions. Curve c shows the electric ouput generated in straight solar operation and curve d the solar-generated portion of the electrical output at constant load – with supplementary fossil fuel combustion.

In hybrid operation better utilization of the solar energy is achieved in periods of reduced insolation since overall the design efficiency of the cycle can be kept constant with the result that the solar-generated portion of the electrical output (curve d) attains higher values on the slopes of the insolation curve than in the case of straight solar operation as represented by curve c.

The solar-generated daily electrical work for the two modes of operation is calculated as the integral of curves c and d:

Downloaded 01 Jun 2010 to 171.66.16.62. Redistribution subject to ASME license or copyright; see http://www.asme.org/terms/Terms_Use.cfm

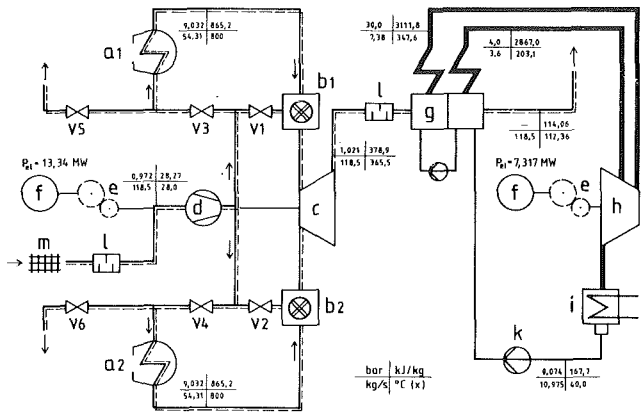

Fig. 13 Schematic diagram of reference plant: Two pressure stage CGS cycle Thermal output of receivers Q_C = 2 × 27.92 MJ/s electrical output: a1, a2 = receiver, b1, b2 = combustion chamber; c = gas turbine; d = compressor; e = mechanical gear; f = generator; g = waste heat steam generator; h = steam turbine; i = condenser; k = boiler feed pump; l = silencer; m = inlet air filter; Design point (June 21st, 12 h)

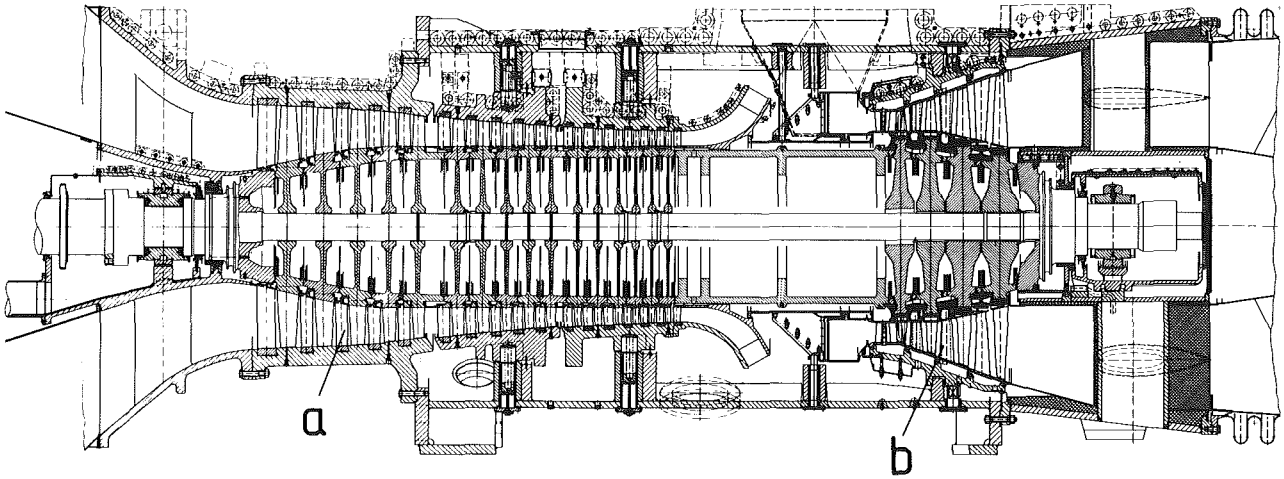

Fig. 14 Longitudinal sectional view of gas turbine type V 94: a = compressor; b = turbine

$$A_c = \int_0^{1d} P_{el,c}\,dt = 204 \text{ MWh} \tag{21}$$

$$A_d = \int_0^{1d} P_{el,d}\,dt = 230 \text{ MWh} \tag{22}$$

The difference between the two solar-generated daily outputs is $\Delta A/A_c$ = 12.75 percent in favour of hybrid operation.

If the combustion chamber outlet temperature is raised to 1000°C by means of supplementary fossil fuel combustion with otherwise unchanged external conditions with respect to insolation ($\dot{Q}_C$ = 60 MW at 12.00 h) the power and efficiency curves shown in Fig. 12 are obtained. Curves a and b represent the thermal solar and the fossil fuel power input to the cycle $\dot{Q}_{C,SOL}$ and $\dot{Q}_{C,FOS}$. Curve *c* is the electric power output in straight solar operation at 800°C $P_{el,SOL}$ and curve d the portion of the electric power generated by fossil fuel combustion $\Delta P_{el,FOS}$. It is to be noted that not only the cycle efficiency is raised from η_C = 42 to 47.7 percent (curve e) and the terminal output from P_{el} = 25.2 to 41 MW (curve f) but also that a high degree of utilization of the fossil fuel can be achieved. This is defined by:

$$\eta_{FOS} = \frac{P_{SOL+FOS} - P_{SOL,800°C}}{\dot{Q}_{C,FOS}} \tag{23}$$

and during the hours of sunshine, according to curve g results in

$$47.7 \text{ percent} \leq \eta_{FOS} \leq 60 \text{ percent}$$

Reference Concept

In contrast to the optimum cycle several practical considerations which fall under the following criteria apply to the pilot plant to be constructed:

- utilization of proven technology for the energy conversion system,
- simple plant structure, which means that the third pressure stage in the waste heat steam generator is to be omitted,
- trouble-free supplementary combustion during periods of reduced or no insolation,
- efficiency improvement potential for subsequent extension or later commercial plants, and
- optimum utilization of the manufacturing potential available in the industrial consortium.

Downloaded 01 Jun 2010 to 171.66.16.62. Redistribution subject to ASME license or copyright; see http://www.asme.org/terms/Terms_Use.cfm

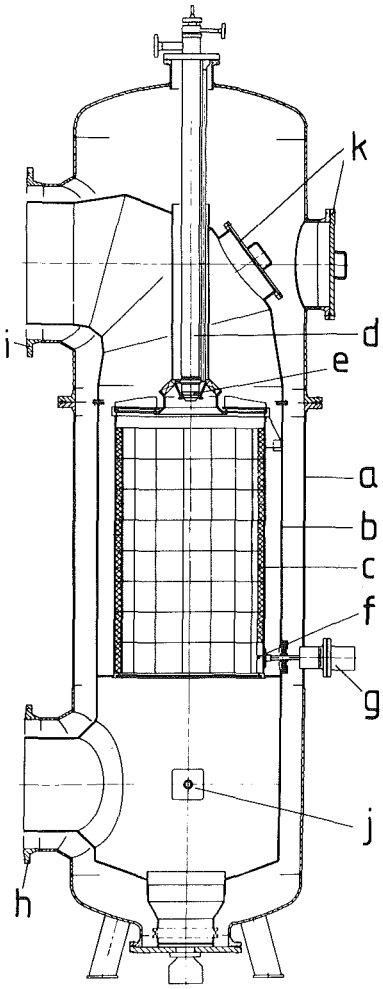

Fig. 15 Cross-sectional view of combustion chamber adapted for solar and fossil operation: a = pressure shell; b = shield; c = flame tube; d = burner; e = combustor; f = openings with variable cross section; g = actuating valve; h = turbine flange; i = flange to concentric pipe from and to receiver; j = fixed point; k = man hole

The selected reference plant is shown in the schematic diagram on Fig. 13.

Two combustion chambers b1 and b2 are provided, one for each of the two receivers a1 and a2. They are flanged on to the right and left hand sides of the gas turbine c in accordance with the proven KWU heavy duty design. The gas turbine drives the compressor d mounted on the same shaft and the generator f via the mechanical gear e. The exhaust gas of the turbine passes to a waste heat steam generator g with two pressure stages to heat a tailing steam turbine cycle. During periods of no insolation or in the event of receiver failure straight fossil operation of the CGS plant is possible, in which the bypass valves V1 and V2 are opened and the receiver valves V3 and V4 closed. The blow-off valves V5 and V6 are actuated when an emergency situation arises. The thermodynamic data are also stated. The cycle efficiency may be given as a reference value of $\eta_C \approx 37$ percent to make allowance for the somewhat different boundary data from those used in the optimization study.

The gas turbine of the KWU type V 64 to be employed is planned to be derived from the V 94 design as shown in Fig. 14. Compressor and turbine are to be scaled down by a factor of 0.5 and the speed doubled accordingly in order to retain aerodynamic and mechanical similarity. In this way the mass flow is to be adapted to the requirements of the solar power plant.

The design of the combustion chamber had to be modified extensively because of the connection to the solar receiver (Fig. 15). The design principles which call for service life of 100.000 h for all main parts including hot liners are to be complied with. A double concentric pipe (a) at the top of each combustion chamber connects the gas turbine to the receivers. As a result the pressurized casing is completely shielded against the high temperatures of the inner liners. The extremely high fluctuations of the inlet temperature due to the varying irradiated heat flow in the receiver (curve a in Fig. 11) make additional modifications to the combustion chamber concept necessary. The fixed cross-sections of the conventional design result in high pressure loss changes because of the varying density of the air entering the flame tube.

Therefore a design which is suited for optimum efficiency calls for low pressure losses that are kept constant in all modes of operation.

As the inlet temperature increases, the heat input by combustion is to decrease. Then only a small amount of combustion air (primary air) is necessary.

These requirements for the flow system give rise to the triple-shell design in the area of the flame tube in Fig. 15 (walls a, b, c). The preheated air from the receiver is partially routed to secondary air openings with variable cross-sections f.

Conclusions

1 It has been demonstrated that a combined gas and steam cycle (CGS) is better suited to adaptation for use as an energy conversion system in a gas-cooled solar power plant in the 20 MW electric capacity class than a recuperative process with intercooling.

2 The limits of an optimum CGS three pressure stage process under the specified preconditions were indicated by means of the thermodynamic optimization method described.

3 The part-load characteristic along the insolation curve in straight solar operation was studied. It transpired that in the case of the variable speed procedure two counteractive effects not encountered in the constant speed mode come to bear; on the one hand, the cycle efficiency is improved considerably, on the other, the receiver efficiency drops substantially at reduced mass flow rate.

4 The results for the daily outputs of both procedures indicate marginal superiority of the variable speed mode. It is to be concluded from this result that although this procedure is not suitable for application in the solar power plant it will certainly be of advantage in conventional CGS power plants to be operated at part-load.

5 It is shown that the conversion rate from solar to electrical energy is higher in solar power plants with supplementary fossil fuel combustion as in the case of constant load than in straight solar operation (Fig. 11). Furthermore a particularly high degree of utilization of the fuel used in conjunction with solar energy can be attained although this is only to be seen in relation to the additional electric output generated.

6 In the optimization of the gas cycle the optimum pressure level of 9 bar required for the receiver was achieved to a good approximation so that, in selecting a CGS cycle concept, a high degree of compatibility between the subsystem, gas cycle, and receiver has been attained.

7 Great importance was attached to simplicity and proven gas turbine technology in the further, detailed planning of the pilot plant. For this reason a CGS cycle with just two pressure stages in the waste heat steam generator are envisaged in the reference concept. It was demonstrated that a KWU gas turbine of the V 64 type with a modified combustion chamber is especially well suited to installation in a gas- cooled solar power plant for the desired rating of 20 MW electric.

Downloaded 01 Jun 2010 to 171.66.16.62. Redistribution subject to ASME license or copyright; see http://www.asme.org/terms/Terms_Use.cfm

Acknowledgment

The Federal Ministry of Research and Technology of West Germany (BMFT) is sponsoring the planning and development of a 20 MW electric Gas-cooled Solar Tower Power Plant (GAST). The project is an industrial joint venture between the partners Internationale Atomreaktorbau Gesellschaft GmbH (INTERATOM), Maschinenfabrik Augsburg-Nürnberg AG, New Technology Division (MAN), Messerschnitt-Bölkow-Blohm GmbH, Space Division (MBB) and Dornier System GmbH (Dornier). The BMFT has appointed the Deutsche Versuchsanstalt fur Luft und Raumfahrt (DFVLR) to take over project supervision.

Kraftwerk Union AG (KWU) is participating as a subcontractor to Interatom in the design and optimization of the power conversion cycle. The authors wish to express their thanks to the Ministry for funding the work and to the companies involved, in particular to Interatom and MAN, for their support and to Professor K. Bammert for his kind advice.

References

1 Kostrzewa, S., "Survey of the 20 MW Electric Gas-cooled Solar Tower Power Plant (GAST)," First BMFT Status Seminar GAST at DFVLR, Cologne, May 1980

2 Feustel, J., "Economic Features of Gas Cooled Solar Power Plants," First BMFT Status Seminar GAST at DFVLR, Cologne, May 1980

3 Bammert, K., "Influence of the Working Fluid on Heat Transfer and Layout of Solar Tower Receivers," *Studies in Heat Transfer*, McGraw-Hill, New York, 1979, pp. 383–400

4 Bammert, K., and Poesentrup, H., "Steam and Gas Turbines for Small Solar Power Plants," *Solar Energy: International Progress*, Pergamon, Vol. 3, 1980, pp. 1338–1350

5 Bammert, K., "Studies of Solar Gas Turbine Modules," Commission of European Communities, Centro EURATOM, Ispra, Italy, Research Project No. 879 - 78 SISP D, Nov. 1979

6 Melchior, E., Fuhrmann, H., Mayrhofer, O., Sprenger, H., "Design of the Nominal Receiver," First BMFT Status Seminar GAST at DFVLR, Cologne, May 1980

7 Franck, E. et al., "Solar Tower Power Plant 20 MW With Gas Turbine Cycle," International Symposium on Solar Thermal Power Systems, Marseilles (France), June 15 to 20, 1980, to be published in "Solar Energy."

Downloaded 01 Jun 2010 to 171.66.16.62. Redistribution subject to ASME license or copyright; see http://www.asme.org/terms/Terms_Use.cfm

Modified Brayton Cycles Utilizing Alcohol Fuels

M.F. Bardon
Mechanical Engineering Department,
Royal Military College of Canada,
Kingston, Ontario, Canada

It is already well known that alcohols can be burned in open-cycle gas turbines by direct firing in the combustor. This paper demonstrates however, that there are significant improvements in thermal efficiency possible by modifying the manner in which alcohols are used in Brayton cycle engines. It is shown that injection of the alcohol during the compression process can materially improve both thermal efficiency and specific work because of the intercooling effect of evaporation. Calculations are given which demonstrate the improvement theoretically possible at representative values of peak turbine inlet temperature. It is also shown that the optimum pressure ratio for both regenerated and unregenerated cycles is different when such compressor evaporative intercooling is used rather than simply injecting the fuel into the combustor.

Introduction

Although there has been considerable recent interest in the use of methyl and ethyl alcohol as fuels for reciprocating engines, their use in gas turbines has received much less study. This has been largely due to the fact that the two major uses of gas turbines at present are for aircraft propulsion and for stationary power generation. The low-energy storage capability of the alcohols compared to conventional hydrocarbons has discouraged their use in aircraft, and closed cycle power plants can often effectively and more economically burn primary energy sources such as coal, wood, or waste directly rather than after conversion to alcohol.

This situation may change in the future because of two factors; namely, that extensive use of regenerator-equipped gas turbines in automobiles is probable [1], and because the extensive development of alcohol fuels for piston engines may make alcohol available in large quantities at competitive prices, particularly in regions where other fuels are unavailable, inconvenient, or costly.

It has been shown [2] that methanol and ethanol can be fired directly in gas turbine combustors with no difficulty and, in fact, that the decrease in flame luminosity observed with methanol results in generally cooler combustion chamber walls than is the case for hydrocarbons. However, there are differences in the properties of the fuels and their combustion products which, if taken into account during the engine design, can significantly increase work output per unit mass of air flow. Furthermore cycle thermal efficiency may be improved as well under certain conditions [3]. However, in order to achieve the potential improvements, it has been shown [3] that optimum pressure ratios required are generally higher for alcohols than for kerosine. For a peak turbine inlet temperature of 1055 K for example, the maximum thermal efficiency of an unregenerated Brayton cycle using methanol was some 9 percent higher than that using kerosine but a pressure ratio of 17 was required to achieve this compared to the optimum value of about 15 for the hydrocarbon. Therefore, firing the methanol in a cycle optimized for kerosine would result in a smaller increase of cycle thermal efficiency than could be achieved if the cycle were designed specifically for methanol.

Direct firing of alcohols in gas turbine engines, although feasible and even attractive in certain respects, would not make best use of the fuels' potential. Because of the low calorific values of alcohols and their very large enthalpies of evaporation, there is a considerable evaporative cooling effect which can substantially alter engine performance. If this unique combination of characteristics is used effectively, there are improvements possible which do not exist for petroleum fuels. Alcohol has been used for many years in spark ignition racing engines largely because of the advantages derived from this phenomenon. It has been shown [4] that there are two opposing effects of fuel evaporation during a compression process. The cooling resulting from fuel evaporation tends to reduce the work of compression thereby raising power output and cycle efficiency; however, the increased quantity of gas (fuel vapor) requires additional work input for whatever further compression remains; this opposes the beneficial effect of the evaporative cooling. It has been demonstrated [4, 5] that, for methanol and ethanol, the cooling effect dominates and there is a net benefit to fuel evaporation during a compression process. For hydrocarbons, on the other hand, the overall effect is generally detrimental because the additional gas requires more work than is saved by the cooling.

Using realistic current component efficiencies and maximum turbine inlet temperatures, this paper shows the potential theoretical effect of allowing alcohol to evaporate in the compressor of a gas turbine engine, rather than injecting it

Contributed by the Gas Turbine Division of THE AMERICAN SOCIETY OF MECHANICAL ENGINEERS and presented at the International Gas Turbine Conference, Houston, Texas, March 8-11, 1981. Manuscript received at ASME Headquarters December 11, 1980. Paper No. 81-GT-103.

Copyright © 1982 by ASME

Downloaded 01 Jun 2010 to 171.66.16.62. Redistribution subject to ASME license or copyright; see http://www.asme.org/terms/Terms_Use.cfm

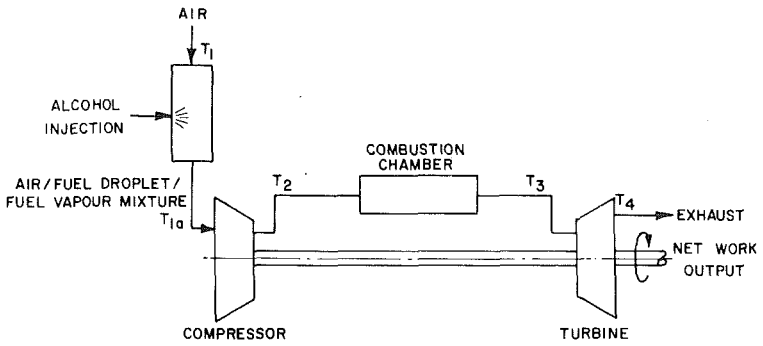

Fig. 1 Unregenerated modified Brayton cycle engine

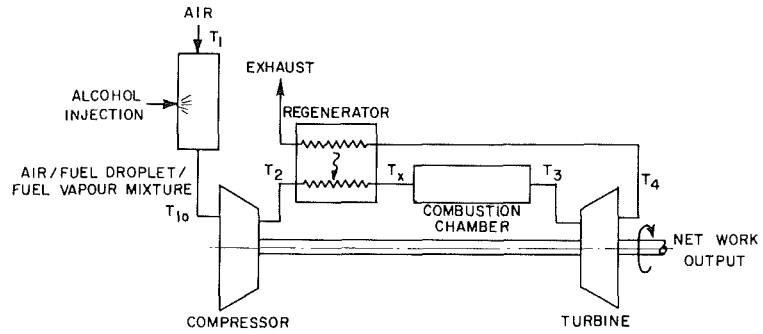

Fig. 2 Regenerator equipped modified Brayton cycle engine

into the combustor in liquid form. Figures 1 and 2 show the arrangement schematically and define the temperatures at various points in the cycle. Since the intent is to evaluate the potential of the concept, the case considered is that which produces the greatest improvement, namely:

1 injection of liquid fuel into the compressor inlet air;
2 evaporation to equilibrium before entering the compressor;
3 compression of the 2-phase mixture of air, fuel vapour and liquid fuel droplets;
4 heat addition in the regenerator if so equipped;
5 combustion without further fuel addition in the combustion chamber;
6 expansion back to the inlet pressure in the turbine; and
7 exhaust (through the regenerator if so equipped).

The implications and limitations of this assumed cycle are discussed in a subsequent section.

Calculation Methods

Gas Properties. In order to determine the properties of the gases at various points during the cycle, the components were

Nomenclature

A,B,C = constants used in Antoine equation (32)
a = coefficient used in equation (1)
b = coefficient used in equation (1)
c = coefficient used in equation (1)
C_p = constant pressure molar specific heat J/mol K
d = coefficient used in equation (1)
e = coefficient used in equation (1)
H = total enthalpy, J
$\bar{h}$ = molar specific enthalpy, J/mol
ln = natural logarithm
LHV = lower constant pressure enthalpy of combustion of liquid fuel
n = number of moles
P = pressure (total mixture pressure if unsubscripted)
$\bar{R}$ = universal gas constant = 8.314 J/mol K
S = total entropy, J/K
$\bar{s}$ = molar specific entropy J/mol K
T = absolute temperature, K
V = volume of a given quantity of fuel air mixture
VF = vapour fraction = n_g/n_l
W = work done on fuel air mixture
η = efficiency

Subscripts and Superscripts

a = value for air
b = referring to the combustion chamber
c = referring to the compressor
f = value for fuel if no superscript is used
$\overset{0}{f}$ = used for enthalpy of combustion i.e. h_f^0
fg = change in property during evaporation
$\overset{0}{fg}$ = change in property during evaporation at reference temperature, 25°C
g = referring to fuel vapour
i = referring to ith component of a mixture
l = referring to liquid fuel
r = referring to regenerator
s = referring to state after an isentropic process
t = referring to turbine
1,2 = general sequential values
1,1a,2,x,3,4 = points during cycle as defined in Figs. 1 and 2
° = value at reference temperature, 25°C

Downloaded 01 Jun 2010 to 171.66.16.62. Redistribution subject to ASME license or copyright; see http://www.asme.org/terms/Terms_Use.cfm

Table 1 Coefficients for specific heat-equation 1 [adapted from reference [6]]

	(Temperature in K, C_p in J/mol K)				
Gas	a	b	c	d	e
0_2	48.178	0	3 556	− 536	0
N_2	39.6	0	− 8 066	0	1 498 000
$C0_2$	67.8	0	− 15 200	0	1 821 000
H_20	83.09	0	17 400	− 1 860	0

assumed to behave both individually and collectively as ideal gases with temperature-dependent specific heats of the following form:

$$C_p = a + bT + cT^{-1} + dT^{-½} + eT^{-2} \tag{1}$$

where

C_p = constant pressure molar specific heat, J/mol K
a,b,c,d,e = coefficients characteristic of the gas concerned
T = absolute temperature, K

Table 1 shows the values of the coefficients used in the above equation for the gases considered in this study. Air was taken to be composed of 21 mole percent oxygen and the remainder nitrogen. Combustion was assumed to be essentially complete as far as gas composition was concerned; therefore, only $C0_2$ and H_20 were produced during the burning of the fuel, which was considered to be completely consumed in the combustor. Consequently, the gas entering the turbine consisted only of the original nitrogen, excess oxygen, and the two products of combustion.

With the assumptions stated above, the enthalpy change of a gas between any temperatures T_1 and T_2 is

$$\bar{h}_2 - \bar{h}_1 = \int_1^2 C_p dT$$

$$= a(T_2 - T_1) + \frac{b}{2}\left[T_2^2 - T_1^2\right] + c\ln\left\{\frac{T_2}{T_1}\right\} + 2d\left[T_2^{½} - T_1^{½}\right] - e\left[T_2^{-1} - T_1^{-1}\right] \tag{2}$$

where

$\bar{h}$ = molar specific enthalpy, J/mol

Likewise, the entropy may be expressed as

$$\bar{s}_2 - \bar{s}_1 = \int_1^2 \frac{C_p}{T} dT - \bar{R}\ln(P_2/P_1)$$

$$= a\ln(T_2/T_1) + b(T_2 - T_1) - c\left[T_2^{-1} - T_1^{-1}\right] - 2d\left[T_2^{-½} - T_1^{-½}\right] - \frac{e}{2}\left[T_2^{-2} - T_1^{-2}\right] - \bar{R}\ln(P_2/P_1) \tag{3}$$

where

$\bar{s}$ = molar specific entropy, J/mol K
$\bar{R}$ = universal gas constant, 8.314 J/mol K
P_2/P_1 = ratio of total pressures (which equals the ratio of each component's partial pressures)

For a mixture of N gases, the above equations become:

$$H_2 - H_1 = \sum_{i=1}^{N} n_i a_i (T_2 - T_1) + \sum_{i=1}^{N} \frac{n_i b_i}{2}\left[T_2^2 - T_1^2\right] + \sum_{i=1}^{N} n_i c_i \ln(T_2/T_1) + 2\sum_{i=1}^{N} n_i d_i \left[T_2^{½} - T_1^{½}\right] - \sum_{i=1}^{N} n_i e_i \left[T_2^{-1} - T_1^{-1}\right] \tag{4}$$

where n_i = number of moles of component i in the mixture. Likewise, equation (3) becomes

$$S_2 - S_1 = \sum_{i=1}^{N} n_i a_i \ln(T_2/T_1) + \sum_{i=1}^{N} n_i b_i (T_2 - T_1) - \sum_{i=1}^{N} n_i c_i \left[T_2^{-1} - T_1^{-1}\right] - 2\sum_{i=1}^{N} n_i d_i \left[T_2^{-½} - T_1^{-½}\right] - \frac{1}{2}\sum_{i=1}^{N} n_i e_i \left[T_2^{-2} - T_1^{-2}\right] - \sum_{i=1}^{N} n_i \bar{R}\ln(P_2/P_1) \tag{5}$$

Liquid Properties and Changes of State. In the calculations performed during this study, liquids were assumed to have constant specific heats.

Enthalpy of evaporation $\bar{h}_{fg}$ at any temperature T was evaluated as follows:

$$\bar{h}_{fg} = \bar{h}^0_{fg} + (\bar{h}_{fg} - \bar{h}^0_{fg}) = \bar{h}^0_{fg} + (\bar{h}_g - \bar{h}_l - \bar{h}^0_g + \bar{h}^0_l) \tag{6}$$

where

$\bar{h}^0_{fg}$ = enthalpy of evaporation at the reference temperature T^0, J/mol
$\bar{h}^0_l, \bar{h}^0_g$ = enthalpy of saturated liquid and saturated vapour at the reference temperature
$\bar{h}_l, \bar{h}_g$ = enthalpy of saturated liquid and saturated vapour at T

Using the previous assumption of variable specific heat for the vapour and constant specific heat C_{pl} for the liquid, equation 6 becomes

$$\bar{h}_{fg} = \bar{h}^0_{fg} + \int_{T^0}^{T} C_p dT - C_{pl}(T - T^0) \tag{7}$$

Equation (2) is used to evaluate the integral.

Now the change in entropy during the evaporation process $\bar{s}_{fg}$ is

$$\bar{s}_{fg} = \frac{\bar{h}_{fg}}{T} \tag{8}$$

Hence entropy of evaporation may be evaluated after enthalpy of evaporation has been found using equation (7).

Component Efficiencies. Using the state points defined in

Downloaded 01 Jun 2010 to 171.66.16.62. Redistribution subject to ASME license or copyright; see http://www.asme.org/terms/Terms_Use.cfm

Figs. 1 and 2, the component efficiencies were defined in their conventional forms as described below.

Compressor Efficiency. Adiabatic compressor efficiency is usually defined as

$$\eta_c = \frac{\bar{h}_{2s} - \bar{h}_1}{\bar{h}_2 - \bar{h}_1} \tag{9}$$

where

$\bar{h}_1$ = enthalpy at compressor inlet
$\bar{h}_2$ = enthalpy at compressor outlet
$\bar{h}_{2s}$ = enthalpy which would exist after an isentropic compression from state 1 to the same compressor exit pressure, P_2.

However, this expression is not useful for the present case because the state of the mass at the compressor outlet and inlet is not uniform as it is in a conventional cycle. The presence of two phases requires a weighted summation of properties. By using the same principle, namely that efficiency is the ratio of isentropic work to actual work, the following analagous expression can be used for the 2-phase compression.

$$\eta_c = \frac{\sum_{i=1}^{N} n_{i2s}\bar{h}_{i2s} - \sum_{i=1}^{N} n_{i1a}\bar{h}_{i1a}}{\sum_{i=1}^{N} n_{i2}\bar{h}_{i2} - \sum_{i=1}^{N} n_{i1a}\bar{h}_{i1a}} \tag{10}$$

Here liquid and vapour values are computed individually.

Combustion Chamber Efficiency. Efficiency of the combustion chamber is defined as the ratio of the difference in total sensible enthalpy between outlet and inlet to the chemical energy ideally released by conversion of reactants to products. Since there may be both liquid and vapour fuel present at the combustor inlet under certain conditions, it is necessary to take into account the differences in the enthalpies of combustion of liquid and gaseous fuel, which is merely the enthalpy of evaporation. Combustion chamber efficiency is therefore defined as

$$\eta_b = \frac{\sum_{i=1}^{N}\left[n_i(\bar{h} - \bar{h}^0_f)_i\right]_3 - \sum_{i=1}^{N}\left[n_i(\bar{h} - \bar{h}^0_f)_i\right]_2}{n_f\left[\mathrm{VF}_2(\mathrm{LHV} + \bar{h}_{fg}) + (1 - \mathrm{VF}_2)\mathrm{LHV}\right]} \tag{11}$$

where

$(\bar{h} - h^0_f)_i$ = sensible enthalpy of component i above its enthalpy of formation at the standard condition (25°C)
VF = that fraction of the fuel in the form of vapor
LHV = lower constant pressure heat of combustion of liquid fuel at 25°C, J/mol
n_f = total moles of fuel mixed with the given amount of air.

Pressure loss in the combustor is assumed to be negligible.

In the case of the regenerated cycle, the combustor inlet state would be x instead of 2.

Turbine Efficiency. Turbine adiabatic efficiency is defined in the usual manner since there is no longer any liquid present in the working fluid.

$$\eta_t = \frac{\bar{h}_3 - \bar{h}_4}{\bar{h}_3 - \bar{h}_{4s}} \tag{12}$$

where

$\bar{h}_3$ = enthalpy at turbine inlet
$\bar{h}_4$ = enthalpy at turbine exhaust
$\bar{h}_{4s}$ = enthalpy after an isentropic expansion from state 3 to the same turbine exit pressure.

Regenerator Efficiency. An ideal regenerator would heat the air leaving the compressor from T_2 to T_4, the temperature of the turbine exhaust, thereby reducing the quantity of fuel necessary. In a real regenerator, the temperature rise and hence fuel saving is less than in the ideal case and the regenerator efficiency is usually expressed as:

$$\eta_r = \frac{\bar{h}_x - \bar{h}_2}{\bar{h}_4 - \bar{h}_2} \tag{13}$$

where

$\bar{h}_2$ = enthalpy of the air leaving the compressor
$\bar{h}_4$ = enthalpy of the air if it were at T_4
$\bar{h}_x$ = actual enthalpy of the air leaving the regenerator and entering the combustion chamber.

Since there may be 2 phases present in the regenerator during this modified cycle, the following more general form of equation (12) is used:

$$\eta_r = \frac{\sum_{i=1}^{N} n_i h_{ix} - \sum_{i=1}^{N} n_i h_{i2}}{\sum_{i=1}^{N} n_i h_{i4} - \sum_{i=1}^{N} n_i h_{i2}} \tag{14}$$

The different properties of liquid and gaseous phases are thus accounted for. As in the case of the combustion chamber, pressure losses in the regenerator are assumed to be negligible.

Evaporation. The evaporation is assumed to occur adiabatically and irreversibly so that the mixture entering the compressor is at equilibrium. Pressure loss is assumed to be negligible.

Table 2 shows the component efficiencies taken in this study to be representative of typical current values.

Table 2 Component efficiencies

Compressor	0.85
Combustor	0.98
Turbine	0.90
Regenerator	0.75

Derivation of Equations for a 2-phase Isentropic Process. In order to determine actual compressor exit conditions it is first necessary to find the conditions at state 2s after an isentropic compression from the same initial state to the same final pressure. Equation (10) may then be used to find state 2. This section shows the derivation of the necessary equations.

For any adiabatic and reversible process between states 1 and 2:

$$S_2 - S_1 = 0$$

where

S_2 = total mixture entropy at state 2
S_1 = total mixture entropy at state 1

For a mixture of air, fuel vapour and liquid fuel this becomes

$$n_a(\bar{s}_{a2} - \bar{s}_{a1}) + n_{g2}\bar{s}_{g2} - n_{g1}\bar{s}_{g1} + n_{l2}\bar{s}_{l2} - n_{l1}\bar{s}_{l1} = 0 \tag{16}$$

where

n_a = number of moles of air
n_g = number of moles of fuel vapor
n_l = number of moles of liquid fuel
$\bar{s}_a$ = molar specific entropy of air, J/mol K
$\bar{s}_g$ = molar specific entropy of fuel vapor, J/mol K
$\bar{s}_l$ = molar specific entropy of liquid fuel, J/mol K

Downloaded 01 Jun 2010 to 171.66.16.62. Redistribution subject to ASME license or copyright; see http://www.asme.org/terms/Terms_Use.cfm

This may be expressed as

$$n_a(\bar{s}_{a2}-\bar{s}_{a1})+n_{g2}\bar{s}_{g2}+(n_{g2}-n_{g1})\bar{s}_{g1}-n_{g2}\bar{s}_{g1}+n_{l2}\bar{s}_{l2}+(n_{l2}-n_{l1})\bar{s}_{l1}-\bar{n}_{l2}\bar{s}_{l1}=0 \quad (17)$$

Rearranging,

$$n_a(\bar{s}_{a2}-\bar{s}_{a1})+n_{g2}(\bar{s}_{g2}-\bar{s}_{g1})+(n_{g2}-n_{g1})\bar{s}_{g1}+n_{l2}(\bar{s}_{l2}-\bar{s}_{l1})+(n_{l2}-n_{l1})\bar{s}_{l1}=0 \quad (18)$$

Since the decrease in the quantity of liquid during evaporation is equal to the increase in the quantity of fuel vapor,

$$(n_{l2}-n_{l1})=-(n_{g2}-n_{g1}) \quad (19)$$

Substituting into equation (18) gives

$$n_a(\bar{s}_{a2}-\bar{s}_{a1})+n_{g2}(\bar{s}_{g2}-\bar{s}_{g1})+(n_{g2}-n_{g1})(\bar{s}_{g1}-\bar{s}_{l1})+n_{l2}(\bar{s}_{l2}-s_{l1})=0 \quad (20)$$

Expanding the last term

$$n_{l2}(\bar{s}_{l2}-\bar{s}_{l1})=n_{l2}(\bar{s}_{g2}+\bar{s}_{l2}-\bar{s}_{g2}+\bar{s}_{g1}-\bar{s}_{l1}-\bar{s}_{g1}) \quad (21)$$

By definition, the entropy change during evaporation is

$$\bar{s}_{fg}=\bar{s}_g-\bar{s}_l \quad (22)$$

Therefore equation (21) may be written

$$n_{l2}(\bar{s}_{l2}-\bar{s}_{l1})=n_{l2}(-\bar{s}_{fg2}+\bar{s}_{fg1}+\bar{s}_{g2}-\bar{s}_{g1}+\bar{s}_{fg1}) \quad (23)$$

$$=n_{l2}(\bar{s}_{fg1}-\bar{s}_{fg2})+n_{l2}(\bar{s}_{g2}-\bar{s}_{g1}) \quad (24)$$

Introducing equation (24) into equation (20) and noting that the total number of moles of fuel, n_f, is at all times equal to the sum of the quantities of liquid and vapor present; that is,

$$n_f=n_{g2}+n_{l2}=n_{g1}+n_{l1} \quad (25)$$

then it follows that

$$n_a(\bar{s}_{a2}-\bar{s}_{a1})+n_f(\bar{s}_{g2}-\bar{s}_{g1})+(n_{g2}-n_{g1})s_{fg1}+(n_f-n_{g2})(\bar{s}_{fg1}-\bar{s}_{fg2})=0 \quad (26)$$

Using the definition of vapor fraction

$$\mathrm{VF}=\frac{n_g}{n_l} \quad (27)$$

this may be written

$$n_a(\bar{s}_{a2}-\bar{s}_{a1})+n_f(\bar{s}_{g2}-\bar{s}_{g1})+n_f(\mathrm{VF}_2-\mathrm{VF}_1)\bar{s}_{fg1}+n_f(1-\mathrm{VF}_2)(\bar{s}_{fg1}-\bar{s}_{fg2})=0 \quad (28)$$

Collecting terms

$$n_a(\bar{s}_{a2}-\bar{s}_{a1})+n_f\left[(\bar{s}_{g2}-\bar{s}_{g1})+(\mathrm{VF}_2-\mathrm{VF}_1)\bar{s}_{fg1}+(1-\mathrm{VF}_2)(\bar{s}_{fg1}-\bar{s}_{fg2})\right]=0 \quad (29)$$

This equation was used to determine the state after an isentropic 2-phase compression - that is, to determine T_2.

The evaluation of the entropy changes of the air and fuel vapour was done using equation (3). Vapor fractions were found by noting that fuel vapor and air occupy essentially the same volume because the specific volume of the liquid is negligibly small compared to that of the gas.

Since ideal gas behavior has already been assumed, the vapor fraction VF may then be found as follows:

$$\frac{\mathrm{VF}\,n_f\bar{R}\,T}{P_f}=\frac{n_a\bar{R}\,T}{P_a}=V \quad (30)$$

where

P_f = partial pressure of fuel vapor at the mixture temperature T

P_a = partial pressure of the air

V = mixture volume

Using the fact that total pressure P is the sum of the partial pressure of fuel and air, equation (30) becomes

$$\mathrm{VF}=\frac{n_aP_f}{n_f(P-P_f)} \quad (31)$$

In order to evaluate vapor fraction it is therefore necessary to evaluate fuel vapor pressure at the conditions concerned. Since both alcohols are pure fuels, vapor pressure is a function of temperature only and may be evaluated using the Antoine Equation [7].

$$\log_{10}P_f=A-B/(C+T) \quad (32)$$

Table 3 Antoine equation constants P_f in kP_a T in K

	A	B	C
Methanol [8]	7.022 40	1 474.08	−44.02
Ethanol [7]	7.169 84	1 554.3	−50.5

In order to evaluate the work done during any process between successive states 1 and 2, the First Law of Thermodynamics may be used in the following form:

$$W=n_a(\bar{h}_{a2}-\bar{h}_{a1})+n_{g2}\bar{h}_{g2}-n_{g1}\bar{h}_{g1}+n_{l2}\bar{h}_{l2}-n_{l1}\bar{h}_{l1} \quad (33)$$

where

W = work done on the $(n_a + n_f)$ moles of mixture

n_g = number of moles of vapor

n_l = number of moles of liquid

By algebraic manipulation similar to that used to derive equation (29), equation (33) becomes

$$W=n_a(\bar{h}_{a2}-\bar{h}_{a1})+n_f\left[(\bar{h}_{g2}-\bar{h}_{g1})+(\mathrm{VF}_2-\mathrm{VF}_1)\bar{h}_{fg1}+(1-\mathrm{VF}_2)(\bar{h}_{fg1}-\bar{h}_{fg2})\right] \quad (34)$$

Equation (34) is the expanded form used to evaluate both ideal and actual compression work, (numerator and denominator of the equation for compressor efficiency-equation (10)).

Calculation Procedure. Calculations were performed on a Burroughs 6700 computer. In general, Newton-Raphson iteration was used to determine the temperature at the end of any isentropic process. The same technique was also employed to determine the temperature change corresponding to a known change of enthalpy.

The following were the steps in the calculation at each cycle pressure ratio studied:

(i) Air was assumed to enter the evaporator at ambient temperature and standard atmospheric pressure where a trial quantity of liquid fuel at the same temperature was injected. The evaporator was considered to be adiabatic and therefore equation 34 was used to determine the outlet conditions knowing that there is no work done during the process. The fuel evaporation results in a decrease in temperature and there was usually found to be a mixture of air, fuel vapour and liquid fuel in equilibrium at the evaporator outlet.

(ii) Taking evaporator outlet state as input conditions for the compressor, equation (29) was used to determine the conditions after an isentropic compression of the initially two phase mixture. From the known ideal compressor outlet temperature, the ideal enthalpy change was found from equation (4); then equation (10), coupled with the assumed value of compressor efficiency provided actual compressor outlet enthalpy and hence temperature.

(iii) Using compressor outlet conditions and equation 11, combustor outlet temperature was found. If calculated combustor outlet temperature was not equal to the desired

Downloaded 01 Jun 2010 to 171.66.16.62. Redistribution subject to ASME license or copyright; see http://www.asme.org/terms/Terms_Use.cfm

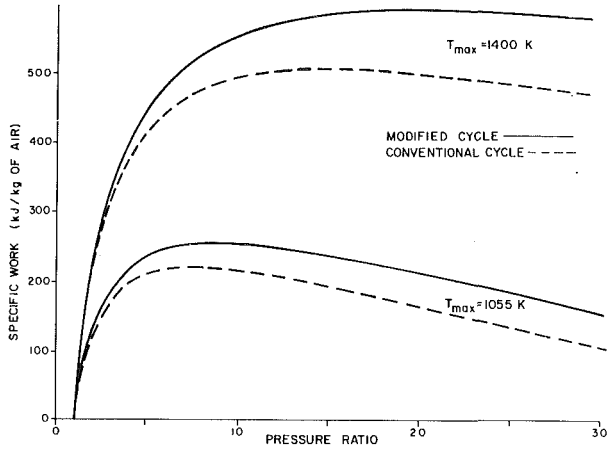

Fig. 3 Work output of unregenerated cycles using methanol

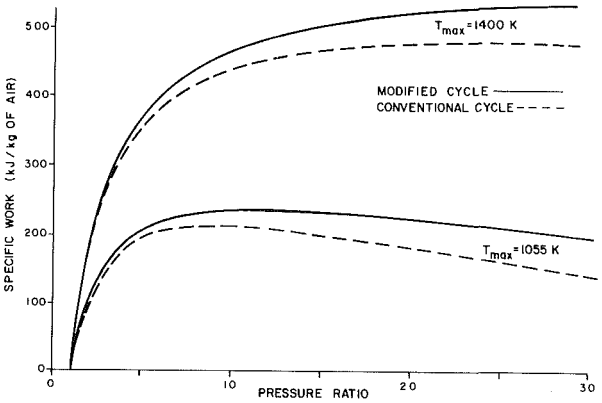

Fig. 4 Work output of regenerator equipped cycles using methanol

Table 4 Other data used in calculations

Property	Methanol	Ethanol
Lower enthalpy of combustion of liquid fuel at 25°C [kJ/mol] [13]	569.2	1 028
Enthalpy of evaporation at 25°C [kJ/mol] [14]	37.4	42.3
Specific heat of liquid [J/mol K] [13]	82.1	117
Air intake temperature (K)	289	289
Initial temperature of liquid fuel (K)	289	289

turbine inlet temperature, steps (i) to (iii) were repeated for a new value of fuel-air ratio determined by the Newton-Raphson technique.

(iv) After the fuel-air ratio necessary for the specified maximum cycle temperature was found, the turbine work was found similarly to that for the compressor except that the working fluid was composed only of gaseous products of combustion.

(v) In the case of the regenerated cycle shown in Fig. 2, the turbine outlet temperature determined the heat transferred to the fluid between the compressor outlet and combustor inlet. Therefore, further iteration was required because the reduction in fuel flow changes the fluid properties and hence turbine outlet temperature. A method of successive approximations was used in which outlet temperature after each set of calculations was reintroduced into the regenerator until no further change occurred.

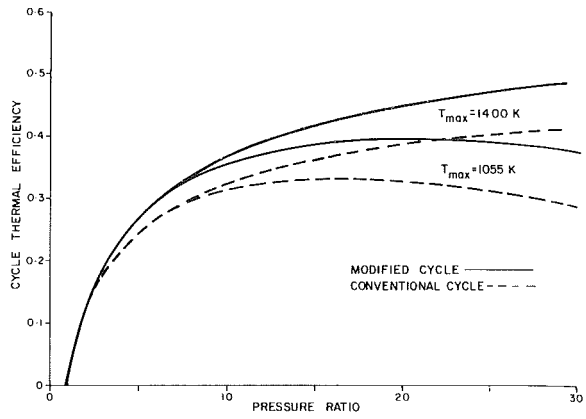

Fig. 5 Thermal efficiency of unregenerated cycles using methanol

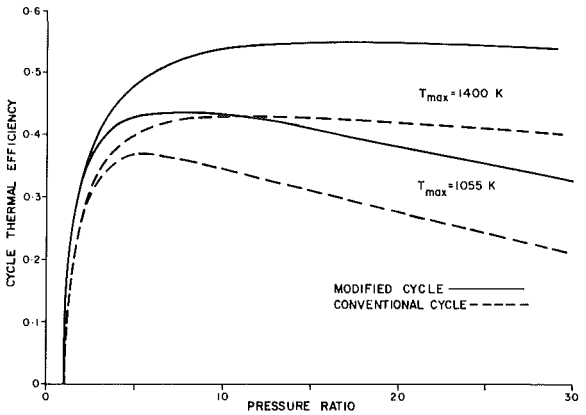

Fig. 6 Thermal efficiency of regenerator equipped cycles using methanol

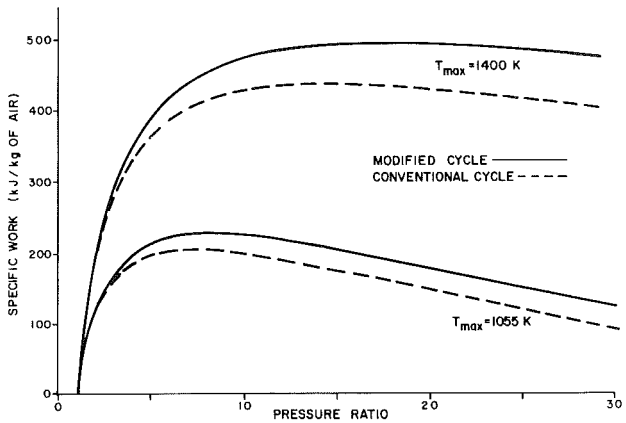

Fig. 7 Work output of unregenerated cycles using ethanol

(vi) Net cycle work output was taken as the difference between turbine and compressor work. Cycle thermal efficiency was defined as the net work divided by the lower enthalpy of combustion of the liquid fuel required.

(vii) To provide a basis of comparison, specific work output and thermal efficiency were determined for a conventional gas turbine cycle burning alcohol injected into the combustion chamber in the usual way. Details of these calculations are given in reference [3].

Results

Figures 3-10 show results of the calculations for methanol

Downloaded 01 Jun 2010 to 171.66.16.62. Redistribution subject to ASME license or copyright; see http://www.asme.org/terms/Terms_Use.cfm

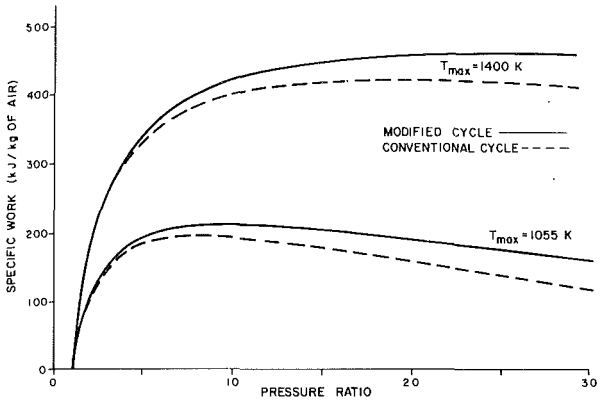

Fig. 8 Work output of regenerator equipped cycles using ethanol

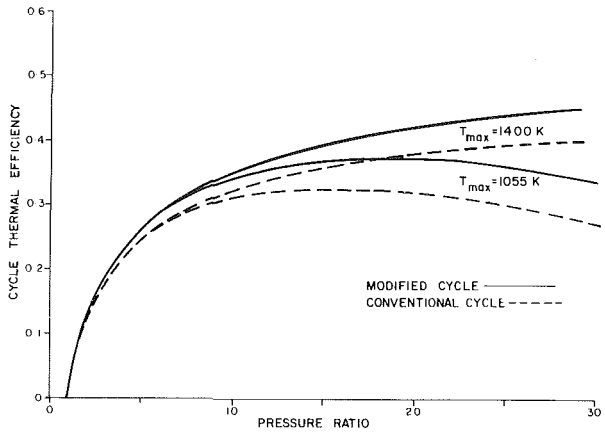

Fig. 9 Thermal efficiency of unregenerated cycles using ethanol

and ethanol at the two values of turbine inlet temperature for both regenerated and unregenerated cycles.

Discussion

The most conspicuous result evident in all the figures is that evaporative intercooling significantly increases both overall cycle thermal efficiency and work output per unit mass of air entering the engine. For example, at a pressure ratio of 15 and a maximum temperature of 1 400 K, the unregenerated cycle using methanol evaporation has a thermal efficiency nearly 15 percent higher than a conventional cycle. Specific work output is similarly improved.

That thermal efficiency is higher in the modified cycle may seem paradoxical in that intercooling in a closed cycle (external heat addition) without regeneration reduces efficiency. However, the explanation lies in the fact that the energy necessary to evaporate the fuel comes ultimately from the fuel's heating value and represents an energy penalty in any case. By utilizing evaporative cooling to reduce compressor work, no additional energy is required than for the usual Brayton cycle configuration but net work output is increased.

The work output improvement results from two cumulative effects. The first is the reduction in compressor work described above, but there is also a major contribution due to the greater overall fuel-air ratio allowable in the modified cycle for a given maximum temperature. The increased fuel flow raises turbine work output because of the difference in the number of moles of combustion products as well as their greater heat capacity. This latter effect is responsible for the disproportionate increase in specific work when methanol is substituted for kerosine in conventional cycles. [3]

There are several practical considerations which may prevent the attainment of the potential improvements predicted by this study. At large pressure ratios and high turbine inlet temperatures (i.e. comparatively rich mixtures) it is conceivable that the fuel-air mixture might ignite spontaneously in the latter stages of the compressor. There is a lack of data on high pressure high temperature flammability of alcohols but the mixtures in this case are well below the lean flammability limit at normal temperature and pressure and the lean limit normally expands but slightly with temperature and pressure [9,10]. This, coupled with the fairly short residence time in the compressor and long ignition delay of both alcohols makes it unlikely that spontaneous ignition will present difficulties. Similarly, flashback from the combustion chamber does not likely pose a serious problem and is somewhat more tractable in any case since flame arrestors could be used between the compressor and combustor.

A more serious difficulty is the opposite effect, namely that

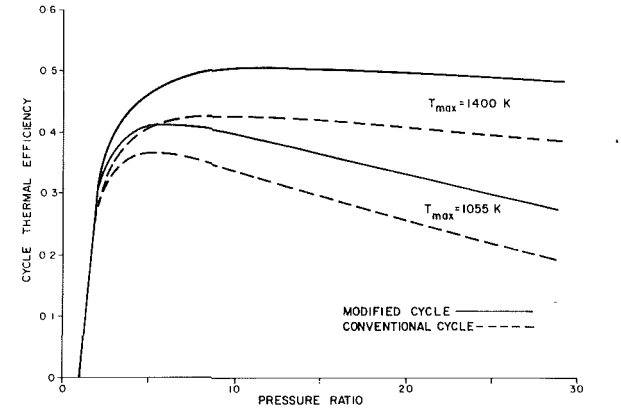

Fig. 10 Thermal efficiency of regenerator equipped cycles using ethanol

the mixture is too lean for stable homogeneous combustion. The catalytic combustion chambers presently being actively investigated would solve this problem nicely although they are not yet sufficiently developed for commercial application. A simpler and already feasible solution would be to pilot the combustion by injecting a portion of the fuel into the combustor to burn heterogeneously as in normal combustors. This would of course reduce some of the gains achieved by the modified cycle; however, a relatively small amount such as 10 percent of total fuel flow would probably be sufficient and significant improvements would therefore still be possible.

The gains in this system would also be reduced if the evaporation deviated too far from the assumed continuous equilibrium in the compressor. Thus fine atomization is necessary during the evaporator injection. In the event that evaporation rate were too slow to maintain equilibrium, it might be necessary to inject some of the alcohol into the compressor after several stages of compression has raised the fluid temperature. If carefully designed, possibly with several points of injection, the cycle efficiency need not drop unduly.

A further advantage possible with this modified Brayton Cycle lies in the possibility of reducing peak turbine inlet temperature without loss of efficiency. An engine could be designed so as to give the same efficiency as a particular conventional cycle but would then have a longer turbine blade and combustor liner life due to considerably cooler temperatures in these components.

Figures 3-10 also show that the pressure ratio giving maximum efficiency and work output is higher in the modified cycle than the conventional one. The curves are relatively flat in this range, however, so operating the

Downloaded 01 Jun 2010 to 171.66.16.62. Redistribution subject to ASME license or copyright; see http://www.asme.org/terms/Terms_Use.cfm

evaporative cycle using equipment manufactured for the optimum pressure ratio of a conventional cycle would still give improved performance.

Conclusions

1. Modifying a Brayton cycle so as to evaporate alcohol fuel in the compressor offers the potential for significant improvement in cycle thermal efficiency and work output per unit mass of air flow.
2. Designing this system so as to achieve efficiency comparable to that of a conventional cycle would result in cooler turbine inlet and combustor liner temperatures and hence extended life for these components.
3. In general, peak efficiency and specific work occur at higher pressure ratios in the modified cycle.
4. Attainment of the potential improvement depends upon component design specifically for the changed conditions. For example, compressor gas flow rate is not constant as in the usual case.

References

1 "Should We Have a New Engine? An automobile power systems evaluation," Vol. 1, JPL SP 43-17, Jet Propulsion Laboratory, California Institute of Technology, Pasadena, 1975.

2 Klapatch, R.D., "Gas Turbine Emissions and Performance on Methanol Fuel," ASME-IEE Joint Power Generation Conference, Portland, Sept. 28 - Oct. 1, 1975.

3 Bardon, M.F., "Methanol and Ethanol as Gas Turbine Fuels," *Proceedings on the IV International Symposium on Alcohol Fuel Technology*, Sao Paulo, Brazil, Oct. 5-8, 1980.

4 Bardon, M.F., "Thermodynamic Calculations for Otto Cycle Engines Using Methanol as a Fuel," 2nd Miami International Conference on Alternative Energy Sources, 10-12 Dec., 1979.

5 Hilliard, J.C., "Calculations Relevant to the Fueling of Alcohols in Spark Ignited IC Engines," *Proceedings of the III International Symposium on Alcohol Fuel Technology*, Asilomar, Calif., May 28-31, 1979.

6 Wark, R., *Thermodynamics*, McGraw-Hill, New York, 1977.

7 *Lange's Handbook of Chemistry*. 11th Edition, J.A. Dean, Editor, McGraw-Hill, N.Y. 1973.

8 Wilhoit, R.C., and B.J. Zwolinski, "Physical and Thermodynamic Properties of Aliphatic Alcohols," *J Phys Chem Ref Data*, Vol. 2, Supp. 1, 1973, pp. 1.40 to 1.54.

9 Lewis B., and G. von Elbe, *Combustion Flames and Explosions of Gases* 2nd edition, Academic Press, N.Y. 1961.

10 Goodger, E.M. *Hydrocarbon Fuels*, Macmillan, London, 1975.

11 Krill, M.V., Kesselring, J.P., and Chu, E.K., "Catalytic Combustion for Gas Turbine Applications," ASME paper #79-GT-188 presented at 1979 Gas Turbine Conference, San Diego, Mar. 12-15, 1979.

12 Cerkanowicz, A.E., Shaw, H., and Stevens, J.G., "Environmental Assessment of Advanced Open Cycle Gas Turbine Power Plants," ASME paper #79-GT-187 presented at 1979 Gas Turbine Conference, San Diego, Mar. 12-15, 1979.

13 *Standard Handbook for Mechanical Engineers*, 7th edition. T. Baumeister, Editor, McGraw-Hill, 1967.

14 Spiers, H.M. *Technical Data on Fuel*, British National Committee, World Power Conference, London, 1952.

Downloaded 01 Jun 2010 to 171.66.16.62. Redistribution subject to ASME license or copyright; see http://www.asme.org/terms/Terms_Use.cfm

Effect of Temperature Dependent Mechanical Properties on Thermal Stress in Cooled Turbine Blades

J. M. Allen
Westinghouse Electric Corporation,
Combustion Turbine Systems Division,
Engineering Department,
Concordville, Pa. 19331
Mem. ASME

Finite element analyses show that maximum thermal stresses in a typically cooled turbine blade are approximately 40 percent larger than they are if calculated assuming constant, average temperature material properties—even though the local-to-average properties vary only 2 to 3 percent. An error of this size in stress leads to an order of magnitude over prediction of cyclic life. This surprisingly large effect is explained by means of the solution for thermal stress in a flat plate with a thermal gradient through its thickness. In general, finite element computer codes allow for temperature dependency of properties, but some do not permit this dependency within an element. It is shown that this can be a serious limitation with higher-order elements.

Introduction

Thermal stresses are caused by differential thermal expansions that arise from an uneven distribution of temperature through the body in question. Since mechanical properties, notably Young's modulus (E) and coefficient of thermal expansion (α), are temperature dependent they too vary throughout the body. Although the variation in these properties is small, compared to the non-uniformity in temperature, failure to take it into account can lead to surprisingly large errors in thermal stress.

Most modern computer codes for calculating stress allow for the temperature dependency of mechanical properties, but some finite element programs only allow E and α to vary from element to element. This is not a serious limitation for the constant stress element because so many are required to construct a good model in the first place. However, it was found to be a serious limitation with higher-order elements where a comparatively small number of elements is otherwise required. The practical importance of these conclusions is illustrated by two-dimensional and three-dimensional steady-state stress analyses of a cooled gas turbine blade.

The following paragraphs discuss the results of finite element analyses in which E and α are temperature dependent in the first case, and completely or partially independent of temperature in the latter case. The substantial differences are explained utilizing the solution for thermal stress in a flat plate with variable temperature through its thickness.

Cooled Turbine Blade

A typical mid-height cross section of a cooled gas turbine blade is shown in Fig. 1. High velocity cooling air extracts heat at the small spanwise holes located along the middle surface of the cross section. This gives rise to large temperature gradients through the thickness, as well as a substantial variation in the chordwise direction.

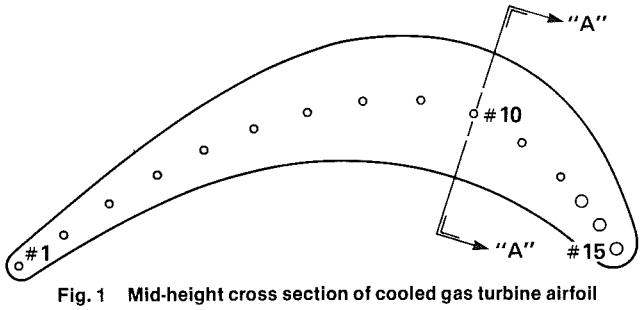

Fig. 1 Mid-height cross section of cooled gas turbine airfoil

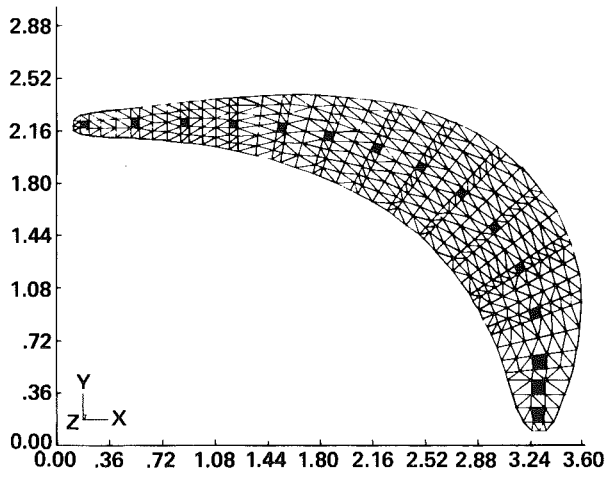

Fig. 2 Finite element model of cooled airfoil mean section

A two-dimensional finite element model of the cross section, shown in Fig. 2, was used for both heat conduction and

Contributed by the Gas Turbine Division of THE AMERICAN SOCIETY OF MECHANICAL ENGINEERS and presented at the International Gas Turbine Conference and Products Show, Houston, Texas, March 8-11, 1981. Manuscript received at ASME Headquarters, December 11, 1980. Paper No. 81-GT-105.

Copyright © 1982 by ASME
Downloaded 01 Jun 2010 to 171.66.16.62. Redistribution subject to ASME license or copyright; see http://www.asme.org/terms/Terms_Use.cfm

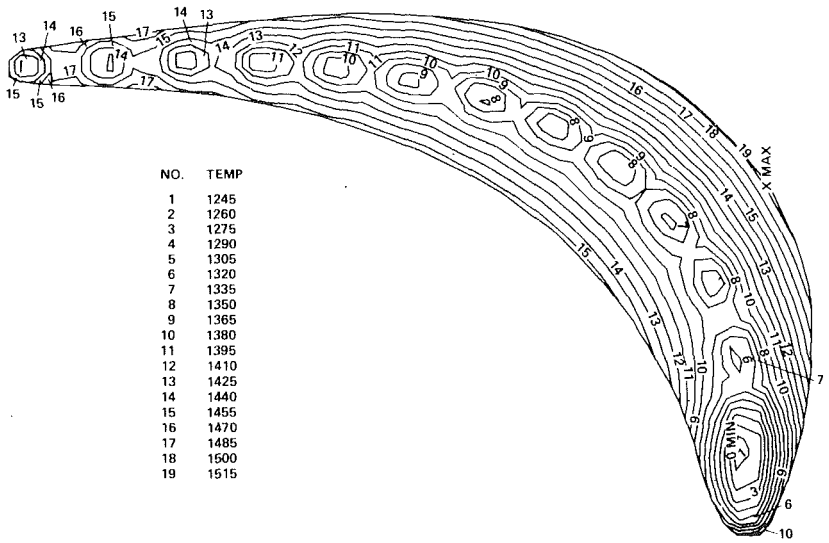

Fig. 3 Isotherms

stress analyses. The heat conduction element permits a linear variation of temperature from node to node. Round cooling holes were replaced by roughly square ones with equal heat removing capability (surface area times heat-transfer coefficient is the same), as shown by the darkened elements (Fig. 2).

Coolant heat transfer-coefficients were applied to the edges of the elements joining the darkened ones. No convective cooling was done on any edge of the darkened hole elements, which had the conductivity of the metal. Isotherms from the heat conduction calculation are shown in Fig. 3. The large through-the-thickness variation at the thickest part of the airfoil is particularly noteworthy.

Stresses resulting from this temperature pattern were calculated utilizing generalized plane strain triangular constant stress elements. Generalized plane strain is an approximation of the actual three-dimensional problem, in which strains normal to the cross section are a linear function of the cross-sectional dimensions, and the shearing strains ϵxy and ϵyz are zero (plane sections remain plane after deformation). This amounts to superimposing a uniform strain (translation) plus pure bending strains (rotations about x and y axes) to the plane strain solution, the magnitudes of which must satisfy equilibrium of the external z force and external moments about x and y. The generalized plane strain solution yields exact results for cross sections well removed from the ends (say a chord length or more), provided that the geometry is prismatic and thermal expansion is linear or constant in the z direction.

The holes were not modeled in the stress analysis. Since the material contained within the darkened squares (Fig. 2) was assumed to be the same as the blade, the stresses calculated in the hole areas are nominal and must be multiplied by appropriate stress concentration factors to obtain actual peak stress.

Table 1 Stress in cooled airfoil with (1) E and α temperature dependent and (2) E and α constant

	Pressure Surface		Suction Surface		Cooling Hole		
Case	σ_I*	σ_{II}	σ_I*	σ_{II}	σ_I*	σ_{II}	σ_{III}
Temperature Dependent E & α	−19.5	−33.9	−21.9	−28.6	37.1	27.2	4.6
Temperature Indpendent E & α	−10.6	−24.3	−12.0	−20.7	28.6	19.1	3.4

All stresses in KSI, 1 KSI = 6.895 MPa

*Includes 10 KSI cf stress

The largest principal stresses generally occur in the thickest part of the airfoil and are essentially perpendicular and parallel to a line such as AA (Fig. 1). The state of stress on the pressure and suction surfaces and at cooling hole number 10 are listed in Table 1, where σ_I is the component perpendicular to the cross section; σ_{II} is the component perpendicular to AA in the plane of the cross section; and σ_{III} is the in-plane component parallel to AA.

Two cases are tablulated. The first set of results was obtained with E and α temperature dependent. The temperature dependence of these quantities is shown in Fig. 4. The second set of results was calculated assuming that E and α are constant and equal to the values that occur at the mean temperature of the cross section.

Thermal stresses are approximately 40 percent larger for the temperature dependent case, even though the local values of E and α are only about 3 percent higher or lower than the

Nomenclature

C_1 = equation (5)
C_2 = equation (6)
E = Young's modulus, psi
f = cyclic frequency, cpm
N_f = cycles to failure
r = radius of curvature, in
t = distance from mid-surface of plate, in
$\bar{t}$ = distance of Young's modulus weighted centroid from middle surface of plate (equation (3)), in
t' = equation (4)
T = temperature, °F
T_0 = reference temperature from which thermal expansion coefficient measured, °F
α = linear coefficient of thermal expansion, in/in-°F
σ_I = principal stress normal to cross section, psi
σ_{II} = principal stress normal to line AA (Fig. 1), psi
σ_{III} = principal stress parallel to line AA (Figure 1), psi
$\Delta\sigma$ = cyclic stress, psi
ν = Poisson's ratio

Downloaded 01 Jun 2010 to 171.66.16.62. Redistribution subject to ASME license or copyright; see http://www.asme.org/terms/Terms_Use.cfm

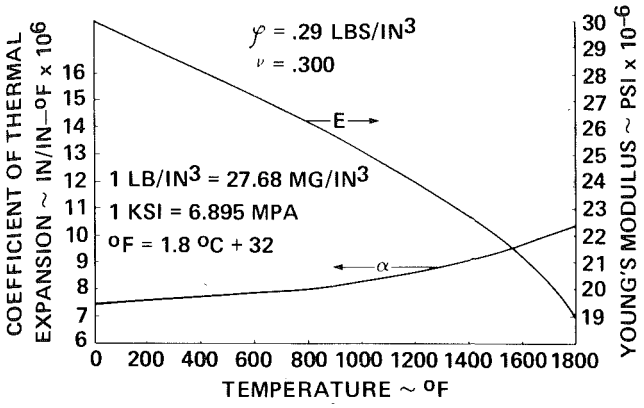

Fig. 4 Temperature dependent mechanical properties of cast U500 nickel base superalloy

average values. The practical implications are significant. In the area of the holes, the local σ_{II} stress is given by the solution for stress around a hole in an infinite plate (1), because the holes are far apart (4 diameters or more). Hence, the peak stresses are $(3 \times 27.2 - 4.6) = 77.0$ ksi for the variable E and α case, and $(3 \times 19.1 - 3.4) = 53.9$ ksi for the constant E $-$ α case. The low cycle fatigue behavior of the blade material has been determined by Leven [2] over a temperature range of 1200°F to 1800°F and frequencies of 1 cycle per min (1 cpm) to 1 cycle per hr (1 cph). The cyclic life at 1340°F and moderate cyclic stress levels (completely elastic behavior) is given by the following:

$$N_f = \left(\frac{431{,}200}{\Delta\sigma}\right)^{7.463} f^{.5112} \tag{1}$$

Cyclic life is strongly dependent on stress. In this example, the predicted life for the temperature dependent E $-$ α case (43 percent higher stress) is only 7 percent of what it is for the constant E $-$ α case. That is, a 30 percent error in stress results in an error of 1332 percent in predicted life.

To determine why this dependency of E and α on temperature is so important, it is useful to study the solution for thermal stress in a flat plate with a temperature gradient through its thickness. Since stresses along line A-A can be reasonably approximated this way, a detailed examination of the flat plate solution should reveal why significant differences occur.

Flat Plate With Temperature Variation Through its Thickness

The solution is well known for thermal stress in a flat plate with a temperature variation through its thickness and temperature independent material properties (1). This equation may be modified to allow for temperature dependent properties by carrying E, α, and v under the integral signs during the derivation:

$$\sigma_I = \sigma_{II} = \frac{E}{(1-v)}\left[\epsilon_0 + \frac{t'}{r} - \alpha(T - T_0)\right] \tag{2}$$

where

$$\bar{t} = \frac{\int_{-h/2}^{h/2} \frac{E}{(1-v)} t\,dt}{\int_{-h/2}^{h/2} \frac{E}{(1-v)}\,dt} \tag{3}$$

$$t' = t - \bar{t} \tag{4}$$

$$C_1 = h/2 - \bar{t} \tag{5}$$

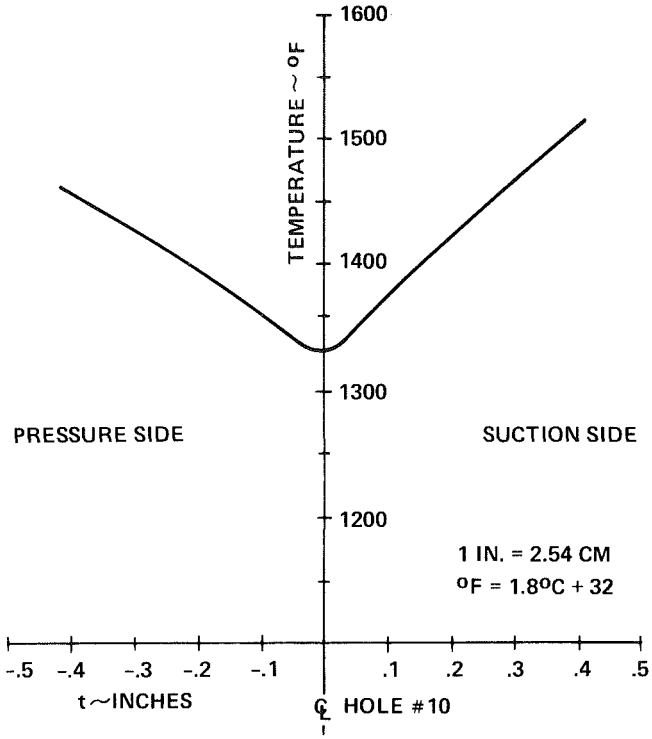

Fig. 5 Temperature distribution through thickness (along "A-A") of airfoil

$$C_2 = h/2 + \bar{t} \tag{6}$$

$$\epsilon_0 = \frac{\int_{-C_2}^{C_1} \frac{E\alpha(T - T_0)dt'}{(1-v)}}{\int_{-C_2}^{C_1} \frac{E\,dt'}{(1-v)}} \tag{7}$$

$$\frac{1}{r} = \frac{\int_{-C_2}^{C_1} \frac{E\alpha\,(T - T_0)t'dt'}{(1-v)}}{\int_{-C_2}^{C_1} \frac{E}{(1-v)}(t')^2 dt'} \tag{8}$$

The temperature variation through the thickness of the airfoil along line AA is plotted in Fig. 5. The thermal stresses resulting from application of the flat plate formula, equation (2), shown in Fig. 6, are a good approximation of the finite element results. The maximum stresses from the temperature dependent property case are about 44 percent greater than for the constant E-α case, in which E and α were taken at the average through the thickness temperature. To demonstrate why this occurs, values of the individual terms in equation (2) are tabulated in Table 2.

Table 2 Terms in flat plate equation for pressure surface on airfoil where (1) E and α temperature dependent and (2) E and α constant

TERM	Temp. Dependent E & α = (1)	Temp. Independent E & α = (2)	Ratio (1) ÷ (2)
ϵ_0	.012239	.012246	.99942
t'/r	−.00045102	−.00031097	1.4504
$\alpha(T - T_0)$	.012886	.012686	1.0158
$\epsilon_0 - \alpha(T - T_0)$	−.000647	−.00044000	1.4705
$E/(1-v)$	31.78×10^6	32.3×10^6	.98390
σ_{II}	−34,895	−24,256	1.4386

Downloaded 01 Jun 2010 to 171.66.16.62. Redistribution subject to ASME license or copyright; see http://www.asme.org/terms/Terms_Use.cfm

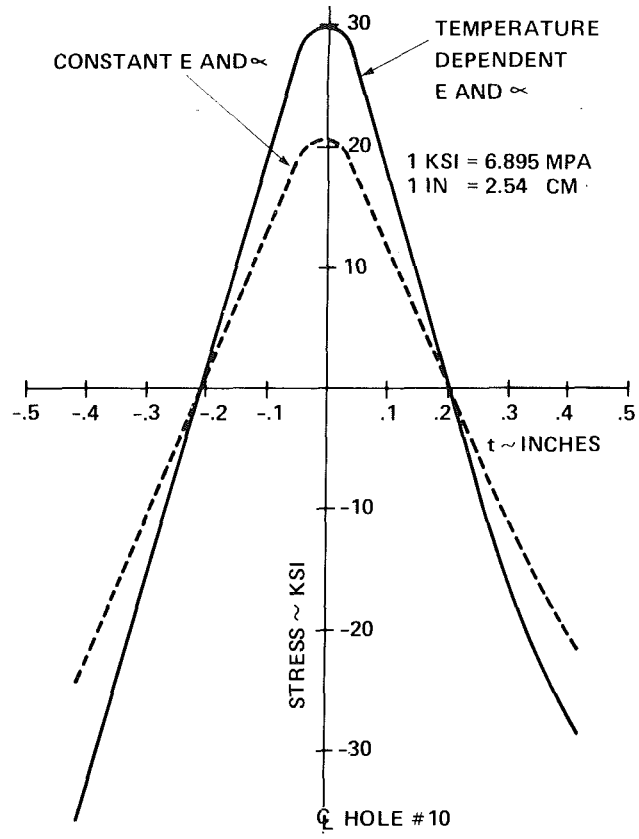

Fig. 6 Flat plate stresses due to through-the-thickness temperature distribution (Fig. 5)

This is a classic case in which stress depends on the difference between two nearly equal numbers. While the average expansion ϵ_0 is essentially the same, and while the local expansion $\alpha(T-T_0)$ is only 1.6 percent greater, the difference between the two (the extensional component of mechanical strain) is 47 percent larger.

Since the same is true for the bending term t'/r, it is the temperature dependency of expansion coefficient that is primarily responsible for the difference in stress. The effect of Young's temperature dependent modulus should be of the same order as the ratio of local E to average E, which is 0.9839 for the preceding flat plate example.

It is apparent that maximum error is introduced when the thermal gradients and stresses are small. Although there is little interest in what the magnitude of maximum error might be if the stresses are of no practical importance, it is clear that large errors can be introduced at stress levels of practical concern as demonstrated by the cooled blade example.

Effect on Finite Element Modeling

The restriction that E and α can vary only from element to element is not serious in terms of the constrant strain triangle element, because many are required to model the problem properly, as in the cooled blade example described earlier (Fig. 2).

The trend today is to employ higher order isoparametric elements that can accurately represent the body with a much smaller number of elements, and more accurately describe curved boundaries. If, however, the isoparametric element does not permit the temperature dependency of E and α from integrating point to integrating point, serious errors in thermal stress can result in an otherwise adequate model.

A three-dimensional model of the same blade using 20 node, quadratic, isoparametric elements is shown in Fig. 7. A total of 320 elements were used (16 chordwise × 10 radially × 2 thick). Heat was removed by convection link elements (point heat sink elements) located at the corner nodes of elements coincident with the cooling holes. The effect of radial gas temperature profile on mid-chord surface thermal stress was the primary objective of this study, and in view of the nearly linear variation in strain from cooling hole to surface (Fig. 6), it was judged to be a reasonable model for calculating these particular stresses.

The first calculation was carried out with E and α variable

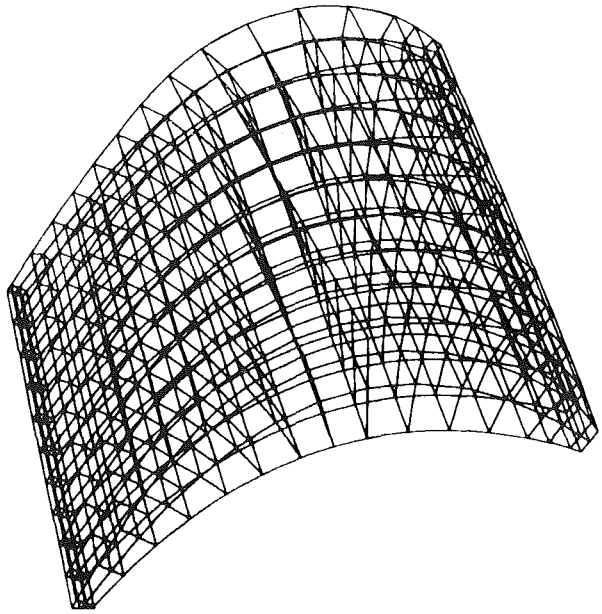

Fig. 7(a) Three-dimensional Isoparametric model of airfoil

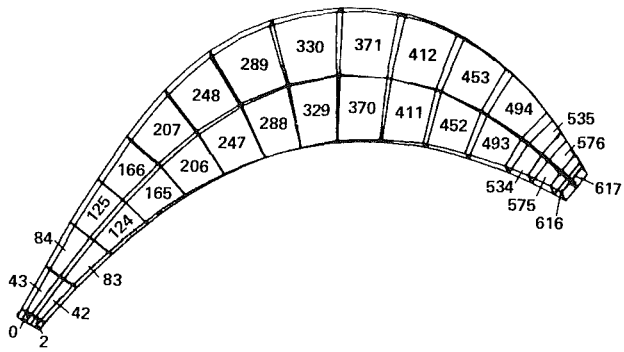

Fig. 7(b) Base section elements

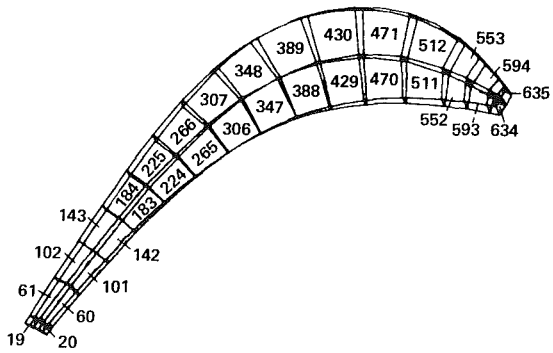

Fig. 7(c) Tip section elements

Downloaded 01 Jun 2010 to 171.66.16.62. Redistribution subject to ASME license or copyright; see http://www.asme.org/terms/Terms_Use.cfm

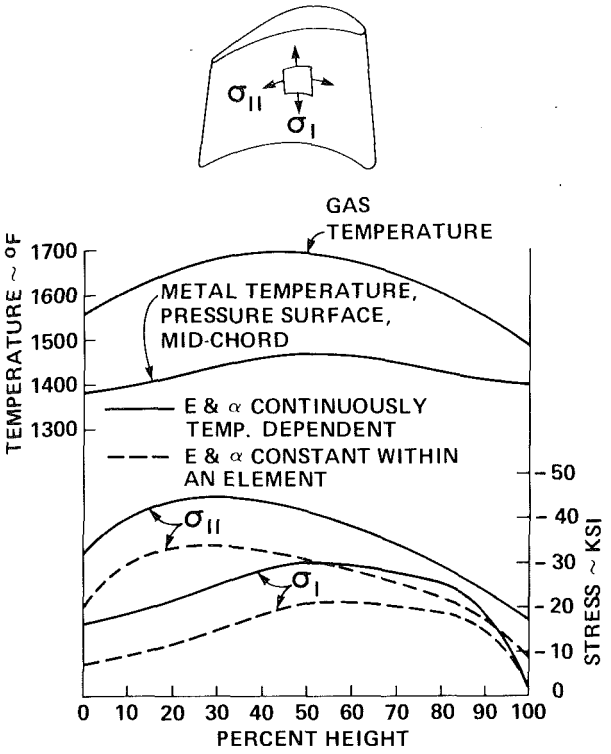

Fig. 8 Effect of element E and α temperature dependency on stress in three-dimensional isoparametric model of cooled airfoil

from element to element – that is, constant within an element and equal to the values corresponding to element average temperature. A second calculation was performed utilizing the same elements after the code was modified to allow for the temperature dependency of mechanical properties from integrating point to integrating point. The mid-chord surface thermal stresses in the latter calculation were 34 percent higher, as shown in Fig. 8. This is not surprising because with only two elements through the thickness, E and α are essentially constant with thickness in the former case. Thus, in thermal stress problems of this kind, the advantages of the higher order elements are considerably reduced if E and α are not allowed to vary continuously with temperature.

It is also important to remember that there is an inherent incompatibility between heat conduction and stress in any finite element. This occurs because thermal strain is proportional to the temperature while the total strain is obtained from differentiating the total displacement function, which is of the same degree as the temperature. Therefore, if the temperature is quadratic, then so is the thermal strain; but the total strain can, at most, be linear because the displacement is only quadratic. To avoid this problem the element model should always be constructed fine enough so that the temperature is apt to vary one degree less than the element permits.

Conclusions

Although the variation in Young's modulus and thermal coefficient of expansion is small compared to the variation in temperature in thermal stress problems, failure to take it into account can lead to large errors in thermal stress. For example, the maximum thermal stresses in a typically cooled gas turbine blade was calculated to be approximately 40 percent higher than it is when E and α were held constant at average temperature values. Such a large error in stress would lead to an order of magnitude over prediction in cyclic life.

This phenomenon occurs because thermal stresses are caused by differential expansions, which are affected (percentage-wise) more than total thermal strains are affected by the temperature dependency of α. This effect is explained by a detailed examination of the solution for thermal stress in a flat plate with a thermal gradient through its thickness (like those encountered through the thickest part of the blade).

In general, finite element codes allow for the temperature dependency of mechanical properties. However, some do not permit this dependency within an element. This is not a serious restriction for constant strain elements because so many elements are required to construct a good model. However, it can be a serious limitation for higher order elements.

References

1 Timoshenko, S., and Goodier, J.N., *Theory of Elasticity,* McGraw-Hill, New York, 1951, pp. 78–82; 401.

2 Leven, M.M., "The Effect of Frequency and Temperature on the Low Cycle Fatigue Behavior of Cast Udimet 500," Westinghouse Research Report, 72-1E7-MEMAT-R1, Dec. 29, 1972.

Downloaded 01 Jun 2010 to 171.66.16.62. Redistribution subject to ASME license or copyright; see http://www.asme.org/terms/Terms_Use.cfm

Nonlinear Damage Cumulation in Solution-Treated and Aged Titanium 6Al-4V

J. H. Adams
Detroit Diesel Allison Division,
General Motors Corp.,
Indianapolis, Ind. 46206

A procedure for determining the functional form of the exponent in the nonlinear damage equation from a limited number of block loading fatigue tests is presented. The theory and experimental details are demonstrated for solution-treated and aged Ti 6-4 at 278°C[1]. The predictive accuracy of the derived functional fit is then shown for additional independent block loading fatigue tests.

Introduction

The duty cycle for most turbine components consists of a complex load versus time mission. Miner's [1] linear damage rule has historically been used to evaluate the fatigue damage caused by these missions. For a given load level the linear rule represents the damage cumulation as

$$D = n_i / N_i \tag{1}$$

Failure is assumed to occur when the damage sum exceeds unity. Figure 1 illustrates the linear damage rule. The linear rule's ease of application has made it an attractive design tool.

Studies [2,3] have shown, however, that the use of the linear rule can lead to grossly nonconservative life predictions for typical gas turbine engine missions. These inaccuracies are apparently caused by small subcycles in the mission which contribute more damage than they would if they were applied independently. Marco and Starky [4] proposed a mechanistic explanation for this phenomena. Their argument was based on experimental observations which indicated that high-stress fatigue cycles produced more microcracks than low stress fatigue cycles. They deduced that this would lead to an increased rate of damage cumulation for low-stress fatigue cycles when they were applied after a set of high-stress cycles. They noted that a nonlinear damage rule proposed earlier by Richart and Newmark [5] could analytically model this effect. The damage cumulation curve for this nonlinear rule has the form

$$D = (n_i / N_i)^{\alpha_i} \tag{2}$$

where α_i is a function of the fatigue life (N_i). Figure 2 shows the nonlinear damage curve. For mission type loading conditions the nonlinear rule cumulates damage in the manner illustrated in Fig. 3. The illustrated mission consists of n_1 of the N_1 type cycle, n_2 of the N_2 type cycle, n_3 of the N_3 type cycle, and n_4 of the N_4 type cycle. By adjusting the relative value of α for each type of cycle, the longer life cycles can be made more damaging. A functional relationship between α and fatigue life (N) is therefore necessary to apply this nonlinear rule.

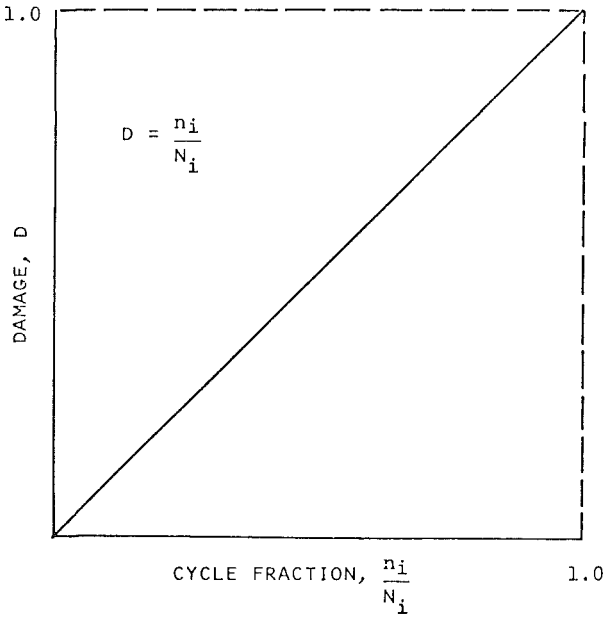

Fig. 1 Nonlinear damage cumulation

This report presents and demonstrates an experimental and analytical program which for a given material provides this functional description of α. The derived nonlinear rule is then applied to a series of fatigue tests which simulate engine mission loading.

Approach

A set of block loading, strain-controlled fatigue tests are used to derive the functional form of α. The first block consists of one large subcycle plus several applications of a

[1]Funding for a portion of the material testing was provided by AFWAC/POTC Contract F33657-77-C-0374 under the direction of Lt. William Prince.

Contributed by the Gas Turbine Division and presented at the International Gas Turbine Conference and Products Show, Houston, Texas, March 9-12, 1981, of THE AMERICAN SOCIETY OF MECHANICAL ENGINEERS. Manuscript received at ASME Headquarters December 10, 1980. Paper No. 81-GT-106.

Copyright © 1982 by ASME

Downloaded 01 Jun 2010 to 171.66.16.62. Redistribution subject to ASME license or copyright; see http://www.asme.org/terms/Terms_Use.cfm

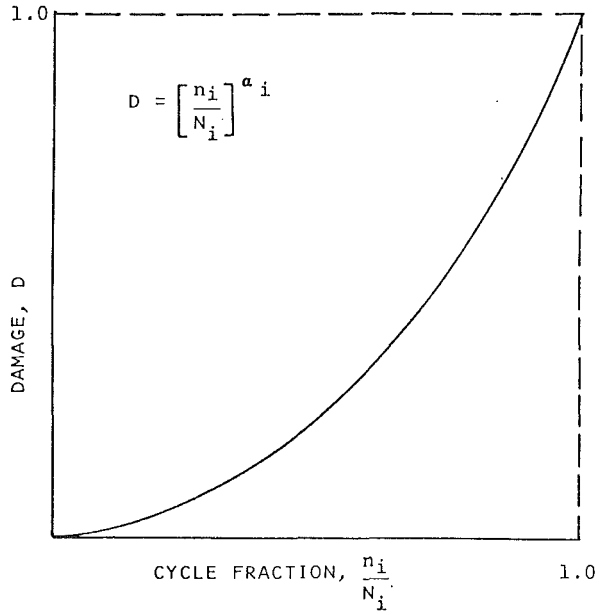

Fig. 2 Nonlinear damage cumulation

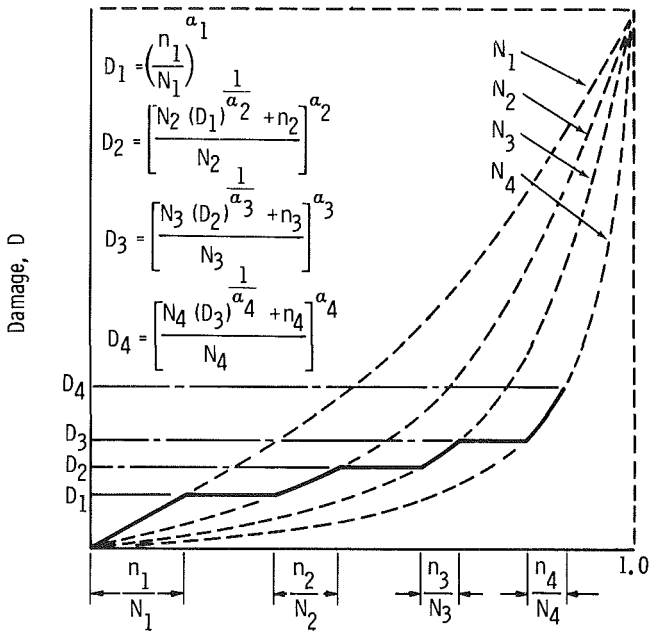

Fig. 3 Nonlinear damage cumulation for mission loading

second smaller subcycle. The second block consists of the first block plus several applications of a third smaller subcycle. The third block consists of the second plus several applications of a fourth smaller subcycle. This pattern can be extended to more blocks depending on the accuracy desired for the functional determination. Each additional block provides one additional data point of α versus the fatigue life. Figure 4 shows the three blocks designed for this study. Several low-cycle fatigue specimens are then subjected to each loading block until failure occurs. An average fatigue life in terms of missions is then calculated for each block. If the exponent corresponding to the largest subcycle α_1 is assumed to be one, then the relative values of the exponents for the other subcycles can be calculated.

The exponent for the second largest subcycle α_2 is determined from the results of the first block loading fatigue tests. The value of α_2 is determined which will yield a calculated damage sum of one after the observed number of blocks to failure. The value of α_3 for the third subcycle is calculated using the previously determined values, α_1 and α_2, and by finding the value of α_3 which will yield a calculated damage sum of one after the observed number of blocks to failure for the second block fatigue tests. The exponents associated with the additional subcycles can be determined in a similar way using the results of the additional block loading fatigue tests. The results from this procedure allow the determination of the functional dependence of the exponent α versus the fatigue life corresponding to each subcycle. This functional relationship can then be used in the nonlinear damage rule to analyze the fatigue lives of engine parts subjected to complex missions.

Experimental Details and Results

Solution-treated and aged titanium 6Al-4V was used in the demonstration of this procedure. This titanium consists of an equi-axed primary alpha phase in an aged transformed beta matrix. All specimens were vacuum-stress relieved after machining to eliminate residual surface stresses. All tests were strain-controlled and performed at 278°C (500°F). The smooth specimen design used in the program is shown in Fig. 5.

The basic relationship between the fatigue life and the stress-strain response was defined by sixty-seven constant amplitude fatigue tests. Fatigue failure was considered to be the initiation of a small crack approximately 0.64 mm (0.025 in.) in surface length. The initiation of such a flaw was detected by the deviation of the load history from a stabilized trend. The data were represented by a fatigue model proposed by Jaske [6]. This model uses a cubic polynomial representation of the logarithm of fatigue life versus an equivalent strain quantity

$$\mathrm{LOG}(N) = a_0 + a_1 \epsilon_{eq} + a_2 \epsilon_{eq}^2 + a_3 \epsilon_{eq}^3 \tag{3}$$

The equivalent strain is defined by Walker's [7] equation and is a function of the maximum stress and strain range

$$\epsilon_{eq} = \frac{\sigma_{max}}{E}\left[\frac{\Delta\epsilon E}{\sigma_{max}}\right]^m \tag{4}$$

Figure 6 demonstrates this representation for the titanium 6A1-4V.

The functional form of α in the nonlinear damage rule (equation (2)) was derived using the loading block sequences

Nomenclature

a_0, a_1, a_2, a_3 = material constants in fatigue life versus equivalent strain equation
D = fatigue damage
E = Young's modulus
m = material constant in Walker equation
n_i = number of cycles applied at load level i
N_i = constant amplitude fatigue life for load level i
α_i = exponent in nonlinear damage rule for load level i
ϵ_{eq} = Walker equivalent strain
$\Delta\epsilon$ = strain range
σ_{max} = maximum stress

Downloaded 01 Jun 2010 to 171.66.16.62. Redistribution subject to ASME license or copyright; see http://www.asme.org/terms/Terms_Use.cfm

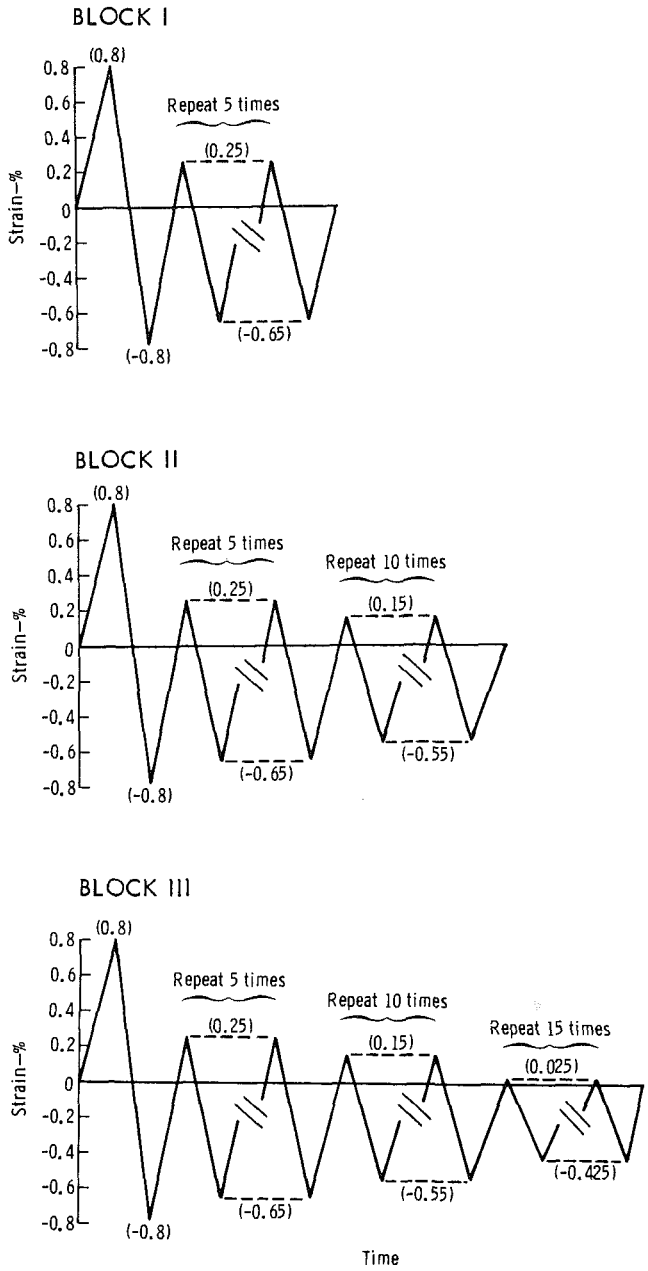

Fig. 4 Block loading sequences for determination of functional form of α

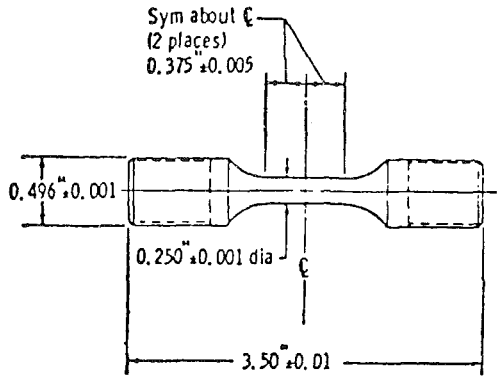

Fig. 5 Smooth LCF specimen design

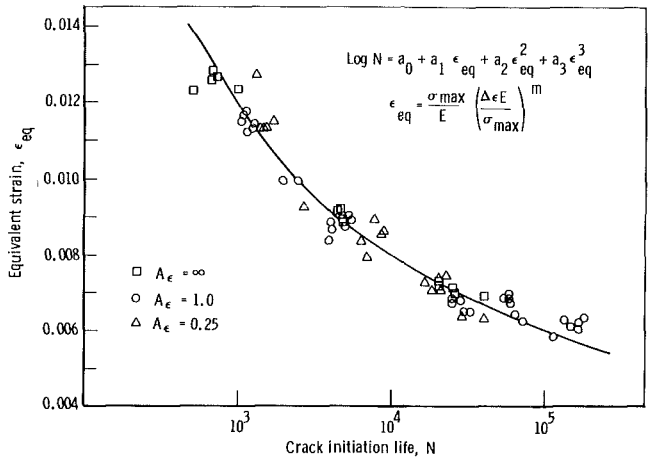

Fig. 6 Fatigue data and fit curve for Ti 6-4

Table 1 Results from baseline block loading tests

Block Type	Observed Life (Missions)
Block I	1692
Block I	1768
Block I	1735
Block I	1569
Block II	1095
Block II	1149
Block II	1329
Block II	1269
Block III	983
Block III	874
Block III	1153
Block III	1018

in Fig. 4. The three loading blocks contain the same four types of subcycles. Each successive block consists of the same load history as the previous block plus one additional type of subcycle. Four specimens were subjected to the repeated application of each block until crack initiation was detected. Table 1 lists the results from these tests which show that the minor subcycles ($N > 10^5$) in block II and block III contribute significant damage. A rainflow counting technique was used to reduce each block history into a corresponding set of subcycles. The strain range and maximum stress for each subcycle were calculated from the prescribed strain limits and the average test loads measured at half-life. Fatigue lives corresponding to the four types of subcycles were then determined based on the constant amplitude fatigue data. The exponent α for each type of subcycle was derived using the nonlinear summation technique illustrated in Fig. 3 and the average fatigue life associated with each loading block. These exponents provide values which drive the calculated damage sums to unity for the observed number of missions to crack initiation. Figure 7 shows the calculated values of α as a function of the constant amplitude fatigue life for each subcycle. A second order polynomial in log-log space was judged to provide a good fit for the derived data

$$\log\ \alpha_i = b_0 + b_1 \log N_i + b_2 (\log\ N_i)^2 \qquad (5)$$

Five independent loading blocks were used to verify the accuracy of the derived fit. Figure 8 shows the strain histories of these five blocks. The strain profiles were designed to simulate typical turbine engine loading patterns. Four specimens were subjected to each simulated mission. Each test was analyzed using the rainflow counting technique and the constant

Downloaded 01 Jun 2010 to 171.66.16.62. Redistribution subject to ASME license or copyright; see http://www.asme.org/terms/Terms_Use.cfm

amplitude data described previously. Life predictions were then made for these tests using both the linear and derived nonlinear damage rules. Predictions were also made based on the nonlinear damage curve approach in reference [2] where it was suggested that the exponent α in equation (2) should have the form

$$\alpha_i = C\ N_i^{.4} \tag{6}$$

where C is an arbitrary constant. Table 1 shows the experimental fatigue lives and the results of these predictions for both the baseline blocks and the simulated mission tests. Plots of the predicted versus measured fatigue lives are shown in Fig. 9 and 10.

Figure 9 shows that the experimentally derived nonlinear rule (equation 5) back-predicts the baseline block loading tests very well. The predictions based on the linear rule, by contrast, tended toward nonconservative results for block types II and III where minor subcycles were present. The nonlinear predictions based on reference [2] and equation (6) provided results better than the linear predictions but less accurate than the nonlinear predictions based on equation (5). Figure 10 shows that the same trends were observed for the predictions of the simulated mission tests. The nonlinear predictions based on equation (5) were accurate within a factor of two in all cases. The linear predictions were consistently nonconservative and in several cases off by a factor of three or greater. The nonlinear predictions based on equation (6) were

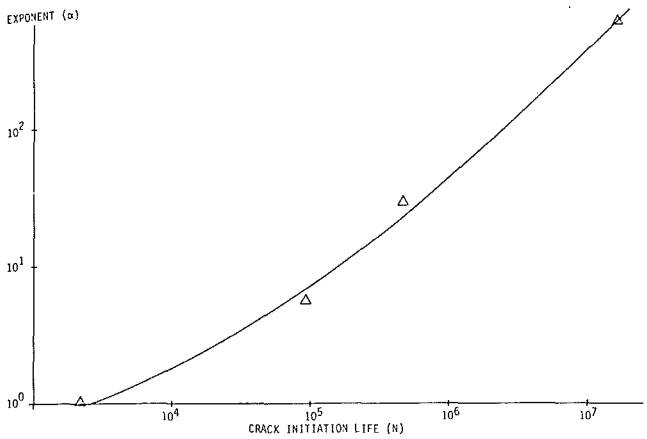

Fig. 7 Functional form of α versus fatigue life

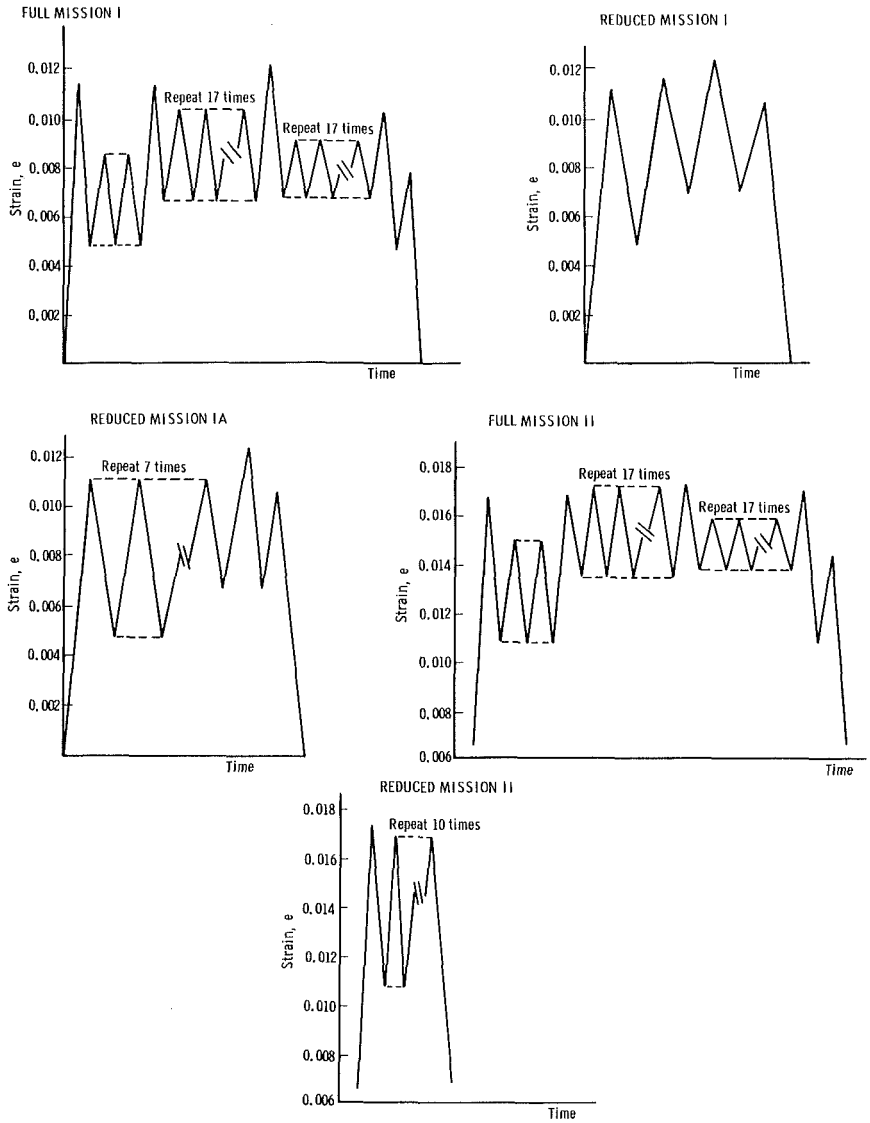

Fig. 8 Simulated turbine engine missions

Downloaded 01 Jun 2010 to 171.66.16.62. Redistribution subject to ASME license or copyright; see http://www.asme.org/terms/Terms_Use.cfm

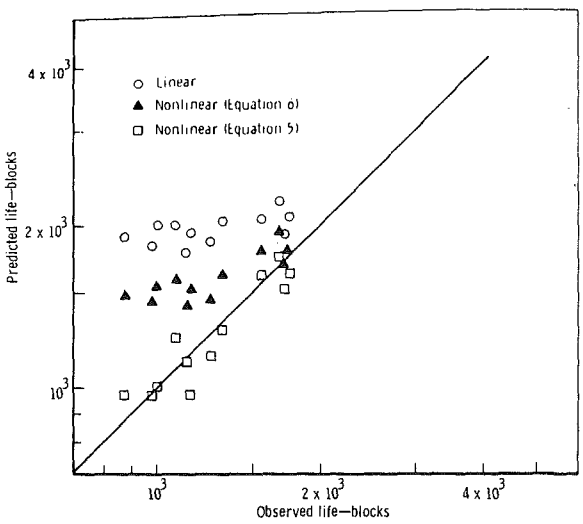

Fig. 9 Back-predictions for block loading tests

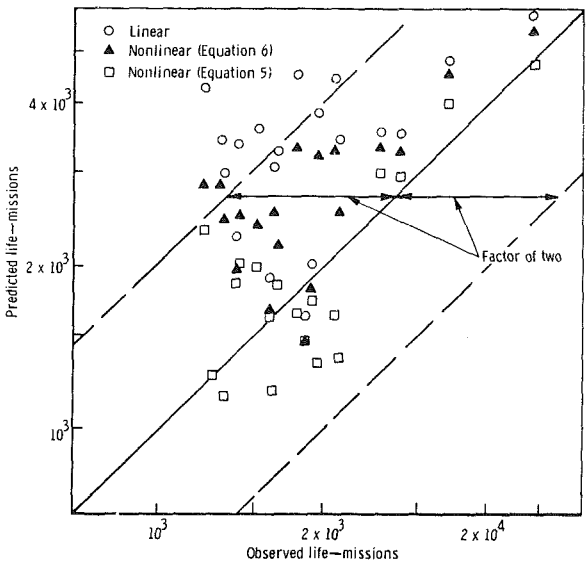

Fig. 10 Life predictions for simulated missions

Table 2 Results of predictions for baseline block loading and simulated mission tests using linear and nonlinear damage rules

Block Type	Observed Life (Missions)	Predicted Life (Linear)	Predicted Life (Nonlinear Equation 6)	Predicted Life (Nonlinear Equation 5)
Block I	1692	2244	1955	1754
Block I	1768	2070	1806	1628
Block I	1735	1939	1695	1532
Block I	1569	2057	1791	1618
Block II	1095	2001	1593	1248
Block II	1149	1782	1424	1130
Block II	1329	2046	1625	1272
Block II	1269	1817	1454	1150
Block III	983	1840	1441	942
Block III	874	1912	1489	972
Block III	1153	1936	1522	977
Block III	1018	2013	1548	1007
Full Mission I	1624	3065	2515	1172
Full Mission I	1318	2986	2446	1150
Full Mission I	1302	3427	2838	1257
Full Mission I	1975	3846	3206	1330
Reduced Mission I	4898	5816	5480	4739
Reduced Mission I	2795	3503	3271	2940
Reduced Mission I	3404	4881	4578	4017
Reduced Mission I	2555	3560	3324	2985
Reduced Mission IA	1533	3600	2384	2003
Reduced Mission IA	1222	4247	2838	2338
Reduced Mission IA	1414	3340	2482	2023
Reduced Mission IA	1670	3278	2187	1850
Full Mission II	1790	4515	3338	1635
Full Mission II	2153	3440	2525	1352
Full Mission II	2130	4454	3298	1622
Reduced Mission II	1867	1622	1427	1432
Reduced Mission II	1911	2067	1804	1725
Reduced Mission II	1373	2284	1985	1857
Reduced Mission II	1610	1905	1667	1621

Table 3 Evaluation of accuracy for predictive techniques

Predictive Technique	Mean Residual	Standard Deviation
Linear	.2413	.1516
Nonlinear (Equation 6)	.1500	.1202
Nonlinear (Equation 5)	−.0015	.1196

Downloaded 01 Jun 2010 to 171.66.16.62. Redistribution subject to ASME license or copyright; see http://www.asme.org/terms/Terms_Use.cfm

generally more accurate than the linear prediction but less accurate than the nonlinear predictions based on equation (5). Table 3 quantifies these observations by listing the mean residual and the standard deviation from the mean for each of the three predictive techniques applied to the simulated mission tests. The residual is defined as

$$\text{Residual} = \text{LOG}(N_{\text{measured}}) - \text{LOG}(N_{\text{predicted}}) \quad (7)$$

Conclusions

The results shown in Fig. 7 indicate that the functional form of the exponent α in equation (2) is α is higher order function of the fatigue life. Unless the life range of the minor subcycles is restricted, the linear relationship with a slope of 0.4 proposed in reference [2] will not model the observed functional form.

The predictions for the simulated mission tests indicate that the proposed experimental procedure can provide an accurate representation of the exponent in equation (2) and an improved life prediction technique for general loading cases. It should be noted that the technique proposed in reference [2] also provides improved predictions and in the absence of test data may be a valuable tool.

It should also be noted that the functional form of α will depend not only on the material but also on the fatigue model used to represent the constant amplitude fatigue data. Different models will extrapolate to high lives differently and may result in different functional forms for α. The use of this nonlinear approach appears to compensate for the lack of high life constant amplitude data and the inaccuracies in the extrapolation of the fatigue model to long lives.

References

1 Miner, M.A., "Cumulative Damage in Fatigue," ASME *Journal of Applied Mechanics*, Vol. 12, 1945, pp. 159–164.

2 Manson, S.S., and Halford, G.R., "Practical Implementation of the Double Linear Damage Rule and Damage Curve Approach for Treating Cumulative Fatigue Damage," to appear in *International Journal of Fracture*.

3 Johnsen, S.E., and Doner, M., "A Statistically Appropriate Form of Miner's Rule," *Proc. of the Symposium on Methods for Predicting Material Life in Fatigue*, Dec. 1979, The American Society of Mechanical Engineers, New York, eds: Ostergren, W.J., and Whitehead, J.R., pp. 221–234.

4 Marco, S.M., and Starkey, W.L., "A Concept of Fatigue Damage," Trans. ASME, Vol. 76, 1954, pp. 627–632.

5 Richart, F.E., and Newmark, N.M., *American Society for Testing and Materials*, Vol. 48, 1948, pp. 767–800.

6 Jaske, C.E., et al., "Analysis of Fatigue, Fatigue Crack Propagation and Fracture Data," Final Report to NASA-Langley Research Center, NASA CR 132332, 1973.

7 Walker, K., "The Effect of Stress Ratio During Crack Propagation and Fatigue for 2024-T3 and 7075-T6 Aluminum," *Effects of Environment and Complex Load History on Fatigue Life*, ASTM, STP 462, 1970, pp. 1–14.

Downloaded 01 Jun 2010 to 171.66.16.62. Redistribution subject to ASME license or copyright; see http://www.asme.org/terms/Terms_Use.cfm

A. Brown
Reader.
Mem. ASME

B. W. Martin
Professor and Head.

Department of Mechanical Engineering
and Engineering Production,
University of Wales Institute of
Science and Technology,
Cardiff, Wales

Flow Transition Phenomena and Heat Transfer Over the Pressure Surfaces of Gas Turbine Blades

Detailed examination of flow measurements over concave pressure surfaces suggests that interaction of Taylor-Goertler vorticity with mainstream turbulence exerts only limited influence in enhancing laminar boundary-layer heat transfer. While transition is primarily controlled by the Launder laminarisation criterion, the Goertler number at which it subsequently occurs is not solely determined by turbulence intensity. Adoption of $K \geq 2.5.10-6$ as a design criterion for the pressure surfaces of turbine blades would appear to have significant advantages in terms of reduced heat transfer, increased lift, and lower aerodynamic drag.

Introduction

It is widely accepted that boundary-layer behavior over the concave pressure surfaces of gas turbine blades is less well understood than that over the convex suction surfaces. This is reflected in the generally poor agreement between predictions and measurements of local heat transfer over concave surfaces, in whose upstream regions heat transfer levels are higher than those for a laminar boundary layer (but below those of a fully turbulent boundary layer) and usually exhibit substantial chordwise fluctuations not readily identifiable with transition. Moreover, as the authors [1] have pointed out, since they do not typically occur in laminar regions on suction surfaces, they cannot convincingly be ascribed to any of the characteristics of mainstream turbulence, or in any obvious way to curvature effects on the boundary-layer flow. The other major problems with pressure surfaces, where the pressure gradients are mostly strongly favourable, are the inadequacies of existing procedures for predicting the onset and extent of transition, and the heat transfer in extended transition regions.

Having suggested that Taylor-Goertler vortices might account for the observed irregularities in, and levels of, heat transfer in laminar boundary layers developing on turbine blades in cascade, Martin and Brown [1] confirmed the likelihood of their occurrence under engine operating conditions by calculating the range of Goertler number $G_\theta = (U_\infty \theta/\nu)^2 \theta/r_c$ over the pressure surface of the PVD blade of 0.05 m surface length for which Martin, et al. [2] had previously reported heat transfer measurements. These were for trailing-edge Reynolds numbers of 8.10^5 and $8.8.10^5$ and passage throat Mach numbers between 0.79 and 0.94, and were made in entirely favorable pressure gradients. Yeo [3] has since shown that the above calculations of G_θ, which were based on the Thwaites [4] relation for incompressible flow, given by

$$\frac{U_\infty}{\nu}\frac{d\theta^2}{dx} = 0.45 - 6\Lambda \tag{1}$$

are well confirmed for compressible flow by his solution of the Gruschwitz [5] equations

$$\frac{U_\infty \theta}{\nu}\frac{d\theta}{dx} = F_1(k) - \frac{k}{d}[2 - M^2 F_2(k)] \tag{2}$$

$$d = \left[\frac{1+(\gamma-1)M^2}{2}\right]\left[\frac{1+M^2F_3(k)}{1+M^2F_4(k)}\right] \tag{3}$$

$$k = \frac{\theta^2 d}{\nu}\cdot\frac{dU_\infty}{dx} = \Lambda d \tag{4}$$

where $F_1(k)$, $F_2(k)$, $F_3(k)$ and $F_4(k)$ are universal functions of k. For the mainstream velocity distribution considered, the error in G_θ neglecting compressibility is less than 9.5 percent even at the trailing edge for M up to 0.7, and is then no more than 2.6 percent at mid-chord, where Martin, et al. [2] observed transition.

In the pre-transition region the local heat transfer for $Re_{x2} = 8.8.10^5$ exceeded that predicted by the standard laminar flat-plate correlation by a factor of about 2 and was almost insensitive to variation of mainstream turbulence intensity U'_∞/U_∞ in the range 0.066 to 0.091. Confirmation that this enhancement is attributable to vortex action is provided by the measurements of McCormack, et al. [6], which yielded the same multiplication of laminar heat transfer for uniform velocity flow in the range $5.10^4 < Re_{x2} < 8.8.10^4$ and $U'_\infty/U_\infty = 0.01$ over a concave surface where Taylor-Goertler vortex motion was observed. Martin and Brown [1] calculated that, over the PVD blade of Martin, et al. [2], vortex development would lead to an increase in wavelength λ from about 0.87 mm at vortex inception (at 6 percent of surface length), to about 2.08 mm at transition. They hypothesized that since there must always be an even number of paired opposed vortices covering a given blade span, increases in λ implied the progressive shedding of paired vortices, possibly by alternating oscillatory spanwise jumps.

Contributed by the Gas Turbine Division of THE AMERICAN SOCIETY OF MECHANICAL ENGINEERS and presented at the Gas Turbine Conference and Products Show, March 9-12, 1981, Houston, Texas. Manuscript received at ASME Headquarters December 11, 1980. Paper No. 81-GT-107.

Copyright © 1982 by ASME
Downloaded 01 Jun 2010 to 171.66.16.62. Redistribution subject to ASME license or copyright; see http://www.asme.org/terms/Terms_Use.cfm

These would cause transverse velocity fluctuations and hence fluctuations in local heat transfer measurements in the longitudinal direction at stations where vortices happened to be shed.

The measurements of Kemp [7] for $U'_\infty/U_\infty = 0.01$ over the pressure surface of a blade of chord 0.15 m at $Re_{x2} \simeq 2.5.10^5$ tend to support the foregoing observations. Kemp also used the Thwaites [4] relation coupled, as did Martin and Brown [1], with Smith's [8] predictions, to calculate the range of vortex wavelengths, which compared well with his measurements. He found the most "dangerous" wavelength, corresponding to transition, with amplification of initially small disturbances by a factor of $e^{10} = 2.2.10^4$, to be similarly about 2.0 mm. Kemp also noted that the strong acceleration experienced by the flow beyond 70 percent of the blade chord arrested boundary-layer transition.

The limited study of Martin and Brown [1] shed little light on the extent to which laminar boundary-layer heat transfer in the presence of vortices increases with U'_∞/U_∞. In this paper a wider and more detailed analysis of available measurements for flow over concave surfaces is attempted, which suggests that even for relatively high levels of mainstream turbulence intensity, heat transfer is still generally below that of a fully-turbulent boundary layer. The analysis also further strengthens the belief that boundary-layer transition cannot occur in flow regions where the velocity gradient factor $K = (\nu/U_\infty^2)\, dU_\infty/dx \gtrsim 2.5.10^{-6}$. The boundary layer then remains laminar or is laminarized, as was originally shown by Launder [9,10]; indeed Jones and Launder [11] predict that for $K > 3.2.10^{-6}$ no turbulent solution exists to their two-equation model of turbulence for energy dissipation rate and turbulence kinetic energy.

While the Launder criterion seems to place an overriding embargo on transition if K exceeds $2.5.10^{-6}$, transition will not necessarily occur immediately K falls below that value because, as Martin and Brown [1] suggested, it then depends on other parameters. For instance, Liepmann's [12] transition measurements in zero pressure gradient along two concave surfaces of different curvature show a transition range $6.3.10^4 \le Re_x \le 1.6.10^6$ (as in Fig. 3), associated with which are values of transition Goertler number which diminish with increasing U'_∞/U_∞. The present analysis attempts to identify this dependence more precisely than does the exponential relation of Forest [13] over a wider range of U'_∞/U_∞. What remains uncertain is the influence of K for values below $2.5.10^{-6}$ and whether, despite this critical value there is, on the one hand, a value of Re_x below which transition cannot occur, and on the other, an upper limit to Re_x above which transition cannot be prevented.

The unpredictable but increased heat transfer following transition leads the authors to propose that it should be avoided by blade design based on the Launder criterion, such that over the pressure surface K is never less than $2.5.10^{-6}$. This paper examines the consequences for high-temperature compressible flow with and without work extraction for trailing-edge Mach numbers up to unity. The mainstream velocity distribution along the pressure surface is found to be convex-downward over the surface length, so that up to mid-chord velocities are relatively low and large accelerations occur only towards the trailing edge. For a given velocity distribution over the suction surface the net lift force is thus increased when compared to linear or concave distributions. There are the further advantages that the aerodynamic drag and local heat transfer over the pressure surface are reduced. Some current designs of cooled blades already employ a convex-downward velocity distribution to avoid the

Nomenclature

a = coefficient in viscosity-temperature relationship
b = index in viscosity-temperature relationship
c = length of pressure surface, m
C_p = specific heat at constant pressure, J/kgK
d = function of M and K defined in equation (3)
f = friction coefficient
$F_1(k) \ldots F_4(k)$ = universal functions of k
G_θ = Goertler number based on boundary-layer momentum thickness $(= [U_\infty\theta/\nu]^2\theta/r_c)$
h = heat transfer coefficient, W/m^2K
k = function of M and Λ defined in equation (4)
k' = thermal conductivity, W/mK
K = velocity gradient factor $(= [\nu/U_\infty^2]dU_\infty/dx)$
K_c = critical value of K
m = Mach number ratio $(= M/M_2)$
M = Mach number
p = pressure, bar
Pr = Prandtl number
r = stagnation pressure ratio $(= p_0/p_{0_1})$
r_c = radius of curvature of pressure surface, m
R = gas constant, J/kgK
Re_x = length Reynolds number $(= U_\infty x/\nu)$
Re_θ = momentum-thickness Reynolds number $(= U_\infty\theta/\nu)$
s = proportion of surface length $(= x/c)$
St_x = Stanton number
t = stagnation temperature ratio $(= T_0/T_{0_1})$
T = temperature, K
U_∞ = local mainstream velocity, m/s
U'_∞/U_∞ = mainstream turbulence intensity
x = distance downstream from blade leading edge, m
α = rate of stagnation temperature reduction
β = rate of stagnation pressure reduction
γ = ratio of specific heats
θ = boundary-layer momentum thickness, mm
λ = wavelength of Taylor-Goertler vortices, mm
Λ = modified Pohlhausen parameter $(= [\theta^2/\nu]dU_\infty/dx)$
μ = dynamic viscosity, kg/ms
ρ = density, kg/m^3
τ = shear stress, N/m^2
ν = kinematic viscosity $(= \mu/\rho)$, m^2/s

Subscripts

0 = stagnation condition
1 = leading-edge condition
2 = trailing-edge condition
t = transition condition
x = based on distance along surface
θ = based on boundary-layer momentum thickness

Downloaded 01 Jun 2010 to 171.66.16.62. Redistribution subject to ASME license or copyright; see http://www.asme.org/terms/Terms_Use.cfm

possibility of flow separation near the leading edge; the foregoing provides additional arguments for so doing.

Analysis of Flow, Heat Transfer and Transition Measurements over Concave Surfaces

Possibly the earliest authenticated measurements of flow over concave surfaces are those of Liepmann [12], referred to above, and interpreted by Dryden [14], mainly in zero pressure gradient and for U'_∞/U_∞ up to 0.003. Transition from laminar flow in the presence of Taylor-Goertler vortices was determined from boundary-layer measurements for two radii of curvature (0.76 m and 6.10 m), from which Dryden concluded that $G_{\theta t}$ diminished from 81 for very low U'_∞/U_∞ to 36 for U'_∞/U_∞ of 0.003. Subsequent investigations, including those of Tani [15], Wortmann [16,17], Tani and Aihara [18] and Winoto, Durao and Crane [19], have been essentially concerned with visualization of, and velocity measurements in, the laminar boundary layer to identify the system of vortices on concave surfaces, and their effects on transition. Tani and Aihara [18] concluded that these were indirect in modifying the development of Tollmien-Schlichting waves by inducing a spanwise variation of boundary-layer thickness. To the authors' knowledge, only

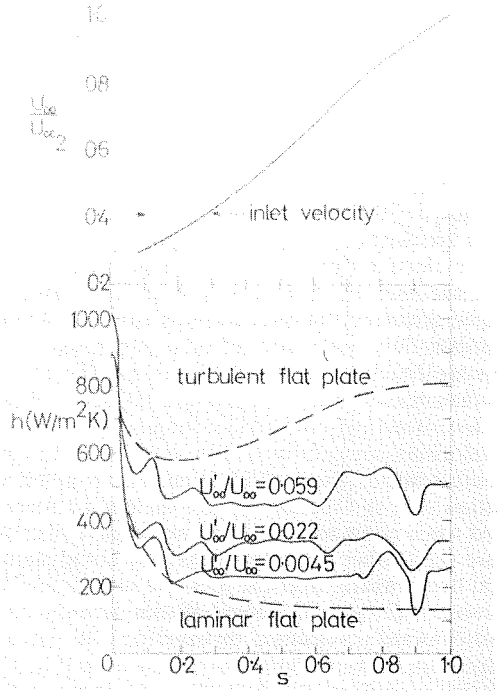

Fig. 1 Pressure surface velocity distribution and local heat transfer measurements of Turner [20]

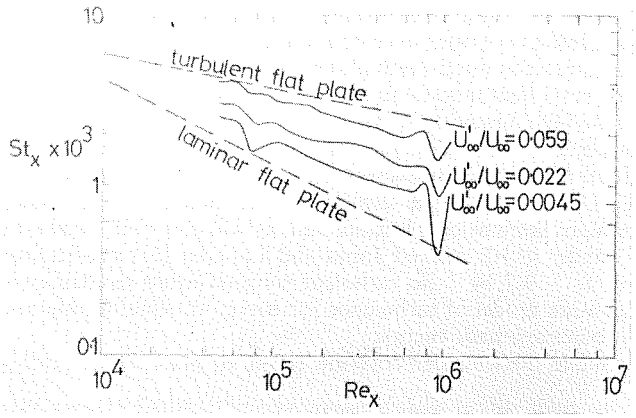

Fig. 2 Non-dimensionalized heat transfer measurements of Turner [20]

Table 1

Author	U'_∞/U_∞	$K_t \times 10^6$	$Re_{xt} \times 10^{-5}$	$Re_{\theta t}$	$G_{\theta t}$	$(G_\theta r_c/x)_t$
Bayley and Priddy (24)	0.005-0.17	1.90	4.86	238	20.7	27.7
Bayley and Priddy (24)	0.005-0.17	0.72	12.2	350	26.6	35.1
Daniels (23)	< 0.003	2.77	5.49	201	12.3	14.8
Garrett (25)	0.005	2.58	4.02	219	14.3	26.1
Garrett (25)	0.04	2.58	4.02	219	14.3	26.1
Garrett (25)	0.08	2.58	4.02	219	14.3	26.1
Garrett (25)	0.17	2.58	4.02	219	14.3	26.1
Kohler et al (22)	0.04	2.94	3.33	163	5.2	13.0
Martin et al (2)	0.042	1.87	2.50	193	8.9	28.8
Martin et al (2)	0.057	1.87	2.50	193	8.9	28.8
Martin et al (2)	0.083	1.87	2.50	193	8.9	28.8
Martin et al (2)	0.066	1.72	2.91	179	6.2	19.7
Martin et al (2)	0.088	1.72	2.91	179	6.2	19.7
Martin et al (2)	0.091	1.72	2.91	179	6.2	19.7
Turner (20)	0.0045	0.93	9.2	321	14.9	35.9
Turner (20)	0.022	0.93	9.2	321	14.9	35.9
Turner (20)	0.059	0.93	9.2	321	14.9	35.9
Walker and Markland (21)	0.02?	0.74	1.57	205	37.1	55.3
Walker and Markland (21)	0.02?	1.07	1.90	239	32.0	71.5

Downloaded 01 Jun 2010 to 171.66.16.62. Redistribution subject to ASME license or copyright; see http://www.asme.org/terms/Terms_Use.cfm

the investigation of McCormack, et al. [6] included both velocity and heat transfer measurements, and none of the above involved transition measurements in strongly favorable pressure gradients with significant mainstream turbulence.

With the exception of the work of Liepmann [12] and Dryden [14], the present analysis of flow over concave surfaces is therefore based exclusively on reported observations for the pressure surfaces of turbine blades in cascade. Representative of these are the velocity distribution, of nearly uniform velocity gradient, and local heat transfer coefficient h, which increases with U'_∞/U_∞ for given $s = x/c$, as measured by Turner [20] and depicted in Fig. 1. The fluctuations in h (which the authors associate with the shedding of paired vortices) make for difficulty in identifying the location of transition, but when the data are presented as in Fig. 2 in the form of local Stanton number St_x versus Re_x, the transition point is more evident. This dimensionless presentation also facilitates comparison with the standard laminar and fully-turbulent local heat-transfer relationships for boundary-layer flow over a flat plate, shown in Fig. 2 and given respectively by

$$St_x = 0.332\, Re_x^{-0.5} Pr^{-0.67} \tag{5}$$

and

$$St_x = 0.029\, Re_x^{-0.2} Pr^{-0.67} \tag{6}$$

These relationships are superimposed in dimensional form in Fig. 1.

Similar analyses of the measurements of Walker and Markland [21], Kohler, et al. [22], Martin, et al. [2], Daniels [23], Bayley and Priddy [24], and Garrett [25] suggest that, as reported by Brown and Burton [26] and Brown and Martin [27], U'_∞/U_∞ has little or no additional effect on laminar heat transfer at values greater than about 0.06, even in the presence of Taylor-Goertler vorticity. While the heat transfer is greater than that of equation (5), it is still appreciably below that of equation (6). Kemp's [7] measurements cannot be analyzed because his mainstream velocity distribution is not given.

Table 1 gives transition values of K, Re_x, Re_θ, G_θ and $G_\theta r_c/x$ obtained by analysis of the pressure-surface measurements of the workers listed, together with quoted values of U'_∞/U_∞. The authors attach great significance to the fact that in no case does K_t exceed $2.94.10^{-6}$, though as Table 1 shows, it can be as much as a factor of four less, with an average value of $1.89.10^{-6}$. This general adherence to the Launder [9,10] criterion is further illustrated in Fig. 3 which plots $G_\theta r_c/x$ against Re_x to show a comparison of the transition values in Table 1 and those of Liepmann [12] with the Blasius equation for zero pressure gradient, together with curves for $K = 2.5.10^{-6}$ of potential flow, constant velocity gradient flow and constant K flow. The equations for these cases based on the Thwaites [4] relation (1), as previously determined by Martin and Brown [1], are respectively

$$G_\theta r_c/x = 0.3019\, Re_x^{0.5} \tag{7}$$

$$G_\theta \frac{r_c}{xRe_x^{0.5}} = \left[\frac{0.45}{5KRe_x + 1}\right]^{1.5}; \quad -0.1 \le KRe_x \le \infty \tag{8}$$

$$G_\theta \frac{r_c}{xRe_x^{0.5}} = \left[\frac{0.075}{KRe_x}[1-(1-KRe_x)^6]\right]^{1.5}; \quad -0.14 \le KRe_x \le 1 \tag{9}$$

$$G_\theta \frac{r_c}{xRe_x^{0.5}} = \left[\frac{0.1125}{KRe_x}[1-(1+KRe_x)^{-4}]\right]^{1.5}; \quad -0.137 \le KRe_x \le \infty \tag{10}$$

As indicated above, Yeo [3] has established the acceptability of the Thwaites [4] relation for subsonic compressible flow.

The proximity of the curves for equations (8, 9) and (10) in Fig. 3 is felt to be sufficient for the potential flow distribution of equation (8) to be regarded as representative of the investigations detailed in Table 1. This lower bound distribution for $K = 2.5.10^{-6}$ also implies larger K in the region below the curve, in which there is no reported instance of transition; all transition measurements in Table 1 lie in the zone of lower K, between equation (8) for $K = 2.5.10^{-6}$ and equation (7), which latter is in satisfactory agreement with Liepmann's [12] transition measurements in zero pressure gradient. The measurements cover a wide range of turbulence intensities, from 0.003 to 0.17. It should also be noted that a single data

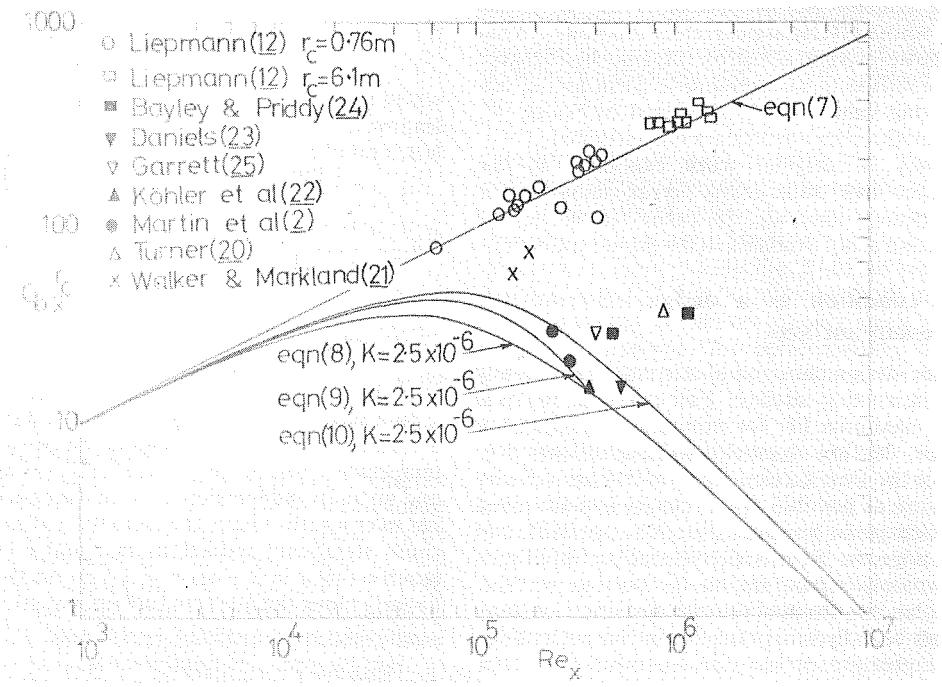

Fig. 3 Experimental transition measurements of $G_\theta r_c/x$ in relation to those for zero pressure gradient and those for specified velocity distributions at $K = 2.5.10^{-6}$

Downloaded 01 Jun 2010 to 171.66.16.62. Redistribution subject to ASME license or copyright; see http://www.asme.org/terms/Terms_Use.cfm

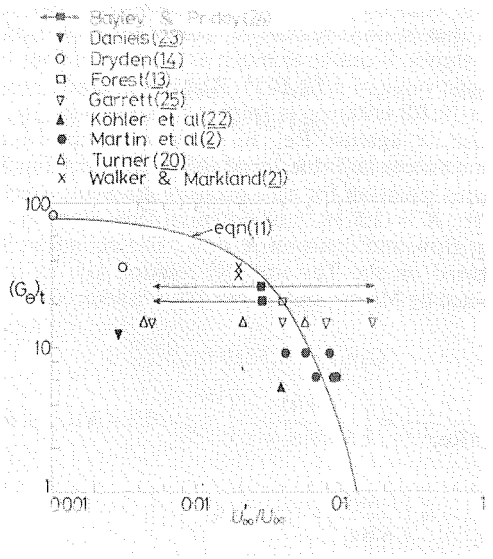

Fig. 4 Transition measurements of $G_{\theta t}$ in relation to U'_∞/U_∞

point may represent several experimental runs, as in the case of Martin, et al. [2].

In Fig. 4, the transitional Goertler number $G_{\theta t}$ is plotted in relation to U'_∞/U_∞ for the investigations in Table 1. Also shown are the transition measurements of Dryden [14] and Forest [13] and the latter's proposed exponential relation between $G_{\theta t}$ and U'_∞/U_∞, given by

$$G_{\theta t} = 81 \exp(-34.6\, U'_\infty/U_\infty) \tag{11}$$

which, despite the considerable scatter, adequately predicts some of the transition values of Martin, et al. [2], Turner [20], Walker and Markland [21] and Garrett [25]. The quoted values of U'_∞/U_∞ are usually based on measurements upstream of the cascade; it is therefore possible that the intervening but unmeasured decay may account for some of the scatter, particularly for very low and very high values of U'_∞/U_∞. The scatter is, however, more likely to be attributable to the influence of other parameters, such as the scale and frequency of turbulence, flow Mach number, radius of curvature and velocity gradient factor (even for values below $2.5.10^{-6}$), whose effects are currently unknown. What is certain is that however valid equation (11) may be for large $G_{\theta t}$, it must be modified to an asymptotic form as $G_{\theta t}$ approaches the limiting value of 0.09 predicted by Smith [8], below which Taylor-Goertler vortices are not sustained.

The wide variety of original work examined in the foregoing precludes any satisfactory error analysis, or estimate of uncertainty intervals. In many instances, the necessary information is not available in the papers quoted.

Laminarization condition as a design criterion for turbine blade pressure surfaces

In turbine blade design most emphasis has traditionally been placed on the suction surface. For example, in PVD blades aiming at maximum lift for minimum chord with a given turning angle, the flow channel is so designed that over the suction surface the flow accelerates to maximum velocity in as short a distance as possible. This velocity is maintained nearly constant for as great a surface distance as possible and near the trailing edge the flow is decelerated as rapidly as possible while avoiding separation on the suction surface. (Although particular mainstream velocity distributions may differ in detail they broadly satisfy the above characteristics). Over the concave pressure surface, on the other hand, the velocity mostly increases throughout, sometimes linearly at constant velocity gradient but often through two constant velocity gradient regions which are sometimes connected by a short decelerating region sufficient to cause laminar separation. Of the accelerating regions, the stronger is near the leading edge with the weaker extending over the greater (downstream) part of the pressure surface. The overall distribution thus presents a concave-downward appearance.

The foregoing analysis of flow over concave surfaces reinforces the conclusion that boundary-layer transition from laminar flow, even in the presence of Taylor-Goertler vortices, is determined primarily by the velocity gradient factor, such that if $K \geq 2.5.10^{-6}$ transition is impossible and that an already-turbulent boundary layer will relaminarise. This suggests the use of this property as a design criterion, with the atttendant potential advantages of lower gas-to-blade heat transfer, increased lift and reduced aerodynamic drag, as discussed below.

The condition to be satisfied for a blade pressure surface over which transition is thus inhibited over its whole length is therefore that

$$\frac{\nu}{U_\infty^2}\frac{dU_\infty}{dx} = \frac{\mu}{\rho U_\infty^2}\frac{dU_\infty}{dx} = K_c \tag{12}$$

where the minimum possible value of K_c is $2.5.10^{-6}$. Assuming a simple power relation for air between μ and T, together with the conventional gas dynamic relations for compressible flow, we have

$$\mu = aT^b = aT_0^b\left[1 + \frac{\gamma-1}{2}M^2\right]^{-b} \tag{13}$$

whence equation (12) can be rewritten

$$\frac{aT_0^{0.5+b}}{2p_0}\left[\frac{R}{\gamma M^2}\right]^{1/2}\left[1+\frac{\gamma-1}{2}M^2\right]^{\frac{\gamma+1}{2(\gamma-1)}-b}$$

$$X\left[\frac{2}{M^2[2+(\gamma-1)M^2]}\frac{dM^2}{dx} + \frac{1}{T_0}\frac{dT_0}{dx}\right] = K_c \tag{14}$$

Let

$$t = \frac{T_0}{T_{0_1}};\ r = \frac{p_0}{p_{0_1}};\ m = \frac{M}{M_2};\ s = \frac{x}{c},$$

where subscripts 1 and 2 refer respectively to pressure-surface leading and trailing-edge conditions. From equation (14), the Mach number distribution is then described by

$$\frac{a(T_{01}t)^{0.5+b}}{2p_{0_1}rc}\left[\frac{R}{\gamma m^2 M_2^2}\right]^{1/2}\left[1+\frac{\gamma-1}{2}m^2M_2^2\right]^{\frac{\gamma+1}{2(\gamma-1)}-b}$$

$$X\left[\frac{2}{m^2[2+(\gamma-1)m^2M_2^2]}\frac{dm^2}{ds} + \frac{1}{t}\frac{dt}{ds}\right] = K_c \tag{15}$$

In a static blade cascade or through the blade stator row of a turbine the changes in stagnation pressure and stagnation temperature will be small and r and t will remain close to unity and virtually independent of s. In the case of expansion of hot gas over a rotor blade, the extraction of mechanical work will cause significant reductions in t and r as s increases. If we assume that $t = 1-\alpha s$, $r = 1-\beta s$, so that t and r diminish linearly along the pressure surface, equation (15) becomes

$$\frac{(1-\alpha s)^{0.5+b}}{(1-\beta s)}\left[1+\frac{\gamma-1}{2}m^2M_2^2\right]^{\frac{\gamma+1}{2(\gamma-1)}-b}$$

Downloaded 01 Jun 2010 to 171.66.16.62. Redistribution subject to ASME license or copyright; see http://www.asme.org/terms/Terms_Use.cfm

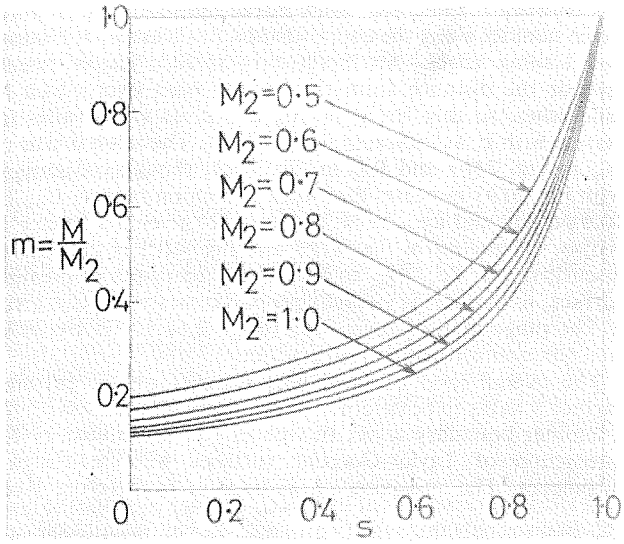

Fig. 5(*a*) Mach number distribution over pressure surface of a stator blade for $K = 2.5.10^{-6}$ and $\gamma = 1.4$

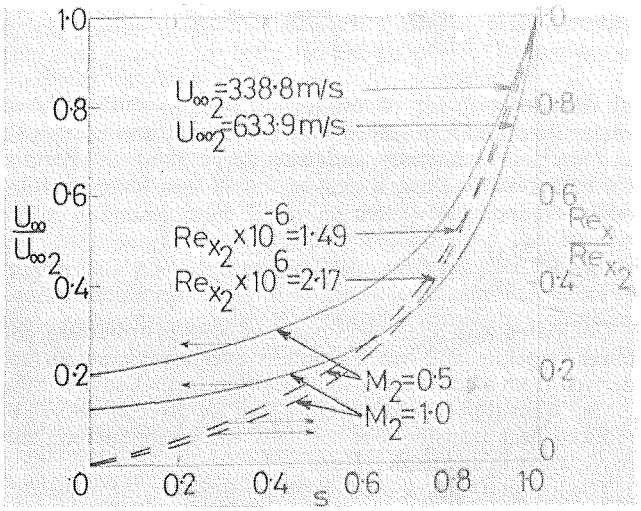

Fig. 5(*b*) Velocity and Reynolds number distributions over pressure surface of a stator blade for $K = 2.5.10^{-6}$ and $\gamma = 1.4$

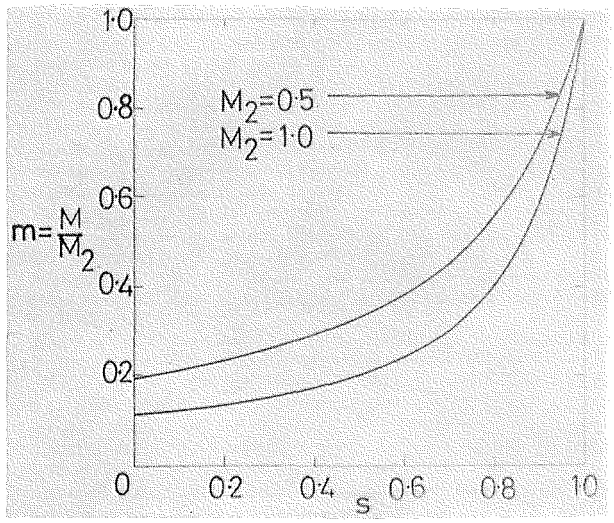

Fig. 6(*a*) Mach number distribution over pressure surface of a stator blade for $K = 2.5.10^{-6}$ and $\gamma = 1.33$

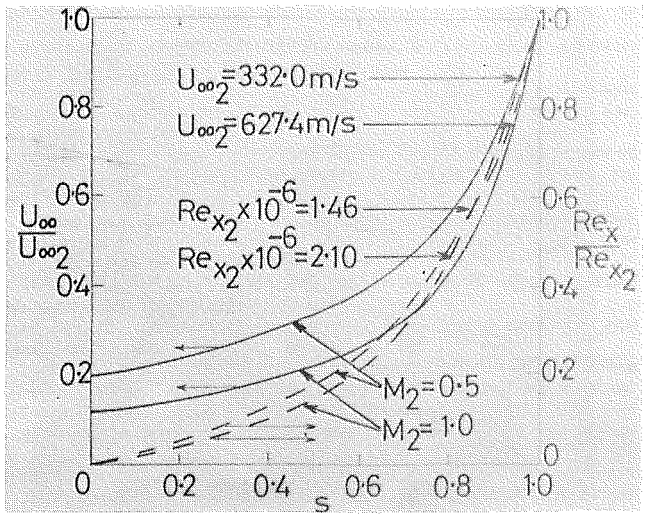

Fig. 6(*b*) Velocity and Reynolds number distributions over pressure surface of a stator blade for $K = 2.5.10^{-6}$ and $\gamma = 1.33$

$$X\left[\frac{2}{m^2[2+(\gamma-1)m^2M_2^2]}\frac{dm^2}{ds}-\frac{\alpha}{(1-\alpha s)}\right] = \frac{2K_c p_{01} c}{aT_{0_1}^{\,0.5+b}}\left[\frac{\gamma m^2 M_2^2}{R}\right]^{1/2} \quad (16)$$

The above equation has been integrated numerically to predict m as a function of s for $p_{01} = 15$ bar, $T_{01} = 1200$K, $K_c = 2.5.10^{-6}$, where for air $R = 289$ J/kg, $a = 6.4.10^{-7}$ kg/ms K^b and $b = 0.6$. By refinement of the steps of integration, an accuracy within 0.1 percent has been established for given trailing-edge boundary conditions.

Figure 5(*a*) shows calculated mainstream Mach number distributions for $0.5 \leq M_2 \leq 1.0$ and $\gamma = 1.4$ for a cascade or stator blade whose pressure surface length $c = 0.05$m. Figure 5(*b*) shows the corresponding mainstream velocity and Reynolds number distributions for $M_2 = 0.5$ and $M_2 = 1.0$. These distributions illustrate the principal distinguishing characteristics which result from inhibiting boundary-layer transition; they are convex-downward in shape so that, as opposed to linear or concave distributions, up to mid-chord mainstream velocities are relatively low and large accelerations occur only towards the trailing edge of the pressure surface. The effect of increasing M_2 in Fig. 5(*a*) is to reduce $m = M/M_2$ along the pressure surface in such a way that the leading-edge Mach number remains substantially constant at about 0.1. In Fig. 5(*b*) an increase in $U_{\infty 2}$ from 338.8 m/s to 633.9 m/s, resulting from increasing M_2 from 0.5 to 1.0, has an almost equally small effect on $U_{\infty 1}$. As might be expected, the corresponding increase in Re_x is greatest at the trailing edge, where the doubling of Mach number increases Re_{x2} by only 45 percent, from $1.49.10^6$ to $2.17.10^6$.

It is evident from Figs. 6(*a*) and (*b*) that the substitution in equation (16) of the more realistic value for γ of 1.33 for otherwise the same conditions has negligible effect on the distributions of M, U_∞ and Re_x along the pressure surface. Figures 7(*a*, *b*) and (*c*) show the same distributions for $\gamma = 1.33$ in the case of a rotor blade where over its length the stagnation temperature falls by 20 percent ($\alpha = 0.2$) and the stagnation pressure by 50 percent ($\beta = 0.5$). These figures also illustrate the effect on the distributions of pressure-surface length, for values of c of 0.025, 0.05 and 0.1 m.

Comparison of Figs. 6(*a*) and 7(*a*) shows that for given

Downloaded 01 Jun 2010 to 171.66.16.62. Redistribution subject to ASME license or copyright; see http://www.asme.org/terms/Terms_Use.cfm

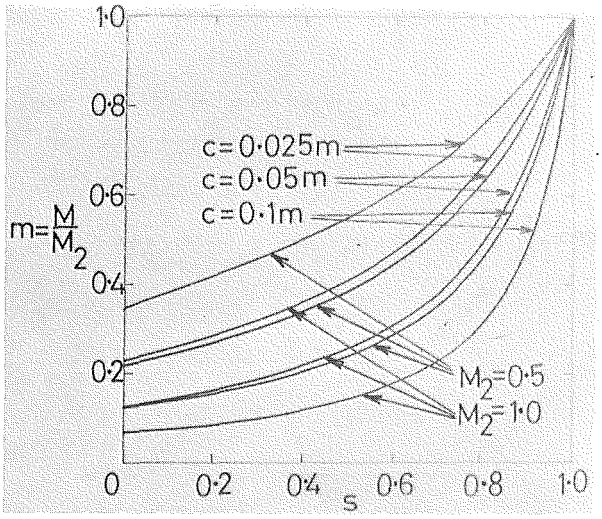

Fig. 7(*a*) Mach number distributions over pressure surface of a rotor blade for $K = 2.5.10^{-6}$ and $\gamma = 1.33$

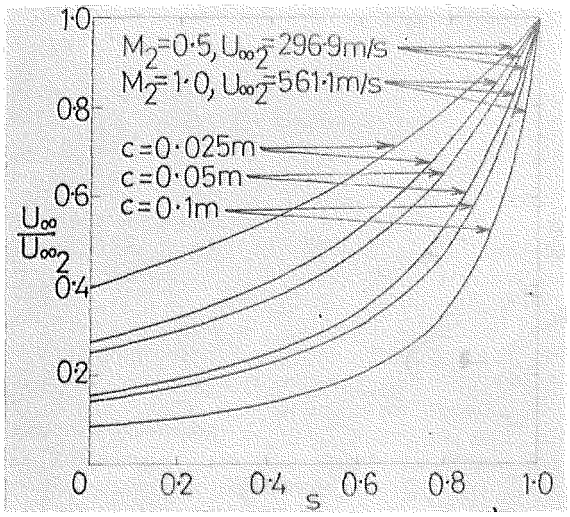

Fig. 7(*b*) Velocity distributions over pressure surface of a rotor blade for $K = 2.5.10^{-6}$ and $\gamma = 1.33$

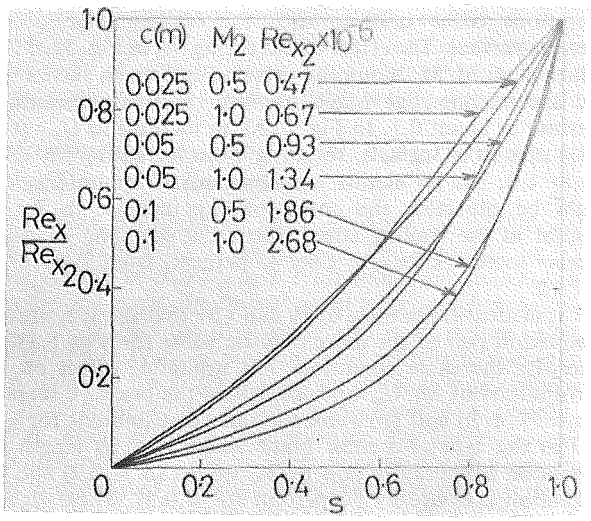

Fig. 7(*c*) Reynolds number distributions over pressure surface of a rotor blade for $K = 2.5.10^{-6}$ and $\gamma = 1.33$

M_2 between 0.5 and 1.0, work extraction increases the local Mach number along the entire surface, but least at the leading and trailing edges. An increase in surface length merely spreads the distance from the trailing edge over which M diminishes, so that for given M_2 and s, its value varies inversely with c, as indicated in Fig. 7(a). The same is true of U_∞ in Fig. 7(b) and Re_x in Fig. 7(c), though comparison with Fig. 6(b) indicates that work extraction reduces $U_{\infty 2}$ by 10.6 percent and Re_{x2} by 36.1 percent for given M_2 when c = 0.05m. Of interest in Fig. 6(b) and Fig. 7(c) is the relative insensitivity of Re_x/Re_{x2} to M_2 for a fixed length of pressure surface, so that Re_x is virtually proportional to Re_{x2} at a given s. The range of Re_{x2} from $4.65.10^5$ to $2.68.10^6$ is felt to be well representative of current practice.

The overall level of local heat transfer on the pressure surface is likely to be determined primarily by equation (5) for a laminar boundary layer, though this be multiplied by the interaction of Taylor-Goertler vorticity with mainstream turbulence. The "baseline" heat transfer is therefore given by:

$$Nu_x = 0.332\, Re_x^{0.5} Pr^{0.33} \tag{17}$$

whence

$$h \propto \left[\frac{\rho U_\infty}{\mu}\right]^{0.5} \left[\frac{\mu C_p}{k'}\right]^{0.33} k' \tag{18}$$

By equation (13) for viscosity, with the previously-adopted values for a and b, together with similar relationships for Pr and thermal conductivity, and using the gas dynamic relations for compressible flow, it can be shown that for $\gamma = 1.33$, relation (18) may be written

$$h \propto \frac{p_0^{0.5} M^{0.5}}{T_0^{0.087}} (1 - 0.319M^2 + 0.077\,M^4 \ldots .) \tag{19}$$

Compared with linear or concave velocity distributions, the lower velocities and Mach numbers over a pressure surface derived from a convex distribution of uniform K sufficient to inhibit transition should therefore lead for given p_0 and T_0 to reduced heat transfer over virtually the entire surface, but particularly in upstream regions.

The lift on a turbine blade is proportional to the integrated difference betwen the static pressures on the pressure and suction surfaces. Hence for fixed suction surface velocity and static pressure profiles, the lift will be a positive function of the pressure surface static pressure distribution. For given p_0, the lower velocities and Mach numbers resulting from convex distributions will give rise to increased static pressures and, hence, increased lift per unit blade surface area.

Aerodynamic drag is directly related to shear stress $\tau = (f/2)\rho U_\infty^2$, whence for laminar flow

$$\tau \propto \frac{\rho U_\infty^2}{Re_x^{1/2}} \propto (\rho U_\infty^3 \mu)^{1/2} \tag{20}$$

Using the procedure used to derive equation (19) it may be shown that

$$\tau \propto p_0^{0.5} T_0^{0.55} M^{1.5} (1 - 0.425M^2 + 0.126M^4 \ldots .) \tag{21}$$

so that as for h, the shear stress and drag will be reduced for given p_0 and T_0 over most of the pressure surface by the lower velocities and Mach numbers associated with convex distributions of uniform K. Finally, it is readily shown from continuity considerations that

$$\rho U_\infty \propto \frac{p_0 M}{T_0^{0.5}} (1 - 0.583M^2 + 0.219M^4 \ldots .) \tag{22}$$

Since M < 1, over most of the pressure surface the mass flow per unit channel width will therefore also be less for convex velocity and Mach number distributions than for linear or

Downloaded 01 Jun 2010 to 171.66.16.62. Redistribution subject to ASME license or copyright; see http://www.asme.org/terms/Terms_Use.cfm

concave distributions. The apparent implication of increased channel section for a given mass flow may not be valid when account is taken of the increased lift noted above.

Conclusions

Our current inability to satisfactorily predict heat transfer over the concave pressure surfaces of turbine blades stems partly from inadequate knowledge of how this is promoted by interaction in the laminar boundary layer between Taylor-Goertler vorticity and mainstream turbulence. It equally stems from ignorance of how these factors influence the onset and extent of boundary-layer transition in the strong favourable pressure gradients characteristic of flow over pressure surfaces, and the local heat transfer in extended transition regions.

The analysis and evaluation of reported measurements on turbine blades in cascade described in this paper suggests that the multiplication of laminar heat transfer caused by longitudinal vortices and their interaction with mainstream turbulence is limited to levels generally below those of a fully-turbulent boundary layer and is restricted to turbulence intensities below about 0.06. Periodic spanwise vortex shedding may well account for the observed chordwise fluctuations in local heat transfer.

Possibly the major conclusion to be drawn from the analysis is that irrespective of the velocity distribution, there is a limiting positive value of the velocity gradient factor K, corresponding to the Launder laminarisation criterion, above which boundary-layer transition does not occur. This "no-go" condition appears to apply irrespective of the Goertler number and the value of U'_∞/U_∞, at least over the ranges examined; the inverse relation between transitional values of these parameters at lower K seems to involve other variables, but there is insufficient evidence to determine their influence on $G_{\theta t}$.

The proposed adoption of the laminarization value of K as a design criterion for the pressure surfaces of turbine blades would not only remove present uncertainty about the location and extent of transition, and the heat transfer in extended transition regions, because transition would never occur; the resulting velocity and Mach number distributions over both fixed and moving blades, from which work is extracted, are shown to provide the additional benefits of reduced heat transfer, increased lift and lower aerodynamic drag when compared to more conventional distributions.

Acknowledgments

The work reported herein was carried out under the terms of a grant from the Science Research Council. The authors also wish to thank Miss A. Clements for her help in preparing this paper.

References

1 Martin, B.W., and Brown, A., "Factors Influencing Heat Transfer to the Pressure Surfaces of Gas Turbine Blades," *International Journal of Heat and Fluid Flow,* Vol. 1, No. 3, 1979, pp. 107–114.

2 Martin, B.W., Brown, A., and Garrett, S.E., "Heat Transfer to a PVD Rotor Blade at High Subsonic Passage Throat Mach Numbers," *Proceedings of the Institution of Mechanical Engineers,* Vol. 192, 1978, pp. 225–235.

3 Yeo, K.H., Personal Communication, 1980.

4 Thwaites, B., "Approximate Calculation of Laminar Boundary Layer," *Aeronautical Quaterly,* Vol. 1, 1949, pp. 245–280.

5 Gruschwitz, E., "Calcul Approché de la Couche Limite Laminaire en Ecoulement Compressible sur une Paroi Non-Conductrice de la Chaleur," *ONERA Publication* No. 47, Paris, 1950.

6 McCormack, P.D., Welker, H., and Kelleher, M., "Taylor-Goertler Vortices and their Effect on Heat Transfer," ASME *Journal of Heat Transfer,* Vol. 92, 1970, pp. 101–112.

7 Kemp, A., "The Boundary Layer on the Pressure Face of a Turbine Blade in Cascade," *Euromech 72,* University of Salford, Apr. 1976.

8 Smith, A.M.O., "On the Growth of Taylor-Goertler Vortices along Highly-Concave Walls," *Quarterly of Applied Mathematics,* Vol. 8, No. 3, 1955, pp. 233–262.

9 Launder, B.E., "Laminarisation of the Turbulent Boundary Layer by Acceleration," MIT Gas Turbine Laboratory, Report No. 77, 1964.

10 Launder, B.E., "Laminarisation of the Turbulent Boundary Layer in a Severe Acceleration," ASME *Journal of Applied Mechanics,* Vol. 31, 1964, pp. 707–708.

11 Jones, W.P., and Launder, B.E., "The Prediction of Laminarisation with a Two-Equation Model of Turbulence," *International Journal of Heat and Mass Transfer,* Vol. 15, 1972, pp. 301–314.

12 Liepmann, H.W., "Investigation of Boundary-Layer Transition on Concave Walls," NACA Wartime Report W-87, 1945.

13 Forest, A.E. "Engineering Predictions of Transitional Boundary Layers," AGARD CP 224, Vol. 22, 1977.

14 Dryden, W.L., "Recent Advances in the Mechanics of Boundary-Layer Flow," *Advances in Applied Mechanics* (ed. R. von Mises and Th. von Karman) 1948, Part I, New York, pp. 1–40.

15 Tani, I., "Production of Longitudinal Vortices in the Boundary Layer on a Concave Wall," *Journal of Geophysical Research,* Vol. 67, No. 8, 1962, pp. 3075–3080.

16 Wortman, F.X., "Experimentelle Untersuchungen Laminarer Grenzschichten bei Instabiler Schichtung," *Proceedings of the 11th International Congress on Applied Mechanics,* Munich, 1964, pp. 815–825.

17 Wortman, F.X., "Visualization of Transition," *Journal of Fluid Mechanics,* Vol. 38, 1969, pp. 473–480.

18 Tani, I., and Aihara, Y., "Goertler Vortices and Boundary-Layer Transition," *Z.A.M.P.,* Vol. 20, 1969, pp. 609–618.

19 Winoto, S.H., Durao, D.F.G., and Crane, R.I., "Measurements within Goertler Vortices," ASME *Journal of Fluids Engineering,* Vol. 101, 1979, pp. 517–520.

20 Turner, A.B., "Local Heat Transfer Measurements on a Gas Turbine Blade," *Journal of Mechanical Engineering Science,* Vol. 13, No. 1, 1971, pp. 1–12.

21 Walker, L.A., and Markland, E., "Heat Transfer to Turbine Blading in the Presence of Secondary Flow," *International Journal of Heat and Mass Transfer,* Vol. 8, 1965, pp. 729–748.

22 Köhler, H., Hennecke, D.K., Pfaff, K., and Eggebrecht, R., "Hot Cascade Test Results of Cooled Turbine Blades and their Application to Actual Engine Conditions," AGARD CP 229, 1977, pp. 6-1-6-12.

23 Daniels, L.C., "Film Cooling of Gas Turbine Blades," D.Phil. thesis, University of Oxford, 1978.

24 Bayley, F.J., and Priddy, W.J., "Effects of Free-Stream Turbulence Intensity and Frequency on Heat Transfer to Turbine Blading," ASME JOURNAL OF ENGINEERING FOR POWER, Vol. 103, 1981, pp. 60–64.

25 Garrett, S.E., Personal Communication, 1980.

26 Brown, A., and Burton, R.C., "The Effects of Free Stream Turbulence Intensity and Velocity Distribution on Heat Transfer to Curved Surfaces," ASME JOURNAL OF ENGINEERING FOR POWER, Vol. 100, 1978, pp. 159–168.

27 Brown, A., and Martin, B.W., "Heat Transfer to Turbine Blades, with Special Reference to the Effects of Mainstream Turbulence," ASME Paper No. 79-GT-26, 1979, pp. 1–12.

Downloaded 01 Jun 2010 to 171.66.16.62. Redistribution subject to ASME license or copyright; see http://www.asme.org/terms/Terms_Use.cfm

Design and Preliminary Results of a Fuel Flexible Industrial Gas Turbine Combustor

A. S. Novick
Program Manager.
Mem. ASME

D. L. Troth
Research Engineer.

Detroit Diesel Allison,
Division of General Motors Corp.,
Indianapolis, Ind.

H. G. Yacobucci
Technical Manager,
NASA Lewis Research Center,
Cleveland, Ohio

The work described in this paper is a part of the DOE/LeRc "Advanced Conversion Technology Project" (ACT). The program is a multiple contract effort with funding provided by the Department of Energy and Technical Program Management provided by NASA LeRc. It is anticipated that future industrial gas turbine engines will require fuel flexibility. The emphasis in this paper is the fuel flexible combustor technology developed under the "Low NO_x Heavy Fuel Combustor Concept Program" for application to the Detroit Diesel Allison (DDA) Model 570-K industrial gas turbine engine. The technology, to achieve emission goals, emphasizes dry NO_x reduction methods. Due to the high levels of fuel bound nitrogen (FBN) control of NO_x can be effected through a staged combustor with a rich initial combustion zone. A RICH/QUENCH/LEAN (RQL) variable geometry combustor is the technology that will be presented to achieve low NO_x from alternate fuels containing FBN. The results will focus on emissions and durability for fuel flexible operation.

Introduction

Detroit Diesel Allison (DDA) is among five gas turbine engine manufacturers participating in the "Low NO_x Heavy Fuel Combustor Concept Program"[1]. The technology focus at DDA is the Allison Model 570-K industrial gas turbine engine. This combustor must be capable of sustained, environmentally acceptable "dry" operation on minimally processed heavy petroleum residuals (RESID), synthetic coal derived liquids (CDL) and petroleum distillate (ERBS) fuels. From a fuel flexibility viewpoint, the advanced combustion technology developed under this DOE/LeRC program, and presented in this paper, is essential to the future industrial engine market. Declines and uncertainties in the availability of petroleum distillate fuel and increasing demands for natural gas coupled with continually rising cost leads one to conclude that in the future industrial gas turbine users will require multifuel capability. As a result of fuel flexibility, uninterrupted operation will be preserved. Fuels such as petroleum residuals or "synthetics" are most likely to become prominent for the utility and industrial user. Generally, RESID's and CDL's have significant levels of fuel bound Nitrogen (FBN). In developing a fuel flexible combustion system the control of NO_x emissions from this pollutant source is a major challenge for the engine manufacturer. Significant technological advances from contemporary combustion systems are essential in order to operate gas turbine engines in an environmentally acceptable manner when using these fuels. Because of general air pollution problems within the U.S. the exhaust emissions from all fuel burning devices have been or are planned to be regulated by both federal and state governments. Recently enacted Federal regulations for stationary gas turbine engines specify pollutant emission concentration levels which are below the current applied technology. Pollutant emissions produced by gas turbines using petroleum distillate fuels are carbon monoxide (CO) and unburned hydrocarbons (UHC) at low power conditions, and oxides of nitrogen (thermal NO_x) at high power conditions.

Reductions of CO and UHC in contemporary combustors can be achieved by relatively straightforward approaches [2,3]. However, these approaches are subject to tradeoffs in operating range capabilities, combustion system complexities and control of thermal NO_x. The reduction of thermal NO_x is not as straightforward because the most favorable conditions for minimum NO_x is in opposition to combustion stability, production of CO and UHC and operating range. Control of NO_x from FBN is less understood but exploratory research [4] indicates control can be effected through a rich (excess fuel) combustion process. The flexibility to operate with non-standardized fuels presents performance problems apart from emissions. High viscosity makes atomization, vaporization and distribution a difficult task, thus necessitating innovative fuel injector design and development. Distillation variations (residual fuel has end points in excess of 1100°F (867K)) requires special consideration as related to combustor sizing. Reduced hydrogen content or high aromatics, especially for CDL's, presents a problem in the area of liner durability due to high radiation loads. In essence, all facets of combustor design and development require careful review and advancements when multi-fuel capability is the goal. The air-staged combustor presented in this paper consist of an initial RICH burning zone followed by a QUENCH zone and LEAN reaction and dilution zone. This combustor is referred to as

Contributed by the Gas Turbine Division of THE AMERICAN SOCIETY OF MECHANICAL ENGINEERS and presented at the Gas Turbine Conference and Products Show, March 9-12, 1981, Houston, Texas. Manuscript received at ASME Headquarters December 11, 1980. Paper No. 81-GT-108.

Copyright © 1982 by ASME

Downloaded 01 Jun 2010 to 171.66.16.62. Redistribution subject to ASME license or copyright; see http://www.asme.org/terms/Terms_Use.cfm

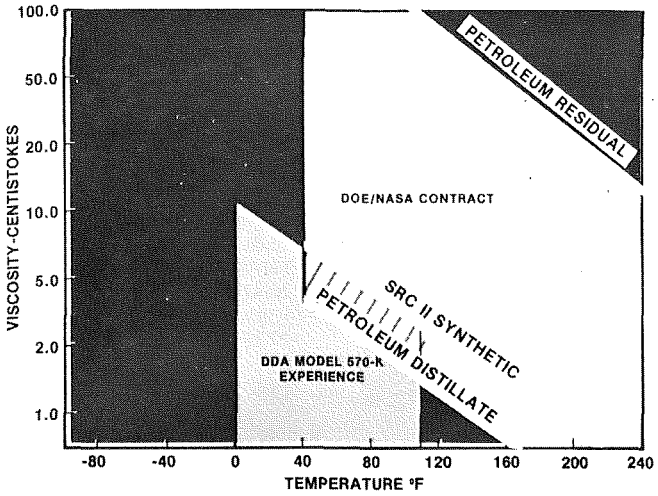

Fig. 1 Effect of temperature on fuel viscosity

Table 1 Fuel properties

	Petroleum Distillate (ERBS)	Petroleum Residual (RESID)	Synthetic-CDL (SRC-II)
Hydrogen, wt percent	12.88	11.24	8.81
Carbon, wt percent	87.05	87.39	85.84
Nitrogen (FBN) wt percent	0.013	0.27	0.88
10 percent, Dist. °F (K)	375 (464)	572 (573)	410 (483)
End point °F (K)	645 (614)	1026 plus (825)	597 (587)
Pour point, °F (K)	−35 (236)	40 (278)	−50 (228)

the RQL combustor. Unique to this RQL combustor is the feature that all air entries are regulated by variable geometry. This permits combustor performance/emission optimization over the entire engine operating range. Tradeoffs between the complexities of variable geometry and performance/emission results will determine the feasibility of this design.

Design Features

The objective of this DOE/LeRC program is to generate and demonstrate the advanced technology required to develop a durable, low emission gas turbine combustor for utility and industrial applications capable of operation on minimally processed petroleum residual or synthetic fuels. Also, the combustor technology should provide for operation on a wide variety of potential fuels, with varying properties, which might be available in the future. The three fuels which are to be tested are illustrated in Fig. 1 and their key properties enumerated in Table 1. Note that ERBS [5] is a research fuel, which is a special blend of kerosene and hydrotreated catalytic gas oil. It represents a future fuel should it become necessary to broaden current kerojet specifications.

Design criteria for multi-fuel operation are dictated by the program goals and are shown in Table 2.

The control of NO_x requires specific reaction zone stoichiometry. In general, oxides of nitrogen are formed when nitrogen in the atmosphere is subjected to high temperatures over a finite period of time in the presence of oxygen. The oxidation of atmospheric nitrogen can be minimized by operating at reaction zone temperature levels below approximately 2500°F (1644K). Unfortunately, in the excess oxygen state of lean combustion FBN will react to produce

Table 2 Emissions and performance goals

Performance Goals	
Combustion Efficiency	99 percent (operating range)
Total Pressure Loss	6 percent (base load power)
Outlet Temp. Pattern Factor	0.25 (base and peak load)
Outlet Temp. Profile	Equivalent to typical production
Emissions Goals	
Oxides of nitrogen (at 15 percent O_2)	90 ppm FBN < 0.015 percent 140 ppm FBN > 0.25 percent
Sulfur Dioxide	(limits fuel sulfur content)
SAE Smoke number	20

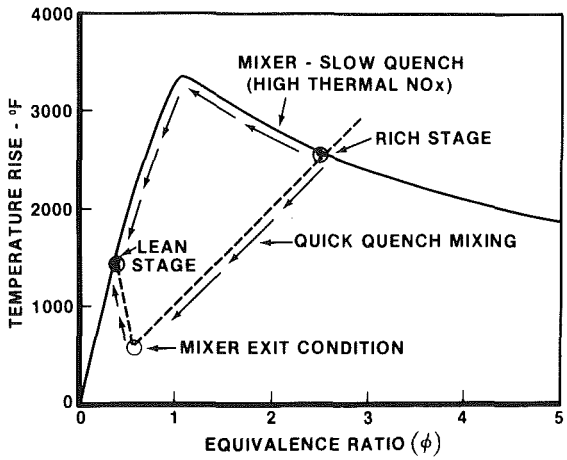

Fig. 2 Operational considerations for rich/quench/lean staged combustor

excessive levels of NO_x. It has been postulated and later demonstrated in fundamental experiments that a fuel rich combustion zone can be effective to minimize NO_x from FBN[4, 6, 7]. The equivalence ratio for minimum NO_x has to be determined through experimentation and is a significant part of this program. The DDA design rational is to inhibit NO_x formation from FBN in a rich burning zone and quickly/uniformly quench the exiting hot products so that a minimum of thermal NO_x will be formed in the final lean reaction zone. This staged air RQL combustion process is illustrated through the temperature rise curve shown in Fig. 2. Transition from a rich zone to a lean zone requires a very rapid uniform quench to prevent high temperatures resulting from stoichiometric streaks. The lean zone equivalence ratio is a function of thermal NO_x with due consideration for the consumption of CO and smoke. The reaction of CO requires time and temperature which is in direct opposition to the NO_x reactions. Therefore, the operating equivalence ratio for this lean zone must also be carefully controlled to satisfy both emissions requirements. The dilution zone will tailor the exit temperature pattern for turbine durability and receives the balance of air after combustion and cooling are satisfied.

A very important area in the design of this combustor, from a combustion point of view, is the dimensional definition of the combustor reaction flow path; ie., combustor diameter and length. Combustor diameter is interrelated to combustor throughput (reference) velocity. It is also dependent on the number of combustors which can physically be utilized in a can-annular combustion system. Vaporization time requirements, especially important for RESID, are, among other things, a direct function of the combustor length, i.e. residence time. Also, factored into the specification of a combustor volume is the geometric consideration for a flow

Downloaded 01 Jun 2010 to 171.66.16.62. Redistribution subject to ASME license or copyright; see http://www.asme.org/terms/Terms_Use.cfm

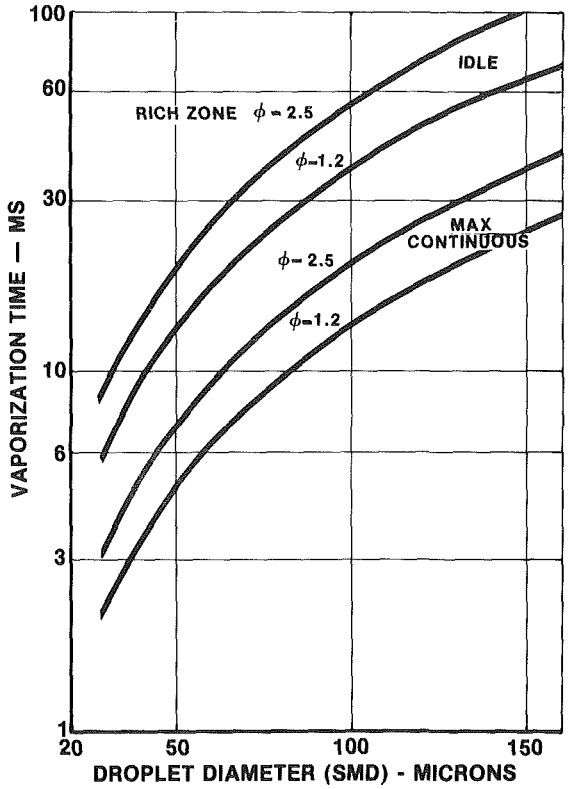

Fig. 3 Effect of atomization on RESID vaporization time

recirculation/mixing pattern. With regard to this variable geometry RQL combustor each zone has to be sized based on the criteria for its operation.

The combustors physical size was calculated for a can-annular combustion system with associated operating conditions (Wa, P and T), for the Allison Model 570-K engine. Rich zone residence time was determined under the assumption that fuel evaporation is the rate controlling phenomena. Inherent in the assumption is the fact that fuel-air mixing or reaction rates are not the limiting items. The analytical formulation for 100 percent vaporization is given by the following expression [8].

$$t = \frac{5.50\,(10^{-9})SpGr\,D^{1.5}}{\sqrt{(1+[\phi_{R.Z.}\,(f/a)_{st}]^{-1})W_f\mu_g}\ln(1+B)}$$

where: t = time (ms);
$SpGr$ = specific gravity;
D = droplet Sauter mean diameter (μm);
$\phi_{R.Z.}$ = rich zone equivalence ratio;
$(f/a)_{st}$ = stoichiometric fuel air ratio;
W_f = fuel flow (lb/hr);
B = transfer number; and
μ_g = gas viscosity lb/s-ft.

Vaporization time as a function of droplet diameter for the RESID fuel is shown in Fig. 3.

Combustion stability limits and liner pressure drop are also factors considered in establishing a reference velocity. Rich combustion stability was of concern since the concept is to react with a fuel rich mixture in the initial combustion zone. From a stability point of view, operational difficulties [9-12] are generally associated with low pressure conditions such as encountered in very high altitude aircraft operation and thus no significant limitations were obvious for the operating range typical of the Allison Model 570-K industrial gas turbine engine. Based on current experience with the can annular combustion system in Allison Model 501K industrial engine the pressure drop goal of 6 percent provides adequate

Table 3 Combustor size

	Rich Zone		Lean Zone
Design Length	11.00 in.(27.94 cm)		5.50 in.(13.97 cm)
Requirement	Vaporization		Reaction (θ)
	$\phi = 1.8$	$\phi = 1.3$	$\phi = 0.6$
Max. Rated	8.23 in. (20.91)	10.28 in. (26.11)	2.77 in. (7.04)
Max. Continuous	8.20 in. (20.83)	10.24 in. (26.01)	3.62 in. (9.19)
70 percent Power	8.32 in. (21.13)	10.40 in. (26.42)	4.33 in. (11.00)
50 percent Power	8.55 in. (21.72)	10.70 in. (27.18)	5.42 in. (13.77)
Idle	8.95 in. (22.74)	11.24 in. (28.55)	8.37 in. (21.26)

mixing and air management and is not detrimental to engine performance.

The θ reaction rate parameter was used to establish the lean combustion zone volume based on correlations with DDA engine operating experience on DF-2 fuel.

Based on the above criteria and engine size considerations, a combustion system of ten liners having a diameter of 5.53 in. (14.05 cm) was selected. The resulting reference velocity is 55.6 ft/s (16.95 m/s) at max continuous power operation. The combustion zones design lengths, compared to the calculated requirements for two rich zone equivalence ratios are shown in Table 3. A conservative estimate of an SMD of 100 at max power operation for RESID was used in this design. Note that the length specification is set by the low power operating conditions and the equivalence ratio. This comes about due to the velocity variations in the rich zone as a consequence of operating conditions and air staging.

The design length provides for complete fuel vaporization over an anticipated range of droplet SMD at all operating conditions except idle. Since it is not a continuous operating condition for pollutant emissions the compromise at idle is reasonable. Also, sizing is directly dependent upon the atomizing performance of a fuel injector and it was deemed prudent to concentrate on achieving better atomization at low power than to provide increased combustor length at the expense of durability.

As previously stated the capability to uniformly and quickly quench the hot gas exiting the rich zone is essential. Since the variable geometry RQL combustor is designed to operate over a range of rich and lean zone equivalence ratios (1.2-2.5) and (0.4-0.6), respectively, the quench mixer must be capable of providing uniform transition between the two combustion zones throughout this equivalence ratio range. Two competing conditions arise regarding the quench phenomena. For a fixed lean zone equivalence ratio increased quantities of quench air are required with increases in the rich zone equivalence ratio. This results in effective quench area increases at a fixed pressure drop. However, as the rich zone equivalence ratio increases the quench jet momentum ratio (quench momentum/hot gas momentum) also increases due to the decrease in mass flow and temperature through the rich zone. These two conditions are in the direction of increasing jet penetration and thus non optimum mixing over a range of equivalence ratios. Also, in designing the quench mixer consideration has to be given to the fact that it must initiate a flow field in the lean zone conducive to stable combustion.

Based on experimental test the quench zone was designed with a 4 in. (10.2 cm) dia and an L/D of 1. The reduced diameter forces the hot gas from the rich zone to acceleratre into the quench jets inhibiting any upstream diffusion. It also provides for an expansion into the lean zone to initiate a stable combustion region. Variable area circumferentially

Downloaded 01 Jun 2010 to 171.66.16.62. Redistribution subject to ASME license or copyright; see http://www.asme.org/terms/Terms_Use.cfm

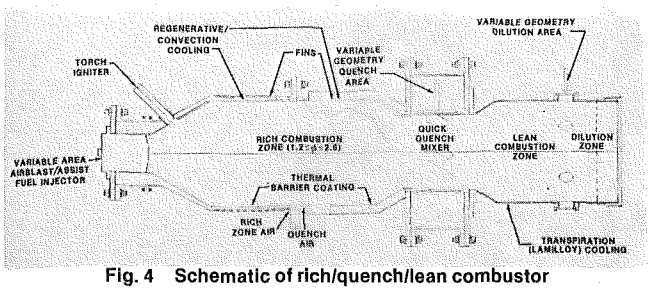

Fig. 4 Schematic of rich/quench/lean combustor

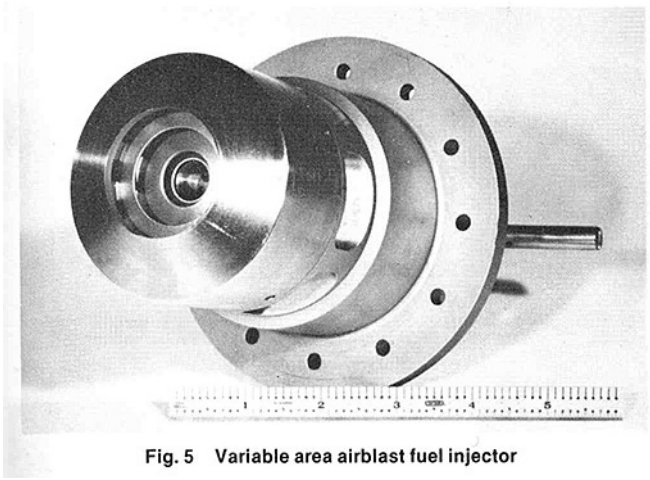

Fig. 5 Variable area airblast fuel injector

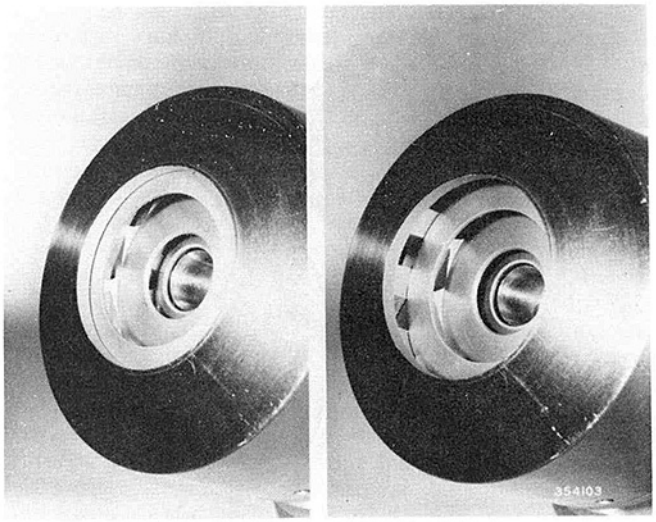

Fig. 6 Variable area airblast fuel injector

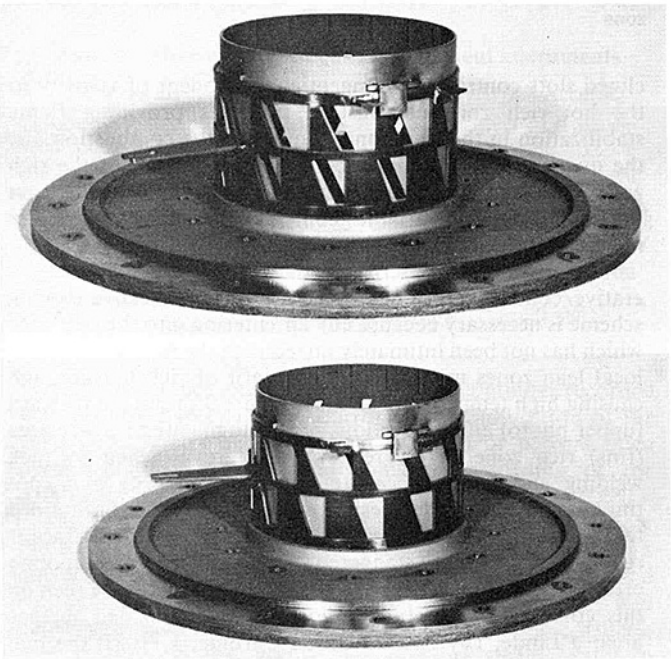

Fig. 7 Variable area quick quench zone

inclined slots are used to admit the quench air into this quench zone. These slots, which compensate for area and momentum ratio variation, with be discussed in the following section.

RQL Combustor Description

A schematic of the Concept I RQL fuel flexible combustor depicting its' key features is shown in Fig. 4. Unique features of this combustor are its' air staging, variable geometry and regenerative/convective cooling. Three axial locations of variable geometry are used in order to vary rich/lean zone equivalence ratios in concert or independently while maintaining a specified pressure drop. A description and illustration of the key features of this combustor follow in this section.

Shown in Fig. 5 is a variable area airblast fuel injector designed by Parker Hannifin Corp. Gas Turbine Fuel Systems Div. to operate with RESID fuel. This injector includes two constant area orifices, two variable area swirlers and a fuel pre-filming orifice. The area variation is accomplished through meshing of the swirlers and is shown in Fig. 6. The photo on the right depicts the maximum airflow configuration while the minimum airflow configuration is shown on the left. The center shroud and fuel entry point traverses approximately 0.25 inches (0.64 cm) axially when operating over the airflow (equivalence ratio) range. In the closed position the air to fuel ratio of 3 is acceptable for good atomization. Results of ambient spray analysis tests are shown in Table 4.

All the rich zone air is admitted to the combustor through the single fuel nozzle. In addition to maximizing air blast atomization, this single point injection allows for intimate mixing between the rich zone air and fuel. Prior to entering the nozzle the air is first used to convectively cool the forward portion of the augmented surface area rich zone. Regenerative use of cooling air provides the potential for improved fuel vaporization and added combustion stability within the rich stage due to the elevated inlet temperatures. It also provides for a wider range of parametric operation since designated cooling air is minimized.

Table 4 Airblast fuel nozzle spray analysis summary, 12 CTS fluid

Variable Area Position	Fuel Flow PPH (g/sec)	Air ΔP PSI (KPa)	SMD (Microns)
Closed	40.8 (5.1)	0.7 (4.8)	60
Closed	40.8 (5.1)	1.4 (9.7)	46
Closed	297.0 (37.4)	1.0 (6.9)	145
Closed	297.0 (37.4)	2.0 (13.8)	75
Half Open	40.8 (5.1)	0.7 (4.8)	95
Half Open	297.0 (37.4)	1.0 (6.9)	66
Open	40.8 (5.1)	0.7 (4.8)	70
Open	297.0 (37.4)	1.0 (6.9)	57

The variable geometry quick quench zone is shown in Fig. 7. Two rows of twelve circumferentially inclined slots having a 4:1 aspect ratio (in the full open position) define the quench air entry ports. Inclining of the slots with respect to the axial direction serves a two fold purpose. First, the arrangement results in more uniform mixing over a shorter length in comparison to circular holes or axial slots. Second, the in-

Downloaded 01 Jun 2010 to 171.66.16.62. Redistribution subject to ASME license or copyright; see http://www.asme.org/terms/Terms_Use.cfm

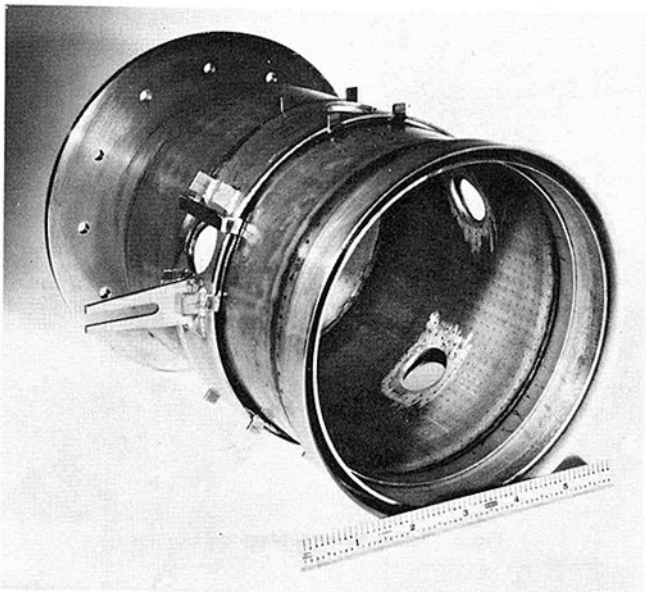

Fig. 8 Transpiration cooled lean combustor variable area dilution zone

clined slots contribute a tangential component of velocity to the hot rich zone combustion products providing flame stabilization in the lean zone. Similar to the combustion air, the quench air convectively cools the aft section of the rich zone. The lean combustion and dilution zone are shown in Fig. 8. The dilution variable geometry consist of circular holes metered by an elevated rotating band.

As previously described the rich zone is regenerative/convectively cooled. The use of a convective cooling scheme is necessary because any air entering into the rich zone which has not been intimately mixed with the fuel will result in local lean zones minimizing the benefit of rich burning and causing high temperature streaks. Figure 9 shows the forward (upper photo) and aft sections of the augmented surface area (fins) rich zone hardware. The fins are attached by tack welding and braze to ensure structural integrity and continuous surface contact, respectively. Due to space limitations the number of fins on the forward section conical surface is reduced, and they are staggered to promote increased cooling effectiveness. A provision for the torch ignitor can be seen on this conical surface. In addition to the augmented surface area; a Linde, Division of Union Carbide, LTB-8B thermal barrier coating has been applied to the inside surface of the rich and quench zones. This added thermal protection, afforded by the coating, is especially desireable when using the CDL fuel with its low hydrogen content and consequently high radiation loads. The lean combustion and dilution zone section, downstream of the quick quench mixer, shown in Fig. 8, uses Lamilloy[R,1] transpiration wall cooling. The use of Lamilloy minimizes cooling air requirements for fuel flexible combustors. Lamilloy hole sizes, patterns, and passage heights are specifically designed to satisfy the wall cooling requirements.

The assembled RQL combustor is shown in Figure 10. Forward and aft sections of the rich zone are enclosed by shells which guide the cooling air over the finned surface before it enters the nozzle and quench zone, respectively. The large annulus enclosing the quick quench mixer is necessary for uniform flow through each of the slots and to contain the variable geometry mechanism.

The RQL combustor is designed in a building block concept for ease of fabrication, assembly and modification. All

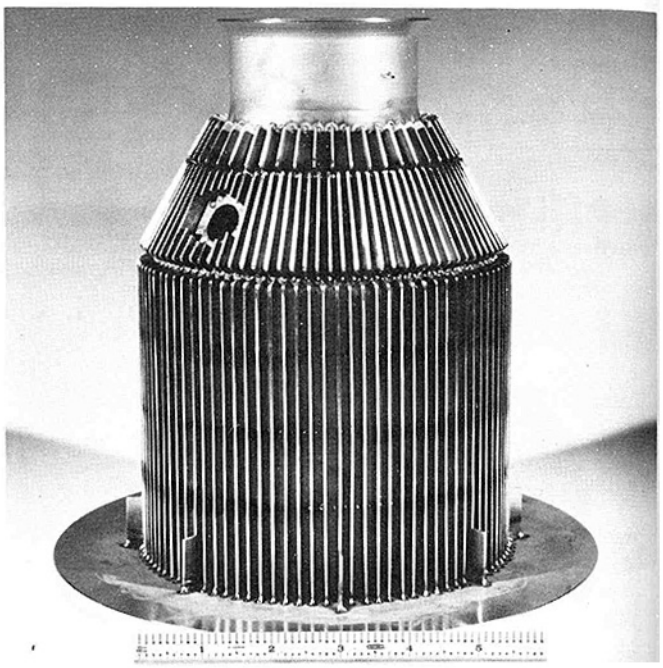

Forward section

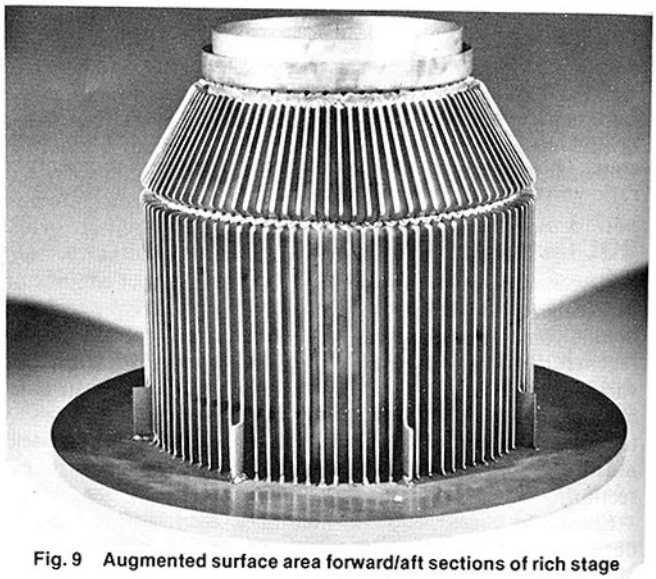

Fig. 9 Augmented surface area forward/aft sections of rich stage

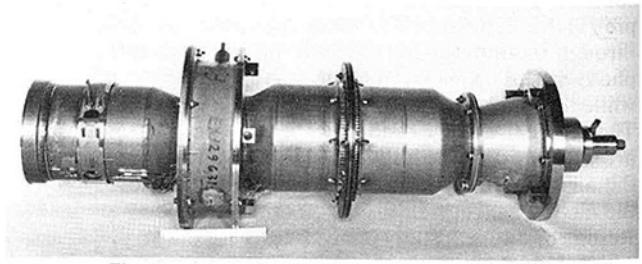

Fig. 10 Assembled rich/quench/lean combustor

sections are bolted together. If preheat is necessary to enhance RESID vaporization the nozzle assembly and front spool piece can be replaced with a Concept II fuel vaporizor as shown in Fig. 11. The vaporizor length has been sized to prevent autoignition [13]. The variable geometry nozzle (Fig. 6) is used as the main fuel injector for the vaporizor. Fuel is supplied to the small Lamilloy burner through a low flowing airblast/air assist nozzle.

[1] Lamilloy is a registered trademark of the General Motors Corp. (1967).

Downloaded 01 Jun 2010 to 171.66.16.62. Redistribution subject to ASME license or copyright; see http://www.asme.org/terms/Terms_Use.cfm

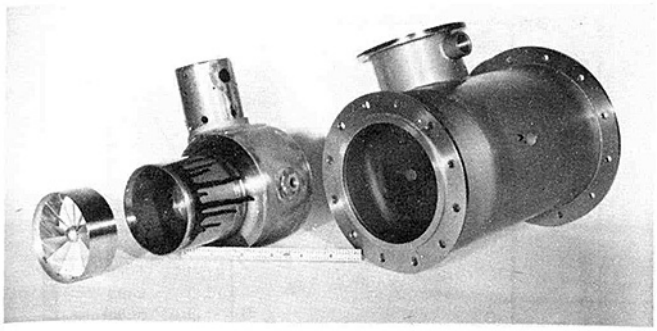

Fig. 11 RESID fuel vaporizer

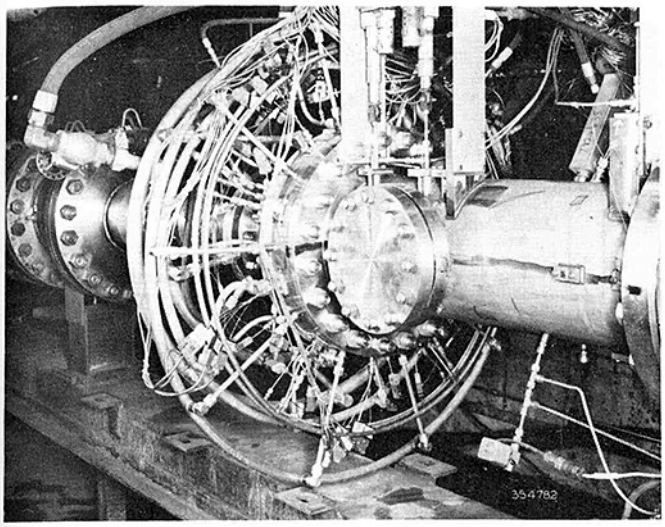

Fig. 12 Test rig for remotely actuated variable geometry RQL combustor

Table 5 Engine/combustor operating conditions

Power Point	Airflow (lb/sec) (Kg/s)	Inlet Temp. °F (K)	Inlet Pressure psia (kPa)	Fuel Flow (lb/hr) (g/s)
Max Rated	3.87 (1.75)	688 (638)	177.1 (1221.1)	331.4 (41.8)
Max Cont.	3.70 (1.68)	661 (623)	165.6 (1141.8)	296.9 (37.4)
70% Load	3.22 (1.46)	592 (584)	135.4 (933.6)	212.2 (26.7)
50% Load	2.89 (1.31)	547 (559)	116.2 (801.2)	164.2 (20.7)
Idle	1.61 (0.73)	342 (445)	52.0 (358.5)	40.8 (5.1)

Test Facilities and Procedures

Airflow calibration and combustion testing of the fuel flexible RQL combustor has been carried out in a DDA high pressure test facility. The test cell dedicated to this program is capable of operation at the Allison Model 570-K rated engine conditions. High pressure, filtered facility air is supplied to the test rig through gas fired heaters which are used to elevate inlet temperatures in order to simulate compressor discharge characteristics. The operating conditions at which the combustor is to be evaluated are enumerated in Table 5.

A plenum type test rig, shown in Fig. 12, accommodates the variable geometry combustor. Unique to this test rig are three remotely controlled variable geometry actuators. These permit independent sizing of the nozzle, quench and dilution air entries from the control room. Thus, many configurations can be examined in an efficient test procedure.

Data of interest are the inlet and exit pressures and temperatures, emissions, internal static pressures, combustor metal temperatures and variable geometry positions. Inlet measurements are consistent with standard DDA test procedures, including sharp edged orifices and appropriate pressure and temperature instrumentation. Exit instrumentation consist of five equally spaced five-element Platinum-Rhodium thermocouple rakes with one rake having a sixth element on the centerline. These are used to evaluate temperature rise and pattern factor. Water cooled emission probes are arranged in a similar manner, with the exclusion of a centerline port. The emission probes are manifolded to a common, heated sample line leading to the exhaust gas measurement instruments described in Table 6. If necessary, the emission probes can also be used as total pressure instrumentation. This exit instrumentation provides sufficient coverage for meaningful evaluation of the combustors performance. Each combustion zone and plenum section of the RQL combustor are instrumented for static pressures, while the plenums also include thermocouples to measure the cooling air temperature rise. Combustor liner durability is monitored through twenty-nine embedded wall thermocouples.

Table 6 On-line exhaust gas measurement instruments

Exhaust Gas	Instrument	Accuracy
Carbon Monoxide (CO)	Beckman Model 865-NDIR	± 1.0 percent
Unburned Hydrocarbons (UHC)	Beckman Model Model 402-heated FID	± 1.0 percent
Total Nitrogen Oxides (NO_x)	TECO Model 10A-CL	± 1.0 percent
Carbon Dioxide (CO_2)	Beckman Model 864-NDIR	± 1.0 percent
Smoke	ARP 1179 procedure	± 3 SN

All performance and emissions data are computer recorded with on-line display in the control room. Calibration of the variable geometry actuators as a function of percent open permit digital read out and computer recording of the combustor configuration.

The fuel storage system entails three 275 gallon tanks for the RESID, ERBS, and SRCII fuels. In order to maintain a uniform nonstratified temperature, an internal heater and recirculating system are part of the RESID tank. The rig fuel delivery system includes electrically heated lines, filters, recirculation circuits, and a high pressure steam heater to elevate the RESID temperature immediately upstream of the fuel nozzle. Also, the capabilities to inject Pyridine into the fuel line through a metered, low flowing, high pressure pump and to blend any two fuels during testing are part of this system. Flotrons are used for all fuel flow measurements. This automated fuel system is well suited for extensive combustor interrogation testing when multiple fuels and blends are involved.

Due to the importance of precise zone equivalence ratio control experimental airflow calibrations were carried out to evaluate the complex combustor airflow circuits and the three variable area air entries. The effective area of each entry and zone pressure drops were determined through sequential testing. The cold flow test procedure used was as follows. The airflow characteristics of the variable area nozzle were determined in an independent test fixture. Utilizing these results in conjunction with parametric tests of the quench air ports and the nozzle, while the Lamilloy and dilution area were sealed, permitted calibration of the variable quench area. A third series of parametric test incorporating the variable geometry dilution resulted in lean zone cooling air and dilution area airflow calibration. Thus, during com-

Downloaded 01 Jun 2010 to 171.66.16.62. Redistribution subject to ASME license or copyright; see http://www.asme.org/terms/Terms_Use.cfm

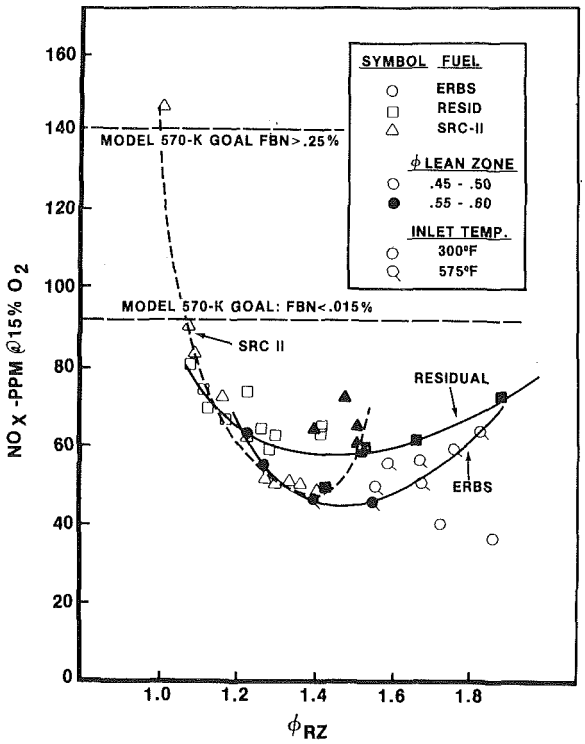

Fig. 13 NO_x versus rich zone equivalence ratio

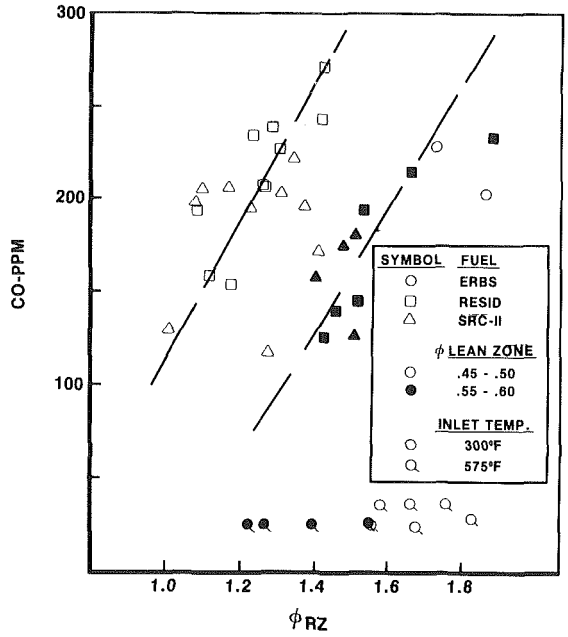

Fig. 14 CO versus rich zone equivalence ratio

bustion testing, zone equivalence ratios are determined by utilizing the variable geometry positions and design pressure drop as input to the performance maps. Throughout the testing this is a set and confirm procedure; i.e., test configurations are selected utilizing the maps and subsequent confirmation of the test point is determined based on the experimental measurements. All data transfers, reductions and correlations are processed through the DDA computer system.

The principal procedure for combustor evaluation testing involved operation at inlet conditions representative of a fixed engine operating point while varying the combustor configuration. Since there are three stations of variable geometry many configurations can be evaluated during a single rig buildup. Also, the ability to vary reaction zone equivalence ratios while maintaining the overall fuel/air and pressure drop permits correlation of all configurations without scaling. Since durability is paramount in this program and novel cooling schemes are being used, continuous real time monitoring of liner temperatures was carried out. The first requirement of an acceptable configuration is liner integrity. Based on satisfaction with this criteria, performance and emissions data are acquired and a new configuration initiated.

Results and Discussion

Evaluation of the RQL combustor has been carried out utilizing the three baseline fuels. Optimizing zone (rich/lean) equivalence ratios to meet performance, emissions and liner durability goals are the objectives of this testing. Early test results reported in this paper are for conditions near max continuous power operation. Emphasis is placed on this operating condition since it is the highest continuous power operating point for the engine, thus potentially producing the highest sustained levels of NO_x and smoke emissions. Further testing will be carried out over the engine operating range later in the program.

Initial RQL combustor tests with ERBS fuel illustrated two areas detrimental to successful operation. First is the potential for carbon deposition in the rich zone. This occurred when the equivalence ratio was of the order of two and above. The cause was determined to be excessively rich operation in a very "lazy" zone. The limited quantity of air required to achieve the high equivalence ratios, recalling that design fuel flow is maintained, coupled with combustor temperatures significantly lower than stoichiometric, result in reduced gas velocities. The consequences of low gas velocities are extreme rich zone residence times, unstable recirculation patterns, and non-uniform mixing. All items contribute to the carbon deposits. As a result of these data, operation at high equivalence ratios was determined to be impractical and subsequent testing was limited to equivalence ratios less than two.

A second area requiring immediate attention was overheating of the liner in the fuel nozzle piloting area. Examination of the liner indicated that air leaking past the nozzle initiated local stoichiometric combustion zones when interacting with the fuel rich mixture. A ramification of this is the detriment to overall combustor durability due to inefficient mixing within the entire rich zone. A modification of the convective cooling passage and the sliding seal arrangement, in proximity to the nozzle, alleviated the problem.

Emission results as a function of rich zone equivalence ratio, at near the max continuous power operating point for the Allison Model 570-K engine, are shown in Figs. 13-15 for the three baseline fuels. (Note that parametric variation in equivalence ratio inherently includes variation in rich zone residence time and swirl strength.) The capability of the RQL combustor to achieve low NO_x with significantly different fuels and levels of FBN is clearly demonstrated in Fig. 13. Because the levels of FBN in the RESID and SRC-11 fuels exceed 0.25 wt. percent, the NO_x goal under this DOE/NASA program is 140 ppm. (The EPA Stationary Gas Turbine NO_x standard for the Allison Model 570-K is 230 ppm). Unburned hydrocarbon emissions from the combustor are not presented since the levels measured at maximum continuous power were all below 20 ppm and nearly half the measurements were below 5 ppm. To achieve the goal of 99 percent combustion efficiency, CO emissions must be kept below 970 ppm at maximum continuous operation (310 ppm at idle). The goal for exhaust smoke is a maximum smoke number of 20.

Downloaded 01 Jun 2010 to 171.66.16.62. Redistribution subject to ASME license or copyright; see http://www.asme.org/terms/Terms_Use.cfm

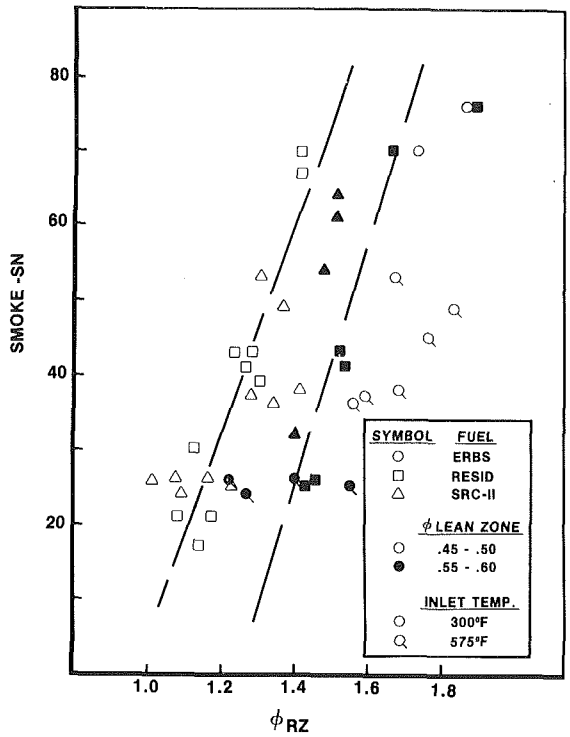

Fig. 15 Smoke versus zone equivalence ratio

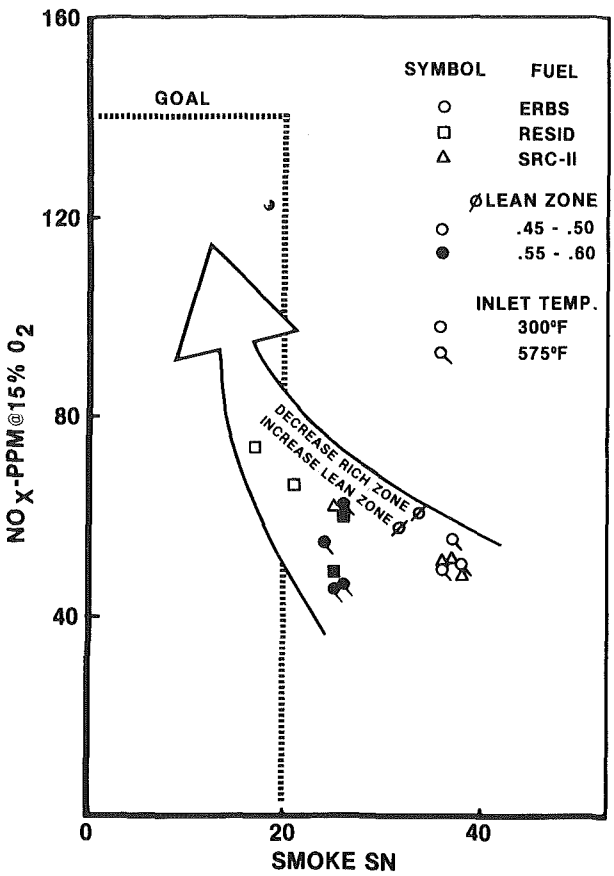

Fig. 16 NO_x versus smoke at optimum rich zone equivalence ratio

The emissions data shown in Figs. 13-15 were measured at a variety of different conditions. First there are three different fuels represented: ERBS, RESID, and SRC-II. Next there are two combustor inlet temperatures plotted: 300°F (422K) and 575°F (575K) (flagged points). Finally there are two ranges of lean zone equivalence ratios and total mass flow represented: lean zone equivalence ratio ranges of 0.45 to 0.50 and 0.55 to 0.60 with total mass flows of rated airflow and 125 percent rated airflow (20 percent reduction in residence time). However, for all test the overall fuel air ratio is maintained at maximum continuous power specification. The variations in both rich and lean zone equivalence ratios occurred because of adjustments to the combustor variable geometry required to maintain a 6 percent system pressure drop, while varying both rich zone equivalence ratio and total mass flow. Inlet temperatures were below the normal operating level of 661°F (622K) to avoid high metal temperatures in the combustor rich zone hardware due to air leakage. The temperature of the rich zone hardware varies directly with rich zone equivalence ratio. As equivalence ratio increases cooling air decreases, thus reducing cooling effectiveness of the regenerative/convective cooling system.

Even though the data in Fig. 13 show some scatter, trend lines drawn through the NO_x data for each baseline fuel show a minimum in the NO_x curve in the region of 1.4 rich zone equivalence ratio. Only the ERBS fuel was operated at two different inlet temperatures. Comparing the ERBS data illustrates how NO_x increased while CO and smoke in Figs. 14 and 15 decreased as inlet temperature was raised.

No_x emissions appear to be controlled only by inlet temperature and the rich zone equivalence ratio. Changes in the lean or dilution zone had no observable effect on NO_x. Carbon monoxide emissions and smoke, on the other hand, were influenced significantly by both rich zone and lean zone equivalence ratio, as well as by combustor inlet temperature. Both CO and smoke vary directly with rich zone equivalence ratio and inversely with lean zone equivalence ratio. The higher temperatures in the lean zone due to either a higher equivalence ratio or a higher inlet temperature increase the CO reaction rate and resulted in lower CO in the combustor exhaust.

To simultaneously achieve the NO_x and smoke goals might necessitate a slight compromise to achieving minimum NO_x. Because of the sizable margin in the NO_x signature (see Fig. 13) and the requirement to reduce smoke (see Fig. 15), the combustor can be operated at a nonoptimized for NO_x rich zone equivalence ratio, in the 1.2 to 1.3 range, to produce less smoke in the rich zone while accepting an increase in NO_x. Also, it appears desirable to operate at higher lean zone equivalence ratios, in the range of 0.60 to 0.65 (increasing thermal NO_x) to consume more of the smoke in the lean zone. This NO_x versus smoke tradeoff is indicated in Fig. 16 where the data represents rich zone equivalence ratios of 1.4.

Conclusions

A fuel tolerant, variable geometry, regenerative/convectively cooled staged air combustor has been designed and tested. Preliminary test results indicate that the concept has the potential to meet emissions requirements at maximum continuous power operation. However, airflow sealing and improved fuel/air mixing are necessary in order to meet program goals. Further testing will be carried out to determine the staged air configuration which meets all emissions requirements and determine operational characteristics over the entire engine operating range.

Acknowledgments

The work described in this paper is a part of the DOE/LeRc "Advanced Conversion Technology Project" (ACT). The program is a multiple contract effort with funding provided

Downloaded 01 Jun 2010 to 171.66.16.62. Redistribution subject to ASME license or copyright; see http://www.asme.org/terms/Terms_Use.cfm

by the Department of Energy and Technical Program Management provided by NASA LeRc.

The DOE Program Manager is Mr. Warren Bunker of the Heat Engines and Heat Recovery Division of the Office of Coal Utilization.

Prof. A. H. Lefebvre, Riley Prof. of Combustion at Purdue University, is acknowledged for his contribution to the design criteria for this combustor.

The authors would like to express their appreciation to Mr. J. G. Tomlinson and Mr. S. B. Reider of DDA Combustion Research and Development and Mr. R. L. Johnson of the DDA Test Department for their contribution to the design and testing of this combustor. The efforts of Linde Div. of Union Carbide Corp. and Parker Hannifin Corp. in thermal barrier coating and fuel injection, respectively, were also significant.

References

1 Lister, E., Niedzwiecki, R. W., and Nichols, L., "Low NO_x Heavy Fuel Combustor Program," ASME Paper 80-GT-69, 1980, Gas Turbine Conference, New Orleans.

2 Troth, D. L., "Investigation of Aircraft Gas Turbine Combustor Having Low Mass Emissions," ASME Paper 74-GT-36, 1974 Gas Turbine Conference, Zurich, Switzerland.

3 Verdouw, A. J., "Evaluation of a Staged Fuel Combustor for Turboprop Engines," ASME Paper 76-WA/GT-5, 1976, Winter Annual Meeting, New York, N.Y.

4 Pierce, R. M., Smith, C. E. and Hinton, B. S., "Low NO_x Combustor Development for Stationary Gas Turbine Engines," *Proceedings of the Third Stationary Source Combustion Symposium EPA-600/7-79-050 C*, Vol. III, Feb. 1979.

5 Prok, G. M., and Seng, G. T., "Initial Characterization of an Experimental Referee Broadened-Specification (ERBS) Aviation Turbine Fuel," NASA TM 81440, Jan. 1980.

6 Martin, F. J., and Dederick, P. K., "NO_x From Fuel Nitrogen In Two-Stage Combustion," Sixteenth Symposium (International) on Combustion, 1976.

7 Takagi, T., Tatsumi, T., and Ogasawara, M., "Nitric Oxide Formation from Fuel Nitrogen in Staged Combustion: Roles of HCN, and NH_i," *Combustion and Flame*, Vol. 35, 1979.

8 Ballal, D. R., and Lefebvre, A. H., "Combustion Efficiency of Gas Turbine burning Alternate Fuels," AIAA/SAE 14th Propulsion Conference, Paper No. 78-1000.

9 Longwell, J. P., et al, "Flame Stabilization by Bluff Bodies and Turbulent Flames in Ducts," *Fourth Symposium (International) on Combustion*, Williams and Wilkins, 1953, pp. 90–97.

10 Williams, G. C., et. al., "Flame Stabilization and Propagation in High Velocity Gas Streams," *Third Symposium on Combustion Flame and Explosion Phenomena*, Williams and Wilkins, 1949.

11 Longwell, J. P., et al, "Flame Stabilization by Baffles in a High Velocity Gas Stream," *Third Symposium on Combustion Flame and Explosion*, Williams and Wilkins, 1949.

12 Herbert, M. V., "A Theoretical Analysis of Reaction Rate Controlled System: Part II," *Eighth Symposium (International) on Combustion*, Williams and Wilkins, 1962.

13 Spadaccini, L. J., "Autoignition Characteristics of Hydrocarbon Fuels at Elevated Temperatures and Pressures," ASME Paper No. 76-GT-3, 1976.

Downloaded 01 Jun 2010 to 171.66.16.62. Redistribution subject to ASME license or copyright; see http://www.asme.org/terms/Terms_Use.cfm

Low NOx Combustion Systems for Burning Heavy Residual Fuels and High-Fuel-Bound Nitrogen Fuels

D. J. White

A. Batakis

R. T. LeCren

Solar Turbine Incorporated,
San Diego, Calif. 92138

H. G. Yacobucci

NASA Lewis Research Center,
Cleveland, Ohio 44135

The work described in this paper is a part of the Department of Energy/Lewis Research Center (DOE/LeRC) "Advanced Conversion Technology" (ACT) project. The program is a multiple contract effort with funding provided by the Department of Energy and technical program management provided by NASA LeRC. The increasingly critical situation concerning the world's petroleum supply necessitates the investigation of alternate fuels for use in industrial gas turbines. Environmentally acceptable operation with minimally processed petroleum based heavy residual and coal derived synthetic fuels requires advanced combustor technology. The technology described in this paper was developed under the DOE/NASA Low NOx Heavy Fuel Combustor Concept Program (Contract DEN3-145). Novel combustor concepts were designed for dry reduction of thermal NOx, control of NOx from fuels containing high levels of organic nitrogen, and control of smoke from low hydrogen content fuels. These combustor concepts were tested by burning a wide variety of fuels including a middle distillate (ERBS), a petroleum based heavy residual, a coal derived synthetic (SRC-II), and various ratios of blends of these fuels which included nitrogen doping with pyridine. The results of these tests show promise that low NOx emissions and high efficiencies can be obtained over most of the operating range of a typical industrial gas turbine engine.

Introduction

The Environmental Protection Agency has recently promulgated emission standards for stationary gas turbines. These standards at present are composed of three groups differentiated by the energy input level into the gas turbine. For engines with energy input levels below 10.7 GJ/h, no NOx emission limits have been imposed. Gas turbines with fuel energy inputs between 10.7 and 107.2 GJ/h are required to meet a limit of 150 ppm NOx converted to 15 percent O_2 for the next five years and then 75 ppm thereafter. Engines with higher than 107.2 GJ/h energy needs must meet the NOx level of 75 ppm corrected to 15 percent O_2. Emission regulations for CO and hydrocarbons are not presently required and do not appear likely in the future in light of high efficiency requirements normally imposed by the user.

Currently, the only means available for meeting these standards involves water (or steam) injection into the combustor. Unfortunately, this technique involves a capital cost of at least 10 to 15 dollars per kw and a fuel consumption increase on the order of 2 to 3 percent. In addition, increased maintenance costs are probable. For obvious reasons, a system which can avoid the use of water injection is desirable.

In addition the specter of diminishing petroleum supplies has, in the U.S., spurred growing interest in utilizing coal-derived fuels especially for utility and industrial gas turbines. Fuels derived from coal, and in particular liquids, contain much higher levels of fuel bound nitrogen than the equivalent petroleum fuel that is to be displaced.

The fuel bound nitrogen in such fuels can be almost quantitatively converted (up to 80 percent) in conventional combustors, and in combustors employing lean primary zones, aimed at reducing thermal NOx. In this paper, the low emission combustion of SRC-II, a fuel derived from coal, is addressed together with the combustion of ERBS a petroleum based fuel resembling JP-5.

In burning the former, a staged combustion system employing a rich primary and lean secondary zone was adopted, this being one of the more promising approaches for reducing fuel nitrogen conversion. For the latter, a lean primary approach was selected, which was based on extensive past work.

The goals of the work described herein were to obtain NOx emissions of 75 ppm corrected to 15 percent O_2 for fuel bound nitrogen levels up to one percent by weight and 37 ppm at 15 percent O_2 for the ERBS fuel. These emission goals were to be attained without any sacrifice of engine efficiency. Thus, limits on combustion efficiency (99.0 percent), pressure drop (6 percent) and pattern factor (0.25) were also imposed at all conditions including base load power and at peak power conditions.

Combustor Concepts

The following paragraphs contain a brief description of the

Contributed by the Gas Turbine Division of THE AMERICAN SOCIETY OF MECHANICAL ENGINEERS and presented at the Gas Turbine Conference and Products Show, March 9-12, 1981, Houston, Texas. Manuscript received at ASME Headquarters December 11, 1980. Paper No. 81-GT-109.

Copyright © 1982 by ASME

Downloaded 01 Jun 2010 to 171.66.16.62. Redistribution subject to ASME license or copyright; see http://www.asme.org/terms/Terms_Use.cfm

basic combustor concepts evaluated in this study for achieving low NOx emissions.

In all the combustor concepts investigated, limited (low) reaction temperatures are required for low NOx production, and because of this all chemical reaction rates are slowed. The resultant slow burnout of partially oxidized fuel material can, if not accounted for, produce low combustion efficiencies. Thus, long residence time combustors maximizing, the uniformity of all temperature distributions, mixing rates, and zonal efficiencies were selected as the most appropriate systems.

Rich-Lean Configuration. The primary basic combustor approach utilized by Solar for the minimization of both thermal and fuel-bound NOx involves staged combustion, using a rich primary zone and a lean secondary zone. In this staged-combustion system the fuel-rich primary zone burns approximately 70 percent of the total fuel in an oxygen-deficient primary reaction zone. Overall and local reaction temperatures and oxygen concentrations are controlled in this system to provide a homogeneous reaction. The partially oxidized combustion gases then mix with secondary air. These later reactions are inhibited sufficiently to allow complete mixing to be accomplished. Complete burnout of the remaining fuel in the premixed secondary reaction zone then occurs at the limiting NOx generation temperature. Conversion control of both atmospheric nitrogen and fuel-bound nitrogen to NOx is thus possible with this combustion process. The feasibility of this concept had been demonstrated on a previous in-house program by burning nitrogen doped natural gas in a full-scale atmospheric rig. The more complex liquid fuel injection process utilized in the combustors described was modelled on the natural gas injection scheme by a potentially simple fuel injection system.

In a rich-lean system an effective primary zone should operate fuel-rich overall, consume nearly all of the fast reacting species while using up most of the available oxygen, and leave behind only the slow reacting carbon monoxide (CO) and intermediaries. Thereby little NOx would be produced. Little or no reaction is desired during the critical secondary air addition until a completely premixed continuum is achieved. During this mixing process the local air-fuel ratio passes through its stoichiometric value where reaction must be avoided to maintain low NOx production. To achieve this, the secondary reaction zone must maintain a level of premixedness on the microscale that permits fuel burnout at limited reaction temperatures, thus avoiding secondary NOx production.

Lean-Lean. The second basic approach tested was the lean-lean combustion system. In this low NOx combustion approach, air and fuel is vaporized and mixed as far as is possible before the charge enters the lean primary zone of the combustor. The overall fuel/air rato in this vaporization/mixing device is maintained at or below the stoichiometric fuel/air ratio. Vaporization and mixing is maximized through the provision of the longest possible residence time consistent with the avoidance of autoignition and flashback. The primary zone itself is a near well-stirred reactor to ensure as near a homogeneous mixture of reactants and products as possible.

The justification for the inclusion of this approach is twofold; in the first instance, because of its proven track record in providing low thermal NOx, it was used as a standard or baseline for the other concepts. Essentially the lean system will provide low thermal NOx but high levels of fuel bound nitrogen NOx (probably close to complete conversion of the fuel bound nitrogen). Thus any system that can produce lower levels of NOx must be providing a measure of inhibition to the conversion of fuel bound nitrogen and is worthy of further development. The secondary reason for the inclusion of this approach was simply one of "safety", if a serious fuel-bound sulfur-nitrogen interaction had been discovered, one that produces high levels of NOx, it would have been necessary to adopt the lean approach and accept the emissions obtained.

Summary of NOx Control Techniques Effective for Fuel Bound Nitrogen. Conversion of organic fuel-bound atomic nitrogen such as reported by Fenimore, de Soete, and Levy becomes dominant when high nitrogen content fuels are burned. Since local reaction temperatures have little effect on the rate of NO formation based on this mechanism, local oxygen concentration is the only control parameter.

Effective NO emission reduction in combustion systems burning fuels with a high nitrogen content is possible by staged combustion, exhaust gas recycle at or above stoichiometric conditions, or a combination of both.

Burning fuel in a fuel-rich environment will limit local reaction temperatures as well as oxygen availability. The slower NO formation reaction has to compete with the much faster radical oxidation for the viable oxygen, thereby inhibiting the NO formation. This first stage is followed by a mixing zone stage in which the partially reacted air/fuel mixture must be followed by a mixing zone stage in which the partially reacted air/fuel mixture must be thoroughly mixed with fresh secondary air without significant reaction. The burnout of the remaining fuel will then be completed in the fuel-lean secondary zone similar to the concept mentioned above.

Since the overall NOx exhaust emission must be reduced, both thermal and fuel NOx must be minimized in any given system. This can be best achieved with a two-stage combustion process wherein 70 to 80 percent of the fuel is reacted under reducing (rich) conditions and fuel burnout following secondary air mixing in a fuel-lean controlled reaction temperature environment.

A staged combustion process was thus adopted wherein all the fuel is partially reacted in the fuel-rich primary zone, and having adequate residence time to permit fuel nitrogen to convert into nitrogen compounds other than NO or NO_2. Secondary air is introduced in a continuous manner, so as to achieve a high degree of mixedness in a microscale level without significant reaction. Fuel burnout of the fully premixed, partially oxidized fuel, air, gas, and secondary air mixtures at a lean air/fuel ratio, will complete the second-stage reaction before addition of dilution air.

Summary of NOx Control Techniques Effective for Minimizing Atmospheric Nitrogen Fixation. The conversion of atmospheric nitrogen to NO and then to NO_2 as described earlier depends strongly on the reaction zone oxygen concentration and temperature conditions. Both these factors are controlled by the zonal fuel/air ratio or equivalence ratio, and to a lesser by the inlet air temperature and pressure. The latter two factors influence the reaction temperature to an extent, but to a much lesser degree than the fuel/air ratio.

Because of the strong dependence on oxygen concentration and temperature the fuel/air ratio in the primary zone is critical and must be controlled within relatively narrow limits. Because of the nature of the reaction rates between air and a hydrocarbon, there are generally two fuel/air ratios at which low NO could be produced. One at a lean fuel/air or equivalence ratio (of the order of half of stoichiometric), and the other at a rich equivalence ratio (of the order of 1.2 to 1.5 times stoichiometric). The lean equivalence ratio point achieves low NOx levels mainly by controlling the temperature in the reaction zone to below a critical value. This latter temperature level can only be maintained through a

Downloaded 01 Jun 2010 to 171.66.16.62. Redistribution subject to ASME license or copyright; see http://www.asme.org/terms/Terms_Use.cfm

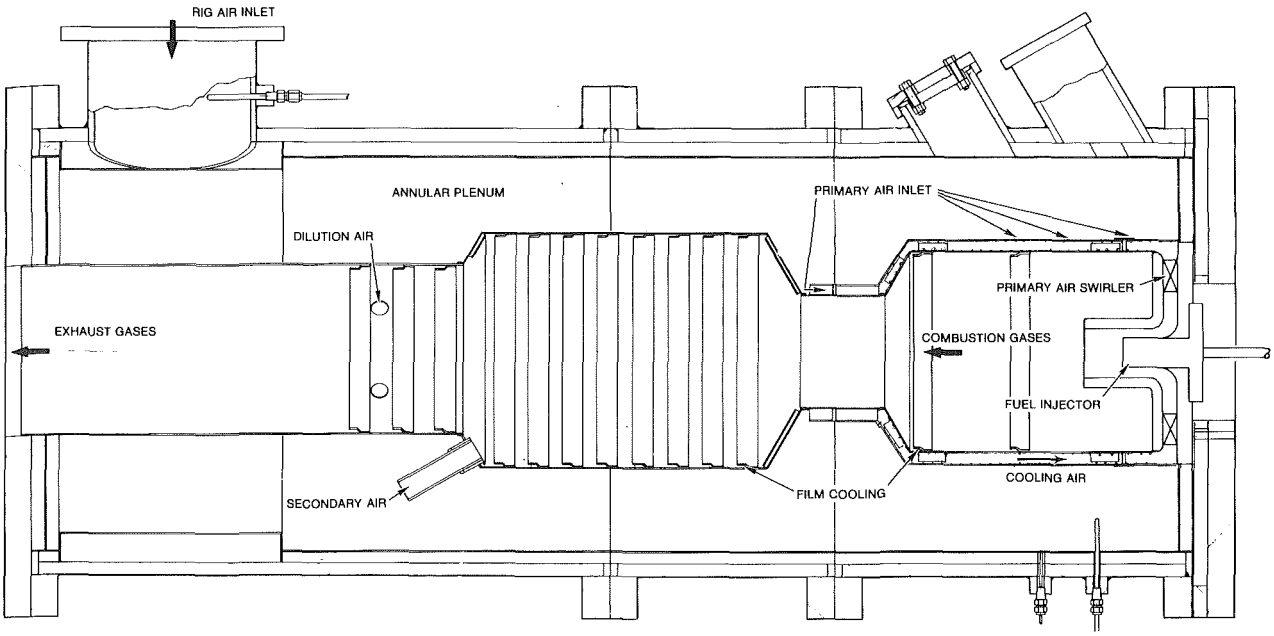

Fig. 1 Lean-lean combustion system

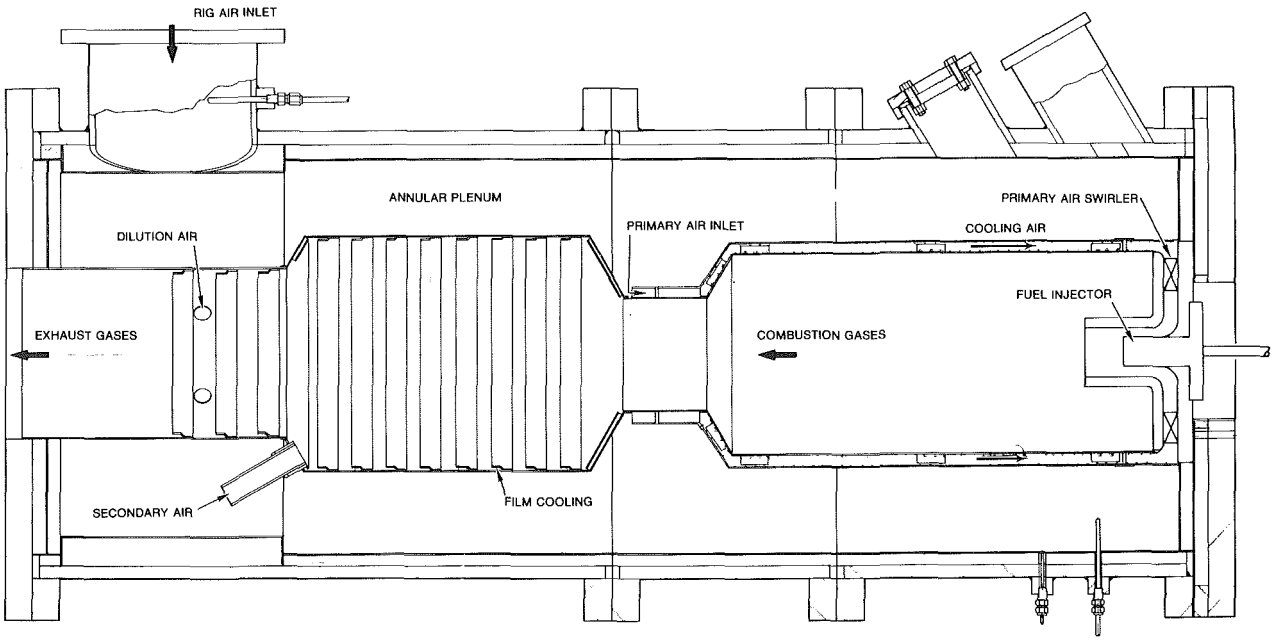

Fig. 2 Original rich-lean combustor configuration

careful control of the fuel/air ratio entering the reaction zone. Premixing of the fuel and air can provide the required control and this technique has been proven in the past both on test rig combustors and in engines.

The fuel rich point utilizes both reduced temperature and oxygen levels to control the formation of NO. As a consequence reaction temperatures can be higher than the lean equivalence ratio point. In addition it appears that less precision is needed in the control of the fuel/air ratio. Generally a range of equivalence ratios as mentioned above can be tolerated and this lessens the need for high levels of "mixedness" in the entering fuel/air charge.

The process required for the minimization of thermal NOx is one of either control of reaction temperature alone, or control of both reaction temperature and oxygen concentration. This can be achieved in a singularly fashion by operating the reaction zone at a very fuel lean condition or in a fuel rich fashion. Other ways of reducing the reaction temperature have been proposed and these usually involved operating the primary zone under non-adiabatic conditions. Water cooling and radiation cooling have all been proposed and investigated with mixed success.

To achieve the control over reaction zone temperature and oxygen concentrations (with the exception of the nonadiabatic systems) premixing of the fuel and air to some degree will be needed.

Combustor Design

The actual lean-lean and staged rich-lean combustors tested

Downloaded 01 Jun 2010 to 171.66.16.62. Redistribution subject to ASME license or copyright; see http://www.asme.org/terms/Terms_Use.cfm

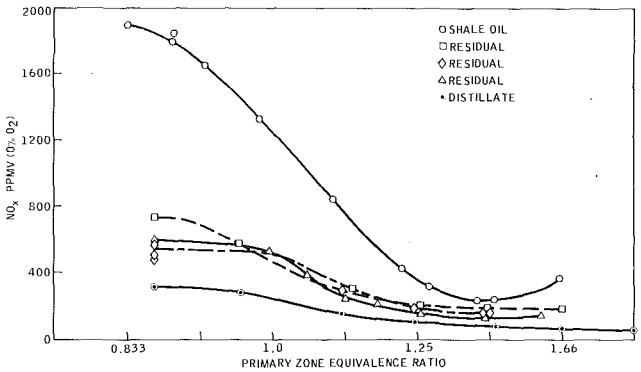

Fig. 3 NO_x emissions signature for various heavy fuels

Table 1 Carbon formation limits for various fuels

FUEL	CRITICAL O/C RATIO FOR INCIPIENT CARBON FORMATION		EQUIVALENCE RATIO FOR CARBON FORMATION AT WELL-STIRRED CONDITIONS
	PRE-MIXED BUNSEN FLAME (FROM REFERENCE 1)	WELL-STIRRED CONDITION (FROM REFERENCE 2)	
ETHYLENE	1.67	1.43	2.11
PROPYLENE	1.79	1.40	2.16
BUTENE	2.08	1.48	2.04
BENZENE	1.75	1.75	1.538
TOLEUNE	1.92	1.71	1.50
XYLENE	2.08	1.80	1.46

in this study are shown schematically in Figs. 1 and 2, respectively. The staged rich-lean system has been modified twice during the course of testing for mechanical integrity reasons and these modifications are described with the test results. The lean-lean and rich-lean combustors which will be described here share many general design features. Any unique features pertaining to a particular configuration are pointed out.

Air at the desired inlet pressure and temperature fills the annular plenum surrounding the combustor, and enters each combustor section from there. The primary zone of the combustor utilizes a regenerative cooling scheme in which the primary air is pre-heated while convectively cooling the primary liner wall. This is accomplished by passing the air through an annulus surrounding the primary zone in a direction opposite to the main combustor gas flow. Preheating the primary combustion air is advantageous to fuel vaporization, particularly when burning heavy fuels, and this enhances pre-mixing of the fuel and air. In addition to this convective cooling, the lean-lean system utilizes two film cooling strips on the primary wall. The primary air in both combustors after being used for cooling, passes through a swirler prior to the point of fuel injection. The swirlers for each of the combustors have been carefully sized to provide the correct air flow-pressure drop characteristics.

The secondary zone of the combustor utilizes opposed-jet mixing to accomplish rapid and thorough mixing of the secondary air with the primary exhaust gases. The secondary zone approaches the condition of a well-stirred reactor and assures complete overall combustion. The linear of the secondary zone is cooled with film cooling air drawn from the rig plenum.

The transition from the primary zone to the secondary zone is a necked down throat section with a decreased flow area. This contraction prevents entrainment of the secondary air into the primary zone recirculation eddy, and also increases the velocity of the gases entering the secondary zone, for better mixing. After leaving the secondary zone, the combustion gases pass through a dilution section, with film-cooled walls, and exit the combustor.

The fuel injectors used in these combustion systems were designed to provide varying degrees of premixedness and to operate over the full range of test conditions. Each of the injectors used in these combustors utilized some form of air assist to atomize the fuel as it flowed over a sharp lip. These injector designs were based on previous fuel injector development work conducted in-house at Solar Turbines Incorporated.

Generally, the preliminary design of both the rich and lean primary zone combustors in terms of geometric size is based on empirical correlations. For the design of the rich primary zone for example, a minimum volume was selected that would provide carbon monoxide levels below 100 ppmv (at 15 percent O_2), from a parameter, defined as $\Theta = (p^{1.75} \times \text{vol} \times \exp(T/300) \times [10 \times \phi]^{0.82})/\text{w}$.

From past work, the value of θ necessary to provide a low CO level (high efficiency) has been fixed in the area of 70 to 75 $\text{atm}^{1.75}$ s per m^3/kg. A length to diameter ratio of 2 has also been estimated as being desirable in terms of minimizing surface area to length while providing a reasonable cross-sectional flow area to maintain low frictional pressure losses.

From the above a minimum diameter and length was established for each of the main operating power points. The correlation of NO reversion as a function of residence time provided in reference [1] was then used to check the necessary rich zone total residence time requirement. A "design level" equal to the program NOx goal of 75 ppmv (at 15 percent O_2) for a fuel with bound nitrogen of the order of 0.6 percent by weight was selected on this basis for determining a nominal primary zone residence time of 60 ms. This later residence time was found to be the limiting factor on geometry, and produced a much larger volume than the above correlation. Arbitrarily the length to diameter ratio of two was retained for the increased residence time requirement.

The lean secondary reaction zone was similarly designed based on a theta (θ) factor derived from earlier work. Generally this correlation factor was found to lie between 9 and 10 $\text{atm}^{1.75}$ s per m^2kg, and the present unit was designed to provide such a level A length to diameter ratio for the zone of 1.3 was also fixed again based on past work and on the requirement of the 30 deg. angled jets to merge before dome impact. This resulted in a nominal secondary residence time of 24 ms. Dilution zone dimensions were also fixed from conventional design considerations. The length and diameter were fixed based on obtaining an outlet pattern factor of 0.25. Generally correlations of pattern factor with dilution zone length to diameter for various values of the pressure drop divided by the dynamic head into the zone were used to estimate lengths and cross-sectional areas or diameters.

The rich-lean combustion system has been designed to run at a nominal primary zone equivalence ratio of 1.3. Supporting data for the selection of the 1.3 value for the equivalence ratio of the fuel rich primary zone is provided by Fig. 3, which shows that low conversions of fuel bound nitrogen can be obtained at equivalence ratios greater than 1.2. Data on smoke production from the combustion of various pure compounds likely to be found in coal oils (see Table 1) show that smoke is likely to be produced at equivalence ratios greater than 1.45. Thus an equivalence ratio of 1.3 (adjustable to 1.35) was chosen as representing a reasonable compromise.

The lean secondary zone of this system operates at a nominal equivalence ratio of 0.5. This value was chosen to keep the flame temperatures below approximately 1427°C (2600°F) and thus inhibit thermal NOx formation.

Downloaded 01 Jun 2010 to 171.66.16.62. Redistribution subject to ASME license or copyright; see http://www.asme.org/terms/Terms_Use.cfm

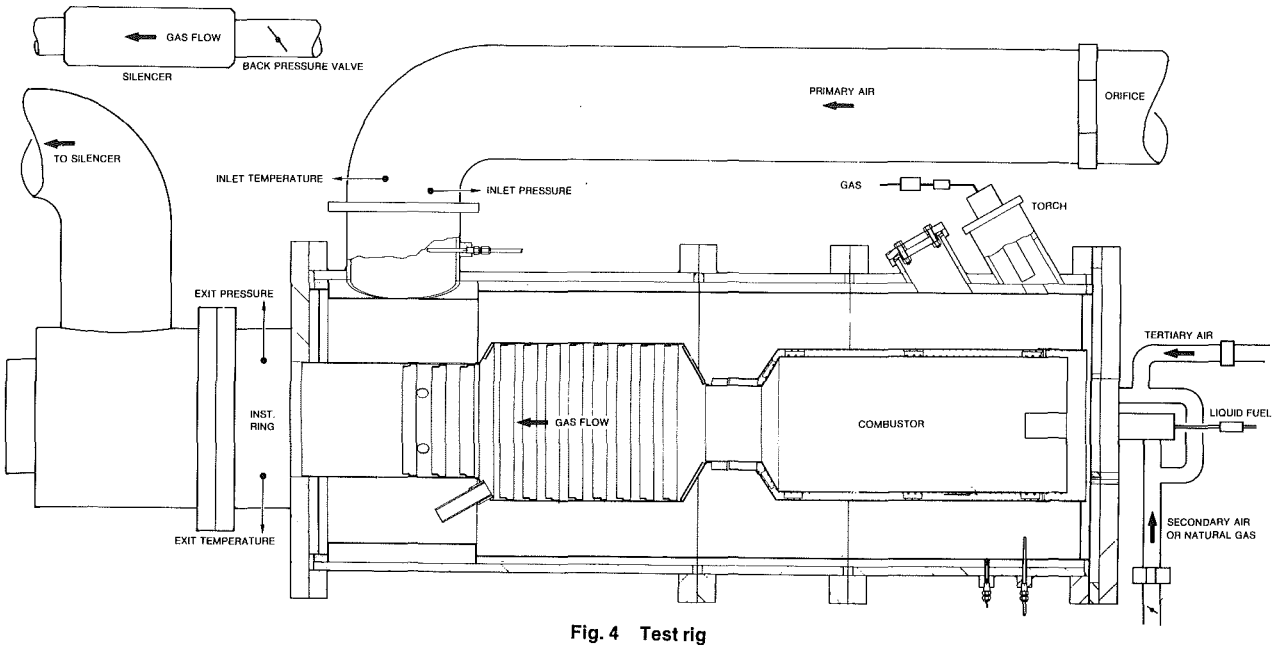

Fig. 4 Test rig

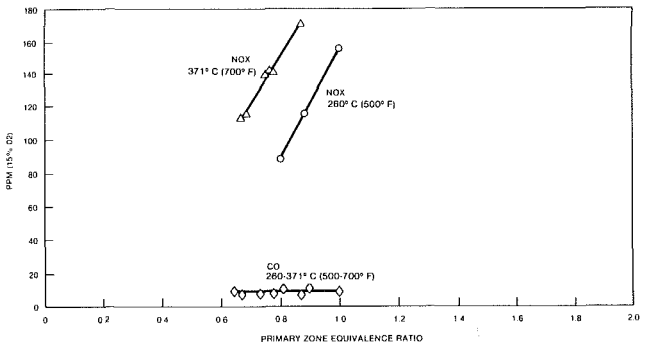

Fig. 5 Effect of inlet air temperature on emissions from lean-lean combustor burning ERBS fuel (0.1 percent N) at C584 kPa

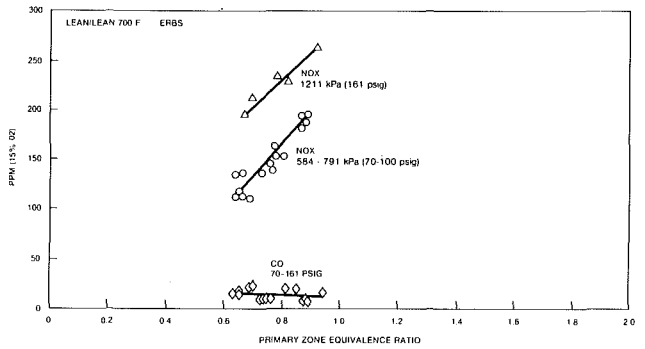

Fig. 6 Effect of pressure on emissions from lean-lean combustor burning ERBS fuel (0.1 percent N) with 371°C inlet air

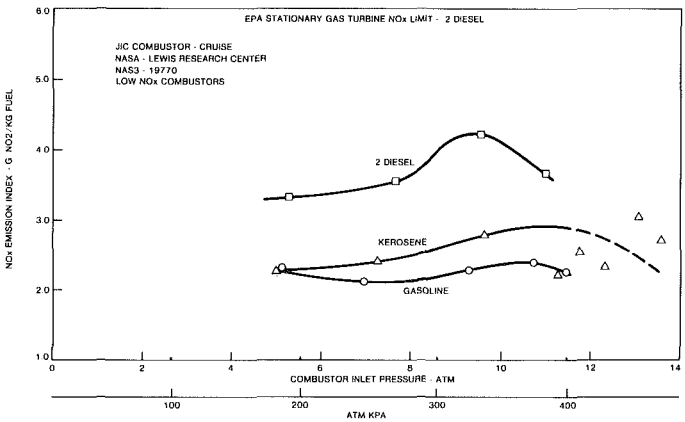

Fig. 7 Comparative emissions from a typical jet induced combustor (JIC)

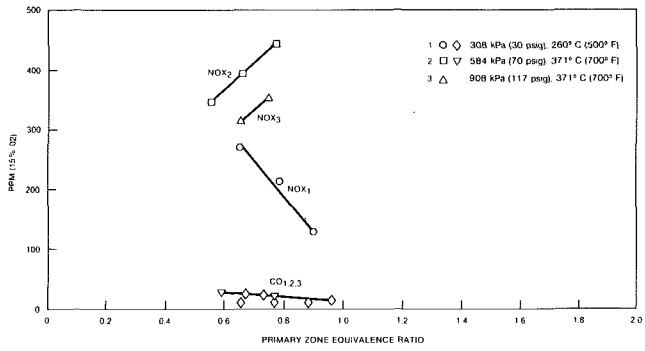

Fig. 8 Emissions from lean-lean combustor burning SRC-II middle distillate fuel (1 percent N) at several inlet conditions

Rig Description. A schematic of the basic test rig is shown in Fig. 4. The rig air supply is raised to the appropriate combustor inlet temperature with an indirect, gas-fired preheater. The preheater is rated up to a maximum pressure of 1723.5 kPa (250 psia) and is capable of raising the air supply from normal ambient temperature levels to a maximum of 593°C (1100°F) over a range of mass flows from 0.09 to 1.59 kg/s (0.2 to 3.5 pps). At inlet temperatures up to 204°C (400°F) the preheater is capable of operating with mass flows up to 2.268 kg/s (5.0 pps). The airflow is supplied from a system of electric motor driven reciprocating compressors capable of supplying up to 2.22 kg/s (4.9 pps) at a maximum of 1723.5 kPa (250 psia) on a continuous basis. Higher mass flows at somewhat lower pressures are available from a pair of Solar Saturn driven centrifugal air compressors.

Flow from the preheater is passed through insulated ducting containing an ASME orifice run for metering purposes to an annular plenum surrounding the combustor. Air flows from this plenum through the combustor and is

Downloaded 01 Jun 2010 to 171.66.16.62. Redistribution subject to ASME license or copyright; see http://www.asme.org/terms/Terms_Use.cfm

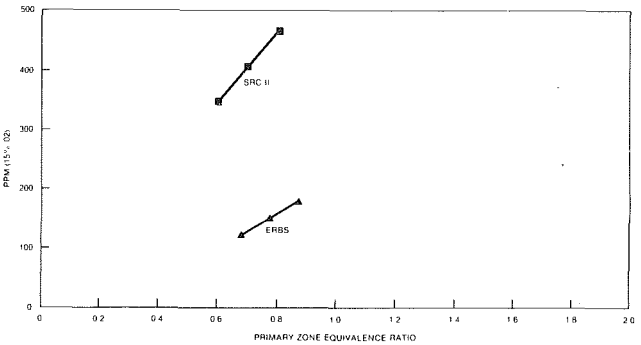

Fig. 9 Comparison of emissions produced from ERBS (0.1 percent) and SRC-II middle distillate fuel (1 percent N) fuels burned in the lean-lean combustor at 584 kPa with 371°C inlet air

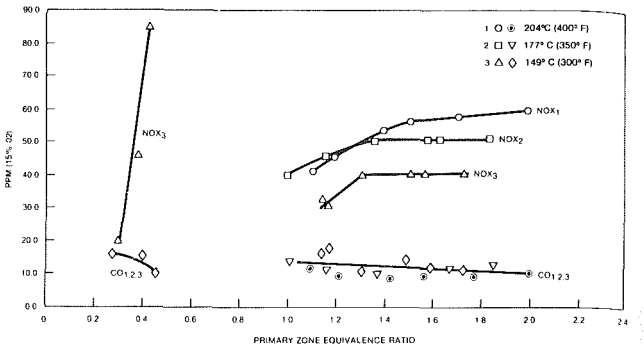

Fig. 10 Emissions from rich-lean combustor burning natural gas fuel at 308 kPa

exhausted to atmosphere via a back pressure butterfly valve, an instrumented tailpipe section and a silencer. The instrumented tailpipe section measures exhaust gas temperatures, pressures and samples the exhaust gases for emissions analysis. An exhaust duct piece arranged as a "Tee" contains a high pressure quartz window which allows a view of the combustor along its axis and thus provides a view of the flame.

The combustor is mounted on a flange which is attached to the end of the test rig. This allows easy removal and installation of the combustor. The fuel injector is also mounted on this flange and can be removed separately from the combustor. The rig itself has removable spool pieces which can be used to adjust its length to accommodate various combustor configurations.

The fuel supply consists of two 50 gallon drums located outside of the actual test cell. Fuel is pumped from these drums via a low pressure boost pump which ffeeds a high pressure pump. This system is capable of supplying fuel at 5515 kPa (800 psig) over the range of fuel flows required in this study. A valving arrangement allows easy switching from one barrel of fuel to the other during testing. This is particularly useful when switching from one type of fuel to another. A series of drains and flush lines have been provided to avoid contamination between the various fuels to be used, and to allow the removal of debris and varnish deposits in the turbine flow meters and other sensitive equipment pieces. The flushing fluid is kerosene but nitrogen can also be used to purge and dry the fuel lines.

Typical instrumentation includes C – A thermocouples for combustor inlet and outlet total temperatures, Kiel probes for combustor section inlet and outlet total pressures with both total and static pressures displayed on Bourdon type gages, or manometers, and turbine meters for fuel flows. In addition to this, temperatures and pressures (via pressure transducers) are continuously scanned by a high speed Accurex data aquisition system and displayed on a CRT. This is particularly useful for continuous monitoring of liner skin temperatures during testing; critical temperatures are also displayed on individual temperature displays. The Accurex data aquisition system has the additional capability of storing temperature and pressure data continuously on a floppy disk, for direct computer input, or printing the data on paper tape.

Instrumentation for monitoring combustor exhaust emissions include a Beckman 315-A NDIR for CO_2 and CO, a Beckman 420 FID for unburned hydrocarbons, a Thermo Electron Corporation 10A Chemiluminescent analyzer for NO and NOx and Von Brand for particulates. The gas analysis instrumentation is maintained and operated per the provisions of SAE ARP 1256.

Test Procedure. The following test procedure has been established for all combustor tests conducted in this study. Prior to light-off, airflow through the combustor is maintained at 310 kPa (30 psig) inlet pressure, the desired inlet temperature and a specified pressure drop. Ignition is accomplished using a natural gas torch located upstream of the primary air swirler. Flame from this torch enters the primary zone with the main air and provides ignition as the primary fuel is brought in. Natural gas is used as the primary fuel initially, due to its controllability and safe ignition properties. The torch is shut off immediately after ignition is achieved.

An exit temperature of approximately 927°C (1700°F) is established using natural gas fuel. The liquid fuel to be tested is then brought in slowly as the natural gas flow is reduced, maintaining a constant exit temperature. Once the combustor is running completely on liquid fuel, the air inlet pressure and air flow are adjusted to the desired operating point. Data is generally taken over range of equivalence ratios while maintaining constant inlet pressure, inlet temperature, and airflow.

Changing from one fuel to another merely involves turning two valves in the fuel system. An adequate purge time is required to allow the new fuel to completely purge the old fuel from the system. After flowing SRC II middle distillate fuel, the system is always purged with ERBS or Kerosene.

Data is recorded by hand and by a paper tape printout on the data acquisition system. This involves reading manometers, pressure gages, digital flowmeter displays and temperature readouts.

Results and Discussion

Lean-Lean. The lean-lean combustor configuration shown in Fig. 1 was tested on both ERBS and SRC II middle distillate fuels at several different inlet temperatures and pressures. Data from these tests are presented in Fig. 5-8.

The effect of combustor inlet temperature on emissions from the ERBS fuel are shown in Fig. 5. The high thermal NOx is attributed to insufficient premixing of the fuel and air, and is thought to be a problem with the fuel injector. As expected, higher inlet temperatures increased the NOx emissions for a given equivalence ratio. The CO emissions levels were consistantly low at all conditions evaluated. Unburned hydrocarbons were negligible and no smoke was detectable throughout these tests.

The effect of inlet pressure on emissions from the ERBS fuel are shown in Fig. 6. Increasing the inlet pressure tended to increase the NOx emissions while the CO emissions level remained quite low. Note that a pronounced change in NOx was observed as the inlet pressure was raised from 793 to 1200 kPa (100 to 161 psia), while a rather negligible change was observed between 586 to 793 kPa (85 and 115 psia). This trend is similar to that observed by NASA when investigating the

Downloaded 01 Jun 2010 to 171.66.16.62. Redistribution subject to ASME license or copyright; see http://www.asme.org/terms/Terms_Use.cfm

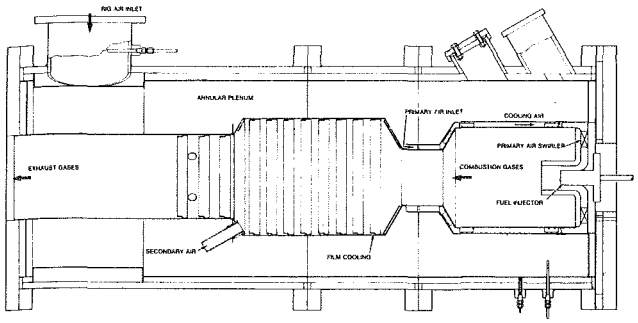

Fig. 11 Rich-lean combustor with shortened primary zone

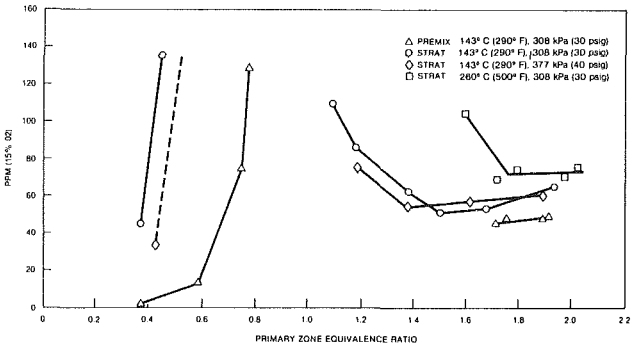

Fig. 12 NO_x emissions from rich-lean combustor burning ERBS fuel (0.1 percent N) at several different inlet conditions and with two different fuel injectors

effect of pressure on NOx emissions from No. 2 Diesel and Kerosene (see Fig. 7). As shown in Fig. 6, pressure has a pronounced effect on NOx emissions between 793 and 1206 kPa (115 and 175 psia). Again, the high thermal NOx observed from the ERBS fuel indicates insufficient pre-mixing of the fuel and air.

Emissions data from the SRC II middle distillate fuel are presented in Fig. 8, for several different inlet conditions. The reason for the negative slope of the data taken at 276 kPa (45 psia) and 260°C (500°F) is not certain. It is interesting to note that increasing the inlet pressure from 586 to 910 kPa (85 to 132 psia), while maintaining a 371°C (700°F) inlet temperature, resulted in a decrease in NOx emissions. The reverse effect was observed using the ERBS fuel (see Fig. 6). Note that the CO emissions remained low using the SRC II middle distillate fuel. No smoke was detectable and unburned hydrocarbons were negligible throughout these tests.

A comparison of the NOx emissions obtained from the ERBS fuel with those obtained from the SRC II middle distillate fuel is shown in Fig. 9. The difference between the two is largely attributed to fuel bound nitrogen. In general, the NOx emissions from the SRC II middle distillate are about three times higher than those from the ERBS fuel.

Rich-Lean Combustor. The original rich-lean combustor configuration, shown in Fig. 2, was tested using natural gas fuel. This fuel was throught to be safer and have easier light-off characteristics than liquid fuel. Tests were conducted at an inlet pressure of 310 kPa (45 psia) and at three different inlet temperatures, 149 (300), 177 (350) and 204°C (400°F). Data from these tests are presented in Fig. 10.

For rich primary zone conditions, NOx emissions were below 60 ppm (corrected to 15 percent O_2) and tended to decrease with decreasing inlet temperature. Low CO and negligible unburned hydrocarbon emissions were observed at all conditions evaluated. Unfortunately, no data were obtained between equivalence ratios of 0.6 and 1.0 because excessive liner skin temperatures were encountered in this region.

To reduce the liner cooling requirement, the rich-lean combustor was modified by shortening the length of the primary zone. Unpublished inhouse work proceeding in parallel with the study indicated that much shorter residence times could be tolerated without any change in NOx. Thus the shortening of the combustor was not considered to be detrimental to performance. A schematic of the modified combustor is shown in Fig. 11. This configuration showed significant improvement in liner skin temperatures and testing was accomplished using liquid ERBS fuel. Tests were conducted at inlet pressures of 310 and 379 kPa (45 and 55 psia) and inlet temperatures of 143 and 260°C (290 and 500°F). Data from these tests are presented in Fig. 12.

For rich primary zone conditions, NOx emissions dropped below 75 ppm (corrected to 15 percent O_2) and increased sharply as stoichiometric primary zone conditions were approached. Low CO emissions were observed at all conditions evaluated. Excessive liner skin temperatures were again encountered in the region of a stoichiometric primary zone, which prohibited testing in this area. Greater range was obtained using a stratified charge fuel injector than using a pre-mix fuel injector, although no significant difference in emissions was noted at the rich primary zone conditions.

To increase the range of operation, another modification of the primary liner cooling scheme was made to the rich/lean combustor. In this third and final configuration, shown schematically in Fig. 13, the primary liner skin is convectively cooled by both the primary air and a portion of the secondary air. This modified configuration showed still further improvement in liner skin temperatures and testing was accomplished using both ERBS and SRC II middle distillate fuels. Tests were conducted at inlet pressures from 586 to 910 kPa (85 to 132 psia) and inlet temperatures of 143 and 260°C (290 and 500°F). Data from these tests are presented in Figs. 14-22. The solid horizontal lines shown in these latter figures represents the NOx emissions limits determined from the program goals for large engines (low limit) and small engines (high limit). Each of these limits is obtained by adjusting the baseline emissions goal of 75 and 150 ppm (corrected to 15 percent O_2), for large and small engines respectively, for combustor efficiency and fuel bound nitrogen, according to recent federal regulations. The adjusted values are obtained from

$$\text{NOx (STD)} = 14.4\left(\frac{X}{Y}\right) + F \tag{1}$$

where X is the baseline emissions goal (ppm), Y is the heat rate (KJ/W-hr), and F is a constant determined by the amount of fuel bound nitrogen. For this study, $Y = 8.6$ KJ/W-hr, which is representative of the Mars gas turbine co-generation engine produced by Solar Turbines Incorporated. The values of F are 40 ppm for ERBS (0.1 percent N) and 50 ppm for SRC II middle distillate fuel (1 percent N).

The resulting adjusted NOx emissions limits are 176 ppm (SRC II) and 166 ppm (ERBS) for large engines and 301 ppm (SRC II) and 291 ppm (ERBS) for small engines. In addition to these, there is another NOx emissions limit, for ERBS fuel only, based on a more stringent program baseline goal of 37.5 ppm and adjusted to 103 ppm (corrected to 15 percent O_2) according to equation (1). This limit is represented by a dotted horizontal line in Fig. 14-17.

Data acquired using the ERBS fuel are shown in these latter figures. At each of the four conditions evaluated, the NOx emissions appear to reach a minimum below the most stringent program goal of 103 ppm, for rich primary zone conditions. Near the stoichiometric primary zone condition, the NOx emissions sharply increase but only exceed the upper NOx emissions limit (for small engines) in a narrow band of

Downloaded 01 Jun 2010 to 171.66.16.62. Redistribution subject to ASME license or copyright; see http://www.asme.org/terms/Terms_Use.cfm

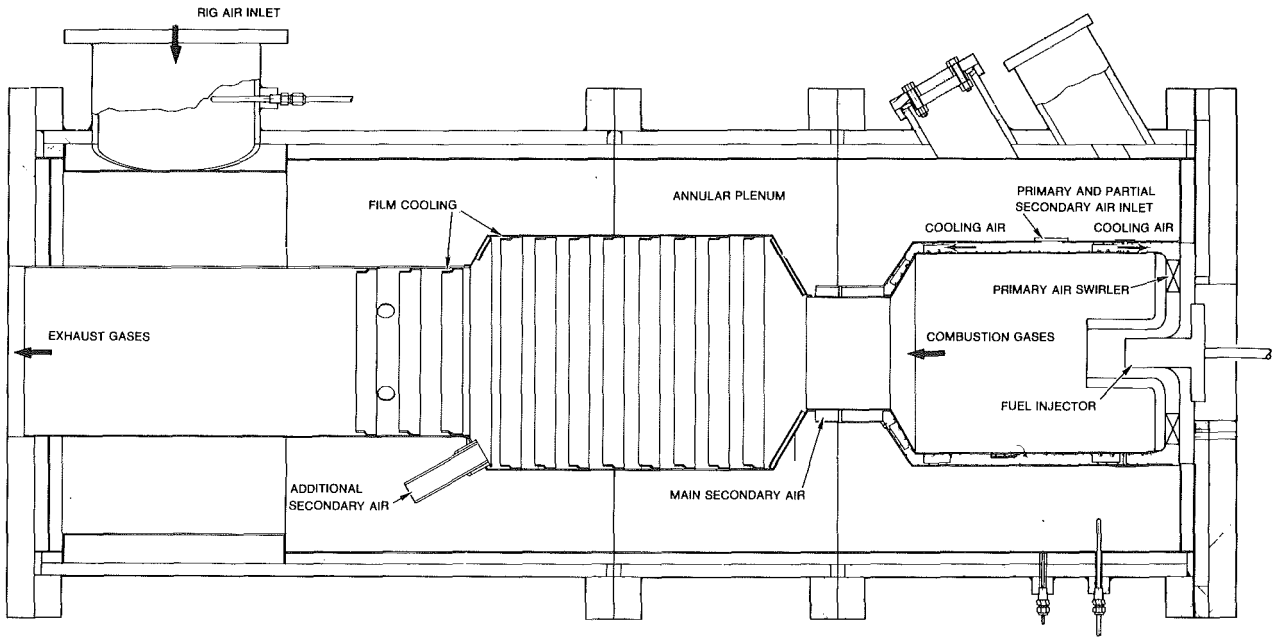

Fig. 13 Final configuration of rich-lean combustor

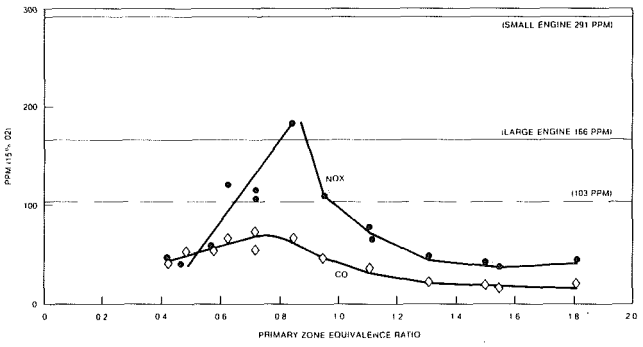

Fig. 14 Emissions from rich-lean combustor burning ERBS fuel (0.1 percent N) at 308 kPa with 143°C inlet air

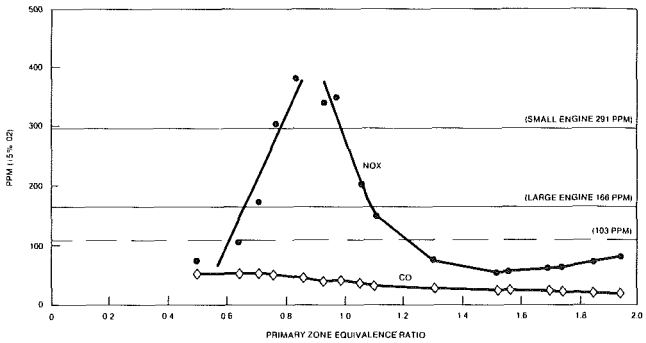

Fig. 16 Emissions from rich-lean combustor burning ERBS fuel (0.1 percent N) at 446 kPa with 260°C inlet air

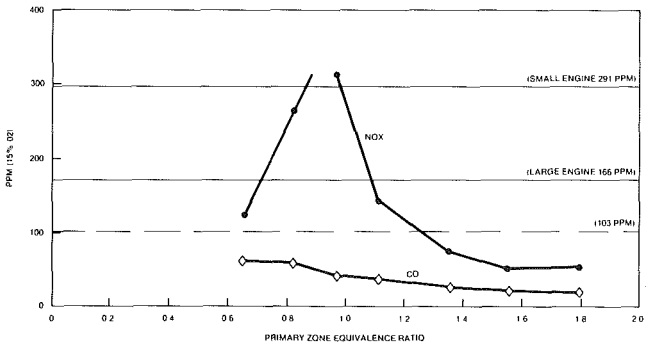

Fig. 15 Emissions from rich-lean combustor burning ERBS fuel (0.1 percent N) at 308 kPa with 260°C inlet air

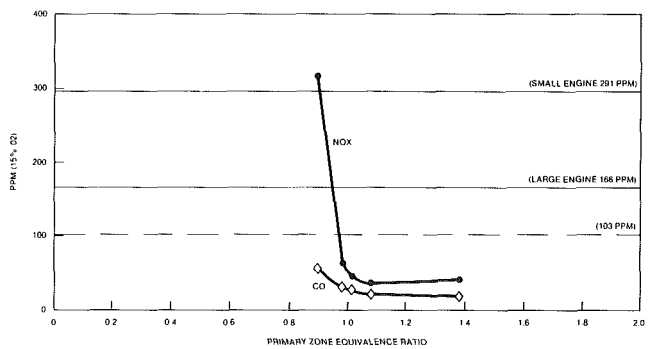

Fig. 17 Emissions from rich-lean combustor burning ERBS fuel (0.1 percent N) at 908 kPa with 143°C inlet air

equivalence ratios. The CO emissions levels are consistantly low; combustion efficiencies were always above 99 percent. No smoke was detectable and UHC emissions remained negligible throughout these tests.

The effect of inlet pressure on NOx emissions from the ERBS fuel appears to be negligible, although additional data at higher pressures should be acquired to verify this. Increasing the inlet temperature does not seem to affect the NOx emissions for rich primary zone conditions, but does appear to increase NOx emissions as stoichiometric primary zone conditions are approached. This data should also be supplemented with more testing before any firm conclusions are drawn however.

Data acquired using the SRC II middle distillate fuel are presented in Figs. 18-22, and represent three different inlet conditions. Although the data shown in Figs. 20 and 21 were acquired at the same inlet conditions, each set was taken on a different day and the two sets do not agree well. Agreement

Downloaded 01 Jun 2010 to 171.66.16.62. Redistribution subject to ASME license or copyright; see http://www.asme.org/terms/Terms_Use.cfm

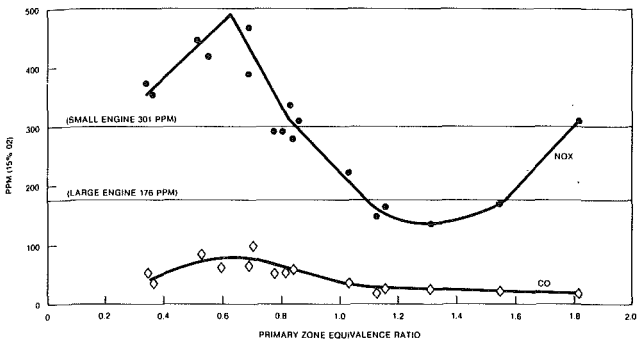

Fig. 18 Emissions from rich-lean combustor burning SRC-II middle distillate fuel (1 percent N) at 308 kPa with 143°C inlet air

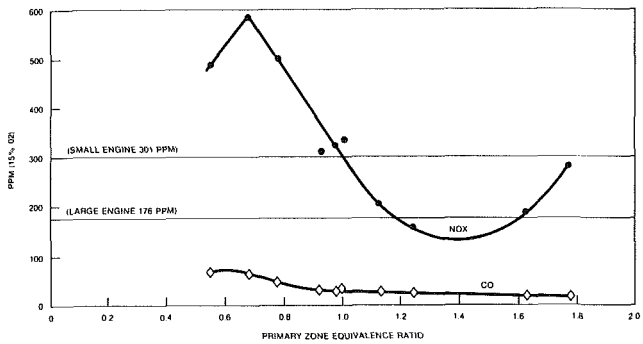

Fig. 19 Emissions from rich-lean combustor burning SRC-II middle distillate fuel (1 percent N) at 308 kPa with 260°C inlet air

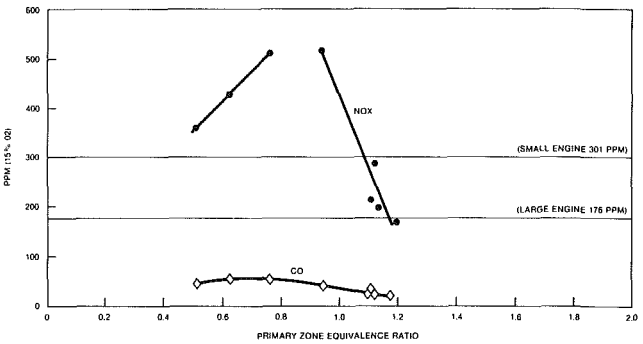

Fig. 20 Emissions from rich-lean combustor burning SRC-II middle distillate fuel (1 percent N) at 446 kPa with 260°C inlet air

between the two can be made, however, if one curve is shifted along the abscissa. This indicates a possible error in the actual values of equivalence ratio use for one or both plots. In fact, there is some question as to the accuracy of the equivalence ratios used in Figs. 18-22, since it was expected that the peak of the emissions curve would occur closer to stoichiometric primary zone conditions than indicated by these figures. Some fuel injector trouble was encountered during the latest tests which may also have affected the resulting data.

At each inlet condition evaluated, the NOx emissions appear to reach a minimum below the lower (large engine) NOx emissions limit, for rich primary zone conditions. On either side of this minimum, the NOx emissions rise sharply and exceed the upper (small engine) NOx emissions limit. The

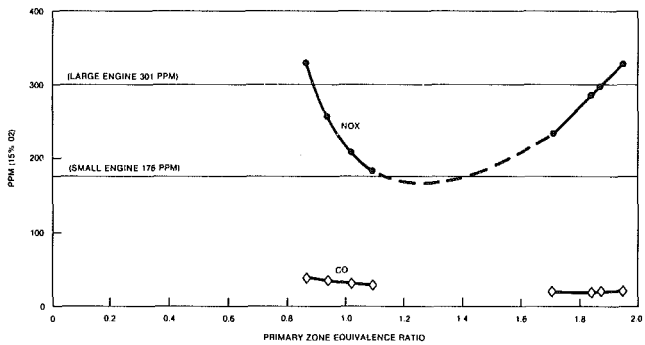

Fig. 21 Emissions from rich-lean combustor burning SRC-II middle distillate fuel (1 percent N) at 446 kPa with 260°C inlet air

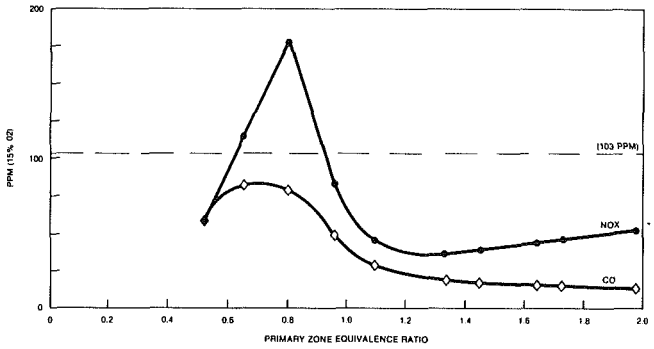

Fig. 22 Emissions from rich-lean combustor with center point pressure atomizing fuel injector burning ERBS fuel (0.2 percent N) at 308 kPa with 143°C inlet air

CO emissions level is consistantly low; combustion efficiencies remained above 99 percent. No smoke was detectable and UHC emissions remained negligible throughout these tests.

From these data, neither inlet temperature nor pressure appear to have a significant effect on NOx emissions from SRC-II middle distillate fuel, for rich primary zone conditions. Increasing the inlet temperature does seem to increase NOx emissions near the peak of the emissions curve and may decrease the width of the minimum NOx "bucket", however. Again, more data should be accumulated before any firm conclusions are made regarding this combustion system.

Acknowledgments

The work described in this paper is a part of the DOE/LeRC "Advanced Conversion Technology" (ACT) project. The program is a multiple contract effort with funding by the Department of Energy (DOE), and technical program management by NASA Lewis Research Center. The DOE Program Manager is Mr. Warren Bunker of the Heat Engines and Heat Recovery Division of the Office of Coal Utilization.

References

1 "Advanced Combustion System for Stationary Gas Turbine Engines: Volume III. Combustor Verification Testing," Interagency Energy/Environment R/D Program Report, Department of Energy.

Downloaded 01 Jun 2010 to 171.66.16.62. Redistribution subject to ASME license or copyright; see http://www.asme.org/terms/Terms_Use.cfm

An Aerothermodynamic Analysis of Transonic Compressor Rotors Containing Three-Dimensional Shocks

Xu Jian-zhong
Research Associate Professor.

Jiang Zuo-ren
Research Associate.

Yang Jin-sheng
Research Assistant.

Zhang Ying
Research Assistant.

Du Zhuan-she
Research Assistant.

Institute of Engineering Thermophysics,
Academia Sinica
Peking, China

Based on the basic aerothermodynamic equations in the differential and integral forms on an arbitrary stream surface in an arbitrary nonorthogonal curvilinear coordinate system derived in this paper, the relations between gas parameters ahead of and behind a shock on such a stream surface are established. These relations are greatly different from the relations for a plane shock because they contain the normal direction of the spatial shock, and the correlations between the stream surfaces are closer. Assuming the location and shape of the shock and using the above relations, calculations on the generalized surfaces of revolution are made, and the iterations between these calculations and the calculation on the central S_2 stream surface are completed. These computational results and comparison with those of the conventional throughflow calculation demonstrate some important features of the three-dimensional shock and the tranconic flow in an axial compressor rotor. They are also useful for the aerothermodynamic design of compressors.

Introduction

To research and develop high performance turbomachines, it is necessary to get detailed knowledge about its complicated internal flow process. Since the general theory of solving three-dimensional flow by use of two kinds of relative stream surfaces had been suggested by Wu [1] in the early 50's, much progress has been made. Using nonorthogonal curvilinear coordinates and velocity components and tensor analysis, the equations in references [2] and [3] are generalized.

In the development of transonic turbomachines, it is necessary to calculate the flow field with shock on two kinds of stream surfaces. Both theoretical and experimental works must be done to study the features of the shock wave. Recently, many interesting works have been carried out and some helpful results have been obtained (e.g. [4–13]).

In order to study the flow nature in transonic compressors, under the leadership and participation of Prof. Wu, a single-stage research compressor was designed with the "three-dimensional flow theory" [14]. In 1976, in the computation on arbitrary surfaces of revolution with supersonic inlet flow of this compressor, it was found that the jump of $\Delta(V_\theta r)$ across the shock is a significant part of total $\Delta(V_\theta r)$ across the whole cascade passage. This is one of the important features of transonic compressors. By analyzing changes of the velocity triangle across the shock, a theoretical analysis of the jump of parameters, such as $V_\theta r$, $\Delta s/R$ and total pressure, is made [15]. After five iterations of calculations between the arbitrary surfaces of revolution, on which the shock discontinuity was included, and the central S_2 stream surface, final results were obtained. To investigate the three-dimensional shock wave, a research report [16] on shock relations was completed in Jan. of 1978. In the report it is pointed out that through the shock the stream surfaces deflect suddenly, the thickness of the streamfilament is discontinous, and the approximate assumption on the arbitrary stream surface of revolution, which had been extensively used in subsonic and supersonic flow calculations, is no longer valid due to the existence of the shock. A concept of the generalized surface of revolution is then introduced. For the purpose of solving three-dimensional shocked flow on two kinds of stream surfaces, by extension of steady stream surface, a system of basic equations on two kinds of unsteady stream surface in four-dimensional "space" and the boundary and initial conditions suitable to solve the steady problem were given [17].

In the present paper, based upon the basic aerothermodynamic equations on an arbitrary stream surface in terms of arbitrary nonorthogonal curvilinear coordinates, shock relations on such surface are developed, which are the extension of [16]. By use of these relations, calculations on the generalized surface of revolution were made. These results were iterated with those along the central S_2 stream surface.

Contributed by the Gas Turbine Division and presented at the International Gas Turbine Conference and Products Show, Houston, Texas, March 9–12, 1981, of THE AMERICAN SOCIETY OF MECHANICAL ENGINEERS. Manuscript received at ASME Headquarters, December 16, 1980. Paper No. 81-GT-120.

Copyright © 1982 by ASME

Downloaded 01 Jun 2010 to 171.66.16.62. Redistribution subject to ASME license or copyright; see http://www.asme.org/terms/Terms_Use.cfm

Aerothermodynamic Equations on an Arbitrary Stream Surface in an Arbitrary Nonorthogonal Coordinate System

There is intercorrelation between two kinds of stream surfaces, S_1 and S_2, the aerothermodynamic equations on which can be expressed with a unified form.

In a nonorthogonal coordinate system, consider an arbitrary stream surface formed by all streamlines passing through the points on an arbitrary curve which is not a streamline

$$S(x^1,x^2,x^3)=0$$

Then

$$\frac{\partial S}{\partial x^i}dx^i=0 \quad i=1,2,3.$$

From the definition of the stream surface,

$$n_i\, w^i = 0$$

or

$$n^i\, w_i = 0$$

On such arbitrary stream surface, there are only two independent coordinate variables. With no restriction of generality, we may assume they are x^α ($\alpha = 1,2$), i.e.,

$$x^3=x^3(x^1,x^2)$$

Any parameter q on the stream surface can be expressed as a function of x^1 and x^2

$$q=q(x^1,x^2,x^3)=q[x^1,x^2,x^3(x^1,x^2)]$$

Introducing partial derivatives along a stream surface, we may find its relations with spatial partial derivatives are

$$\frac{\bar\partial q}{\bar\partial x^\alpha}=\frac{\partial q}{\partial x^\alpha}-\frac{n_\alpha}{n_3}\frac{\partial q}{\partial x^3} \quad \alpha=1,2$$

Its rate of change along a streamline on the stream surface is

$$\frac{\bar d q}{\bar d t}=w^\alpha\frac{\bar\partial q}{\bar\partial x^\alpha}$$

It is convenient to obtain the basic aerothemodynamic equations on the arbitrary stream surface from the equations in reference [1], which describe steady, inviscid, adiabatic flow in a relative coordinate system rotating with a constant angular velocity ω.

1 The Equation of Continuity. In the case of three-dimensional flow, it is

$$\nabla\cdot(\rho\mathbf{W})=0 \text{ or } \frac{1}{\sqrt g}\frac{\partial(\sqrt g\rho w^i)}{\partial x^i}=0,$$

where g is Jacobian determinant.

Using the partial derivatives along the stream surface, we have

$$\frac{\bar\partial(\sqrt g\rho w^\alpha)}{\bar\partial x^\alpha}=-\frac{n_i}{n_3}\sqrt g\rho\frac{\partial w^i}{\partial x^3}$$

Defining the thickness of the stream filament

$$\frac{\bar D\ln\tau}{\bar Dt}=\frac{n_i}{n_3}\frac{\partial w^i}{\partial x^3}$$

we finally get the continuity equation on the arbitrary stream surface

$$\frac{\bar\partial(\sqrt g\rho w^\alpha\tau)}{\bar\partial x}=0 \tag{1}$$

i.e.,

$$\bar\nabla\cdot(\tau\rho\bar{\mathbf{W}})=0 \tag{1a}$$

where $\bar{\mathbf{W}}$ is the vector sum of the two components w^α (or w_α) of $\mathbf{W}$ on the stream surface.

2 The Equation of Momentum. Applying the equation for the 3-D motion

$$\frac{d\mathbf{W}}{dt}-|\omega|^2\mathbf{r}+2\omega\times\mathbf{W}=-\frac{1}{\rho}\nabla p$$

or

$$\frac{1}{2}\nabla|\mathbf{W}|^2-\mathbf{W}\times(\nabla\times\mathbf{W}+2\omega)-|\omega|^2\mathbf{r}=-\frac{1}{\rho}\nabla p$$

to the stream surface we obtain

$$\frac{1}{2}\frac{\bar\partial}{\bar\partial x^1}(w^1w_1+w^2w_2+w^3w_3)w^2\left(\frac{\bar\partial w_2}{\bar\partial x^1}\frac{\bar\partial w_1}{\bar\partial x^2}\right)-w^3\frac{\bar\partial w_3}{\bar\partial x^1}$$

$$+2\sqrt g(w^3\omega^2-w^2\omega^3)-|\omega|^2r_1=-\frac{1}{\rho}\frac{\bar\partial p}{\bar\partial x^1}+f_1' \tag{2a}$$

$$\frac{1}{2}\frac{\bar\partial}{\bar\partial x^2}(w^1w_1+w^2w_2+w^3w_3)-w^3\frac{\bar\partial w_3}{\bar\partial x^2}+w^1\left(\frac{\bar\partial w_2}{\bar\partial x^1}-\frac{\bar\partial w_1}{\bar\partial x^2}\right)$$

$$+2\sqrt g(w^1\omega^3-w^3\omega^1)-|\omega|^2r_2=-\frac{1}{\rho}\frac{\bar\partial p}{\bar\partial x^2}+f_2' \tag{2b}$$

$$w^1\frac{\bar\partial w_3}{\bar\partial x^1}+w^2\frac{\bar\partial w_3}{\bar\partial x^2}+2\sqrt g(w^2\omega^1-w^1\omega^2)-|\omega|^2r_3=f_3' \tag{2c}$$

where $\mathbf{n}_s$ is the unit normal vector of the stream surface and

$$\mathbf{f}'=-\frac{\mathbf{n}_s}{n_3}\left\{\frac{1}{2}\frac{\partial}{\partial x^3}(w^iw_i)-w^i\frac{\partial w_i}{\partial x^3}+\frac{1}{\rho}\frac{\partial p}{\partial x^3}\right\} \tag{3}$$

In addition, the following relation can be derived

$$\frac{d\mathbf{W}}{dt}=\frac{\bar d\mathbf{W}}{\bar dt}+\frac{\mathbf{n}_s}{n_3}\left\{\frac{1}{2}\frac{\partial}{\partial x^3}(w^iw_i)-w^i\frac{\partial w_i}{\partial x^3}\right\} \tag{4}$$

3 The Equation of Energy. For the 3-D flow the equation is

Nomenclature

- $\mathbf{f}$ = force between stream surfaces
- G = mass flow
- I = stagnation rothalpy of gas per unit mass
- l = meridional line
- M = Mach number
- $\mathbf{n}$ = unit vector normal to surface
- p = pressure
- s = entropy of gas per unit mass
- $\mathbf{V}$ = absolute velocity of gas
- $\mathbf{W}$ = relative velocity of gas
- x^i = nonorthogonal curvilinear coordinates
- β = relative flow angle of gas
- ρ = density of gas
- τ = thickness of streamfilament
- ω = angular velocity of blade

Superscripts

- o = stagnation state
- i = contravariant component of vector

Subscripts

- 0 = at inlet
- 1 = before shock
- 2 = after shock
- i = covariant component of vector

Downloaded 01 Jun 2010 to 171.66.16.62. Redistribution subject to ASME license or copyright; see http://www.asme.org/terms/Terms_Use.cfm

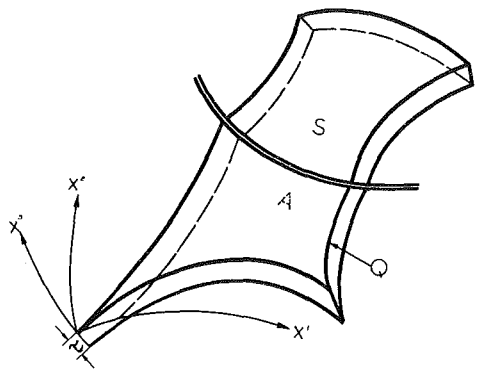

Fig. 1 Arbitrary stream surface in an arbitrary nonorthogonal coordinate system and shock on it

$$\frac{dI}{dt}=0 \quad \text{or} \quad w^i\frac{\partial I}{\partial x^i}=0$$

On the stream surface the energy equation becomes

$$w^\alpha\frac{\bar\partial I}{\bar\partial x^\alpha}=0 \tag{5}$$

It is easy to clarify that in the corresponding special cases equations (1) and (5) can be transformed to the continuity and energy equations in [1] and [3], respectively. Equations (2*a*), (2*b*), (2*c*) and (3) are consistent with the momentum equation and the expression for $\mathbf{f}'$ in [1] and [3] although in some cases both sides of the equation may have an identical additional term.

As we know, two kinds of stream surfaces are needed to solve the three-dimensional flow in turbomachines. From the derivation, it is seen that the streamfilament thickness τ and the steamfilament force $\mathbf{f}'$ in these equations which connect the two kinds of stream surfaces by the way of the relationship between the partial derivatives along the stream surfaces and the spatial derivatives. Therefore, it is important to calculate τ and $\mathbf{f}'$ correctly while iterating between the calculations on two kinds of stream surfaces.

Shock Relations on an Arbitrary Stream Surface

Let us formulate the basic eqs. in the integral form for a thin streamfilament, such that its central surface coincides with the considered arbitrary stream surface, and its thickness in the x^3 direction is $\tau(x^1, x^2)$. Figure 1 shows the lower half of the streamfilament. The area of the central surface is denoted by S. The volume, the total surface area, and the side surface area of the streamfilament are V, A and Q. The unit vecters $\mathbf{n}_A$ and $\mathbf{n}_Q$ are normal to A and Q, respectively. Then equations of continuity, momentum and energy may be written as follows:

$$\frac{d}{dt}\iiint_V \rho dV=\frac{d}{dt}\iiint_V \rho\sqrt{g}dx^1dx^2dx^3$$
$$=\frac{d}{dt}\iiint_V \rho\sqrt{\frac{g}{a}}dx^3(\sqrt{a}dx^1dx^2)$$
$$=\frac{\bar d}{\bar dt}\iint_S \tau\rho dS=0 \tag{6}$$

$$\frac{\bar d}{\bar dt}\iint_S \tau\rho\mathbf{W}dS=\iint_S \tau\rho(\omega^2\mathbf{r}-2\omega\times\mathbf{W})dS-\oint\!\!\!\oint_A p\mathbf{n}_s dA \tag{7}$$

$$\frac{\bar d}{\bar dt}\iint_S \tau\rho\left(e+\frac{|\mathbf{W}|^2}{2}-\frac{U^2}{2}\right)dS=-\iint_Q p\mathbf{W}\cdot\mathbf{n}_Q dQ \tag{8}$$

where a is the subdeterminant of g.

Obviously, they are still correct even for flow with shocks. If there is no shock, they may be reduced correspondingly to equations (1), (2*a*), (2*b*), (2*c*) and (5) in the last section.

Now we assume there is a shock surface Σ_s in the flow field. The whole field then is divided into two parts with continuous motion. In this condition, for any function F there exists the following relation [18]:

$$\frac{d}{dt}\iiint_V FdV=\iiint_V\left(\frac{dF}{dt}+F\nabla\cdot\mathbf{W}\right)dV+\iint_{\Sigma_s}^{s}[F\theta_{\Sigma_s}]d\Sigma_s \tag{9}$$

where $\theta_{\Sigma_s}=W_n=\mathbf{W}\cdot\mathbf{n}_{\Sigma_s}$, $[F]$ is the jump of F across the shock. If we use Σ as the intersection of the stream surface with the shock surface Σ_s, $\mathbf{n}_\Sigma$ as the unit normal vector of Σ on the stream surface, along the stream surface equation (9) becomes

$$\frac{\bar d}{\bar dt}\iint_S \tau F dS=\iint_S \tau\left\{\bar\nabla\cdot(F\bar{\mathbf{W}})+\frac{n_i}{n_3}F\frac{\partial w^i}{\partial x^3}\right\}dS+\int_\Sigma[\tau F\theta_\Sigma]d\Sigma \tag{10}$$

where $\theta_\Sigma=\bar{\mathbf{W}}\cdot\bar{\mathbf{n}}_\Sigma$.

With the aid of (10), equations (6), (7), and (8) can be, respectively, expressed as

$$\iint_S \bar\nabla\cdot(\tau\rho\bar{\mathbf{W}})dS+\int_\Sigma[\tau\rho\theta_\Sigma]d\Sigma=0$$

$$\iint_S \tau\rho\left\{\frac{\bar d\mathbf{W}}{\bar dt}+\frac{n_s}{n_3}\frac{1}{2}\frac{\partial}{\partial x^3}(w^iw_i)-\frac{\mathbf{n}_s}{n_3}\left(w^i\frac{\partial w_i}{\partial x^3}\right)\right\}dS$$
$$+\int_\Sigma[\tau\rho\theta_\Sigma\mathbf{W}]$$

$$d\Sigma=\iint_S \tau\rho(\omega^2\mathbf{r}-2\omega\times\mathbf{W})dS-\iint_S\left(\bar\nabla p+\frac{\mathbf{n}_s}{n_3}\frac{\partial P}{\partial x^3}\right)dS$$
$$-\int_\Sigma\left[\frac{\tau}{\cos\sigma}p\right]\mathbf{n}_{\Sigma_s}d\Sigma$$

$$\iint_S \tau\rho\bar{\mathbf{W}}\cdot\bar\nabla\left(e+\frac{|\mathbf{W}|^2}{2}-\frac{|U|^2}{2}+\frac{p}{\rho}\right)dS$$
$$+\int_\Sigma\left[\tau\rho\left(e+\frac{|\mathbf{W}|^2}{2}-\frac{|U|^2}{2}\right)\theta_\Sigma\right]$$

$$d\Sigma=-\int_\Sigma[\tau p\mathbf{W}\cdot\mathbf{n}_\Sigma]d\Sigma$$

in which σ is the angle between two planes at a certain point, one tangent to the three-dimensional shock Σ_s and the other, to the surface formed by Σ and x^3 coordinate line.

Substituting the eqs. of continuity, momentum and energy in the preceding section into these three formulae, we obtain the shock relations on an arbitrary stream surface:

$$\tau\rho\bar{\mathbf{W}}\cdot\bar{\mathbf{n}}_\Sigma]=0 \tag{11}$$

$$[\tau\rho(\bar{\mathbf{W}}\cdot\bar{\mathbf{n}}_\Sigma)\mathbf{W}]+\left[\frac{\tau}{\cos\sigma}p\right]\mathbf{n}_{\Sigma_s}=0 \tag{12}$$

$$[I]=0 \tag{13}$$

It is obvious that for S_1 and S_2 stream surfaces in the cylindrical coordinates, equations (11)–(13) become (8)–(10) or (14)–(16) in [16], respectively, and τ is b or Br separately.

From these shock relations on an arbitrary stream surface, the relative stagnation rothalpy of the gas is constant across a

Downloaded 01 Jun 2010 to 171.66.16.62. Redistribution subject to ASME license or copyright; see http://www.asme.org/terms/Terms_Use.cfm

shock. It indicates that the relative stagnation rothalpy along the streamline is an invariant in the steady, adiabatic flow of an inviscid gas.

The above relations point out that the jump of the gas parameters across the shock is dependent on the streamfilament thickness τ and the normal direction $\mathbf{n}_{\Sigma_s}$ of the spatial shock surface. So there are great differences between the shock relations on a stream surface and those of a plane oblique shock. If the plane shock relations are used to calculate the gas parameters after the three-dimensional shock on the stream surface, the correct answer can not be expected.

We have found that the influence of the shock spatiality is reflected in the appearance of τ and $\mathbf{n}_{\Sigma_s}$, and the former is closely dependent on the latter. In fact, due to the spatial direction of the shock each streamline on the stream surface undergoes a sudden turning while passing through the shock, so the whole stream surface undergoes a sudden turning, and the streamfilament thickness becomes discontinuous. Therefore, in the foregoing shock relations the normal direction of the shock surface plays an important role. Consequently, the correlations between the stream surfaces of the same family, and between one family and the other, are closer in shock flows than in subsonic and isentropic supersonic flows. This means that in order to calculate the gas parameters behind the shock on one family of stream surfaces, the jump of the streamfilament thickness should be obtained from the calculations on the other family of stream surfaces, taking the same three-dimensional shock into account. Also this sort of calculation is directly dependent on the spatial normal direction of the shock surface. That is one of the important features of turbomachinery gas flows with three-dimensional shocks. Because of this, the study on the supercritical blade profile in the turbomachine is unusually difficult.

It has been shown that the deflection of the stream surface and the discontinuity amount of the stream filament thickness across a three-dimensional shock is dependent on the spatial orientation of the shock surface. So it is not permited to solve the shocked flow on the stream surface with any given shape. Particularly, even though the stream surface before the shock can be considered as an arbitrary surface of revolution, the assumption of arbitrary surface of revolution behind the shock is no longer valid. This is a result of the fact that the turning location of each streamline across the shock on the stream surface is different and the jump of the stream filament thickness is not equal.

For this reason, the concept of the generalized stream surface of revolution is suggested in [16]. Its thickness is a function of both ζ and φ, and may be discontinuous. The component n_u of its normal vector, and hence the component f_u' of the streamfilament force, can be ignored. It is known that f_u' generally is small in an axial flow compressor. After the shock τ varies with ζ and φ and f_u' is no longer negligible. If the obliquity of the 3-D shock surface on each S_2 stream surface is not great, or if its spatial orientation is almost the same, then f_u' could be relatively small for all streamlines on the stream surface passing through the shock. In this case, τ is regarded as the function of ζ and φ, and the assumption about the generalized surface of revolution can be accepted. Obviously, the deviation of the stream surface immediately behind the shock from the surface of revolution is considerable. As a matter of fact, the approximation of the generalized surface of revolution neglects the details of this region in order to calculate the flow in a simple form.

For the generalized surface of revolution, the shock relations may be obtained from equations (11)-(13) as follows:

$$[\tau\rho(\mathbf{W}\cdot\bar{\mathbf{n}}_\Sigma)]=0 \tag{14}$$

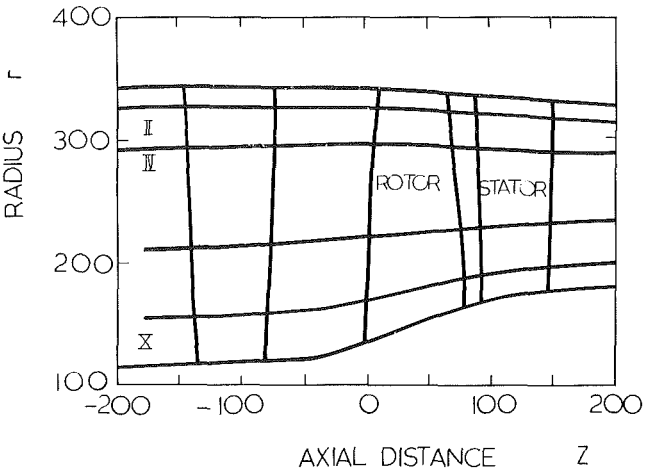

Fig. 2 Flowpath

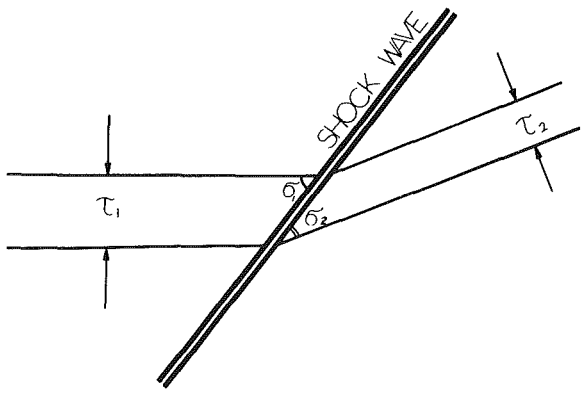

Fig. 3 Turning of the stream surface and discontinuity of the stream filament thickness

$$[\tau\rho(\mathbf{W}\cdot\bar{\mathbf{n}}_\Sigma\mathbf{W})]+\left[\frac{\tau}{\cos\sigma}p\right]\mathbf{n}_{\Sigma_s}=0 \tag{15}$$

$$[I]=0 \tag{16}$$

where τ is the normal thickness of the surface of revolution and σ is the angle between two planes at a certain point tangential to the three-dimensional shock Σ_s and to the surface formed by Σ and τ-direction line.

It is also noted that to ensure there is no turning at the shock termination, S_1 stream surface should be normal to the shock surface at this place. The problem on the shock termination region will be discussed in another paper.

Computational Results and Discussion

For the aerothermodynamic analysis on the surface of revolution with a supersonic inlet flow, it is necessary to know the precise location and shape of the shock near the leading edge of the cascade. In the case of a cylindrical cascade with uniform inlet flow, W. E. Moeckel's bow shock model [19] can be used. For the cascade on the surface of revolution the location and shape of the shock can be calculated by solving flow field with the help of the characteristic equations, the compatibility conditions of the inlet flow, the shape of the airfoil, the structure of the cascade and the interaction between the blades are taken into account.

In the region bounded by the bow shock and the passage shock (not including a small subsonic part around the leading edge), the flow may be solved by the method of characteristics

Downloaded 01 Jun 2010 to 171.66.16.62. Redistribution subject to ASME license or copyright; see http://www.asme.org/terms/Terms_Use.cfm

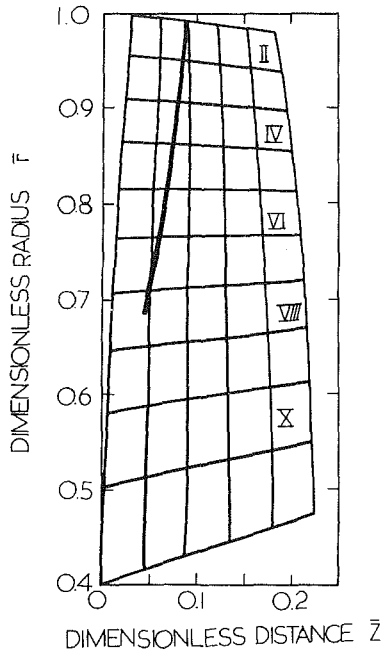

Fig. 4 Meridional projection of the intersection of the shock with S_{2c}

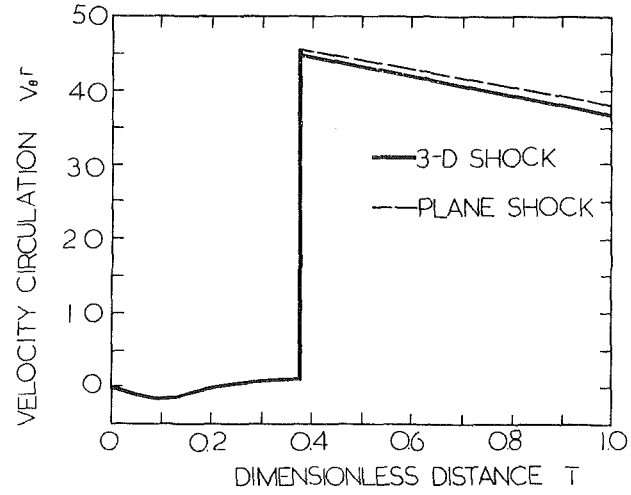

Fig. 5 Distributions of $V\theta r$ along central streamline on surface II

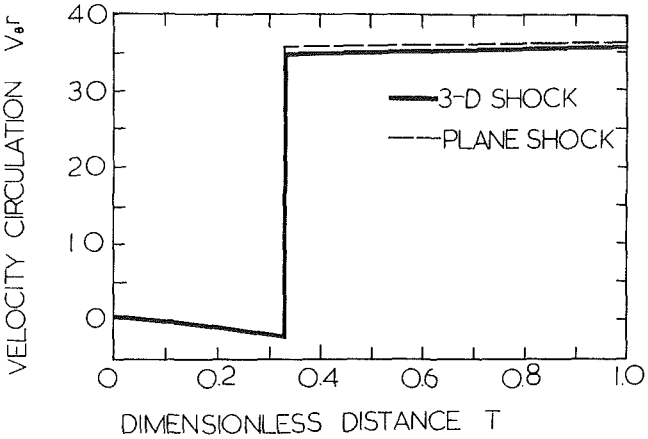

Fig. 6 Distributions of $V\theta r$ along central streamline on surface IV

[20–22] in which the changes of the thickness τ and radius r of the streamfilament are involved. In the subsonic region after the passage shock, the flow field matrix solution can be used.

Using the solution method described above and the shock relations (14)–(16) and assuming the location of the passage shock, some calculations on generalized surfaces of revolution at the upper region of the rotor (Fig. 2) in reference [14] are made with the turning of the stream surface and the discontinuity of the stream filament thickness across the shock. The turning of the stream surface across the shock can be obtained either from comparison between calculations of the three-dimensional shock and the two-dimensional shock on the stream surface, or from iteration between separate calculations of two-dimensional shocks on the S_1 and S_2 stream surfaces. As the first approximation, the turning of the S_1 stream surface may be calculated by the use of the plane oblique shock relations on the S_2 stream surface. From the turning of the S_1 stream surface, the jump amount of its stream filament thickness can be calculated (Fig. 3):

$$\tau_2 = \tau_1 \cos\sigma_1 / \cos\sigma_2$$

Incorporating the results of the aforementioned calculations and the subsonic flow calculations along arbitrary surfaces of revolution near the hub region into the calculation on the central S_2 stream surface (S_{2c}), a complete cycle of calculations is made. The thickness of revolution may be got from that of the arbitrary streamfilament of revolution and its jump amount across the shock. The projection of the intersection of shock surface and the central S_2 stream surface on the meridional plane is drawn in Fig. 4 in accordance with the locations of the shock on the surface of revolution. Additional computation results are shown in Figs. 5–11. The abscissa of these figures is the ordinary dimensionless distance along the generator of the surface of revolution.

The distributions of $(V_\theta r)$ of gas along the central streamlines of the two generalized surfaces of revolution on which the inlet Mach numbers are 1.31 and 1.23 are given in Figs. 5 and 6, respectively. It is seen that after the shock $V_\theta r$ increases to a high value. This result is very similar to that from the analysis on the arbitrary surface of revolution based on the plane shock relations [15]. For surface IV with a lower inlet Mach number, $\Delta(V_\theta r)$ across the shock is about 98 percent of that in the whole cascade passage. On surface II with a higher inlet Mach number, $V_\theta r$ behind the shock is even higher than that at the passage exit, and after the shock the flow along the central streamline of the compressor rotor cascade behaves like the turbine flow. Of course, this does not mean that the flow in the entire cascade passage after the shock is in the same condition, because the shape and strength of the passage shock at various points are quite different. However, it does indicate that at least acceleration in some part of the compressor cascade passage is possible, and careful aerothermodynamic design is needed to ensure the proper strength of the shock and the acceptable flow conditions after the shock.

Computational results from the plane oblique shock relations are also shown in these two figures $\Delta(V_\theta r)$ produced in the plane shock is greater than that produced in the three-dimensional shock, even though the Mach numbers ahead of both shocks are same. In addition, it is found from the comparisons of the differences between these two kinds of calculations of surfaces II and IV that the difference on surface IV is greater than that on surface II. Thus the strength of the three-dimensional shock is weaker than that of the plane shock. The three-dimensional effect of the shock is more distinct on surface IV than on surface II, for the shock at the intersection of the S_{2c} stream surface and surface II is nearly normal and the shock on surface IV is more oblique. Hence, in the middle part of the shock the three-dimensional

Downloaded 01 Jun 2010 to 171.66.16.62. Redistribution subject to ASME license or copyright; see http://www.asme.org/terms/Terms_Use.cfm

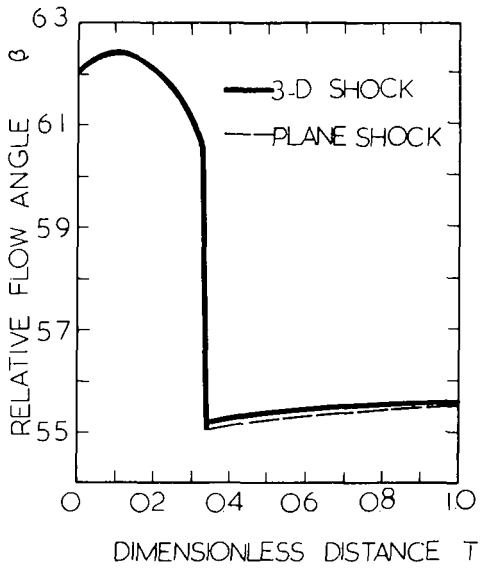

Fig. 7 Variations of relative flow angle along central streamline on surface II

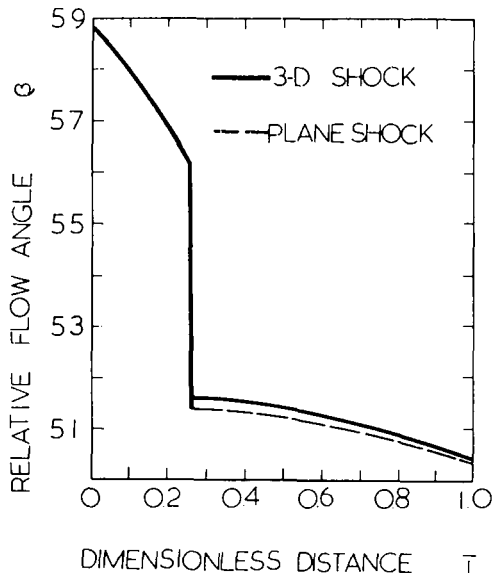

Fig. 8 Variations of relative flow angle along central streamline on surface IV

effect is stronger and larger error would be resulted if the plane oblique shock relations are used.

Variations of flow angles along the central streamlines on the two generalized surfaces of revolution are shown in Figs. 7 and 8. Consistent with the variations of $V_\theta r$, the flow angles across the shock suddenly decrease. On surface IV the flow angle behind the shock is less than that ahead of the shock by 4.41 deg and is a little higher than that at the exit. On surface II the flow angle after the shock is decreased by 5.46 deg, and is lower than that at the exit. As a comparison, the jumps in flow angles from the calculations of the arbitrary surface of revolution, on which the turning of the stream surface and the discontinuity of the streamfilament are not taken into consideration, are 4.63 deg and 5.51 deg respectively. These differences are also attributed to the three-dimensional effects of the shock.

Gas parameters, which are calculated from the plane and spatial oblique shock relations, are given in Table 1. Similar to the cases for $\Delta(V_\theta r)$ and β, the jump amounts of any other parameters across the spatial three-dimensional shock are smaller than those due to the plane two-dimensional shock. In addition, the difference between the jump quantities of two-dimensional and three-dimensional shocks is greater on surface IV than that on surface II. For example, the difference between entropy increases of two-dimensional and three-dimensional shocks for surface II is less than 2 percent, but is more than 6 percent for surface IV.

In order to demonstrate the variation of the thickness of the central S_2 stream filament, the distributions of $(p-t)/\zeta p$, (p – the pitch of the cascade, t – its thickness, ζ – the ratio of

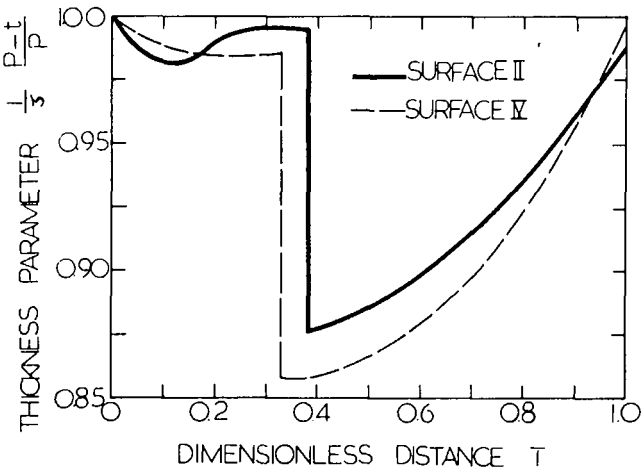

Fig. 9 Distributions of $\frac{1}{\zeta}\frac{p-t}{p}$ along central streamlines

ρW_t at the central streamline to its average on the cascade) along the central streamlines of the two surfaces of revolution are shown in Fig. 9. Like other parameters, $(p-t)/\zeta p$ is also suddenly changed across the shock. This confirms from the computation that across the shock the central S_2 stream surface undergoes a turning.

In Figs. 10 and 11 the relative Mach numbers on surfaces II and IV which are taken from the calculation along the central S_2 stream surface [23], are shown. Their characteristic

Table 1 Comparison of parameters behind the shock from the calculations for two types of shock

		M_0	β_0	M_1	β_1	M_2	β_2	$(V_\theta r)_2$	P°_2/P°_1	$(\Delta S/R)_2$
surface II	2-D shock	1.309	62.13	1.324	60.60	0.821	55.09	45.46	1.754	.0227
	3-D shock	1.309	62.13	1.324	60.60	0.824	55.14	45.20	1.749	.0224
surface IV	2-D shock	1.225	58.96	1.315	56.04	0.811	51.41	36.17	1.650	.0206
	3-D shock	1.225	58.96	1.315	56.04	0.825	51.63	34.95	1.627	.0193

Downloaded 01 Jun 2010 to 171.66.16.62. Redistribution subject to ASME license or copyright; see http://www.asme.org/terms/Terms_Use.cfm

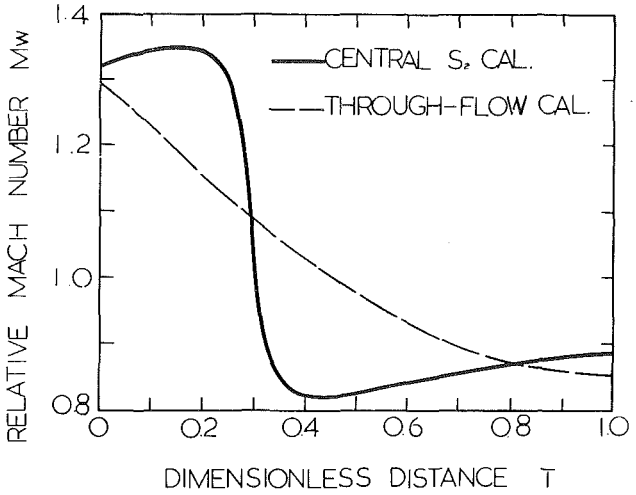

Fig. 10 Variations of relative Mach number along central streamline on surface II

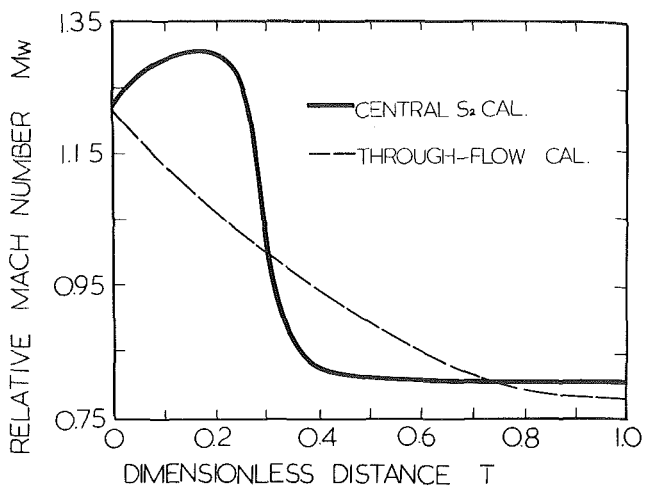

Fig. 11 Variations of relative Mach number along central streamline on surface IV

features are as follows. At their first part, in connection with the supersonic expansion at the inlet region, the Mach number of the gas flow increases gradually and reaches its maximum ahead of the shock. Across the shock Mach number decreases rapidly. For surface IV the Mach number immediately after the shock is higher than that at the cascade exit and the gas is decelerated in this subsonic region. For surface II it is lower than that at the exit and the gas is accelerated in the passage. It is interesting to note that, from the comparison of the computation results on S_{2c} and the corresponding generalized surface of revolution, the distributions of Mach number, $V_\theta r$ and other parameters obtained from the aforementioned two kinds of calculations are quite close. This shows that their results are consistent. It is necessary to point out that owing to small number of the calculating stations along axial direction within the blade passage in S_{2c} flow field line relaxation solution, the computational results must be continuous.

In Figs. 10 and 11 the variations of Mach number from the conventional through-flow calculation, in which $\zeta = 1$ and the effects of the shock are not taken into account, are also given for the purpose of comparison with those from the S_{2c} calculations. It is noted that the differences between two types of S_2 calculations are considerable, especially near the shock. Before the shock Mach numbers in the conventional through-flow calculation are much less, and after the shock are much greater than those in the S_{2c} calculation. It suggests that in order to make the aerothermodynamic design computation accurately for transonic compressors, it is necessary to use the S_{2c} calculations with the three-dimensional shock computation results on the generalized surface of revolution as its inputs.

Concluding Remarks

A shock in a turbomachine is three-dimensional. Because of that, the correlations between the stream surfaces are closer. In calculating gas parameters behind the shock it is necessary to take the three-dimensional effects of the shock into account, that is to estimate the turning of the stream surface and the discontinuity of the streamfilament across the shock.

Calculations according to the three-dimensional shock relations developed in this paper show that the strength of the three-dimensional shock is weaker than that of the plane shock and the three-dimensional effect of the shock at the midspan of the compressor rotor is greater than that near the tip assuming that the surface of revolution at the tip is normal to the shock.

The aerothermodynamic analyses with the three-dimensional shock on the generalized surfaces of revolution demonstrate that along the central streamline, the flow angle decreases suddenly and $V_\theta r$ increases suddenly while passing through the shock. $\Delta(V_\theta r)$ produced by the shock is a significant part of that in the whole cascade passage. In some cases, it may exceed the latter and the compressor cascade passage after the shock acts as a turbine cascade passage.

Computation results on the central S_2 stream surface iterated with those on the generalized surfaces of revolution are greatly different from the results of the conventional through-flow calculation, especially in the region near the shock. They may represent some distinguishing features of the supersonic flow on the stream surface of a compressor rotor and give some useful suggestions to designers.

Acknowledgment

This paper is completed under the supervision of Director Wu Chung-hua. The authors wish to thank him for his guidance and encouragement.

References

1 Wu, Chung-hua, "A General Theory of Three-Dimensional Flow in Subsonic and Supersonic Turbomachines of Axial-, Radial-, and Mixed- Flow Types," ASME Paper No. 50-A-79, Nov. 1952, or NACA TN 2604, 1952.

2 Wu, Chung-hua, "Basic Aerothermodynamic Equations Governing Fluid Flow in Turbomachines Expressed in Terms of Non-Orthogonal Curvilinear Coordinates," Research Note, Academia Sinica, 1963.

3 Wu, Chung-hua, "Three-Dimensional Turbomachine Flow Equations Expressed with Respect to Non-Orthogonal Curvilinear Coordinates and Methods of Solution," *Proceedings of 3rd ISABE,* 1976, pp. 233-252.

4 Wisler, D.C., "Shock Wave and Flow Velocity Measurement in a High Speed Fan Rotor Using the Laser Velocimeter," *Journal of Engineering for Power,* Vol. 99, Apr. 1977, pp. 181-188.

5 Dunker, R.J., Strinning, P.E., and Weyer, H.B., "Experimental Study of the Flow Field Within a Transonic Axial Compressor Rotor by Laser Velocimetry and Comparison with Through-Flow Calculations," ASME Paper No. 77-GT-28, 1977.

6 Dunker, R.J., and Hungenberg, H.G., "Study of Flow Field Behind a Transonic Axial Compressor Rotor Using Laser-Anemometry and Unsteady Pressure Measurement," *Proceedings of 4th ISABE,* 1979, pp. 269-276.

7 Benser, W.A., Bailey, E.E., and Gelder, T.F., "Holographic Studies of Shock Waves Within Transonic Fan Rotors," ASME Paper No. 74-GT-46, 1974.

8 Epstein, A.H., "Quantitative Density Visualization in a Transonic Compressor Rotor," ASME JOURNAL OF ENGINEERING FOR POWER, Vol. 99, July 1977, pp. 460-475.

9 Bilwakesh, K.R., Koch, C.D., and Prince, D.C., Jr., "Final Report on Task II, Contract NAS3-11157 Performance of a 1500 Feet-per-second Tip Speed Transonic Fan Stage with Variable Geometry Inlet Guide Vanes and Stator," NASA CR 72880, June 1972.

10 Epstein, A.H., Kerrebrock, J.L., and Thompkins, W.T., Jr., "Shock Structure in Transonic Compressor Rotors," *AIAA Journal,* Vol. 17, Apr. 1979, pp. 375-379.

Downloaded 01 Jun 2010 to 171.66.16.62. Redistribution subject to ASME license or copyright; see http://www.asme.org/terms/Terms_Use.cfm

11 Thompkins, W.T., Jr., "An Experimental and Computational Study of the Flow in a Transonic Compressor Rotor," MIT GTL Report No. 129, May 1976.

12 Prince, D.C., Jr., "Three-Dimensional Shock Structures for Transonic/Supersonic Compressor Rotors," *Journal of Aircraft,* Vol. 17, Jan. 1980, pp. 28–37.

13 Haymann-Haber, G., and Thompkins, W.T., Jr., "Comparison of Experimental and Computational Shock Structure in a Transonic Compressor Rotor," ASME Paper No. 80-GT-81, 1980.

14 Academia Sinica, and Shenyang Aeroengine Company, "Theory, Method and Application of Three-Dimensional Flow Design of Transonic Axial-Flow Compressor," Research Report, 1976; or *Chinese Journal of Engineering Thermophysics,* Vol. 1, No. 1, 1980, pp. 44–54.

15 Xu, Jian-Zhong, Jiang, Zuo-ren, Yang, Jin-sheng, Zhang, Ying, and Du, Zhuan-she, "A Theoretical Analysis on Arbitrary Surface of Revolution with Supersonic Inlet Flow in a Transonic Axial Compressor," to be published in *Chinese Journal of Engineering Thermophysics,* Vol. 2, No. 1, 1981.

16 Xu, Jian-Zhong, "Shock Relations in Turbomachines," *Chinese Journal of Mechanical Engineering,* Vol. 16, No. 3, 1980, pp. 61–69.

17 Xu, Jian-Zhong, "A General Theory of Three-Dimensional Flow in Transonic Turbomachines with Shocks," *Chinese Journal of Engineering Thermophysics,* Vol. 1, No. 2, 1980, pp. 120–127.

18 Serrin, J., "Mathematical Principle of Classical Fluid Dynamics," *Handbuch der Physik,* Band V111/I, Springer-Verlag, 1959, pp. 125–263.

19 Moeckel, W.E., "Approximate Method for Predicting Form and Location of Detached Shock Waves Ahead of Plane and Axially Symmetric Bodies," NACA TN 1921, 1949.

20 Wu, Chung-hua, and Costilow, E.L., "A Method of Solving the Direct and Inverse Problem of Supersonic Flow along Arbitrary Stream Filaments of Revolution in Turbomachines," NACA TN 2492, 1951.

21 Xu, Jian-Zhong, "Aerothermodynamic Equations of Supersonic Flow on Arbitrary Surface of Revolution in Turbine-machines Expressed with Respect to Non-Orthogonal Curvilinear Coordinates and Method of Characterastics," Research Report, Institute of Engineering Thermophysics, Academia Sinica, 1980.

22 Liu, Cui-e, and Wu, Wen-quan, "Computer Program of Supersonic Flow Past Inlet of Cascade Section on an Arbitrary Stream Filament of Revelution and Determining Unique Inlet Flow Angle," *Chinese Journal of Engineering Thermophysics,* Vol. 1, No. 3, 1980, pp. 264–271.

23 Zhu, Rong-guo, "Flow-Field Line Relaxation Solution for Inverse Problem of Flow Along S_2 Relative Stream Surface Employing Non-Orthogonal Curvilinear Coordinates and Corresponding Non-Orthogonal Velocity Components," *Chinese Journal of Engineering Thermopohysics,* Vol. 1, No. 1, 1980, pp. 35–42.

Downloaded 01 Jun 2010 to 171.66.16.62. Redistribution subject to ASME license or copyright; see http://www.asme.org/terms/Terms_Use.cfm

Computation of Three-Dimensional Flow Fields Through Rotating Blade Rows and Comparison With Experiment

K. P. Sarathy
Research Engineer, Compressor Analysis and Technology Development, Pratt and Whitney Aircraft, East Hartford, Conn. 06108
Mem. ASME

A three-dimensional inviscid time-marching calculation solving the unsteady Euler equations in a coordinate system rotating with the blade row has been developed, based on the Denton flow solver. This calculation was used to compute the flow field through the rotor of a transonic axial compressor and compared to measurements made with an advanced laser velocimeter at DFVLR. The comparison is made at design speed at pressure ratio corresponding to peak efficiency. Comparisons of the calculated and experimentally determined Mach number contours indicate excellent agreement in the entrance region where the viscous blockage effects are small. The methodology of the analysis is also described in this paper.

Introduction

In current turbofan engines, fan rotor inlet Mach numbers in the relative frame range from subsonic at the rotor hub to supersonic over the outer parts of the rotor span. In the supersonic regions, leading edge shocks in the rotating frame are formed causing a complicated three-dimensional flow field. The associated three-dimensional shock structures can cause severe shock losses and various types of shock-boundary layer interactions. Losses are also caused and transported by three-dimensional boundary layers on the blades and by radial wake mixing. The transonic and three-dimensional nature of these fan flow fields have made this computational problem the subject of much long term research.

Recent analysis methods for fan rotors employ a quasi three-dimensional approach, in which the flow fields through the fan rotors is computed iteratively between an axisymmetric through flow calculation and a blade-to-blade surface calculation [1]. Through flow calculations are solved by a streamline curvature method which is mathematically elliptical in nature. Flow fields in the blade-to-blade surfaces are analyzed using time marching methods. Time marching methods are generally applicable to mixed supersonic and subsonic flows. By retaining the time dependency in the system of equations, the differential equations remain hyperbolic in time irrespective of the Mach number and thus only one type of differential equation is solved. Thus, there is some inconsistency between the types of equations solved in the quasi three-dimensional approach. Time-marching methods work naturally with a prescribed pressure ratio rather than prescribed mass flow, thus avoiding the problems of finding the choking mass flow. An important aspect of the solution is that shocks are formed naturally as part of the computed flow field.

Time marching methods have been used to solve for the two-dimensional blade-to-blade flow fields by Gopalakrishnan [2], McDonald [3], Veuillot [4], Erdos, et al. [5]. Gopalakrishnan solved the Euler equations in differential form, transformed from the physical domain into a rectangular computational domain. He used the McCormack scheme without time splitting, which is second-order accurate in time and space. Veuillot solved the Euler equations in integral form using the McCormack scheme. Erdos, et al. [5] solved the unsteady flow on a blade-to-blade stream surface through a stage using a finite-difference method. Thomkins [6] modified and extended Oliver's [7] three-dimensional time-dependent calculation of flow-through rotors using the McCormack scheme with time splitting. McDonald solved the equations of motion in integral form using a six-sided grid in the physical domain, conserving fluxes of mass, momenta and energy for each element.

Denton [8,9] improved McDonald's method by using a simpler four-sided grid, a one-step scheme in time, and using correction factors to smooth out the fluxes and obtain second order-accuracy in space. The Denton scheme is partially implicit, since the new values of the pressure are used in the subsequent momentum equations. Denton extended this method to solve flow equations in three-dimensions. Denton and Singh [9] computed the flow field through a stage using absolute flow quantities and conservation equations referenced to a stationary frame of reference.

Contributed by the Gas Turbine Division and presented at the International Gas Turbine Conference and Products Show, Houston, Texas, March 9-12, 1981, of THE AMERICAN SOCIETY OF MECHANICAL ENGINEERS. Manuscript received at ASME Headquarters, December 11, 1980. Paper No. 81-GT-121.

Copyright © 1982 by ASME
Downloaded 01 Jun 2010 to 171.66.16.62. Redistribution subject to ASME license or copyright; see http://www.asme.org/terms/Terms_Use.cfm

The present work is an adaptation of Denton's three-dimensional calculation to solve the transonic flow in a rotor with the conservation equations referenced to the rotating frame of reference. This work was developed concurrently and independently of Denton and Singh [9]. The calculation has been modified to account for rotational effects (coriolis and centrifugal forces) and solve an additional equation for the conservation of energy. Advantages of using a rotating frame of reference are application to shrouded fan sections and modelling viscous corrections. This method is a natural extension of the two-dimensional blade-to-blade solutions to a full three-dimensional analysis of the fan rotor flow field.

Governing Equations

The equations and their derivations for the stationary vane and rotor are given by Denton [9]. The governing equations which define the inviscid flow are the equations of conservation of mass, momenta and energy. It is convenient to work with the equations written in a frame rotating with the blade in an orthogonal cylindrical coordinate system (r, θ, x). The energy equation has to be included since the rothalpy may not be radially uniform in the inlet plane.

The relevant equations written in flux conservation form are:

Continuity

$$\Delta t\ \Sigma(\rho W_x dS_x + \rho W_\theta dS_\theta + \rho W_r dS_r) = \Delta V\ \Delta\rho$$

Axial Momentum

$$\Delta t\ \Sigma\{(p+\rho W_x{}^2)dS_x + \rho W_x W_\theta dS_\theta + \rho W_x W_r dS_r\} = \Delta V\ \Delta(\rho W_x)$$

Angular Momentum

$$\Delta t\Sigma\{\rho W_x r\ W_\theta dS_x + (p+\rho W_\theta{}^2) r\ dS_\theta + \rho W_r r W_\theta dS_r\} - \Delta t\ 2\ \Omega r\ W_r \Delta V = \Delta V\ \Delta(\rho r\ W_\theta)$$

Radial Momentum

$$\Delta t\ \Sigma\{\rho W_r W_x dS_x + \rho W_\theta W_r dS_\theta + (p+\rho W_r{}^2)dS_r\} + \Delta t\ \Sigma\ p\ \delta\theta\ dS_\theta + \Delta t \frac{\rho V_\theta{}^2}{r}\ \Delta V = \Delta V(\rho W_r)$$

Energy

$$\Delta t\ \Sigma(\rho W_x I\ dS_x + \rho W_\theta I\ dS_\theta + \rho W_r I\ dS_r) = \Delta V\ \Delta(\rho E_r)$$

where

$$I \equiv H - UV_\theta = H_{\text{rel}} - \frac{U^2}{2} = C_p T_{o_{\text{rel}}} - \frac{U^2}{2}$$

$$E_r = C_v T - \frac{U^2}{2} + \frac{W^2}{2}$$

and the static pressure is computed at each point using the equation of state for thermally and calorically perfect ideal gas

$$p = \rho RT = \rho(\gamma - 1)\left(E_r - \frac{W^2}{2} + \frac{U^2}{2}\right)$$

$$\gamma = C_p / C_v$$

Computational Mesh

The foregoing equations are solved in the physical domain on a grid which is basically an extension of grids used in time marching codes for calculation of two-dimensional flow in the blade-to-blade plane. It is formed by surfaces equally spaced between the blade pressure and suction surfaces, axially spaced surfaces running from hub to tip (quasi-orthogonal surfaces), and the meridional quasi-stream surfaces equally spaced in the radial direction between the hub and tip.

Numerical Scheme

The numerical scheme employed is the same as that developed by Denton. The scheme in essence is equivalent to using upwind differences for mass and momentum flux gradients but downwind differences for pressure gradients. The basic scheme is modified to achieve greater accuracy with the same number of grid points by adding correction factors to the fluxes and pressures acting on the pitchwise faces of the element. The correction factors are computed such that when they are added to the flux or pressure acting at the pitchwise face, they result in fluxes equivalent to those obtained using curve fits along quasi streamlines. To preserve stability, changes in correction factors are damped to lag behind changes in the main flow properties.

No explicit artificial viscosity is used in the scheme, although a slight smoothing in the pitchwise direction is used after each time step to eliminate the slight waviness in the pitchwise direction.

Boundary Conditions

The necessary boundary conditions to yield a unique and stable converged solution have been derived based on experience and are very similar to Denton's. At the upstream boundary the inlet relative stagnation pressure and temperature are specified and held constant. At the upstream boundary the static pressure gradient along the quasi-streamline is assumed to be zero at each radial location. Since, in the relative frame of reference, the incoming Mach numbers may be supersonic and their axial components subsonic, upstream propagation of disturbances is felt at the

Nomenclature

C_v = specific heat at const volume
C_p = specific heat at const pressure
E_{rel} = relative total internal energy $= C_v T + W^2/2$
H = total enthalpy in the absolute system $= h + V^2/2$
H_{rel} = total enthalpy in the relative frame of reference $= h + W^2/2$
h = enthalpy $= C_p T$
I = rothalpy
p = static pressure
R = gas const for air = 1718 ft^2/sec^2 °R
r = coordinate in the radial direction
T = static temperature
t = time
dS = area of any face of the control volume
U = wheel speed $= (\Omega r)$
V = velocity in absolute frame of reference
W = velocity in relative frame of reference
X = coordinate in axial direction
Δ = change in any variable
γ = ratio of specific heats $= C_p/C_v$
Ω = rotational speed in rad/sec
ρ = density
θ = coordinate in the tangential direction

Subscripts

x = component or projected area in the x direction
r = component or projected area in the r direction
θ = component or projected area in the θ direction

Downloaded 01 Jun 2010 to 171.66.16.62. Redistribution subject to ASME license or copyright; see http://www.asme.org/terms/Terms_Use.cfm

upstream boundaries. To satisfy unique incidence, absolute swirl angles are held constant and relative flow angles computed as a result of the calculation.

At the downstream boundary the static pressure is specified at the inner radius of the flowpath and held constant. The radial variation of static pressure satisfying radial equilibrium at the downstream boundary is determined in the calculation. Also, a condition of zero velocity gradient in the axial direction is maintained at the downstream plane. The specified axisymmetric flow far downstream suppresses radial vorticity at that plane, though numerical dissipation tends to smear out the gradient downstream (numerical mixing), and thus it is not really clear if the errors introduced due to this approximation are significant.

The blade surface boundary condition has not been changed from the stator case. It requires that no mass flux cross the boundaries and that the velocities normal to the blade surface be set equal to zero. A form of the Kutta condition is imposed at the trailing edge by stipulating that the pressure and flow angles be equal on the pressure and suction surfaces at the trailing edge grid point.

Since they effectively feed into the same element, this discontinuity in radial velocity is immediately spread over three grid points. Vorticity shed from the trailing edge appears as a discontinuity in the spanwise velocity at trailing edge.

Initial Condition

Since the asymptotic solution in time is of interest, the initial conditions need only be approximate. In the interests of saving computing time, the initial flow field is built by stacking radially two-dimensional (axisymmetric) flow fields.

Stability

Since the scheme is basically explicit, the time step for stability is found from the Courant Friedrich Lewy (CFL) condition, which requires that the domain of dependence of the numerical difference equation include the physical domain of dependence of the original differential equations.

Convergence

Convergence of the flow field is defined to be achieved when the maximum change in axial velocity at any grid point in successive time steps is within a tolerance of 0.05 percent.

Results

Recent laser-two-focus (L2F) velocity measurements by the DFVLR [10] in a single-stage, transonic fan rotor have provided an excellent series of cases for testing three-dimensional flow calculations. The comparison case shown here is the 100-percent design speed, maximum efficiency condition. At this measured condition the fan rotor efficiency is 89.6 percent. The measured and computed flow properties are shown in Table 1.

Table 1

	Measured	Computed
Mass flow	37.8 lb/s 17.15 kg/s	36.22 16.43 kg/s
Total pressure ratio	1.626	1.657
Total temperature ratio	1.164	1.161

The flowpath and the location of the laser velocimetry measuring stations are shown in Figs. 1(*b*) and 1(*c*). Information required to use the three-dimensional rotor analysis includes blade and flowpath geometry, and rotor rotational speed. Aerodynamic input required are absolute stagnation conditions at an arbitrary inlet plane and a value of static pressure at the inner radius of the flowpath far downstream.

The calculation was performed with a grid network formed by the intersections of 60 axial surfaces, 12 tangential surfaces and 11 radial surfaces. This input computing grid at each spanwise location was constructed based on relative air angles obtained from a streamline calculation. To initialize the flow field, upstream relative Mach numbers have also been obtained from a streamline solution. In the absence of any such information, approximate guesses may be made for these variables. The projection of the grid on the meridional plane is shown in Fig. 2. Input blade section geometry in the hub cylindrical surface is shown in Fig. 3.

The computational grid is obtained by radially interpolating at equidistant surfaces between the endwalls. Typical computing grids are shown in Figs. 4 and 5 for the hub and tip walls. For this grid, a flow field solution was obtained in 25 min of CPU time on the IBM 370/3033 system. This was achieved in 1500 time steps with a convergence criteria requiring the maximum change in axial velocity at any point in the flow field in the final iteration to be less than 0.05 percent. The time per grid point per time step is about 1.1×10^{-4} s. For a grid of $20 \times 60 \times 20$ the code requries 3000K bytes of storage. The test case required CPU time comparable to a quasi-3D analysis, with less engineer interaction.

Comparison with Experiment

The measured laser-two-focus (L2F) velocity data in conjunction with standard pressure and temperature measurements were reduced by the DFVLR to relative Mach number contours on approximate blade-to-blade stream surfaces and on radial planes at constant axial locations. The locations of these surfaces are shown in Fig. 1(*b*). The Mach number contours calculated using the three-dimensional rotor analysis program have been interpolated to these same measurement surfaces, for ease of comparison.

Figures 6(*a*) and 6(*b*) compare the measured and computed relative flow field at 18 percent (Surface 2) blade span. The incoming flow is subsonic but accelerates to sonic velocities on the blade suction surface. Mach number contours of 0.95, 0.9, 0.85 and 0.8 are clearly shown in both the data and the calculation, and the agreement in location is excellent. Inside the blade passage, Mach levels of 0.7 and 0.65 appear further back along the suction surface for the measured data than for the calculated levels. Toward the trailing edge it may be seen that the measured Mach numbers are larger than the computed values. This is probably due to the absence of any viscous blockage effects in the calculation. The absence of blockage produces a larger effective flow area and lower average Mach numbers.

Mach number contours for the 45-percent span surface are shown in Figs. 7(*a*) and 7*b*) (surface 4, in Fig. 1(*b*)). The incoming flow is slightly supersonic. The detached shock wave is observed at the blade channel entrance. The leading edge shock wave appears to be standing off the blade leading edge, indicating spilling of the flow. This feature of the flow field is predicted by the calculation also. The shock decelerates from Mach 1.2 to 0.85 at the suction surface. The match between measurement and analysis is again very good in the entrance region. In the covered passage the Mach number levels of 0.85 and 0.8 are further back in the passage for the measured data. Trailing edge Mach numbers of 0.7 are experimentally observed, the calculation giving 0.6. Again, viscous effects probably account for this difference.

Mach number contours for the 68-percent span surface are shown in Figs. 8(*a*) and 8(*b*) (surface 6 in Fig. 1(*b*)). The measured data indicate a typical leading edge bow shock at Mach number 1.25, propagating upstream and interacting with the expansion waves from the convex suction side. The shock interacting with the suction surface boundary layer causes a shock pattern and the spreading of Mach lines due to

Downloaded 01 Jun 2010 to 171.66.16.62. Redistribution subject to ASME license or copyright; see http://www.asme.org/terms/Terms_Use.cfm

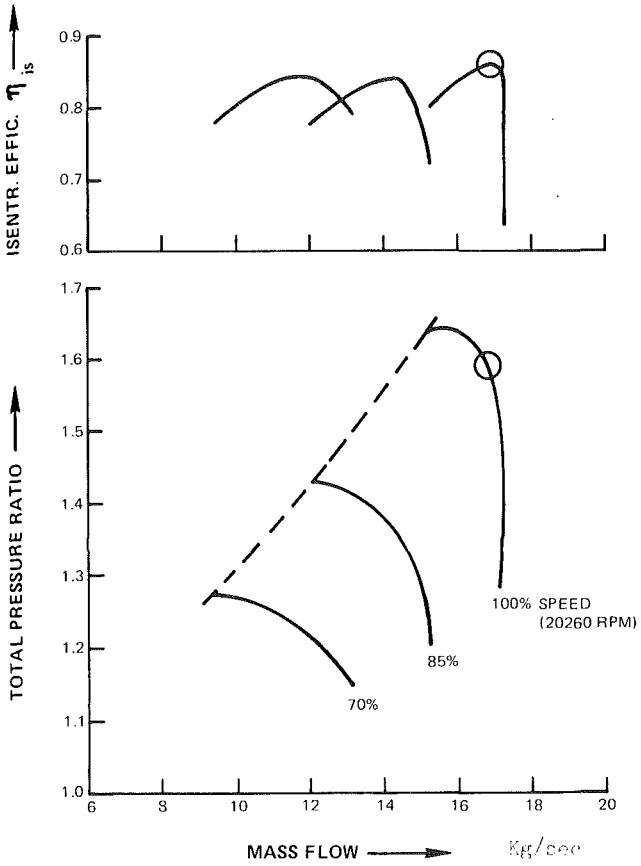

Fig. 1(*a*) Compressor stage performance

a gradual diffusion in the viscous regions. The analysis shows a leading edge oblique shock at Mach number 1.25 shocking down to 0.95. A Mach number level of 0.95 is observed in the analysis and in the data at identical locations.

Figures 9(*a*) and 9(*b*) show the results of measurements and analysis for the 89-percent span surface (surface 8 in Fig. 1(*b*)). The leading edge oblique shock at a Mach number of 1.3 is observed in both the calculation and measurement. A region of Mach number 1.4 is observed in the calculation and in the data. The weak oblique shock gradually diffuses to the subsonic Mach numbers of 0.85 at the trailing edge plane for the measured flow field. The calculation predicts a weak oblique shock and a subsequent normal shock at the trailing edge of the suction surface. A downstream Mach number of 0.85 is observed in the analysis also.

Figures 10(*a*) and 10(*b*) show for the data and analysis, respectively, lines of constant relative Mach number plotted in a plane perpendicular to the engine center line extending from root to tip in the radial direction and from the suction surface (SS) to the pressure surface (PS) at an axial location corresponding to about 40 percent from the blade leading edge. This is measuring plane 11 in Fig. 1(*b*) as seen looking in the direction of flow. The measurements indicate sonic velocity at 40-percent span on the suction surface and the sonic line extends to 90-percent span on the pressure surface. The shape of the sonic line may be an indication of the three-dimensional nature of the shock structure. The analysis predicts the sonic line at the same location. At the hub, computed Mach numbers of 0.55 are lower as compared to measured values of 0.65. What looks like a tip vortex in the measurements is not predicted by the calculation. Mach numbers calculated in the tip region are generally larger than measured. The presence of viscous effects, whether in the form of blockage or vortices is, of course, not included in the calculation, probably accounting for differences in Mach number levels within the blade passage.

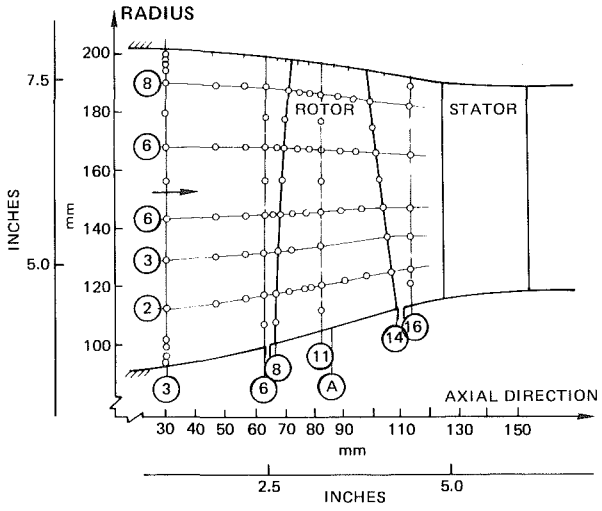

Fig. 1(*b*) Compressor flowpath with the laser measuring stations

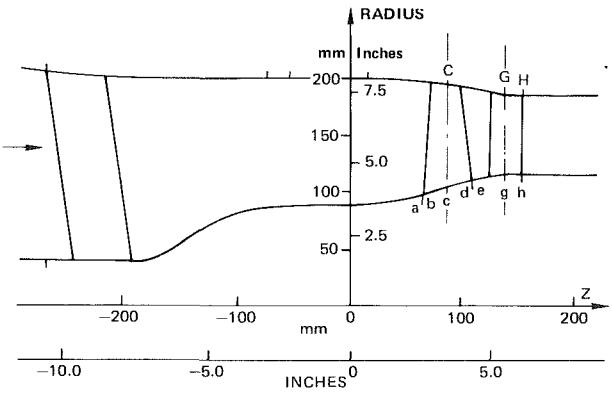

Fig. 1(c) Complete flowpath of the stage

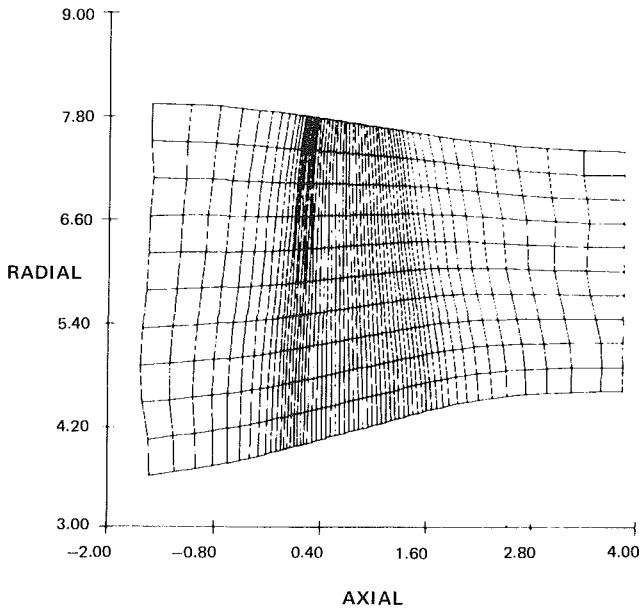

Fig. 2 Computational grid projected on the meridional plane

Conclusions

The Denton fully three-dimensional time marching

Downloaded 01 Jun 2010 to 171.66.16.62. Redistribution subject to ASME license or copyright; see http://www.asme.org/terms/Terms_Use.cfm

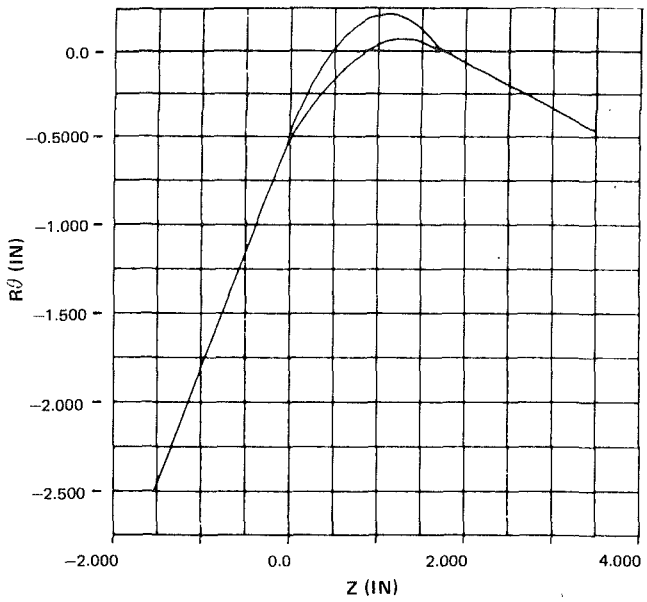

Fig. 3 Input geometry at the root section

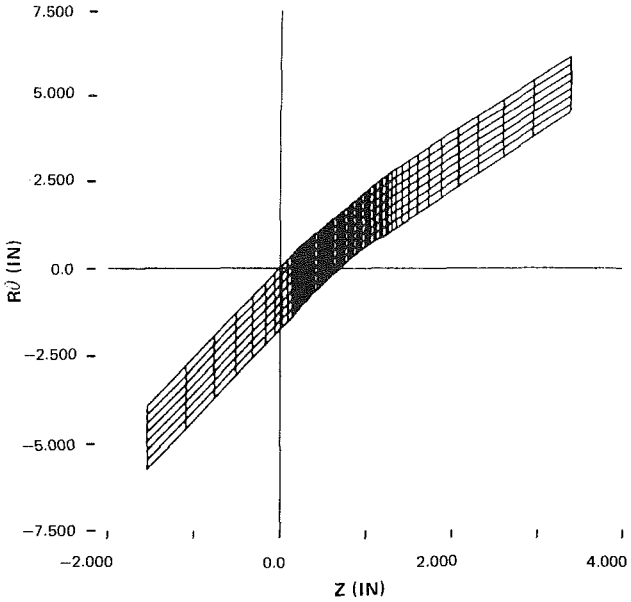

Fig. 5 Computational grid at the tip

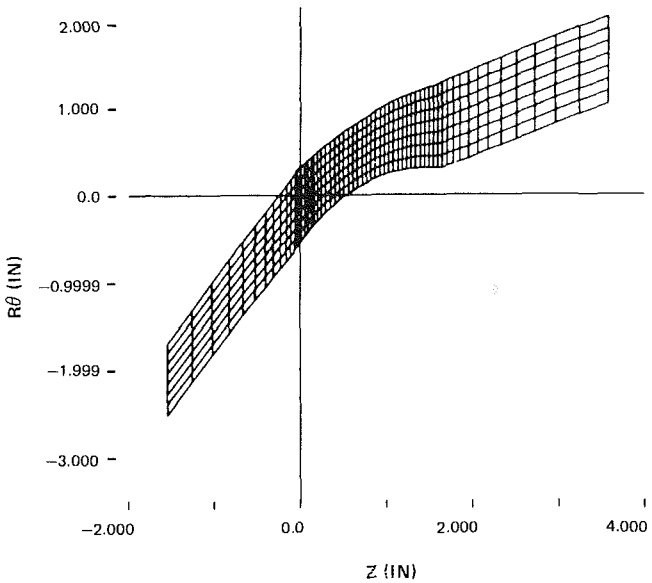

Fig. 4 Computational grid at the root

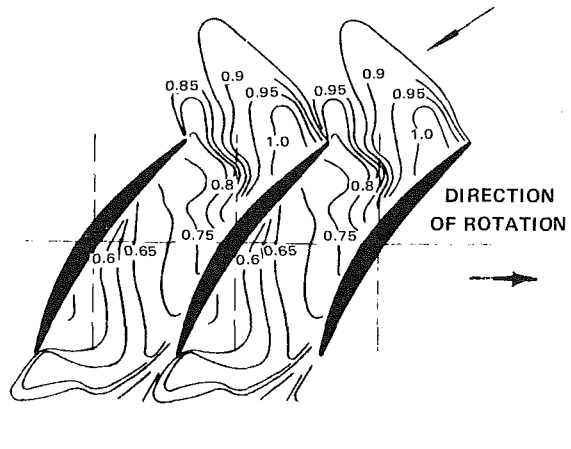

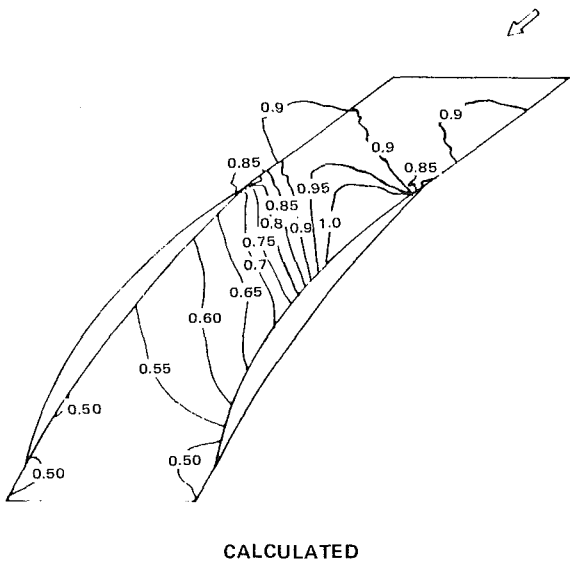

Fig. 6 Lines of constant relative Mach number through the blade passage at 18 percent span (surface 2 in Fig. 1(*b*))

calculation has been developed to calculate the flow in transonic compressor rotors referenced to a rotating frame of reference. The modification consists of solving the system of equations in the relative frame rotating with the blade row, including additional terms for coriolis and centrifugal forces in the momentum equations and solving an additional equation for the conservation of energy. The modified program has been used to compute the three-dimensional flow field through the DFVLR fan rotor at the 100-percent design speed, maximum efficiency condition. Comparisons with laser-two-focus velocity measurements indicate that the inviscid calculation accurately models the transonic flow field in the upstream portion of the blade passages, with the viscous effects mainly influencing the downstream portions.

Acknowledgment

The author wishes to thank Dr. John Denton (Cambridge

Downloaded 01 Jun 2010 to 171.66.16.62. Redistribution subject to ASME license or copyright; see http://www.asme.org/terms/Terms_Use.cfm

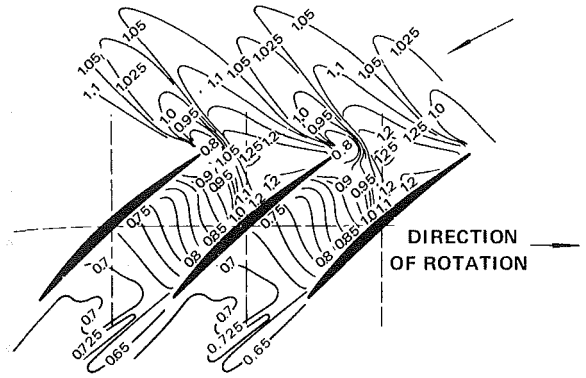

MEASURED

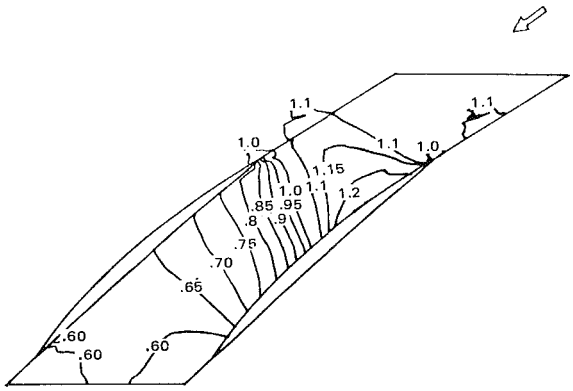

CALCULATED

Fig. 7 Lines of constant relative Mach number through the blade passage at 45 percent span (surface 4 in Fig. 1(*b*))

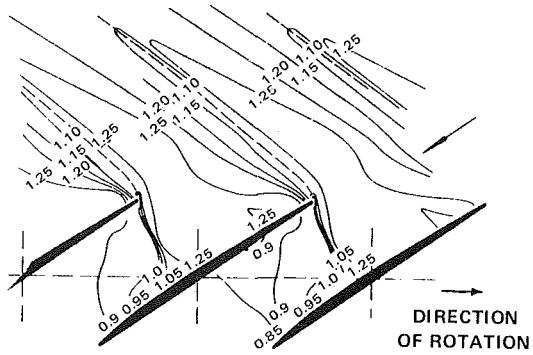

MEASURED

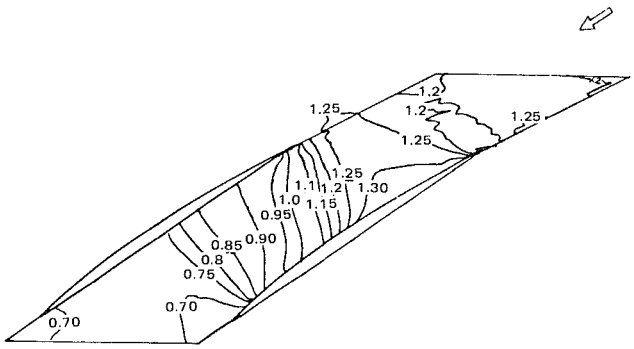

CALCULATED

Fig. 8 Lines of constant relative Mach number through the blade passage at 68 percent span (surface 6 in Fig. 1(*b*))

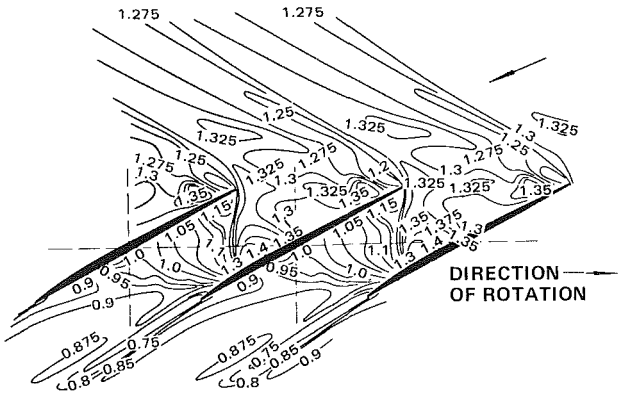

MEASURED

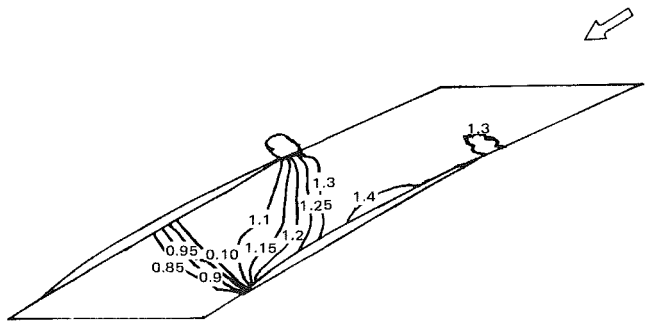

CALCULATED

Fig. 9 Lines of constant relative Mach number through the blade passage at 89 percent span (surface 6 in Fig. 1(*b*))

Downloaded 01 Jun 2010 to 171.66.16.62. Redistribution subject to ASME license or copyright; see http://www.asme.org/terms/Terms_Use.cfm

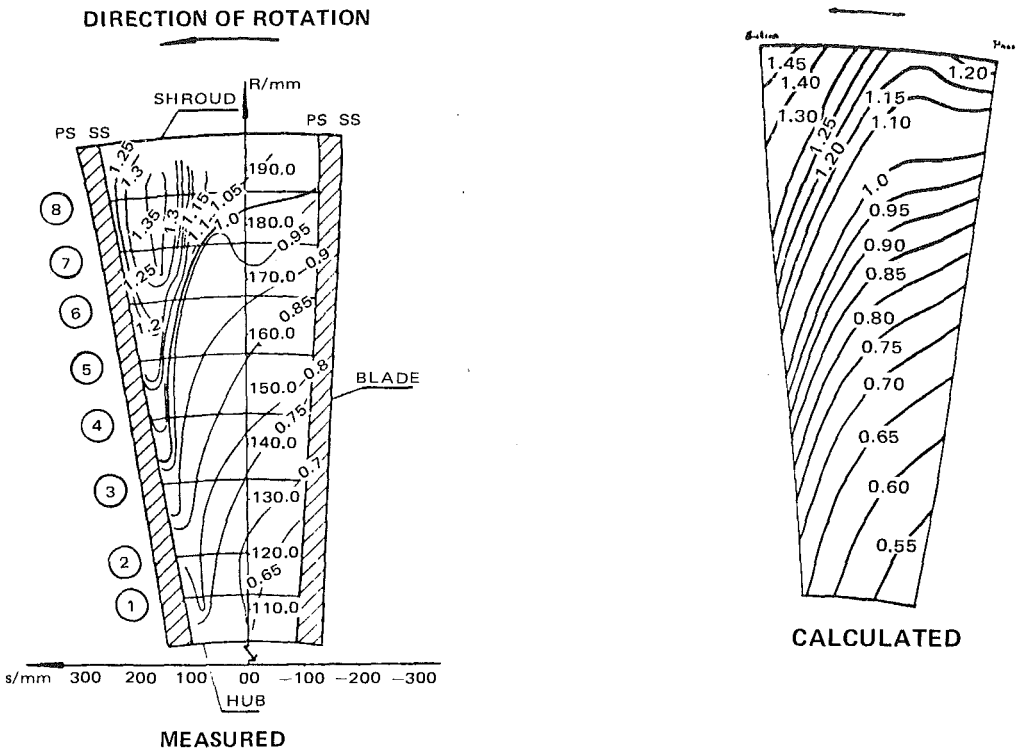

Fig. 10 Lines of constant relative Mach number plotted over one blade channel within the rotor (Plane 11)

University) for the many helpful discussions during this project, and David Hobbs for his support and other useful discussions. The author also thanks the management of Pratt and Whitney Aircraft for permission to present this paper, and Dr. Weyer of DFVLR for the details of the blade geometry and the laser data.

References

1 McDonald, P. W., Bolt, C. R., Dunker, R. J. and Weyer, H. B., "A Comparison Between Measured and Computed Flow Fields in a Transonic Compressor Rotor," ASME Paper No. 80-GT-7.

2 Gopalakrishnan, S., "Fundamentals of Time Marching and Application of the Time Dependent Technique to Turbomachinery Cascades," *VKI Lecture Series 59, Transonic Flows in Turbomachinery*, May 1973.

3 McDonald, P. W., "The Computation of Transonic Flow Through Two-Dimensional Gas Turbine Cascades," ASME Paper No. 71-GT-89.

4 Veuillot, J. P., "Calculation of the Quasi Three-Dimensional Flow in a Turbomachine Blade Row," ASME Paper No. 76-GT-56, 1976.

5 Erdos, J. I., Alzner, E., and McNally, W., "Numerical Solution of Periodic Transonic Flow through a Fan Stage," *AIAA Journal*, Vol. 15, No. 11, Nov. 1977, pp. 1559–1568.

6 Thompkins, W. T., Jr., "An Experimental and Computational Study of the Flow in a Transonic Compressor Rotor," MIT GTL Report No. 129, May 1976.

7 Oliver, D. A., and Sparis, P., "A Computation Study of Three-Dimensional Transonic Shear Flow in Turbomachine Cascades," AIAA Paper No. 71-83.

8 Denton, J. D., "Extension of the Finite Area Time Marching Method to Three-Dimensions," *VKI Lecture Series 84, Transonic Flows in Axial Turbomachinery*, February 1976.

9 Denton, J. D., and Singh, U. K., "Time Marching Methods for Turbomachinery Flow Calculation," *VKI Lecture Series 7*, 1979.

10 Weyer, H. B., and R. Dunker, "Laser Anemometer Study of the Flow Field in a Transonic Compressor Rotor," AIAA Paper 78-1, Jan. 1978.

Downloaded 01 Jun 2010 to 171.66.16.62. Redistribution subject to ASME license or copyright; see http://www.asme.org/terms/Terms_Use.cfm

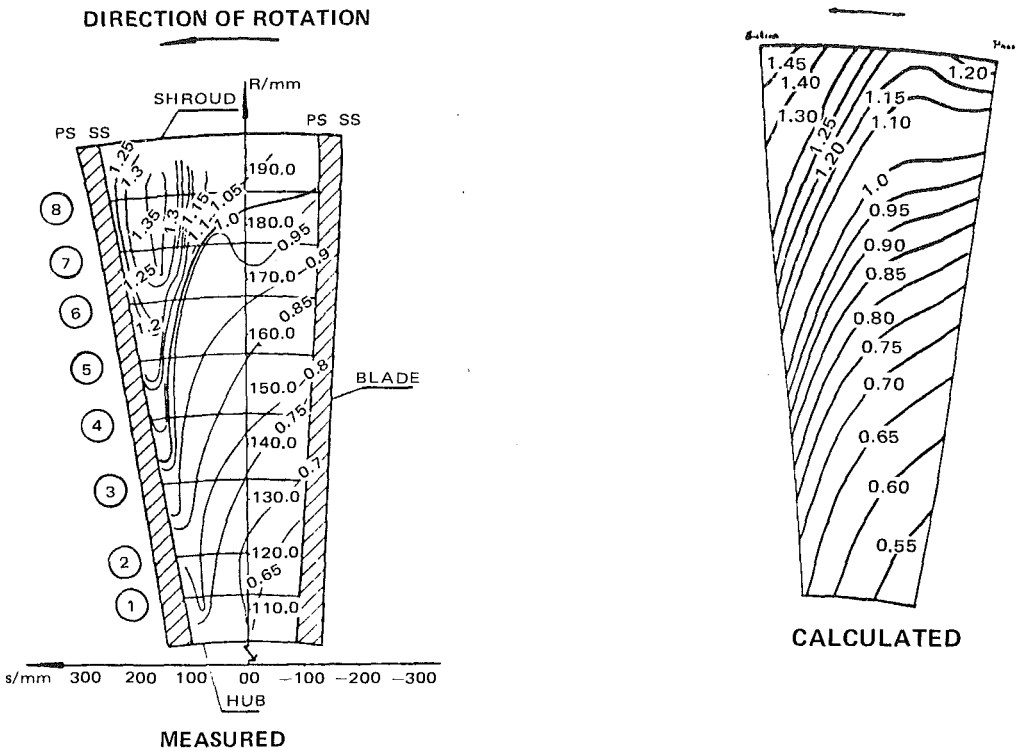

Fig. 10 Lines of constant relative Mach number plotted over one blade channel within the rotor (Plane 11)

University) for the many helpful discussions during this project, and David Hobbs for his support and other useful discussions. The author also thanks the management of Pratt and Whitney Aircraft for permission to present this paper, and Dr. Weyer of DFVLR for the details of the blade geometry and the laser data.

References

1 McDonald, P. W., Bolt, C. R., Dunker, R. J. and Weyer, H. B., "A Comparison Between Measured and Computed Flow Fields in a Transonic Compressor Rotor," ASME Paper No. 80-GT-7.

2 Gopalakrishnan, S., "Fundamentals of Time Marching and Application of the Time Dependent Technique to Turbomachinery Cascades," *VKI Lecture Series 59, Transonic Flows in Turbomachinery*, May 1973.

3 McDonald, P. W., "The Computation of Transonic Flow Through Two-Dimensional Gas Turbine Cascades," ASME Paper No. 71-GT-89.

4 Veuillot, J. P., "Calculation of the Quasi Three-Dimensional Flow in a Turbomachine Blade Row," ASME Paper No. 76-GT-56, 1976.

5 Erdos, J. I., Alzner, E., and McNally, W., "Numerical Solution of Periodic Transonic Flow through a Fan Stage," *AIAA Journal*, Vol. 15, No. 11, Nov. 1977, pp. 1559–1568.

6 Thompkins, W. T., Jr., "An Experimental and Computational Study of the Flow in a Transonic Compressor Rotor," MIT GTL Report No. 129, May 1976.

7 Oliver, D. A., and Sparis, P., "A Computation Study of Three-Dimensional Transonic Shear Flow in Turbomachine Cascades," AIAA Paper No. 71-83.

8 Denton, J. D., "Extension of the Finite Area Time Marching Method to Three-Dimensions," *VKI Lecture Series 84, Transonic Flows in Axial Turbomachinery*, February 1976.

9 Denton, J. D., and Singh, U. K., "Time Marching Methods for Turbomachinery Flow Calculation," *VKI Lecture Series 7*, 1979.

10 Weyer, H. B., and R. Dunker, "Laser Anemometer Study of the Flow Field in a Transonic Compressor Rotor," AIAA Paper 78-1, Jan. 1978.

DISCUSSION

D. C. Prince, Jr.[1]

A conspicuous feature of the results in this paper is the deficiency in calculated flow, more than 4 percent, as compared with the experimental flow. This result is in sharp contrast with reference [1], in which the measured mass flow for the same experiment was used successfully as the boundary condition for matching the measured pressure profiles. The result would be consistent if the effective critical passage area as seen by the code were several percent too small. But if the critical passage area is correct, and the upstream capture area, evidenced by the calculated flow, is 4 percent too small, the possibility that a 20 percent inconsistency in average velocity level exists.

There seems to be a need for a standard procedure for evaluating the accuracy and reliability of computational analyses of compressor rotors. The problem is not peculiar to three-dimensional solutions; many two-dimensional solutions have also attributed a theoretical impossibility to the measured flow through transonic cascades. I would like to propose standard evaluation procedures for application to compressor cascade analyses. These procedures are in three parts – the first involving satisfaction of conservation of mass, the second covering conservation of momentum, and the third presenting velocity or pressure profiles along stream surface intersections taken at mid passage and at 10 percent flow away from pressure and suction surfaces. For the first two parts, a standard control volume is to be defined which should be as simple as possible to assist in physical understanding of the results.

To test conservation of mass, a suitable control volume could be based on orthogonals to the flow in S_1 surfaces (blade-to-blade stream surfaces, which may or may not be

[1] Consulting Engineer, General Electric Co., Aircraft Engine Group, Cincinnati, Ohio 45215.

Copyright © 1982 by ASME

Downloaded 01 Jun 2010 to 171.66.16.62. Redistribution subject to ASME license or copyright; see http://www.asme.org/terms/Terms_Use.cfm

defined from revolution of meridional flow streamlines), originating on the pressure surface at five leading edge radii downstream from the stagnation locus. The volume would be extended upstream along the airfoil surfaces to the stagnation locus and then, in principle, along the S_2 surface (hub-to-tip stream surface) extensions of the airfoils. The upstream boundary is to be taken in a region of uniform flow, parallel to leading edges for two-dimensional solutions and in a plane perpendicular to the axis of rotation for three-dimensional solutions. Considering no net flow across the S_2 surface boundaries, comparison of the flow across the downstream boundary of this region with the upstream flow is analogous to the throat margin evaluation inherent in transonic compressor design procedures. Assuming that the passage inlet area is evaluated correctly, one would surely expect that the choked flow across it should be at least as high as the design flow, and that any significant deficiency below the choked flow should be a consequence of very large velocity differences according to the standard A/A^* versus M relationship. In the absence of excessive boundary layer allowances, the computed flow should be higher than the measured flow. It is suggested that a 1/2 percent discrepancy between the flow across the upstream boundary and the flow through the critical passage area should be cause for serious concern.

A logical control volume for a momentum balance could be based on the passage inlet shock. My personal experience is that the passage inlet shock is perpendicular to the S_1 surface flow (i.e., roughly coincides with the control volume boundary suggested for checking conservation of mass) for relative Mach numbers between 0.9 and 1.2, approximates the wave direction for maximum deflection for Mach numbers between 1.4 and 1.8, and is slightly oblique to the S_1 surface flow in the in-between range. The surface location needs to be chosen in a way to make it convenient to evaluate the momentum flux vector across it near the pressure surfaces, separately with reference to local flow angles upstream of the leading edge, and with reference to the pressure surface metal angle at the point five leading edge radii downstream of the leading edge.

It is recognized that time-marching methods face formidable problems in obtaining good resolution in regions of rapid deceleration. These problems need to be taken seriously. The relative flow angle upstream of the leading edge is expected to be closely related to the suction surface metal angle across the passage in the upstream characteristic direction. If this flow angle is different from the pressure surface metal angle, as is usually the case, standard shock equations predict a pressure difference. The present paper, in contrast to some previous presentations, recognizes the need for that pressure difference at all radii. An effort to evaluate the level of pressure difference would be appreciated.

The objective in the use of the momentum control volume is to demonstrate that the momentum flux upstream of the shock differs from the flux far upstream by an amount predictable from the pressure distribution on the open suction surface and that the momentum flux change across the shock is consistent with the shock equations. In company with other investigators, observe that measured shock discontinuities are usually much smaller than my training leads me to expect. I have not identified any mechanism to justify theoretical predictions different from those implied by simple normal shock equations. Reference [11], however, reports a quite extensive series of experiments on normal shock pressure rises, averaging about 60 percent of conventional predictions. Although the author of reference [11] discusses theoretical considerations at some length, his main thrust is an empirical correlation of the results. Considering the frequent appearance of deficient experimental pressure rises, it could be misleading to use these to support the discontinuities in analytical simulations. Violation of conservation of momentum by the experimental data do not normally permit analytical simulations to do the same.

The third step in the proposed evaluation procedure is designed to facilitate direct comparisons among velocities, between two-dimensional and three-dimensional analyses, and between analysis and experiment. Contour plots are valuable as overall presentations of the flow patterns, but may be misleading for efforts at direct comparison of velocity magnitudes. My recommendation for comparison at 10 percent flow away from pressure and suction surfaces (specifically along the S_1 surface-S_2 surface intersection at 10 percent flow) is designed to avoid dependence on anomalous experimental data taken close to an airfoil surface and on the difficulty in representing the details of shock reflections and shock-boundary layer interactions. Visual examination of the experimental result presented in the paper in Fig. 9 for a curve at 10 percent flow from the pressure surface suggests:

1 a rapid deceleration from Mach number 1.325 to 1.25 at about 50 percent chord upstream of the leading edge – the bow wave from the adjacent airfoil;
2 a gradual expansion back to Mach number 1.325, with the minimum at about 5 percent chord upstream of the leading edge;
3 a rapid deceleration to Mach number 1.125 across the pressure surface branch of the leading edge bow wave;
4 a nearly constant Mach number plateau extending opposite the first 15 percent chord of the pressure surface;
5 a nearly linear deceleration to 0.9 Mach number at 85 percent chord;
and
6 a final region of equalization with the dowstream flow conditions.

The calculated results show no equivalent to items (1) and (2), a deceleration of somewhat greater amplitude to below 1.10 corresponding to (3), a plateau covering 50 percent chord corresponding to (4), a rapid deceleration over no more than 10 percent chord, centered on 55 percent chord, and going below 0.85, corresponding to (5), and no further detail. If the overall deceleration from Mach number 1.3 to 0.9 is taken as the reference velocity level in a comparison, calculated velocities appear to oscillate around the measured velocities, departing as much as 10 percent from the reference level in either direction.

It is to be hoped that the author might report the results of control volume analyses for his calculations, including, especially, his assessment of the critical passage area situation.

Additional References

11 Sinnott, C. S., "On the Prediction of Mixed Subsonic/Supersonic Pressure Distributions," *Journal of Aerospace Sciences*, Vol. 27, No. 10, Oct. 1960, pp. 767-778.

Author's Closure

The author thanks Dr. Prince for his detailed discussions. McDonald et al. in the quasi-three-dimensional analysis (reference [1]) use a streamline calculation to compute the flow field in the meridional surface where mass flow is a prescribed boundary condition. Time marching methods do not compute for defined preset mass flows.

The boundary conditions used in the three-dimensional time marching calculation as stated in the paper are: (a) total pressure and temperatures upstream maintained constant at an input level, (b) static pressure on the hub at exit station input, and exit spanwise variation computed based on radial equilibrium. These boundary conditions set the mass flow. The results presented in the paper were computed using

Downloaded 01 Jun 2010 to 171.66.16.62. Redistribution subject to ASME license or copyright; see http://www.asme.org/terms/Terms_Use.cfm

measured total conditions upstream and a far downstream static pressure condition, which was derived from a measured trailing edge value without correcting for the converging area change. This larger static pressure induced a lower than measured mass flow. A lower back pressure could be used to give the correct mass flow, but this should be done in conjunction with boundary layer modeling to be meaningful. The blade untwist due to rotation was accounted for but no corrections due to boundary layer buildup on the blades or endwalls were made. Modeling this is quite complex since this involves computing three-dimensional boundary layers with shock interactions present. To assess the convergence of each calculation, mass flow conservation and changes in axial velocity at any point in the field between time steps are checked. Mass flow computed at each axial station of the computational grid was conserved within 0.25 percent for that run.

Also, the computation smears the shock through three or four grid points. Thus a discontinuity is smoothed and approximated by a continuous distribution. Hence, a solution requiring discontinuous jumps in the flow field, to satisfy continuity and conservation of momenta, is approximated by continuous, smeared shocks, and is in error. The magnitude is determined by the smoothing of the shock.

A momentum balance check similar to the one suggested has been used in the two-dimensional version of the program and has been found to be equal to the load (integral of the static pressures on the surface in the tangential direction) on the blade within 0.15 percent. Discrepancies in the Mach number fields between the calculation and the data at a location 10 percent gap from the blade surfaces could be associated with lack of boundary layer modeling on the surfaces.

In conclusion, the paper is intended to demonstrate the quality of an inviscid three-dimensional solution. It is not attempting to present a fully developed strong viscous-interaction, inviscid-blade row solution, of which it is only a component part.

Downloaded 01 Jun 2010 to 171.66.16.62. Redistribution subject to ASME license or copyright; see http://www.asme.org/terms/Terms_Use.cfm

Evaluation of Methods for the Treatment of Mean Stress Effects on Low-Cycle Fatigue

M. Doner

K. R. Bain

J. H. Adams

Detroit Diesel Allison Division,
General Motors Corporation,
Indianapolis, Ind. 46206

Several methods proposed for the treatment of mean stress effects on time-independent low cycle fatigue (LCF) lifetime were critically evaluated using LCF crack initiation data on a number of materials used in gas turbine design. The methods evaluated included Jaske's equivalent strain (ϵ_{eq}) formulation, Manson's mean stress correction method and nonlinear Goodman diagram representation of the strain-controlled LCF data. LCF crack initiation data on STA Ti-6-4 (533K), Ti-5522S (783K), IN-706 (866K) and MAR-M246 (1033K) were utilized in the evaluations. The evaluations were carried out in terms of each method's capability to back-predict the experimetnal data used in its construction. Also considered were the implications associated with the type and the extent of data required for each method.

Introduction

The current low cycle fatigue (LCF) crack initiation life prediction methods are based on the assumption that a smooth, strain-controlled LCF specimen simulates the behavior of the material at the geometric discontinuities in a component. Consequently strain-controlled LCF data is generated extensively in order to construct material LCF models for life prediction analysis. The large volume of strain-controlled LCF data generated on materials used in gas turbine design, as well as data available in literature on other structural alloys, indicate that the LCF crack initiation life is strongly affected by the mean stresses that develop in a given material. Consequently, mean stress effects, whenever they are present, must be included in the material LCF models. A number of factors influence the magnitude of mean stresses developed in a material subjected to strain cycling. These include the ratio of elastic to inelastic strain range, temperature, cycle frequency, hold time (duration as well as where applied in the cycle), the degree with which the material properties change with temperature,[1] the phase difference between temperature and strain,[1] etc.

The present study, first, attempts to provide a brief overview of some of the most prominent methods that are available for the treatment of mean stress effects on LCF life. This, then, is followed by an evaluation of these methods using an extensive LCF data base on a number of materials used in gas turbine design. The evaluations are carried out in terms of each method's capability to back-predict the experimental data.

Experimental Observations on Mean Stress Effects

Before proceeding with a discussion of various methods proposed for the treatment of mean stress effects, it seems appropriate to describe briefly the magnitude of mean stresses that can develop in materials used in gas turbine design and the extent with which they affect the crack initiation lifetimes.

Figure 1 is a typical example illustrating the dependence of the mean stress (developed in strain-controlled LCF specimens) on the total strain range ($\Delta\epsilon_T$) and the strain ratio (A_ϵ). The material is a wrought nickel-base superalloy used primarily in turbine disk applications. In Fig. 1, the linear portions of the curves indicated by dotted lines correspond to conditions where the peak stress in the cycle is below the proportional limit of the material. In this regime $A_\sigma = A_\epsilon$. As the strain range is increased, however, the material eventually yields and part of the total strain in the hysteresis loop becomes inelastic. From this point on $A_\sigma \pm A_\epsilon$ and A_σ continually increases with $\Delta\epsilon_T$. As the total strain range is further increased, the σ_o versus $\Delta\epsilon_T$ curve at each strain ratio goes through a maximum and then drops off continuously with $\Delta\epsilon_T$. Finally, when the total strain range (and, correspondingly, the ratio of inelastic to total strain range) become sufficiently large, the hysteresis loops become completely reversed (i.e., $\sigma_o = 0$) for both A_ϵ ratios. An examination of the corresponding crack initiation lives clearly illustrates the effects of mean stress in this material. At $\Delta\epsilon_T$ = 0.005 in./in., for example, the mean stresses sustained by the material are 414 MPa for $A_\epsilon = 0.25$,255 MPa for $A\epsilon = 1.0$ and essentially zero for $A_\epsilon = \infty$. The corresponding crack initiation lives at this strain range level are 5×10^4 cycles for

[1] These factors apply to thermal-mechanical cycling only.

Contributed by the Gas Turbine Division and presented at the International Gas Turbine Conference and Products Show, Houston, Texas, March 9-12, 1981, of THE AMERICAN SOCIETY OF MECHANICAL ENGINEERS. Manuscript received at ASME Headquarters, December 15, 1980. Paper No. 81-GT-122.

Copyright © 1982 by ASME

Downloaded 01 Jun 2010 to 171.66.16.62. Redistribution subject to ASME license or copyright; see http://www.asme.org/terms/Terms_Use.cfm

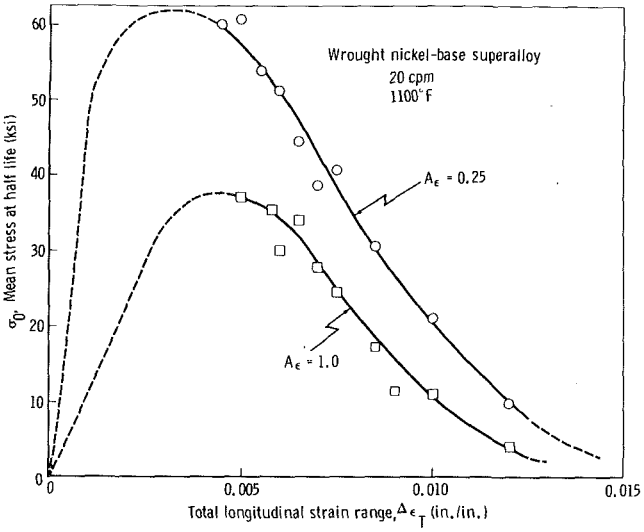

Fig. 1 Dependence of mean stress on strain range at various strain ratios in a wrought nickel-base superalloy at 1100°F (866K)

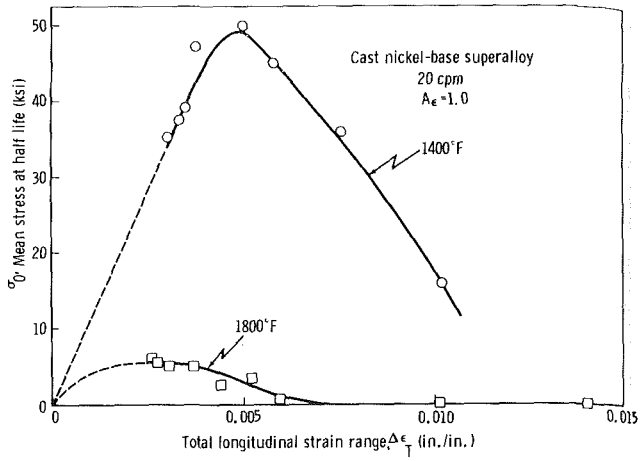

Fig. 2 Mean stress versus strain range at 1400°F (1033K) and 1800°F (1255K) for A_ϵ = 1.0 in a cast nickel-base superalloy

A_ϵ = 0.25, 10^5 cycles for A_ϵ = 1.0 and approximately 10^6 cycles for $A_\epsilon = \infty$. On the other hand, at $\Delta\epsilon_T$ = 0.013 in./in., where the hysteresis loops for all three strain ratios are essentially completely reversed, the crack initiation lives are essentially the same at about 10^3 cycles.

Figure 2 illustrates the mean stress versus strain range relationship in a cast nickel-base superalloy for A_ϵ = 1.0 at two different temperatures: 1033K and 1255K. The behavior exhibited at 1033K in this material is similar to that observed in Fig. 1. The crack initiation life in this alloy is also strongly influenced by the mean stress. At $\Delta\epsilon_T$ = 0.005 in./in., for example, the crack initiation life for A_ϵ = 1.0 (with a mean stress of 345 MPa) is approximately an order of magnitude less than that for $A_\epsilon = \infty$, where the mean stress is zero. The difference between the A_ϵ = 1.0 and $A_\epsilon = \infty$ lives increases as the strain range is lowered below 0.005 in./in. On the other hand, at strain ranges above 0.011 in./in., the level of mean stress sustained by the material becomes almost negligible and, correspondingly, the crack initiation lives become essentially the same.

The behavior exhibited at 1255K in Fig. 2, however, is entirely different, in that the highest level of mean stress that can be sustained by the material is about 5 ksi, and at total strain ranges above about 0.005 in./in. the hysteresis loops become essentially completely reversed. Correspondingly, the total strain range vs life curves for A_ϵ = 1 and $A_\epsilon = \infty$ at this temperature are essentially identical within a life range of approximately 10^2 to 10^5 cycles.

Methods Proposed for the Treatment of Mean Stress Effects

As the results presented in the preceding sections indicate, the determination of mean stress effect on crack initiation lifetimes of materials requires the generation of strain-controlled LCF data at a number of strain ratios. Experience indicates that at least three strain ratios be utilized for this purpose, e.g., $A_\epsilon = \infty$, 1.0 and 0.25. A number of approaches can then be utilized to model the resultant data. The following paragraphs describe some of these methods proposed specifically for the treatment of mean stress effects in the absence of any time-dependent effects on materials LCF life. The treatment of mean stresses effects when the fatigue crack initiation process is time-dependent is outside the scope of this study.

One common method in which the mean stress effects on LCF crack initiation life can be directly expressed is based on the utilization of nonlinear Goodman diagrams, as illustrated schematically in Fig. 3. This approach generally requires strain-controlled testing of specimens at a minimum of three strain ratios. Analytical representations of strain versus life are first constructed for each strain ratio. The well-known Manson-Coffin relationship provided satisfactory fits for the materials and strain ratios examined in this study. There may be cases, however (especially for strain ratios other than fully reversed), where the Manson-Coffin relationship is not appropriate and other representations should be used. The specimen response data is then used to construct the half-life stress-strain curve and the half-life mean stress versus strain relationship for each strain ratio. For any given life, the iso-life line of the nonlinear Goodman diagram can then be constructed. Several relationships can be used to describe these iso-life lines. One such relationship, used in the present study is as follows:

$$\frac{\sigma_A}{\sigma_{CR}} + \left(\frac{\sigma_0}{\sigma_U}\right)^\beta = 1.0 \qquad (1)$$

where σ_A is the alternating stress (at half-life), σ_{CR} is the

Nomenclature

A_ϵ = strain ratio (alternating strain/mean strain)
$A\sigma$ = stress ratio (alternating stress/mean stress)
$\bar{D}$ = differences between back-predicted and observed log lives
E = elastic modulus
N_f = number of cycles to failure
N_i = number of cycles to crack initiation
β = exponent for modified Goodman diagram
ϵ_A = total strain amplitude
ϵ_{eq} = equivalent strain parameter
σ = standard deviation of differences between back-predicted and observed log lives
σ_A = alternating stress (at half-cycle)
σ_{CR} = alternating stress (at half-life) for completely reserved ($A = \infty$) cycling
σ_{max} = maximum stress (at half-life)
σ_o = mean stress (at half-life)
σ_U = ultimate tensile strength
$\Delta\epsilon_T$ = total strain range

Downloaded 01 Jun 2010 to 171.66.16.62. Redistribution subject to ASME license or copyright; see http://www.asme.org/terms/Terms_Use.cfm

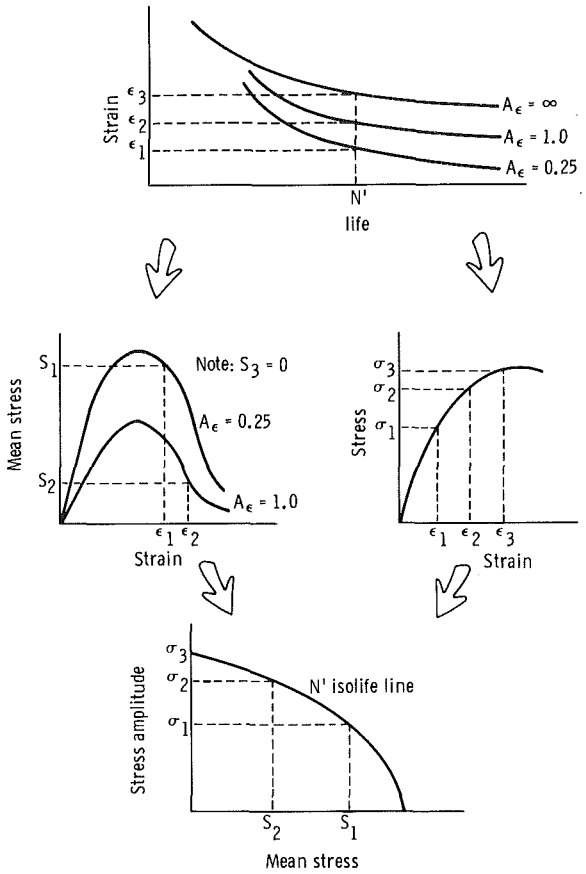

Fig. 3 Representation of mean stress effects through the use of nonlinear Goodman diagrams

alternating stress (at half-life) corresponding to $A_\epsilon = \infty$, σ_o is the mean stress (at half-life) and σ_u the ultimate tensile strength. The exponent β is determined so as to provide the best fit to the experimental data and may be a function of life.

Using an iterative procedure the nonlinear Goodman equation can be used to calculate the equivalent completely reversed stress amplitude for any combination of stress amplitude and mean stress. The equivalent stress amplitude is then converted to an equivalent strain amplitude using the half-life cyclic stress-strain curve. The life calculation is then made based on equivalent fully reversed strain amplitude and the strain amplitude versus life curve for the fully reversed strain cycling, i.e., $A_\epsilon = \infty$.

Other methods have beenproposed in which the LCF crack initiation life is directly expressed in terms of mean stress along with other pertinent parameters. One such method has been described by Manson [1,2]

$$\frac{\Delta\epsilon}{2} = \epsilon_f'(2N_f)^c + \frac{\sigma_f' - k\,\sigma_0}{E}(2N_f)^b \tag{2}$$

where σ_o is the mean stress, k is a constant which is related to material's sensitivity to mean stress, and all other parameters have their usual meaning in terms of SAE modified notation. The approach is based essentially on modification of the elastic line of completely reversed cyclic life relationships. When $k = 1$, the mean stress modification takes the form suggested by Morrow [3]. The value of k, for a given material, can be determined experimentally [2].

A number of methods have been suggested in which the LCF crack initiation life has been expressed in terms of a parameter called "Equivalent Strain," ϵ_{eq} [4]. At least three formulations of ϵ_{eq} have been proposed [4]:

Walker's Formulation

$$\epsilon_{eq} = (\sigma_{max}/E)\quad (\Delta\epsilon_T \,.\, E/\sigma_{max})^m \tag{3a}$$

Topper-Sandor Formulation

$$\epsilon_{eq} = \epsilon_A + \sigma_o^a/E \tag{3b}$$

Stulen's Formulation

$$\epsilon_{eq} = \epsilon_A + d\;\sigma_o/E \tag{3c}$$

In these expressions, $\Delta\epsilon_T$ is the total range, ϵ_A the total strain amplitude, σ_{max} the maximum stress, σ_o the mean stress and E is the modulus of elasticity. For each formulation the fatigue life can be expressed as a polymial[2] in ϵ_{eq}. The parameters m, a and d are determined, using a nonlinear programming technique, to give the best fit to the data.

Still another method in which the mean stress effects on life are expressed analytically has been proposed by Cruse and Meyer [5].

$$N_f = A\;\Delta\epsilon_T^B 10^{C\sigma_o} \tag{4}$$

where N_f is the fatigue life, and A, B and C are material parameters determined by regression analysis. This method, however, is expected to have a limited range of applicability, since for $\sigma_o = 0$, i.e., $A_\epsilon = \infty$, a log-log plot of N_f versus $\Delta\epsilon_T$ results in a straight line over the entire life range, which is not often supported by experimental results.

Evaluation of Proposed Methods

Of the various methods described in the preceding section, some were previously evaluated by one of the authors [6]. These included the use of "equivalent strain" parameter based on Walker's, Topper-Sandor's and Stulen's formulations, as given by equations 3(*a*) to 3(c), and the method proposed by Cruse and Meyer [5]. LCF crack initiation (and failure) data on INCO-901 (generated under strain-controlled testing using strain ratios of ∞, 1.0 and 0.25) were utilized in this evaluation. The methods were compared in terms of the quality of fits (based on sum of squared residuals). The results are presented in Table 1.

Table 1 Comparison of quality of fits for several methods [6]

Method	N_i data	N_f data
Equivalent strain (Walker)	0.7616	0.7978
Equivalent strain (Topper-Sandor)	1.787	3.349
Equivalent strain (Stulen)	1.940	3.388
Cruse and Meyer	0.8512	1.4915

As seen in Table 1, this comparison indicates that the equivalent strain parameter based on Walker's expression is superior to all other methods for the modeling of both N_i and N_f data on this material. (equivalent strain representation of this data is provided in Fig. 7 of reference [7].) A similar result was obtained in the modeling of an extensive LCF data on STA Ti-6-4 at 500°F (533K) in another program [8]. Consequently, in the evaluations carried out in the present study, the equivalent strain formulations based on equations 3(*b*) and 3(*c*), and the method proposed by Cruse and Meyer were not included. The methods critically evaluated in the present study, therefore, were as follows:

- Nonlinear Goodman diagrams
- Manson's mean stress corrections (equation (2))
- Equivalent strain parameter based on Walker's expression (equation (3*a*))

[2] In the present study a cubic polynomial function was used to describe life as a function of ϵ_{eq}.

Downloaded 01 Jun 2010 to 171.66.16.62. Redistribution subject to ASME license or copyright; see http://www.asme.org/terms/Terms_Use.cfm

Table 2 LCF crack initiation data used in the present study for the evaluation of methods dealing with means stress effects

Material	Temperature (°K)	Cycle frequency (cpm)	Strain-ratio (A)	No. of data points
Ti-6-4 (STA)	533	20	∞,1.0,0.25	62
Ti-5522S (STA)	783	20	∞,10,0.25	34
IN-706 (AMS 5703)	866	20	∞,1.0,025	36
MAR-M246	1033	20	∞,0	24

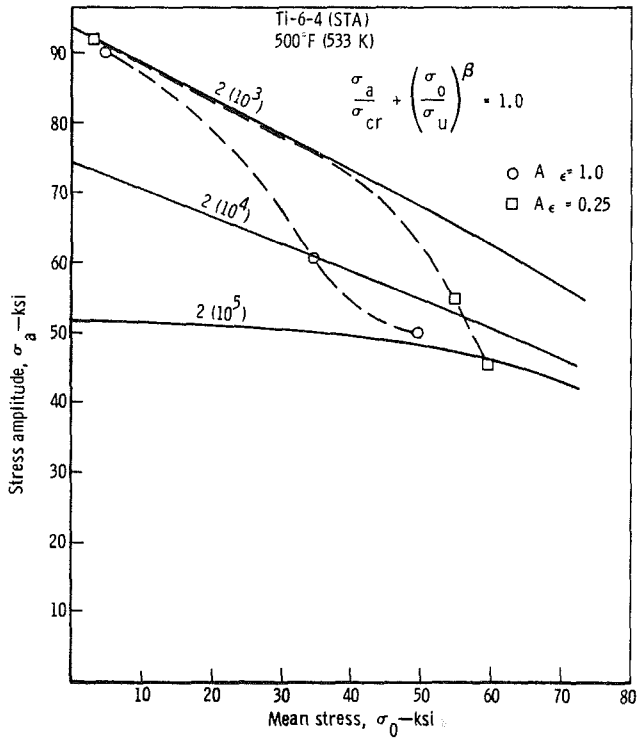

Fig. 4 The nonlinear Goodman diagram for Ti-6-4 (STA) alloy at 500°F (533K)

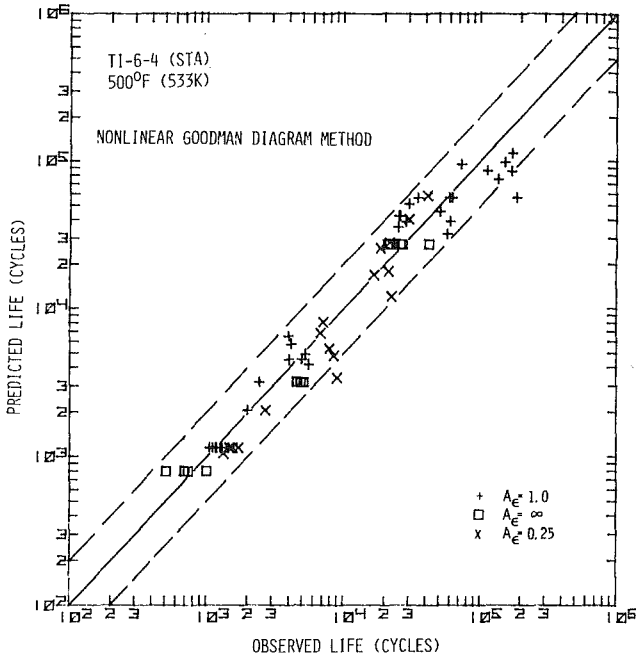

Fig. 5 Predicted versus observed crack initiation life for Ti-6-4 (STA) alloy based on nonlinear Goodman diagram method

The type and the extent of experimental data used in these evaluations are given in Table 2.[3]

In the discussion to follow, each of the aforementioned methods will be examined in terms of plots of back-predicted versus experimentally observed crack initiation lives. This will, then, be followed by a comparison in terms of the standard deviation of differences between the back-predicted and the experimental lives.

A typical nonlinear Goodman diagram (applicable to STA Ti-6-4 at 533K) is illustrated in Fig. 4. This diagram, as well as those for the other materials listed in Table 2, were constructed in the manner described previously. The plots of the back-predicted versus experimentally observed crack initiation lives for the four materials are presented in Figs. 5 to 8. It is seen in these plots that, with the exception of Ti-5522S alloy (Fig. 6), the crack initiation lives can be back-predicted within approximately a factor of 2 using the nonlinear Goodman diagram approach. The method, however, appears to break down in the case of Ti-5522S alloy, expecially for the $A_\epsilon = 0.25$ test results. The examination of the experimental data for this material indicates that the scatter is unusually large in the $A_\epsilon = 1.0$ and 0.25 test results

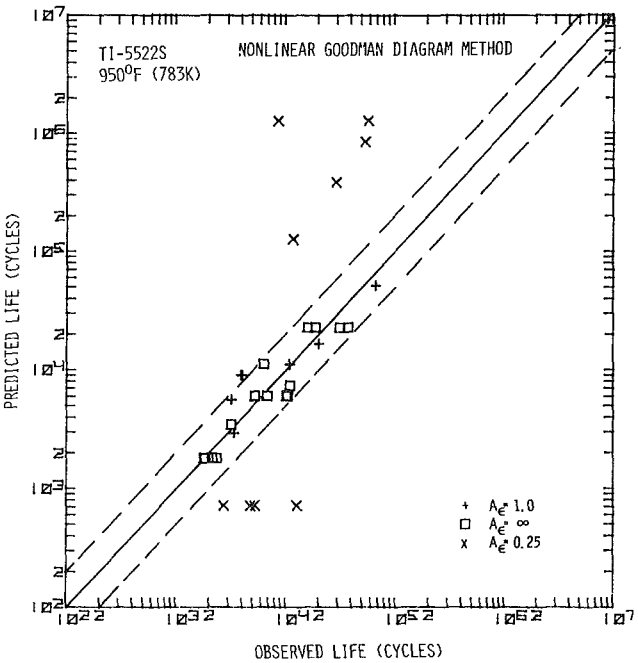

Fig. 6 Predicted versus observed crack initiation life for Ti-5522S alloy based on nonlinear Goodman diagram method

[3]The generation and analysis of LCF data on Ti-6-4 (STA) were accomplished under "Turbine Engine Structural Life Prediction/Correlation Program," USAF Contract F33657-77-C-0374 Detroit Diesel Allison Division, General Motors Corporation.

Downloaded 01 Jun 2010 to 171.66.16.62. Redistribution subject to ASME license or copyright; see http://www.asme.org/terms/Terms_Use.cfm

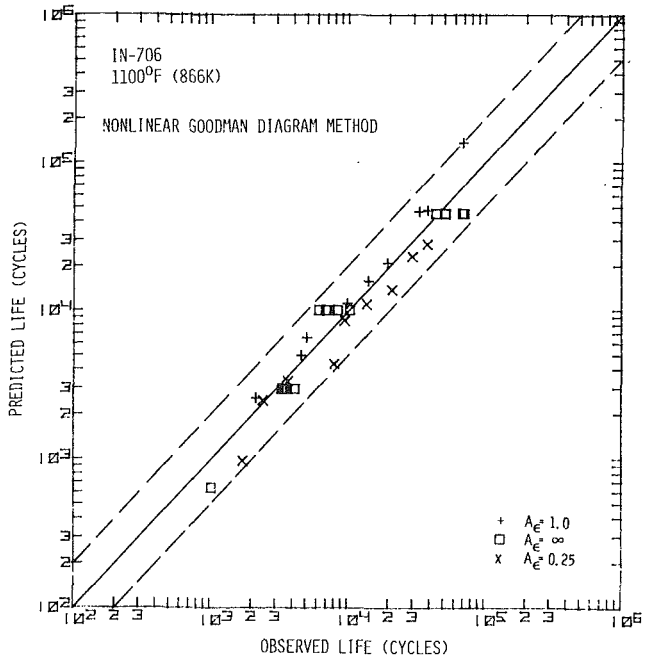

Fig. 7 Predicted versus observed crack initiation life for IN-706 alloy based on nonlinear Goodman diagram method

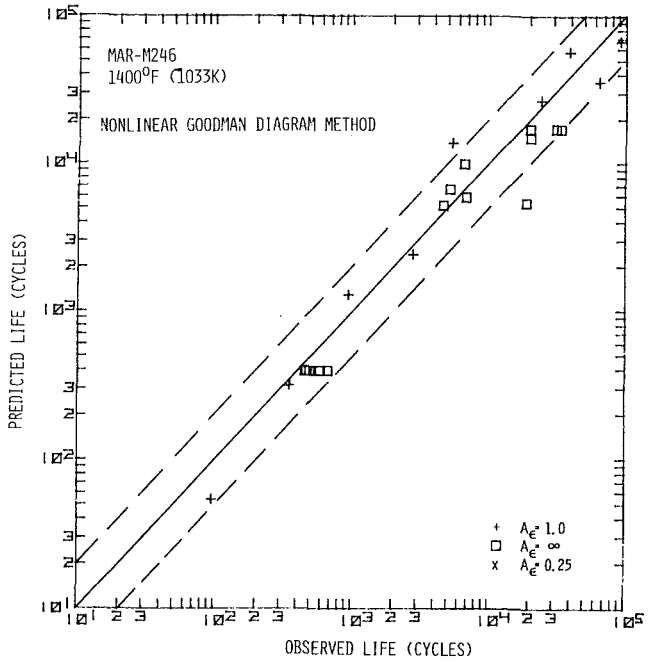

Fig. 8 Predicted versus observed crack initiation for MAR-M246 alloy based on nonlinear Goodman diagram method

and that the corresponding strain range versus life relationships are not well defined. One consequence of this behavior was that the analytically determined iso-life lines of the nonlinear Goodman diagram crossed each other at the lower strain (stress) ratio regime. This problem, however, could perhaps be alleviated by additional testing to provide a better definition of strain range versus life relationships.

In the use of Manson's mean stress correction method [1,2] the calculation of the parameter k is accomplished by rearranging equation (2) as follows

$$\frac{E}{(2N_i)^b}\left[\epsilon_f'(2N_i)^c + \frac{\sigma_f'}{E}(2N_i)^b\frac{\Delta\epsilon_T}{2}\right] = k\sigma_o \qquad (5)$$

A plot of the quantity on the left side of eqaution (5) (for test results in which the mean stress, σ_o, is not zero) versus σ_o should yield the slope k.

(The exponents b and c, and intercepts ϵ_f' and σ_f' are obtained from the Manson-Coffin representation of the completely reversed, i.e. $A_\epsilon = \infty$ data.) The line is required to pass through the origin since the left side of equation (5) is zero, when the mean stresses are zero which is the assumption made in the determination of the exponents b and c and the intercept ϵ_f' and σ_f' in equation (2) through the use of $A_\epsilon = \infty$ data.

The examination of the $A_\epsilon = \infty$ data for all four materials used in this study indicates, however, that the assumption of $\sigma_o = 0$ is not always satisfied. For the alloys Ti−6−4, Ti-5522S and IN-706, the mean stress (at half-life) were primarily compressive and were, for some specimens, as large as −41 MPa. In the case of MAR-M246 alloy, however, they were all tensile and were, for some specimens, as large are 114 MPa. Consequently, for the materials used in this study, the exponents b and c and the intercepts ϵ_f' and σ_f' (equation (2)) do not necessarily represent the strain amplitude versus number of reversals relationships for the casde when the mean stress, σ_o, is zero for the entire life regime.

Additionally, in the determination of the mean stress constant k, the line through the data points, i.e., in the plots of the quantity in the left side of equation (5) versus σ_o, was forced through the origin as required by equation (5). Almost

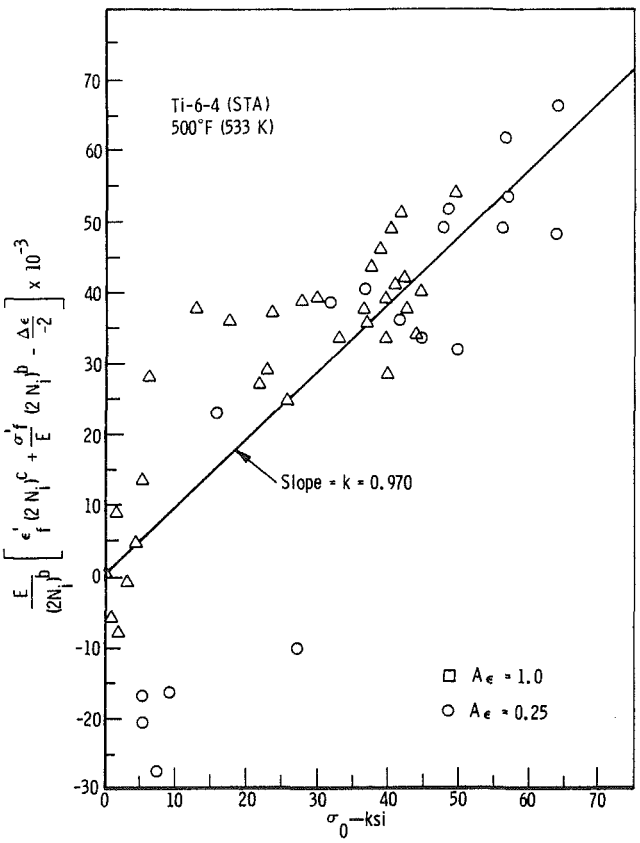

Fig. 9 The left side of equation (5) versus mean stress, σ_o, for Ti-6-4 (STA) alloy for the determination of mean stress parameter k

in all cases, however, a least-squares line through the data points yielded an intercept which varied in value from about −8.5 (IN-706) to 6.0 (Ti-5522S alloy).

A typical plot of the left side of equation (5) versus the mean stress, σ_o, is shown in Fig. 9, which is for the Ti-6-4 alloy at 533K. Similar plots were made for the other materials

Downloaded 01 Jun 2010 to 171.66.16.62. Redistribution subject to ASME license or copyright; see http://www.asme.org/terms/Terms_Use.cfm

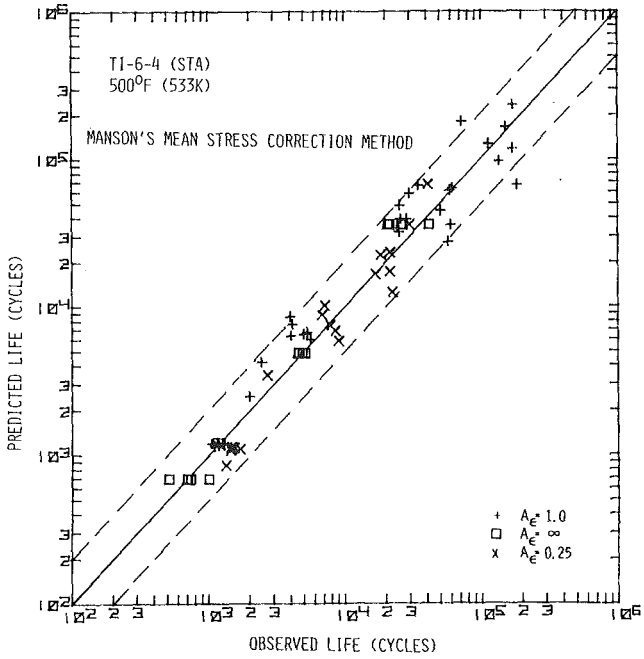

Fig. 10 Predicted versus observed crack initiation life for Ti-6-4 (STA) alloy based on Manson's mean stress correction method

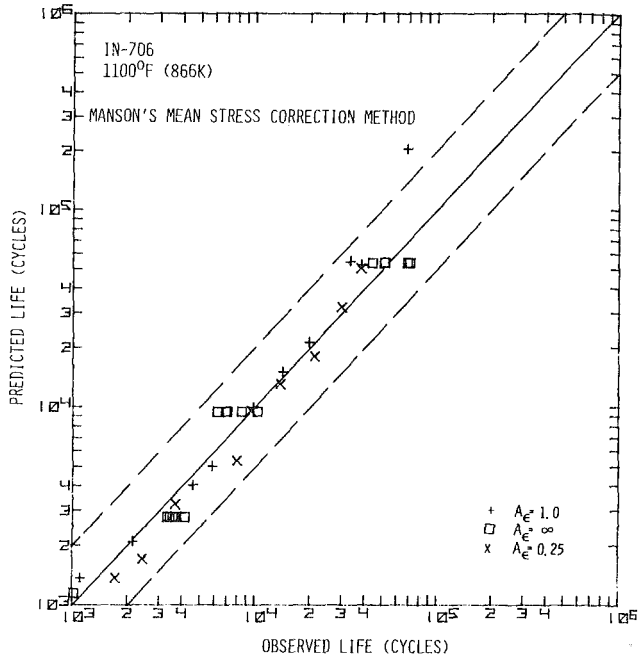

Fig. 12 Predicted versus observed crack initiation life for IN-706 alloy based on Manson's mean stress correction method

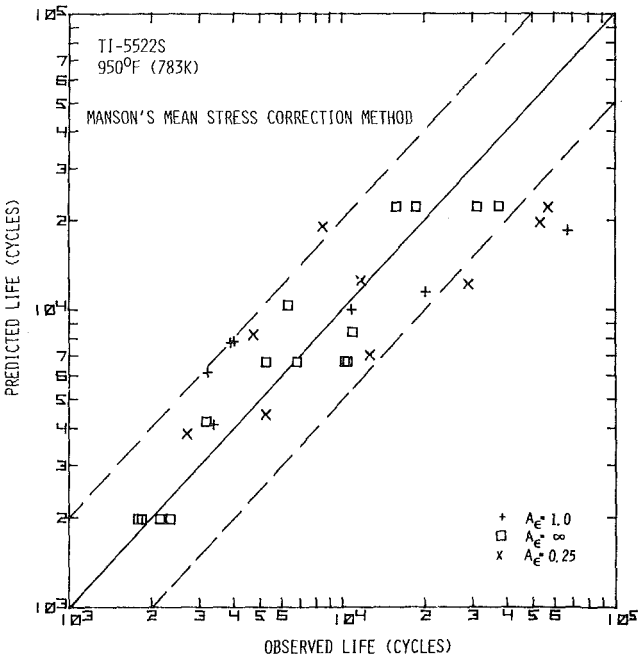

Fig. 11 Predicted versus observed crack initiation life for Ti-5522S alloy based on Manson's mean stress correction method

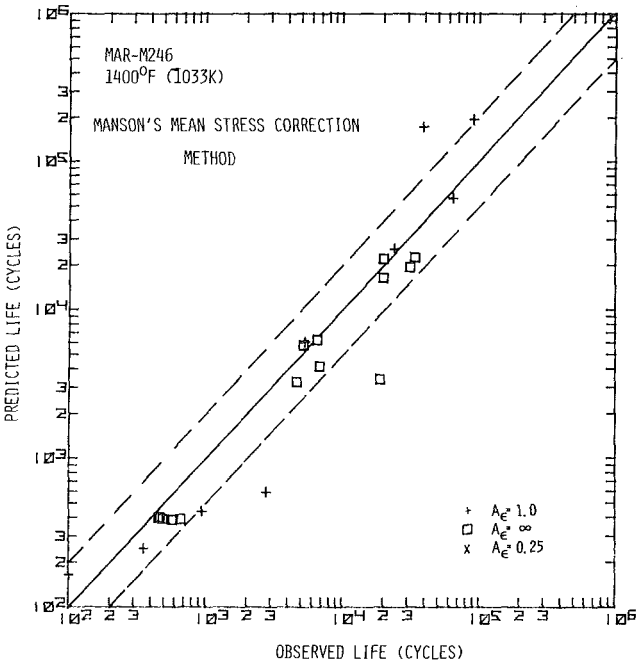

Fig. 13 Predicted versus observed crack initiation life for MAR-M246 based on Manson's mean stress correction method

as well, and the resultant mean stress parameter, k, values are listed in Table 3.

Table 3 The values of the mean stress parameter k for materials used in the present study

Material	Test temp. (K)	k
Ti-6-4 (STA)	533	0.970
Ti-5522S (STA)	783	1.279
IN-706	866	1.019
MAR-M246	1033	1.1614

It is seen in Table 3 that for the alloys Ti-6-4 (533K) and IN-706 (866K) the value of k is very close to 1.0, indicating that these materials behave essentially in accordance with Morrow's hypothesis [3]. The largest value of k corresponds to Ti-5522S alloy, indicating that, of the four materials evaluated, this alloy exhibits the greatest sensitivity to "mean stress" effects. It is also noted in Table 3 that k values listed are considerably smaller than that obtained by Welcher, et al. [2] for the Ti-6-4 alloy at 350K.

The plots of back-predicted versus the experimentally observed crack initiation lives for the four materials studied are presented in Figs. 10 to 13. A comparison of Figs. 10 and

Downloaded 01 Jun 2010 to 171.66.16.62. Redistribution subject to ASME license or copyright; see http://www.asme.org/terms/Terms_Use.cfm

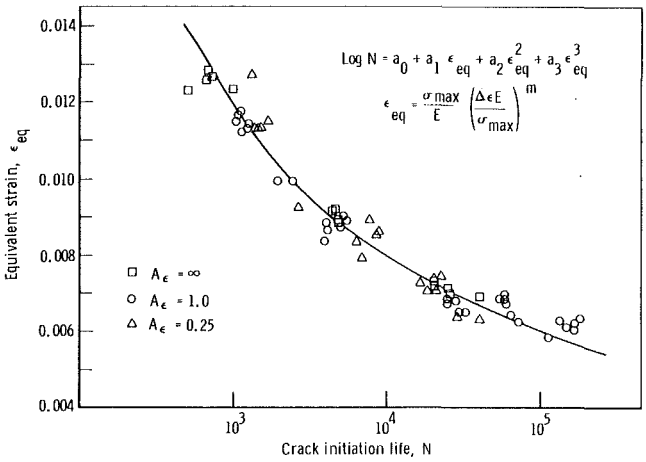

Fig. 14 Use of equivalent strain method for the representation of crack initiation data on Ti-6-4 (STA) alloy at 500°F (533K)

12 with Figs. 5 and 7 indicates that for the alloys Ti-6-4 and IN-706 both the use of Manson's mean stress correction method (equation (2)) and the nonlinear Goodman diagram approach, provide essentially the same degree of correlation of the data in the treatment of mean stress effects. In all cases, the crack initiation lives are back-predicted within about a factor of 2.

A comparison of Fig. 6 and 11, indicate that Manson's mean stress correction method is far superior to the nonlinear Goodman Diagram approach in the treatment of mean stress effects for the Ti-5522S alloy. On the other hand, Manson's method appears to be inferior to the nonlinear Goodman Diagram approach in the case of Mar-M246 alloy. (See Figs. 7 and 12.)

The last method evaluated in the present study was Jaske's [4] equivalent strain method based on Walker's expression (equation 3(*a*)). In this method, the so-called "mean stress effects" are treated through the use of peak tensile stress, σ_{max}. The equivalent strain representation of the crack initiation data for the STA Ti-6-4 alloy at 533K is presented in Fig. 14 [9]. A similar representation of the LCF crack initiation data carried out for the other materials as well, resulted in the values for the exponent m given in Table 4.

Table 4 The values of exponent m for materials used in the present study

Material	Test temp. (K)	m
Ti-6-4 (STA)	533	.518
Ti-5522S(STA)	783	0.391
IN-706	866	0.565
MAR-M246	1033	0.426

The values of m in Table 4 indicate that, of the four materials studied, Ti-5522S alloy exhibits the greatest sensitivity to mean stress effects, as was also observed previously in terms of mean stress parameter k values tabulated in Table 3.

The corresponding plots of back-predicted versus the experimentally observed crack initiation lives for the four materials used are presented in Figs. 15 to 18. A comparison of these figures with those corresponding to the other methods evaluated previously, indicates that, except for the case of Ti-5522S alloy, Jaske's equivalent strain method provides the best correlation of the LCF crack initiation data for the treatment of the so-called mean stress effects. As for the Ti-5522S data, Manson's mean stress correction method appears to provide a slightly better correlation.

A further comparison of the three methods evaluated is provided in Table 5 in terms of the standard deviation, σ, and the mean, $\bar{D}$, of the differences between the back-predicted and the experimentally observed log lives. Taking the standard deviation, σ, as the primary measure of the data correlation, the ranking shown in Table 6 is obtained. The results presented in Table 6, clearly indicate that Jaske's equivalent strain method provides the best overall means of treating the mean stress effects on LCF crack initiation lifetimes of the materials investigated in this study. Additionally, an examination of $\bar{D}$ values in Table 5 indicates that this method results in the lowest values of $\bar{D}$ for all four alloys. (A low value of $\bar{D}$ implies that the bias in back-predicted lives, in terms of conservatism or nonconservatism, is small.)

The results of Tables 5 and 6 also indicate that Manson's mean stress correction method (equation (2)) is the second

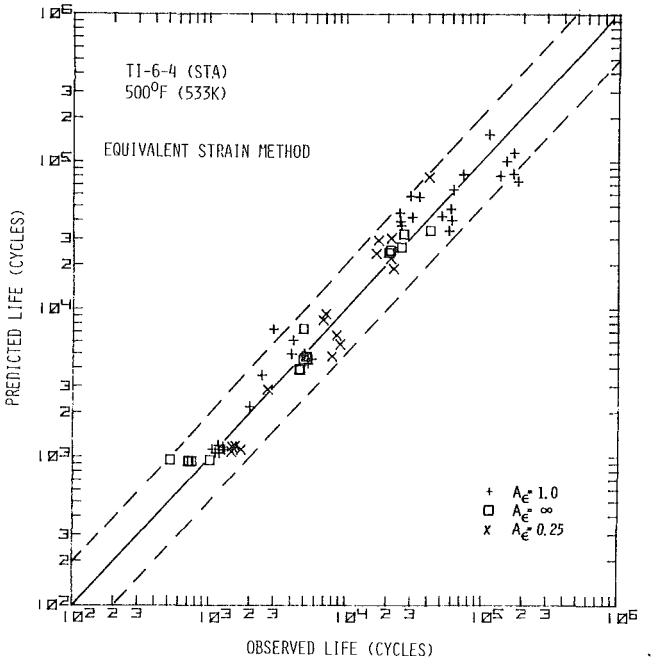

Fig. 15 Predicted versus observed crack initiation life for Ti-6-4 (STA) alloy based on equivalent strain method

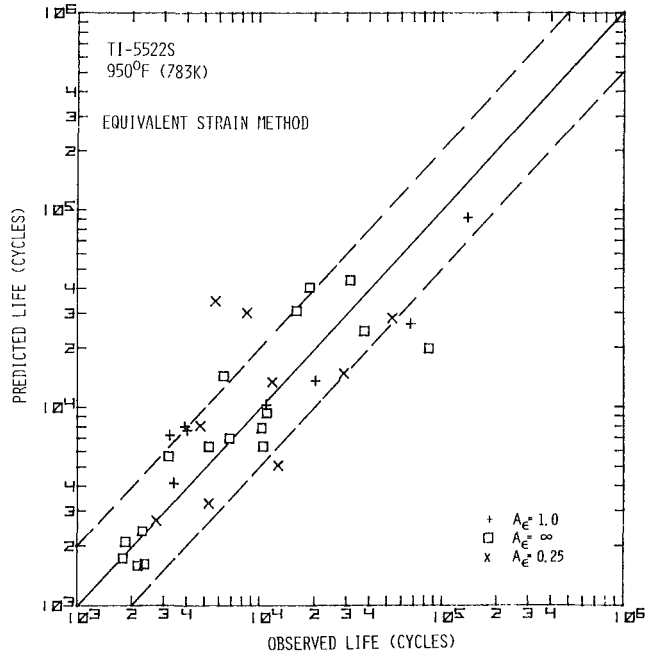

Fig. 16 Predicted versus observed crack initiation life for Ti-5522S alloy based on equivalent strain method

Downloaded 01 Jun 2010 to 171.66.16.62. Redistribution subject to ASME license or copyright; see http://www.asme.org/terms/Terms_Use.cfm

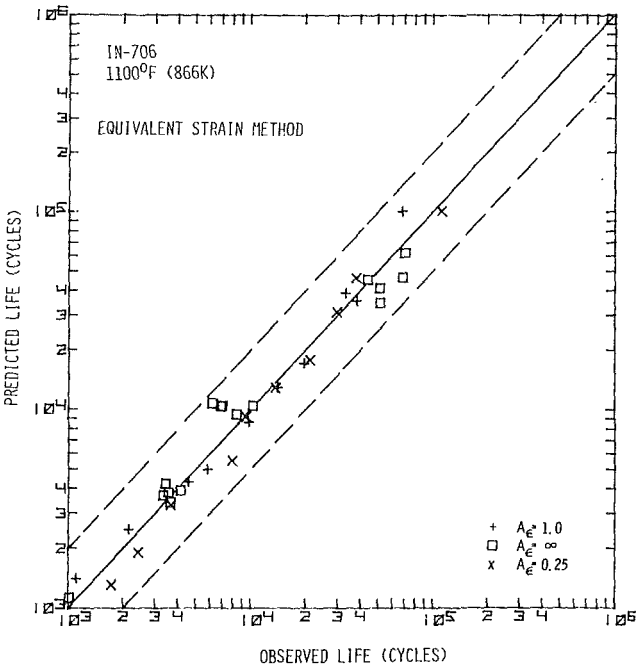

Fig. 17 Predicted versus observed crack initiation life for IN-706 alloy based on equivalent strain method

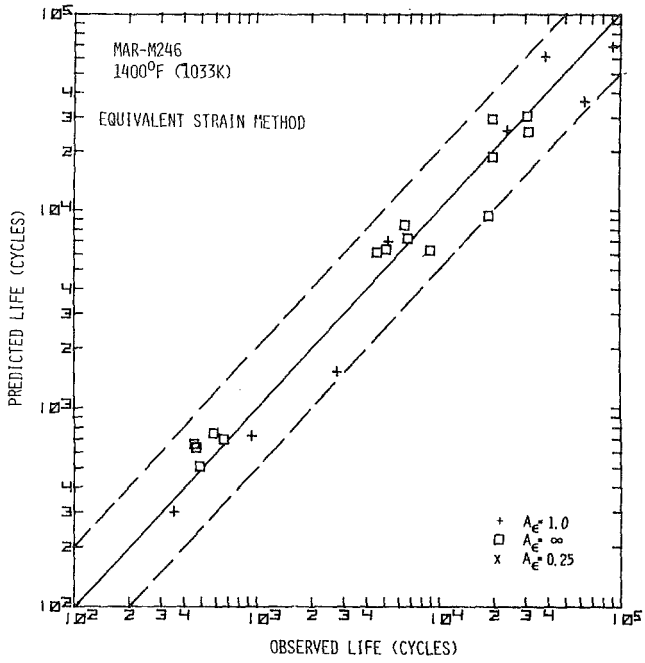

Fig. 18 Predicted versus observed crack initiation life for MAR-M246 alloy based on equivalent strain method

Table 5 Comparison of the Three Methods Evaluated in Terms of Statistical Parameters

Material	Test temp. (K)	Nonlinear Goodman diagram method		Manson's mean stress correction method		Jaske's equivalent strain method	
		σ	$\bar{D}$	σ	$\bar{D}$	σ	$\bar{D}$
Ti-6-4	533	0.1637	0.0367	0.1628	−0.0299	0.1533	−0.00002
Ti-5522S	783	0.6715	−0.0850	0.2365	−0.0311	0.2469	0.0160
IN-706	866	0.1323	0.0245	0.1300	0.0072	0.09841	0.0016
MAR-M246	1033	0.1955	0.0686	0.3063	−0.0944	0.1430	0.0070

Table 6 Ranking of the Three Methods Evaluated on the Basis of Standard Deviation, σ

Material	Nonlinear Goodman diagram method	Manson's mean stress correction method	Jaske's equivalent strain method
Ti-6-4	3	2	1
Ti-5522A	3	1	2
IN-706	3	2	1
MAR-M246	2	3	1

best method among the approaches evaluated. It is possible, however, that the predictions of this method can be further improved, at least in cases where noticeable mean stresses are present in the completely reversed (i.e., $A_\epsilon = \infty$) data, by the simultaneous determination of all constants (i.e., b, c, ϵ_f', σ_f', and k) in equation (2) by means of a nonlinear programming approach using the entire data base available.

It is also reasonable to conclude that, of the three methods evaluated, the nonlinear Goodman diagram approach requires the largest data base, since this method depends upon the use of well defined strain range versus life relationships preferably for at least two other strain ratios besides $A_\epsilon = \infty$. An examination of the results on Table 5 substantiates this conclusion, in that, in the case of Ti-6-4 alloy for which an extensive data base was available (Table 2), the differences between the three methods evaluated appear to be extremely small.

Summary and Conclusions

Three methods of treating mean stress effects on time-independent LCF lifetimes of materials were critically evaluated. These consisted of nonlinear Goodman diagram approach, Manson's mean stress correction method and Jaske's "Equivalent Strain" formulation. LCF crack initiation data on four materials (Ti-6-4, Ti-5522S, IN-706 and MAR-M246) were used in the evaluations. The evaluations were carried out in terms of each method's capability in back-predicting the experimentally observed crack initiation lifetimes. The results indicated that Jaske's equivalent strain formulation provides the best overall means of treating the mean stress effects on LCF crack initiation lifetimes. The results also indicate that Manson's mean stress correction method is the second best method among the approaches evaluated and that the predictions of this method could possibly be improved further (especially in cases when

Downloaded 01 Jun 2010 to 171.66.16.62. Redistribution subject to ASME license or copyright; see http://www.asme.org/terms/Terms_Use.cfm

mean stresses are present in the $A = \infty$ data) if all constants in equation (5) are determined simultaneously by a nonlinear programming approach. Further, of the three methods evaluated, the nonlinear Goodman diagram approach appears to require the largest data base.

Acknowledgments

The authors are deeply indebted to Detroit Diesel Allison, GMC, for the support of a part of this work and for permission to publish the results.

References

1 Manson, S.S., "Inversion of the Strain-Life and Stress-Strain Relationships for use in Metal Fatigue Analysis," *Journal of Fatigue of Engineering Materials and Structures*, Vol. 1, 1979, pp. 37–57.

2 Walcher, J., Gray, D., and S.S. Manson, "Aspects of Cumulative Fatigue Damage Analysis of Cold End Rotating Structures," AIAA/SAE/ASME 15th Joint Propulsion Conference, Paper No. 79-1190, Las Vegas, June 18–20,1979.

3 Morrow, J., *Fatigue Design Handbook (A Guide for Product Design and Development Engineers)*, SAE, Vol. 4, 1968.

4 Jaske, C.E., et al., "Analysis of Fatigue, Fatigue Crack Propagation and Fracture Data," Final Report to NASA-Langley Research Center, NASA Cr-132332, 1973.

5 Cruse, T.A., and Meyer, T.G., "Structural Life Prediction and Analysis Technology," Final Report, AFAPL-TR-78-106, Dec. 1978.

6 Doner, M., "Mean Stress and Hold Time Effects on Crack Initiation Life in INCO-901," to be published.

7 Johnsen, S.E.J., and Doner, M., "A Statistical Simulation Model of Miner's Rule," *Methods for Predicting Material Life in Fatigue*, ed., W.J. Ostergren and J.R. Whitehead, ASME, New York, 1979, p. 221.

8 "Turbine Engine Structural Life Prediction/Correlation Program," USAF Contract F33657-77-C-0374, Detroit Diesel Allison Division, General Motors Corporation.

9 Adams, J.H., "Nonlinear Damage Cumulation in Solution Treated and Aged Ti 6A1-4V," to be presented at 1981 ASME Gas Turbine Conference, Houston, Tex.

Downloaded 01 Jun 2010 to 171.66.16.62. Redistribution subject to ASME license or copyright; see http://www.asme.org/terms/Terms_Use.cfm

mean stresses are present in the $A = \infty$ data) if all constants in equation (5) are determined simultaneously by a nonlinear programming approach. Further, of the three methods evaluated, the nonlinear Goodman diagram approach appears to require the largest data base.

Acknowledgments

The authors are deeply indebted to Detroit Diesel Allison, GMC, for the support of a part of this work and for permission to publish the results.

References

1 Manson, S.S., "Inversion of the Strain-Life and Stress-Strain Relationships for use in Metal Fatigue Analysis," *Journal of Fatigue of Engineering Materials and Structures*, Vol. 1, 1979, pp. 37-57.

2 Walcher, J., Gray, D., and S.S. Manson, "Aspects of Cumulative Fatigue Damage Analysis of Cold End Rotating Structures," AIAA/SAE/ASME 15th Joint Propulsion Conference, Paper No. 79-1190, Las Vegas, June 18-20,1979.

3 Morrow, J., *Fatigue Design Handbook (A Guide for Product Design and Development Engineers)*, SAE, Vol. 4, 1968.

4 Jaske, C.E., et al., "Analysis of Fatigue, Fatigue Crack Propagation and Fracture Data," Final Report to NASA-Langley Research Center, NASA Cr-132332, 1973.

5 Cruse, T.A., and Meyer, T.G., "Structural Life Prediction and Analysis Technology," Final Report, AFAPL-TR-78-106, Dec. 1978.

6 Doner, M., "Mean Stress and Hold Time Effects on Crack Initiation Life in INCO-901," to be published.

7 Johnsen, S.E.J., and Doner, M., "A Statistical Simulation Model of Miner's Rule," *Methods for Predicting Material Life in Fatigue*, ed., W.J. Ostergren and J.R. Whitehead, ASME, New York, 1979, p. 221.

8 "Turbine Engine Structural Life Prediction/Correlation Program," USAF Contract F33657-77-C-0374, Detroit Diesel Allison Division, General Motors Corporation.

9 Adams, J.H., "Nonlinear Damage Cumulation in Solution Treated and Aged Ti 6A1-4V," to be presented at 1981 ASME Gas Turbine Conference, Houston, Tex.

DISCUSSION

G. R. Halford[1] and S. S. Mason[2]

We would like to compliment the authors on their thorough evaluation of several prominent models for dealing with mean stresses in the low-cycle fatigue regime. The contribution to the field of high temperature fatigue life prediction is assuredly a worthly one that would have been even more valuable had the raw data been made available for other researchers to analyze for the purpose of developing new models or refining existing ones. As a case in point, an important improvement has been made recently by the discussors to the Manson mean stress correction method (which in itself is an improvement of Morrow's original model, [10]), which places the approach on a sounder physical basis. Qualitatively, the change recognizes the need to shift, equally, the elastic *and* plastic strain range versus life relationships when accounting for the presence of a mean stress rather than shifting only the elastic component as has been done in the past. The simplest way to accomplish the desired shift is to displace the transition fatigue life as shown in Fig. 19 in accordance with the following equation:

$$N'_T = \frac{1}{2}\left[(2N_T)^{-b} - \frac{2k\sigma_0}{E\Delta\epsilon_T}\right]^{-\frac{1}{b}} \tag{1}$$

The notation is the same as that used by the authors with the exception of N'_T and N_T, which are the transition fatigue lives with and without a mean stress, respectively. The transition fatigue life is the life corresponding to the elastic and plastic strain ranges, being equal to each other and equal to the transition strain range $\Delta\epsilon_T$. Recent experience [11] has shown that the transition strain range is not a function of the mean stress and, hence, can be determined from the original total strain range versus life relation obtained in the absence of mean stresses. Hence,

$$\frac{\Delta\epsilon_T}{2} = \frac{\sigma'_f}{E}(2N_T)^b = \epsilon'_f(2N_T)^c \tag{2}$$

The total strain range versus life relationship with a mean stress can thus be written in the same relatively simple form as the relationship without mean stress [12],

$$\frac{\Delta\epsilon}{\Delta\epsilon_T} = \left(\frac{N_f}{N'_T}\right)^b + \left(\frac{N_f}{N'_T}\right)^c \tag{3}$$

The only difference between the two equations is the value of the transition life as defined by equation (3). Thus, the application of equations (3) and (1) defines a mean stress constant k in the same manner as that discussed in reference [13]. It would therefore be interesting to determine whether the revised life relationship would improve the correlations presented for the Manson method.

Since the data published by the authors are insufficient to permit accurate evaluation of the revised method, we would encourage the authors to make such an evaluation. We would also be pleased to volunteer our services in such an effort.

Additional References

10 Morrow, J., "Fatigue Properties in Metals," Section 3.2, *Fatigue Design Handbook*, SAE Advances in Engineering, Vol. 4, Graham, J. A., ed., 1968, pp. 21-29.

11 Manson, S. S., and Halford, G. R., "Recent Developments in Practical Implementation of the Double Linear Damage Rule," *International Journal of Fracture*, Vol. 17, No. 3, 1981 (in press).

12 Manson, S. S., "Predictive Analysis of Metal Fatigue in the High Cycle Life Range," *Methods of Predicting Material Life in Fatigue*, ASME, 1979, pp. 145-183.

13 Walcher, J., Gray, D., and Manson, S. S., "Aspects of Cumulative Fatigue Damage Analysis of Cold End Rotating Structures," Paper No. 79-1190, AIAA/SAE/ASME Joint Propulsion Conference, Las Vegas, Nev., June 18-20, 1979.

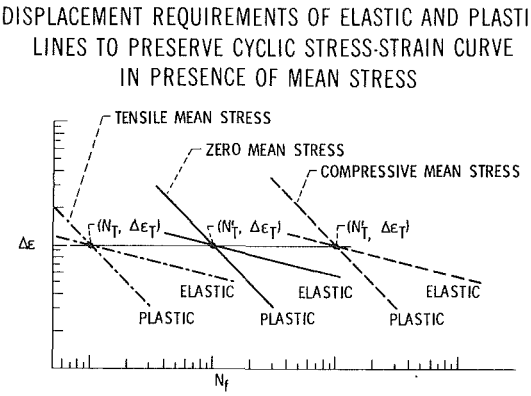

Fig. 19 Displacement of transition fatigue life to account for mean stress effects in low-cycle fatigue

[1] NASA-Lewis Research Center

[2] Case Western Reserve University, Cleveland, Ohio

Copyright © 1982 by ASME

Downloaded 01 Jun 2010 to 171.66.16.62. Redistribution subject to ASME license or copyright; see http://www.asme.org/terms/Terms_Use.cfm

M. D. Rothrock
R. L. Jay
R. E. Riffel

Cascades and Flow Systems Research,
Detroit Diesel Allison Division,
General Motors Corporation,
Indianapolis, Ind. 46206

Time-Variant Aerodynamics of High-Turning Blade Elements

Basic experimental data has been obtained from a linear cascade of five turbine airfoil sections undergoing torsional oscillation. A high-turning subsonic/transonic cascade was tested and both steady-state and time-variant data were obtained. A quasi-static investigation was conducted to compare static pressure distributions with the pressure distributions from the time-variant investigation. During the time-variant data acquisition, six values of interblade phase angle were investigated at each of four expansion ratios. Unsteady pressures were measured by flush-mounted Kulite pressure transducers on the center airfoil and compared with an oscillating flat-plate cascade analysis.

Introduction

Aerodynamically induced vibration of fan, compressor and turbine airfoils is a commonly encountered problem in the development of gas turbine engines. These vibrations occur when a periodic aerodynamic forcing function has a frequency close to the natural frequency of a blade. A problem results when the resonant response of the airfoil exceeds the allowable stress value dictated by engine life requirements.

Current design systems are capable of accurate predictions of the natural frequencies of bladed-disk systems. Some sources of various aerodynamic stimuli are also known by reference to past experience. These considerations locate the system resonances in terms of rotor speed, but cannot determine the actual value of resonant stresses. If stresses beyond the allowable values are measured in engine or rig testing, the designer must make changes to reduce the stresses and perform costly test iteration until life requirement goals are met. An accurate analytical technique to predict the stress levels of a blade in resonance with an aerodynamic forcing function is thus a pressing need.

To calculate the unsteady aerodynamic forces acting on the cascaded airfoils in a particular assembly, an accurate prediction of the magnitude and phasing of the unsteady pressures along the surface of the airfoil is required. These pressure distributions are due to both the time-related variations of the aerodynamic field from disturbances being swept past an assumed nonresponding airfoil, as well as from the movement of the airfoil in the aerodynamic field. The first of these effects has been labeled the "gust" loading, and the second termed the "aerodynamic damping." A solution which relates the gust loading, the ensuing blade motion and the generated aerodynamic damping is necessary to properly predict the total response of a particular airfoil.

The aerodynamic "gust" problem has been analyzed by several investigators. Kemp and Sears [1], Horlock [2], Naumann and Yeh [3], and Goldstein and Atassi [4] considered isolated airfoils acted on by various input gust profiles to determine unsteady or time-variant loadings of the airfoils. These investigators contributed to the overall understanding of the gust problem, yet the results were not amenable for application to turbomachinery blading rows.

D. S. Whitehead [5] analyzed a cascade of flat plate airfoils subjected to a wake due to periodic obstructions far upstream and presented the induced gust loading as functions of cascade variables for incompressible flow. Smith [6] extended this analysis to include the effects of compressibility in the subsonic flow regime. Henderson and Daneshyar (7) used thin airfoil theory to derive an expression for the unsteady lift acting on a two-dimensional cascade of thin, slightly cambered airfoils moving through a sinusoidal disturbance in an incompressible velocity field. In a later analysis, Henderson and Horlock [8] analytically investigated a moving cascade of airfoils experiencing a sinusoidal disturbance in inlet axial velocity. Two dimensional, inviscid and incompressible flow was assumed for highly cambered cascades with low blade loading. The purpose of these analyses was to analytically describe the time-variant loading of an airfoil due to wake-type disturbances.

Due to the limiting assumptions in these and other analyses, experimental data to validate results and indicate needed improvements in the analytical models were needed. Investigators such as Commerford and Carta [9], Ostdiek [10], Henderson and Franke [11] and Fleeter, Novick and Riffel [12] furnished sets of initial correlative data. More recently, Fleeter, Bennett and Jay [13-16] have provided measurements of rotor-wake-induced time-variant surface pressures on a highly cambered stator vane. The pressures were related to the strength of the incoming velocity defect typifying the rotor wake. Variations of parameters including reduced frequency, solidity, axial spacing and interblade phase angle has provided an extensive data bank for correlation of gust analyses in the subsonic flow regime.

Contributed by the Gas Turbine Division and presented at the International Gas Turbine Conference and Products Show, Houston, Texas, March 9-12, 1981, of The American Society of Mechanical Engineers. Manuscript received at ASME Headquarters, December 11, 1980. Paper No. 81-GT-123.

Copyright © 1982 by ASME

Downloaded 01 Jun 2010 to 171.66.16.62. Redistribution subject to ASME license or copyright; see http://www.asme.org/terms/Terms_Use.cfm

The aerodynamic damping portion of the overall forced vibration problem has been analytically investigated by several authors mentioned previously. Since the aerodynamic damping analyses are necessary to predict flutter, this area of research has been vigorously attacked. Whitehead [5], Smith [5], and Fleeter [17] are but a few of those who have presented analyses for the subsonic flow regime. The common assumption in many of these analyses has been that of a zero thickness flat plate. Atassi and Akai [18] presented an analytical formulation for analyzing oscillating airfoils in cascade in uniform incompressible flows. The theory accounts for the geometry of the airfoils. Experimentally, the efforts of Carta and St. Hilaire [19] and Fleeter and Riffel [20] in two-dimensional, rectilinear wind tunnels have furnished basic experimental damping for correlations in the low subsonic and supersonic flow regimes.

Platzer [21] presented a review of unsteady flows in turbomachinery which included the efforts of investigators in both the areas of gust response and aerodynamic damping. This survey was concluded with an emphasis on the need for evaluation of the various analytical formulations by comparison with experimental data, specifically in the area of highly loaded, transonic cascades.

The purpose of the experimental research program described in the following was to furnish basic time-variant data acquired from controlled torsional oscillations of a cascade of highly cambered airfoils operating transonically. The results of varying operating conditions and interblade phase angles on the measured time-variant surface pressures are discussed. Comparisons between pressures measured during quasi-static motion and dynamic motion of the airfoils are shown as well. The steady-state and time-variant data/theory correlations are also discussed. This research effort is reported completely in reference [22].

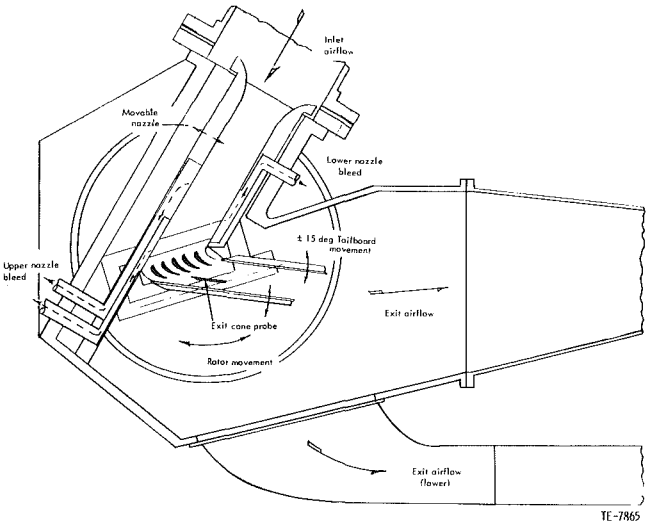

Fig. 1 Schematic of turbine rotor

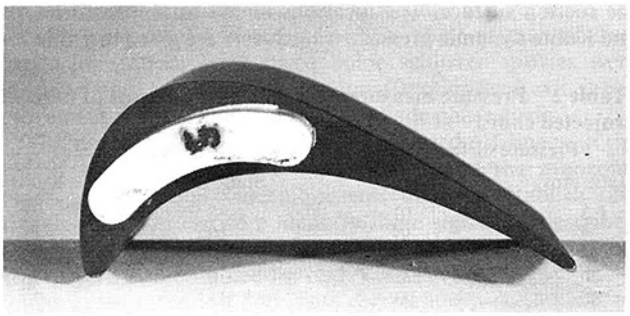

Fig. 2 High-turning turbine rotor hub section

Experimental Facility

The Detroit Diesel Allison (DDA) rectilinear turbine cascade facility was conceived and built as a research tool to evaluate the steady and time-variant aerodynamic characteristics of turbine blade sections having high turning. The facility is a continuous-flow, nonreturn, pressure-vacuum-type wind tunnel, with the test section evacuated by means of two primary steam ejectors. Up to 10 lbm/s of filtered, dried, and temperature-controlled air may be used.

The major features of this facility include:

- Continuous operation for extended time periods.
- A mechanized test section for changing cascade incidence angle.
- A schlieren optical system for visual observation and photography of the facility in both steady and unsteady operation.
- Bleed systems on all four cascade inlet sidewalls.
- A sophisticated instrumentation system centered around two digital minicomputers.

In the cascade facility, the entrance flow to the test section is generated by parallel nozzle blocks, shown in Fig. 1, which set the inlet flow direction. The upper nozzle block is movable to ensure that all the flow is directed through the cascade. The cascade inlet Mach number is determined by the cascade geometry under test. A secondary steam ejector is used to provide sidewall and nozzle-wall bleed for inlet periodicity adjustments. The cascade has dummy end blades presenting one surface to the flow with adjustable porous tailboards hinged on them to aid in setting expansion ratio and exit periodicity.

To acquire the steady-state and dynamic data from this facility requires the use of a minicomputer interfaced to both a Scanivalve pressure cabinet and a high-speed analog-to-digital multiplexer. A smaller minicomputer is used in conjunction with the first to precisely control the oscillatory motion of the cascade blades under dynamic test by switching the DC power supplies which energize the drive system electromagnets. Other facility equipment includes amplifiers and signal conditioners for strain gages and pressure transducers, and a 14-channel magnetic tape recorder.

Airfoil Cascade and Instrumentation

The two-dimensional cascade used in this investigation is comprised of five airfoils having the profile of a high-turning turbine rotor hub section as shown in Fig. 2. Trunnions were attached to both ends of each airfoil for support in the cascade sidewalls. The physical dimensions of the airfoils are a 7.62 cm (3.00 in.) span, a 6.58 cm (2.59 in.) chord, a maximum thickness of 1.34 cm (0.53 in.), and 1.95 rad (112 deg) of turning. The cascade physical parameters are listed in Table 1.

Table 1 Description of turbine airfoil cascade

Physical parameters	
Span	3.00 in.
Chord	2.59 in.
Solidity	1.891
Setting angle	25.5 deg
Turning	112 deg
Maximum thickness/chord	0.205
Leading edge radius/chord	0.024
Trailing edge radius/chord	0.009
Axial chord projection	2.34 in.
Torsion axis location	35.5% (from L.E.)

Downloaded 01 Jun 2010 to 171.66.16.62. Redistribution subject to ASME license or copyright; see http://www.asme.org/terms/Terms_Use.cfm

The cascade airfoils consist of injection-molded fiberglass with a Kevlar outer wrap. Steel trunnions were attached to both ends of each airfoil using screw clamps and pins. These trunnions were supported in bearings, and the airfoil setting angle was maintained by the clamps of the cascade drive system. Paths for the instrumentation wires and pressure tubes were machined into the blade surface, and the trunnions of the instrumented blade were hollow to allow the wires and tubes to exit the cascade.

The instrumentation used to describe the steady-state aerodynamic performance of the cascade included sidewall static pressure taps at the inlet and exit, upstream total pressure and temperature probes, and a five-hole conical probe to survey the exit. Schlieren flow visualization was also used to help establish exit periodicity in the transonic cases.

For the steady-state and quasi-static testing, the center blade of the cascade was instrumented with 9 static pressure taps per surface for definition of the surface pressure distributions at each operating condition. For the time-variant phase of the experiment, the center blade of the cascade was instrumented with 12 miniature high-response Kulite pressure transducers. These Kulites were staggered across the center 50 percent span of the airfoil, 5 on the pressure surface and 7 on the suction surface. The locations of the static pressure taps and Kulite dynamic pressure transducers are given in Table 2.

Table 2 Pressure measurement locations in terms of percent projected chord

Pressure surface		Suction surface	
Static taps	Kulites	Static taps	Kulites
1.3	10	5	5
5	30	10	15
10	60	20	30
20	75	30	55
30	90	45	70
45		60	80
60		70	92.5
80		80	
95		90	

A new installation technique was used on the Kulite-instrumented airfoils of this test to reduce the perpendicular acceleration sensitivity of the pressure transducers. Each transducer is embedded in the airfoil under a perforated metal screen made flush with the airfoil surface as shown in Figure 3. This technique has an advantage over a previous method, which used an RTV coating directly contacting the transducer diaphragm, because there is no increase in the effective mass of the diaphragm.

The torsion mode drive system is a spring bar and hammer arrangement with a driving electromagnet. Each airfoil is driven on both ends to ensure rigid-body motion with no spanwise twisting or bending. The trunnions are held with "battery-clamps" and are suported by bearings in the cascade windows. Figure 4 shows the torsion drive system assembled on a bench rig for test and calibration.

In operation, the electromagnets are powered by DC supplies which are switched on and off at the resonant frequency (345 Hz) of the torsional system by a computer trigger. The hammers swing through an arc causing the spring bars to flex resulting in corresponding torsional deflection of the airfoil. Strain gages are attached to each spring bar and calibrated to indicate the amount of deflection, and thus airfoil torsional amplitude is obtained. The computer triggering allowed precise phasing of the pulse trains to the power supplies to obtain specific interblade phase angles.

Data Acquisition and Analysis

The primary components of the data acquisition system are shown schematically in Fig. 5. Calibrations were performed to determine the transfer functions throughout the measurement system. These included strain gage dynamic amplitude sensitivities, Kulite static/dynamic pressure sensitivities, Kulite amplitude and phase shift components due to oscillation, amplifier and signal conditioner gains, and phase shifts between channels of the magnetic tape recorder. The calibration factors were stored in the computer for on-line

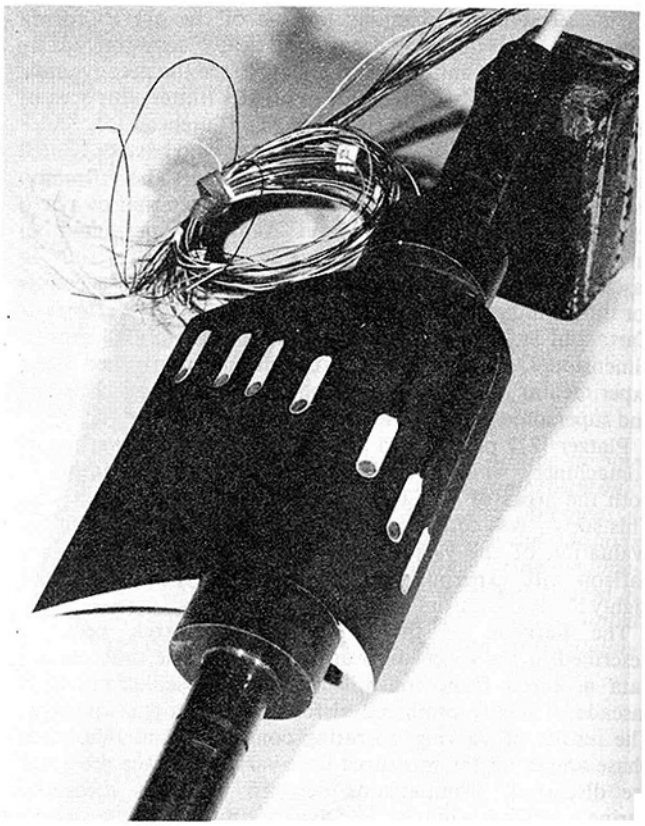

Fig. 3 Kulite transducer installation – suction surface

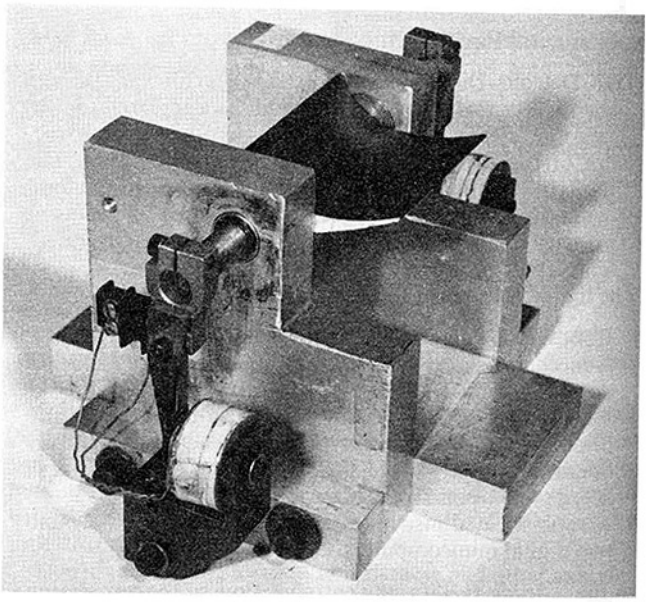

Fig. 4 Torsion drive system bench rig

Downloaded 01 Jun 2010 to 171.66.16.62. Redistribution subject to ASME license or copyright; see http://www.asme.org/terms/Terms_Use.cfm

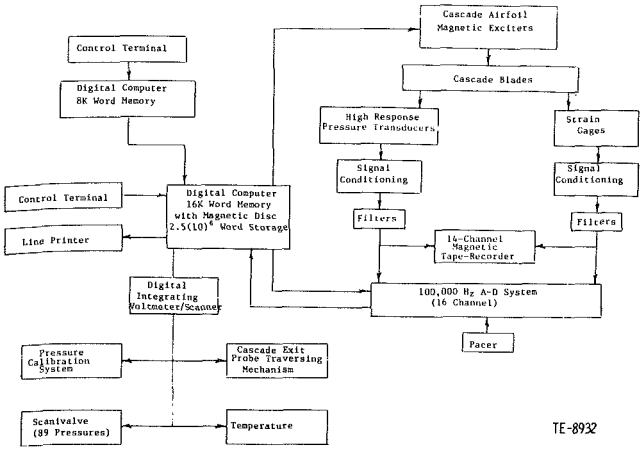

Fig. 5 Schematic of data acquisition system

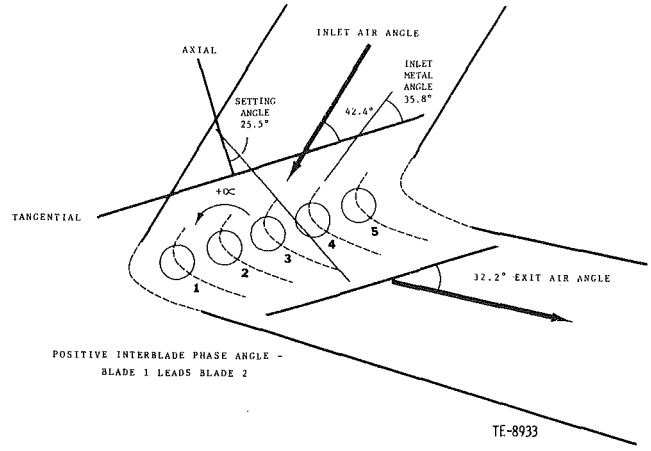

Fig. 6 Torsion cascade geometry

signal corrections and conversions to engineering units on the output.

With the tunnel in operation at specific ratios of upstream total pressure to downstream static pressure (expansion ratio), steady-state pressure and temperature data were measured by the computer data acquisition system. Sidewall static pressures were measured to set up a periodic inlet and exit flow field at each expansion ratio, and then a computer-actuated exit cone-probe survey was made to yield aerodynamic performance, wake definition, and mass-averaged properties. Schlieren photographs were also taken at the supersonic exit operating points to show trailing edge shock structures. Airfoil surface static pressures were measured at each steady-state condition as well as at the two expansion ratios of the quasi-static test.

The quasi-static experiment was conducted at two expansion ratios. The steady-state pressures on the center airfoil were measured as the cascade was reset to fixed setting angles representing temporal angular positions in the torsional cycle of oscillation at zero interblade phase angle. Quarter cycle angular positions at zero interblade phase angle corresponded physically to nominal, maximum open, nominal, and maximum closed setting angles. A 1 deg peak torsional amplitude was used in this study.

For the time-variant phase of the experiment, the center blade was instrumented with Kulite high-response miniature pressure transducers. The torsion drive systems were tuned to equal resonant frequencies and maximum amplitudes. An operating condition described by steady-state data was established and then the airfoils of the cascade were oscillated at the desired interblade phase angle under control of the smaller minicomputer. Minor adjustments to the phase were made via the DC power supply voltage controls. The minicomputer interfaced to the high-speed analog to digital multiplexer acquired, averaged, and printed out the amplitudes and phase angles of each blade (referenced to the center blade signal) as adjustments in the interblade phase angles were made.

After the desired interblade phase angle was established, the signals from the Kulite pressure transducers were recorded on the magnetic tape recorder with a center-blade strain gage signal for phase reference. This procedure was repeated for six values of cascade interblade phase angle at each of four expansion ratios. High-speed color schlieren movies were taken to observe the airfoil torsional motion and exit shock movement at 0 deg and 180 deg interblade phase angle.

The recorded Kulite signals were analyzed off-line with the aid of the analog-to-digital multiplexer and the minicomputer. An averaging technique was used to establish raw signals. Corrections were made to these signals as described by calibration information. Pressure amplitude and phase angles were thus obtained for each Kulite in the data set.

The autocorrelation and cross-correlation procedures used in the analysis are described in the reference [20]. In the average technique, the reference blade square wave driving signal acts as a trigger. Six cycles of oscillation are acquired for each desired signal to represent one coherently triggered sample. One hundred samples are collected and averaged, thus providing an enhanced signal for analysis. This data enhancement technique is similar to that described in reference [13], the only difference is in the trigger source.

Results

A summary of the cascade operating points is presented in Table 3. All four expansion ratios, denoted by R_e, were obtained at the same incidence angle and nearly equal inlet mach numbers by adjusting the exit tailboards and downstream exit air valve. The cascade inlet static pressure was adjusted to slightly below ambient to reduce the load on the cascade sidewalls and trunnion seals, and the inlet temperature was controlled to 100°F.

Figure 6 shows the turbine cascade geometry and airfoil numbering system. Figure 7 is a schlieren photograph of the 2.3 expansion ratio point from the same viewpoint as Fig. 6. The exit shock structures indicate the periodicity of the exit flow field by their identical wave angles.

Table 3 Steady-state operating points

Ideal inlet total to exit static expansion ratio	Mass-averaged expansion ratio	Inlet Mach no.	Inlet static pressure (psia)	Cascade incidence angle (deg)	Mass-averaged exit Mach no.
1.5:1	1.53	0.50	12.74	−6.6	.78
1.8:1	1.84	0.52	12.16	−6.6	0.95
2.3:1	2.34	0.52	12.05	−6.6	1.13
2.8:1	2.71	0.53	12.30	−6.6	1.25

Downloaded 01 Jun 2010 to 171.66.16.62. Redistribution subject to ASME license or copyright; see http://www.asme.org/terms/Terms_Use.cfm

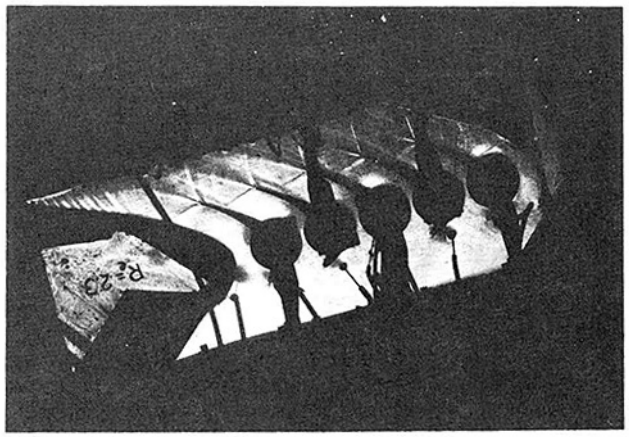

Fig. 7 Schlieren photograph at 2.3 expansion ratio

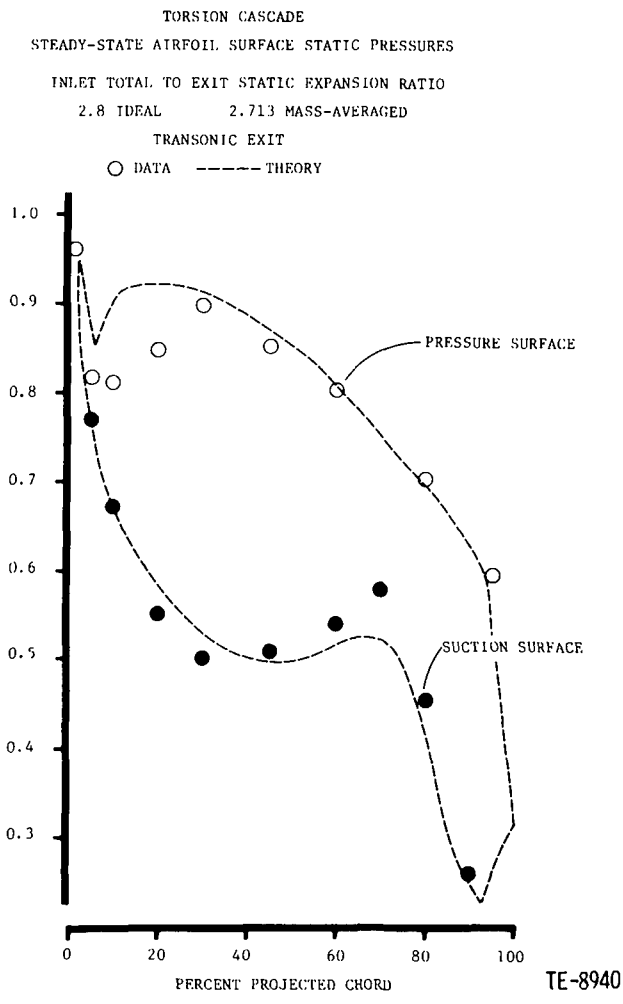

Fig. 8 Steady-state airfoil surface static pressures for 2.8 expansion ratio

The surface static pressure distributions obtained at 2.8 expansion ratio are shown in Fig. 8 and compared with a steady-state analysis based on the work of Couston [23]. The analysis is in good overall agreement with the experimental data with the exception of the 5 to 30 percent projected chord region of the pressure surface leading edge where local flow separation is suspected. The analysis also misses the severity

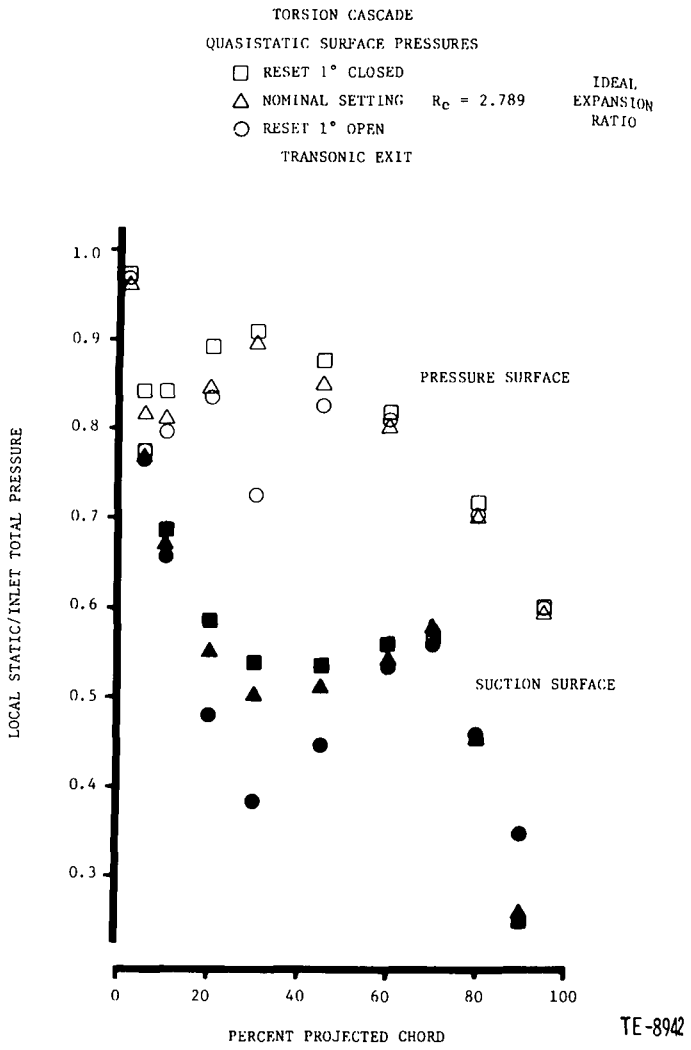

Fig. 9 Quasi-static surface pressure distributions for 2.8 expansion ratio

of the local deceleration trend at about 70 percent projected chord of the suction surface.

The quasi-static experiment was conducted at 1.5 and 2.8 expansion ratios. The setting angles of the cascade blades were changed to measure the static pressure distributions on the center airfoil at the maximum open and closed positions of in-phase cascade oscillation with one deg peak amplitude. Figure 9 shows the resulting changes in static pressure for the 2.8 expansion ratio case. Opening the cascade (trailing edges moving down in Fig. 6) increased the velocity and thus decreased the static pressure on the airfoil surface, while closing the cascade setting angles did the opposite. In order to compare these quasi-static results to the time-variant data, a peak differential pressure was calculated and normalized by twice the product of the dynamic head and the peak torsional amplitude of the airfoil:

$$\text{Normalized } P = (P_{\text{closed}} - P_{\text{open}})/\rho V^2 \alpha$$

Figure 10 shows the resulting normalized quasi-static pressure for the suction surface of the airfoil at 2.8 expansion ratio compared to the amplitude of the normalized time-variant pressure at the same condition. The trailing-edge points are influenced by the impinging shock wave in both cases. The trend appears to be similar, but the dynamic pressure amplitude is attenuated by the oscillation. Dividing through by the maximum pressure in each case yields Fig. 11,

Downloaded 01 Jun 2010 to 171.66.16.62. Redistribution subject to ASME license or copyright; see http://www.asme.org/terms/Terms_Use.cfm

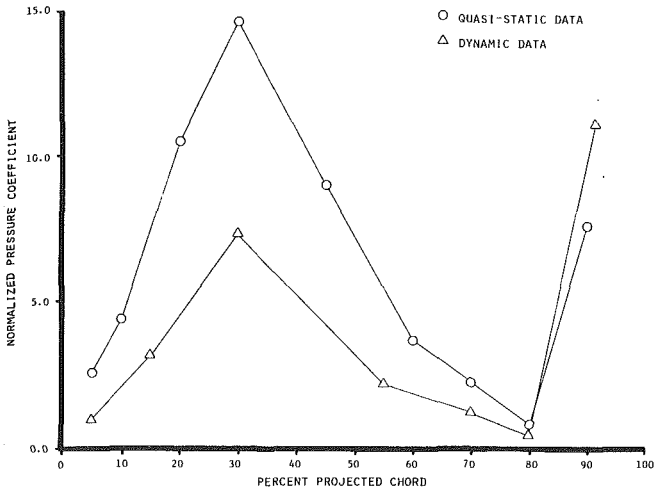

Fig. 10 Comparison of normalized pressure coefficients on the suction surface for 2.8 expansion ratio

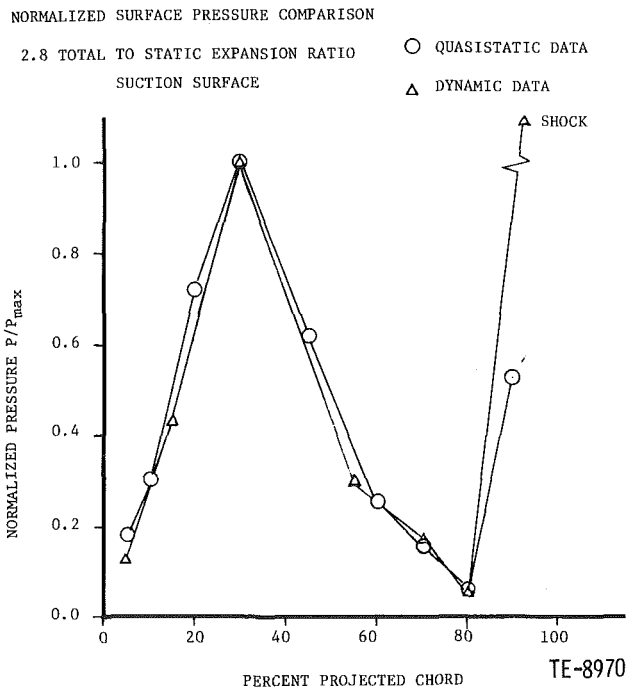

Fig. 11 Comparison of quasi-static and dynamic data on suction surface at 2.8 expansion ratio

which indicates an exact trendwise correlation of the two kinds of data. This same matching was evident in the comparison of the quasi-static and dynamic data on the pressure surface, and on both surfaces at 1.5 expansion ratio.

Time-variant data were obtained at all four expansion ratios for six interblade phase angles: 0 deg, ±45 deg, ±90 deg, and 180 deg. All of the data were at 345 Hz with blade amplitudes of about 0.1 deg peak, though all five blades were not at a uniform amplitude due to slightly different resonant frequencies in the drive systems. Typical normalized pressure amplitude and phase lag data are shown in Figs. 12 and 13 for 2.8 expansion ratio and 0 deg interblade phase angle. The Kulite transducer at 30 percent projected chord on the pressure surface was inoperative, but the quasi-static results indicate that a peak amplitude would have occurred near its location. The suction surface amplitude data are affected by

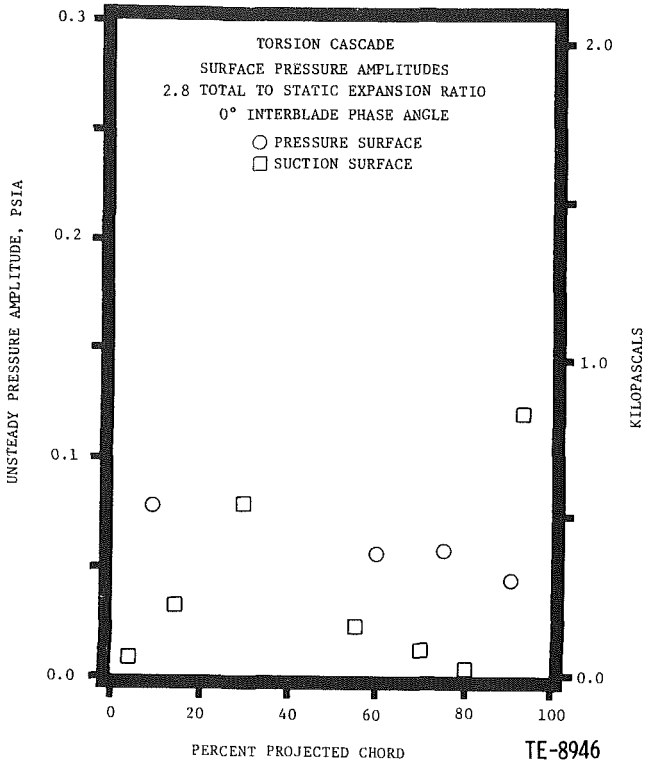

Fig. 12 Time-variant surface pressure amplitude plot for 2.8 expansion ratio and 0 deg interblade phase angle

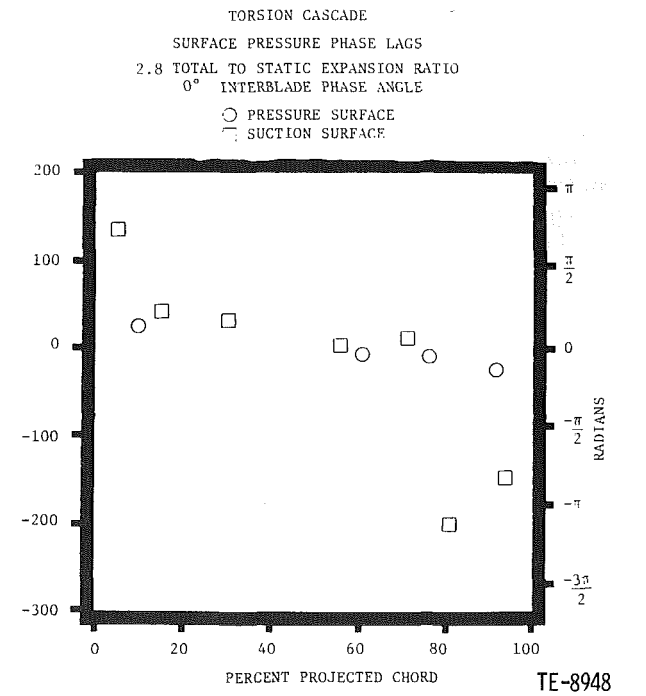

Fig. 13 Time-variant surface pressure phase lag plot for 2.8 expansion ratio and 0 deg interblade phase angle

an impinging shock wave on the last transducer, though the phase lag is relatively unaffected.

By oscillating each cascade airfoil by itself and observing the effect on the Kulites of blade 3, it was found that the primary unsteady pressure effects came from blade 3, with smaller effects from adjacent blades and relatively little effect from blades 1 and 5.

Downloaded 01 Jun 2010 to 171.66.16.62. Redistribution subject to ASME license or copyright; see http://www.asme.org/terms/Terms_Use.cfm

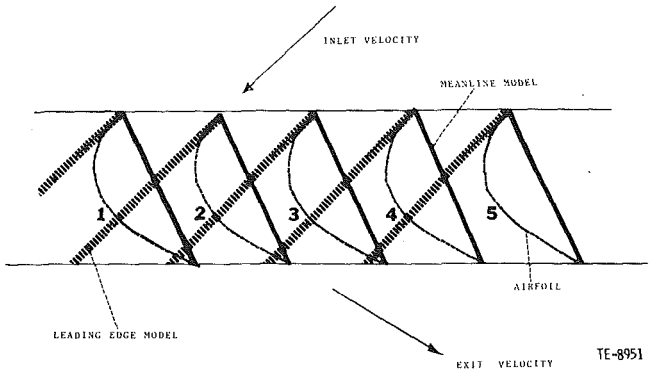

Fig. 14 Assumed flat plate cascades

Table 4 Conditions assumed for analytical study

Parameter	Leading edge	Meanline
Solidity (chord/spacing)	2.532	1.890
Reduced frequency (based on chord)	1.060	0.843
Setting angle, deg	47.6	25.5
Mach number	0.500	0.489
Interblade phase angle	Variable	Variable

A time-variant flat-plate cascade analysis based on the method outlined by Smith [6] was used to correlate with the experimental data. Two different geometries were assumed in an attempt to "best fit" a flat-plate cascade to the highly cambered turbine airfoils, as shown in Fig. 14. The first of these, labelled the leading edge cascade, was aligned with the inlet velocity vector of the cascade. The parameters necessary to analyze this assumed cascade were based on inlet quantities. The second cascade was formulated such that flat plate airfoils were aligned with the setting angle of the turbine airfoils. The reduced frequency and Mach number were based on an average velocity of the fluid along the meanline from the leading to the trailing edge. The parameters used in both cascades are listed in Table 4.

Only the 1.5 expansion ratio theory is shown on the example data/theory correlations to follow, as little change occurs in the unloaded analysis from the small variations in the experimental inlet Mach numbers. The normalized pressure coefficient is obtained from the experimental data by dividing the magnitude of the peak time-variant pressure difference across the meanline of the airfoil by the product of twice the dynamic head and the peak torsional amplitude. The transducers were arranged on each surface so as to symmetrically straddle the airfoil meanline on a line normal to the meanline. A normalized length along the meanline was calculated for each transducer pair in order to compare to distance down the flat-plate airfoils of the analysis. The nonfunctioning pressure surface transducer causes the large gap in the data. As shown in Fig. 15, the trends of pressure coefficient are predicted by both analytical methods, but the leading-edge analysis does a better job on the amplitude. This was generally true for all the data cases. The phase lag comparison is shown in Fig. 16, with a positive angle indicating that the phase of the pressure signal lags the airfoil motion, which is positive for counterclockwise rotation. The phase agreement was generally better using the meanline analysis for all the data comparisons since it more closely approximated the increase in phase lag over the rear portion of the airfoil.

Figure 17 indicates the trends of normalized pressure coefficient with interblade phase angle at the 57.8 percent meanline distance transducers. The data and theory are fairly

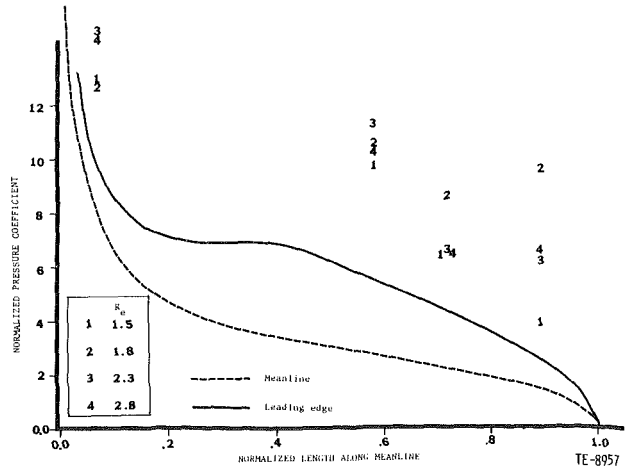

Fig. 15 Normalized pressure coefficients for −90 deg interblade phase angle

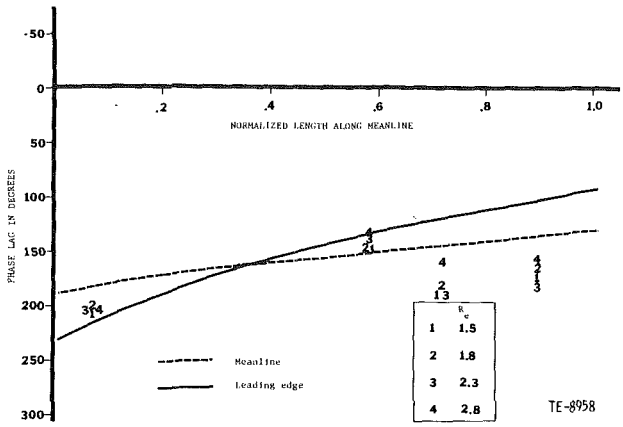

Fig. 16 Phase lag for −90° phase angle

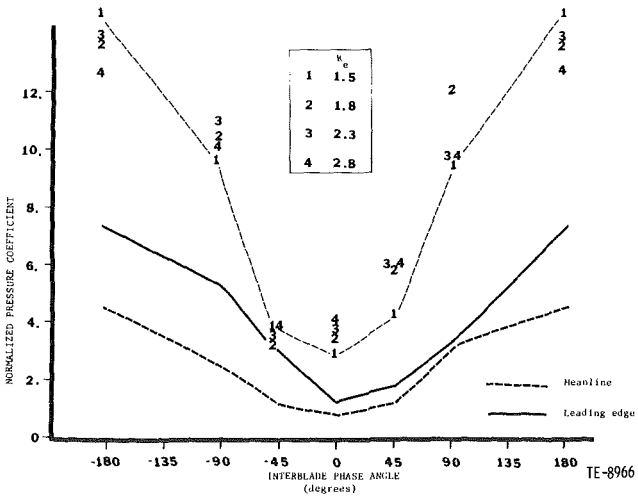

Fig. 17 Normalized pressure coefficient as a function of interblade phase angle at 57.8 percent meanline station

symmetrical about zero interblade phase angle with minimum unsteady pressures occurring for in-phase oscillation and maximum coefficients for 180 deg oscillation. The better leading-edge analysis amplitude agreement is again seen.

Phase lag is plotted against interblade phase angle in Fig. 18

Downloaded 01 Jun 2010 to 171.66.16.62. Redistribution subject to ASME license or copyright; see http://www.asme.org/terms/Terms_Use.cfm

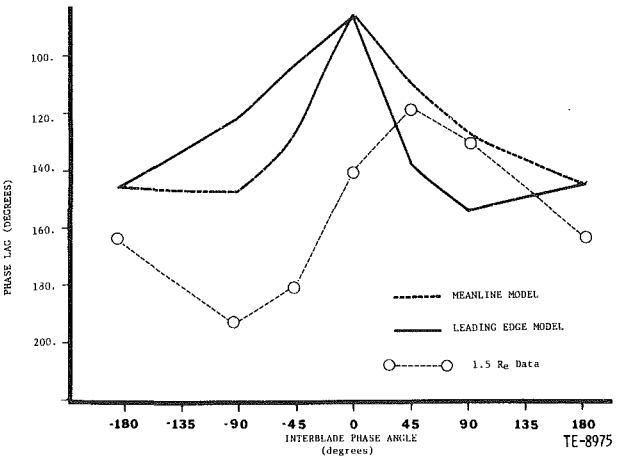

Fig. 18 Pressure phase lag as a function of interblade phase angle at 71.2 percent meanline station

at the 71.2 percent meanline station. The meanline prediction more closely follows the trend of the experimental data, but the data peaks at a more positive interblade phase angle.

Summary and Conclusions

A five-bladed cascade of high-turning airfoils was investigated to obtain steady-state and time-variant torsion-mode airfoil surface pressure data for four values of expansion ratio and six interblade phase angles. These data were then correlated with state-of-the-art analytical predictions. A comparison of quasi-static and time-variant data was also performed. These data form an important experimental base to aid in the development and verification of analytical predictions of the unsteady aerodynamic forces acting on the cascaded airfoils of bladed-disk systems undergoing aerodynamically-induced vibrations.

The most significant result of the experiment was the identification of the almost exact correspondence in surface pressure trends obtained from the quasi-static and time-variant testing. This similarity suggests that an empirical attenuation function could be determined to calculate the unsteady pressure amplitudes of in-phase cascade oscillation at any frequency from quasi-static pressure data. Also the data suggests that the coupling between the steady flow field and the time-variant aerodynamics should definitely be included in any analysis of thick, highly cambered airfoils.

The flat-plate unloaded cascade analysis can be used to demonstrate data trends for a highly loaded, large-turning airfoil section, but cannot be used to assess the quantitative magnitude of time-variant pressure distributions on the airfoil surface. The experimental data consistently demonstrates a higher pressure coefficient than that predicted by the analytical model. Thus this analysis would not be a conservative tool in a forced response analysis until further experimentation defines a factor of safety for its use.

The time-variant flow field appears to be predominantly affected by averaged flow properties rather than inlet flow properties, as evidenced by the better phase angle correlation of the experimental data which the meanline analysis.

Recommendations based on this research are as follows:

1 Develop and correlate analytical codes which model and couple the steady and time-variant aerodynamic fields to establish a predictive tool for aerodynamic damping in the forced response problem,

2 Investigate the relationship between the quasi-static and time-variant aerodynamic fields at various levels of airfoil loading, airfoil turning, interblade phase angles and reduced frequencies,

3 Examine the validity of analytical models in translational motion both normal and parallel to the chordline of high-turning airfoils.

Acknowledgment

This investigation was sponsored in part by the Naval Air Systems Command, Code Air 310, Washington, D.C., with Dr. H. J. Mueller as Technical Administrator.

References

1 Kemp, N.H. and Sears, W.R., "Aerodynamic Interference Between Moving Blade Rows," *Journal of the Aeronautical Sciences,* Vol. 20, No. 9, Sept. 1953.

2 Horlock, J. H., "Fluctuating Lift Forces on Airfoils Moving Through Transverse and Chordwise Gusts," ASME, *Journal of Basic Engineering,* Vol. 90, No. 4, Dec. 1968.

3 Naumann, H., and Yeh, H., "Lift and Pressure Fluctuations of a Cambered Airfoil Under Periodic Gusts and Applications in Turbomachinery," ASME JOURNAL OF ENGINEERING FOR POWER, Vol. 95, No. 1, Jan. 1973, pp. 1-10.

4 Goldstein, M.E., and Atassi, H., "A Complete Second-Order Theory for the Unsteady Flow About an Airfoil Due to a Periodic Gust," *Journal of Fluid Mechanics,* Vol. 74, 1976.

5 Whitehead, D.S., "Force and Moment Coefficients for Vibrating Airfoils in Cascade," *Aeronautical Research Council R and M 3254,* Feb. 1960.

6 Smith, S. M., "Discrete Frequency Sound Generation in Axial Flow Turbomachines," University of Cambridge, Department of Engineering *Report CUED/A-Turbo/TR 29,* 1971.

7 Henderson, R. E., and Daneshyar, H., "Theoretical Analysis of Fluctuating Lift on the Rotor of an Axial Turbomachine," *Aeronautical Research Council R and M 3684,* Sept. 1970.

8 Henderson, R. E., and Horlock, J. H., "An Approximate Analysis of the Unsteady Lift on Airfoils in Cascade," ASME JOURNAL OF ENGINEERING FOR POWER, Oct. 1972.

9 Commerford, G. L., and Carta, F. O., "Unsteady Aerodynamic Response of a Two-Dimensional Airfoil at High Reduced Frequency," *AIAA Journal,* Vol. 12, No. 1, 1974.

10 Ostdiek, F. R., "A Cascade In Unsteady Flow," Ph D thesis, The Ohio State University, 1975.

11 Henderson, R. E., and Franke, G. F., "Investigation of the Unsteady Pressure Distribution on the Blades of an Axial Flow Fan," *Final Report, NASA Grant No. NGR 39-009-275,* Mar. 1978.

12 Fleeter, S., Novick, A. S., and Riffel, R.E., "The Unsteady Aerodynamic Response of an Airfoil Cascade to a Time-Variant Supersonic Inlet Flow Field," *Unsteady Phenomena in Turbomachinery,* AGARD-CP-177, 1975.

13 Fleeter, S., Jay, R. L., and Bennett, W. A., "Rotor Wake Generated Unsteady Aerodynamic Response of a Compressor Stator," ASME Paper No. 78-GT-112, Apr. 1978.

14 Fleeter, S., Bennett, W. A., and Jay, R. L., "Time-Variant Aerodynamic Measurements in a Research Compressor," *Proceedings of the Dynamic Flow Conference 1978,* Sept. 1978.

15 Fleeter, S., Jay, R. L., and Bennett, W. A., "Wake Induced Time-Variant Aerodynamics Including Rotor-Stator Axial Spacing Effects," *Journal of Non-Steady Fluid Dynamics,* Dec. 1978.

16 Fleeter, S., Bennett, W. A., and Jay, R. L., "The Time-Variant Response of a Stator Row Including the Effects of Airfoil Camber," ASME Paper No. 79-GT-110, Mar. 1979.

17 Fleeter, S., "Fluctuating Lift and Moment Coefficients for Cascaded Airfoils in a Nonuniform Compressible Flow," *AIAA Journal of Aircraft,* Vol. 10, No. 2, Feb. 1973.

18 Atassi, H., and Akai, T. J., "Aerodynamic and Aeroelastic Characteristics of Oscillating Loaded Cascades at Low Mach Number," ASME paper No. 79-GT-111, Mar. 1979.

19 Carta, F. O., and St. Hilaire, A. O., "An Experimental Study on the Aerodynamic Response of a Subsonic Cascade Oscillating Near Stall," ASME Paper No. 77-GT-47.

20 Fleeter, S., and Riffel, R. E., "Aerodynamic Phenomena in an Oscillating Transonic MCA Airfoil Cascade including Loading Effects," AGARD-CP-227, Sept. 1979.

21 Platzer, M. F., "Unsteady Flows in Turbomachines — A Review of Recent Developments," AGARD-CP-227, Sept. 1977.

22 Jay, R. L., Rothrock, M. D., Riffel, R. E., and Sinnet, G. T., "Time-Variant Aerodynamics for Torsional Motion of Large-Turning Airfoils," DDA EDR 10192, Final Report, NASC Contract N00019-79-C-0087, Jan. 1980.

23 Couston, M., "Time Dependent Solution of Euler's Equations to Solve the Transonic Blade to Blade Flow in Turbomachinery," von Karman Institute for Fluid Dynamics, Dec. 1975.

Downloaded 01 Jun 2010 to 171.66.16.62. Redistribution subject to ASME license or copyright; see http://www.asme.org/terms/Terms_Use.cfm

Application of a Fast Pseudo-Unsteady Method to Steady Transonic Flows in Turbine Cascades

J.A. Essers
Assistant Professor,
Von Karman Institute for Fluid Dynamics and University of Liege, Belgium

F. Kafyeke
Former Student,
University of Liege, Belgium

New very fast artificial time-dependent techniques for isentropic inviscid steady transonic flows are applied to turbine cascades. An explicit dissipative finite volume scheme with splitting of the space operators is used. The efficiency of the new technique is tested for turbine blades with a relatively thick rounded supersonic trailing edge, and is compared with that of other classical methods. Different models used to apply the Kutta condition and to predict the base pressure accounting for the separation occuring in that region are fully described and tested. For a comparable accuracy, the new method is found to be faster than most of the classical numerical techniques generally applied to similar problems.

Introduction

Up to now, essentially two different categories of numerical methods have been extensively used to compute steady transonic cascade flows: the physical time-dependent (PTD) and the overrelaxation techniques. The PTD techniques consist in solving the physical unsteady Euler equations at successive time levels until reaching the sought steady solution. They generally use explicit schemes with either finite-difference or finite-volume space discretizations. Several different such methods have been developed by various authors, e.g., Gopalakrishnan [1], Mac Donald [2], Couston [3], Van Hove [4]. Nearly all PTD techniques are relatively time consuming. This is mainly due to the lack in the Euler equations for any strong dissipation that could lead to an efficient elimination process of the unsteady perturbation waves and, therefore, to a fast convergence to the steady state.

For various transonic potential flows, fast overrelaxation iterative techniques with a considerably increased rate of convergence have been developed, e.g., by Dodge [6] for cascade flows. However, because of the non-conservative character of its discretization, the method of Dodge does not lead to correct shock captures. Moreover, it cannot compute certain oblique shocks, such as those occuring downstream of transonic turbine cascades, because of the use of an upstream excentered scheme in the supersonic regions. More recently, fully conservative space centered overrelaxation techniques have been developed by Hafez and Murman [5]. As far as we know, they have never been applied to cascade flows, but might be of potential applicability for such problems.

Recently, Essers [7–10] developed new fast artificial time-dependent techniques which bring together the advantages of the PTD and overrelaxation techniques, but eliminate most of their disadvantages. They have been applied to various transonic flows in nozzles and around airfoils. In those techniques, unphysical time-dependent equations are solved, which are constructed by adding a purely artificial unsteady operator to the steady physical equations so as to lead to a large rate of convergence. Among those techniques, the so-called "quasi-natural" method is the less sophisticated. Its large rate of convergence is essentially due to the optimization of the elimination effect of the boundary conditions during their interaction with the perturbation waves [10]. Other pseudo-unsteady numerical methods have been developed by different authors. A thorough review of those techniques has been recently presented by Viviand [11].

The aim of this paper is to discuss results obtained applying the "quasi-natural" technique to isentropic transonic turbine cascade flows. The quasi-natural equations are discretized using an explicit dissipative finite-volume technique with quadrilateral elements. In order to optimize the efficiency of the discretization from the viewpoint of its required CPU times, we have performed a splitting of the space operators rather similar to that initially proposed by Mac Cormack and Paullay [12–13] for the Euler equations. In the problems we have treated, the blades exhibit a relatively thick rounded supersonic trailing edge. Different models proposed for the treatment of the base region are fully described and tested.

The Quasi-Natural Technique

Two-dimensional steady isentropic potential flows are governed by the following system of equations:

$$F_1(u, v) \equiv \frac{\partial}{\partial x}(\rho u) + \frac{\partial}{\partial y}(\rho v) = 0$$

Contributed by the Gas Turbine Division and presented at the International Gas Turbine Conference and Products Show, Houston, Texas, March 9–12, 1981, of The American Society of Mechanical Engineers. Manuscript received at ASME Headquarters, Paper No. 81-GT-124.

Copyright © 1982 by ASME
Downloaded 01 Jun 2010 to 171.66.16.62. Redistribution subject to ASME license or copyright; see http://www.asme.org/terms/Terms_Use.cfm

$$F_2(u, v) \equiv \frac{\partial}{\partial y} u - \frac{\partial}{\partial x} v = 0 \tag{1}$$

where the specific mass ρ is actually a known function of the velocity components u, v obtained by expressing the uniform character of entropy and total enthalpy. To obtain the solution of those equations, Essers proposed to solve an initial value problem governed by the following artificial time-dependent equations [10]:

$$\begin{aligned} \frac{\partial u}{\partial t} &= \frac{c}{\sqrt{u^2+v^2}} \left(\frac{u}{\rho} F_1 - b\, v\, F_2 \right) \\ \frac{\partial v}{\partial t} &= \frac{c}{\sqrt{u^2+v^2}} \left(\frac{v}{\rho} F_1 + b\, u\, F_2 \right) \end{aligned} \tag{2}$$

b and c being known positive functions to be chosen in order to optimize the rate of convergence. When the time derivatives asymptotically vanish at the steady state, it is obvious that the correct solution of equations (1) is obtained.

A detailed analysis of the mathematical properties of system (2) has been presented in [10]. That paper namely investigates the behaviour of unsteady perturbation waves governed by those "quasi-natural" equations, and proves that the waves elimination processes due to their interaction with the boundaries are much more efficient than for the Euler equations [8, 10]. Moreover, the latter are more complicated than equations (2). For all those reasons, the quasi-natural method generally proves to be significantly faster than the classical PTD techniques, especially at transonic and at low speed flow regimes. To optimize the rate of convergence, factor b should be expressed as a function of the local Mach number by

$$b_{\text{opt}} = |1 - M^2| \tag{3}$$

However for that choice of b, the equation $F_2 = 0$ would not be satisfied on the sonic line at the steady state. To avoid that difficulty, b has been chosen as follows in our computations:

$$b = \begin{cases} 1 - \mathrm{M}^2 & \text{if } \mathrm{M}^2 < 1 - \epsilon \\ \epsilon & \text{if } 1 - \epsilon \le \mathrm{M}^2 \le 1 + \epsilon \\ \mathrm{M}^2 - 1 & \text{if } 1 + \epsilon < \mathrm{M}^2 \end{cases} \tag{4}$$

where ϵ is a small positive constant whose choice is somewhat arbitrary.

In the continuity equation, the term expressing the time derivative of the specific mass becomes very small at low speed regime and completely vanishes for incompressible flows. For such flows, the PTD techniques can therefore not be applied. For the same reason, the application of most of the PTD techniques to transonic cascades lead to a highly oscillating solution near the stagnation point. All those remarks are not valid for the quasi-natural method because the latter introduces a strong artificial compressibility. As a result, that method has proved to lead to a rather accurate computation of the stagnation regions and to be applicable to low speed compressible and to fully incompressible flows without a significant reduction of the rate of convergence.

Finite Volume Discretization

The Euler equations as well as the quasi-natural system (2) can be written in the following general form:

$$\frac{\partial}{\partial t} \mathbf{s} = c\, H(\mathbf{s}) \left[\frac{\partial}{\partial x} \mathbf{f}(\mathbf{s}) + \frac{\partial}{\partial y} \mathbf{g}(\mathbf{s}) \right] \tag{5}$$

where $\mathbf{s}$ is a vector field whose N components s_i are the fundamental unknowns of the problem. For equations (2), $N = 2$ and $\mathbf{s}$ is the velocity vector. $\mathbf{f}$, $\mathbf{g}$, and H, respectively, denote 2 vector fields and a matrix which are functions of the s_i but not of their derivatives. c is a positive function of x, y, t whose optimal choice is discussed in the forthcoming.

For the Euler equations, H is the unit matrix and equation (5) is therefore written in the classical conservative form. That

Nomenclature

b, c = positive variable coefficients to optimize the rate of convergence
c = blade chord length
$\mathbf{f}, \mathbf{g}$ = vector fields depending on the unknowns (dimension N)
n = number of internal inviscid steps in a cycle
p = static pressure
$\tilde{p}$ = ratio of local static pressure to upstream total pressure
$\mathbf{s}$ = vector field of the fundamental unknowns (dimension N)
t = time
u, v = velocity components along x and y axes
x, y = coordinates in directions, respectively, parallel and perpendicular to the axial chord
$\tilde{x}$ = coordinate along the actual blade chord
D_1, D_2 = artificial viscosity operators
$\mathbf{F}, \mathbf{G}$ = flux vectors through element sides (dimension N)
H = matrix depending on the unknowns (dimension $N \times N$)
J = number of mesh points along m = constant lines
L_m, L_j = inviscid elementary steps
M = Mach number
N = number of fundamental unknowns
PTD = physical time-dependent technique
R = number of mesh points along j = const lines
S = area of a quadrilateral element
V_m, V_j = artificial viscosity fractional steps
β = inlet or outlet flow angle (with respect to axial direction)
γ = specific heat ratio
δ = angle made by the local velocity vector with the x axis
μ = angle made by the wave vector of a plane perturbation wave with the x axis
ν_1, ν_2 = artificial viscosity coefficients
ρ = specific mass
σ = safety coefficient
Δ, ∇ = forward and backward difference operators
Δt = time step
$\Delta t_m, \Delta t_j$ = local CFL maximum value of Δt for $L_m(\Delta t)$ and $L_j(\Delta t)$ steps
$\overline{\Delta t}_m, \overline{\Delta t}_j$ = minimum value of Δt_m and Δt_j on the whole domain

Subscripts

1 = inlet
2 = outlet
ax = axial
b = base
is = isentropic
j, m = integer numbers used to identify each mesh point

Superscripts

1 = integer number used to identify each time step

Downloaded 01 Jun 2010 to 171.66.16.62. Redistribution subject to ASME license or copyright; see http://www.asme.org/terms/Terms_Use.cfm

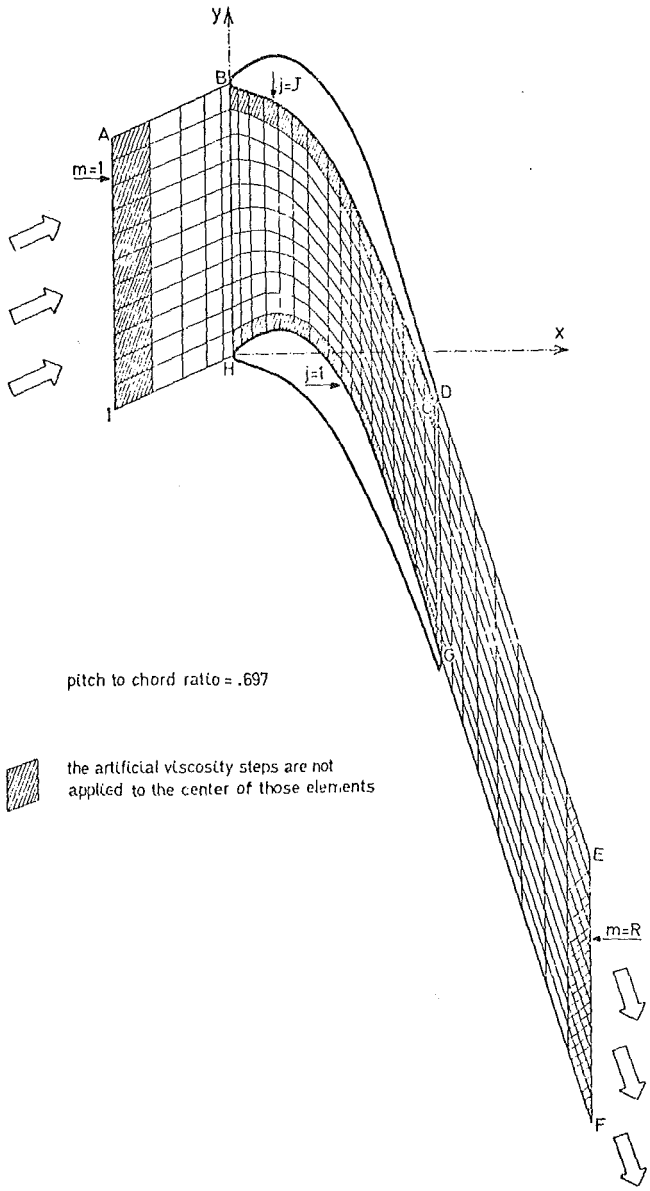

Fig. 1 Gas turbine rotor blade section (coarse mesh is for illustrative purpose only)

remark is however not valid for the quasi-natural equations. Nevertheless, it is obvious that if the term between brackets appearing in the right-hand side of equation (5) is discretized in a conservative form, the quasi-natural technique can lead to a correct capture of relatively weak (i.e., nearly isentropic) shocks at the steady state.

Fig. 1 presents a typical computational domain used in our calculations of turbine cascades. It is discretized by a mesh of $R\ X\ J$ quadrilateral elements. The various mesh points, i.e., the quadrilateral apices, will be denoted by $A_{m,j}$, m and j being integer numbers ($m = 1, \ldots, R$ and $j = 1, \ldots, J$). The coordinates of $A_{m,j}$ are $\bar{x}_{m,j}$ and $\bar{y}_{m,j}$. We denote by $S_{m,j}$ the area of quadrilateral (m, j) (Fig. 2) and by $0_{m,j}$ its center with coordinates $x_{m,j}$ and $y_{m,j}$.

In the finite volume discretization we used, the unknowns are not computed at the mesh points $A_{m,j}$ but at the element centers. Integrating system (5) on each quadrilateral, we obtain

$$\int_{S_{m,j}} \left(\frac{1}{c} H^{-1} \frac{\partial}{\partial t} \mathbf{s}\right) dS_{m,j} = \int_C (\mathbf{f}\, n_x + \mathbf{g}\, n_y)\, dC \qquad (6)$$

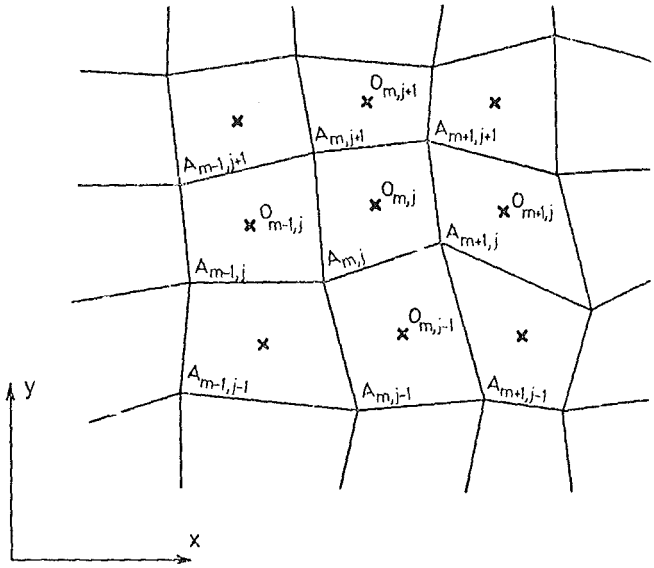

Fig. 2 Quadrilateral elements used in the finite volume technique

where n_x and n_y represent the x and y components of the external unit vector perpendicular to the closed contour limiting the element. Equation (6) is discretized as follows by assuming that $\mathbf{f}$ and $\mathbf{g}$ are constant along each element side and equal to the average of their values at the centers of two adjacent quadrilaterals

$$\frac{d}{dt}\mathbf{s}_{m,j} = \frac{c_{m,j}}{S_{m,j}} H_{m,j} (\mathbf{F}_{m+1,j} - \mathbf{F}_{m,j} + \mathbf{G}_{m,j+1} - \mathbf{G}_{m,j}) \qquad (7)$$

where $\mathbf{F}_{m,j}$ and $\mathbf{G}_{m,j}$, respectively, denote flux terms through sides $A_{m,j}\,A_{m,j+1}$ and $A_{m,j}\,A_{m+1,j}$. They are supposed to be positive when they correspond to fluxes in the direction of increasing m and j. For the quasi-natural equations, their two components are actually the mass flux and the circulation along the quadrilateral sides. For all such sides, except those located on the boundaries, they are computed from the following formulas:

$$\begin{aligned}
\mathbf{F}_{m,j} &= \frac{1}{2}(\mathbf{F}_{m,j,-} + \mathbf{F}_{m,j,+}); \\
\mathbf{G}_{m,j} &= \frac{1}{2}(\mathbf{G}_{m,j,-} + \mathbf{G}_{m,j,+}) \\
\mathbf{F}_{m,j,+} &= (y_{m,j+1} - y_{m,j})\,\mathbf{f}_{m,j} \\
&\quad + (x_{m,j} - x_{m,j+1})\,\mathbf{g}_{m,j} \\
\mathbf{F}_{m,j,-} &= (y_{m,j+1} - y_{m,j})\,\mathbf{f}_{m-1,j} \\
&\quad + (x_{m,j} - x_{m,j+1})\,\mathbf{g}_{m-1,j} \qquad (8) \\
\mathbf{G}_{m,j,+} &= (y_{m,j} - y_{m+1,j})\,\mathbf{f}_{m,j} \\
&\quad + (x_{m+1,j} - x_{m,j})\,\mathbf{g}_{m,j} \\
\mathbf{G}_{m,j-1} &= (y_{m,j} - y_{m+1,j})\,\mathbf{f}_{m,j-1} \\
&\quad + (x_{m+1,j} - x_{m,j})\,\mathbf{g}_{m,j-1}
\end{aligned}$$

Downloaded 01 Jun 2010 to 171.66.16.62. Redistribution subject to ASME license or copyright; see http://www.asme.org/terms/Terms_Use.cfm

To discretize the differential equations (7), we use an explicit scheme with splitting of the space operators initially proposed by Mac Cormack and Paullay [13] for the solution of the Euler equations. From the point of view of the required CPU, that discretization is actually well known to be more efficient than other explicit nonsplitted schemes, especially when very different mesh sizes are used in the two space directions. A certain number of similar time cycles are computed successively until reaching the steady state. Each cycle is composed of different successive elementary steps. Two different types of such steps are used, respectively, denoted by $L_m\ (\Delta t)$ and $L_j\ (\Delta t)$, where Δt indicates the time interval covered by those steps. They, respectively, correspond to discretizations of the following one dimensional equations obtained from a splitting of system (7):

$$L_m \text{ step} : \frac{d}{dt}\mathbf{s}_{m,j} = \frac{2c_{m,j}}{S_{m,j}} H_{m,j}(\mathbf{F}_{m+1,j} - \mathbf{F}_{m,j})$$

$$L_j \text{ step} : \frac{d}{dt}\mathbf{s}_{m,j} = \frac{2c_{m,j}}{S_{m,j}} H_{m,j}(\mathbf{G}_{m,j+1} - \mathbf{G}_{m,j})$$

Those equations are discretized using a predictor-corrector sequence, which is actually a generalization of a finite difference dissipative scheme proposed by Mac Cormack [12] for one-dimensional problems. That sequence is, e.g., the following for the $L_m\ (\Delta t)$ step:

$$\text{Predictor} : \hat{\mathbf{s}}^{l+1}_{m,j} = s^l_{m,j} + \frac{2\Delta t \bar{c}_{m,j}}{S_{m,j}} \bar{H}_{m,j}(\mathbf{F}^l_{m+1,j,-} - \mathbf{F}^l_{m,j,-})$$

$$\text{Corrector} : \mathbf{s}^{l+1}_{m,j} = \frac{1}{2}\left[\hat{\mathbf{s}}^{l+1}_{m,j} + \mathbf{s}^l_{m,j} + \frac{2\Delta t \bar{c}_{m,j}}{S_{m,j}} \bar{H}_{m,j} (\hat{\mathbf{F}}^{l+1}_{m+1,j,+} - \hat{\mathbf{F}}^{l+1}_{m,j,+})\right]$$

where $\mathbf{s}^l_{m,j}$ represents the value of $\mathbf{s}_{m,j}$ at time $t = l\Delta t$ ($l = 0, 1, 2, \ldots$). Symbols $\bar{c}_{m,j}$ and $\bar{H}_{m,j}$ indicate that those coefficients are computed at the beginning of each cycle and kept constant during the whole cycle.

Each L_m and L_j step is not consistent with equations (7), but the whole sequence of such steps forming a cycle should obviously be. To obtain consistency, the total time intervals, respectively, covered by the L_m and L_j steps should be the same. Additionally, the sequence of elementary steps should be symmetric to obtain second order accuracy with respect to time. The following two types of cycles can therefore be used:

Cycle of type m:

$$L_m(\Delta t) \cdot \frac{L_j\left(\frac{2\Delta t}{n}\right) \ldots L_j\left(\frac{2\Delta t}{n}\right)}{n \text{ steps}} \cdot L_m(\Delta t) \qquad (10)$$

Cycle of type j:

$$L_j(\Delta t) \cdot \frac{L_m\left(\frac{2\Delta t}{n}\right) \ldots L_m\left(\frac{2\Delta t}{n}\right)}{n \text{ steps}} \cdot L_j(\Delta t) \qquad (11)$$

Δt and the integer number n are chosen to satisfy the following CFL stability condition for each elementary step at each element center:

$$\text{For } L_m(\Delta t) \text{ steps:} \quad \Delta t \le \Delta t_m \qquad (12)$$

$$\text{For } L_j(\Delta t) \text{ steps:} \quad \Delta t \le \Delta t_j \qquad (13)$$

If we first suppose that the factor c appearing in the right hand side of equations (2) and (5) is taken equal to 1, the local maximum time steps Δt_m and Δt_j at element center (m, j) are given by

$$\Delta t_m = \frac{S_{m,j}}{2W_{m,j,1}} \quad ; \quad \Delta t_j = \frac{S_{m,j}}{2W_{m,j,2}} \qquad (14)$$

where

$$W_{m,j,1} = \text{Max}_{\text{all } i=1,\ldots,N}[\lambda_{m+1,j} |w_{i,m,j,1}|; \lambda_{m,j} |w_{i,m,j,3}|]$$

$$W_{m,j,2} = \text{Max}_{\text{all } i=1,\ldots,N}[\theta_{m,j+1} |w_{i,m,j,2}|; \theta_{m,j} |w_{i,m,j,4}|]$$

$\lambda_{m,j}$ and $\theta_{m,j}$ are the length of sides $A_{m,j}A_{m,j+1}$ and $A_{m,j}A_{m+1,j}$ (Fig. 2); whereas $w_{i,m,j,1}$, $w_{i,m,j,2}$, $w_{i,m,j,3}$, $w_{i,m,j,4}$ represent the N possible phase velocities ($i = 1, \ldots, N$); computed at center (m, j) of plane perturbation waves propagating in directions, respectively, perpendicular to sides $A_{m+1,j}A_{m+1,j+1}$, $A_{m,j+1}A_{m+1,j+1}$, $A_{m,j}A_{m,j+1}$ and $A_{m,j}A_{m+1,j}$. For system (2), the two possible velocities of waves propagating in a direction forming the angle μ with the x axis are given by

$$w_{\pm} = \frac{1}{2}\left[|b + \mathrm{M}^2 - 1|\,|\cos\mu| \pm \sqrt{(b+1-\mathrm{M}^2)^2\cos^2\mu + 4b\sin^2\mu}\right]$$

computed at each element center. The program then evaluates

$$\overline{\Delta t_m} = \text{Min}_{\text{all } m,j} \Delta t_m \text{ and } \overline{\Delta t_j} = \text{Min}_{\text{all } m,j} \Delta t_j$$

It is possible to prove that the best computational efficiency is obtained when cycles of type m and j are chosen if $\overline{\Delta t_m}$ is, respectively, larger or smaller than $\overline{\Delta t_j}$. That choice is automatically performed by the program. To satisfy the stability condition at each center for each elementary step, Δt and n are, e.g., taken as follows for a cycle of type m

$$\Delta t = \sigma \overline{\Delta t_m}$$

and

$$n = \text{smallest integral such that } n \ge \frac{2\overline{\Delta t_m}}{\overline{\Delta t_j}} \qquad (15)$$

when σ is a safety coefficient that should in principle be slightly smaller than 1.

Computation of the c Factor

If that factor is taken equal to 1, the local CFL maximum time step is Δt_m and Δt_j, respectively, for $L_m\ (\Delta t)$ and $L_j\ (\Delta t)$ steps. However, if Δt_m and Δt_j are subject to important variations in the domain, Δt cannot be larger than the smallest of those values. The time step can therefore be significantly smaller than the local stability limit in large regions of the domain, thus leading to a considerable wasting of the rate of convergence. To avoid that wasting, c should be chosen variable in the domain and such that the local maximum value of Δt becomes equal to any positive constant in the whole domain. As the value of that constant can easily be proved to do not influence the rate of convergence, it has been taken equal to 1 in our programs. At the beginning of each cycle, the c factor has been computed at each element center and kept constant during the whole cycle. For instance if $\overline{\Delta t_m} > \overline{\Delta t_j}$, the following cycle of type m is used:

$$L_m(\sigma) \cdot \frac{L_j\left(\frac{2\sigma}{n}\right) \ldots L_j\left(\frac{2\sigma}{n}\right)}{n \text{ steps}} \cdot L_m(\sigma) \qquad (16)$$

with

Downloaded 01 Jun 2010 to 171.66.16.62. Redistribution subject to ASME license or copyright; see http://www.asme.org/terms/Terms_Use.cfm

$$c = \text{Min}\left(\Delta t_m, \frac{n\Delta tj}{2}\right),$$

n being given by (15).

The choice of $\sigma = 1$ theoretically corresponds to the stability limit. However that coefficient can be slightly larger in practice. This is due to the following reasons:

- A cycle can be stable even if some of its elementary steps are not.
- CFL stability conditions (14) can be slightly too restrictive when the mesh elements are not parallelograms.
- To prevent nonlinear instabilities, we have introduced a small artificial viscosity as explained below. The latter can slightly improve the stability properties of the cycle.

In our computations of turbine cascades, σ was taken equal to 1.3 - 1.4. The use of a slightly too large value of σ (e.g., 1.5) also led to a stable computation, but significantly reduced the rate of convergence.

Boundary Conditions

A typical domain used in our computations is presented on Fig. 1. As the flow is assumed to be isentropic, not only the total temperature but also the total pressure are supposed to be uniform and known. To apply the Kutta condition accounting for the supersonic separation at the relatively thick rounded trailing edge, the latter is generally truncated, and CD, which will be referred to as "the base element side," is subject to a special treatment described in the next section. The technique used to compute the fluxes through all other boundary element sides is presented below.

The unknowns u and v at the center of elements located near the boundaries are computed in the same way as any other elements. However for element sides located on the boundaries, the components of flux vectors such as $\mathbf{F}_{m,j}$ and $\mathbf{G}_{m,j}$, i.e., the mass flux and the circulation along boundary sides, are not computed from formulas (8), but from equations accounting for the boundary conditions.

Impermeable Blade Surface. Consider (Fig. 3) the element side RJ located on the blade surface. The mass flux through RJ is obviously taken equal to zero. By expressing that the circulation along the closed contour PTSQP is equal to zero, the tangential velocity U_p at the center P of RJ can be computed as a function of u and v at points T, S, Q taken at the same time level. The circulation along RJ is then approximated by the product of U_p by the length of that side.

Upstream Boundary AI. The inlet angle β_1 is given at each point of the upstream boundary. Suppose that the element side RJ (Fig. 3) is located on that boundary. Because of the nearly uniform character of the fully subsonic flow in that region, we can write: $u_p = u_S$ and $v_p = u_p tg\beta_1$. From those values of u_p and v_p, the mass flux and the circulation along RJ can easily be computed.

Downstream Boundary EF. On that boundary, the flow is supersonic, but the normal velocity component is supposed to be smaller than the local speed of sound. Two options are available in the program.

In the first option, the outlet angle β_2 is given at the center P of each boundary side RJ. The norm of the velocity vector, and therefore the pressure at that point, is computed as a function of u and v at centers Q, S, T by expressing that the circulation along the contour PTSQP is equal to zero.

In the second option, the ratio of the outlet static pressure to the upstream total pressure is given. That condition is equivalent to give the norm of the local velocity vector at any center P. If we can now determine the outlet angle at each of those points, the velocity components u_p and v_p, and therefore the mass flux and circulation along boundary side RJ will easily be computed. Two different techniques have been used to compute the slope of the velocity vector. In the first one, it is expressed as function of slopes at centers S and K by linear extrapolation. In the second so-called "mass conservation technique," the slope of the velocity vector at point P is obtained by expressing that the mass flux through the closed contour PTSQP is equal to zero.

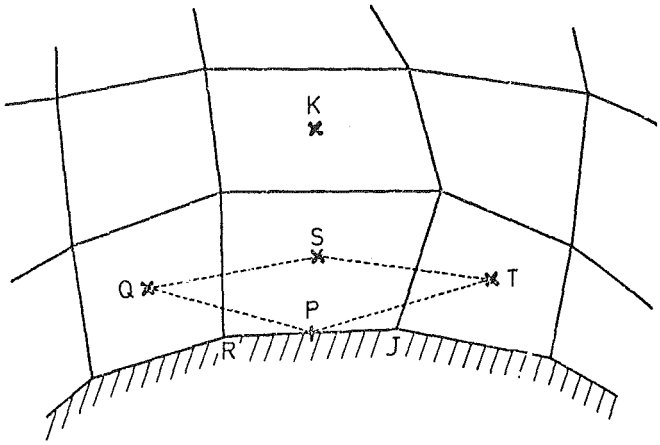

Fig. 3 Numerical treatment of boundary element sides

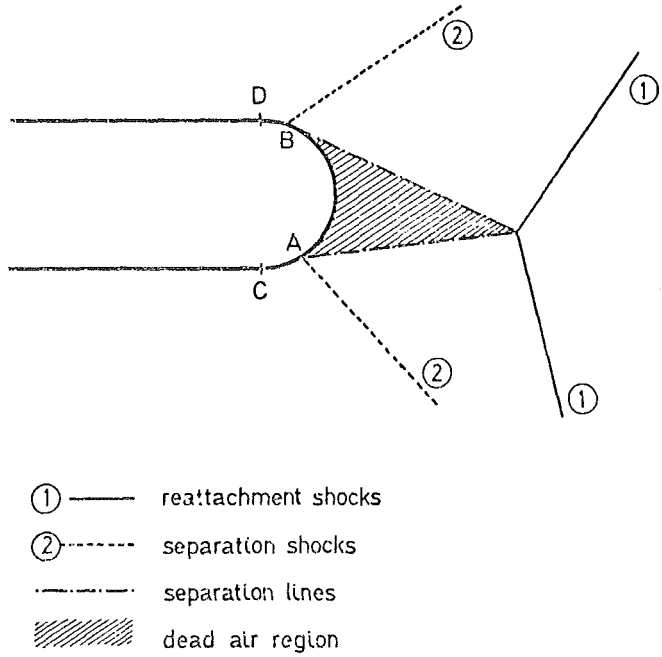

Fig. 4 Flow near a blunt supersonic trailing edge

Periodicity Boundary Conditions. Because of the periodic character of the flow, the flux vectors that correspond to any side of boundaries IH and GF are the same as those corresponding to other sides located on AB and DE (Fig. 1). Those fluxes are computed using equations (8). However, as some of those formulas use values of the unknowns at certain points that do not belong to the computational domain, those values are computed at other points located inside the domain using the periodicity properties.

Treatment of the Base Region

The blades used in our computations have a relatively thick rounded trailing edge. In that region, the flow is supersonic

Downloaded 01 Jun 2010 to 171.66.16.62. Redistribution subject to ASME license or copyright; see http://www.asme.org/terms/Terms_Use.cfm

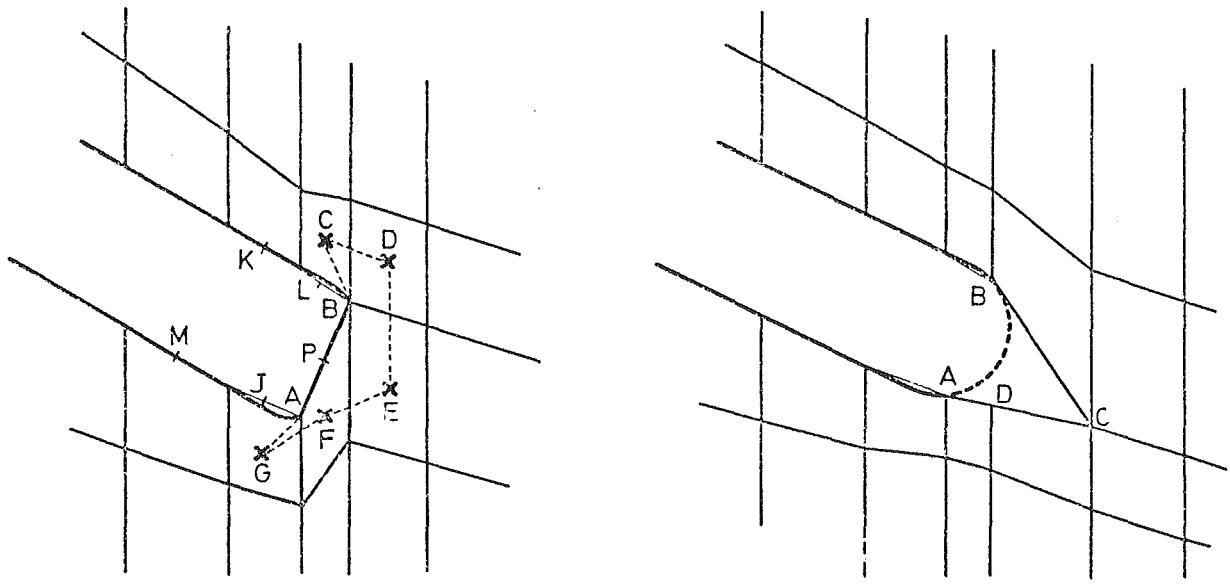

(a) Truncated trailing edge models *(b) Dead air region models*

Fig. 5 Numerical treatment of the base region

on both suction and pressure sides, and separates on the blunt trailing edge. The base region is schematically described on Fig. 4. A more detailed description can namely be found in [3].

From measurements performed by Sieverding and his collaborators [14], the following conclusions can be obtained. The dead air region can roughly be considered as isobaric. Separation shocks are generally very weak, and can therefore be neglected in simple computational models. When the boundary layers are fully turbulent upstream of separation points A and B, a simple separation criterion due to Sieverding can be used to predict the position of those points. The base pressure to outlet static pressure ratio is not very different from 1. An estimation of its value depending on several parameters can be obtained from an experimental correlation proposed by Sieverding.

An accurate prediction of the flow in the base region is obviously not possible from a purely inviscid calculation. However to avoid important errors on the pressure distribution mainly in the supersonic part of the suction side, our program should be capable of leading to a reasonable prediction of the base pressure. We have tested the following four different models for the treatment of the base region.

Impermeable Truncated Trailing Edge. The experiments of Sieverding prove that the base pressure is not significantly modified when the blade is truncated at the trailing edge as shown on Fig. 5(*a*) if A and B are not too different from the actual separation points. Couston [3] therefore used such a truncated blade in his PTD finite volume calculations. In some of our computations, the base element side AB has been assumed to be impermeable. The mass flux through that side has therefore been taken equal to zero, whereas the circulation was computed by expressing that the circulation along the closed contour ABCDEFGA is equal to zero. A rather poor accuracy was obtained with that model because an important unphysical overexpansion occurred in the base region, thus leading to a significantly too weak base pressure.

Constant Pressure Truncated Trailing Edge. To avoid the overexpansion mentioned in the foregoing, the base element side AB is no longer impermeable. The pressure is supposed to be constant along that side. It is taken equal to the base pressure p_b, which is computed as follows at the beginning of each cycle and kept constant during the whole cycle. The velocity at points A and B is computed by linear extrapolation from its known value at points M, J, K, L. The pressures p_A and p_B can then be obtained from the isentropic approximation. The base pressure p_b is taken equal to the average of p_A and p_B.

The norm of the velocity vector on AB is easily obtained from the value of p_b. To compute the slope of the velocity vector $\mathrm{tg}\delta_b$ on that side, a mass conservation technique through contour ABCDEFGA is used. If the velocity component in the direction perpendicular to AB is found larger than the local speed of sound, that technique is however not valid and can lead to instabilities. This is due to the fact that two boundary conditions should then be imposed on AB, and δ_b should therefore be obtained from physical considerations. The program then automatically performs another computation of δ_b. The flow at points A and B is supposed to be deflected by a Prandtl-Meyer expansion or an isentropic oblique shock until reaching the calculated base pressure p_b. The value of tg δ_b is then taken equal to the average of the slopes of the velocity vectors obtained at points A and B after deflection. In our calculations, a good accuracy was obtained with that model. Because of an unphysical blowing occurring through the base element side, the base pressure was however slightly overestimated.

Impermeable Triangular Dead Air Region. In that model, the dead air region is simulated by triangle BCA (Fig. 5(*b*)). The mesh is modified near the trailing edge, and we now have several base element sides (e.g., BC, CD and AD on that figure), which are supposed to be impermeable. We obtained a good accuracy by choosing those sides a priori as follows, and keeping them constant during the whole computation. The position of A and B is chosen from the separation criterion of Sieverding [14]. The one-dimensional theory is used to obtain a rough estimation of the position of sonic points on both pressure and suction sides. The sonic flow at those points is supposed to be deflected by Prandtl-Meyer expansions until reaching the base pressure estimated from

Downloaded 01 Jun 2010 to 171.66.16.62. Redistribution subject to ASME license or copyright; see http://www.asme.org/terms/Terms_Use.cfm

Sieverding's correlations. The pseudo-separation lines BC and AC are then taken parallel to the flow after deflection.

Constant Pressure Dead Air Region. The pseudo-separation lines are no longer supposed to be impermeable, but isobaric. The pressure on those lines is taken equal to the base pressure at the beginning of each cycle. Up to now, we however did not succeed in obtaining convergence with that model. The pressure in the trailing edge region was actually found to exhibit important oscillations.

Artificial Viscosity

In our computations, we have introduced a weak artificial viscosity. The value $\tilde{s}_{m,j}$ of the unknowns obtained at the end of the inviscid part of each cycle (i.e. of the sequence of several L_m and L_j steps), has been modified using the following two V_m and V_j implicit viscosity steps successively:

$$V_m \text{ step} : \hat{\mathbf{s}}_{m,j} = \tilde{\mathbf{s}}_{m,j} + 4\sigma\bar{c}_{m,j} D_{1,m,j}\hat{\mathbf{s}}_{m,j}$$

$$V_j \text{ step} : \mathbf{s}_{m,j} = \hat{\mathbf{s}}_{m,j} + 4\sigma\bar{c}_{m,j} D_{2,m,j}\mathbf{s}_{m,j}$$

with

$$D_{1,m,j}\ \mathbf{s}_{m,j} \equiv \frac{1}{\bar{d}_m} \nabla_m \left(\frac{\nu_{1,m,j}}{d_m}\Delta_m\right)\mathbf{s}_{m,j}$$

$$D_{2,m,j}\ \mathbf{s}_{m,j} \equiv \frac{1}{\bar{d}_j} \nabla_j \left(\frac{\nu_{2,m,j}}{d_j}\Delta_j\right)\mathbf{s}_{m,j}$$

∇ and Δ being backward and forward difference operators, and

$$d_m = [(x_{m+1,j}-x_{m,j})^2 + (y_{m+1,j}-y_{m,j})^2]^{\frac{1}{2}}$$

$$\bar{d}_m = \frac{1}{2}[(x_{m+1,j}-x_{m-1,j})^2 + (y_{m+1,j}-y_{m-1,j})^2]^{\frac{1}{2}}$$

Our program has been written in such a way that the small positive artificial viscosity coefficients ν_1 and ν_2 can be chosen variable in the whole field. However the results presented in the forthcoming have been obtained with constant viscosity coefficients ($\nu_1 = \nu_2 = 0.001$). The artificial viscosity is not applied to certain elements located near the boundaries. For the elements that are hatched on Fig. 1, we actually take $\mathbf{s}_{m,j} = \hat{\mathbf{s}}_{m,j} = \tilde{\mathbf{s}}_{m,j}$

The viscosity steps are implicit and therefore unconditionally stable. The computation of the V_m and V_j steps actually require the solution of a linear algebraic system for each j = constant or m = constant line, respectively. For most of those lines, the matrix is tridiagonal, and the solution can therefore be obtained using the fast classical Thomas algorithm. However for m = constant lines located upstream and downstream of the cascade, the matrix is only quasi-tridiagonal, i.e. tridiagonal with corner elements, because of the periodicity boundary conditions. For those lines, we used another algorithm [17] which only requires 1.5 - 2 times as much CPU time as the Thomas algorithm.

Presentation of Some Results

In all computations described in the forthcoming, the initial fields have been chosen from the quasi-one-dimensional isentropic theory. The total number of L_m and L_j steps per cycle, which are actually automatically selected by the program, was typically found of the order of $5(n = 3)$. A rather severe convergence test was used. At the end of each complete cycle, the program computes two convergence parameters ϵ_1 and ϵ_2. The latter, respectively, represent the

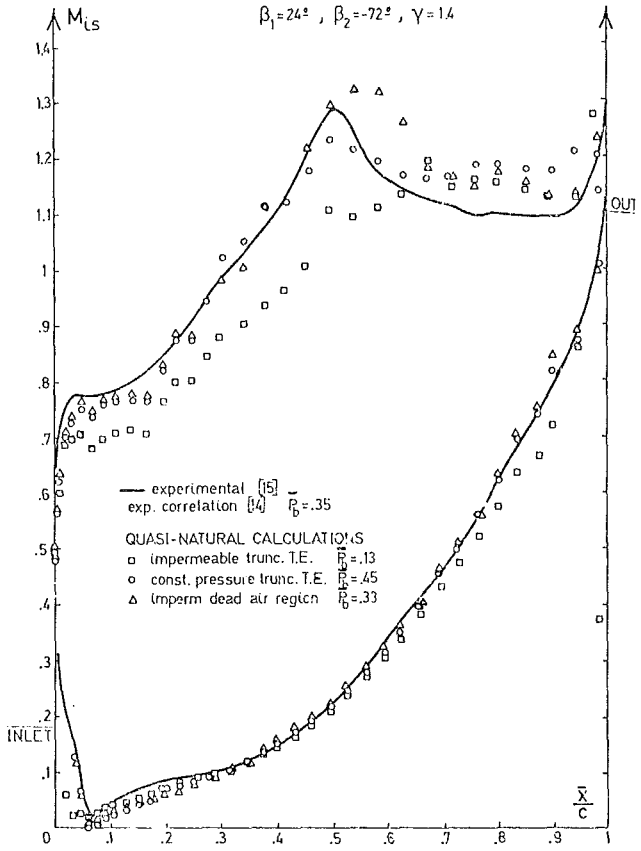

Fig. 6 Gas turbine rotor blade section Isentropic Mach number along blade surface

average and the maximum value of $|\bar{p} - \bar{p}^\circ|$ for the center of all element sides located on the blade surface (including the base sides), $\bar{p}$ being the ratio of the local static pressure obtained at the end of the cycle that has just been computed to the upstream total pressure, and $\bar{p}^\circ$ being the value of that ratio obtained ten cycles earlier (i.e., approximately fifty time steps earlier). The convergence was assumed to be achieved when ϵ_1 and ϵ_2, respectively, became smaller than 0.005 and 0.02.

We first performed various computations on a transonic gas turbine rotor blade section (Fig. 1), which was designed by P. Mac Donald and is fully described in [15]. The mesh we used was much finer than that presented on Fig. 1. It actually uses 63 × 23 mesh points, 74 such points being located on the blade surface. In all computations, the inlet flow angle is given ($\beta_1 = 24$ deg). Either the outlet flow angle or the outlet isentropic Mach number is fixed ($\beta_2 = -72$ deg, or $M_2 = 1.14$).

Fig. 6 and 7 present the isentropic Mach number obtained along the blade pressure and suction sides as a function of the normalized coordinate measured along the blade chord.

If we compare the various numerical results with those obtained from experiments performed by Sieverding [15], the following conclusions can be obtained. As expected the results obtained with the impermeable truncated trailing edge model are not excellent. A strong unphysical circulation occuring from the suction to the pressure side at the trailing edge leads to a deceleration of the pressure side flow in that region, and to a much too weak value of the base pressure. The constant pressure truncated trailing edge and the impermeable dead air region models both lead to an excellent prediction of the Mach number on the whole pressure side and on the part of the suction side located upstream of the shock. The Mach number is however slightly overestimated downstream of the latter. We obtain a too weak shock and a too-high value of the base

Downloaded 01 Jun 2010 to 171.66.16.62. Redistribution subject to ASME license or copyright; see http://www.asme.org/terms/Terms_Use.cfm

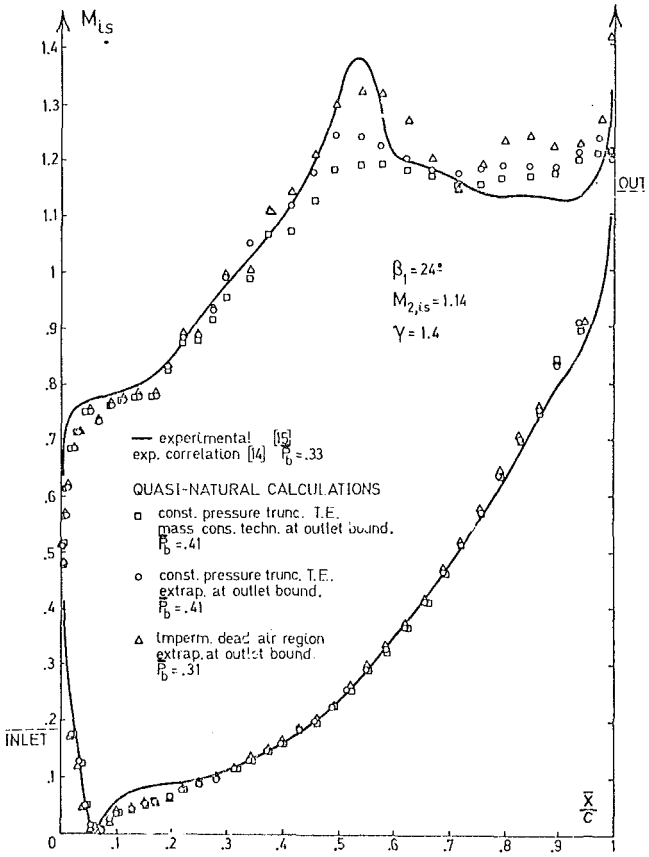

Fig. 7 Gas turbine rotor blade section Isentropic Mach number along blade surface

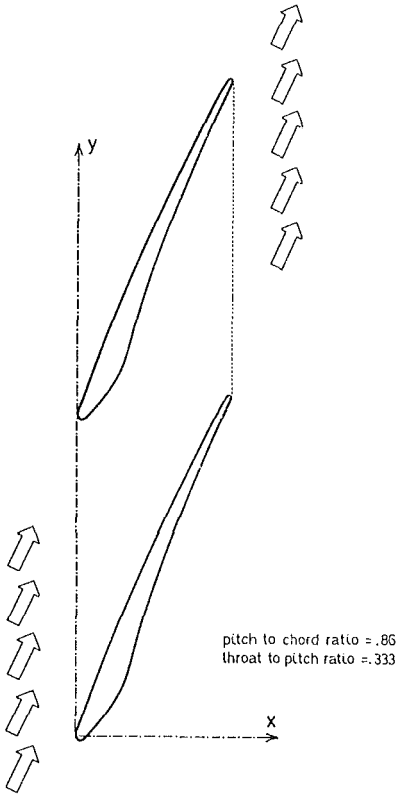

Fig. 8 Steam turbine tip section

pressure with the constant pressure truncated trailing edge model. In our opinion, that behaviour can be explained by the unphysical blowing occuring in the base region. The impermeable dead air region model actually leads to a much better prediction of the shock strength and of the base pressure. The latter results are in good agreement with unpublished preliminary results not presented here, obtained by other authors using a PTD technique. That technique also yields a slightly too weak shock. The Mach number in the stagnation region and the position of the stagnation point are accurately predicted by all quasi-natural calculations. This is an important advantage with respect to most of the PTD techniques, which frequently lead to important oscillations in that region.

The quasi-natural technique has also been applied to the transonic streamturbine tip section of Fig. 8, which is fully described in [16]. Our results are presented on Fig. 9. They are compared to the experimental results of Sieverding [16] and to those obtained by Couston using a PTD finite volume technique with the same mesh [3]. The latter are found in reasonably good agreement with our results. However as opposed to ours, the PTD method leads to oscillations on the pressure side near the trailing edge. For both PTD and quasi-natural calculations, the agreement with the experimental results is good, except on the downstream part of the suction side where the Mach number is overestimated.

For reasons explained above, the quasi-natural technique is very fast. For all our calculations the required total CPU time has been found of the order of 0.22 sec per mesh point on IBM 370/158. The convergence has, e.g., been obtained in 325 s and 65 cycles (i.e., nearly 325 elementary steps) for the computation of the cascade of Fig. 1 using a mesh with 1449 mesh points. For the same fine mesh, the PTD technique of Couston obtains convergence after 1000 time steps and 0.75 s

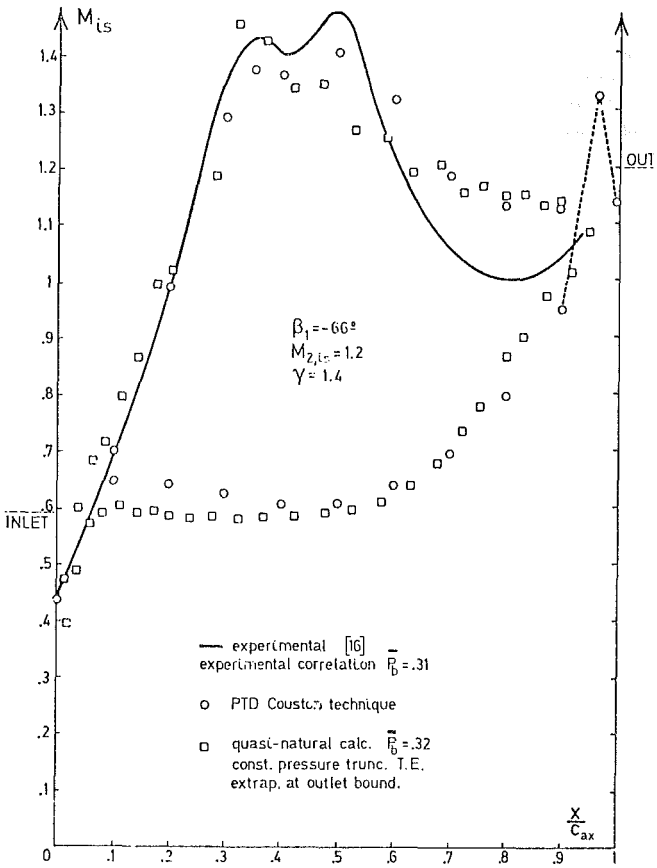

Fig. 9 Steam turbine tip section – isentropic Mach number along blade surface

Downloaded 01 Jun 2010 to 171.66.16.62. Redistribution subject to ASME license or copyright; see http://www.asme.org/terms/Terms_Use.cfm

Table 1 Comparison of various methods for the computation of transonic cascade flows

Method	Relative CPU times	Conservative character	Isentropic character	Ability to compute oblique shocks
Gopalakrishnan [1] PTD finite difference	8	yes	no	yes
Mac Donald [2] PTD finite volume	2	yes	yes	yes
Couston [3] PTD finite volume	1	yes	no	yes
Dodge [6] overrelaxation finite difference	0.5	no	yes	no
present	$0.2-0.3^{(a)}$	yes	yes	yes

$^{(a)}$ Depending whether the computations are performed using a coarse and a fine mesh successively

per mesh point on the same computer. However, Couston uses two different meshes. 500 time steps are first computed with a coarse mesh corresponding to a mesh size twice large than that of the fine mesh, which is itself used to compute the 500 other next steps. We estimate that if we had used those two different meshes, the total CPU time of the quasi-natural technique could have been reduced to 0.15 s per point of the fine mesh. We can therefore conclude that the quasi-natural method is nearly 5 times faster than that of Couston, which is actually among the fastest PTD techniques for transonic turbine cascades. Our method also appears to be faster than the over-relaxation technique of Dodge [6].

Table 1 summarizes different important properties of various numerical methods used to compute transonic cascade flows. One of the columns entitled "Relative CPU times" has been obtained from informations presented in [3]. It gives an estimation of the ratio of the CPU times required by each method to those corresponding to the PTD technique of Couston for the same mesh and the same computer. Such informations about the relative efficiency of different methods should however be used very cautiously, because the CPU times depend on many different factors, such as, e.g., the chosen initial conditions and the convergence criteria, about which very few informations are generally given in the literature. Therefore before considering that the advantages of the quasi-natural technique have been definitely proved, the latter should obviously still be applied to several test problems.

Conclusions

A new fast isentropic artificial time-dependent technique has been successfully applied to transonic flows in turbine cascades. Different models have been tested for the treatment of the base region. For some of them, a good accuracy is obtained, namely for the prediction of the base pressure. That "quasi-natural" method appears to be faster than most of the classical numerical techniques generally used to compute transonic cascade flows. As opposed to the overrelaxation method of Dodge, it can be used to compute weak oblique shocks. It additionally leads to a reasonably accurate prediction of the flow near stagnation points, and can be applied to low speed flows without a significant reduction of the rate of convergence as opposed to most of the PTD techniques.

In future, we intend to develop a generalized non isentropic quasi-natural method [10], which could be applied to both turbines and compressors. The use of other pseudo-unsteady techniques developed by the first author [7-9], which are actually more sophisticated but still faster than the quasi-natural method, would also be interesting.

Acknowledgment

The authors are grateful to Prof. Sieverding and to Mr. Arts who provided them with several comparative experimental and numerical results obtained at the Von Karman Institute.

References

1 Gopalakrishnan, S., and Bozzola, R., "A Numerical Technique for the Calculation of Transonic Flows in Turbomachinery Cascades," ASME Paper No. 71-GT-42.

2 Mac Donald, P.W., "The Computation of Transonic Flow through Two-Dimensional Gas Turbine Cascades," ASME Paper No. 71-GT-89.

3 Couston, M. "Méthode de Calcul de l'Ecoulement Inter-aubes Pseudo-tridimensionnel en Régime Transsonique," PhD thesis, VKI-University of Brussels, Sept. 1976.

4 Van Hove, W., "Time Marching Methods for Turbomachinery Flow Calculations: Methods of Improving Convergence, *"VKI Lect. Series 57 on Application of Numerical Methods to Flow Calculations in Turbomachines,* Rhode-Saint-Genèse, Apr. 1979.

5 Hafez, M.M., and Murman, E.M., "Artificial Compressibility Methods for Numerical Solution of Transonic Full Potential Equation," AIAA Paper No. 78-1148.

6 Dodge, P.R., "A Transonic Relaxation Method for Cascade Flow Systems," VKI Lect. Series 59 on Transonic Flow in Turbomachinery, Rhode-Saint-Genèse, 1973.

7 Essers, J.A. "Méthods Nouvelles pour le Calcul Numérique d'Ecoulement Stationnaires de Fluides Parfaits Compressibles," PhD thesis, Univ. of Liège, June 1977.

8 Essers, J.A., "Evolution Approaches to the Numerical Treatment of Inviscid Internal Flows," *Computational Fluid Dynamics, a VKI book,* ed., W. Kollman, Hemisphere Publishing Corp., Washington D.C., 1980, pp. 329-400.

9 Essers, J.A., "New Fast Super-dashpot Time-Dependent Techniques for the Numerical Simulation of Steady Flows, — Part I: Numerical Formulation," *Computers and Fluids,* Vol. 8, No. 3, Sept. 1980, pp. 351-368.

10 Essers, J.A., "Quasi-natural Numerical Methods for the Computation of Inviscid Potential or Rotational Transonic Flows," *Applied Mathematical Modelling,* Vol. 3, No. 1, Feb. 1979, pp. 55-66.

11 Viviand, H., "Pseudo-Unsteady Methods for Transonic Flow Computations," Seventh Intern. Conference on Numerical Methods in Fluid Dynamics, Stanford Univ., June 1980.

12 Mac Cormack, R.W., Paullay, A.J., "Computational Efficiency Achieved by Time-splitting of Finite Difference Operators," AIAA Paper No. 72-154.

13 Mac Cormack, R.W., and Paullay, A.J., "The Influence of the Computational Mesh on Accuracy for Initial Value Problems with Discontinuous or Non Unique Solutions," *Computers and Fluids,* Vol. 2, No. 3/4, 1974, pp. 339-361.

14 Sieverding, C.H., Stainislas, M., and Snoek, J., "The Base Pressure Problem in Transonic Turbine Cascades," ASME Paper No. 79-GT-120.

15 Sieverding, C.H., "The Base Pressure Problem in Transonic Turbine Cascades. Part I: Cascade Tests," *VKI Lect. Series 84 on Transonic Flows in Axial Turbomachines,* Rhode-Saint-Genèse, 1976.

16 Sieverding, C.H., Decuypere, R., and Hautot, G., "Investigation of Transonic Steam Turbine Tip Sections with Various Section Side Blade Curvature," VKI Paper No. C195/79.

17 Essers, J.A., and Kafyeke, F., "A New Fast Artificial Evolution Numerical Method for Transonic Flows in Turbine Cascades," VKI Tech. Note No. 136, 1980.

Downloaded 01 Jun 2010 to 171.66.16.62. Redistribution subject to ASME license or copyright; see http://www.asme.org/terms/Terms_Use.cfm

M.B. Cutrone
Manager.

M.B. Hilt
Manager.
Mem. ASME

General Electric Company,
Schenectady, N.Y. 12345

A. Goyal
Engineer.

E.E. Ekstedt
Manager.

General Electric Company,
Evendale, Ohio 45215

J. Notardonato
Manager,
NASA/Lewis Research Center,
Cleveland, Ohio 44135

Evaluation of Advanced Combustors for Dry NOx Suppression With Nitrogen Bearing Fuels in Utility and Industrial Gas Turbines

The work described in this paper is part of the DOE/LeRC Advanced Conversion Technology Project (ACT). The program is a multiple contract effort with funding provided by the Department of Energy, and technical program management provided by NASA LeRC. Combustion tests are in progress to evaluate the potential of seven advanced combustor concepts for achieving low NOx emissions for utility gas turbine engines without the use of water injection. Emphasis was on the development of the required combustor aerothermodynamic features for burning high nitrogen fuels. Testing was conducted over a wide range of operating conditions for a 12:1 pressure ratio heavy-duty gas turbine. Combustors were evaluated with distillate fuel, SRC-II coal-derived fuel, residual fuel, and blends. Test results indicate that low levels of NOx and fuel-bound nitrogen conversion can be achieved with rich-lean combustors for fuels with high fuel-bound nitrogen. In addition, ultra-low levels of NOx can be achieved with lean-lean combustors for fuels with low fuel-bound nitrogen.

Introduction

Background. A decline in the availability of petroleum fuels is projected to occur in the 1980's and accelerate throughout the 1990's. This is particularly true with regard to the petroleum distillate fuels currently used in many stationary power generation sources. Faced with declining supply, these are expected to be devoted to transportation and other consumer use. The availability decline will be accompanied by continued cost increases.

Fuel supplies for power generation equipment must thus move towards the utilization of petroleum products of lower cost and quality, and increasingly towards the combustion of coal-derived liquids (CDL) and gaseous fuels. Furthermore, because of the projected higher costs, increasingly stringent emissions requirements, and the unreliability in the projected mix of fuels to be available, combustion systems for gas turbines must be efficient, environmentally acceptable and have fuels flexibility. Lower quality petroleum (residual) fuels and CDL's have higher fuel nitrogen content and lower hydrogen content which thus require significant improvements in current production combustor technology to meet emissions and operational performance requirements.

Program Objectives. The objectives of the program described in this paper are to develop low NOx combustor technology to meet current U.S. EPA NSPS emissions requirements and operational performance standards for turbine operation with high nitrogen fuels, and with fuels flexibility. A goal was established to meet these requirements dry, i.e., without the use of water injection for NOx suppression. Dry operation leads to improved cycle efficiency to offset expected higher fuel costs, and to eliminating investment and operating expenses required for water injection systems. Furthermore, water and steam injection is successful in reducing thermal NOx but does not remove NOx from fuel-bound nitrogen sources.

Seven advanced combustor concepts are being tested, including three-rich-lean and three lean-lean staged combustors, and one lean reaction catalytic burner. Initial screening tests are being used to evaluate the potential of each concept, followed by selection of the most promising concepts for development to meet the program dry low NOx goals. The rich-lean concepts are expected to have the highest potential for low conversion of fuel nitrogen to NOx.

Tests are being conducted with 20-cm- dia combustors over a range of operating conditions from ignition to peak load for a 12:1 pressure ratio heavy duty gas turbine cycle characteristic of the General Electric MS7001E machine. Test emphasis is on the development of combustor aerothermodynamic features for low NOx burning of petroleum residual and SRC-II fuels.

Contributed by the Gas Turbine Division and presented at the International Gas Turbine Conference and Products Show, Houston, Texas, March 9-12, 1981, of THE AMERICAN SOCIETY OF MECHANICAL ENGINEERS. Manuscript received at ASME Headquarters, December 15, 1980. Paper No. 81-GT-125.

Copyright © 1982 by ASME

Downloaded 01 Jun 2010 to 171.66.16.62. Redistribution subject to ASME license or copyright; see http://www.asme.org/terms/Terms_Use.cfm

This paper is a report of the interim status of this program and presents the combustor concepts studied, test results obtained, interim conclusions and plans for the remaining development testing.

Specific Goals. Program emissions goals are based on the EPA Standard F.R. 40 CFR Part 60 and are contained in Table 1.

Table 1 Emissions goals

Pollutant	Maximum level	Operating condition
Oxides of nitrogen	75 ppm at 15% 0	All
Sulfur dioxide	150 ppm at 15% 0	All
Smoke	S.A.E. no. = 20	All

Key combustor operational performance goals are listed in Table 2.

Table 2 Performance goals

Combustion efficiency	>	99% at all operating conditions
Total pressure loss	<	6% at base power load
Outlet temperature pattern factor	=	0.25 at base load and load power
Combustor exit radial temperature profile	=	Equivalent to production comb. values

Test equipment and procedures

Air Supply Facility and Test Cell. The combustion tests were conducted in the General Electric facilities located in Evendale, Ohio. The test cell used in this program has an air supply capability of approximately 5.4 kg/s at temperatures up to 866 K and 2.07 mPa pressure. The air supply is heated by an indirect gas fired preheater so that unvitiated air is supplied to the combustor test section. The fuel supply system is capable of supplying any of three types of fuels or blends of the fuels during the tests. In addition, the fuels or fuel blends could be doped with pyridine to increase the nitrogen content. The system was configured to enable changing of fuel type, blend ratios or the amount of pyridine doping with the combustor in operation. Fuel samples were taken during the tests and analyzed to verify fuel blend ratios and pyridine content as measured by flow meters.

Test cell data acquisition systems included smoke measurement and on-line gas analysis equipment. The smoke emissions are measured using a filter stain method. The on-line gas analysis equipment consists of four basic instruments: a flame ionization detector (FID) for measuring total HC concentrations; two nondispersive infrared analyzers for measuring CO and CO_2; and, a heated chemiluminescent analyzer for measuring NO and NO_2. This system conforms to SAE ARP 1179 and is used to determine the exhaust emission concentrations/emission indices, combustion efficiency and sample fuel-air ratio.

Test Rig. The test rig used to evaluate the combustors during this program consisted of a 25.4-cm- dia duct divided into several spool pieces including an inlet section, a combustor housing section and an exit instrumentation section. The spool pieces included various ports to accommodate the fuel nozzle supply lines, instrumentation rake mountings and lead out of thermocouples mounted on the combustors. The combustion section had two two spool pieces for ease of assembly and to accommodate combustors of various lengths. The test rig is mounted on a dolly used to transport the assembly between the test cell and the buildup area. The dolly also includes quick disconnect fittings for the thermocouple and pressure instrumentation hookup in the test cell. The inlet of the test rig is supplied with air from a settling or plenum chamber in the test facility. The discharge of the test rig is connected to a facility exhaust system with back pressuring valves.

Instrumentation at the combustor exit consisted of four three-element gas sampling rakes and four three-element thermocouple rakes. The gas sampling rakes were also utilized for measuring combustor exit total pressures and for extracting the smoke samples. The three elements on each rake were mounted on centers of equal area at the combustor exit with one element of one gas sample rake located on the combustor centerline. The gas samples could be read as twelve individual samples for a detailed analysis of the gas stream profiles or manifolded together for extracting overall average gas samples. When read individually, the gas samples could also be used to calculate local temperatures and used along with the thermocouple readings for more detailed examination of the combustor exit temperature distribution.

Test Fuels. Three types of fuels and blends of these fuels were used during the program. In addition, pyridine was added in various percentages to increase the concentration of fuel nitrogen. The fuel properties are presented in Table 3. The ERBS fuel was a middle petroleum distillate with 12.95 percent hydrogen and essentially no fuel-bound nitrogen.[1] The solvent refined coal SRC-II fuel was a middle-distillate, coal-derived fuel supplied by the Pittsburg and Midway Coal Mining Co. This coal-derived fuel had only 9.07 percent hydrogen content and a high level of fuel-bound nitrogen at 0.87 percent by weight. The residual had a 294 K pour point and contained significant levels of vanadium and fuel-bound

[1] Prock, G.M., and Seng, G. T., NASA Technical Memorandum 81440, "Initial Characterization of an Experimental Referee Broadened Specification (ERBS) Aviation Turbine Fuel," NASA LeRC, Jan. 1980.

Nomenclature

CO = carbon monoxide emissions
EI = emissions index, g/kg fuel
ERBS = Experimental Referee Broad Specification petroleum distillate
f/a = fuel-air mass ratio
ISO = International Standards Organization reference humidity condition, 0.0063 g H_2O/g dry air
MWe = power, megawatts electrical output
NOx = oxides of nitrogen emissions
P_3 = combustor inlet pressure, mPa
ppm = parts per million, by volume
PF = pattern factor = $\dfrac{(T_4)_{max} - \bar{T}_4}{\bar{T}_4 - T_3}$
T_3 = combustor inlet temperature, K
T_4 = combustor exhaust temperature, K, at radial location r
$\bar{T}_4$ = average combustor exhaust temperature
UHC = unburned hydrocarbon emissions
V_{ref} = reference velocity, m/s
ϕ = reaction zone equivalence ratio

Downloaded 01 Jun 2010 to 171.66.16.62. Redistribution subject to ASME license or copyright; see http://www.asme.org/terms/Terms_Use.cfm

Table 3 Fuels properties

	ERBS[a]	SRC-II	Residual
Spec. grav. @ 289/289 K	0.8377	0.9796	0.9440
Hydrogen content, percent	12.95	9.07	11.52
Sulfur content, percent	0.085	0.20	0.49
Net heat of combustion, MJ/kg	42.5	38.1	41.3
Viscosity, m^2/s @ 311 K	1.36×10^{-6}	3.55×10^{-6}	1.345×10^{-3}
Nitrogen content, percent	0.0054	0.87	0.23
Surface tension, N/M	–	–	3.29×10^{-2} @ 339 K
Surface tension, N/M	–	–	3.06×10^{-2} @ 366 K
Pour point, K	244	255	294
Vanadium, ppm by wt	–	–	26

[a] Experimental Referee Broad Specification (ERBS) petroleum distillate fuel

Table 4 Combustor test conditions

P_3, mPa	T_3, K	V_{ref}[a], m/s	Fuel-air ratio	Engine condition
Ambient	Ambient	11.3	0.023	Ignition
.882	564	43.6	0.0054	Full speed no load
1.025	588	38.4	0.0141	50% load
1.080	596	36.9	0.0183	70% load
1.145	606	35.1	0.0235	Base load (92%)
1.166	609	34.4	0.0253	Peak load (100%)

[a] Velocity in test rig duct forward of combustor dome

nitrogen. Heated storage tanks and fuel supply lines were required when using this fuel. The viscosity at 311 K was $1.345 \times 10^{-3} m^2/s$. With the three types of fuel used, plus the blending and the pyridine doping, a very wide range of fuel properties was available for evaluating the combustor concepts.

Test Conditions. The operating conditions used in evaluation tests of these combustors are representative of the General Electric MS7001E utility engine. The MS7001E engine has a baseload rating of 72.9 MWe at a turbine inlet temperature of 1353 K, pressure ratio of 11.7 and airflow of 271 kg/s. The matrix of test conditions is shown in Table 4. The standard procedure was to evaluate the combustor over the load range for the MS7001E engine and to conduct additional tests as appropriate. Other test variables were also adjusted during the tests. For example, fuel-air ratios above and below design levels were tested for diagnostic purposes. Also, the fuel flow split between the pilot and main stage for combustors with two fuel states was varied to determine the optimum operating conditions. In addition, the atomizing air pressure ratio for the fuel nozzles was varied and had some effect on performance.

Description of Test Combustors

Two-Stage Rich-Lean Combustor Concepts. Previous work has shown the potential of two-stage rich-lean combustion for producing low NOx emissions with high nitrogen fuels. The work described here is aimed at development of this concept for practical application to combustion systems of heavy duty stationary gas turbines.

In this combustion mode, a rich mixture of fuel and air ($\phi \simeq 1.7$) is burned in the first stage producing incomplete combustion at low temperatures in an oxygen-deficient environment. Under these conditions, little thermal NOx is produced while fuel nitrogen is released with minimal conversion to NOx. This incompletely combusted mixture is then mixed with additional combustion air in a low residence time quench zone to produce a lean mixture ($\phi \simeq 0.5$) with combustion completed in the lean second stage.

Two key problems are associated with the development of rich-lean combustors capable of low NOx emissions, and are addressed in the combustor designs studied in this program. These are (*a*) the potential for smoke production in the rich first stage, and (*b*) the need for an acceptable heat transfer design of the rich stage which avoids NOx production by eliminating a locally stoichiometric zone associated with combustion liner film cooling air. Smoke production is avoided by proper selection of rich stage equivalence ratio and the provision of fuel-air mixing systems to provide for mixture homogeneity. Rich stage cooling in the test hardware was accomplished by backside convective cooling.

Rich-Lean Combustor with Premixing, Concept 1. Concept 1 contains a single fuel nozzle and swirl cup in a premixing tube ahead of the rich stage. This should provide uniform mixing of fuel and air and avoid smoke production. Following the rich stage is a necked-down quench zone where secondary air is introduced and mixed with the products of combustion from the rich stage in minimum time. This shifts the stoichiometry from rich to lean and is followed by combustion in the final lean stage. Figure 1 shows Concept 1 with the premix tube at the top of the figure, followed by the convectively cooled rich stage, quench zone, and lean stage. The elongated holes in the converging section of the quench zone provide for entrance of secondary air to be rapidly mixed with the rich stage products while accelerating through the necked-down section between rich and lean stages. Rich-stage liner cooling is accomplished by convection cooling of the outside of the liner. A thermal barrier coating was applied to the inside of the rich stage to minimize heat transfer from combustion gases to the liner wall.

Nominal rich-stage equivalence ratios of 1.4 to 1.7 have been tested, with a lean stage equivalence ratio of 0.54. The test combustor is 20 cm in diameter with an overall length of 137 cm., including the premix tube and downstream dilution section.

Rich-Lean Combustor with Multiple Nozzle Dome, Concept 2. This combustor was designed to have the same rich and lean stage equivalence ratios as Concept 1, but has multiple fuel nozzles and swirlers to prepare the rich stage fuel-air mixture. Figure 2 shows combustor Concept 2 with eight fuel nozzles and swirl cups in the head end of the rich stage. Following the rich stage is the necked-down quench zone followed by the lean stage. In addition to the multiple nozzle head-end, this combustor differs from Concept 1 in that the rich stage was shorter (38 cm compared to 51 cm for 1) and the holes for admission of mixing air to the products leaving the rich stage are in the smaller-diameter quench zone. Note in Fig. 2 that the rich stage is again not cooled by air

Downloaded 01 Jun 2010 to 171.66.16.62. Redistribution subject to ASME license or copyright; see http://www.asme.org/terms/Terms_Use.cfm

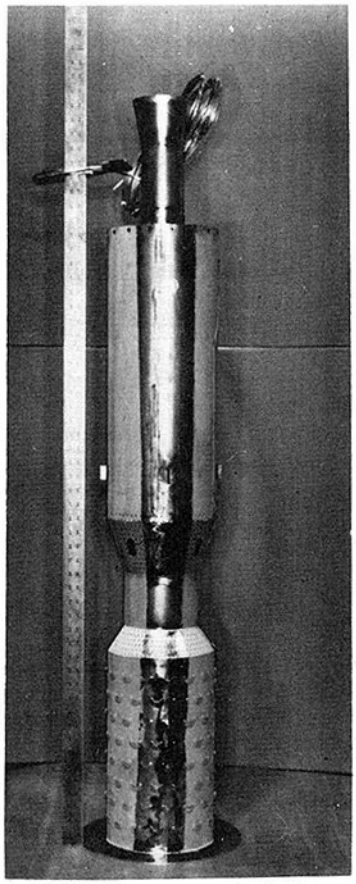

Fig. 1 Rich-lean combustor with premix, Concept 1

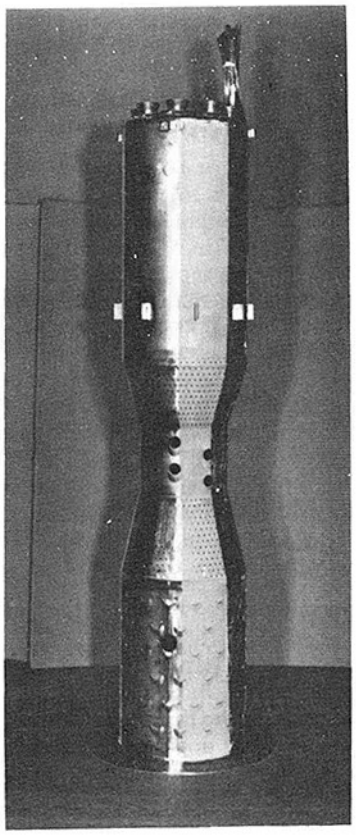

Fig. 2 Multiple-nozzle rich-lean combustor, Concept 2

penetrating the rich stage through liner cooling holes, but rather by backside convection cooling and the application of a thermal barrier coating to the inside surface of the rich stage. The test combustor is 20 cm in diameter with an overall length of 125 cm.

Rich-Lean Combustor, Concept 3. Concept 3 is a rich-lean combustor with multiple fuel nozzles and swirl cups. Following the rich stage is a narrow passage mixing stage, where secondary and dilution air are introduced and mixed with the products of combustion from the rich stage in minimum time so as to produce minimum additional thermal NOx. This combustor has the same multi-nozzle fuel injector/air swirler head end and rich and lean stage equivalence ratios as for Concept 2. It differs in the design of the mixing passage between rich and lean stages.

As for combustor Concepts 1 and 2, the rich stage liner is convectively cooled on the backside and sprayed with thermal barrier coating on the inside.

Two Stage Lean-Lean Combustor Concepts. Lean-Lean combustors burn lean in both stages to avoid high combustion gas temperture and, thus avoid generation of thermal NOx. In general, local average dome fuel air ratios are maintained at less than 6/10 equivalence ratio. However, minimum local fuel-air ratios must be maintained high enough to avoid poor combustion and generation of unburned hydrocarbons and CO. In order to achieve these objectives, two stages of combustion are employed. At low engine power conditions when the total fuel flow rates are low, only the primary or pilot stage of the combustor is fueled. At higher power conditions when the engine fuel flow rate is adequate to fuel both stages of the combustor, fuel is introduced into the main stage dome and the pilot dome fuel flow is reduced. As the

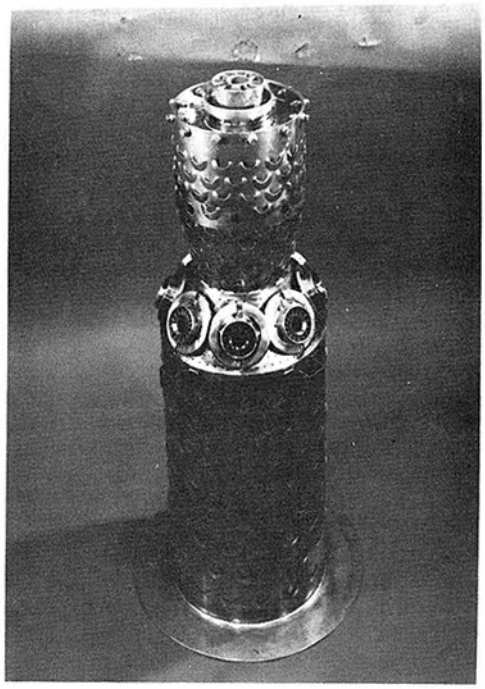

Fig. 3 Series-staged lean-lean combustor, Concept 4

engine power and fuel flow rates are increased, the fuel-air ratio in the main stage is increased and generally reaches an equivalence ratio of approximately six tenths at max power.

Basic problems associated with lean-lean two-stage combustors include high fuel-air ratios and consequent smoke from the pilot stage before the main stage is in operation, and CO generation when the main stage is initially fueled.

Downloaded 01 Jun 2010 to 171.66.16.62. Redistribution subject to ASME license or copyright; see http://www.asme.org/terms/Terms_Use.cfm

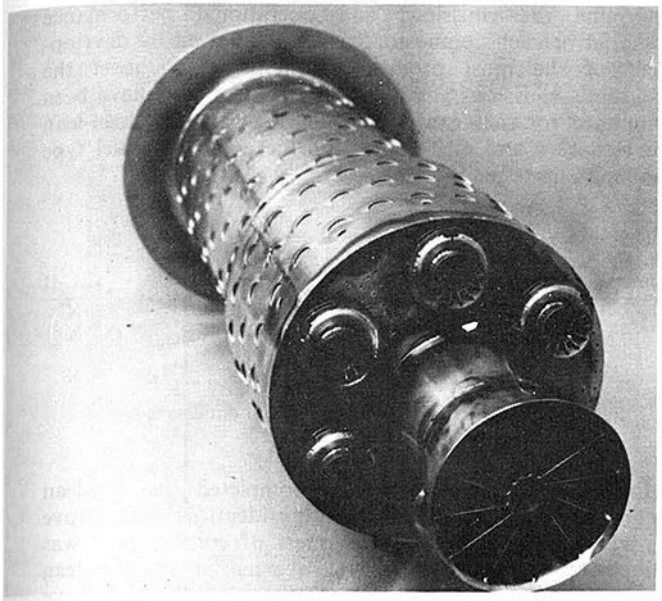

Fig. 4 Series-staged combustor with premix, Concept 5

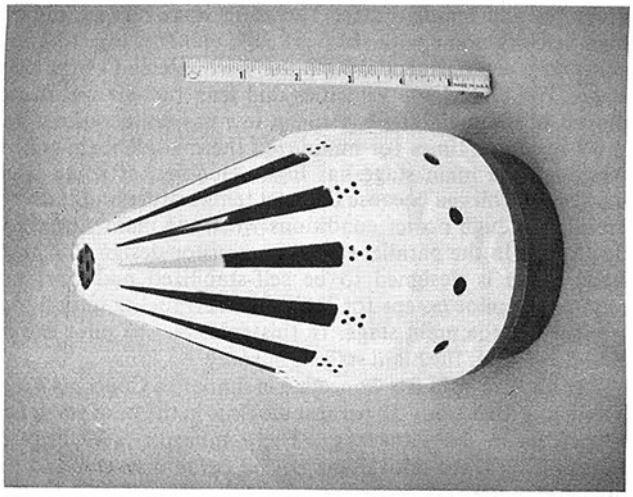

Fig. 5 Premixing duct details, Concept 5

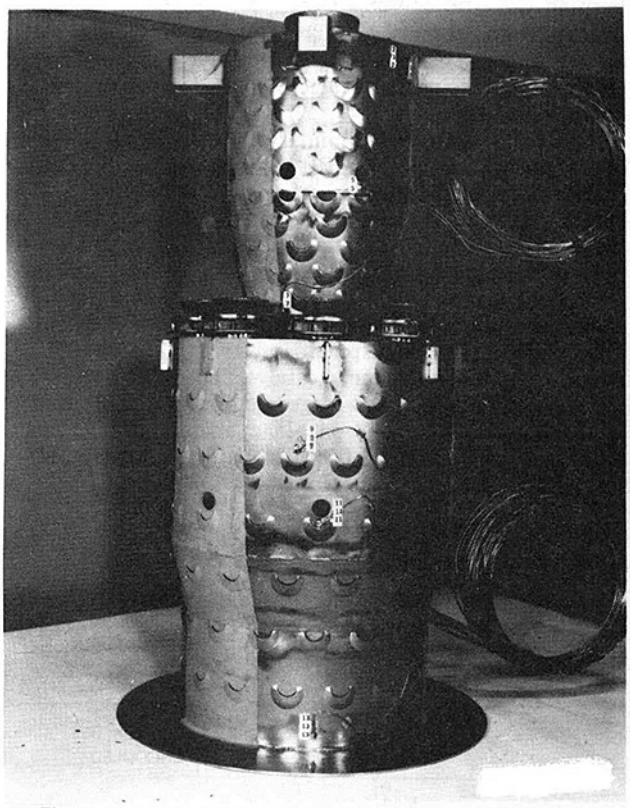

Fig. 6 Parallel-staged lean-lean combustor, Concept 6

Series-Staged Lean-Lean Combustor, Concept 4. A series-staged lean burning combustor is illustrated in Figure 3. This combustor has a pilot stage utilizing a single-air atomizing fuel injector and a two-stage counter-rotating swirl cup at the forward end. This pilot burner is used for lightoff and operation up to approximately seventy percent of peak engine power rating. Combustion air is introduced into the pilot dome through the swirler and through a band of eight dilution holes located approximately one dome height aft of the fuel nozzle tip.

The main stage employs eight single-stage swirlers and air atomizing fuel injectors. For this combustor, the objective is to obtain rapid mixing of the fuel and air in the main dome. No attempt is made to generate a strong, flame-stabilizing recirculation zone in the main stage. This is to avoid long gas residence times associated with recirculating zones that generate thermal NOx. Instead, ignition of the main stage gases is provided by the hot gases from the pilot dome which is used at all engine operating conditions. For the combustor shown in Fig. 3, 34.8 percent of the combustion air is used in the pilot stage and 65.2 percent is used in the main stage. At peak load conditions, 65 percent of the fuel is introduced in the main stage and the main stage average equivalence ratio based on the swirler air flow is 0.61. At peak load, the pilot stage equivalence ratio based on the swirler, dome cooling and pilot dilution air is approximately 0.51.

The overall length of this combustor is 64.8 cm, the pilot dome diameter is 15.2 cm and the aft liner diameter is 20.3 cm. Approximately 24.5 percent of the combustor air is used for liner cooling.

Series-Staged Lean-Lean Combustor with Premixed Main Stage, Concept 5. This combustor is shown in Fig. 4 and has a pilot stage with six dual counter-rotating swirlers arranged in an annulus around the main stage premixing duct. The main stage fuel is introduced into the forward end of the duct and mixed with the air prior to entering the combustion zone through twelve axial slots at the aft end of the premixing duct. Details of the premixing cone are shown in Fig. 5. The hot gases from the pilot dome flow in the spaces between the slots shown in Fig. 5 and mix with the main stage mixture to provide ignition. The velocity in the premixing duct is 73.2 m/s and the bulk mixture residence time in the premixing duct is about four ms. Air atomizing fuel nozzles are employed for both the pilot and main stage of this combustor.

The air flow split for this combustor is similar to that of Concept 4 with 35 percent of the combustion air admitted to the pilot stage and 65 percent admitted in the main stage and aft end of the combustor. The equivalence ratio in the premixing duct is 0.61 at peak load conditions. The design fuel split between pilot and main stage at peak load conditions is 35 percent in the pilot and 65 percent in the main stage.

Parallel-Staged Lean-Lean Combustor, Concept 6. This combustor is shown in Fig. 6. This concept has a low velocity pilot stage with a single swirl cup and air atomizing fuel injector at the dome end. The pilot dome is designed for ease of ignition and efficient combustion at low power conditions with low overall engine fuel-air ratios and with low inlet

Downloaded 01 Jun 2010 to 171.66.16.62. Redistribution subject to ASME license or copyright; see http://www.asme.org/terms/Terms_Use.cfm

pressures and temperatures. The main stage has an annular high-velocity dome with six swirl cups and fuel injectors in a concentric arrangement around the discharge end of the pilot stage. The high dome velocities and lean fuel-air ratios employed in the main stage result in low gas temperatures and short residence times for minimized thermal NOx emissions. Although the main stage has high velocities, efficient combustion is achieved because the inlet temperature and pressure are high at high power conditions when the main stage is in operation. In the parallel-staged combustor design, the main stage dome is designed to be self-stabilized and does not require the pilot except for ignition when fuel is initially introduced in the main stage. In this concept, the pilot can be shut down after the main stage is burning.

The air flow split for Concept 6 is similar to Concepts 4 and 5 with approximately 37 percent air flow in the pilot stage and 63 percent in the main stage. The combustor is 52.7 cm in overall length, the pilot dome is 15.2 cm in diameter and the diameter at the main stage dome is 22.9 cm.

Lean Burning Catalytic Combustor, Concept 7. A lean burning catalytic combustor has been designed to demonstrate ultra-low thermal NOx performance for the combustion of low nitrogen fuels at gas turbine cycle conditions. The combustor is being fabricated and will be operated in a planned future test.

Figure 7 presents a preliminary design schematic for this combustor. A fuel preparation section precedes the catalytic reactor main stage and contains seven fuel nozzles. A 38-cm length is expected to provide thorough premix and prevaporization of ERBS and SRC-II fuels and partial prevaporization of the heavy petroleum residual fuel, while providing margin against auto-ignition. This section is followed by the main stage catalytic reactor, which consists of an MCB-12 zirconia-spinel substrate coated with a proprietary UOP noble metal catalyst. The reactor is followed by the downstream pilot stage section, which is used for ignition, acceleration and part-load operation to 50 percent load, at which point lightoff ocurs for further load increase to full power.

Results and Discussion

The test plan for this program includes screening tests to determine the emissions and operational performance potential of each combustor concept, followed by development of the most promising combustors to meet the program's emissions goals. Initial screening tests have been completed for rich-lean combustors 1 and 2 and lean-lean combustors 4 and 6. Table 5 lists the combustor-fuel type combinations tested.

Table 5 Test matrix

Combustor concept	ERBS	RESID	SRC-II
LL4	X	X[(a)]	X
LL6	X[(a)]	X[(a)]	X
RL1	X[(a)]		
RL2	X[(a)]	X	X

[(a)] Fuel doped with pyridine to increase fuel-bound nitrogen

Extensive screening tests were completed for lean-lean combustors 4, 6, modifications were identified to improve emissions performance, and a retest of combustor 4 was completed. Initial testing was less extensive for rich-lean combustors 1 and 2. However, these combustors have demonstrated very low conversion of fuel-bond nitrogen to NOx, modifications have been identified, and further tests of combustors 1 and 2 are underway.

Rich-Lean Combustor Tests.

Rich-Lean Combustor with Multiple Nozzle Dome, Concept 2. Initial screening tests were run for combustor Concept 2 with SRC-II and residual fuels. Testing was limited to fuel-air ratios characteristic of only the higher load points for the reference engine cycle. This was done to maintain fuel-rich first stage stoichiometry, thereby avoiding imposing unacceptable heat flux to the rich-stage liner wall which would result from near-stoichiometric conditions. Future development in Phase II of this program will consider air-staging for part-load performance.

Figure 8 presents the NOx emissions plotted as emissions index (g NOx/kg fuel) corrected to ISO humidity (0.0063 g H_2O/g dry air) versus engine load and corresponding fuel-air ratio for the reference engine cycle. NOx emissions were well above the program goals in these initial tests of the as-manufactured hardware, and about the same as found in tests

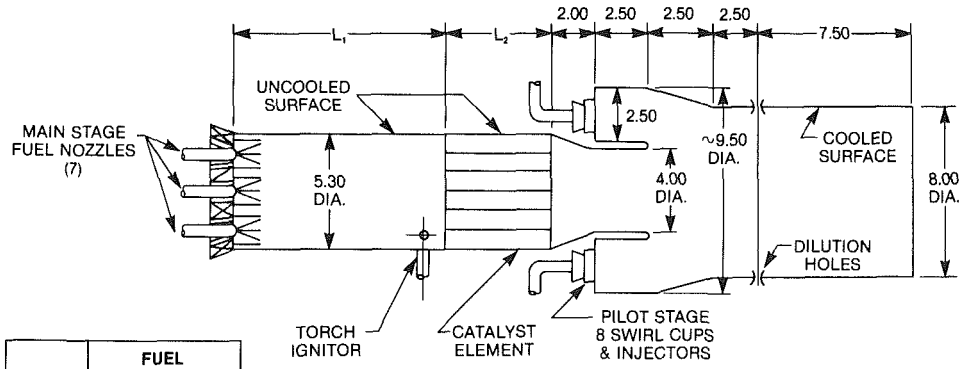

LENGTH	FUEL	
	RESIDUAL	#2
L_1	15.0	15.00
L_2	~10.00	5.00

NOTE: LARGER L_2 DIMENSION IS SPECIFIED TO PERMIT INCLUSION OF A SPLIT CATALYST ELEMENT

Fig. 7 Parallel-staged lean reaction catalytic combustor, Concept 7

Downloaded 01 Jun 2010 to 171.66.16.62. Redistribution subject to ASME license or copyright; see http://www.asme.org/terms/Terms_Use.cfm

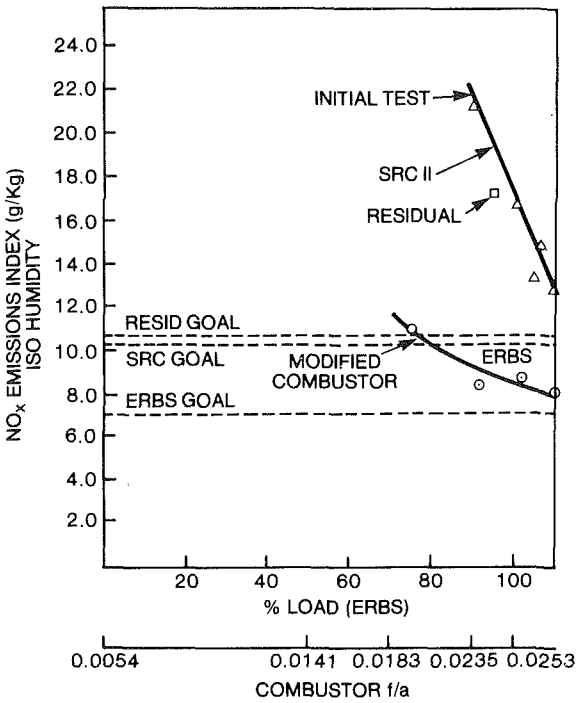

Fig. 8 NOx emissions versus load, Concept 2

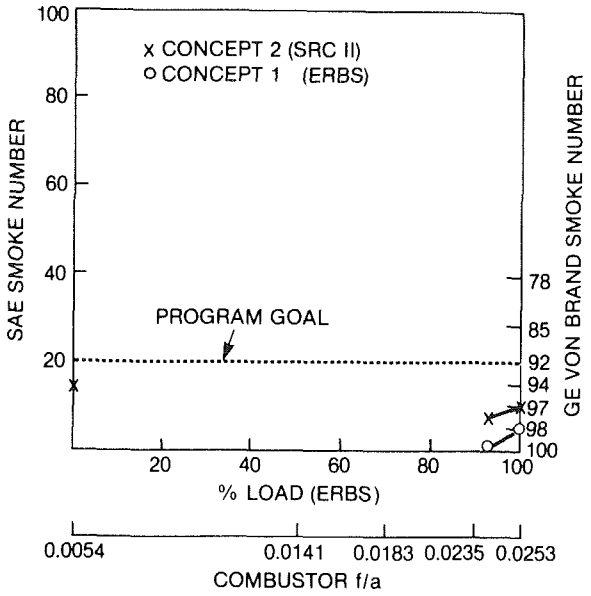

Fig. 9 Smoke performance, Concepts 1 and 2

of lean-lean combustor 4 (discussed later) with residual and SRC-II fuels. This unexpected results indicated that the full potential of this rich-lean concept had not been realized. In fact, Fig. 8 shows that NOx decreased rapidly with increasing fuel-air ratio and, at the highest fuel-air ratios tested (f/a = 0.029, corresponding to 110 percent load), NOx emissions approached the EPA limit for high-nitrogen fuels. A significant reduction in NOx is thus expected to be realized by redistributing the combustor air flow to operate with a richer first stage. The NOx emissions index should pass through a local minimum at high loads and tests scheduled with the first stage equivalence ratio increased should serve to locate this optimum point.

As seen in Fig. 9, smoke performance of this combustor was excellent, with an SAE smoke number of approximately 5 at base load and less than 10 at all other load conditions, compared to the goal of SAE-20. Increasing the first stage equivalence ratio will eventually be limited by excessive smoke formation in the rich stage. However, the smoke data shows that even at a fuel-air ratio of approximately 0.029 on SRC-II fuel (at which point NOx emissions approach the NSPS goals), smoke number was approximately 18, which is within the program limit of 20. Improved fuel atomization and more rapid first stage fuel-air mixing are modifications that could potentially reduce the onset of smoke.

Combustible emissions (CO, UHC) were well within program goals. The CO emissions were approximately 20 ppm at baseload conditions. Combustion efficiency exceeded 99 percent for all test points.

The maximum liner metal temperature measured in the rich stage was approximately 925 K, well within materials limits. Combustor pressure drop met the program goals, as did measured pattern factors and combustor exit temperature profiles.

Combustor Concept 2 was then modified to increase the rich stage equivalence ratio for the next series of tests. Preliminary test results for the modified combustor with ERBS fuel are also shown on Fig. 8. These data show the NOx emissions index for ERBS at baseload to be approximately 8, approaching the program goal of 7 for this fuel. Furthermore,

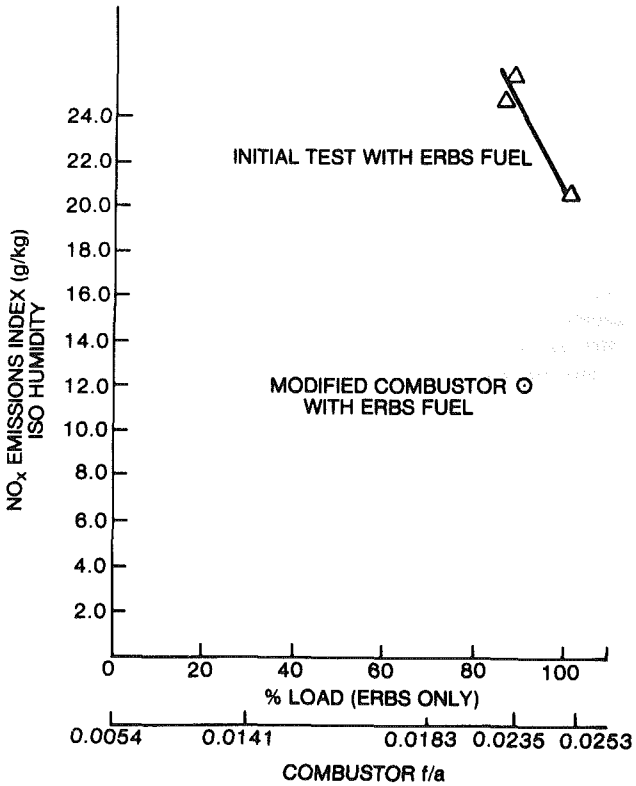

Fig. 10 NOx emissions, rich-lean, Concept 1

data with ERBS fuel doped with pyridine to nitrogen contents of 0.18 percent and 0.87 percent (approximately equal to the nitrogen levels in residual and SRC-II fuels, respectively), show the NOx emissions at baseload are within 10–15 percent of the program goals for these fuels. The corresponding fuel-bound nitrogen conversion rates were approximately 30 percent for residual and 10 percent for SRC-II fuels. More extensive tests of this combustor are planned with all program fuels and fuel blends.

It appears that this combustor has the potential for meeting program goals for residual and SRC-II fuels, i.e., with fuels

Downloaded 01 Jun 2010 to 171.66.16.62. Redistribution subject to ASME license or copyright; see http://www.asme.org/terms/Terms_Use.cfm

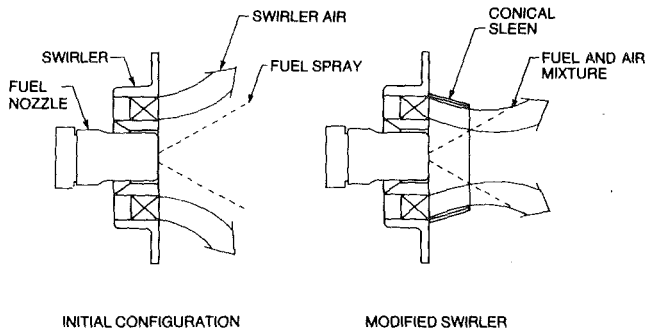

Fig. 11 Fuel nozzle/swirl cup spray pattern

having bound nitrogen contents approaching one weight percent. Encouragingly low yield was observed and further tests with the increased rich-stage equivalence ratio is expected to demonstrate meeting emissions goals with all program fuels.

Rich-Lean Combustor with Premixing, Concept 1. Initial screening tests have been completed with ERBS fuel only, and with ERBS doped with pyridine to assess fuel-bound nitrogen conversion to NOx. Figure 10 shows that NOx emissions were high. This was found to be caused by misalignment of the fuel nozzle at the entrance to the premix tube. This resulted in fuel spraying on the premix walls presenting an asymmetric fuel-air distribution at the entrance to the rich stage. This was confirmed by an observed skew in the emissions and temperature profiles at the combustor exhaust. However, as with combustor Concept 2, Fig. 10 shows that NOx emissions decreased rapidly with increasing rich-stage fuel-air ratio. As for Concept 2, a significant reduction in NOx is expected to be realized by increasing the rich-stage equivalence ratio.

Smoke emissions were exceptionally low, as seen in Fig. 9. The data indicates that sufficient smoke margin is available to allow significant increase in the rich-stage equivalence ratio, thus taking advantage of the rapid decrease in NOx emissions versus fuel-air ratio seen in Fig. 10.

Combustible emissions (CO, UHC) were well within program goals. Combustion efficiency exceeded 99 percent for all conditions tested.

Combustor Concept 1 was subsequently modified to provide proper fuel nozzle alignment and to increase the rich stage equivalence ratio. Preliminary test results with ERBS fuel are also shown on Fig. 10. The NOx emissions index at baseload was approximately 12, much improved over the initial test results but still above the program goal and higher than that observed for multi-nozzle Concept 2. Test data indicates that this is due to thermal NOx formation in the downstream section of the rich stage. This is caused by lean stoichiometry in that location resulting from the admission of quench air through holes in the converging throat section, as opposed to quench air admission through holes in the narrow diameter throat of Concept 2. NOx emissions data with ERBS doped with pyridine to nitrogen levels approaching that for residual and SRC-II fuels indicate yields of 30 percent and 20 percent, respectively. It is expected that combustor modifications will further improve performance.

Lean-Lean Combustor Tests

Series-Staged Lean-Lean Combustor, Concept 4. The lean burning series-staged combustor was tested with two levels of pressure drop. During the initial testing, the combustor total pressure drop was 4½ percent of the inlet pressure. Later testing was conducted with the pressure drop increased to 5½ percent. The program goal for pressure drop was 6 percent or

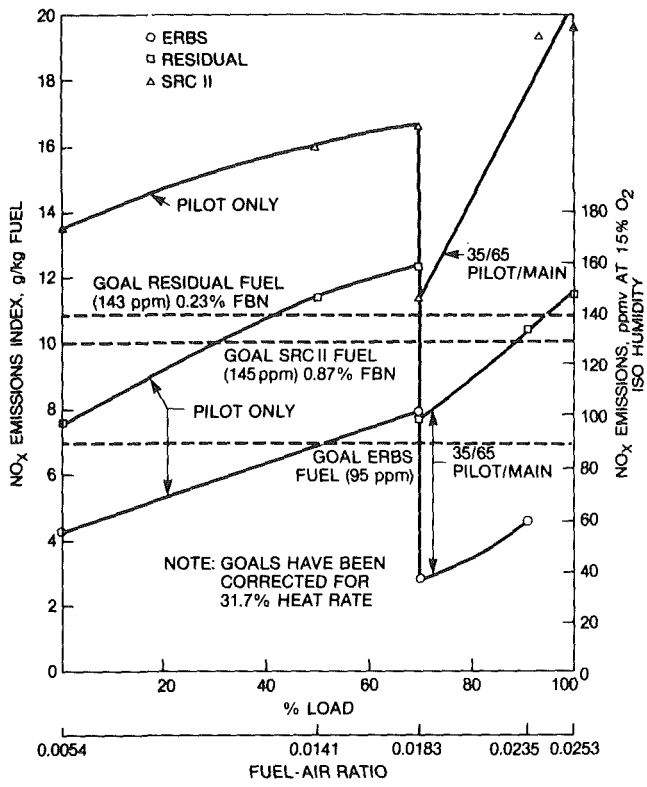

Fig. 12 NOx emissions, lean-lean, Concept 4

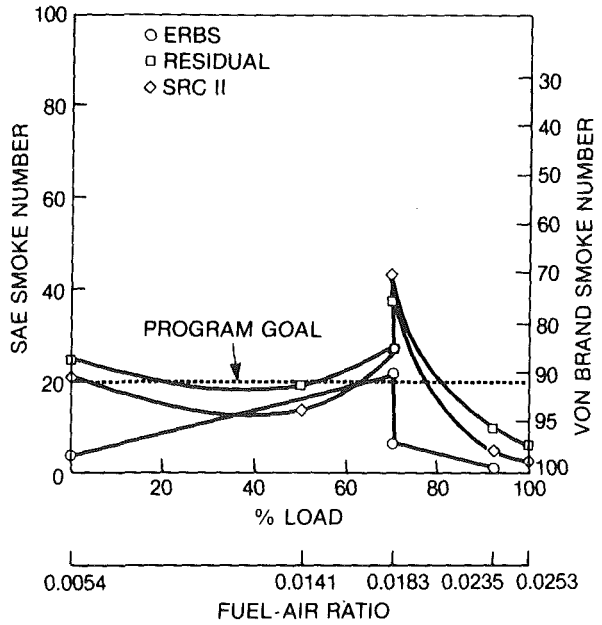

Fig. 13 Smoke data, Concept 4

less. At 4½ percent pressure drop, the NOx emissions were approximately ten percent above the program goals at the base load (92 percent) test condition for both the ERBS and the residual fuels. Also, when operating on the pilot alone at fifty and seventy percent load conditions, the NOx was above the program goal.

Spray tests of the main stage swirlers were subsequently conducted and indicated insufficient mixing of fuel and air. The local rich regions in the main stage prevented reaching the potential NOx emissions levels of this design. Figure 11

Downloaded 01 Jun 2010 to 171.66.16.62. Redistribution subject to ASME license or copyright; see http://www.asme.org/terms/Terms_Use.cfm

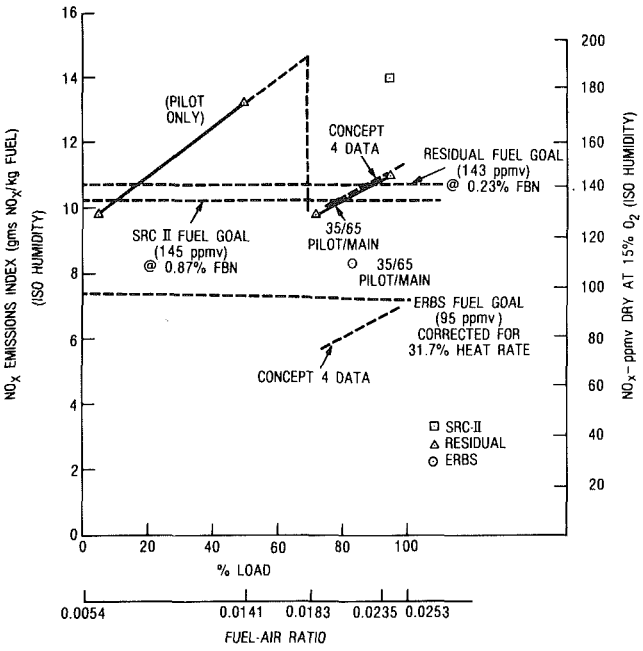

Fig. 14 NOx performance for Concept 6

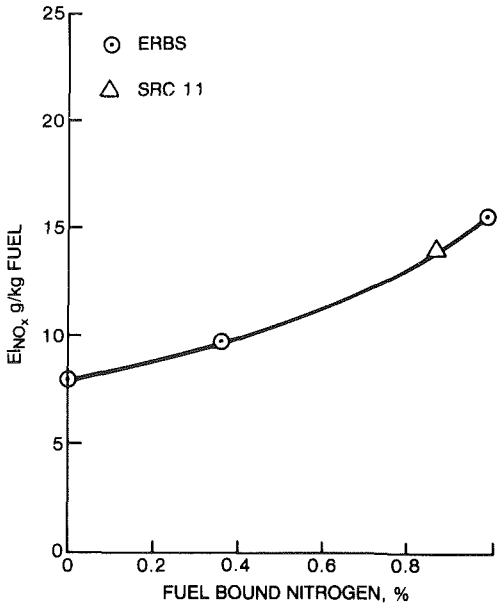

Fig. 15 Effect of FBN on NOx, Concept 6

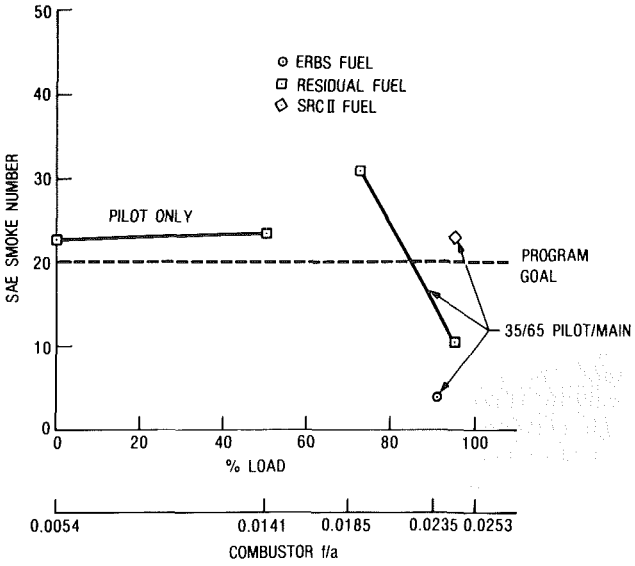

Fig. 16 Smoke emissions, Concept 6

illustrates the initial spray pattern and the spray pattern obtained after a flow guide sleeve was added to the swirler. The combustor pressure drop was increased by approximately one percent to 5½ percent by reducing the cooling flow from approximately 28.4 percent to 27 percent of the combustor flow and some airflow was shifted from the pilot stage dilution holes to the pilot swirler. This latter change was made to reduce carbon deposits in the pilot swirler and also to reduce local fuel-air ratios. The increased pressure drop was expected to improve mixing in both the pilot and main stage.

With the foregoing changes, the NOx level with ERBS fuel was well below the program goal at the base load condition as shown in Fig. 12. On pilot-only operation at the seventy percent load condition, the NOx levels slightly exceeded the limit. With residual fuel, the goals were also met at the base load condition but were above the limit at peak load and at the transition point. With the SRC-II fuel with higher nitrogen content, the NOx emission levels were significantly above the limits owing to relatively high rates of conversion of the fuel nitrogen.

Measured pattern factors and turbine inlet temperature profiles for this combustor met the goals at both pressure levels and with all three fuels. Liner temperatures were low for both pressure drop levels tested and for all three fuels. The maximum measured temperature was approximately 250 K above the inlet temperature with residual fuel. These temperature measurements were made with the cooling flow reduced to 27 percent of the combustor air flow.

Carbon deposits presented no problem with this combustor design. There were some very light deposits in both the pilot and main stage swirlers and on the dome of the main stage. These deposits are believed to have reached a stabilized thickness as the combustor accumulated approximately 16 test hr with seven on the residual fuel during the last test run.

Smoke levels were well below the limits at base and peak level conditions with all three fuel types as shown in Fig. 13. With ERBS fuel, the smoke levels met the requirements at all conditions. With SRC-II and residual, the smoke levels exceeded the limits when operating only on the pilot at the transition point.

Combustion efficiencies were greater than 99 percent at all conditions with all three fuels except at full speed no load where the efficiency was 97 percent and at the pilot-mainstage crossover point where the efficiency was 92 percent after transfer to the main stage.

It appears that this combustor concept has the potential of meeting all program goals with ERBS and possibly a residual fuel with less than 0.25 weight percent fuel nitrogen. In fact, with fuels with low nitrogen content (i.e., ERBS), this concept would meet the NOx emission level with considerable margin. The two minor deficiencies observed, smoke at high pilot fuel-air ratios and low efficiency at lean operating conditions could most likely be overcome with some development including flow split adjustments, additional swirl cup changes and possible additional pressure drop. All other performance parameters including pattern factors, liner temperature and carbon deposits were met on the initial testing. This combustor concept does not appear to have the potential for meeting NOx emission goals with fuels with nitrogen contents much in excess of one quarter of one percent.

Parallel Staged Lean-Lean Combustor, Concept 6. The

Downloaded 01 Jun 2010 to 171.66.16.62. Redistribution subject to ASME license or copyright; see http://www.asme.org/terms/Terms_Use.cfm

parallel staged combustor was tested with a pressure drop of 4½ percent. The NOx emissions levels shown in Fig. 14 were close to the program goals at base load conditions with ERBS fuel (exceeded goal by 12 percent) and residual fuel (exceeded goal by two percent) but were 37 percent above the goal with SRC-II fuel. The measured NOx levels with ERBS and residual fuel were comparable to those of the series-staged combustor at this same combustor pressure drop level. Good mixing of the fuel and air is very important to avoid local rich regions. Therefore, it is likely that this combustor concept would respond to pressure drop increases and swirl cup changes as the series-staged combustor did. Therefore, this concept should also have the potential for very low NOx levels with fuels having moderate levels of fuel-bound nitrogen.

It may be noted that the NOx emissions for Concept 6 were lower at 4½ percent pressure drop than for Concept 4 at 5½ percent pressure drop with SRC-II fuel. This NOx level represents an unexpectedly low level of conversion of fuel-bound nitrogen for a lean burning combustor. NOx levels were also low with ERBS fuel doped with pyridine to one percent fuel nitrogen as shown in Fig. 15. The conversion rate for the doped fuel was approximately 30 percent. The low fuel bound nitrogen conversion rate for this combustor is not fully understood at this stage of testing. If additional testing confirms initial yield estimates, this concept would have the potential for acceptable NOx levels with somewhat higher levels of fuel nitrogen than Concept 4.

Figure 16 presents smoke data for Concept 6. At base load conditions, smoke level was very low even with the residual fuel. Although smoke data was not taken at the transition point (pilot only), it is suspected that the smoke level would be above the program limits, and that some development would be required.

The peak liner temperatures for Concept 6 were approximately 700 K above the inlet temperature. The maximum measured temperatures were located in the main stage liner wall. The increase in liner temperature relative to Concept 4 is attributed to the more confined main stage dome and consequent close proximity of the combustion process to the liner walls. The liner temperature levels do not present a significant problem. However, additional cooling would be required for high pressure ratio engines or regenerative systems with combustor inlet temperatures in excess of 700 K.

The measured pattern factor and temperature profiles were excellent for this configuration. The pattern factor was less than the goal of 0.20 with all fuels tested. Carbon deposits were very light and occurred only in the swirl cup region. Testing duration was approximately 20 hr with ten of these conducted with residual fuel so that the carbon deposits had probably reached a stabilized thickness.

Conclusions

A lean-lean combustor (Concept 4, Series-Staged) has been developed which has the potential for achieving ultra-low NOx emissions (one-half NSPS limits) with petroleum distillate fuel, and meeting emissions goals with petroleum residual fuel or other fuels containing up to 0.25 weight percent fuel nitrogen. CO, smoke and combustion efficiency met program goals except at low loads and at the transition from pilot to dual stage operation. Pressure drop, metal temperature and exhause profile goals were also met. This combustor does not have potential for meeting the NOx emission goals with nitrogen contents much in excess of 0.25 weight percent because of high fuel nitrogen conversion to NOx.

The rich-lean combustors tested show the potential for achieving low yield required to obtain low NOx emissions which meet the NSPS standard with fuels containing up to one percent nitrogen. Although NOx emissions were higher than program goals, NOx was found to decrease rapidly with increased rich-stage equivalence ratio. Smoke emissions were low and appear to provide adequate margin to increase the equivalence ratio while meeting smoke limits. CO, pressure drop and pattern factor limits have been met and acceptable metal temperatures were achieved.

Future Work

Screening tests will continue for rich-lean combustors 1 and 2 with the improvements already identified, and will be completed for rich-lean combustor 3 and lean-lean combustor 5. Based on these results, the combustor offering highest potential will be selected and developed towards program emissions and performance goals. Tests will also be conducted with blends of the three program fuels to assess fuel matrix effects on emissions and to assess the tradeoffs between combustor effects and fuel processing. A conceptual design will be completed for the full-scale combustor to be developed to engine prototype level in Phase II of this three-phase program. The design will incorporate the aerodynamic features of the test combustor which has been developed to meet program goals in this phase of the Low NOx program, and will include air and/or fuel staging to provide required engine turndown capability.

Hardware for catalytic combustor Concept 7 will be fabricated and combustor tests completed.

Acknowledgment

The work described in this paper is part of the DOE/LeRC Advanced Conversion Technology Project (ACT). The program is a multiple contract effort with funding provided by the Department of Energy, and technical program management provided by NASA LeRC. The DOE program manager is Mr. Warren Bunker of the Heat Engines and Heat Recovery Division of the Office of Coal Utilization.

The authors wish to acknowledge the efforts of many individuals who have contributed to this work. Particular mention should go to J. Taylor and the staff of the General Electric Aircraft Engine Group who were responsible for combustor design, fabrication and testing, and to M. Davi, R. Symonds and B. Gerhold of General Electric's Gas Turbine Division who contributed strongly to the design, testing and evaluation of all data.

Downloaded 01 Jun 2010 to 171.66.16.62. Redistribution subject to ASME license or copyright; see http://www.asme.org/terms/Terms_Use.cfm

A Quasi-Three-Dimensional Blade Surface Boundary Layer Analysis for Rotating Blade Rows

W. T. Thompkins, Jr.
Assistant Professor.

W. J. Usab, Jr.
Research Assistant.

Department of Aeronautics and Astronautics,
Massachusetts Institute of Technology,
Cambridge, Mass. 02139

A quasi-three-dimensional, finite difference boundary layer analysis for rotating blade rows has been developed which uses pressure distribution and streamline position data from a three-dimensional Euler equation solver. This analysis uses as coordinate lines the blade normal vector, the local inviscid streamline direction and a crossflow coordinate line perpendicular to both normal and streamline coordinate lines. The equations solved may be determined either by assuming the crossflow velocity to be small or that its variation in the crossflow direction is small. Thus the analysis would not apply to a region where the boundary layer character changes rapidly such as a corner but could be expected to provide good results away from hub or tip casing boundary layers. Modified versions of Keller's box scheme are used to solve the streamwise and crossflow momentum equations as well as the energy equation. Results are presented for a high-tip speed, low aspect ratio rotor designed by NASA Lewis Research Center which show that the three-dimensional boundary layer separates significantly sooner and has a much larger influence on rotor performance than would be expected from a two-dimensional analysis.

Introduction

In recent years there has been a growing effort to predict and improve transonic axial compressor performance. A key element in this effort is a requirement for increased predictive capability for blade profile boundary layer losses and separation points. Designers have attempted to use standard two-dimensional boundary layer calculations, based either on integral methods or finite difference methods, to characterize the flows; but the radial variation of rotor blade row total pressure loss seems only loosely related to this body of boundary layer theory. In order to predict actual boundary layer development and losses for practical machines, designers are forced to rely heavily on experimental data correlations.

It has often been speculated that the poor performance of two-dimensional boundary layer predictions is due to various three-dimensional effects. In fact transonic compressor rotor blades do have large radial twist, low aspect ratios and large Coriolis forces within the boundary layer. These factors should cause large three-dimensional variations within the blade profile boundary layer, but the overall impact on blade losses and separation has been difficult to assess. Available analytical solutions are limited to laminar incompressible flow with only the simplest of blade geometries. The work of Fogary [1] and Tan [2] for helicopter blades and Miyake [3] and Horlock [4] for helical blades are notable. These solutions imply that large, radial velocities, 15 percent to 30 percent of the inviscid edge velocity, may be induced by blade row rotation. These large radial velocities are confined to a thin layer near the surface, and their integrated contribution to blade total pressure losses or their effect on separation points seems small. However, since these solutions neglect the possibility of turbulent flow, consider only constant or zero streamwise pressure gradients and consider only the simplest blade geometries; their relevance to actual compressor flow fields is questionable.

Many axial flow compressor stages have been observed to have much higher total pressure losses near the tip casing than can be explained on the basis of two-dimensional boundary layer calculations [see Kerrebrock [5]]. It seems natural to propose that radial velocities induced by blade row rotation are a mechanism to transport low momentum fluid generated on inboard blade sections to the outer tip sections in spite of the rather negative results from previous work. Such a loss migration rather than loss generation mechanism would overcome some difficulties in explaining anomalous tip region losses since it requires no large increase in local loss generation in order to explain observed experimental results. Past boundary layer calculation schemes are inadequate to establish or disprove the strength of this loss migration mechanism for practical geometries.

Efficient full three-dimensional turbulent boundary layer calculations are now possible for external wing calculations [see Cebeci, Kaups and Ramecy [6]] and direct extension of one of these schemes to blade profile boundary layers would be valuable. Unfortunately, although the inviscid flow solution may be computed (Thompkins [7]), the boundary layer solution schemes would require as input a complete definition of the boundary layer at the hub and tip section of

Contributed by the Gas Turbine Division and presented at the International Gas Turbine Conference and Products Show, Houston, Texas, March 9-12, 1981 of THE AMERICAN SOCIETY OF MECHANICAL ENGINEERS. Manuscript received at ASME Headquarters December 15, 1980. Paper No. 81-GT-126.

Copyright © 1982 by ASME

Downloaded 01 Jun 2010 to 171.66.16.62. Redistribution subject to ASME license or copyright; see http://www.asme.org/terms/Terms_Use.cfm

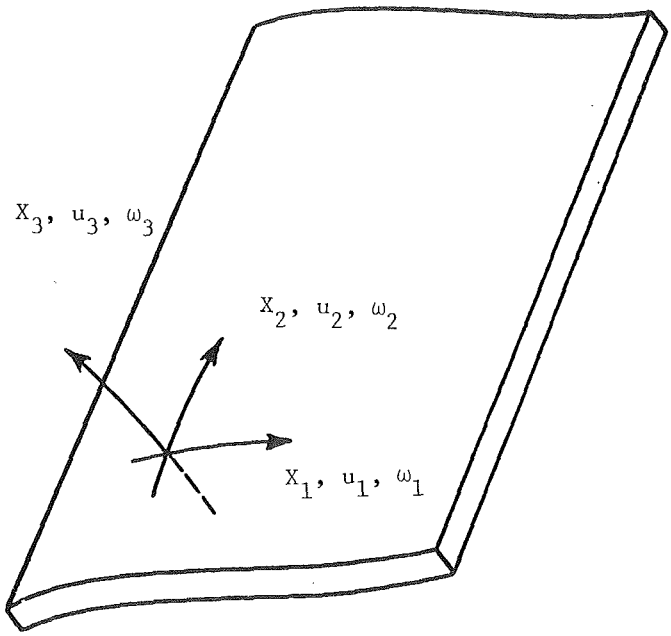

Fig. 1 Orthogonal curvilinear coordinate systems

the blade. This information is not available even in an approximate form. Without these initial data planes any three-dimensional calculation would be of questionable value. In light of the need for a better understanding of three-dimensional blade boundary layers and the difficulty of implementing a full three-dimensional calculation, a quasi-three-dimensional approximation is developed. This calculation includes the effect of nonzero pressure gradients, turbulent flow and blade twist but includes only a simple coupling between streamlines. The resulting set of equations is solved using Keller's Box Scheme [8]. The solution scheme is checked against available incompressible flow solutions and then applied to a NASA Low Aspect Ratio transonic compressor stage for which extensive experimental and computational data are available (see references [9,10]). These results are then used to assess the probable importance of three-dimensional boundary prediction and the possible role of loss migration in determining performance for this stage.

Analysis

Three-Dimensional Boundary Layer Equations. The blade profile boundary layer is analyzed from the framework of an orthogonal, curvilinear coordinate system rotating with the blade row as illustrated in Fig. 1. In this coordinate system, the mean flow is considered to be steady. The three-dimensional compressible, laminar boundary layer equations are expressed by Mager [11], and the three-dimensional compressible, turbulent boundary layer equations in nonrotating reference frame are presented in Cebeci [6] by including the Reynolds stress terms.

As discussed in Mager [11], the coriolis accelerations create a pressure gradient normal to the blade surface which is of $\vartheta(1)$ but, even though this is larger than in usual boundary layer calculations, the total change in pressure across the boundary layer is negligible if the boundary layer thickness is small. This implies the assumption of zero pressure gradient across the boundary layer is still valid. In addition it will be assumed that the coordinate line normal to the blade, X_3 in Fig. 1, is locally straight, which implies that the scale length, h_3, is identically 1. While this approximation is not strictly accurate, it also seems adequate for "thin" boundary layers.

With the addition of the Reynolds stress terms, the equations to be solved in the rotating frame are:

Continuity

$$\frac{\partial}{\partial X_1}(\rho u_1 h_2)+\frac{\partial}{\partial X_2}(\rho u_2 h_1)+\frac{\partial}{\partial X_3}(\rho u_3 h_1 h_2)=0 \tag{1}$$

X_1 Momentum Equation

$$\frac{\rho u_1}{h_1}\frac{\partial u_1}{\partial X_1}+\frac{\rho u_2}{h_2}\frac{\partial u_1}{\partial X_2}+\rho u_3\frac{\partial u_1}{\partial X_3}+\rho u_2\left[\frac{u_1}{h_1 h_2}\frac{\partial h_1}{\partial X_2}-\frac{u_2}{h_2 h_1}\frac{\partial h_2}{\partial X_1}\right]-2\rho\omega_3 u_2-\frac{\rho\omega^2}{h_1}R\frac{\partial R}{\partial X_1}=-\frac{1}{h_1}\frac{\partial P}{\partial X_1}+\frac{\partial}{\partial X_3}\left[\mu\frac{\partial u_1}{\partial X_3}-\rho\overline{u_1' u_3'}\right] \tag{2}$$

X_2 Momentum Equation

$$\frac{\rho u_1}{h_1}\frac{\partial u_2}{\partial X_1}+\frac{\rho u_2}{h_2}\frac{\partial u_2}{\partial X_2}+\rho u_3\frac{\partial u_3}{\partial X_3}+\rho u_1\left[\frac{u_2}{h_1 h_2}\frac{\partial h_2}{\partial X_1}-\frac{u_1}{h_1 h_2}\frac{\partial h_1}{\partial X_2}\right]+2\rho\omega_3 u_1-\frac{\rho\omega^2}{h_2}R\frac{\partial R}{\partial X_2}=-\frac{1}{h_2}\frac{\partial P}{\partial X_2}+\frac{\partial}{\partial X_3}\left[\mu\frac{\partial u_2}{\partial X_3}-\rho\overline{u_2' u_3'}\right] \tag{3}$$

X_3 Momentum Equation

$$\frac{\partial P}{\partial X_3}=0 \tag{4}$$

Energy Equation

$$\frac{\rho u_1}{h_1}\frac{\partial I}{\partial X_1}+\frac{\rho u_2}{h_2}\frac{\partial I}{\partial X_2}+\rho u_3\frac{\partial I}{\partial X_3}=\frac{\partial}{\partial X_3}\left[\frac{\mu}{P_r}\frac{\partial H}{\partial X_3}+\mu\left(1-\frac{1}{P_r}\right)\left(u_1\frac{\partial u_1}{\partial X_3}+u_2\frac{\partial u_2}{\partial X_3}\right)-\rho\overline{H' u_3'}\right] \tag{5}$$

where

I = $H - 1/2(\omega^2 R^2)$ is the rothalpy
ω = blade row rotation speed
ωi = components of angular velocity
R = perpendicular distance from the axis of rotation
H = stagnation enthalpy $\left(C_p T+\frac{1}{2}(u_1^2+u_2^2)\right)$

with the velocity component normal to the surface neglected.

It is convenient at this point to express the Reynolds stress and turbulent energy transport terms by Boussinesq's eddy viscosity concept in the following form:

$$-\rho\overline{u_1' u_3'}=\rho\epsilon_m\frac{\partial u_1}{\partial X_3} \tag{6}$$

$$-\rho\overline{u_2' u_3'}=\rho\epsilon_m\frac{\partial u_2}{\partial X_3} \tag{7}$$

$$-\rho\overline{H' u_3'}=\rho\epsilon_H\frac{\partial H}{\partial X_3}=\rho\left(\frac{\epsilon_m}{P_{r_t}}\right)\frac{\partial H}{\partial X_3} \tag{8}$$

As will be described in a later section, ϵ_m is the eddy viscosity which is to be modeled.

Downloaded 01 Jun 2010 to 171.66.16.62. Redistribution subject to ASME license or copyright; see http://www.asme.org/terms/Terms_Use.cfm

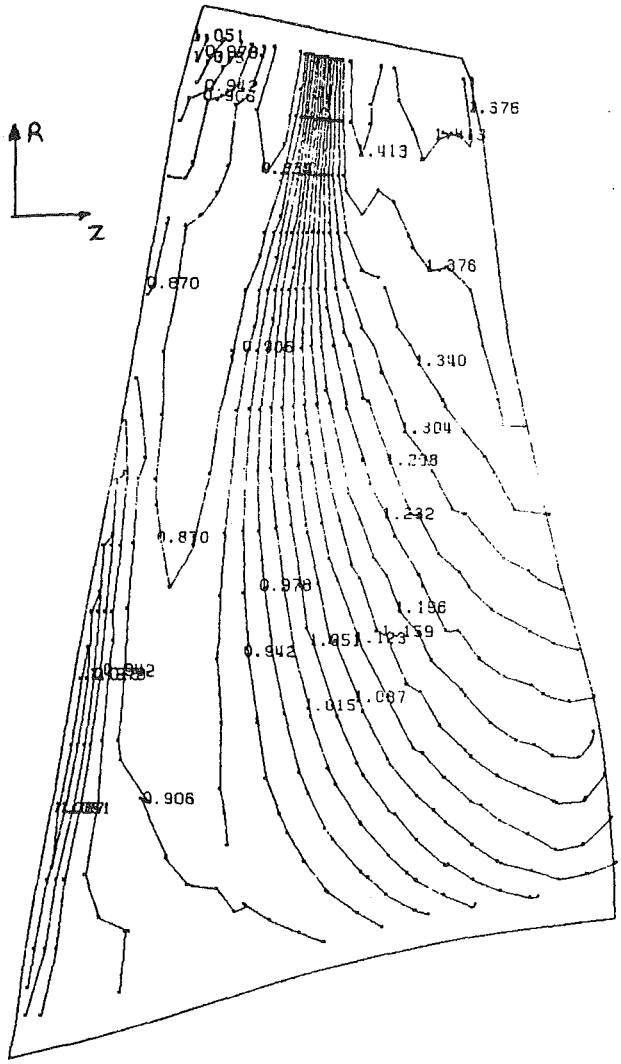

Fig. 2 NASA low-aspect-ratio rotor inviscid pressure contours, pressure surface

The boundary conditions that apply to this set of equations are no-slip at the wall ($X_3 = 0$) and prescribed temperature or temperature gradient. At the outer edge of the boundary layer the velocity components and temperature take on the inviscid external flow values.

Inviscid Flow Variables. Flow variables required at the outer edge of the boundary layer are the pressure, density and streamwise velocity. For the test solutions to be described, analytical pressure distributions are used. For the transonic compressor blade case, flow quantities were determined from numerical, three-dimensional, Euler equation solutions. The computer codes used are described in references [7, 12]. Figure 2 shows typical inviscid results for the low aspect ratio rotor designed at NASA Lewis Research Center by Urasek [9]. This figure shows the pressure distribution on the blade pressure surface at the rotor design point mass flow rate.

Intrinsic Coordinate System. The first step in specializing the boundary layer equations for transonic compressor blades is in the choice of grid geometry on the blade surface. An intrinsic coordinate system was chosen since it greatly simplifies the outer flow boundary conditions. This system uses the inviscid streamlines as one family of coordinate lines, lines of constant X_2. The other coordinate family, lines of constant X_1, are then orthogonal to the inviscid streamlines. The outer

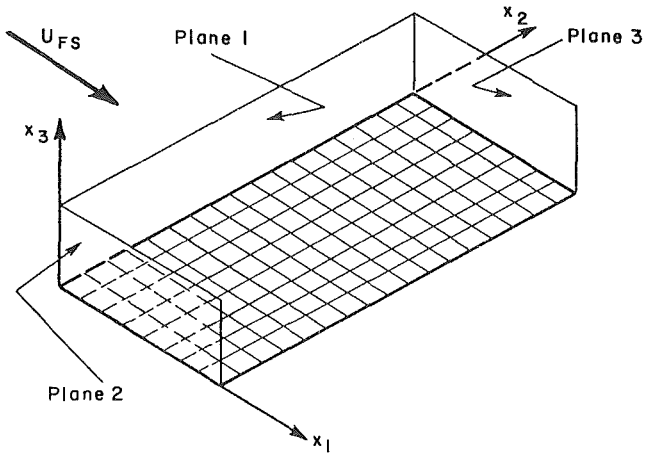

Fig. 3 Simple flat plate blade showing three required initial planes of data

flow boundary conditions and pressure gradient expressions are simplified since the crossflow velocity component is identically zero over the entire inviscid flow field.

Quasi-Three-Dimensional Flow Approximation. With little effort it can be shown that the full three-dimensional boundary layer equations as given in the previous section are of parabolic class type but, as Ketchen, et al. [13] point out, it may be more appropriate to say the equations have a dominant parabolic property with a secondary property hyperbolic in nature. To illustrate the zone of dependence requirements, consider the simplified case of a flat plate blade with a computational grid shown in Fig. 3. Assuming the boundary conditions are known, the u_1 velocity is always positive, and the crossflow velocity u_2 is also positive; they must be defined on two orthogonal initial planes, in order that the flow field be completely defined. Plane 1 along the leading edge of the blade can be generated through a stagnation line solution, a limiting form of the full three-dimensional boundary layer equations, but data on plane 2 at the hub section must come from some other source. Once the initial conditions are defined, standard marching schemes can be used to solve for the boundary layer over the entire surface. If the cross flow velocity u_2 should become negative at some point on the blade, data on yet a third initial plane, plane 3, would be required.

For a complete solution over a general blade with the possibility of negative crossflows, at least three initial planes of data would then be required. Plane 1 is easily found from stagnation line solutions, but the problem of generating the other two planes at hub and tip sections is extremely difficult. In these regions very little is known either experimentally or through numerical solutions. Attempting to provide a full three-dimensional calculation without correct initial conditions in these regions would be of questionable value. The lack of initial data for three-dimensional calculations leads us to look for further simplifications specific to transonic compressor blades which will allow approximate prediction of three-dimensional boundary layers.

The flow equations can be simplified by considering the actual blade geometry of a common transonic compressor blade. Typical blade sections at hub, midspan, and tip are shown in Fig. 4 from which the following points can be seen. The transonic blade shown has a very sharp leading edge. This will later lead to assumptions on the type of stagnation line solution. The sections each have very large radii of curvature, both suction and pressure side. Further Fig. 9 shows typical inviscid streamlines over the surface of the blade. Again the radius of curvature of the streamlines is very large. Since the

Downloaded 01 Jun 2010 to 171.66.16.62. Redistribution subject to ASME license or copyright; see http://www.asme.org/terms/Terms_Use.cfm

total radius of curvature of streamlines on both the pressure and suction sides of this blade are very large, the assumption of no curvature of streamlines ($h_1 = h_2 = 1$) seems to be valid. This statement is nearly correct except that, as will be shown later, the terms containing the curvature of coordinate lines

$$K_1 = \frac{1}{h_1 h_2} \frac{\partial h_1}{\partial x_2} \tag{9}$$

$$K_2 = \frac{1}{h_1 h_2} \frac{\partial h_2}{\partial x_1} \tag{10}$$

may be important in obtaining correct solutions since the acceleration represented by these terms may not be small. It is then important to retain these terms while taking $h_1 = h_2$ approximately 1 elsewhere. This reduces the governing equations to the following:

Continuity Equation

$$\frac{\partial}{\partial X_1}(\rho u_1) + \frac{\partial}{\partial X_2}(\rho u_2) + \frac{\partial}{\partial X_3}(\rho u_3) = 0 \tag{11}$$

X_1 Momentum Equation or Streamwise Equation

$$\rho u_1 \frac{\partial u_1}{\partial X_1} + \rho u_2 \frac{\partial u_1}{\partial X_2} + \rho u_3 \frac{\partial u_1}{\partial X_3} + \rho u_2 (u_1 K_1 - u_2 K_2) - 2\rho\omega_3 u_2 - \rho\omega^2 R \frac{\partial R}{\partial X_1} = \rho_e u_{1e} \frac{\partial u_{1e}}{\partial X_1} - \rho_e \omega^2 R \frac{\partial R}{\partial X_1} + \frac{\partial}{\partial X_3}\left[\mu\left(1 + \frac{\rho\epsilon_m}{\mu}\right)\frac{\partial u_1}{\partial X_3}\right] \tag{12}$$

X_2 Momentum Equation or Crossflow Equation

$$\rho u_1 \frac{\partial u_2}{\partial X_1} + \rho u_2 \frac{\partial u_2}{\partial X_2} + \rho u_3 \frac{\partial u_2}{\partial X_3} + \rho u_1 [u_2 K_2 - u_1 K_1] + 2\rho\omega_3 u_1 - \rho\omega^2 R \frac{\partial R}{\partial X_2} = -\rho_e u_{1e}^2 K_1 + 2\rho_e \omega_3 u_{1e} - \rho_e \omega^2 R \frac{\partial R}{\partial X_2} + \frac{\partial}{\partial X_3}\left[\mu\left(1 + \frac{\rho\epsilon_m}{\mu}\right)\frac{\partial u_2}{\partial X_3}\right] \tag{13}$$

Energy Equation

$$\rho u_1 \frac{\partial H}{\partial X_1} + \rho u_2 \frac{\partial H}{\partial X_2} + \rho u_3 \frac{\partial H}{\partial X_3} - \rho\omega^2 R\left[u_1 \frac{\partial R}{\partial X_1} + u_2 \frac{\partial R}{\partial X_2} + u_3 \frac{\partial R}{\partial X_3}\right] = \frac{\partial}{\partial X_3}\left[\frac{\mu}{P_r}\left(1 + \frac{P_r}{P_{r_t}}\frac{\rho\epsilon_m}{\mu}\right)\frac{\partial H}{\partial X_3} + \mu\left(1 - \frac{1}{P_r}\right)\left(u_1 \frac{\partial u_1}{\partial X_3} + u_2 \frac{\partial u_2}{\partial X_3}\right)\right] \tag{14}$$

NOTE: Subscript (e) refers to inviscid edge values.

It is convenient at this point to call the X_1 momentum equation the streamwise momentum equation, and the X_2 momentum equation the crossflow equation. In essence the problem has been reduced to the application of an inviscid velocity distribution and an associated coriolis force field to a flat plate blade. The solution of these equations is then the boundary layer solution along inviscid streamlines of the actual blade.

Although consideration of the inviscid flow field, blade geometry, and coordinate system has reduced the equations to a much simpler form, the resulting equations still remain a highly coupled system. It will now be assumed that gradients of all flow properties in the X_2 direction are zero, with the exception of the coriolis force terms. This reduces the coupling of the X_2 momentum equation with the other equations. This assumption is valid at least in a first approximation over a majority of the blade, and provides insight to the characteristic of the boundary layer three dimensionality without having to deal with the complications of a full three-dimensional calculation. It must be realized that, although of great value, this approximation is not as accurate as the standard boundary layer approximations used to this point and cannot be strictly accurate near a separation point.

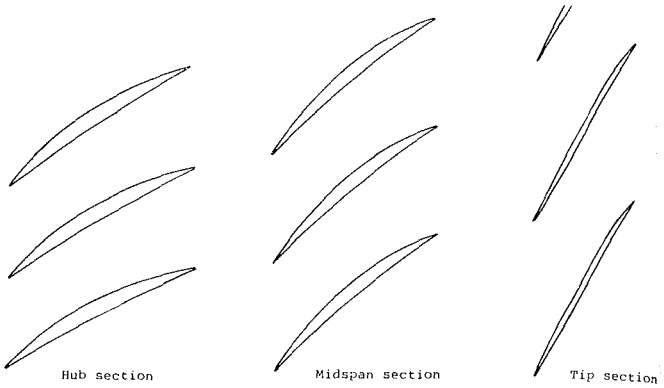

Fig. 4 Typical blade sections of NASA low-aspect-ratio rotor

Finally, considering the curvature terms (terms containing K_1 or K_2 defined by equations (9) and (10)), the term containing K_2 is usually of smaller order than that containing K_1 and is therefore negligible. K_2 represents the curvature of the coordinate lines normal to the inviscid streamlines and will be significant only if the streamlines are not locally parallel. Referring back to Fig. 9 it is apparent that the streamlines are nearly locally parallel, which would imply $K_2 = 0$.

For generality no assumptions about the relative ordering of the coriolis acceleration terms will be made since it requires no additional effort to include them and those terms that are higher order will not affect the calculation. After dropping the terms mentioned above, the final equation set results:

$$\frac{\partial}{\partial X_1}(\rho u_1) + \frac{\partial}{\partial X_3}(\rho u_3) = 0 \tag{15}$$

Streamwise Momentum Equation

$$\rho u_1 \frac{\partial u_1}{\partial X_1} + \rho u_3 \frac{\partial u_1}{\partial X_3} + \rho u_1 u_2 K_1 - 2\rho\omega_3 u_2 - \rho\omega^2 R \frac{\partial R}{\partial X_1} = \rho_e u_{1e} \frac{\partial u_{1e}}{\partial X_1} - \rho_e \omega^2 R \frac{\partial R}{\partial X_1} + \frac{\partial}{\partial X_3}\left[\mu\left(1 + \frac{\rho\epsilon_m}{\mu}\frac{\partial u_1}{\partial X_3}\right)\right] \tag{16}$$

Energy Equation

$$\rho u_1 \frac{\partial H}{\partial X_1} + \rho u_3 \frac{\partial H}{\partial X_3} - \rho\omega^2 R\left[u_1 \frac{\partial R}{\partial X_1} + u_2 \frac{\partial R}{\partial X_2} + u_3 \frac{\partial R}{\partial X_3}\right] = \frac{\partial}{\partial X_3}\left[\frac{\mu}{P_r}\left(1 + \frac{P_r}{P_{r_t}}\frac{\rho\epsilon_m}{\mu}\right)\frac{\partial H}{\partial X_3} + \mu\left(1 - \frac{1}{P_r}\right)\left(u_1 \frac{\partial u_1}{\partial X_3}\right)\right] \tag{17}$$

Crossflow Momentum Equation

$$\rho u_1 \frac{\partial u_2}{\partial X_1} + \rho u_3 \frac{\partial u_2}{\partial X_3} - \rho u_1^2 K_1 + 2\rho\omega_3 u_1 - \rho\omega^2 R \frac{\partial R}{\partial X_2} = -\rho_e u_{1e}^2 K_1 + 2\rho_e \omega_3 u_{1e} - \rho_e \omega^2 R \frac{\partial R}{\partial X_2} + \frac{\partial}{\partial X_3}\left|\mu\left(1 + \frac{\rho\epsilon_m}{\mu}\right)\frac{\partial u_2}{\partial X_3}\right| \tag{18}$$

Downloaded 01 Jun 2010 to 171.66.16.62. Redistribution subject to ASME license or copyright; see http://www.asme.org/terms/Terms_Use.cfm

The most important difference between the three-dimensional and the quasi-three dimensional boundary layer equations is the elimination of the term $(\partial/\partial X_2)\ (\rho u_2)$ from the continuity equation. This term is eliminated through the assumption of zero gradient in the X_2 direction and would be strictly true if the pressure gradient in the X_2 direction were everywhere small or zero as in a yawed cylinder problem. The physical phenomena neglected is a buildup of boundary layer thickness caused by a gradient in cross-flow velocity. As can be seen in the example solutions, this term is nearly always positive, and its inclusion in the continuity equation would tend to accelerate boundary layer growth. The neglect of this term is felt to produce a flow solution in which the effect of crossflow velocity is minimized. Examination of the predicted solutions indicates that this effect is probably small except near separation.

Turbulence Modeling. Turbulence modeling can be very complex and at this point in time is often looked upon as a kind of "Black Art" in the sense that there is very little theoretical basis for the choice of one model over another except that a model does or does not fit experimental data. Since the main point of this work is development of an efficient scheme to predict crossflows on compressor blades, no attempt has been made to develop a detailed well tuned turbulence model with complex determination of transition.

The model used in all turbulent calculations is a simple two layer mixing length model described in Cebeci [6], which has been applied to many three-dimensional turbulent calculations such as swept infinite cylinders and wings. In the form presented here the outer region model has been modified as discussed in Mellor [14].

$$(\epsilon_m)_i = L^2\left[\left(\frac{\partial u_1}{\partial X_3}\right)^2 + \left(\frac{\partial u_2}{\partial X_3}\right)^2\right]^{1/2},$$

$$L = 0.4\ X_3\left[1-\exp\left(\frac{-X_3}{A}\right)\right],\quad A = 26\frac{\nu}{u_\tau}\left(\frac{\rho}{\rho_w}\right)^{1/2},$$

$$u_\tau = \left(\frac{\tau_{tw}}{\rho_w}\right)^{1/2},\quad \tau_{wt} = \mu_w\left[\left(\frac{\partial u_1}{\partial X_3}\right)_w^2 + \left(\frac{\partial u_2}{\partial X_3}\right)_w^2\right]^{1/2} \quad (19)$$

Outer Region

$$(\epsilon_m)_o = 0.0168\int_0^\infty X_3\left[\left(\frac{\partial u_1}{\partial X_3}\right)^2 + \left(\frac{\partial u_2}{\partial X_3}\right)^2\right]^{1/2} dX_3 \quad (20)$$

The boundary between the inner and outer regions is at the point where $(\epsilon_m)_i = (\epsilon_m)_o$.

For some comparison calculations, a two-dimensional turbulence model was required and the model selected is reported by Cebeci and Smith [16]:

Inner Region

$$(\xi_m)_i = L^2[\partial u_1/\partial X_3],\quad L = 0.4X_3[1-\exp(-X_3/A)]$$

$$A = 26\frac{\nu}{N}\left(\frac{\tau_w}{\rho_w}\right)^{-1/2}\left(\frac{\rho}{\rho_w}\right)^{1/2},$$

$$N = [1-11.8(\mu_w/\mu_s)\,(\rho/\rho_w)^2 P^+]^{1/2}$$

$$P^+ = (\nu_e u_{1e}/u_\tau{}^3)(du_{1e}/dX_1),\quad u_\tau = (\tau_w/\rho_w)^{1/2} \quad (21)$$

Outer Region

$$(\epsilon_m)_o = 0.0168\left|\int_o^\infty (u_{1e}-u_1)dX_3\right| \quad (22)$$

The boundary between the inner and outer regions is at the point where

$$(\epsilon_m)_i = (\epsilon_m)_o$$

Numerical Solution of the Quasi-Three Dimensional Equation. Before solving the governing equations it is convenient to remove the singularity at $X_1 = 0$ and scale the X_1 and X_3 coordinates by introducing the Levy-Lees transformation as described in Hayes and Probstein [15].

$$d\xi = \rho_e\mu_e u_{1e}dX_1 \quad d\eta = \left[\frac{\rho u_{1e}}{(2\xi)^{1/2}}\right]dX_3 \quad (23)$$

This coordinate stretching not only removes the leading edge singularity, allowing stagnation point calculations, but also removes the large variation in the boundary layer thickness. For laminar calculations the boundary layer thickness and profile remain essentially constant for similar flows and vary only slightly for nonsimilar flows. Even the extreme turbulent boundary layer growth is substantially reduced, although not removed. This scaling then speeds convergence and reduces the need for addition of grid points to capture the boundary layer growth as the computation proceeds.

The continuity equation (15) is satisfied identically through introduction of the streamfunction ψ, where

$$\frac{\partial\psi}{\partial X_3} = \rho U_1 \quad -\frac{\partial\psi}{\partial X_1} = \rho U_3 \quad (24)$$

ψ may be written in terms of a nondimensional streamfunction f, a function of the new coordinates ξ, η.

$$\psi(X_1, X_2) = (2\xi)^{1/2} f(\xi,\eta) \quad (25)$$

In terms of this streamfunction the velocities u_1 and u_3 are:

$$u_1 = u_{1e}f' \quad (26)$$

$$u_3 = \frac{-\rho_e\mu_e u_{1e}}{\rho}(2\xi)^{1/2}\left[\frac{f}{2\xi} + \frac{\partial f}{\partial\xi} + f'\left(\frac{\partial\eta}{\partial\xi}\right)_{X_3}\right] \quad (27)$$

Introducing these transformations into the streamwise equation set, equations (16), (17), (18), yields the following:

Streamwise Equation Set

Streamwise Momentum

$$[bf'']' + ff'' + \beta[c-(f')^2] - D_1 f' w = 2\xi\left[f'\frac{\partial f'}{\partial\xi} - f''\frac{\partial f}{\partial\xi}\right] + E_1 \quad (28)$$

Energy

$$[a_1 g' + a_2 f' f'']' + fg' - \beta^* f' g = 2\xi\left[f'\frac{\partial g}{\partial\xi} - g'\frac{\partial f}{\partial\xi}\right] + E_2 \quad (29)$$

where

$$f' = \frac{u_1}{u_{1e}} \qquad g = \frac{H}{H_e} \qquad w = \frac{u_2}{u_{1e}}$$

$$E_1 = -D_2 w + D_3(1-c) \qquad E_2 = D_5 f' + D_6 w$$

$$b = C(1+\epsilon_m{}^+) \qquad C = \frac{\rho\mu}{\rho_e\mu_e} \qquad c = \frac{\rho_e}{\rho}$$

$$\beta = \frac{2\xi}{u_{1e}}\frac{\partial u_{1e}}{\partial\xi} \qquad \beta^* = \frac{2\xi}{H_e}\frac{\partial H_e}{\partial\xi} \qquad \epsilon_m{}^+ = \frac{\rho\epsilon_m}{\mu}$$

$$a_1 = C\frac{1}{P_r}\left(1+\epsilon_m{}^+\frac{P_r}{P_{r_t}}\right) \qquad a_2 = C\left(1-\frac{1}{P_r}\right)\frac{u_{1e}{}^2}{H_e}$$

$$D_1 = \frac{2\xi}{\rho_e\mu_e u_{1e}}K_1 \qquad D_2 = \frac{4\xi\omega_3}{\rho_e\mu_e u_{1e}{}^2}$$

$$D_3 = \frac{2\xi\omega^2 R}{\rho_e\mu_e u_{1e}{}^3}\frac{\partial R}{\partial X_1} \qquad D_5 = \frac{2\xi\omega^2 R}{\rho_e\mu_e u_{1e}H_e}\frac{\partial R}{\partial X_1}$$

$$D_6 = \frac{2\xi\omega^2 R}{\rho_e\mu_e u_{1e}H_e}\frac{\partial R}{\partial X_2}$$

Crossflow Equation Set

Crossflow Momentum

Downloaded 01 Jun 2010 to 171.66.16.62. Redistribution subject to ASME license or copyright; see http://www.asme.org/terms/Terms_Use.cfm

$$[bw']' + fw' - \beta f' w = 2\xi\left(f' \frac{\partial w}{\partial \xi} - w' \frac{\partial f}{\partial \xi}\right) + E_3 \qquad (30)$$

where

$$E_3 = D_1[C - (f')^2] + D_2[f - C] + D_4[1 - C]$$

$$D_4 = \frac{2\xi\omega^2 R}{\rho_e \mu_e u_{1e}^3} \frac{\partial R}{\partial X_2}$$

NOTE: Primes denote differentiation with respect to η.

Through the assumption of zero gradient in the crossflow direction, all the strong coupling terms have dropped out, with the exception of the coriolis force terms and curvature terms on which no additional assumptions have been made. As a result the crossflow equation is now only weakly coupled to the continuity-streamwise momentum-energy equation set. The two initial data planes at the hub and tip sections are no longer required for solution of the boundary layer over the compressor blade. Instead it is possible to march independently along each streamline in the following manner.

First an attachment line similarity solution is generated for which the streamwise gradients and the crossflow velocities are zero. Then the combined continuity-streamwise momentum-energy equation set is solved without the coupling term followed by solution of the crossflow equation. Then the term dropped in the first set is inserted and iteration between the two equation sets is repeated until convergence. This is then repeated at each point down the streamline.

The quasi-three dimensional approximation to the full boundary layer equations requires numerical solution of the streamwise equation set, which is in essence a modified form of the standard two-dimensional boundary layer equations. Once u_1, u_3 and H are known, the crossflow equation is simply an ordinary differential equation. The numerical method used here, often called Keller's Box Method, was first developed by Keller and later applied to boundary layer problems by Cebeci and Keller [17, 18]. Keller's Box Method is much faster and more flexible than many other methods that exist. In addition, by proper scaling of the equations, similarity solutions are generated with little effort.

The key to the effectiveness of Keller's Box Scheme is expressing each of the governing equations, as a system of first order equations. This is accomplished by defining new unknown functions as normal or X_3 derivatives of the boundary layer variables. Derivatives which appear in each of the other directions are only first order due to the boundary layer approximations already made. The resulting system can then easily be discretized on an arbitrary rectangular mesh using only first order centered-difference quotients and averages at the midpoint of each rectangle to obtain an $\vartheta(\delta^2)$ accurate finite-difference equation set. The resulting system remains highly nonlinear and implicit, requiring application of Newton's Method coupled with an efficient block-tridiagonal factorization shceme to solve. The complete process produces an efficient unconditionally stable scheme.

Results

Quasi-Three Dimensional Calculation Test Cases. Unfortunately at this time there exists little experimental data or numerical solutions for three-dimensional boundary layers on general rotating blades. This is the direct result of the extreme difficulty of making experimental boundary layer measurements of rotating blades and, since these boundary layers are three-dimensional, the governing equations are so complex that exact solutions are rare.

Nearly exact solutions that exist are for simple, laminar, incompressible boundary layers on zero thickness unloaded blades for which similarity or series type solutions exist. Two of the cases were selected as test problems.

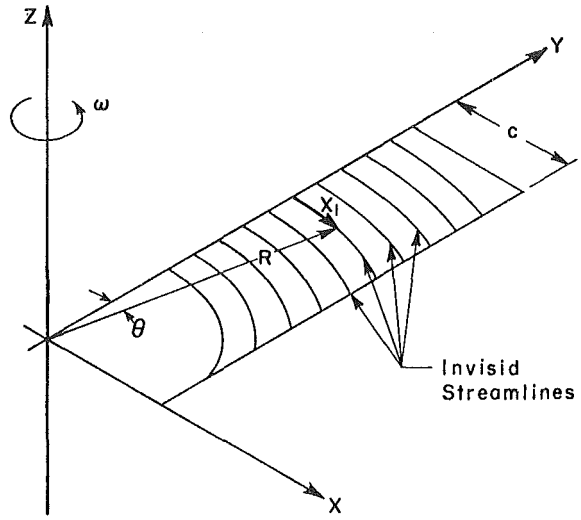

Fig. 5 Flat plate blade

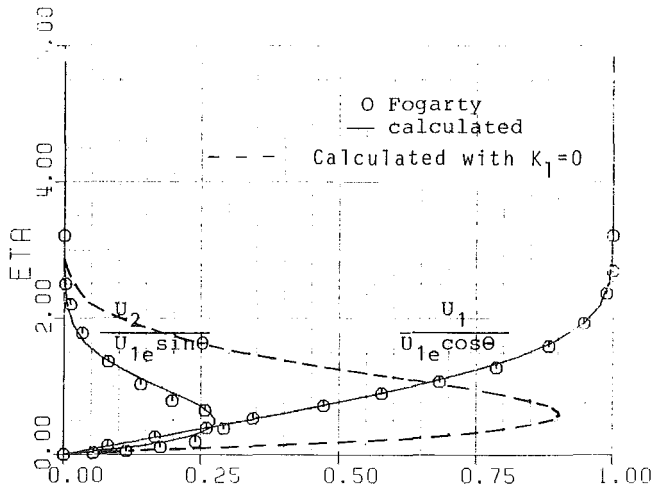

Fig. 6 Comparison of small crossflow solution with Fogarty for flat plate blade $R >> X_1$

The first case is for a rotating flat plate of chord c, as shown in Fig. 5. Fogarty [1] was able to find a similarity-type solution for the small crossflow equations in laminar incompressible form which applied for large R/c stations far out from the hub on the blade. The inviscid flow field for this case in terms of intrinsic coordinate system is

$$u_{1e} = \omega R \qquad u_{2e} = 0 \qquad (31)$$

where the streamlines or lines of constant X_2 are circular arcs of radius R. This case is important since the three-dimensionality of the flow is the result of the centrifugal force due to rotation. Fogarty presented the solution of this flow for the limiting case of $R >> X_1$, or the angle $\theta = X_1/R$ as $\theta \to 0$. This limiting case presented in the similarity form found by Fogarty is compared to the computed small crossflow solution in Fig. 6. ETA is a dimensionless distance from the plate defined as

$$\text{ETA} = X_3\left[\frac{\rho_e u_{1e}}{\mu_e X_1}\right]^{1/2} \qquad (32)$$

the u_1 and u_2 velocities are also scaled as

Downloaded 01 Jun 2010 to 171.66.16.62. Redistribution subject to ASME license or copyright; see http://www.asme.org/terms/Terms_Use.cfm

$$\frac{u_1}{u_{1e}\cos\theta} \quad \text{and} \quad \frac{u_2}{u_{1e}\sin\theta} \tag{33}$$

This case also illustrates the importance of the curvature term containing K_1. Here $K_1 = 1/R$, R being the perpendicular distance from the axis of rotation, would appear to be unimportant for the case $R >> X_1$, but since all the terms in the crossflow momentum equation are $\vartheta(C/R)$ this term is not negligible. This becomes obvious when the term is dropped as also shown in Fig. 6. Without the term the solution is nearly three times what it should be. The effect of this curvature is often important in predicting correct crossflows since, even though the radius of curvature is large, relative to other terms in the crossflow momentum equation, it cannot be dropped.

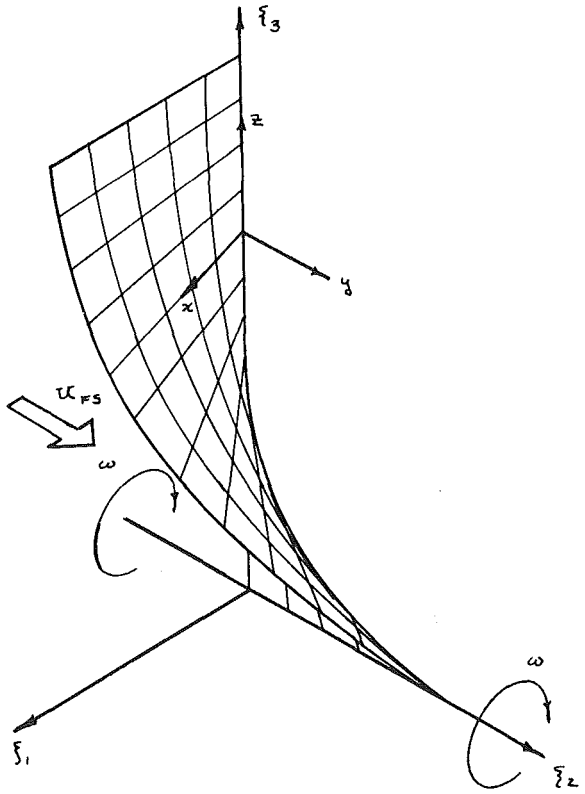

Fig. 7 Helical blade coordinate system

Nonloaded Helical Blade in a Uniform Stream. Miyake and Fujita [3] were able to generate three-dimensional laminar incompressible boundary layer solutions for nonloaded helical blades in a uniform stream as shown in Fig. 7. This case is important since the three-dimensionality of the boundary layer is the result of both centrifugal forces and also the twist of the blades which generate coriolis forces.

The test case is for a uniform upstream velocity U_{FS} with a blade rotating at angular velocity ω. The blade, as shown in Fig. 7, is twisted with the center of twist at the blade leading edge, so the angle of attack becomes zero all along the leading edge. The blade is assumed infinitely long with the effect of the hub and tip casing not taken into account. The inviscid streamlines for this case are the intersection of the blade surface and circular cylinders whose center is the ξ_2 axis as determined by the following equation set:

$$\xi_1 = X\cos\phi \tag{34}$$

$$\xi_2 = X\sin\phi \tag{35}$$

$$\xi_3 = Z \tag{36}$$

$$(\xi_1)^2 + (\xi_3)^2 = R \tag{37}$$

$$\tan\phi = U_{FS}/\omega Z \tag{38}$$

Finally along a given streamline defined by a given R the inviscid velocity is

$$u_{1e} = [U_{FS}{}^2 + (\omega R)^2]^{1/2} \tag{39}$$

Figures 8(*a*) and (*b*) compare streamwise and crossflow boundary layer profiles with those generated by Miyake and Fujita. The profiles are both on the same streamline defined by leading edge angle $\phi_0 = \tan^{-1}(0.2)$, Fig. 8(*a*) for $X_1/R = 0.2$, and Fig. 8(*b*) for $X_1/R = 0.3$ (Recall, X_1 is the distance down the streamline from the leading edge and R is the radius of the streamline.) The computational results prove to be in very good agreement with those computed by Miyake and Fujita.

Transonic Compressor Blade Calculations. Quasi-three dimensional calculations were completed for a low aspect ratio, transonic compressor rotor designed and tested by NASA Lewis Research Center [9]. The inviscid flow was calculated without boundary layer corrections in Thompkins

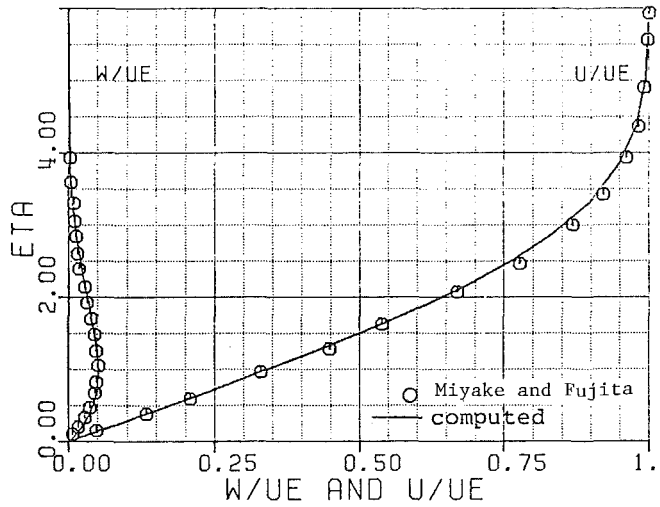

Fig. 8(*a*) Comparison of computed streamwise velocities

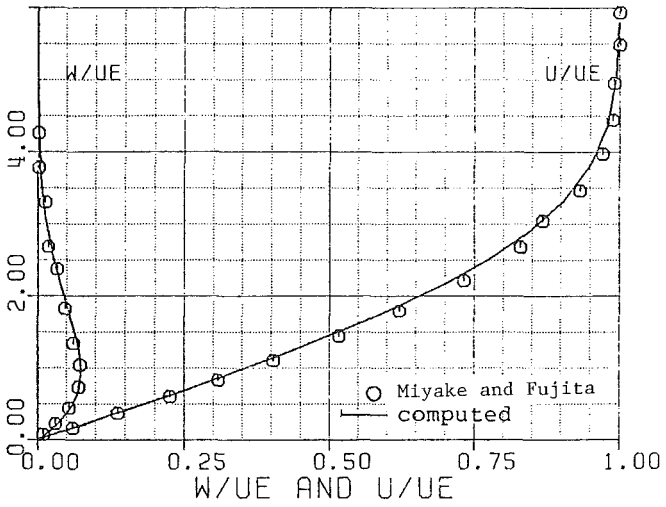

Fig. 8(*b*) Comparison of computed crossflow velocities

Downloaded 01 Jun 2010 to 171.66.16.62. Redistribution subject to ASME license or copyright; see http://www.asme.org/terms/Terms_Use.cfm

[12] and representative pressure distributions were presented in Fig. 2. For the boundary layer calculation it was assumed that the flow would be fully turbulent at the first grid point downstream of the leading edge. In general it was found that while the pressure side boundary layer always remained attached, the suction side boundary layer appeared to separate between an X/C of 0.8 to 0.9 for each of the streamlines. The computed separation line is shown in Fig. 9 and also shown is the direction of the limit streamline just before the separation line. The separation line reported is actually the last calculation station for which converged solutions could be found. Near this line, the boundary layer displacement thickness is increasing rapidly and the skin-friction coefficient is falling rapidly.

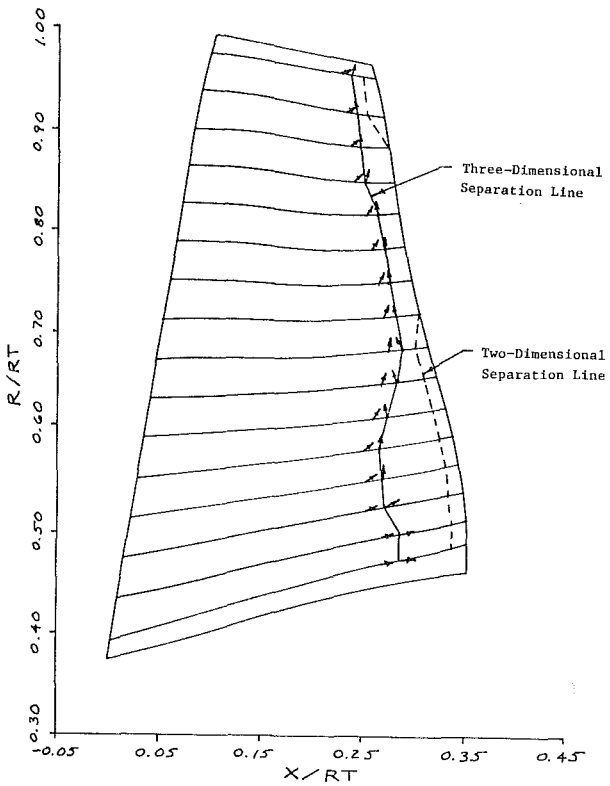

Fig. 9 Separation line and limiting streamline angles for NASA low aspect ratio blade, suction surface

Streamwise velocity profiles for a midspan streamline are shown in Figs. 10 and 11 for the blade pressure and suction surface. The onset of separation is clearly indicated in Fig. 11, and it is interesting to note that a small region of reverse streamwise velocity is actually calculated near the wall. Crossflow velocity profiles for these same streamlines are shown in Figs. 12 and 13. These figures show that both pressure and suction surface boundary layers are far from two-dimensional.

It was attempted to account for the blade boundary layer in the inviscid solution procedure by adding the calculated displacement thickness to the blade geometry and then repeating both the inviscid and boundary layer solutions. This procedure, as might be expected, did not work well and no stable solutions were found using this classical iteration procedure. Viscous-inviscid interaction models are the subject of continuing research and appear necessary to compute even a first order correction to the inviscid solution.

Discussion of Results and Conclusions

The most important goal of this investigation is to determine if a three-dimensional boundary layer analysis is required or useful in predicting transonic compressor performance. A first step in answering this question is to compare the small crossflow separation points and skin friction values to those calculated in a conventional manner. To do this, the small crossflow model was degraded to a two-dimensional scheme. This process sets the crossflow velocity to zero and uses the subset of the three-dimensional turbulence model. The two-dimensional model is that represented by equations (21) and (22). In this calculation, the skin friction coefficient, away from separation, was found to be nearly 30 percent lower than in the quasi-three-dimensional calculation. In addition the pressure side boundary layer remained attached as before, but the suction side boundary layer separated later than the quasi-three-dimensional case. The two-dimensional separation line is shown in Fig. 9. It is not yet possible to demonstrate whether the indicated quasi-three-dimensional separation will involve only a thin layer near the surface as appears likely from Figs. 11 and 13 or a

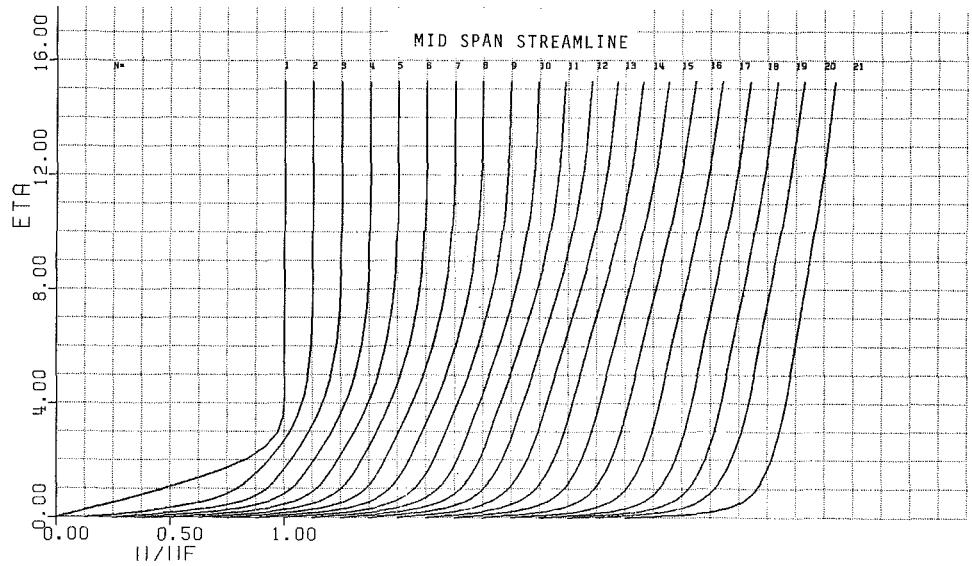

Fig. 10 Streamwise velocity profile development, pressure surface

Downloaded 01 Jun 2010 to 171.66.16.62. Redistribution subject to ASME license or copyright; see http://www.asme.org/terms/Terms_Use.cfm

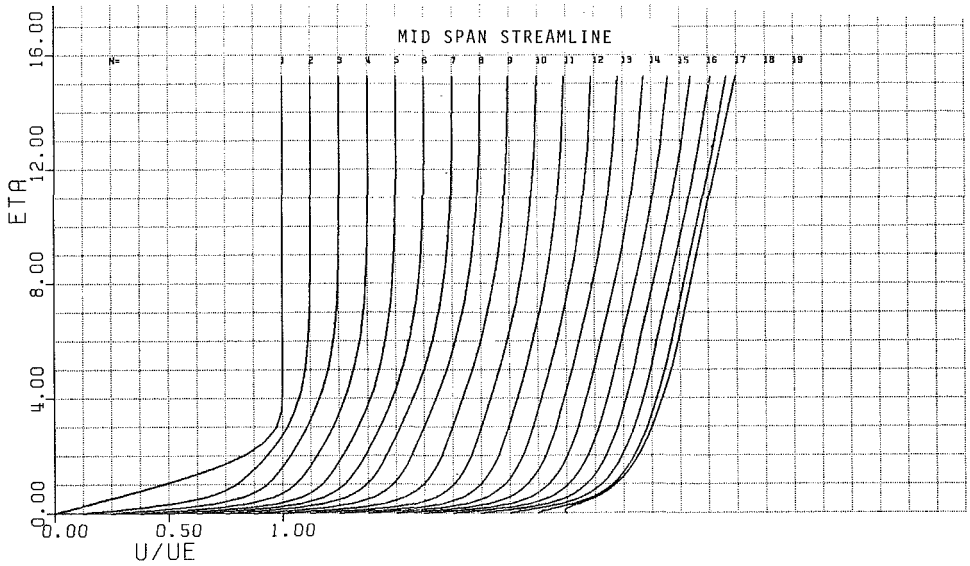

Fig. 11 Streamwise velocity profile development, suction surface

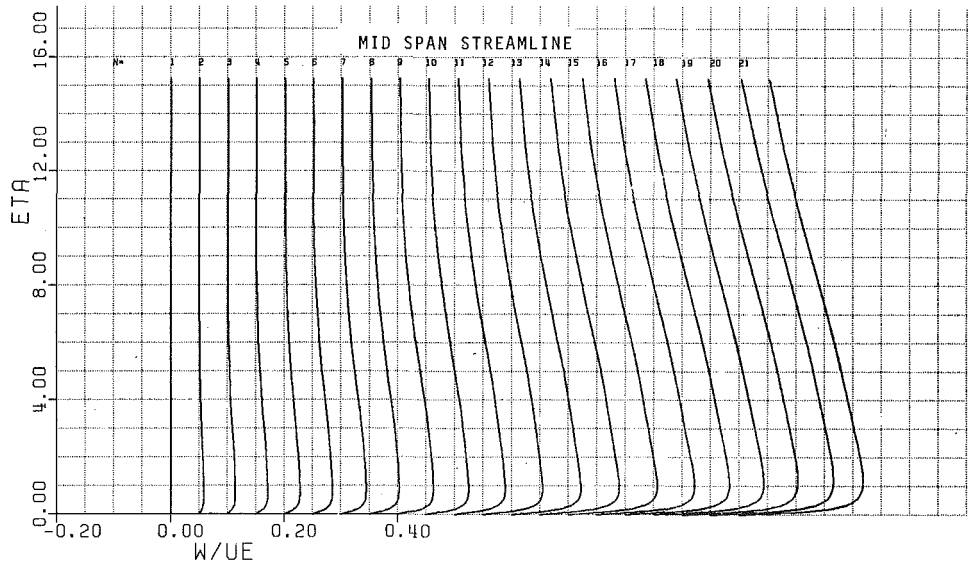

Fig. 12 Crossflow velocity profile development, pressure surface

substantial fraction of the boundary layer. It does appear likely, on the basis of simple force balance arguments, that any separated flow will be centrifuged rapidly outward and collected at the tip radius.

These results are at present poorly understood, in the sense of sensitivity to a particular turbulence model, but suggest that the response of a three-dimensional boundary layer may differ substantially from that of a two-dimensional one even when the crossflow component remains small. Much further effort is required in this area to include viscous-inviscid interactions correctly, but this separation result indicates that further work would be useful.

Experimental measurements of the flow through the NASA low aspect ratio have been performed at NASA LeRC [9] and at MIT [10]. Both sets of test data suggest much lower streamline efficiency near the tip casing than can be explained by shock losses and two-dimensional boundary layer losses, see Fig. 14. Correctly ascribing these unexplained losses to specific mechanisms (casing boundary layer, tip clearance vortex, shock-boundary layer interaction, or profile boundary layer) is a difficult but important task. In order to estimate the possible contribution of the profile boundary layer to these unexplained losses, the following simple but qualitatively correct model is proposed, see Fig. 15 for reference.

Any boundary layer fluid moving radially outward ($\dot{m}_c$) is assumed to move with zero tangential velocity relative to the blade. As this fluid moves outward, work is done on it, and its stagnation temperature is increased. This fluid is assumed to mix near the top radius with some fraction of the total machine mass flow rate ($\dot{m}_{\text{tip}}$) and to lose all its momentum. In addition the nominal compressor performance, temperature and pressure ratio, is assumed to be retained for the tip mass flow, $\dot{m}_{\text{tip}}$. The net effect of any boundary layer fluid migration is to increase the tip mass averaged total temperature ratio while decreasing the mass averaged total pressure ratio. This model is proposed not because of its great accuracy but because it brings into the analysis in a simple way all the important parameters: the ratio of induced mass flux to tip mass flux, the Mach number at which mixing takes place, the blade tip Mach number and the nominal pressure level of the machine.

The fully mixed (mass averaged) exit total temperature may

Downloaded 01 Jun 2010 to 171.66.16.62. Redistribution subject to ASME license or copyright; see http://www.asme.org/terms/Terms_Use.cfm

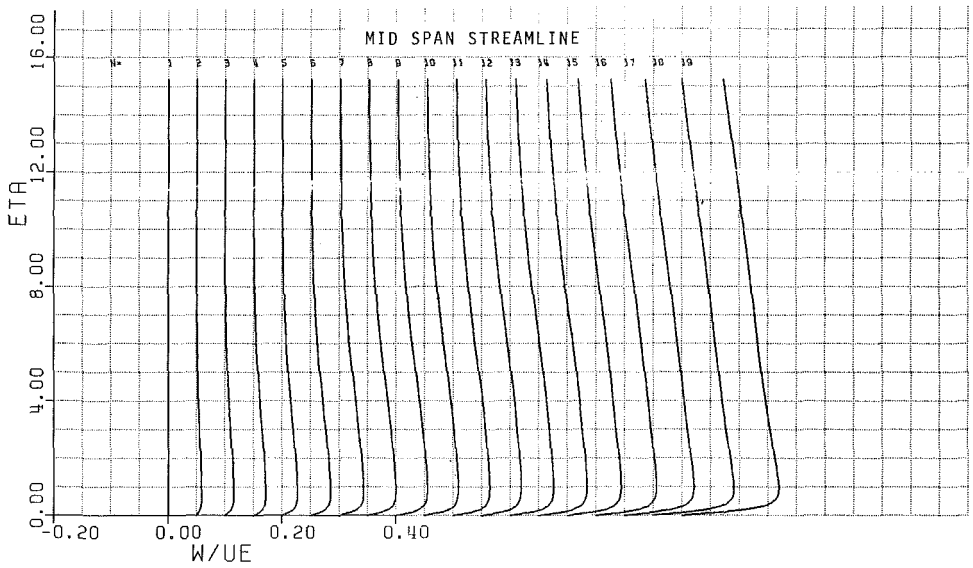

Fig. 13 Crossflow velocity profile development, suction surface

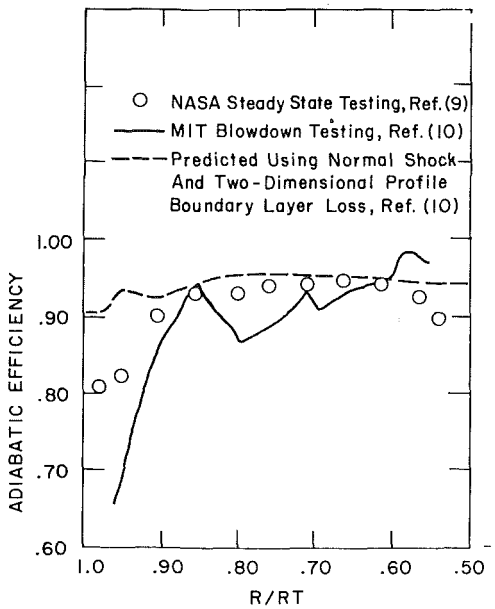

Fig. 14 Comparison of measured and predicted adiabatic efficiency for the NASA low aspect ratio rotor

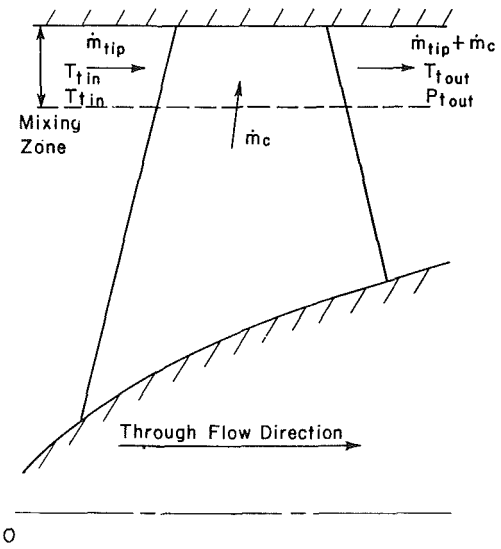

Fig. 15 Simplified crossflow/through-flow mixing model

be expressed as:

$$\frac{T_{t\,\text{out}}-T_{t\,\text{in}}}{T_{t\,\text{in}}}=\left(\frac{\Delta T_t}{T_{t\,\text{in}}}\right)_{\text{nominal}}\left(\frac{1}{1+\dot{m}_c/\dot{m}_{\text{tip}}}\right)+\left(\frac{\Delta h_t}{C_p T_{t\,\text{in}}}\right)_c\left(\frac{\dot{m}_c/\dot{m}_{\text{tip}}}{1+\dot{m}_c/\dot{m}_{\text{tip}}}\right) \tag{40}$$

where $(\Delta T_t/T_{t\,\text{in}})_{\text{nominal}}$ represents the nominal temperature ratio of the rotor, and $(\Delta h_t/C_p T_{t\,\text{in}})_c$ represents the work done on boundary layer fluid centrifuged outward.

The maximum plausible amount of work done on the boundary layer fluid occurs when this fluid is centrifuged to the tip radius and there picks up wheel speed. Since the NASA low aspect ratio rotor also has zero inlet swirl velocity, the Euler turbine equation yields for the work done on the boundary layer fluid

$$\frac{\Delta h_t}{C_p T_{t\,\text{in}}}=(\gamma-1)M_{\text{tip}}^2 \tag{41}$$

where $M_{\text{tip}}^2=(\omega r_{\text{tip}})^2/\gamma R T_{t\,\text{in}}$.

To an adequate approximation, the mixing process may be treated as constant area mixing with, see Shapiro [19]

$$\left(\frac{\Delta P_t}{P_t}\right)_{\text{mixing}}=-\gamma M_{\text{mix}}^2\frac{\dot{m}_c}{\dot{m}_{\text{tip}}} \tag{42}$$

where M_{mix} is the nominal Mach number level at which mixing occurs. The average exit total pressure is then

$$\frac{P_{t\,\text{out}}}{P_{t\,\text{in}}}=\left(\frac{P_{t\,\text{out}}}{P_{t\,\text{in}}}\right)_{\text{nominal}}-\gamma M_{\text{mix}}^2\frac{\dot{m}_c}{\dot{m}_{\text{tip}}} \tag{43}$$

In order to compare directly with Fig. 14 and the usual data presentation forms the effect of mixing boundary layer fluid is expressed as an adiabatic efficiency decrement

$$\Delta\eta=\frac{\left(\frac{P_{t\,\text{out}}}{P_{t\,\text{in}}}\right)^{\gamma-1/\gamma}_{\text{nominal}}-1}{\left(\frac{T_{t\,\text{out}}}{T_{t\,\text{in}}}\right)_{\text{nominal}}-1}-\frac{\left(\frac{P_{t\,\text{out}}}{P_{t\,\text{in}}}\right)^{\gamma-1/\gamma}-1}{\left(\frac{T_{t\,\text{out}}}{T_{t\,\text{in}}}\right)-1} \tag{44}$$

Downloaded 01 Jun 2010 to 171.66.16.62. Redistribution subject to ASME license or copyright; see http://www.asme.org/terms/Terms_Use.cfm

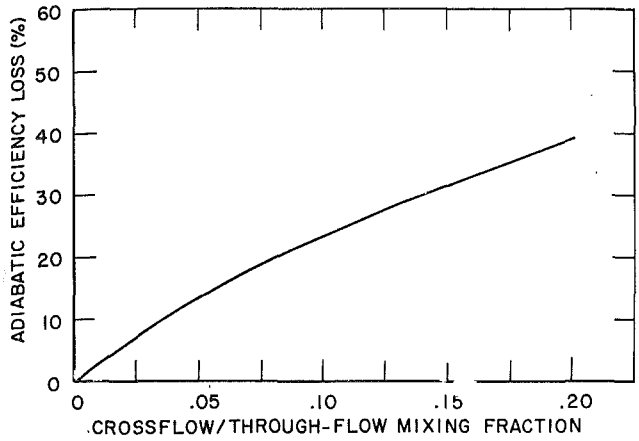

Fig. 16 Adiabatic efficiency loss as a function of mass flow mixing fraction

For the low aspect ratio rotor

$$\left(\frac{T_{t\,\text{out}}}{T_{t\,\text{in}}}\right)_{\text{nominal}} \simeq 1.16\ ,\ \left(\frac{P_{t\,\text{out}}}{P_{t\,\text{in}}}\right)_{\text{nominal}} \simeq 1.60$$

$M_{\text{tip}} \simeq 1.27$ and $M_{\text{mix}} \simeq 0.8$. Figure 16 shows the expected efficiency decrement for these conditions as a function of the mass flow fraction, $\dot{m}_c/\dot{m}_{\text{tip}}$. As would be expected, the adiabatic efficiency falls rapidly as $\dot{m}_c/\dot{m}_{\text{tip}}$ increases. Surprisingly, however, the most important effect is not the loss of total pressure due to mixing, but the work done on the boundary layer fluid as it moves radially outward. Approximately 65 percent of the efficiency decrement is accounted for by this work, equation (41) and only 35 percent of the decrement is accounted for by the total pressure loss, equation (42).

One estimate for the boundary flow migration can be obtained by integrating the quasi-three dimensional crossflow rate along the tip streamline up to separation. Even though large cross-flow velocities exist, the total crossflow is only 0.24 percent of the rotor mass flow rate. If this amount of flow is mixed in the outer 10 percent of the flow annulus as appears likely from Fig. 14, an efficiency decrement of 5 points would result. The measured "unexplained" efficiency decrement is 15 to 25 points.

It is possible but unlikely that a fully three-dimensional analysis would triple the crossflow rate and thus account for the entire efficiency decrement. A more plausible explanation is to recognize that at separation a much larger fraction of the boundary layer fluid could be centrifuged out. The computed suction surface displacement thickness represents about 7 percent of the rotor mass flow rate at separation. If 10 percent of this flow rate, or 0.7 percent of the rotor flow rate, were mixed in the outer 10 percent annulus, an efficiency decrement of 20 points would occur. The entire "unexplained" efficiency decrement could easily be explained by such a mechanism.

This simple analysis shows the great potential of the blade profile boundary layer for influencing the overall rotor efficiency even if the boundary layer does not separate. The major portion of these losses appears to result not from the total pressure loss due to mixing but rather from the nonrecoverable work (recoverable as stagnation pressure) done on the boundary layer fluid as it moves radially outward. In addition, the boundary layer separation points are significantly different from a two-dimensional analysis. It thus appears that a large compressor performance improvement could be made by properly managing the profile boundary layer.

Acknowledgments

This research was supported by the NASA Lewis Research Center under Grant NGL-22-009-383 and monitored by Dr. Roderick Chima.

References

1 Fogarty, L.E., "The Laminar Boundary Layer On a Rotating Blade," *Journal of Aeronautical Sciences*, Vol. 18, No. 4, Apr. 1951, pp. 247-252.

2 Tan, H.S., "On Laminar Boundary Layer Over a Rotating Blade," *Journal of Aeronautical Sciences*, Vol. 20, July 1953, pp. 780-781.

3 Miyake, Y., and Fujita, S., "A Laminar Boundary Layer on a Rotating Three-Dimensional Blade," *Journal of Fluid Mechanics*, Vol. 63, Part 3, 1974, pp. 481-498.

4 Horlock, J.H., and Wordsworth, J., "The Three-Dimensional Laminar Boundary Layer on a Rotating Helical Blade," *Journal of Fluid Mechanics*, Vol. 23, Part 2, 1965, pp. 305-314.

5 Kerrebrock, J.L., "Flow in Transonic Compressors," AIAA Paper No. 80-0124, Jan. 1980.

6 Cebeci, T., Kaups, K., and Ramsey, J.A., "A General Method for Calculating Three-Dimensional Compressible Laminar and Turbulent Boundary Layers on Arbitrary Wings," NASA CR-2777, 1977.

7 Haymann-Haber, G., and Thompkins, W.T., Jr., "Comparison of Experimental and Computational Shock Structure in a Transonic Compressor Rotor," ASME JOURNAL OF ENGINEERING FOR POWER, Paper No. 80-GT-81, Dec. 1979.

8 Cebeci, T., and Smith, A.M.O., *Analysis of Turbulent Boundary Layers*, Academic Press, New York, 1974, pp. 258-297.

9 Urasek, D.G., Gorrell, W.T., and Cunnen, W.S., "Performance of Two-Stage Fan Having Low-Aspect Ratio, First-Stage Rotor Blading," NASA Technical Paper 1493, 1978.

10 Ng, W.F., "Detailed Time Resolved Measurements and Analysis of Unsteady Flow in a Transonic Compressor," SM thesis, MIT, Sept. 1980.

11 Mager, A., "Three-Dimensional Laminar Boundary Layers," *High Speed Aerodynamics and Jet Propulsion*, Vol. 4, Theory of Laminar Flows, Section C, Princeton University Press, N.J., 1964, pp. 286-394.

12 Thompkins, W.T., "A FORTRAN Program for Calculating Three-Dimensional, Inviscid, Rotational Flows with Shock Waves in Axial Compressor Blade Rows," NASA CR Report, to be published Jan. 1981.

13 Kitchens, C.W., Jr., Sedney, R., and Gerber, N., "The Role of Zone of Dependence Concept in Three-Dimensional Boundary-Layer Calculations," *AIAA 2nd Computational Fluid Dynamics Conference Proceeding*, Hartford, Conn., June 1975, pp. 102-112.

14 Mellor, G.L., and Herring, H.J., "Simple Eddy Viscosity Relations for Three-Dimensional Turbulent Boundary Layers," *AIAA Journal*, Vol. 15, No. 6, June 1977.

15 Hayes, W.D., and Probstein, R.F., *Hypersonic Flow Theory*, Academic Press, New York, 1959.

16 Cebeci, T., and Smith, A.M.O., *Analysis of Turbulent Boundary Layers*, Academic Press, New York, 1974, pp. 211-257.

17 Keller, H.B., and Cebeci, T., "Accurate Numerical Methods for Boundary-Layer Flows—I. Two-Dimensional Laminar Flows," Lecture Notes in Physics, Vol. 8, *Proceedings of the Second International Conference on Numerical Methods in Fluid Dynamics*, 1971.

18 Keller, H.B., and Cebeci, T., "Accurate Numerical Methods for Boundary-Layer Flows—II. Two-Dimensional Turbulent Flows," *AIAA Journal*, Vol. 10, Sept. 1972, pp. 1193-1199.

19 Shapiro, A.H., *The Dynamics and Thermodynamics of Compressible Fluid Flow*, Vol. 1, Wiley, New York, 1953, pp. 230-232.

Downloaded 01 Jun 2010 to 171.66.16.62. Redistribution subject to ASME license or copyright; see http://www.asme.org/terms/Terms_Use.cfm

A Baseload Gas Turbine to Meet Utility Requirements for Reliability and Availability[1]

P. E. Grevstad

M. J. Smith

Power Systems Division,
United Technologies Corporation,
South Windsor, Conn. 06074

R. L. Duncan

Electric Power Research Institute,
Palo Alto, Calif.

The coal gasifier, gas turbine, combined cycle is a superior baseload electric generating system. It promises lower fuel cost, lower operating and maintenance cost, and superior siting and environmental characteristics over conventional steam systems with flue gas clean up and fluidized bed combined cycle systems. Two major new components are required: 1) the coal gasifier, and 2) the baseload gas turbine. Several candidate gasifier systems are emerging from development for other applications. Existing gas turbines primarily reflect characteristics of peaking power units. Application of such design philosophies to the demanding performance and durability requirements of baseload operation is questionable. The baseload gas turbine must be designed with the high reliability, high availability, low maintenance characteristics associated with steam turbines. This paper summarizes United Technologies Corporation's investigation of a new gas turbine designed specifically for baseload service with a coal gasifier fueled combined cycle. The design of this machine results from a cooperative effort by Kraftwerk Union, United Technologies Corporation, and Electric Power Research Institute.

Need for a Baseload Gas Turbine

The gas turbine combined cycle, fueled by a coal gasifier, is a superior "coal-fired" central station, baseload electric generating system. This is the conclusion of many studies which have examined the question of how the world's abundant coal reserves can be most wisely used. Compared to conventional and near-term generating systems, the coal gasifier gas turbine combined cycle emerges as having the best combination of efficiency, cost, environmental and siting characteristics.

One approach to a coal gasifier gas turbine-based system is shown schematically in Fig. 1. It consists of a coal gasification and gas clean-up subsystem integrated into a gas turbine-steam turbine combined cycle to maximize the utilization of thermal energy throughout the entire system. The combined cycle can operate on any liquid or gaseous fuel. Efficiencies can be achieved in the order of 50 percent by the combined cycle system without the gasifier. These superior conversion efficiencies, obtainable with conventional equipment, are the primary reason the gas turbine based system with the coal gasifier promises to be the next standard baseload fossil-fueled electric generating system. Key advantages of the system are summarized in the following paragraphs.

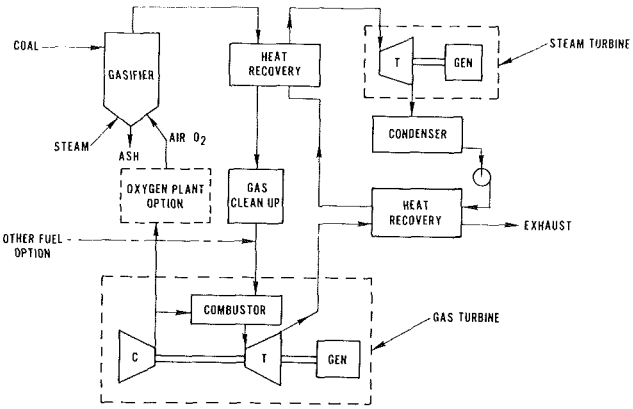

Fig. 1 Coal gasification gas turbine combined cycle

The coal gasifier gas turbine combined cycle system uses less coal to generate electric energy than competing systems. Figure 2 shows predicted system efficiency as a function of operating temperature for the gas turbine combined cycle system and other coal fueled systems. As shown, the coal gasifier gas turbine combination is superior even at introductory ratings consistent with existing technology with turbine inlet temperatures of 2000–2200°F (1090 to 1200°C). Further, as indicated, the gas turbine based system can be improved as increased temperature technology becomes available. In contrast, conventional steam or fluid bed systems have little hope for efficiency improvement because increases in temperature cause fundamental problems.

[1] Work supported in part by Electric Power Research Institute, Contract RP1187-1.

Contributed by the Gas Turbine Division and presented at the International Gas Turbine Conference and Products Show, Houston, Texas, March 9–12, 1981, of THE AMERICAN SOCIETY OF MECHANICAL ENGINEERS. Manuscript received at ASME Headquarters, December 15, 1980. Paper No. 81-GT-127.

 Copyright © 1982 by ASME

Downloaded 01 Jun 2010 to 171.66.16.62. Redistribution subject to ASME license or copyright; see http://www.asme.org/terms/Terms_Use.cfm

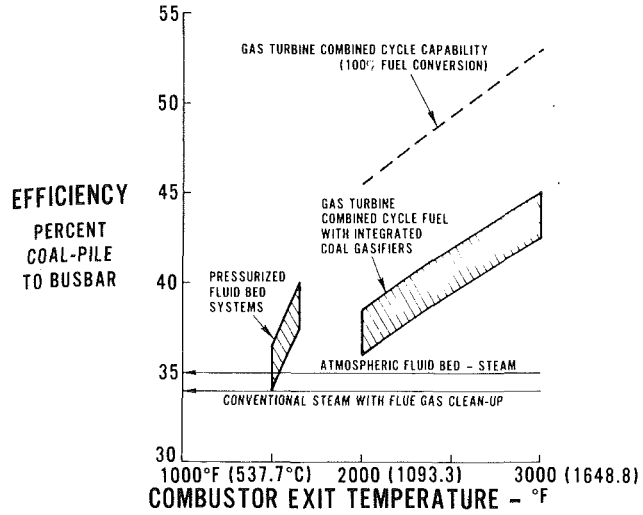

Fig. 2 Efficiencies of coal-fired generating systems

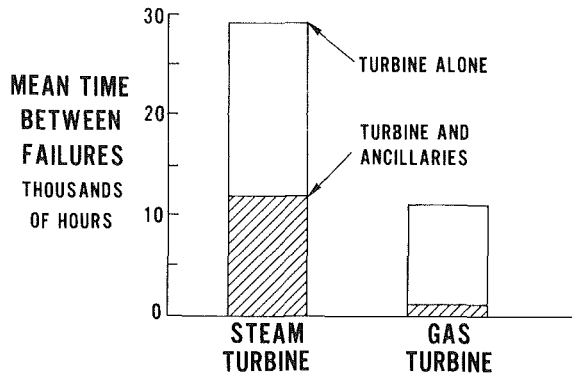

Fig. 3 Reliability comparison – steam turbine and gas turbine 2

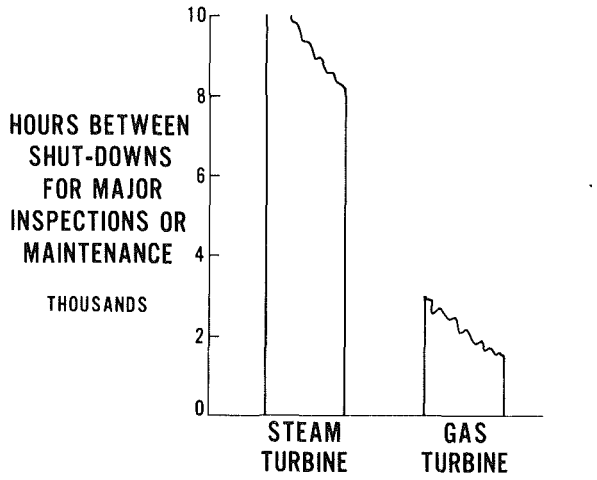

Fig. 4 Maintenance comparison – steam turbine and gas turbine

Coal gasifier gas turbine systems can make environmentally acceptable utilization of coal an economic fact. Low effluent levels are produced compared to coal fired steam plants with flue gas desulfurization. In addition, the gasifier gas turbine system is cost competitive.

Two new components must be developed to high levels of durability, reliability and performance for the coal gasifier combined cycle to achieve its promise. The first is the coal gasifier. Several attractive candidates are emerging as a result of intensive development to meet nonpower producing requirements such as petrochemical and local industrial fuel supply needs. This development is occurring both in the United States and abroad. Additional development, focused by the needs of the electric power industry, is accelerating the adaptation and extension of gasification engineering and technological development to bring it to a state of readiness for central station electric generating plant use. Meeting utility operating standards for reliable, continuous service associated with baseload generating plants will require careful engineering, particularly of the control subsystems and integration with the power producing portions of the complete system.

The purpose of this paper, however, is to address the second "new" component requiring development for the coal gasification gas turbine combined cycle baseload generating plant – the gas turbine itself. The major use of gas turbines by the electric utilities has been for peaking power service. Indeed, the stationary gas turbine industry's existence is a result largely of utility requirements for low cost peaking power generators. Peaking service connotes rapid response, high number of cycles and low operating hours per year; opportunities for maintenance without disturbing the grid are several throughout the year. Peaking power also means pressure for minimum first cost. These are not characteristics of baseload generators. Consequently, many utility executives do not accept the idea of gas turbines as baseload machines. What these executives want and need is the day-in day-out high reliability and availability demonstrated by steam turbines.

The Electric Power Research Institute recognized the dichotomy between perceived or actual gas turbine capabilities and those required to fulfill the coal-fired baseload mission. Research Program 1187, "High Reliability Gas Turbine Combined Cycle Development Program" was set up to systematically examine the reliability and durability problems of gas turbines and to evaluate methods for achieving baseload technical readiness. The gap between reliability and durability characteristics desired of gas turbines for baseload service and that measured from operating gas turbines is illustrated in Figs. 3 and 4. The data, taken from Edison Electric Institute publications [1], show gas turbines fail about three times more frequently than steam turbines. When the ancillaries associated with each are included, i.e., the complete turbine set, gas turbine systems fail 10 times more frequently. These differences occur with gas turbines used approximately 1000 hr per yr (primarily peaking power service), whereas the steam turbine is in service at least 7000 hr per yr. Operating durations before gas turbines are shut down for inspection or maintenance have also been less than desired for baseload service. Hot section inspections and combustor or turbine component replacements are the most frequent reasons.

The total gas turbine picture is not as grim as the two figures indicate. Engines specifically adapted for continuous duty, lower operating temperatures, and clean fuel provide highly reliable service over long operating times.

Electric Power Research Institute Reliable Engine Program

The EPRI/UTC Reliable Engine Program [2] is focused on defining a true baseload gas turbine for central station utility service and available in the mid to late 1980's. The UTC approach to this program is summarized in Fig. 5. Major emphasis is being placed on identifying gas turbine and gas turbine ancillary designs which maximize reliability and durability. Full use is made of design "do's and don'ts" developed by the gas turbine industry as the art has evolved

Downloaded 01 Jun 2010 to 171.66.16.62. Redistribution subject to ASME license or copyright; see http://www.asme.org/terms/Terms_Use.cfm

SUBJECT	REQUIREMENT
RELIABILITY AND DURABILITY	• REDUCED HOT SECTION TEMPERATURES • MINIMUM NUMBER OF PARTS • CONSERVATIVE, PROVEN AERO-MECHANICAL DESIGN PRACTICES • NEW PHILOSOPHY OF ANCILLARY AND HOUSING DESIGN
COMPETITIVE PERFORMANCE	• MAXIMUM COMBUSTOR EXIT TEMPERATURE CONSISTENT WITH DURABILITY GOALS AND AVAILABLE TECHNOLOGY • LOW LOSS FLOWPATH DESIGN
MEETING NEW SYSTEM REQUIREMENTS	• INCORPORATE TECHNOLOGY WHICH IS CURRENTLY IN DEVELOPMENT ONLY WHEN NEEDED FOR DURABILITY OR FOR FUELS EMISSIONS REQUIREMENTS
GROWTH	• PROVIDE CAPABILITY TO INCORPORATE HIGHER TEMPERATURE, HIGHER EFFICIENCY COMPONENTS AS THEY BECOME AVAILABLE

Fig. 5 Design requirements for central station gas turbine

APPROACH		BENEFITS/COSTS
NEW CENTERLINE	PRO	• MAXIMUM POTENTIAL FOR: • HIGHEST RELIABILITY AND DURABILITY • HIGHEST PERFORMANCE • LOWEST FIRST COST • GROWTH
	CON	• LONGER, MORE COSTLY DESIGN AND DEVELOPMENT PROGRAM • HIGHER COST FIELD DEMONSTRATION PROGRAM TO DOCUMENT RELIABILITY AND DURABILITY TO UTILITY SATISFACTION
EVOLVE FROM ESTABLISHED BASE	PRO	• LOWEST COST AND TIME TO FIELD INSTALLATION • DATA BASE EXISTS TO HELP PROVE CLAIMS TO UTILITIES
	CON	• CANNOT INCORPORATE ALL FEATURES DESIREABLE OR POSSIBLE; SOME COMPROMISE IN PERFORMANCE

Fig. 6 Approaches for achieving a gas turbine capable of central station services

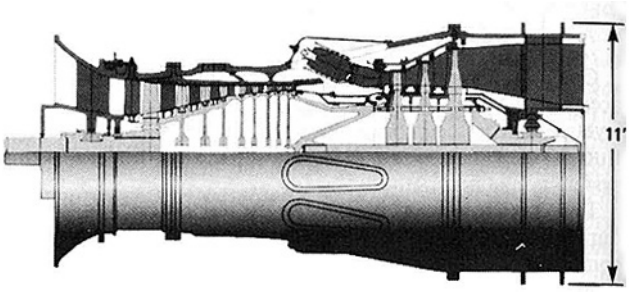

Fig. 7 New centerline 110-MW gas turbine conceptual design

from the 1940's both for aircraft and stationary engine purposes. The most recent state-of-the-art in all component areas has been reviewed for applicability. This was expected to reveal and in fact did show that substantial improvements are possible. This is not surprising in that the technology used in today's stationary gas turbines largely represents that of the 1960's and early 1970's when designs for today's machines were initiated. New technology, most of it provided by the aircraft gas turbine industry, can provide increases in output and efficiency while reducing the severity of environments to which parts are exposed. Thus simultaneous improvements in performance as well as reliability and durability are possible. For example, turbine inlet gas temperature can be increased several hundred degrees with turbine airfoil metal temperature reduced by several hundred degrees.

While full use is made of "up-to-date" technology, a primary criterion used in UTC's Reliable Engine Program evaluations was that no unproven technology would be used unless it provided major gains in reliability and durability or was required to meet newly instituted fuels and emissions requirements. It is in the latter area that unproven technology must be specified since low emissions combustion technology for the wide variety of petroleum and synthetic fuels required in the future is deficient. Additionally, provision is included in the gas turbine design to allow growth to higher levels of economic performance as more efficient and higher temperature capability components become available. The initial service date of mid to late 1980's is needed to permit the coal gasifier combined cycle system to make its timely commercial appearance and begin its contribution to this country's energy needs. Since this system could well become the dominant fossil-fueled generating system, it is important that the reliability/durability heritage established in the 1980's and 90's be extended well beyond the year 2000.

Two approaches to achieving a baseload central station gas turbine are feasible: 1) an all new centerline, "clean sheet of paper" powerplant; 2) an evolutionary growth approach founded on a conservatively designed powerplant with substantial field experience. Both approaches have been investigated under UTC's Reliable Engine Program. Without question, the most reliable, durable and high performance machine would result from the new centerline approach. As Fig. 6 indicates, the machine would be optimized for the baseload mission, which, as discussed in the foregoing, is a new one for the gas turbine. The new centerline approach allows the negative aspects of the gas turbine's peaking power heritage to be left behind. However, the hard cash facts of life will probably not permit this approach. Studies have shown the benefits to society, in the form of lower electricity costs, lower emissions and lower utilization of natural resources, justify funding the development of an optimum coal gasification gas turbine (via the Government). It is doubtful, however, that this will occur [3].

Therefore, an evolutionary improvement approach is a necessity. While the resulting engine will not measure up to the full potential which today's technology and design art could provide, the compromise is small. Also, it will make easier the task of convincing utility executives and the Public Utility Commissions that the gas turbine is capable of fulfilling baseload requirements. Building on the experience of similar engines operating in baseload or near baseload service provides a more rapid route to establishing credibility.

A third approach is also possible for consideration. That is, to evolve a baseload gas turbine from today's peaking machines. Significant difficulties arise in doing this, however, since these gas turbines are based on a design philosophy that made them right for peaking applications, and, hence, wrong for baseload applications.

New Centerline Baseload Gas Turbine

The Utility Turbine 100 (UT100), defined under the initial phase of the EPRI-UTC Reliable Engine Program [4], is an example of what could be achieved with a new centerline approach. To achieve highest reliability, this 110-MW output engine draws on the existing pool of modern gas turbine component technology to perform its function with a minimum number of parts. Its design uses conservative temperatures and design margins to maximize potential for long time between overhauls and total life.

The engine is shown in Fig. 7 in an on-board combustor configuration. Two bearings support the single, 3600 RPM direct drive shaft. Power is removed at the compressor end providing the exhaust gases with a direct route to the waste heat recovery boiler. A 14:1 pressure ratio, an optimum value for combined cycle applications, is provided by a high-

Downloaded 01 Jun 2010 to 171.66.16.62. Redistribution subject to ASME license or copyright; see http://www.asme.org/terms/Terms_Use.cfm

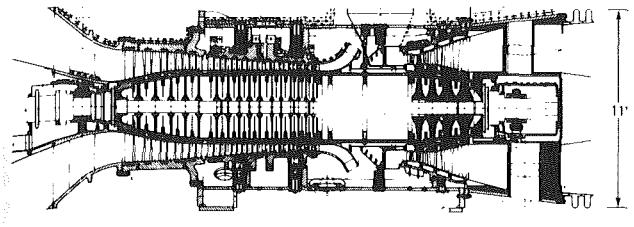

Fig. 8 Kraftwerk Union 110-MW direct drive gas turbine

performance compressor. The series staged rich/lean combustor allows the engine to meet EPA emission requirements without water injection when operating with nitrogen containing as well as nitrogen free fuels. Reliability and durability can be further enhanced by incorporating an off-board combustor as described in the next section. The three stage turbine is convective air cooled using no film cooling. Eliminating film cooling holes increases reliability by making the airfoils completely tolerant to impurities which may be contained in the fuel or air. The short compressor and turbine yield a rugged, stiff shaft eliminating the need for the troublesome, commonly used, middle bearing.

With the exception of the combustor[2], the technology for this machine is in hand. The job of developing such a machine for utility service is just that – development, not technology. Much work in design trade studies, detailed design, component verification testing and engine demonstration testing remains to be done. The cost to do this straightforward work for a new centerline engine is substantial – over $100 million. In the light of the continuing depressed market for stationary gas turbines and in the absence of public support, the plans for considering development of the ideal baseload engine must be put aside and other, lower investment cost means to achieve the goals must be sought.

Evolutionary Baseload Gas Turbine

United Technologies Corporation and the Kraftwerk Union AG, a division of Siemens, of the Federal Republic of Germany, have jointly defined a new family of long life stationary gas turbines based on KWU gas turbines. The KWU engines embody the same electric utility service design philosophy used in UTC's new centerline concept: single shaft, direct drive from the compressor end, two bearings, etc. Figure 8 shows a cross section of a KWU 110-MW 50 Hz (3000 RPM) machine. The large diameter shaft is made up of face splined compressors and turbine disks retained by a central tiebolt. The resulting high stiffness provides large critical speed margins with only two bearings. Compressor and turbine aerodynamics are based on earlier machines, hence sixteen compressor stages provide a 10:1 pressure ratio for the 740 lb/sec air flow; four turbine stages are used. The turbine inlet temperature is 1950°F (1063.3°C).

The major departure from American design practice reflected by the KWU machine is shown in the front view, Fig. 9. Rather than grouping a number of relatively small diameter combustor cans around the engine centerline, only two off-board (silo) combustors are used. Two benefits of major importance to the baseload gas turbine concept result: 1) turbine and combustor durability and reliability are improved many fold, 2) development for low emissions operation using alternate fuels is greatly simplified.

These important benefits are discussed in detail later in this paper. For now it is sufficient to say that the time between maintenance is ten times greater than those of current United States stationary engines.

[2]The combustor design is based on UTC's EPA-supported work [5] to define a durable combustor capable of operation with various fuels. The first phase of a DOE/NASA program [6] to extend and broaden these results is now underway at several contractors.

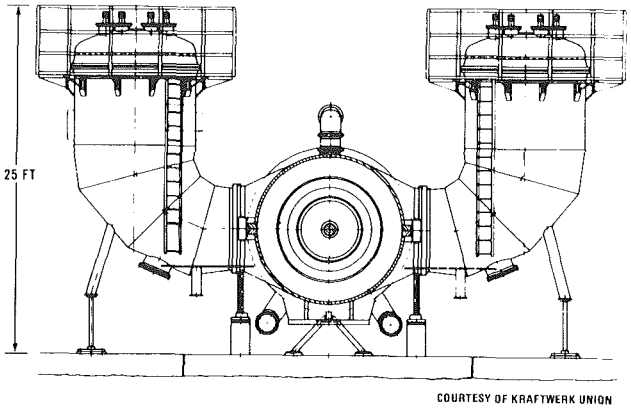

Fig. 9 Kraftwerk Union 110-MW gas turbine showing off-board combustors

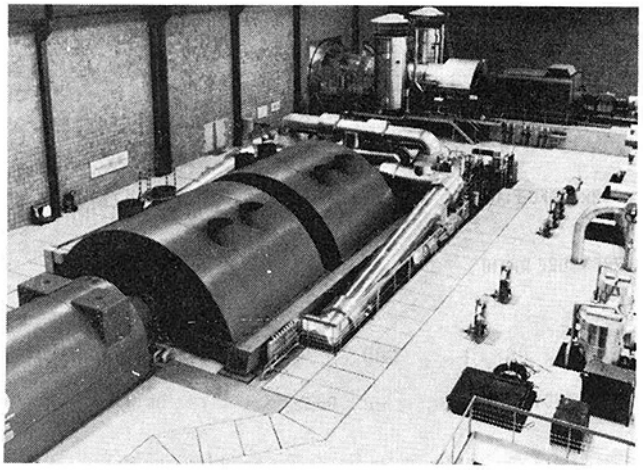

Fig. 10 Kraftwerk Union combined cycle installation

KWU machines are used in open and combined cycle applications; Fig. 10 shows a combined cycle installation. Approximately 37 units of capacity between 70-110 MW have been installed throughout Europe and the Far East. Total operating time is over 1 million hours. Availability of these units in the 1978 time period was 93 percent.

United Technologies and KWU jointly incorporated state-of-the-art aircraft engine technology into the basic KWU engine. Modern compressor and turbine aerodynamics are used to improve efficiency and output power. Low emissions combustor technology developed for UTC's FT4 industrial engine [7] is adapted to the silo combustors. Turbine cooling improvements allow a 260°F (126.6°C) increase in turbine inlet temperature. Figure 11 summarizes the specifics of the design improvements.

Compressor. To increase engine output and efficiency, the 16 stage compressor was redesigned to increase the flow and pressure ratio while retaining its high efficiency, reliability and surge margin. Additional flexibility for part power operation was introduced.

To increase flow from 740 to 860 lb per sec and pressure ratio from 10:1 to 12:1, changes were made to only the first four stages. The outer diameter of the first stage was increased three percent. Loading on each of the four stages was increased slightly. The rear twelve stages were unchanged. Variable inlet guide vanes were introduced to improve the combined cycle part power operating characteristics. Figure 12 compares the results of the compressor redesign.

Downloaded 01 Jun 2010 to 171.66.16.62. Redistribution subject to ASME license or copyright; see http://www.asme.org/terms/Terms_Use.cfm

DESIGN CHANGE	RESULT
INCREASE AIRFLOW 15%	INCREASED OUTPUT
INCREASE PRESSURE RATIO FROM 10:1 TO 12:1	INCREASED EFFICIENCY
REDESIGN BURNER HEAD END	MEET EPA EMISSIONS STANDARDS WITHOUT WATER INJECTION
INCREASE TURBINE DIAMETER	INCREASED OUTPUT AND EFFICIENCY
INCREASE TURBINE TEMPERATURE 250°F	INCREASED OUTPUT
REDUCED TURBINE AIRFOIL METAL TEMPERATURES	IMPROVED DURABILITY

Fig. 11 Component improvements made under joint UTC/KWU program

	BASE	REDESIGN
CORRECTED FLOW	740 LB/SEC	860 LB/SEC
PRESSURE RATIO	10:1	12:1
STAGES	16	16
EFFICIENCY	BASE	-0.1%

Fig. 12 Predicted results of compressor uprating

Extensive structural analysis was performed to ensure the high reliability characteristics of the compressor were retained. The critical design margins used in the initial design were either maintained or exceeded. These included operating stress to material strength margin, as well as vibratory and flutter margins. This was accomplished through slight increases in both blade camber and chord. The increased shaft length resulting from the increased chord was accommodated within the present bearing span.

Combustor. Off-board or "Silo" combustors provide benefits of fundamental importance to baseload gas turbines in life, availability, and performance compared to on-board combustor engines. These improvements are critical to successful base load operation.

The combustor used in current KWU engines is shown in Fig. 13 [8]. Key characteristics of this off-board design include:

- Large combustion and gas mixing volume.
- Durable ceramic tiles protecting the primary combustion zone.
- The liner is cooled effectively and uniformly by the high velocity cool compressor discharge air on the outside.
- A long flow path providing good mixing resulting in a highly uniform temperature pattern at the turbine inlet.
- No line of sight from the combustion flame to the turbine.
- Configuration flexibility to adapt to a wide variety of fuels with low emissions.

Field data on KWU silo combustors show them to have a life of over 40,000 hr (5 yr) of operation. Comparative on-board combustors are often replaced at 3000-hr intervals, or more frequently than twice a year. This is illustrated in Fig. 14

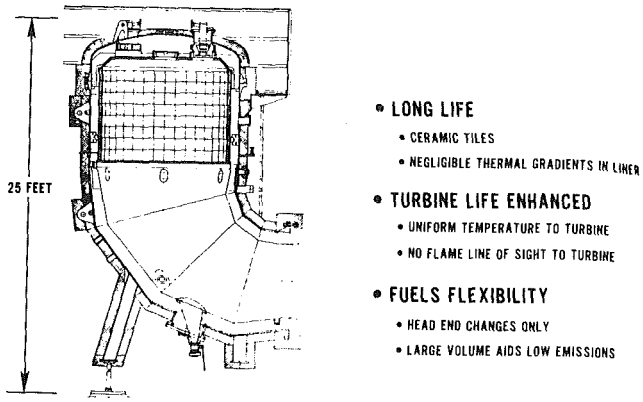

Fig. 13 Off-board combustor characteristics

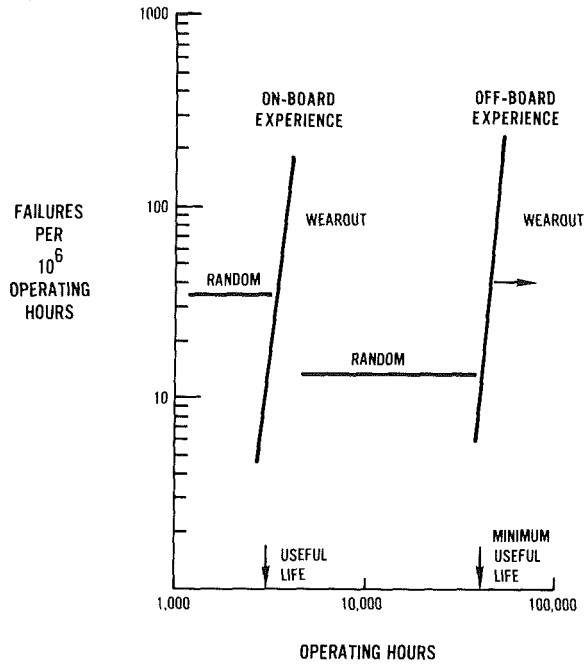

Fig. 14 Reliability and life comparison: off-board versus on-board combustors

which also shows the better reliability (lower mean time between failures) even though on-board combustors receive much more frequent maintenance than do silo type combustors.

The off-board configuration allows easy accessibility for inspection and maintenance. As Figure 13 shows, a man-way access port in the transition duct allows entry for "walk-around" inspection and work.

The good mixing and low velocity flow which takes place in the large volume of the silo provides the turbine with a uniform gas temperature pattern. Figure 15 shows the peak temperature exceeds the average by only about 100°F compared to up to 500°F for a good on-board combustor. In addition, there can be little radiative heating of turbine airfoils as no line of sight exists to the flame. The result is marked improvement in turbine life for the same combustor temperature. This also may be translated into higher operating temperatures for equal turbine environment, thereby increasing efficiency and power. The silo head-end configuration allows for ready incorporation of low emissions lean or rich/lean designs to allow use of a variety of coal derived liquid or other synthetic fuels [9].

Downloaded 01 Jun 2010 to 171.66.16.62. Redistribution subject to ASME license or copyright; see http://www.asme.org/terms/Terms_Use.cfm

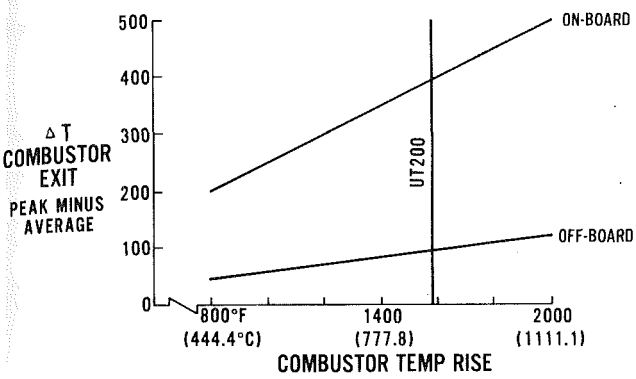

Fig. 15 Severity of turbine cooling requirements reduced by off-board combustors

	BASE	REDESIGN
COMBUSTOR EXIT TEMPERATURE - °F	1950	2210
- °C	(1063.3)	(1210)
NUMBER OF STAGES	4	4
EFFICIENCY - PERCENT	89.6	91.8
NET POWER - PERCENT	BASE	1.58 x BASE
MAXIMUM AIRFOIL TEMPERATURE	BASE	BASE - 150°F (83°C)

Fig. 16 Predicted results of turbine uprating

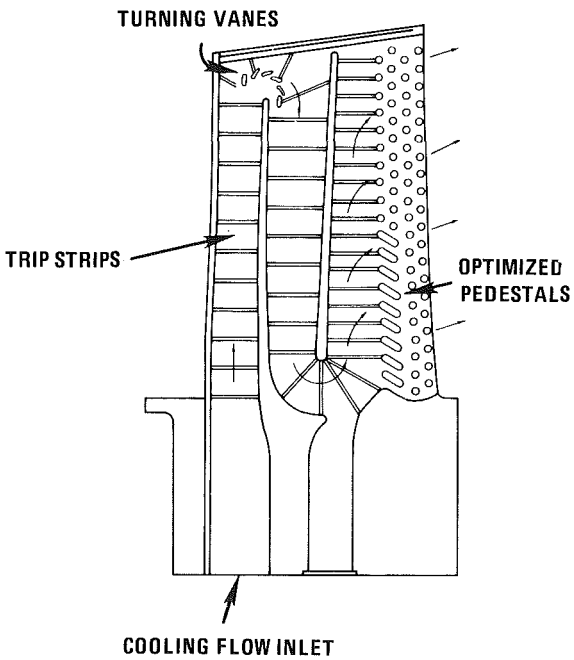

Fig. 17 All-convectively cooled first stage blade

These characteristics result in the conclusion that the silo combustor configuration carries a high priority for achieving multi fuel, low emissions capability in a high performance baseload gas turbine.

Turbine. The turbine output was increased through increased flow, expansion ratio, efficiency and by increasing turbine inlet temperature 260°F. The combination of these increases provided a net power output increase of 58 percent compared to the unmodified machine. Aerodynamic changes included increased diameter, increased annulus area, improved airfoil contours and an optimized exhaust system. A comparison of the turbine redesign is shown on Fig. 16.

The most significant change was the introduction of state-of-the-art airfoil cooling. The 260°F increase in turbine inlet temperature was made possible by cooling designs and airfoil fabrication technology which are current practice in the aircraft gas turbine industry. This high-effectiveness cooling keeps airfoil metal temperatures at or below their current levels. The cooling is done completely internal to the airfoils, no film cooling is used. Potential failure due to clogging of film cooling holes is not possible. Thus, high tolerance to fuel or air-borne contaminants is achieved. Figure 17 shows the cross section of the first stage turbine blade design.

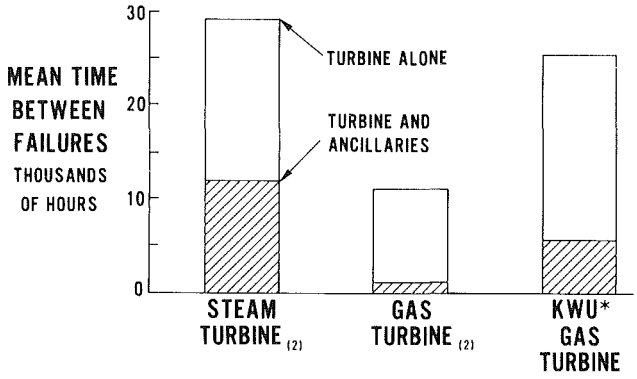

Fig. 18 Reliability Experience Comparison

MODEL	KWU BASE ENGINE (50 Hz)	KWU BASE SCALED TO 60 Hz	UTC UPRATING UT200 OPENED CYCLE	UTC UPRATING UT200 COMBINED CYCLE
POWER OUTPUT - MW	110	76	120	178
HEAT RATE - BTU/KW-HR (HHV)	12,000	12,000	10,800	7400

Fig. 19 Reliable engine design progression

Gas Turbine Design

The UTC/KWU/EPRI baseload gas turbine design, designated UT200, has competitive power and efficiency and superior reliability, life, fuels flexibility and emissions characteristics.

Redesign of the conservative, proven reference engine to obtain competitive performance has been carried out with care to conserve or to further enhance its excellent durability and reliability characteristics. Figure 18 shows these characteristics and compares them with the average for U.S. engines.

The new 120-MW engine has a simple cycle heat rate of 10,800 Btu/kW HR (higher heating value). In engine efficiency terms, this represents a lower heating value efficiency of 34 percent. In combined cycle configuration, overall heat rate and efficiency (using the same definitions as above) are

Downloaded 01 Jun 2010 to 171.66.16.62. Redistribution subject to ASME license or copyright; see http://www.asme.org/terms/Terms_Use.cfm

	RELIABLE ENGINE (UT200)	GROWTH ENGINE (UT202)
• COMPRESSOR		
• PRESSURE RATIO	12:1	14:1
• No. OF STAGES	16	12
• COMBUSTOR	LEAN	RICH/LEAN
• TYPE	DRY NOx	DRY NOx
• CONFIGURATION	SILO	SILO
• EXIT TEMP. – °F	2210	2600
– °C	(1210)	(1426.7)
• TURBINE COOLING		
• TYPE	CONVECTIVE	CONVECTIVE
• COOLANT	AIR	AIR
• COOLANT TEMP. – °F	660 (348.8°C) (COMP. DISCH.)	400 (204.4)
• AIRFOIL CONSTRUCTION	CAST SINGLE PIECE	BONDED, MULTIPLE PIECE

Fig. 20 Reliable engine growth parameters

7430 Btu/kWh and 49 percent, respectively. Figure 19 summarizes the "before and after" power and performance story.

Gas Turbine Growth

The UT200 is capable of growing from an output of 120 MW to 165 MW primarily by introducing new air-cooled turbine airfoil and combustor liner technology. Combined cycle efficiency is improved by 3.5 percentage points.

The introductory rating of the UT 200 is set by durability requirements and today's combustor and turbine state-of-the-art. Technical approaches to increase component efficiency and operating temperatures have been identified which result in substantial increases in output and efficiency. Firing temperatures can be increased to 2600°F and higher without disturbing durability and reliability parameters, i.e., turbine metal temperatures remain constant.

Figure 20 shows the growth scenario when improvements in compressor, combustor and turbine are made. The compressor achieves a 14:1 pressure ratio in 12 stages (versus the 16 stages now required for a 12:1 ratio). A rich/lean silo combustor provides low NOx operation with nitrogenous coal derived liquids as well as other gaseous or liquid fuels. Increased use is made of the ceramic combustor walls used in the present engine; cold-side area augmentation is used to maintain combustor-to-turbine transition duct temperatures. The high reliability turbine cooling design philosophy is retained, i.e., internal convective cooling only, with air as the coolant. No film cooling is used. Extension of all air cooling for service at turbine inlet temperatures to 2600°F and above is made possible by the bonded airfoil technology developed for aircraft engines [10]. Bonded airfoils are formed from two or more pieces cast to final shape and subsequently bonded together. "Opening up" the airfoil allows complex, high surface area cooling passages to be formed inside the airfoil thereby increasing heat transfer capacity substantially. Compressor discharge air, cooled to 400°F, is the coolant.

The result in terms of gas turbine power and heat rate in a combined cycle configuration is shown in Figs. 21 and 22. Power is up 37 percent from 120 to 165 MW. Heat rate (in an oil-fired combined cycle plant configuration) is down to 6900 from 7430 BTU/kW-Hr.

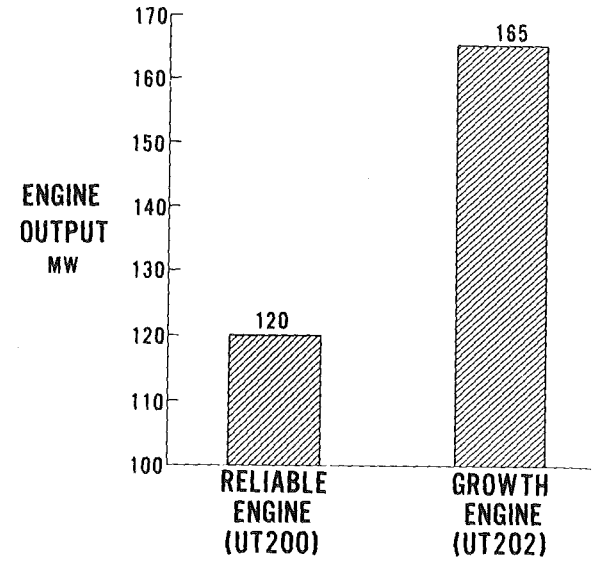

Fig. 21 Power output improvement

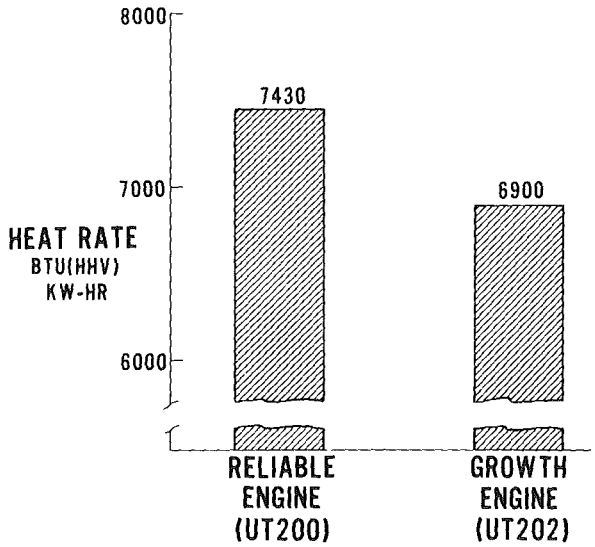

Fig. 22 Heat rate improvement

Conclusion

A new breed of gas turbine is required for the coal gasification combined cycle system to achieve its potential as the lowest cost, lowest emissions central station generator of electricity. The gas turbine described in this paper has been designed to meet the rigorous reliability, durability and emissions requirements associated with baseload, central station service. It has also been designed to meet modern, competitive standards for performance, fuels flexibility and cost. This machine is developable now; no new technology needs to be generated. The present, and likely continuing depressed market for industrial/utility gas turbines, coupled with non-focused public support for solving energy problems will probably delay the introduction of this, or similar machines.

Downloaded 01 Jun 2010 to 171.66.16.62. Redistribution subject to ASME license or copyright; see http://www.asme.org/terms/Terms_Use.cfm

References

1 "Equipment Availability Component Cause Code Summary Report for the Ten-Year Period 1967–1976," EEI-77-64A, Jan. 1979, Ten-Year Period 1968–1977, July 1980.

2 Whitaker, R., "How Much Can We Rely on a Combined-Cycle Plant?," *EPRI Journal,* Volume 5, No. 2, Mar. 1980, pp. 22–27.

3 "Business Venture Analysis Case Study Relating to the Manufacture of Gas Turbines for the Generation of Utility Electric Power," DOE Report No. FE-2483-7, May 5, 1978, DOE Contract EJ-77-C-01-2483.

4 "High Reliability Gas Turbine Combined Cycle Development Program," United Technologies Final Report, GTR-1830, EPRI Contract RP1187-1, Publication Pending.

5 "Advanced Combination Systems for Stationary Gas Turbine Engines," Contract No. 68-02-2136, EPA-Control Systems Laboratory Office of R&D.

6 "Low NO_x Heavy Fuel Combustor Concept Program," Contract No. DEN3-149, NASA LeRC.

7 Lewis, G. D., Holladay, T. E., "Design of a Successful Low Emissions Burner," ASME Paper 80-GT-12, Mar. 1980, 25th Annual International Gas Turbine Conference.

8 Linert, A., "Experience with Large Gas Turbine Combustion Chambers," Paper to be published by ASME for March 1981 Gas Turbine Conference.

9 Krockow, W., Fiorentino, A. J., "Low Emissions Silo Combustor," to be published by ASME for March 1981 Gas Turbine Conference.

10 Mayfield, J., "Computer Controlled Production Gains," *Aviation Week and Space Technology,* December 3, 1979.

Downloaded 01 Jun 2010 to 171.66.16.62. Redistribution subject to ASME license or copyright; see http://www.asme.org/terms/Terms_Use.cfm

New Correlations of the Two-Dimensional Turbine Cascade Aerodynamic Performance

K. F. Qiang
Deputy Chief Engineer,
Marine Boiler and Turbine Research Institute,
Harbin, China

N. X. Chen
Associate Research Professor,
Institute of Engineering Thermophysics,
Chinese Academy of Sciences,
Peking, China

Theoretical evaluation and experimental research have been conducted to verify the performance of steam and gas turbines, including exhaust turbines of superchargers. The simplified channel method and hydroelectrical analog method have been used to calculate blade surface velocity distribution. Based on the "fully developed turbulence" assumption, viscous effects are approximately taken into account by using the boundary layer theory. Theoretical optimum profile loss coefficients are given. Effects of velocity profile on losses are analyzed. Turbine cascades have the characteristics of high solidity, high setting angle, and high air turning angle, which facilitate the use of the channel concept. On this basis, K. W. Todd's "passage convergent gradient," modified O. Zweifel's "tangential load coefficient" and other effective criteria have been chosen and cascade data correlated. Some relatively accurate semiempirical formulas for predicting the aerodynamic performance of cascades are formulated.

Introduction

For over a decade, in the advancement of gas turbines, steam turbines, and exhaust turbines or superchargers, the authors have conducted some theoretical evaluation and experimental research on the aerothermodynamics of turbine cascades. On one hand, the hydroelectrical analog method and the flow channel method were used to solve "the direct problem" of cascades and, in making boundary layer calculations, the rationality in the choice of cascade design parameters was discussed. On the other hand, based on numerous plane cascade tunnel tests, the relationship between the aerodynamic characteristics and the geometric parameters of cascades was studied and some generally applicable semiempirical correlations were obtained.

Theoretical Calculation of Turbine Cascade Aerodynamic Performance

Knowledge of two disciplines of aerodynamics is essential for theoretical research of two-dimensional cascades: nonviscid (potential) and viscous (boundary layer) flow theories. The former provides a key to understanding the velocity distribution and the air outlet angle, and the latter is helpful for evaluating the quality of a specific cascade.

The Turbine Cascade Ideal Flow. Early in 1952, a well-known "mean-stream-line method" was given by Prof. Wu for evaluating the flow past turbine cascades [1]. The method is theoretically well established and has the advantages of ease in taking the compressibility effect into account, simplicity of computation, and sufficient accuracy. It is also conducive to achieving desirable thickness distribution dictated by the strength and cooling requirements.

This method has been further developed and widely adopted in our country. In addition, the electrical analog and the simplified approximate channel method are also used by the authors.

Electrical Analogy. During the 1950s, the hydroelectrical analogy was a popular method for solving cascade flow problems. The method we used is a combination of analogy with conformal transformation [2]. The corresponding conformal transformation relationship between the cascade plane and auxiliary plane (circular cascade or unit circle) is sought out by electrical analogy.

Approximate Channel Method. On the basis of mean-stream-line method, a quick calculating channel method was presented by the authors [3]. It is especially convenient for solving direct problem of cascades, the profiles of which are formed by connecting several circular arcs with straight lines.

For stream-equipotential line coordinate system, the velocity W along the equipotential line (approximately taken to be the conjunction line between two tangential points and the center of inscribed circle in the cascade channel) can be obtained by Taylor series (Fig. 1).

$$W = W_s + \frac{\Delta n}{1}\left(\frac{\partial W}{\partial n}\right)_s + \frac{\Delta n^2}{2}\left(\frac{\partial^2 W}{\partial n^2}\right)_s + \frac{\Delta n^3}{3!}\left(\frac{\partial^3 W}{\partial n^3}\right)_s + \ldots \quad (1)$$

where

Contributed by the Gas Turbine Division of THE AMERICAN SOCIETY OF MECHANICAL ENGINEERS and presented at the Gas Turbine Conference and Products Show, March 9-12, 1981, Houston, Texas. Manuscript received at ASME Headquarters December 15, 1980. Paper No. 81-GT-128.

Copyright © 1982 by ASME

Downloaded 01 Jun 2010 to 171.66.16.62. Redistribution subject to ASME license or copyright; see http://www.asme.org/terms/Terms_Use.cfm

$$\left.\begin{aligned}\frac{\partial W}{\partial n} &= W\frac{\partial \beta}{\partial \ell} = -W\zeta \\ \frac{\partial^2 W}{\partial n^2} &= -W\frac{\partial \zeta}{\partial n} + W\zeta^2 \\ \frac{\partial^3 W}{\partial n^3} &= -W\frac{\partial^2 \zeta}{\partial n^2} + 3W\zeta\frac{\partial \zeta}{\partial n} - W\zeta^3\end{aligned}\right\} \quad (2)$$

The distribution of the streamline curvature along the equipotential line can be assumed by

$$\zeta = \zeta_s + \frac{\zeta_p - \zeta_s}{N}\Delta n \quad (3)$$

Substituting equations (1-3) into the continuity integral relation gives the formulas for calculating velocity distribution of suction and pressure surfaces

$$\left.\begin{aligned}W_s &= W_{1z}t\Big/\left[N - \frac{\zeta_s N^2}{2} + \left(\zeta_s{}^2 - \frac{\zeta_p - \zeta_s}{N}\right)\frac{N^3}{3!} + \left(3\zeta_s\frac{\zeta_n - \zeta_s}{N} - \zeta_s{}^3\right)\frac{N^4}{4!} + \ldots\right] \\ W_p &= W_s\left[1 - \zeta_s N + \left(\zeta_s{}^2 - \frac{\zeta_n - \zeta_s}{N}\right)\frac{N^2}{2} + \left(3\zeta_s\frac{\zeta_p - \zeta_s}{N} - \zeta_s{}^3\right)\frac{N^3}{3!} + \ldots\right]\end{aligned}\right\} \quad (4)$$

For compressible fluid, assuming that the influence of tangential velocity on the velocity distribution of suction and pressure surfaces may be neglected, the following approximation for subsonic flow is used:

$$\left.\begin{aligned}\frac{\lambda_s}{\lambda_p} &= \frac{(W_s)_B}{(W_p)_B} \\ \frac{\lambda_s}{\lambda_m} &= \frac{(W_s)_B}{(W_m)_B}\end{aligned}\right\} \quad (5)$$

Figure 2 is a comparison of the calculated results by the approximate channel method and by experiment. Curves 1 and 2 represent downstream Mach number of 0.8 and 0, respectively; the solid line denotes experimental values and the circles denote calculated values.

Viscous Flow through Cascade of Blade Profiles. The presence of fluid viscosity complicates the problem we are to solve. For this reason, we have paid attention not only to the inviscid flow, but also to the viscous flow problems.

Cascade Flow Coefficient. The cascade flow coefficient is the ratio of the real flow past through the cascade passage to the theoretical flow and it can be expressed by the boundary layer momentum thickness (Fig. 3).

Nomenclature

All angles are measured from cascade axis.

b = airfoil chord

$G = \dfrac{0_1 - 0_2}{L_P}$ = passage convergent gradient

$i = \beta_1' - \beta_1$ = incidence angle

$K = 1 - \left(\dfrac{\sin\beta_2}{\sin\beta_1}\right)^2$ = passage convergence

$\bar{l} = \dfrac{\ell}{b}$ = aspect ratio

L_p = length of passage centerline between inlet and outlet throats

$M = \dfrac{w}{a}$ = Mach number

λ = critical velocity ratio

$0_1, 0_2$ = passage inlet throat and outlet throat

r_1, r_2 = leading edge radius and trailing edge radius

$\sigma = \dfrac{b}{t}$ = cascade solidity

$\mathrm{Re} = \dfrac{Wb}{\nu}$ = Reynolds number

ν = kinematic viscosity

$\bar{t} = \dfrac{t}{b}$ = pitch-chord ratio

T_0 = initial turbulence of overtaking flow

β_1, β_2 = air inlet angle and outlet angle

β_1', β_2' = cascade inlet angle and outlet angle

β_b = setting or stagger angle

$\delta = \beta_2 - \beta_2'$ = deviation angle

$\epsilon = 180 \text{ deg} - (\beta_1 + \beta_2)$ = air turning angle

$H = \dfrac{\delta^*}{\delta^{**}}$ = form parameter

δ = boundary layer thickness

Superscripts

$*$ = displacement or stagnation parameter

$**$ = momentum

$-$ = nondimensional

Subscripts

1 = upstream of the cascade

2 = downstream of the cascade

B = incompressible flow

cr = critical value

e = outside inviscid flow region of the boundary layer

m = mean value

t = trailing edge or theoretical

ad = adiabatic

id = ideal

Downloaded 01 Jun 2010 to 171.66.16.62. Redistribution subject to ASME license or copyright; see http://www.asme.org/terms/Terms_Use.cfm

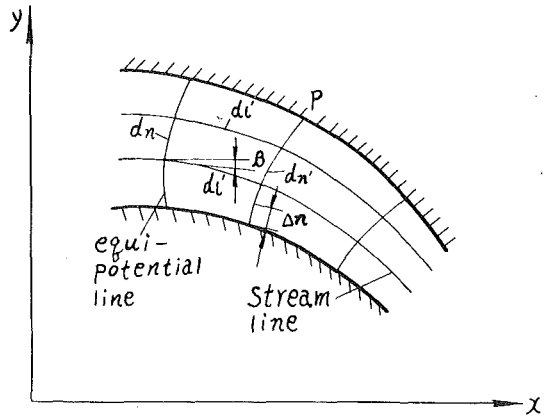

Fig. 1 Coordinate system of equipotential line and streamline

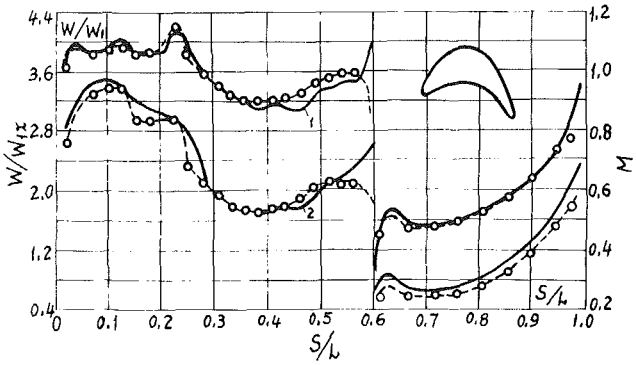

Fig. 2 Comparison of calculated results with cascade test data

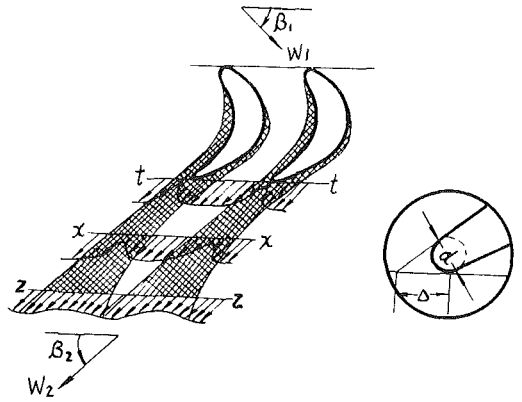

Fig. 3 Sketch of cascade boundary layer and wake

$$\mu_G = \frac{G}{G_t} \simeq \frac{\rho_{te} W_{te}(t-\Delta)\sin\beta_t - \Sigma \rho_{te} W_{te} \delta_t^*}{\rho_{te} W_{te}(t-\Delta)\sin\beta_t} \approx 1 - \frac{\Sigma H_t(\delta_t^{**}/t\sin\beta_t)}{1-\bar{\Delta}} \tag{6}$$

Cascade Loss Coefficient. The cascade loss coefficient is defined as the ratio of energy loss of the gas flow through the cascade $\Delta E = G\, W_{2e}^2 - W_2^2/2gJ$ to the total energy $E = G\, W_{2e}^2/2gJ$:

$$\zeta_p = 1 - \left(\frac{W_2}{W_{2e}}\right)^2 \tag{7}$$

On the assumption that the energy loss only occurred in the boundary layer and wake between sections 1-1 and 2-2, the loss coefficient may be formulated as

$$\zeta_p = \frac{1.73\Sigma(\delta_t^* t\sin\beta_t)}{(1-\bar{\Delta}) - 1.4\Sigma(\delta_t^{**}/t\sin\beta_t)} + 0.1\bar{\Delta} \tag{8}$$

Generalized Method for Calculating Boundary Layers. The momentum integral equation for a compressible fluid flow along arbitrary stream surface of revolution in turbomachinery may be written as

$$\frac{d\delta^{**}}{d\chi} + \delta^{**}\left[\frac{1}{\tau}\frac{d\tau}{d\chi} + \frac{1}{Pe}\frac{dPe}{d\chi} + (2+H)\frac{1}{We}\frac{dWe}{d\chi} - \left(1-\frac{Pm}{Pe}\right)H_{02}\frac{\omega^2\gamma}{We^2}\sin\sigma\sin\beta\right] = \frac{\tau w}{PeWe^2} \tag{9}$$

where $H = \delta^*/\delta^{**}$, $H_{02} = \delta/\delta^{**}$, τ denotes the normal thickness of the stream sheet, and σ is the angle between the axial axis and projection of the streamline on the meridional plane.

The formula for calculating laminar, transient or turbulent boundary layer momentum thickness of two-dimensional incompressible cascade flow can be approximated by the following relation:

$$\delta^{**} = \frac{\nu^{\frac{m}{1+m}}}{We^{\frac{b^*+m}{1+m}}}\left[\left(\frac{a}{A}\right)\int_{\chi_i}^{\chi} We^{b^*} d\chi + K\right]^{\frac{1}{1+m}} \tag{10}$$

This formula contains an integral constant K and four constants a, b^*, A, m, which are related to the boundary layer behavior:

For laminar: $a=0.44,\ b^*=4.75,\ m=1,\ A=1$
For transient: $a=0.90,\ b^*=5.55,\ m=-0.1,\ A=1259$
For turbulent: $a=0.012,\ b^*=4.47,\ m=0.268,\ A=1$
or $a=0.0062,\ b^*=3.7,\ m=0.15,\ A=1$ (11)

The introduction of the compressibility transformation gives a formula for compressible flow as follows:

$$\delta^{**} = \mathcal{K}_e^{-\frac{k+1}{2(k-1)}}\left(\frac{\nu_e^*}{a_0}\right)^{\frac{m}{1+m}} M_e^{-\frac{b^*+m}{1+m}} \cdot\left[\left(\frac{a}{A}\right)\int_{\chi_i}^{\chi} \mathcal{K}_e^{\frac{3k-1}{2(k-1)}} M_e^{b^*} d\chi + K\right]^{\frac{1}{1+m}} \tag{12}$$

where the integral constant $K = [\delta_i^{**}\mathcal{K}_{ei}^{k+1/2(k-1)}]^{1+m}(\nu_e^*/a_0)^{-m} M_{ei}^{b^*+m}$; a_0 is sound speed, which is obtained by the total temperature of the flow outside the boundary layer Te^*, $M_e = W_e/\sqrt{gkRTe}$ is Mach number. $\mathcal{K}_e = T_e/T_e^*$ is the ratio of static to total temperature.

Generally speaking, there is a high turbulence level in the turbomachinery and the boundary layer on the blade surfaces is fully turbulent. For this reason, the method assuming that the boundary layer is fully turbulent is reasonable.

Calculation of Formparameter. Nondimensional formparameter is an important parameter for calculating the boundary layer. For turbulent boundary layer, there exist several criteria for estimating boundary separation. The more reliable criterion for engineering practice is to consider that the separation occurs at $H \geq 1.8 \sim 2.6$. In 1965, an approximate formula for evaluation of turbulent boundary layer formparameter H was suggested by the authors [4] as

$$H = 1.78 - 0.162(\log R^{**})$$

Downloaded 01 Jun 2010 to 171.66.16.62. Redistribution subject to ASME license or copyright; see http://www.asme.org/terms/Terms_Use.cfm

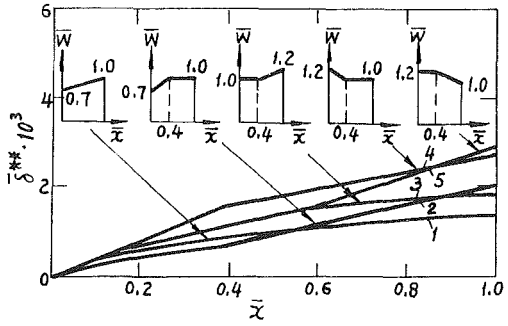

Fig. 4 Variation of boundary layer momentum loss thickness along the profile at different velocity distributions

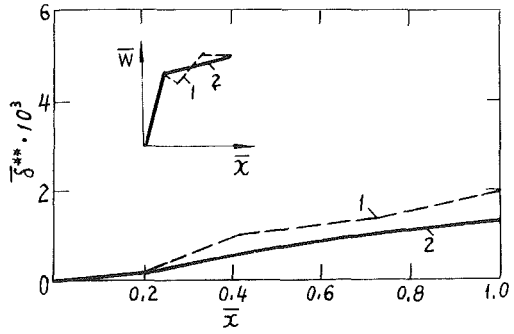

Fig. 5 Variation of boundary layer momentum loss thickness at two different velocity distributions

$$+0.0122(\log R^{**})^2 + 174\left(-\frac{\delta^{**}}{We}\frac{dWe}{d\chi}\right) \qquad (13)$$

where $R^{**} = We\delta^{**}/\nu$ and $dWe/d\chi$ denotes the velocity gradient along the blade surface.

Study on the Velocity Distribution along the Blade Surfaces. The method previously described can be used for qualitative analysis of some simple velocity distributions.

The results of boundary layer thickness calculation on cascades with various surface velocity distributions are given in Figs. 4 and 5.

It is evident that the velocity distribution of the diffusing type gives the maximum loss, while the accelerating velocity distribution the smallest. Therefore, the optimum velocity distribution should be such as to assume an ascending tendency from leading edge to trailing edge. Moreover, the larger the velocity gradient, the smaller the momentum loss thickness of the boundary layer. Owing to the fact that the onset of decreasing velocity (diffusing) is undesirable, the formation of positive pressure gradient is essential. But this will lead to increasing momentum loss thickness of the boundary layer. In serious cases, boundary layer separation takes place. Under such circumstances, it is necessary to restrict the value of profile parameter H which should not exceed 1.8. It is true that at the suction surface outlet section, that is, for cascade with relatively large convergence, the presence of diffusion is sometimes unavoidable.

For the velocity distribution of the increase-constant-decrease type, the maximum velocity ratio W_{max}/W_l has a certain effect on the magnitude of the boundary layer momentum loss thickness, but the influence of velocity ratio W_T/W_L is very small (Fig. 6).

On the basis of the foregoing analysis, curves of theoretical optimum profile loss coefficient of turbine cascade versus air outlet angle and inlet angle are plotted (Fig. 7).

During plotting, several assumptions are made and, therefore, these curves are only for reference.

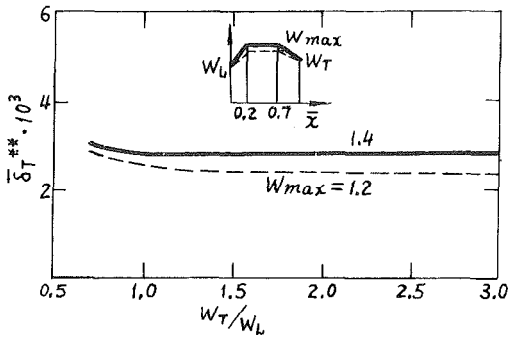

Fig. 6 Variation of boundary layer momentum loss thickness with velocity ratio at different maximum velocity ratios ($X^* = 0.2, X_2' = 0.7$)

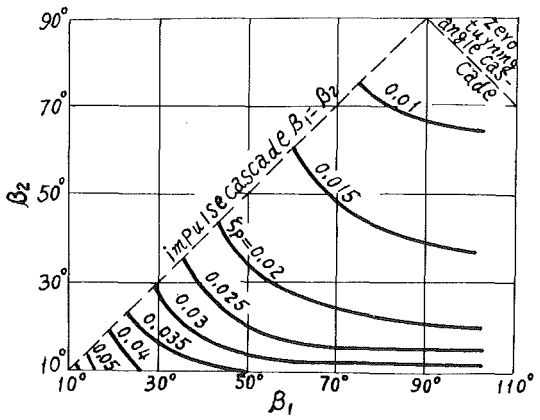

Fig. 7 Variation of theoretical optimum profile loss coefficient with air inlet angle and outlet angle of turbine cascades

Brief Description of the Experimental Investigation

In veiw of the fact that design data on low-speed cascades are already available [5], the authors' chief aim of this investigation is to accumulate and analyze experimental data on high subsonic cascades, which will eventually lead to a reduction and even avoidance of repetition of such similar work.

During plane cascade tunnel tests, special emphasis was given to the study of the uniformity of inlet flow field and the flow two-dimensionality. By taking such measures as the selection of a proper diffuser taper angle, the use of a proper ratio of chamber length to diameter, a rational arrangement of flow-rectifying devices such as screens, correct design of a contraction section contour, and the selection of appropriate number of test blades and aspect ratio, a quite satisfactory flow field was achieved in the cascade tunnel [6]. A systematic study was also conducted on methods of measuring and handling cascade test data. Finally, an appropriate test procedure was selected which insured the necessary testing accuracy and minimized the time required [7].

The chord length and the aspect ratio of the cascade tested were 30 to 40 mm, and 1.5 to 2.0, respectively. The Reynolds number was within the self-simulating range. The initial turbulence of the tunnel overtaking flow measured by a pressure ball was $T_0 = 1.5$ percent. The number of blades was usually 7 to 11.

In the following, instead of describing in detail individual cascade test curves, emphasis will be given to the selection of a proper model and the development of a criterion for test data analysis. Then the various reliable test data will be grouped together. Finally, some simple-in-form, easy-to-use new correlations will be proposed. These semiempirical formulas have been employed to verify the aerodynamic characteristics of steam turbine cascades. The results have shown that the

Downloaded 01 Jun 2010 to 171.66.16.62. Redistribution subject to ASME license or copyright; see http://www.asme.org/terms/Terms_Use.cfm

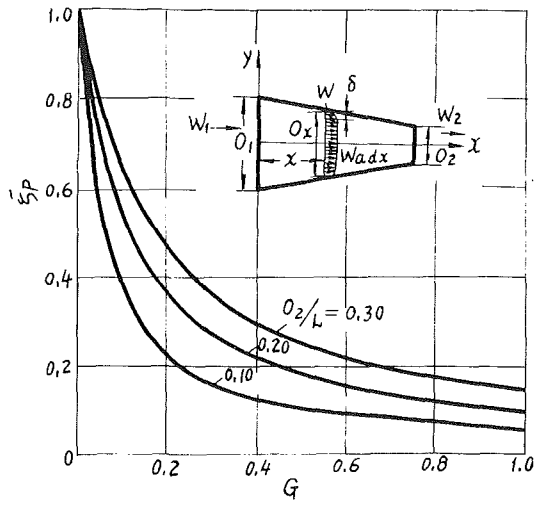

Fig. 8 Variation of loss coefficient ζ_P with convergence gradient G (calculated values)

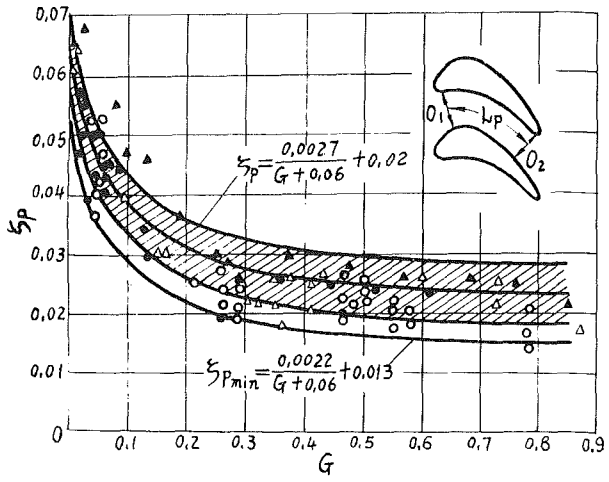

Fig. 9 Variation of profile loss coefficient with convergence gradient of plane turbine cascade

proposed formulas agree with the test data, and excel others in accuracy.

New Correlations of Aerodynamic Characteristics of Plane Turbine Cascades

Profile Loss Coefficient. Among the many factors affecting the losses in turbine cascades, β_1 and β_2 are the most important. When the values of these parameters are fixed, the blade profile and the approximate shape of the cascade passage are basically determined. As has been stated [5], however, it is improper to use only the air turning angle ϵ or the passage convergence K as the criteria for loss analysis.

K. W. Todd [8] uses as the criterion for analyzing blade profile losses the so-called "convergence gradient of blade passage" $G = 0_1 - 0_2/L_p$ which evidently represents the degree of convergence of passage width per unit length of centerline.

Supposing that the plane cascade is taken as a two-dimensional uniformly converging duct and that the flow is one-dimensional and incompressible, after making certain simplified assumptions, we can calculate the loss coefficient as follows:

$$\zeta_p = \frac{C}{Re_L^{\frac{m}{1+m}}} \left(\frac{1}{0_2}\right)^{\frac{m}{1+m}} \left[\frac{1-\left(G\frac{L}{0_2}+1\right)^{1-b^*}}{G}\right]^{\frac{1}{1+m}} \quad (14)$$

where

$$C = \left(\frac{a}{Ab^*}\right)^{\frac{1}{1+m}}$$

$$Re_L = \frac{W_{ad2}L}{\nu}$$

and the factors of a, b^*, A, and m can be calculated according to turbulent flow conditions. The results are shown in Fig. 8, where $\zeta_P = \zeta_P/\zeta_{PG=0}$

As can be seen in the figure, in the self-simulating range, the cascade friction loss is in the main related to two characteristic parameters, the passage convergence gradient G and the ratio $0_2/L$, with the former playing a dominant role.

For this reason, the authors used G as the criterion for analyzing the profile loss. But the proposed approximate formula $\zeta_P = 0.0022/G + 0.015$ from (8) was modified to improve its accuracy in the ranges $G \le 0.1$, $G \ge 0.3$. Pertinent test data were plotted in Fig. 9, and the following semiempirical formulas were obtained:

The mean cascade loss coefficient:

$$\zeta_P = \frac{0.0027}{G+0.06} + 0.02 \quad (15)$$

The minimum cascade loss coefficient:

$$\zeta_{P\min} = \frac{0.0022}{G+0.06} + 0.013 \quad (16)$$

It can be seen that numerous test points crowded near the curve of the formula (15). In cases where a cascade is designed by a well-founded engineering method, the cascade passage width is characterized by a uniform and continuous convergence and a relative thickness of blade trailing edge $r_2/b = 1 \sim 2$ percent, then, under conditions of $M_2 \le 0.7 \sim 0.8$, $Re_2 \ge 2 \sim 3 \times 10^5$, and the initial turbulence of the overtaking flow $T_0 \le 2 \sim 3$ percent, formula (15) will give profile loss results with an accuracy of about ± 0.005, which is comparable to that of measured data and considered to be satisfactory.

At the preliminary design stage, since the throats of the cascade inlet and outlet and the passage centerline cannot be known in advance, we can approximately assume $0_1 = t \sin\beta_1$, $0_2 = t \sin\beta_2$. Thus, substituting them into the formula (14), after some reduction and rearrangement, we have

$$\zeta_P = \frac{C}{Re_b^{\frac{m}{1+m}}} \left(\frac{L}{t\sigma}\right)^{\frac{1}{1+m}} \left[\frac{1-\left(G^{**}\frac{\sigma}{\sin\beta_2}+1\right)^{1-b^*}}{G^{**}}\right]^{\frac{1}{1+m}} \cdot \left(\frac{\sigma}{\sin\beta_2}\right)^{\frac{m}{1+m}} \quad (17)$$

where $G^{**} = (\sin\beta_1 - \sin\beta_2)/\sigma$ is a new convergence gradient.

Since $L/t\sigma \approx 1 \sim 1.5$, the loss coefficient is only a function of G^{**} and $\sigma/\sin\beta_2$, except for the effects of working conditions and boundary layer flow conditions. Thus, an approximate equation (see Fig. 10) is

$$\zeta_P = \frac{0.003}{G^{**}+0.085} + 0.017 \quad (18)$$

Air Outlet Angle. The air outlet angle of the turbine cascade may also be analyzed with the aid of the "passage" concept. By using the continuity equation, the momentum equation, and the simplified conditions to analyze the one-dimensional

Downloaded 01 Jun 2010 to 171.66.16.62. Redistribution subject to ASME license or copyright; see http://www.asme.org/terms/Terms_Use.cfm

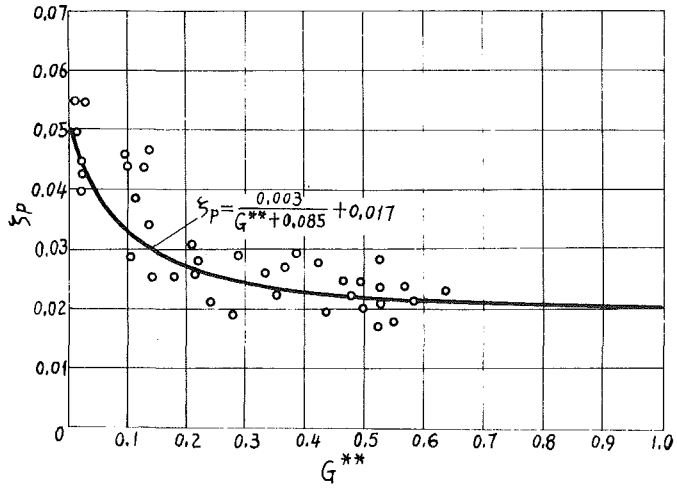

Fig. 10 Variation of loss coefficient with convergence gradient G^*

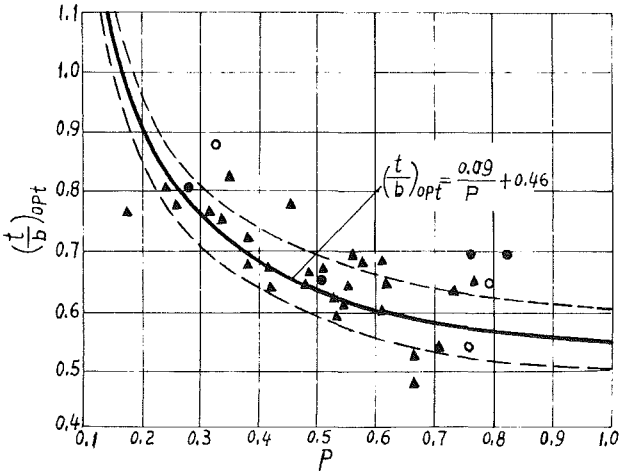

Fig. 11 Optimum relative pitch of plane turbine cascade $\bar{t}_{opt} = f(P)$

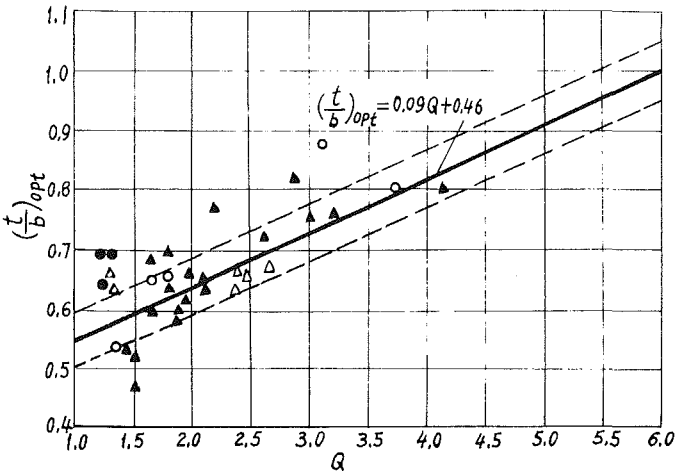

Fig. 12 Optimum relative pitch of plane turbine cascade $\bar{t}_{opt} = f(Q)$

flow in a blade passage, different theoretical approximate equations for calculating the air outlet angle of the turbine cascade can be derived, all of which have the form of sin $\beta_2 = k\ 0_2/t$. Obviously, β_{2ef} = arc sin $(0_2/t)$ is a good characteristic criterion.

However, empirical formulas such as $\beta_2 = \beta_{2ef} =$ arc sin $0_2/t$, $\beta_2 =$ arc sin $0_2/t - \Delta t$, and $\beta_2 =$ arc sin $[0_z + S/t]$ give results with relatively large deviations when $\beta_{2ef} < 18$ deg and $\beta_{2ef} > 30$ deg.

Thus, the use of $\beta_2 = k$ arc sin $0_2/t - k_2$ can enhance accuracy. Some authors recommended $k_1 = 1.143$, $k_2 = 2.1$ or $k_1 = 1.18$, $k_2 = 1.8$. For a higher calculation accuracy, however, different values of k_1 and k_2 should be used, depending on the range of M_2 and β_{2ef}.

On the basis of analyzing considerable test data, the authors propose:

(*a*) When $M_2 \le 0.5$, $k_1 = 1.11$ and $k_2 = 2.0$ may be used over the entire range of β_{2ef}.

(*b*) When $M_2 = 1.0$, a distinction should be made between the following two cases:

(i) If $\beta_{2ef} \ge 18$ deg, then, $k_1 = 1.0$ and $k_2 = 0$.

(ii) If $\beta_{2ef} < 18$ deg, i.e., for high reaction nozzle cascades with very small outlet angle and impulse cascades with large turning angles, β_2 will further decrease at high values of M_2, due to the fact that at low speeds $\beta_2 < \beta_{2ef}$. As available data are not adequate $k_1 = 1.5$ and $k_2 = 9.0$ can be used as an approximation.

J. Dunham [10] expresses by an approximate analytical expression the correction factor given by D. G. Ainley for the effects of changes of M on the air outlet angle.

$$\beta_2 = \beta_{2ef} - 4(\beta_{2i} - \beta_{2ef})(1 - 6M_2 + 9M_2{}^2 - 4M_2{}^3) \tag{19}$$

where β_{2i} is the air outlet angle when $m_2 \le 0.5$.

Concrete checking calculations show that the preceding equation can give satisfactory results in the range of $\beta_{2ef} \ge 18$ deg.

Optimum Pitch-chord Ratio. Since the demand to turbine cascade is to keep the energy loss at a minimum when it turns air flow by a given angle, during analysis "the minimum loss rate" $(\zeta_P/\epsilon)_{min}$ was used to determine the optimum pitch-chord ratio $(t/b)_{opt}$.

Based on the analysis of an ideal incompressible flow through cascade, O. Zweifel [11] found that when the turbine cascade profile loss is at a minimum, the tangential force load coefficient

$$Cu = \frac{T}{T_{id}} = 2\frac{t}{b}\frac{\sin\beta_2 \sin(\beta_1 + \beta_2)}{\sin\beta_1 \sin\beta_b}$$

varied within certain limits of values (normally $Cu = 0.8 - 1.2$) and, consequently, proposed to use it as a criterion for determining the optimum pitch-chord ratio. The value of Cu is evidently a function of ϵ and k.

Based on this, the authors chose the following characteristic criterion:

$$Q = \frac{\sin\beta_1/\sin\beta_2}{\sin(\beta_1 + \beta_2)} \tag{20}$$

Downloaded 01 Jun 2010 to 171.66.16.62. Redistribution subject to ASME license or copyright; see http://www.asme.org/terms/Terms_Use.cfm

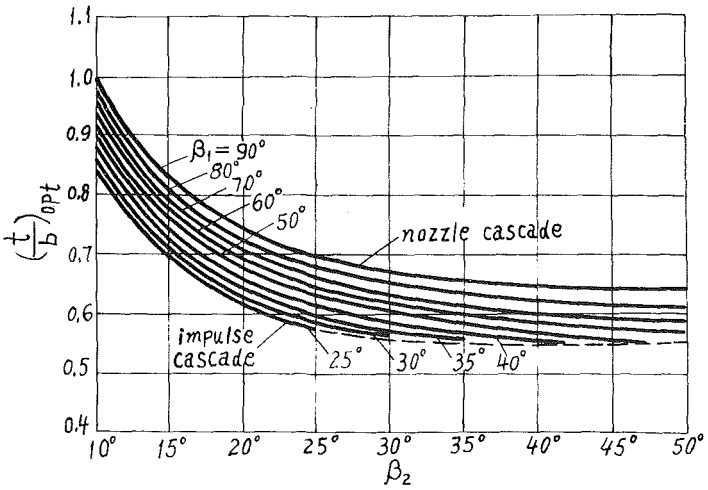

Fig. 13 Optimum relative pitch of plane turbine cascade $(t/P)_{opt} = f(\beta_1, \beta_2)$

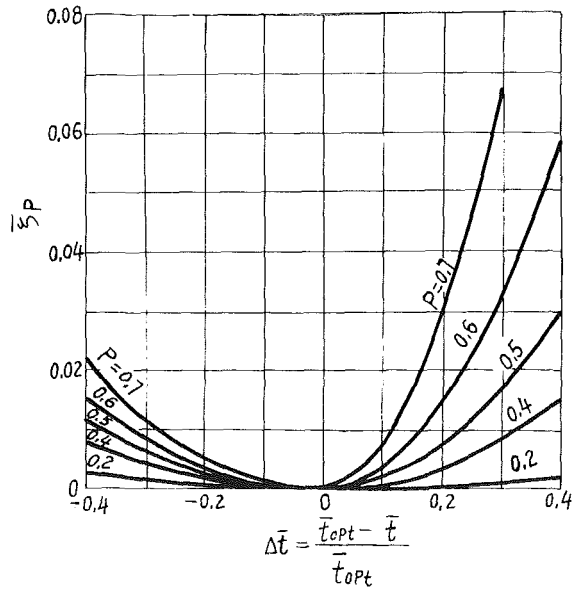

Fig. 14 Empirical curves for predicting profile loss variation when the relative pitch deviates form optimum value

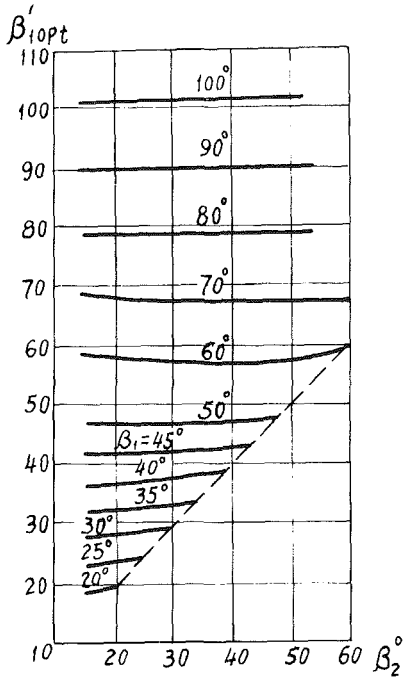

Fig. 15 Diagram for predicting the optimum blade inlet angle β'_{1opt}

and stipulated that it should give the pitch-chord ratio of an isolated wing plate when $\beta_1 = \beta_2 = 90$ deg, so that the plate might be correlated with the cascade. The variation of $(t/b)_{opt}$ with $p = 1/Q$ is shown in Fig. 11. It can be seen that the test points form a quite thick grouping, the average curve of which is

$$\left(\frac{t}{b}\right)_{opt} = \frac{0.09}{P} + 0.46 \tag{21}$$

i.e.,

$$\left(\frac{t}{b}\right)_{opt} = 0.09Q + 0.46 \text{ (see Fig. 12)} \tag{22}$$

Figure 13 also shows the variation of $(t/b)_{opt}$ with β_1 and β_2. It gives values of $(t/b)_{opt}$ ranging from 0.65 to 1.0 for nozzle cascades ($\beta_1 = 90$ deg) and values of the same term ranging from about 0.55 to 0.72 for impulse cascades ($\beta_1 = \beta_2$).

The basic principles of passage analysis can also be used to determine the optimum pitch-chord ratio of a cascade. Practice has shown that a cascade passage converges uniformly near the optimum pitch. Therefore, for a cascade having a uniformly changing passage with its upstream portion without divergence or slightly convergent while its downstream portion is uniformly convergent, the pitch-chord ratio is near its optimum value (the variation curve of $G_i = 0_i - 0_2/L_P \sim (L_i/L_P)$ can be used during plotting).

In actual turbine design, due to such factors as structure, stress, vibration, and cooling, it is often impossible for the turbine cascades to operate at optimum pitch condition. Figure 14 gives a set of curves of

$$\Delta\bar{\zeta}_P = \frac{\zeta_P - \zeta_{P\min}}{1 - \zeta_{P\min}} = K_t \Delta\bar{t}^2$$

where $\Delta\bar{t} = (\bar{t}_{opt} - \bar{t})/\bar{t}_{opt}$. They can be used to evaluate variation of profile loss when the pitch deviates from its optimum value.

It is interesting to note that equations (21) and (22) agree quite well with the empirical data given by (12) in terms of range of values and their variation trends.

Cascade Losses Under Off-Design Conditions. The profile losses have another component—the loss caused by

Downloaded 01 Jun 2010 to 171.66.16.62. Redistribution subject to ASME license or copyright; see http://www.asme.org/terms/Terms_Use.cfm

separation of air flow from the suction surface and the pressure surface of the airflow when the air inlet angle changes. According to the simplified one-dimensional analysis on the basis of incompressible flow through a plate cascade proposed by G. Yu. Stepanov [13], the additional losses caused by off-design conditions are

$$\Delta\zeta_P = B\left[\left(\frac{\sin\beta_2}{\sin\beta_1}\right)^2 - \left(\frac{\sin\beta_2}{\sin\beta_i'}\right)^2\right] + C\left[\frac{\sin(\beta_i' - \beta_1)\sin\beta_2}{\sin\beta_1 \sin\beta_1}\right]^2$$

in which the first term represents the additional loss due to variation of convergence, and the second term indicates the effects of flow separation. Taking into account that the profile loss at blade inlet angle is

$$\zeta_{P0} = A + B\left(\frac{\sin\beta_2}{\sin\beta_i'}\right)^2$$

the total profile losses at off-design air inlet angle β_1 are

$$\zeta_P = \zeta_{P0} + \Delta\zeta_{P0} = A + B\left(\frac{\sin\beta_2}{\sin\beta_1}\right)^2 + C\left[\frac{\sin(\beta_i' - \beta_1)\sin\beta_2}{\sin\beta_i' \sin\beta_1}\right]^2 \quad (23)$$

In order to enhance the calculation accuracy of the foregoing equation, the authors [14] used the factors of $A = 0.017$, $B = 0.048$, and $C = 0.265$, and introduced for the range of positive incidence angles the correction factor

$$D = 1 + 0.7\frac{\sin\beta_2}{\sin\beta_1} \text{ (for negative angles, } D = 1.0)$$

Hence

$$\zeta_P = 0.017 + D\left[0.048\left(\frac{\sin\beta_2}{\sin\beta_1}\right)^2 + 0.265\left(\frac{\sin i \sin\beta_2}{\sin\beta_1' \sin\beta_1}\right)^2\right] \quad (24)$$

The improved equation (24) agrees relatively well with the test results.

By use of equation (24), the optimum incidence angle i_{opt} (or the optimum blade inlet angle β'_{iopt}) of a turbine cascade can also be determined. Recommended curves are presented in Fig. 15.

Concluding Remarks

Earlier, the authors have described the theoretical method of ideal air flow and viscous flow through a turbine cascade and qualitatively discussed the optimum pattern of profile velocity distribution. Based on the discussion of flow criteria, the authors have correlated numerous test data and proposed some semiempirical formulas for the calculation of cascade loss, air inlet angle and optimum pitch-chord ratio. The authors came to the conclusion that the task of investigating subsonic turbine cascades has been basically fulfilled; however, as the radial dimensions of the meridional passage change and the Mach number of the air flow increases, it will be necessary to take into account the effects of variation of stream sheet thickness during the quasi-three-dimensional flow calculation. Therefore, further theoretical and experimental work is required on the problem of profiling arbitrary surface of revolution. In addition, there also exists the need to develop a correct and reliable model for loss calculation in the turbine design. In this regard, the data accumulation and investigation of secondary flow are very important. In order to increase the aerodynamic load and improve the adaptability to off-design conditions, it is also necessary to investigate the highly loaded transonic cascade with a large turning angle operating under off-design conditions. For all these, a new leap in the study of theories and a breakthrough in experimental techniques are essential.

Acknowledgment

The authors wish to thank Professor Wu Zhonghua, Doctor Li Genshen, Engineers Ji Guiming, Chen Jinbao, and Ai Xiaoyi for their cooperation and valuable comments and suggestions.

References

1 Wu, C. H., and Brown, C. A., "A Theory of the Direct and Inverse Problems of Compressible Flow Past Cascade of Arbitrary Airfoils," *Journal of Aeronautical Sciences*, Vol. 19, No. 3, Mar. 1952, pp. 183–196.

2 Chen, J. B., et al., "Some Works of the Turbomachinery Aerodynamic Research Group," Report, Apr. 1959.

3 Chen, N. X., "An Approximate Solution of Two-dimensional Turbine Cascades," Report, Apr. 1959.

4 Chen, N. X., "An Approximate Calculation of the Turbulent Boundary Layer with Adverse Pressure Gradient," paper presented at the 1st National Conference of Chinese Society of Aeronautics, 1965.

5 Qiang, K. F., "Systematic Analysis on Some Results from the Low Speed Plane Turbine Cascade Experimental Research," *Chinese Journal of Mechanical Engineering*, Vol. 11, No. 2, 1963.

6 Ai, X. Y., et al., "Readjustment of Flow Field from the Setting Chamber of Two-dimensional Turbine Cascade Wind Tunnel," Report, 1965–1967.

7 Qiang, K. F., and Guiming, Ji, "Simplified Measuring and Handling Method in Two-dimensional Cascade Experiments," Report, 1965–1967.

8 Todd, K. W., "Flow Characteristics in Steam Turbines," *Prace Instytutu Maszyn Przeplywowych, Zeszyt*, 14–16, 1963.

9 Ainley, D. G., and Mathieson, G. C. R., "An Examination of the Flow and Pressure Losses in Blade Rows of Axial-flow Turbines," ARC R & M No. 2891, 1951.

10 Dunham, J., "A Parametric Method of Turbine Blade Profile Design," ASME Paper 74-GT-119, 1974.

11 Zweifel, O., "The Spacing of Turbomachine Blading Especially with Large Angular Deflection," *Brown Boveri Review*, Vol. 32, No. 12, 1945.

12 Clebanov, A. G., and Mamajev, B. E., "Optimum Pitch of Turbine Cascades," *Thermal Energetics*, No. 10, 1969 (in Russian).

13 Stepanov, G. Yu., "Cascade Hydrodynamics of Turbomachinery," 1962 (in Russian).

14 Ji, G. M.., and Qiang, K. F., "Turbine Cascade Off-design Losses and Rational Selection of its Design Incidence," *Ship Engineering*, No. 1, 1979.

15 Qiang, K. F., and Waixing, Z., "Theoretical Calculation and Experimental Investigation of the Flow Past the Two-dimensional Turbine Cascades," *Shipbuilding of China*, No. 66, July 1979.

APPENDIX

We wish to make some supplementary remarks on the cascade tunnel and data measuring and reduction procedures. The working section size is 200 × 60 mm, with the blade height 60 mm. The flow field at the exit section of our turbine cascade tunnel was greatly improved as against the original configurations. With regard to data reduction procedure, a simplified method was developed for saving time. As the loss coefficient of the turbine cascade may be expressed as

$$\xi_p = \frac{M_2^2\phi}{M_2^2 t}$$

where

$$M_2\phi = \sqrt{\frac{2}{k-1}\left[\left(\frac{P^*_1}{P^*_2}\right)^{\frac{k-1}{k}} - 1\right]}$$

and

$$M_{2t} = \sqrt{\frac{2}{k-1}\left[\left(\frac{P_1}{P_2}\right)^{\frac{k-1}{k}} - 1\right]}$$

Downloaded 01 Jun 2010 to 171.66.16.62. Redistribution subject to ASME license or copyright; see http://www.asme.org/terms/Terms_Use.cfm

Originally, one had to calculate n values of local loss ξ_i within one blade pitch t and then get the mean loss

$$\xi_m = \frac{1}{t}\int_0^t \xi_i dt$$

After detailed study, we now calculate the mean pressure ratio instead:

$$\left(\frac{P^*_1}{P^*_2}\right)_m = \frac{1}{t}\int_0^t \left(\frac{P^*_1}{P^*_2}\right) dt$$

After doing this, we finally determine the mean loss coefficient

$$\xi_p = \frac{M_2^2 \phi}{M_2^2 t}$$

Two examples are given below to justify this simplified procedure:

example	inlet angle	Mach number	simplified	conventional	absolute error	relative error
	B_1^0	M_{2t}	$\bar{\xi}^*$	$\bar{\xi}$	$\Delta\xi$	$\delta_u = \frac{\bar{\xi}-\bar{\xi}^*}{\bar{\xi}}$
1	89	0.683	0.0417	0.0401	0.0016	−0.004
2	50	0.712	0.0851	0.0850	0.0001	−0.0012

In measuring the cascade exit angle, during traversing we now do not rotate the wedge-type combined pitot-yaw type probe about its axis. It is proved that by the correct handling of the yaw-angle calibration curve of the probe, the exit angle may be simply and accurately determined.

A new book entitled *Marine Gas Turbines, Aerothermodynamics of Axial-flow Turbomachinery (Theory, Design and Experimental Research)*, Vol. 1 (in Chinese) was recently published in December 1980 in our country. A detailed discussion about cascade measuring and testing methods is given in chapter 7 (pp. 297–328).

Finally, some remarks about the availability of the test data and suggested correlations. When we first began our work, we made comparative tests with several foreign cascades, the geometrical configuration and aerodynamic characteristics of which are all known to us. Great care was taken in the manufacturing of the cascades and the handling of the probe and the flow field of the tunnel. From time to time we repeatedly conducted tests with same cascades in order to ensure the reliability of the results. Detailed analysis suggested that the loss coefficient and exit angle may be determined, even in the extreme cases, with an accuracy within 1 percent and 1, respectively.

The Ainley's correlation given in equation (9) differs from our "new" correlation in two aspects: first, the former was largely based upon turbine rig tests rather than two-dimensional cascades; secondly, they used "conventional profile," the suction surface of which is somewhat straight near the exit region.

Downloaded 01 Jun 2010 to 171.66.16.62. Redistribution subject to ASME license or copyright; see http://www.asme.org/terms/Terms_Use.cfm

Interaction of Compressor Rotor Blade Wake With Wall Boundary Layer/Vortex in the End-Wall Region

B. Lakshminarayana
Director of Computational Fluid Dynamics Studies and Professor of Aerospace Engineering.

A. Ravindranath[1]

Department of Aerospace Engineering, The Pennsylvania State University, University Park, Penn. 16802

This paper reports the experimental study of the three-dimensional characteristics of the mean velocity of the rotor wake inside the annulus- and hub-wall boundary layers. The measurements were taken with a rotating three-sensor hot wire behind the rotor. This set of measurements probably represents the first set of comprehensive measurements taken inside the annulus- and hub-wall boundary layers. The wake was surveyed at several radial locations inside the boundary layer region and at several axial locations. Interaction of the wake with the annulus-wall boundary layer, secondary flow, tip-leakage flow, and the trailing vortex system results in slower decay and larger width of the wake. The presence of a strong vortex and its merger with the wake is also observed. The end-wall boundary layers and the secondary flow were found to have a substantial effect on both the decay characteristics and the profile of the wake. These and other measurements are reported and interpreted in this paper.

Introduction

Compressor rotor wake interaction with the tip leakage flow, secondary flow, scraping vortex, and the annulus and hub-wall boundary layers in the end-wall region probably represents the most complex and highly three-dimensional flow phenomena downstream of a compressor rotor. The resulting flow is extremely complex, as illustrated in Fig. 1, and is very difficult to model analytically or measure experimentally. All the investigations carried out hitherto on this phenomena are confined to a study of one of these flow effects in the absence of other effects. For example, the effects of leakage flow only are reported in reference [1], secondary flow only in reference [2], and rotor wake outside the end-wall region in references [3] and [4]. It is also known that these complex interactions near the tip and root of the blade will deviate the flow to a much larger extent as compared to the cascade prediction.

Lack of knowledge of the flow field downstream of compressor rotor blades, especially near the wall regions, has hampered the progress of compressor design and development, and prediction of losses, noise generation, surge and stall and three-dimensional flow into subsequent blade rows. It is known that the rotation-induced centrifugal and Coriolis forces generate spanwise flows inside the boundary layers, the magnitude of which depends on rotor-blade geometry, angular velocity of the blade, flow coefficient, etc. This

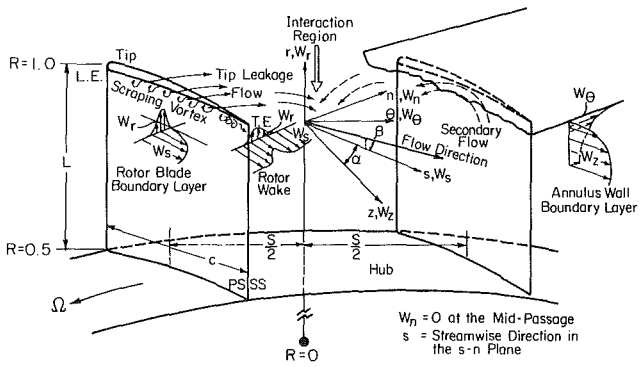

Fig. 1 Nature of flow in the tip region and notations used

spanwise migration of the flow results in a decrease of the boundary layer (and wake width) near the hub and an increase near the tip. These and other flow phenomena at the hub and tip of the rotor are known to contribute substantially to the overall losses in turbomachines. A thorough understanding of this flow is essential to improve the performance and efficiency of rotors.

It is thus essential to carry out a systematic study of the compressor rotor wake and end-wall flow for the prediction of the aerodynamic, acoustic and mechanical performance of compressors. Previous investigations have given an insight into the flow downstream of the rotor blade away from the end wall [3,4]. The present study was conducted near the hub and tip regions in the trailing-edge and near-wake regions of a moderately loaded compressor blade using a tri-axial hot-wire

[1] Presently, AiResearch Manufacturing Company, Phoenix, Ariz.

Contributed by the Gas Turbine Division and presented at the International Symposium on Applications of Fluids Mechanics and Heat Transfer to Energy and Environmental Problems, University of Patras, Greece, June 29–July 3, 1981. Manuscript received at ASME Headquarters April 1, 1981. Paper No. 81-Gr/GT-1.

Copyright © 1982 by ASME

Downloaded 01 Jun 2010 to 171.66.16.62. Redistribution subject to ASME license or copyright; see http://www.asme.org/terms/Terms_Use.cfm

probe in a noninertial frame of reference. The flow-field was surveyed very close to the trailing edge as well as far downstream.

To study the effect of secondary flows, tip-leakage flow and the extent of shear-layer interactions, the wake was surveyed inside the annulus- and hub-wall boundary layers and at several locations downstream. The wake was found to be substantially different in its profile and decay characteristics as compared to that found outside the end-wall regions. All three components of the mean velocity were found to be affected. One of the marked features for the wake inside the annulus-wall boundary-layer was spread of the wake. The secondary flow, tip-leakage flow and scraping vortex in the annulus-wall region made the wake width grow across the entire blade passage. These and other measurements are reported and interpreted in this paper.

Test Facility, Data Acquisition, and Procedure

All the measurements reported in this paper were performed using the axial-flow compressor facility located in the Turbomachinery Laboratory of The Pennsylvania State University. All the data were acquired with a tri-axial hot-wire probe rotating with the rotor. The study included the measurements of the mean velocities, turbulence intensities, Reynolds stresses and their decay characteristics downstream of the blade trailing-edge region. The data outside the end-wall regions are presented in references [4] and [5].

The Axial Flow Compressor Facility. A general description of the compressor stage is given by Smith [6], and a detailed discussion of the facility is given by Lakshminarayana [7]. Good peak efficiencies are exhibited by the rotor. The hub/annulus wall diameter ratio of the facility is 0.5, with the diameter of the annulus wall equal to 0.932 m. The inlet guide vane row, which consists of 45 blades, is followed by the 21-bladed rotor. The rotor is driven by a 37 kW variable-speed motor through a belt and pulley system. The rotor is followed by a stator vane row of 25 blades. Downstream of the stator is located a Joy axial flow fan with variable blade setting for the variation of pressure rise and mass flow. Operating conditions and rotor specifications are as follows: inlet velocity, 29.04 m/s; flow coefficient based on tip speed, 0.56; stage loading coefficient based on tip speed, 0.4864; speed of rotor, 1066 rpm; tip clearance, 0.25 to 0.3 cm. Blade element data at the tip are NASA 65 series; chord, 15.41 cm; spacing, 14.12 cm; maximum thickness, 5.10 percent of chord; stagger angle, 45.0 deg; and camber, 8 percent of chord. The blade profile near the tip section is given in references [6] and [7]. The blade element details of the rotor are given in Table 1.

Table 1 Rotor-blade element details

	Radius Ratio					
	Rotor					
Radius Ratio	0.5	0.6	0.7	0.8	0.9	1.0
Chord, cm	12.39	12.68	13.25	13.68	14.41	15.41
Blade Spacing, cm	6.91	8.35	9.80	11.24	12.68	14.12
C_{L_0}	1.35	1.45	1.5	1.5	1.48	1.32
Thickness (t/c x 100)	9.5	9.1	7.6	6.5	5.9	5.1
Chord Angle, (Stagger) Degrees	22.5	26.0	28.5	34.0	39.0	45.0
Air Outlet Angle, Degrees	19.5	13.5	16.0	19.5	26.0	33.5

Nomenclature

c = blade chord length
C_{l0} = lift coefficient of the corresponding isolated airfoil at zero angle of attack
L = $2(L_s + L_p)/S$ = sum of the characteristic length on the suction and pressure surfaces normalized by semi-blade spacing
L_s, L_p = wake width at half the depth on the suction and pressure surfaces of the rotor blade wake, respectively
PS = pressure side
p = static pressure
q = $(\overline{v_r'^2} + \overline{v_\theta'^2} + \overline{v_z'^2})/2$
R = radius ratio = (r/r_t)
Re = Reynolds number
r = local radius, radial direction
(r,θ,z) = rotating cylindrical coordinate system, radial, tangential, and axial coordinate directions (Fig. 1)
S = blade spacing
SS = suction side
(s,n,r) = natural coordinate system, streamwise, normal, and radial coordinate directions (Fig. 1)
U = blade speed
V = local absolute velocity
v' = fluctuating component of absolute velocity
W = total relative velocity
w = defect in relative velocity
w' = fluctuating component of relative velocity
Y = tangential distance
$(2Y/S)$ = tangential distance normalized by half the blade spacing ($Y = 0$ at wake center)
Z = axial distance from blade trailing-edge normalized by rotor blade chord at the tip
$\bar{\phi}$ = mass-averaged flow coefficient $(\bar{W}_z/U_t)$
$\bar{\psi}$ = mass-averaged stagnation pressure rise coefficient (normalized by $1/2\ U_t^2\rho$)
Ω = speed of rotation of rotor blade
$\bar{\eta}$ = rotor efficiency (Euler) = $\bar{\psi}/\bar{\psi}_{\text{Euler}}$
β = air outlet angle
$\tau_z, \tau_r, \tau_\theta$ = normalized turbulence intensities in the axial, radial, and tangential directions, respectively $(\sqrt{\overline{w_z'^2}}/W, \sqrt{\overline{w_r'^2}}/W, \sqrt{\overline{w_\theta'^2}}/W)$
τ_{sn}, τ_{rn} = normalized streamwise and radial Reynolds stress respectively $(\overline{w_s' w_n'}/W^2, \overline{w_r' w_n'}/W^2)$

Subscripts

c = value at wake center
m,max = maximum value in the wake
0 = value at wake edge/free-stream value
p = pressure side
(r,θ,z) = values in the radial, tangential, and axial coordinate directions, respectively
(s,n,r) = values in the streamwise, normal, and radial coordinate directions, respectively
s = suction side, blade spacing
t = value at the rotor tip, stagnation condition

Superscript

$\bar{}$ = average value

Downloaded 01 Jun 2010 to 171.66.16.62. Redistribution subject to ASME license or copyright; see http://www.asme.org/terms/Terms_Use.cfm

Rotating Probe Traverse Mechanism and Data Acquisition System. The rotating-probe traverse mechanism and the instrumentation system used in these rotor wake measurements are described in detail in references [4] and [7]. The main feature of the rotating-probe traverse gear mechanism is an SLO-SYN motor of 225 in-oz torque driving a 3.81×10^{-2} m (1.5 in.) dia shaft through a planetary reduction gear train. The gear train steps down (1.8 deg/step) the circumferential stepping from 1.8 deg/step to 0.09 deg/step. The probe holder, stepping motor, and probe are mounted inside the rotating hub of the machine. The probe, which is located behind the blade row, traverses in a slot in the hub. The motor is powered and controlled by a stationary traverse indexing device through an eight-channel brush slip-ring unit. The traverse unit and probe are locked, except when indexed. Though the circumferential traverse can be accomplished when the rotor is rotating, the radial and axial motions have to be accomplished manually when the rotor is stationary.

A tri-axial hot-wire probe, similar to that used in references [3] and [4], was employed for all velocity measurements reported in this paper. The probe has been found to measure the three components of velocity and turbulence intensities accurately. The probe sensors were built out of tungsten wire and had a length-to-diameter ratio of 270. The probe calibrations are corrected for the variations of temperature and aging of the wire. The signals from the rotating hot wire, rotating with the rotor, were taken through a ten-channel slip-ring unit to a stationary data-processing system similar to the one employed in references [4] and [7]. The choice of the instrumentation was made such that the raw data from the experiment could be used directly in the data-processing program developed by Gorton and Lakshminarayana [8]. Consistent with the assumptions made in reference [8], a streamline coordinate system was chosen and the hot-wire axis was aligned along the blade stagger. The data was then transformed to the r-θ-z coordinate system where the r-direction is in the direction of the machine radius, z in the axial direction, and θ in the tangential direction, as illustrated in Fig. 1. The stresses were evaluated in the s,n,r system, with τ_{sn} representing the streamwise component and τ_{rn} representing the radial component.

The measurements were taken at several radial and axial stations, and are tabulated in Table 2. The data near the mid-radius (R = 0.6581, 0.7297, 0.7973) are presented in references [4] and [5]. The data near the hub wall (R = 0.5676) and inside the annulus-wall boundary layer (R = 0.9324, 0.9595, 0.973) are presented and interpreted in this paper.

Mean Velocity and Turbulence Profiles Near the Hub Wall

Mean Velocity Profiles. The rotor wake was measured very near the hub at R = 0.5676 (3 cm from the hub). The velocity data presented here are relative velocities (axial, tangential and radial components as indicated in Fig. 1) normalized by the corresponding free stream axial velocity (W_{z0}). Near the hub, the interaction between the secondary flow, hub-wall boundary layer and the blade boundary layer results in a complex three-dimensional flow, characterized often by a separated or "wall stall" region in the corner formed by the hub and the blade.

The axial, tangential, and radial components of mean velocity profiles across the passage at various axial locations are shown in Fig. 2. The wake near the hub-wall region exhibits characteristics which are quite different from those in the annulus-wall region described later. The nature of the secondary flow is such that the wake shows a thicker suction

Table 2 Measurement stations

R	Chord (m)	Axial Location From Trailing Edge Z					
0.973	0.154		0.083	0.125	0.344	0.542	
0.9595	0.150	0.0104	0.0417	0.124	0.240	0.458	
0.9324	0.147	0.0104	0.0412	0.125	0.250	0.458	
0.8615	0.141	0.0104	0.0417	0.125	0.208	0.417	0.625
0.7973	0.137		0.0312	0.146	0.229	0.375	0.563
0.7297	0.134	0.0104	0.0208	0.135	0.219	0.354	0.5313
0.6581	0.130			0.114	0.240	0.458	0.6875
0.5676	0.128			0.125	0.208	0.458	0.656

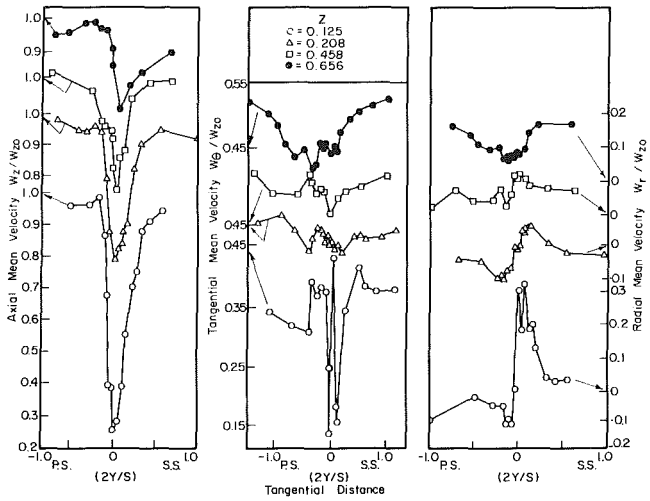

Fig. 2 Axial, tangential and radial velocity profiles near hub at R = 0.5676

surface boundary layer. The defect in the axial mean velocity is far more pronounced near the hub than it is at either the mid-span (reference [4]) or the annulus-wall region and the decay of the defect near the hub is also slower than that of wakes in other regions. An initial axial velocity defect of 0.7 at Z = 0.125 decreases to 0.25 at Z = 0.656, which is slower than those at other radial locations.

The tangential velocity profile shown in Fig. 2 shows appreciable departure from those observed at near mid-span [4]. A defect of 0.3 at Z = 0.125 drops to 0.07 at 0.2 chords downstream, and then increases beyond 0.3 chords. This value is maintained even at 0.65 chords downstream of the blade. This strange behavior can be attributed to the secondary vortex formation downstream of the blade. The tangential velocity profile at Z = 0.125 shows a peak near the wake center, with a minimum value slightly away from the wake center on either side of the wake. This seems to indicate the presence of secondary vortices inside the wake. These vortices, if they have a core, will induce linearly varying tangential velocity profiles on either side of its center, resulting in peak values (in opposite directions) on either side of the vortex center. This hypothesis is in agreement with the measured tangential velocity distribution shown in Fig. 2. As the flow proceeds downstream, the vortex tends to entrain fluid and become stronger. This may account for the increase in the velocity defect as the flow proceeds downstream, as shown in Fig. 2.

The radial velocity distribution shown in Fig. 2 clearly reveals the presence of the secondary vortex. The radial

Downloaded 01 Jun 2010 to 171.66.16.62. Redistribution subject to ASME license or copyright; see http://www.asme.org/terms/Terms_Use.cfm

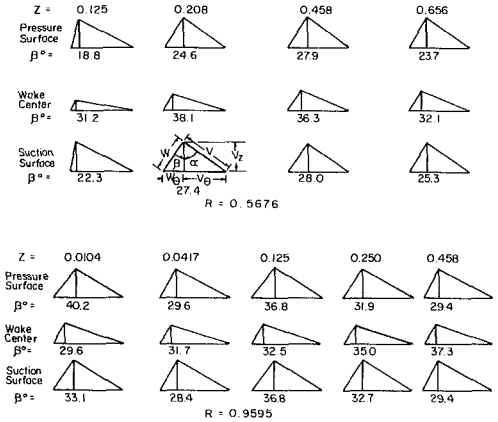

Fig. 3 Velocity triangles at various axial locations for R = 0.5676, 0.9595

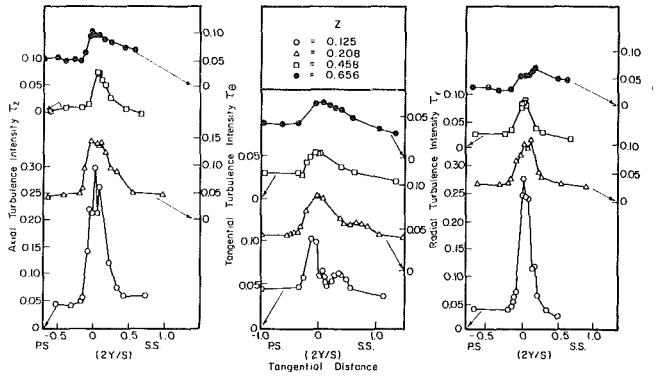

Fig. 4 Axial, tangential and radial turbulence intensity profiles near hub at R = 0.5676

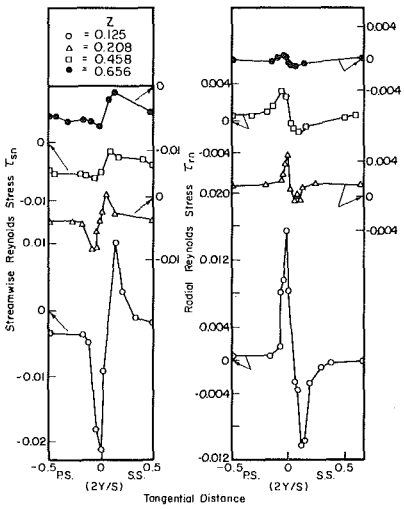

Fig. 5 Streamwise and radial stress profiles at R = 0.5676

velocity due to the wake is outward on both sides of the wake in a rotor, while that caused by the secondary vortex is outward on the suction side and inward on the pressure side of the wake. This results in very high radial outward velocities on the suction side and lower radial outward (or inward) velocities on the pressure side, depending on the extent of the secondary flow. The radial velocity distribution shown in Fig. 2 clearly reveals that the secondary vortex is very strong, causing an inward radial velocity on the pressure side. The vortex seems to persist far downstream. Even at Z = 0.458 the radial velocity distribution shows the dominance of the vortex. Radially outward velocity was observed at all tangential locations at Z = 0.656.

The velocity triangles at the wake center and on the pressure and suction sides at various axial locations are shown in Fig. 3. The outlet relative air angle increases continuously until Z = 0.458, beyond which it decreases. There is a large variation in air outlet angle (β) across the wake, with the maximum value occurring at the wake center at all the axial locations. The absolute tangential velocity decreases continuously downstream of the blade at all the tangential locations.

Turbulence Intensity and Stress. The turbulence intensity profiles at R = 0.5676 are shown in Fig. 4. The turbulence intensities are normalized by the local resultant velocity. At Z = 0.125, axial and radial components of intensities are very high, with peak values of 25 percent near the wake center. The intensities decay very rapidly downstream. The free stream turbulent intensity is nearly isotropic, with a value of approximately 5 percent for all the components. This is higher than the free stream intensities measured near the mid-radius [4].

The decay of the wake turbulence intensity is slower compared to those at locations away from the wall. An axial turbulence intensity of 25 percent at Z = 0.125 has decayed only to 10 percent at Z = 0.656. The corresponding values near mid-span are 60 and 5 percent, respectively [4]. This slower decay reinforces the earlier argument that the presence of the secondary vortex and its growth downstream influence the flow development substantially, even though the wake is decaying. The axial turbulence intensities are of the same order of magnitude as the radial component of intensities. In most nonrotating shear flows (boundary layers and wakes) the transverse component of turbulence intensity is usually smaller than the streamwise component. This clearly reveals the effect of rotation which has a substantial influence on the turbulence quantities, especially the radial component. These data agree with the qualitative predictions of Lakshminarayana and Reynolds [9]. The radial component of turbulence intensity decays faster than the axial component, and has nearly the same value at Z = 0.656. This clearly reveals the vanishing effects of rotation far downstream.

The tangential component of intensities inside the wake at R = 0.5676 is lower and decays more slowly than the axial and the radial components.

The streamwise (τ_{sn}) and radial stresses (τ_{rn}) are shown in Fig. 5. The stresses are nearly zero at the wake center, and the peak values occur a short distance away from it. The usual positive and negative stresses are observed on either side of the wake center. The streamwise stresses decay rapidly until R = 0.458, beyond which there is a slight increase in their value. One of the interesting observations is that the radial component of turbulent stress is of the same order of magnitude as the streamwise stress, a consequence of the effect of the Coriolis force as explained in reference [9].

Mean Velocity and Turbulence Profiles Inside the Annulus-Wall Boundary Layer

Rotating hot-wire measurements were carried out inside the annulus-wall boundary layer to study the effect of this boundary layer on the wake structure, such as the wake profile and the decay. The velocity data presented here are relative velocities and are normalized by the corresponding free stream axial velocity. The data at the radii R = 0.973, 0.9595 and 0.9324 are given here. The first two radii are inside the annulus-wall boundary layer (Fig. 6), while the last radius represents the data near the edge of that layer. The profiles of

Downloaded 01 Jun 2010 to 171.66.16.62. Redistribution subject to ASME license or copyright; see http://www.asme.org/terms/Terms_Use.cfm

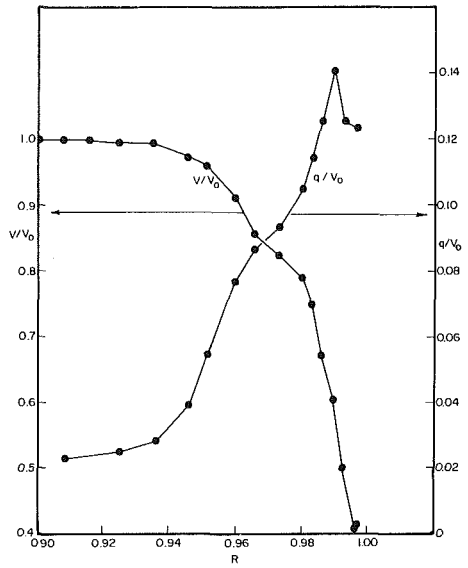

Fig. 6 Absolute velocity and turbulence energy profile in the annulus-wall boundary layer upstream of the rotor

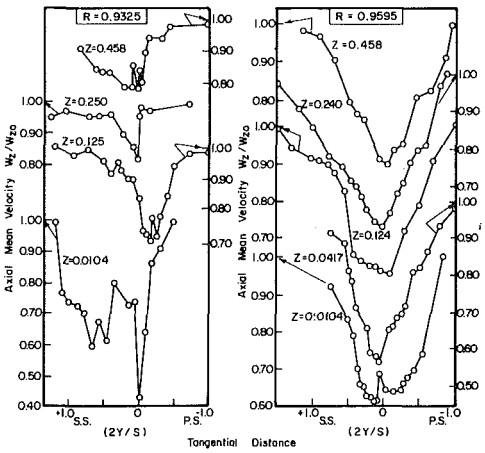

Fig. 7 Axial velocity profile inside the annulus-wall boundary layer at $R = 0.9324, 0.9595$

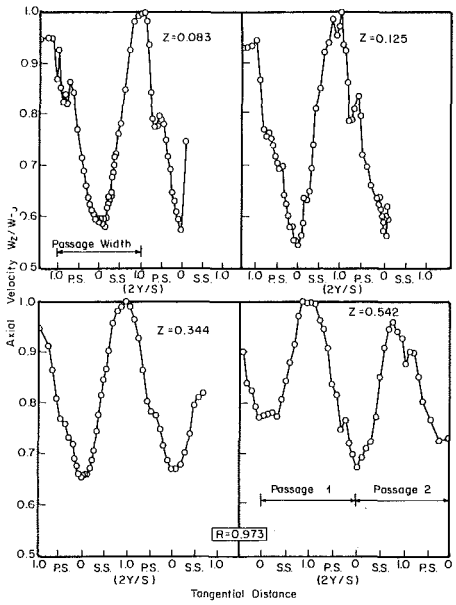

Fig. 8 Axial velocity profile inside the annulus-wall boundary layer at $R = 0.973$

the absolute velocity and the turbulent energy across the annulus-wall boundary layer upstream of the rotor are shown in Fig. 6. The unconventional profile shape is caused by the three-dimensionality (with both streamwise and cross flows). The turbulence intensities are quite high near the wall.

Since no measurements or data are available to predict the effect of the end-wall boundary layers on the wake, it is hoped that the data presented in this paper will be useful in the future development of theoretical analysis on this effect. Additional data derived from a stationary three-sensor probe is given in reference [10].

Axial Velocity Profile. As reported earlier, all the velocities are relative velocities and are normalized by the corresponding axial velocity in the free stream. The velocities are in the r-θ-z coordinate system (Fig. 1).

Variation of the axial velocity across the wake at various radial and downstream locations is shown in Fig. 7 for $R = 0.9324$ and 0.9595, and in Fig. 8 for $R = 0.973$. The data at $R = 0.973$ include more than one passage. The tangential distances are normalized by the semi-blade spacing ($2Y/s$). It is clear that the profiles are asymmetrical about the wake center, indicating the differential growth of the boundary layers on the two surfaces of the blade. The wake in the annulus-wall region exhibits complex behavior. At $Z = 0.0104$ and $R = 0.9595$, the velocity defect is 0.34, which initially increases to 0.40 at $Z = 0.0417$, beyond which it decreases. This characteristic may be attributed to the presence of the tip vortices, secondary flow, as well as the annulus-wall boundary layer in this region. As the vortex grows in strength immediately behind the trailing edge, the defect in the wake increases. Beyond $Z = 0.0417$, the strength of the vortex decreases, and consequently, the usual wake behavior is seen. It can also be observed that the decay of the mean velocity defect as well as the profile is different at each radii, indicating that the radial variation of wake properties are affected by the varying contributions from the blade loading, secondary flow, tip vortex, and the end-wall boundary layer. The wakes in the annulus-wall region ($R = 0.9595$, 0.973) cover one complete passage, indicating fully developed flow in this region. It is also clear that the secondary flow and the tip-leakage flows that exist at the tip of the blades not only distort the wake profile but also slow down the decay rate.

The existence of a tip vortex at $R = 0.9324$ is evident from Fig. 7. A Second dip in the velocity profile at $Z = 0.0104$ at $2Y/s = 0.5$ is a clear indication of the presence of the leakage vortex, which is located near the mid-pasage. This is caused by the relative motion between the blade and the wall. Even though the leakage vortex formation occurs very near the tip, this vortex tends to move inward as the trailing edge is approached. Hence, the leakage vortex is observed only at $R = 0.9324$ and not at higher radii. Furthermore, the vortex decays rapidly, and the interaction between the wake and the vortex results in a very complex wake profile, as can be seen at $R = 0.9324$.

The wake at the radius $R = 0.973$ (Fig. 8), which represents the one closest to the annulus wall, seems to be far more well-behaved compared to the ones at the lower radii. This implies that the boundary layer and the wake are not perturbed by the secondary flow and the leakage vortex in this region. The annulus-wall boundary has a far more pronounced effect on the wake at this location than do the leakage and the secondary flows. This is very clearly seen in the decay of the wake, which shows a much slower decay rate compared to the ones at the lower radii. The measurements at this radial location were carried out in more than one passage. The plots in Fig. 8 indicate that the wakes in adjoining passages are almost identical very near the trailing edge. Appreciable

Downloaded 01 Jun 2010 to 171.66.16.62. Redistribution subject to ASME license or copyright; see http://www.asme.org/terms/Terms_Use.cfm

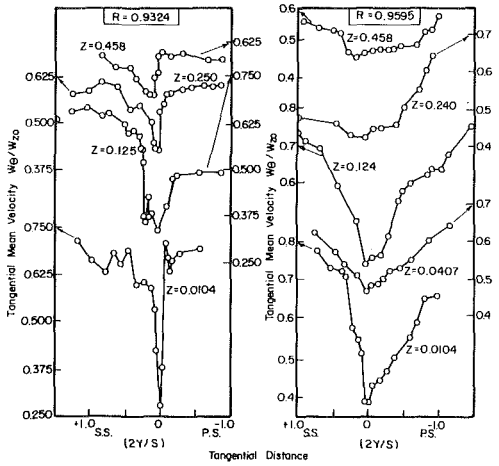

Fig. 9 Tangential velocity profile inside the annulus-wall boundary layer at R = 0.9324, 0.9595

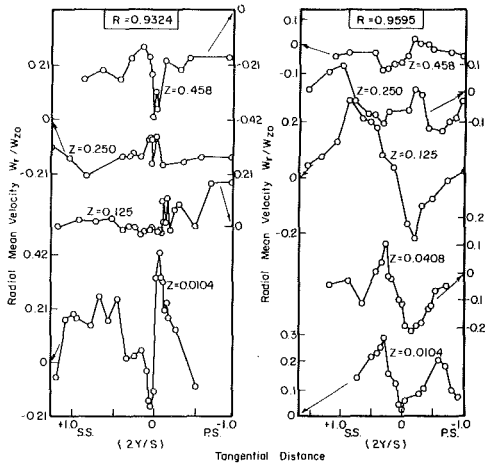

Fig. 11 Radial velocity profile inside the annulus-wall boundary layer at R = 0.9324, 0.9595

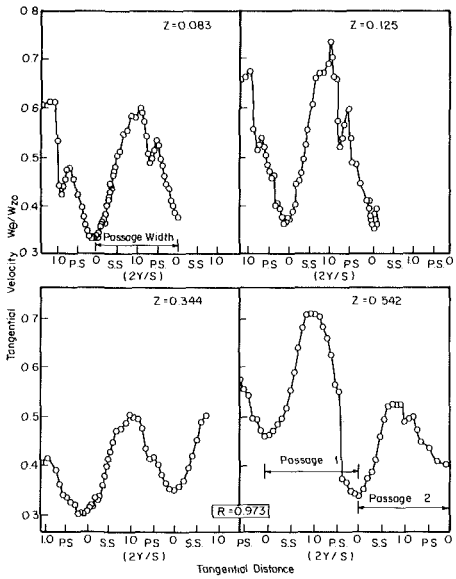

Fig. 10 Tangential velocity profile inside the annulus-wall boundary layer at R = 0.973

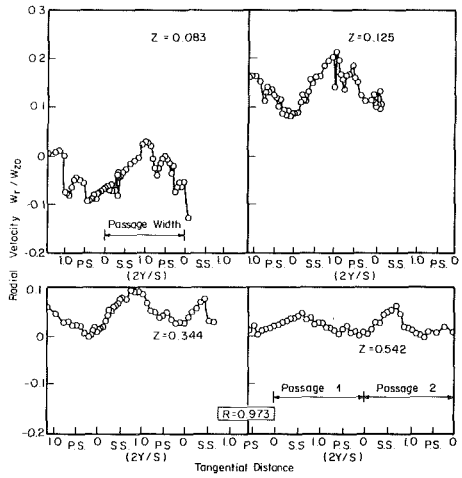

Fig. 12 Radial velocity profile inside the annulus-wall boundary layer at R = 0.973

differences exist between the adjoining wakes only far downstream (Z = 0.542). This indicates that the wakes of adjoining blades decay differently. Another interesting phenomenon observed in Fig. 8 is probably the presence of the scraping vortex. A small dip in the profile near the pressure surface indicates that this dip may have been caused by the scraping vortex near the pressure surface, shown schematically in Fig. 1. This vortex seems to dissipate quickly as the flow proceeds downstream. The wake width covers the entire passage at this location.

Tangential Velocity Profiles. The variation of the tangential mean velocity across the wake at various downstream and radial locations is shown in Figs. 9 and 10 for R = 0.9324, 0.9525 and R = 0.973, respectively. The profiles are very similar to the axial velocity profiles described earlier; hence, the interpretation will be limited only to new features.

The presence of the leakage vortex is evident from the wake profile at Z = 0.0104, R = 0.9324 (Fig. 9). The leakage flow is such as to cause flow underturning (increased relative tangential velocity) in the region. This is evidently the case near the mid-passage at this location. Hence, the "hump" in the velocity profile at Z = 0.0104, R = 0.9324, $2Y/s \approx 0.5$ is caused by the leakage vortex. This confirms the earlier conclusion with regard to the presence of the leakage vortex. *The vortex diffuses or interacts rapidly with the wake as the* flow proceeds downstream, as indicated in Fig. 9. The free stream value of the tangential velocity decrease downstream for R = 0.9324, while the trend for R = 0.9595 and R = 0.973 is not clear. The wake at R = 0.9595, 0.973 covers the entire passage. Substantial differences exist between the wake on the pressure and suction sides at these locations. At R = 0.973, the wakes are identical in adjoining passages near the trailing edge. This trend persists only up to Z = 0.125, beyond which substantial differences are observed between the wakes of the adjoining passages. The presence of the scraping vortex can be seen in Fig. 10 at Z = 0.083.

Radial Velocity Profiles. Radial velocity profiles at various axial locations for the wakes inside the annulus- wall boundary layer region are shown in Fig. 11 for R = 0.9324 and 0.9595 and in Fig. 12 for R = 0.973. It is clear that the radial velocity profiles are quite unique in the trailing-edge region for all the radii under consideration. Also, the radial velocities show trends indicating their strong dependence on the tip vortex. It is known that the maximum radial velocities occur slightly away from the blade surfaces, and that they reach zero magnitude on the surface of the blade. Radial velocities arise due to the imbalance between the radial

Downloaded 01 Jun 2010 to 171.66.16.62. Redistribution subject to ASME license or copyright; see http://www.asme.org/terms/Terms_Use.cfm

pressure gradients and the centrifugal forces, and are strongly dependent on the trailing vortex system, as indicated in reference [4]. Near the end walls, they are also influencd by the constraints imposed by the hub and the annulus walls and presence of the vortex system.

The radial velocities near the edge of the annulus-wall boundary layer at $R = 0.9324$ (Fig. 11) shows trends similar to those observed in the trailing-edge region at lower radii, except that the spread of the wake is considerable. The leakage flow induces radially outward velocity on the pressure side and inward velocity on the suction side, while the wake flow will have outward flow on either side. Thus, the radial outward velocity gets amplified on the pressure side and attenuated on the suction side. This is consistent with the measured data shown in Fig. 11. It is interesting to note that an opposite trend is observed near the hub (Fig. 2), where the secondary flow is the dominant phenomenon. The tip vortex initially grows in strength as it travels downstream before it starts to dissipate, as seen in Fig. 11 for $R = 0.9595$ and $Z = 0.125$. Very complex flow phenomena are evident from these radial velocity profiles inside the annulus-wall boundary layers, where the secondary flow, tip-leakage flow and annulus-wall boundary layer interact.

The large radial component of the velocities indicate the highly three-dimensional nature of the rotor wake. The radially inward or outward flow in the wake will result in an increased dissipation of energy. The spread of the radial velocity profile downstream of the blade is not as marked as in the case of the axial or the tangential component of velocity. Since both the wake and the vortices are decaying very near the trailing edge, it is to be expected that the decay of the radial velocity would be much more rapid than the axial and the tangential velocity components. In the far wake region, the decay rates of all three components of velocity are nearly the same.

At $R = 0.9324$ (Fig. 11), the blade wake is thin, and the wake and the vortex coexist independently near the trailing edge and interact rapidly to provide a complex flow pattern beyond $Z = 0.125$. Radially inward flow is observed at $Z = 0.458$ and $R = 0.9324$.

At $R = 0.9595$ (Fig. 11), radially outward flow occurs on either side of the wake center at $Z = 0.0104$. This trend rapidly changes at $Z = 0.0408$, providing inward flow near the suction side. This may indicate the roll up of the leakage vortex near the middle of the passage. Increased radial velocities and the type of radial velocity distribution measured at $Z = 0.125$, $R = 0.9595$ seem to indicate that the leakage vortex is located near the mid-passage, with rotation in the clockwise direction. This appears to confirm the presence of the leakage vortex and absence of the secondary vortex in this region. The vortex diffuses rapidly, providing very small radial velocities at $Z = 0.458$.

The radial velocities are generally low very near the tip ($R = 0.973$, Fig. 12). The flow is inward very near the trailing edge at $R = 0.973$, while $Z = 0.125$ and beyond, radially outward flow exists. The magnitude of radial velocity is generally lower than at other radii. Radial velocities differ from passage to passage as indicated at $Z = 0.542$ in Fig. 12. Formation and growth of the vortex in combination with the wake flow will result in the observed phenomena.

The velocity triangles at $R = 0.9595$ for several axial and three typical tangential locations are shown in Fig. 3. The outlet air angle increases continuously from the trailing-edge region to far downstream at the wake center, a trend very similar to that observed in the hub region. However, the angles near the edge of the wake decrease continuously, a trend opposite to those observed near the hub.

Axial and Tangential Turbulence Intensity Profiles. The axial turbulence intensity profiles for the wakes inside the annulus wall boundary layer are shown in Fig. 13 for $R = 0.9324$ and 0.9595. The axial turbulence intensities are normalized by the local resultant velocity (W). These plots indicate a very complex turbulence structure in the trailing-edge region. The effect of interaction of the tip-leakage flow and the wake is clear from Fig. 13. Free stream turbulence intensity is much higher than that which exists outside this region (7 to 10 percent as compared to 3 to 5 percent outside the annulus-wall boundary layer). There are also two very distinct peaks in the turbulent intensity profiles. One of these peaks is believed to have been caused by the tip clearance flow and the associated tip vortex, and the other peak is due to the wake. Peak intensity reaches nearly 90 percent at the trailing-edge locations.[2] As the leakage vortex travels downstream, it diffuses and dissipates very rapidly; consequently, the tur-

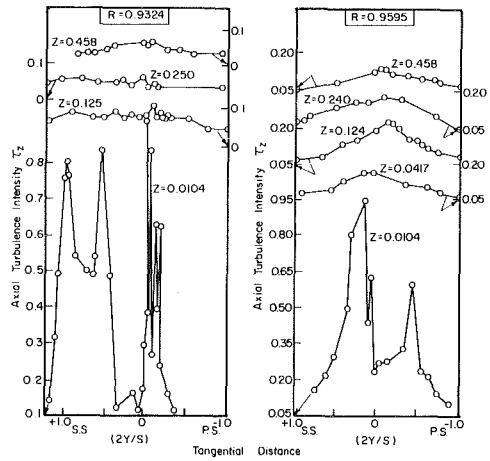

Fig. 13 Axial turbulence intensity profile at $R = 0.9324, 0.9595$

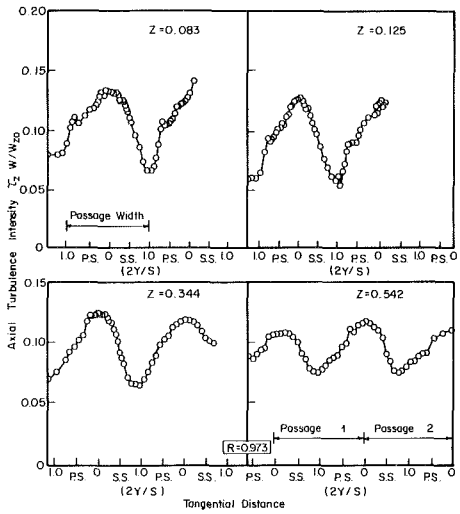

Fig. 14 Axial turbulence intensity profile at $R = 0.973$

[2] Large intensities near the trailing edge, apparent in Figs. 13, 15 and 16, are caused by the fact that the intensities are normalized by the local velocities, which are very small. Substantial error due to the vicinity of the trailing edge (aerodynamic interference with the probe) and the presence of oscillating vortices may be present in the data. The turbulence would then include not only random fluctuations, but also periodic fluctuations in mean velocity due to the movement of the vortices. This reasoning is only speculative and is not supported by detailed measurements near the trailing edge. Hence, at least for now, the turbulence intensities near the trailing edge (first station) should be viewed with caution. The upper limit of the frequency response of the probe and the associated electronics is nearly 10 KHz.

Downloaded 01 Jun 2010 to 171.66.16.62. Redistribution subject to ASME license or copyright; see http://www.asme.org/terms/Terms_Use.cfm

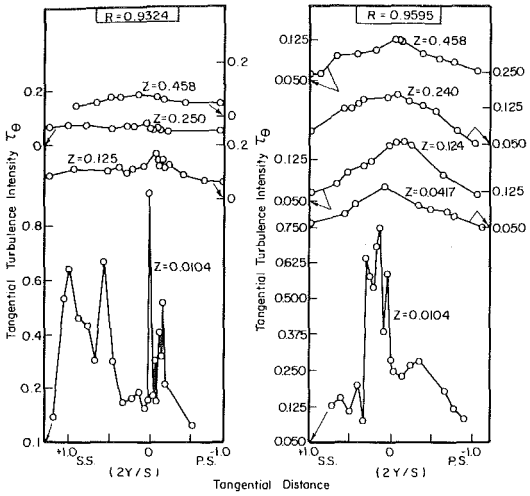

Fig. 15 Tangential turbulence intensity profile at R = 0.9324, 0.9595

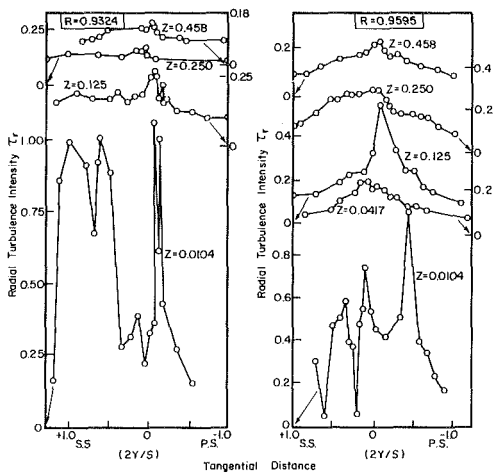

Fig. 16 Radial turbulence intensity profile at R = 0.9324, 0.9595

bulence intensity contributed by it to the overall rotor wake also decays rapidly. For R = 0.9595, a 90 percent peak intensity at Z = 0.0104 drops off to 15 percent at Z = 0.0417. The decay beyond this is rather gradual and the free stream intensity remains high at the value of above 5 percent even at the far downstream location of Z = 0.458. Not only is the turbulence intensity high, but it also extends to most of the passage, which is attributed to the tip vortex arising due to the clearance flow. The interpretation of the decay characteristics of the turbulence intensity in this region is difficult, as we are dealing with the decay of the turbulence as well as the vortex. In the trailing-edge region, the decay is extremely rapid, but becomes very gradual in the far-wake region, with the free stream values of approximately 5 percent. It is interesting to note that the presence of the tip vortex is observed both at R = 0.9595 and R = 0.9324, even though the mean velocity profiles showed such a vortex only at R = 0.9324. It is quite likely that the vortex, which has a core, extends across the entire boundary layer, with its edge located near the radius R = 0.9595. The dip in the intensity profile for the vortex seems to confirm the presence of a core, where the turbulence is suppressed, and an outer region, where the intensities are high.

Very near the tip at R = 0.973, shown in Fig. 14, the axial turbulence intensities exhibit smaller peaks, but the intensities are uniformly high across the entire passage, reaching a free stream intensity of approximately 7 to 8 percent. The adjoining passages seem to have an almost identical distribution of turbulence intensities. The presence of the scraping vortex at Z = 0.083 can also be seen in this figure. It should be noticed that the values of the turbulence intensities in this plot are based on the free stream axial velocity; hence, very high peak intensities such as those observed in Fig. 13 are absent. Furthermore, the closest station at R = 0.973 location is Z = 0.083, where the turbulence intensities are likely to be much lower due to the rapid decay indicated in Fig. 13.

Tangential turbulence intensity profiles are shown plotted in Fig. 15 for R = 0.9324, 0.9595. In these plots, the ordinate represents the tangential turbulence intensity normalized by the local resultant velocity, and the abscissa represents the tangential distance normalized by half the blade spacing. The tangential turbulence intensity profiles are very similar to the axial intensity profiles, with small differences in magnitude. Hence, the interpretation will be limited only to new features. Two distinct profiles for both the wake and the vortex are observed. The tangential turbulence intensity profile for the vortex at R = 0.9324 seems to contain a dip, where the core of the vortex is located, and the peak intensities occur in the outer region. The tangential intensities decay very rapidly, as is the case for the axial intensity. The free stream values vary from 7 to 10 percent. The tangential turbulence intensity profile at R = 0.973 (not included in the paper) is found to be very similar to the axial intensity plotted in Fig. 14.

Radial Turbulence Intensity Profiles. Radial turbulence intensity profiles at the radii R = 0.9324, 0.9595 are shown in Fig. 16. The abscissa in these figures represents the tangential distance normalized by the semi-blade spacing, while the ordinate represents the radial turbulence intensity normalized by the local resultant relative velocity.

The dip that was observed in the axial turbulence intensity profile is also seen in the profile of radial turbulence intensity. At R = 0.9595, another interesting feature is noted; namely, that the intensities decay rather rapidly with a subsequent increase in the peak intensities. Beyond Z = 0.25, the peak values decay very slowly to a value of 0.2 at Z = 0.458. This shows the effect of the leakage vortex on the radial turbulence intensity. In general, the radial turbulence intensities are very high at these locations across the entire passage. The presence of the vortex near the tip is clearly seen in Fig. 16. There are two distinct profiles, one of which is due to the vortex and the other due to the wake.

At Z = 0.125, the peak radial turbulence intensities are 25 and 50 percent at R = 0.9324 and 0.9595, respectively, and the corresponding axial turbulence intensities are 10 percent and 20 percent, respectively. Even the free stream radial turbulence intensities are higher than those of the corresponding axial and turbulence intensities. The radial turbulence intensities are normally influenced by the Coriolis and centrifugal forces arising due to the rotation. This is very clearly seen for the wake at the outer radius (Fig. 16). The radial turbulence intensities at this location are higher than the axial and tangential intensities. Lakshminarayana and Reynolds [9] have provided a theoretical explanation for the redistribution of energy between the three components of fluctuating velocities, and have shown that the effect of the Coriolis force is to redistribute the energy such that $\tau_r \geq \tau_z$, τ_θ in a compressor. This trend is generally true in the present case, with the radial intensities being higher or of the same order of magnitude as the axial and tangential components. However, in a non-rotating case τ_θ, $\tau_z \geq \tau_r$. It is also seen that beyond half-a-chord downstream of the blade, the turbulence becomes isotropic, with all three components of intensities having nearly the same value.

The wake region seems to be very thin compared to the vortex region. The vortex seems to cover almost half of the blade passage near the tip region at R = 0.9324, and 25 percent of the passage at R = 0.9595.

Downloaded 01 Jun 2010 to 171.66.16.62. Redistribution subject to ASME license or copyright; see http://www.asme.org/terms/Terms_Use.cfm

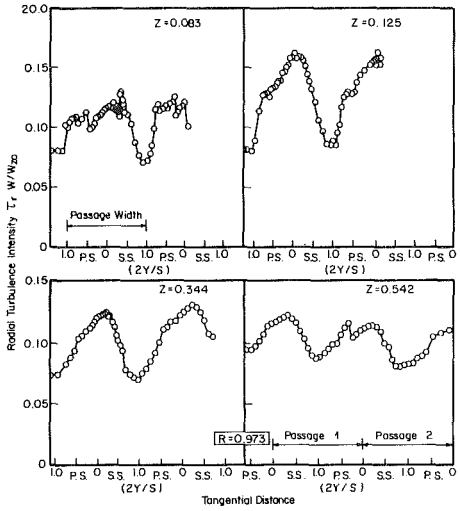

Fig. 17 Radial turbulence intensity profile at $R = 0.973$

The radial turbulence intensity profiles at $R = 0.973$ are shown plotted in Fig. 17. The intensities in this plot are normalized by the free stream axial velocity. The radial component of turbulence intensities at this radius is generally of the same order of magnitude as the axial turbulence intensity (Fig. 14). The effect of rotation on the redistribution of the turbulence energy is not as severe as those at lower radii, and the presence of the leakage vortex is not noticeable. The intensities are high across the entire passage, with free stream values of 7 to 8 percent. This seems to indicate that the turbulence is nearly isotropic in this region (compare Figs. 14 and 17).

Turbulent Shear Stress Profiles. The streamwise (τ_{sn}) and radial (τ_{nr}) components of the Reynolds stresses are shown in Figs. 18 and 19, respectively. Only the data in the natural coordinates are given, as they are the ones of practical interest. All Reynolds stresses given here are normalized by the local dynamic pressure, based on total relative velocity. The tangential distances are normalized by the semi-blade spacing. The turbulent stresses are very small in the free stream and increase in magnitude near the wake center, where they reach peak values. This type of trend is to be expected as the positive and negative stress distribution results from opposite gradients of streamwise mean velocity on either side of the

The variation of the streamwise stress, τ_{sn}, across the wake is shown plotted in Fig. 18 for the radii $R = 0.9324$, 0.9595, which are inside the annulus-wall boundary layer. These plots show the expected reversal of stress at the wake center. The positive and negative stress distribution results from opposite gradients of streamwise mean velocity on either side of the wake center. The profiles are asymmetrical about the wake center, with peak stresses near the pressure surface being lower than the corresponding values near the suction surface at $R = 0.9324$. The stresses are high in the region of the vortex at this radial location. The profiles are asymmetric about the wake center, and the decay of the stresses, unlike the wakes outside the end-wall boundary layers, are rather slow. The dominant effect of the leakage vortex can be seen in Fig. 18. The vortex dissipates rapidly very close to the trailing edge, and the contribution to the Reynolds stresses from this vortex also diminishes rapidly.

The radial components of stresses are shown plotted in Fig. 19. The peak radial stresses near the wake center are much higher than the streamwise stress at $R = 0.9324$. These radial stresses are of the same order of magnitude or higher than the streamwise stress at $R = 0.9595$, even though the radial velocities are much smaller than the streamwise velocities at

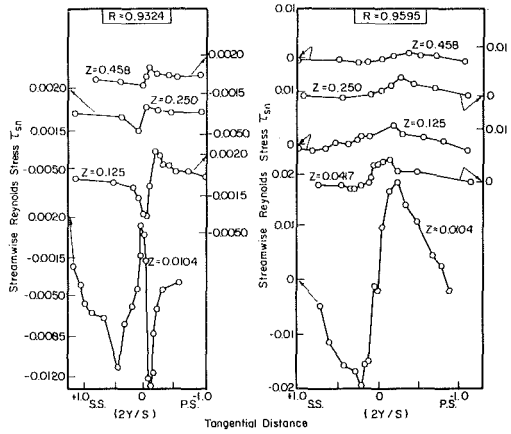

Fig. 18 Streamwise stress profile at $R = 0.9324, 0.9595$

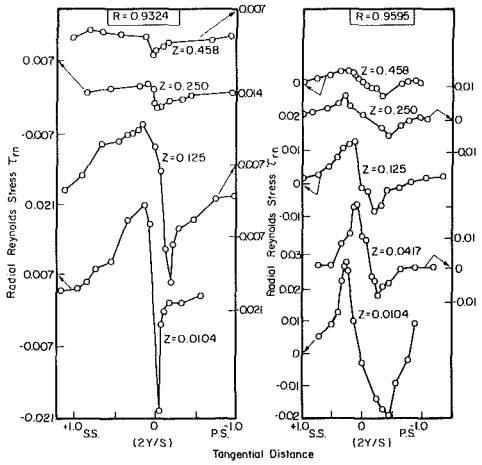

Fig. 19 Radial stress profile at $R = 0.973$

this location. This phenomenon can be attributed to the effects of rotation analyzed in reference [9]. The decay of the radial stress between $Z = 0.0104$ and 0.125 at $R = 0.9324$ is much slower than the corresponding decay in the streamwise component, which is probably caused by the development of the leakage vortex, whose strength increases in the trailing-edge region. The radial components of stress decays slower than the corresponding streamwise component.

Variation of Wake Defect, Maximum Turbulence Intensities and Wake Width

The major characterisitc features of the wake are the velocity of the defect at the center of the wake, maximum turbulence intensities and the wake width. The decay characteristics as well as the radial variation of these properties in the wake near the hub and annulus-wall regions are discussed in this section. Such data are extremely useful in the prediction of the annulus-wall boundary layer, such as that carried out by Hirsch [11].

Variation of Velocity Defects at the Wake Center. Decay of the mean velocity defect is greatly influenced by the pressure gradients and turbulence fluctuations as well as viscous effects that exist near the blade trailing edge. The secondary flow near the hub wall and the tip leakage flow near the annulus wall also contribute to the decay of the wake defect in these regions. The decay rate changes drastically for the wakes inside the annulus and hub wall boundary layers. The decay of the tangential and axial velocity defects and the

Downloaded 01 Jun 2010 to 171.66.16.62. Redistribution subject to ASME license or copyright; see http://www.asme.org/terms/Terms_Use.cfm

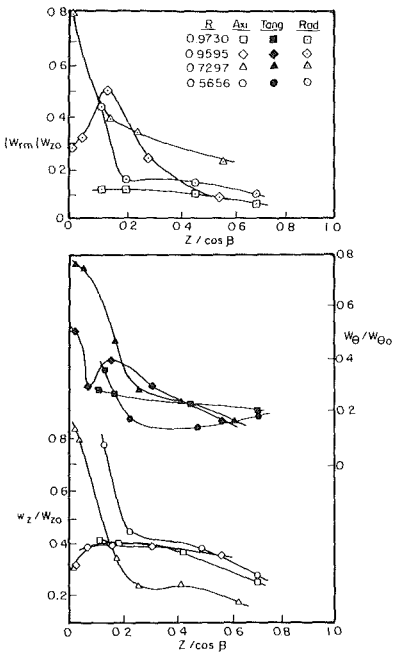

Fig. 20 Decay of maximum axial, tangential velocity defect, and maximum radial velocity in the annulus-wall boundary layer

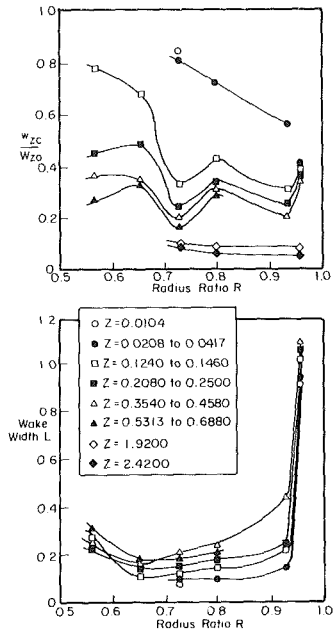

Fig. 21 Radial variation of the axial velocity defect at the wake center and the wake width

maximum radial velocities at the wake center for the hub-wall (R = 0.5676), mid-span (R = 0.7297) and annulus-wall regions (R = 0.9595, 0.973) are shown in Fig. 20. At R = 0.9595, it can be seen that the axial velocity defect and the maximum radial velocity increase initially in the trailing-edge region up to Z = 0.15, beyond which they decrease. The tangential velocity defect decreases initially and then increases up to Z = 0.2, beyond which it decreases. This strange behavior is attributed to the leakage vortex in the tip region. It is also observed that the axial velocity defect near the trailing edge is much smaller in the annulus-wall boundary layer compared to that in the hub-wall boundary layer and mid-span regions. The interesting feature to be noted is that, though the defect is much larger in the hub-wall boundary layer, the decay rate is such as to make the defects nearly the same far downstream. The axial velocity defect in the far-wake region is lowest for the mid-span, highest in the annulus-wall and hub-wall regions. The tangential velocity defect and the maximum radial velocities are about the same in the far wake for all the radii.

The maximum radial velocities are about the highest at the mid-span and hub regions and lowest in the annulus-wall region. The lowest radial velocities occur near the annulus wall (R = 0.973). Surprisingly, the maximum radial velocities are about the same at far downstream stations ($Z/\cos\beta$ = 0.7) for all the radii.

The tangential velocity defect near the trailing-edge region at the center of the wake is maximum at the mid-span and minimum inside the annulus-wall boundary layer. The defect is almost identical for all the radii far downstream. This seems to indicate that the decay rate of the defect in axial and tangential velocities is very low in the annulus-wall boundary layer, even though the magnitude of the defect is lowest in these regions near the trailing edge. A similar trend is observed for the defect in axial velocities.

The radial variation in maximum axial velocity defect at various axial locations is shown in Fig. 21. It is clear from the plot that the defect is maximum at mid-radius at the trailing-edge region and continuously toward the annulus-wall regions. This may have been caused by the presence of high turbulence, leakage flow or secondary flow in this region, all of which accelerate the mixing process. It is also clear that the decay of the defect is much more rapid in the mid-span region. For example, for $Z > 0.04$, the mid-span region has the lowest defect far downstream.

Decay of Maximum Turbulence Intensity. Decay of maximum axial, tangential and radial turbulence intensities normalized by the local relative mean velocity is shown plotted in Fig. 22 for the wakes inside the annulus- and hub-wall boundary layers and at R = 0.7297 (near mid-span). It can be seen that the intensities are very high near the trailing edge and that they decay very rapidly in this region.

Lakshminarayana and Reynolds [9] have given a qualitative analysis on the effects of rotation in turbulence and have shown that the turbulence structure is quite different compared to a stationary case. These authors hold that radial intensities are likely to be higher than the axial and tangential components. The present data seems to confirm this analysis. For the radius R = 0.9324 at Z = 0.0104, the maximum radial component (normalized by the local axial velocity) is 0.99, while the axial and tangential components are 0.836 and 0.8870, respectively.

Not only are the magnitudes of the turbulence intensities at various radii different but also their decay rates. It is seen from Fig. 22 that the decay rate of the axial and tangential components. The present data seem to confirm this analysis. For the radius R = 0.9324 at Z = 0.0104, the maximum maximum intensities are high at all the locations. The values near the mid-span decay more rapidly than the maximum intensities near the wall regions at this location. Further downstream ($Z > 0.2$), the maximum axial turbulence intensities are about the same at all the axial locations. The tangential component of maximum intensities is generally lowest for the hub region, and highest for the annulus-wall region (R = 0.9595) for $Z > 0.1$. The maximum radial intensities are generally lowest at the hub region and highest at the mid-span region for $Z > 0.2$. In the far wake, the maximum radial, tangential and axial intensities in the annulus-wall boundary layer region remain very high, with values ranging from 15—19 percent for the axial component and 25 percent for the radial component.

Downloaded 01 Jun 2010 to 171.66.16.62. Redistribution subject to ASME license or copyright; see http://www.asme.org/terms/Terms_Use.cfm

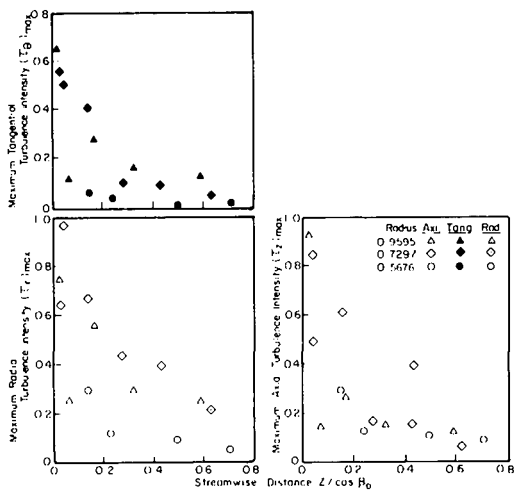

Fig. 22 Decay of maximum axial, tangential and radial turbulence intensity in the annulus-wall boundary layer

Variation of Wake Width. The wake width (L) is defined as twice the width of the wake at half the defect of total relative velocity. The variation of this wake width normalized by the blade spacing is shown plotted in Fig. 23 for the radii R = 0.5676, 0.7297, 0.9324, 0.9595, 0.973. In the case of rotors, because of centrifugal effects, wakes at higher radii tend to be thicker than wakes at lower radii. However, as the hub and annulus-wall regions are approached, the wake width grows enormously due to the complex interaction of the wake with the end-wall boundary layers and secondary flow (and tip leakage in the case of the annulus-wall region).

The wake width near the mid-span (R = 0.7297) is lowest, growing from a negligible value at the trailing edge to 0.2 of the blade spacing. The growth of the wake at R = 0.5675 (hub) and R = 0.9324 (edge of the annulus-wall boundary layer) is about the same. The initial values of wake width in these regions are high and growth rate is small. The wake width far downstream at these locations is approximately 30 to 40 percent. The maximum wake width is observed at R = 0.9595 and 0.973, where the initial wake covers nearly the blade passage and occupies one passage width further downstream. The growth rate for the wake is about the same for all the radii except R = 0.5676. The radial variation of the wake width, shown plotted in Fig. 21, clearly reveals these effects. The wake width is generally low for $R < 0.9$ and $R > 0.6$, and in the hub-wall region it is much lower than that in the tip regions.

Conclusions

The characteristics of the wake in the annulus-wake boundary layer and hub-wall regions of a moderately loaded compressor rotor blade were investigated. All measurements were acquired in the rotor frame of reference using a three-sensor hot-wire probe. Some of the important conclusions that can be drawn based on the results of the present investigation are as follows.

1 Secondary flow in the hub-wall region and leakage flow in the annulus-wall region affect the velocity profiles considerably, resulting in vortex and wake types of distributions. Radial velocities inside the annulus-wall layer are influenced by the tip-leakage flow. The tip vortex, which is strong in this case, dominates the radial velocity profile in this region. The radial outward velocity in the wake on the pressure side in the annulus-wall region gets amplified by the leakage flow. An opposite trend exists on the suction side.

2 The leakage vortex decays very rapidly in the trailing edge region. The interaction between the wake and the leakage flow produces a very complex wake structure.

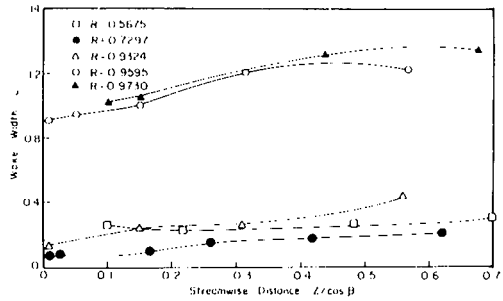

Fig. 23 Variation of semi-wake-width with downstream distance

3 The wake near the outer wall (6 percent of span from the tip) is not influenced by the leakage flow. The wake covers the entire passage, and its decay is slower than wakes at other radii. The wakes of adjoining blades were found to be identical in this region. The presence of a scraping vortex is also observed in this region.

4 The tangential velocity profile near the hub shows a peak near the center of the wake, with a minimum value slightly away from the wake center on either side of the wake. This is caused by the secondary flow in this region. Radial inward and outward velocities confirm this trend.

5 For the wake inside the annulus-wall boundary layer, the axial and tangential velocity defects and the maximum radial velocity initially increase and then decrease. This is attributed to the tip vortex which initially increases in its strength and then decreases downstream of the blade. The decay of velocity defects inside the annulus- and hub-wall boundary layers is far slower compared to the decay rates outside the end-wall boundary layers. The slower decay is attributed to the combined effect of secondary flow (tip vortex in the case of an annulus-wall boundary layer) and the end-wall boundary layers on the wake.

6 Inside the annulus and hub-wall boundary layers the wake width is found to be very large due to the effect of secondary and tip-leakage flows, and the outer 10 percent of the span has fully developed flow. The wake width is lowest at mid-span and highest near the outer wall. The growth rate of the wake is nearly the same at all radii.

7 The free-stream turbulence intensity in the wakes outside the end-wall boundary layers is about the same at all radii. However, for the wakes inside the annulus- and hub-wall boundary layers, the magnitude of the free-stream turbulence is higher, indicating the influence of secondary and tip leakage as well as wall boundary layers on the turbulence intensity.

8 The radial turbulence intensities in the wake near the hub are of the same order of magnitude as the other components. This is caused by the rotation effects. Decay of turbulence intensities is slow in this region.

9 Very high turbulence intensities are measured very near the blade trailing edge in the annulus wall boundary layer. These intensities decay very rapidly. The radial turbulence intensities are generally higher (effect of rotation) and decay more slowly compared to the other two components. The radial component of stresses is found to be of the same order of magnitude as that of the tangential stresses in this region, as a consequence of rotation.

Acknowledgments

This work was supported by the National Aeronautics and Space Administration through the grant NSG 3012, with L. Shaw as the technical monitor. The authors wish to thank R. Davino for the wake data at R = 0.973.

Downloaded 01 Jun 2010 to 171.66.16.62. Redistribution subject to ASME license or copyright; see http://www.asme.org/terms/Terms_Use.cfm

References

1 Lakshminarayana, B., "Methods of Predicting the Tip Clearance Effects in Axial Flow Turbomachinery," ASME *Journal of Basic Engineering*, Vol. 92, 1970, pp. 467–482.

2 Papailiou, K. D., Flot, R., Mathiou, J., "Secondary Flow in Compressor Blading," ASME JOURNAL OF ENGINEERING FOR POWER, 1977.

3 Reynolds, B., and Lakshminarayana, B., "Characteristics of Lightly Loaded Fan Rotor Blade Wakes," NASA Contract Report CR-3188, 1979, 180 pp.

4 Ravindranath, A., "Mean Velocity and Decay Characteristics of the Near and Far Wake of a Compressor Rotor," ASME JOURNAL OF ENGINEERING FOR POWER, Vol. 102, No. 3, 1980, pp. 535–548.

5 Ravindranath, A., and Lakshminarayana, B., "Structure and Decay Characteristics in the Near- and Far-Wake of a Moderately Loaded Compressor Blade," ASME JOURNAL OF ENGINEERING FOR POWER, Vol. 103, No. 1, 1981, pp. 131–140.

6 Smith, L. H., "Three-Dimensional Flow in an Axial Flow Turbomachinery," WADC Technical Report 55-348, Vol. 2, John Hopkins University, 1956.

7 Lakshminarayana, B., "An Axial Flow Research Compressor Facility Designed for Flow Measurement in Rotor Passages," ASME *Journal of Fluids Engineering*, Vol. 102, No. 4, Dec. 1980, pp. 402–411.

8 Gorton, C. A. and Lakshminarayana, B., "A Method of Measuring the Three Dimensional Mean Flow and Turbulence Quantities Inside a Rotating Turbomachinery Passage," ASME JOURNAL OF ENGINEERING FOR POWER, Vol. 98, No. 2, 1976, pp. 137–146.

9 Lakshminarayana, B. and Reynolds, B., "Turbulence Characteristics in the Near Wake of a Compressor Blade," *AIAA Journal*, Vol. 18, No. 11, November 1980, pp. 1354–1362.

10 Davino, R., "Three-Dimensional Mean Flow and Turbulence Characteristics in the Annulus-Wall Region of an Axial Flow Compressor Rotor Blade Passage," M.S. Thesis, Dept. of Aerospace Engr., The Pennsylvania State University, Nov. 1980.

11 Hirsch, Ch., "Endwall Boundary Layer in Axial Flow Compressors," ASME Paper No. 74-GT-72, 1974.

Downloaded 01 Jun 2010 to 171.66.16.62. Redistribution subject to ASME license or copyright; see http://www.asme.org/terms/Terms_Use.cfm

Measurement and Analysis of Total-Pressure Unsteadiness Data From an Axial-Flow Compressor Stage

W. C. Zierke[1]

T. H. Okiishi

Department of Mechanical Engineering,
Engineering Research Institute,
Iowa State University,
Ames, Iowa 50010

A fast-response, total-pressure probe was used with a periodically sampling and averaging data acquisition system to study the unsteady total-pressure field in an axial-flow turbomachine. Periodically unsteady total-pressure data were used to demonstrate some of the ways in which turbomachine blade wake transport and interaction influences the energy transfer involved. Observed trends of periodic variations in local total-pressure values could be explained in terms of the details of energy transfer associated with the different kinds of fluid particles (freestream, wake segment, blade surface boundary layer, mixed) moving through a blade row.

Introduction

Further generalization of turbomachine design procedures to the extent that they more correctly reflect the inherent periodically unsteady flows involved is desirable. This kind of progress is dependent on more of the phenomenological aspects of the unsteadiness of the flow being revealed through experiment and organized by analysis. Research in this direction is important because of the improvements still to be realized in designing turbomachines that are energy efficient, quiet, and able to survive the variety of aerodynamic sources of blade vibration present when the machine is in operation.

The unsteady flow of interest in this paper is the periodically unsteady flow that occurs between blade rows of an axial-flow turbomachine because of rotor/stator wake production, transport and interaction. When the wakes of an upstream blade row are periodically cut by a downstream blade row as suggested in Fig. 1, wake segments are subsequently transported through the cutting blade row. Some of the details of such wake transport and subsequent interaction have been established by a number of researchers including Meyer [1], Lefcort [2], Smith [3], Kerrebrock and Mikolajczak [4], Brandone and Bernard [5], Walker and Oliver [6], Lockhart and Walker [7], Schmidt and Okiishi [8, 9], Fleeter, et al. [10, 11], Adachi and Murakami [12], Wagner, et al. [13], Pfeil and Herbst [14], Gallus, et al. [15] and Larguier [16].

As a wake segment impinges onto the pressure surface of a wake cutting or chopping blade, its motion relative to the chopping blade results in a tendency for the wake segment fluid to move towards the impacted pressure surface as the segment is transported downstream. Fleeter, et al. [10, 11] have presented data that suggest that wake segments travel faster over the suction surface of the wake cutting blade than the pressure surface. Smith [3] recognized that this difference in wake segment velocity would result in turning of the segment during its passage through a blade row. Pfeil and Herbst [14] and Larguier [16] have shown that wake segments affect local boundary layers and can hasten transition. At a location where the wake cutting blade surface boundary layer would otherwise be laminar, intermittent behavior is associated with the passage of wake segments.

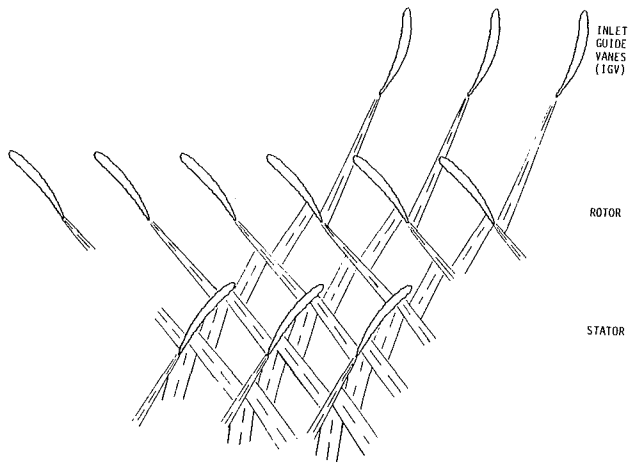

Fig. 1 Simplified sketch of blade-wake cutting, transport and interaction

Calculations (see for example Meyer [1], Lefcort [2]) and measurements (e.g. Lefcort [2], Gallus, et al. [17], Adachi and Murakami [12] and Franke and Henderson [18]) indicate that wake cutting blade surface local pressures vary considerably with cut wake segment location, especially in the leading edge region. These surface pressure fluctuations are large enough to result in significant fluctuations in blade lift force.

[1] Currently Research Assistant, Applied Research Laboratory, The Pennsylvania State University, State College Pa. 16801.

Contributed by the Gas Turbine Division and presented at the International Symposium on Applications of Fluids Mechanics and Heat Transfer to Energy and Environmental Problems, University of Patras, Patras, Greece, June 29–July 3, 1981. Manuscript received at ASME Headquarters April 1, 1981. Paper No. 81-Gr/GT-2.

Copyright © 1982 by ASME

Downloaded 01 Jun 2010 to 171.66.16.62. Redistribution subject to ASME license or copyright; see http://www.asme.org/terms/Terms_Use.cfm

Between blade rows, Smith [3], Walker and his colleagues [6, 7] and Schmidt and Okiishi [8] showed that transported wake segments can have a large effect on the periodic *and* irregular or turbulence related unsteadiness of the flow velocity measured at a point. Schmidt and Okiishi [8, 9] and Wagner, et al. [13] have established that blade-to-blade profiles of periodic-average[1] fluid velocity vary periodically by a considerable amount with rotor sampling position. Alarcon, et al. [19] and Gallus, et al. [15] presented data that suggest that blade-to-blade profiles of periodic-average total pressure also vary periodically with rotor position. On a time-average basis, Kerrebrock and Mikolajczak [4] demonstrated that the collection of rotor wake fluid toward the pressure surfaces of the cutting stator blades resulted in appreciable blade-to-blade variations of fluid stagnation temperature at the stator row exit.

The research summarized in this paper centered on acquiring and analyzing periodically unsteady total-pressure data in the first stage of an axial-flow research compressor. Since total-pressure values are indicative of fluid particle energy addition through work, and energy loss through viscous action, the periodic unsteadiness of turbomachine energy transfer can be studied by observing the periodic unsteadiness of the total-pressure field. A complete description of the experiment may be found in reference [20].

Brief Description of the Experimental Apparatus and Procedure

The low-speed, three-stage, axial-flow research compressor shown in Fig. 2 provided the flow field described herein. There were 37 inlet guide vanes and stator blades and 38 rotor blades per respective row. More information about this compressor was given previously by Schmidt and Okiishi [8] and will not be repeated presently. All of the data were obtained with the compressor operating at 1400 rpm with a flow coefficient of 0.42 (nominal design point). The corresponding reduced frequency, $\pi fc/V_{ax}$, where f = stator blade passing frequency, c = rotor chord length and V_{ax} = blade-to-blade average of time-average axial velocity, is 6 at midspan.

Unsteady total-pressure measurements were obtained with a fast-response probe equipped with a KULITE Model XCS-062-5 pressure transducer. The transducer was installed within the probe close to the impact opening as shown in Fig. 3. Unsteady total-pressure field data for 6 selected sampling positions of a reference rotor blade were acquired by averaging periodically (once per rev) sampled data. A sample size of about 700 instantaneous total-pressure values per periodic-average data value was chosen since only small improvements in precision were realized for larger sample sizes. A schematic of the system used to obtain these periodic-average total-pressure data is shown in Fig. 4. The fast-response probe yaw angle was set at each location in the compressor to the periodic-average value measured there previously (see [21]) with an inclined hot-wire probe. To avoid problems due to zero drifting of the Kulite transducer, the fast response probe was used to measure fluctuating total-pressure values only. At any particular location in the compressor where a measurement was made absolute periodic-average total-pressure values were obtained by adding the periodic-average value of fluctuating total pressure acquired with the fast-response probe to the absolute time-average total pressure measured there previously (see [20]) with a cobra probe. The cobra probe yaw angle was set by balancing the side port pressures except in stator wake regions where the probe was left at the freestream yaw angle setting.

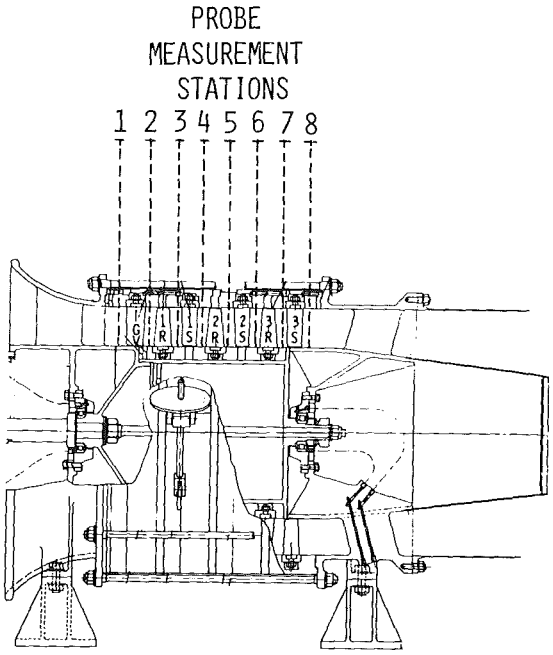

Fig. 2 Research compressor with probe measurement stations

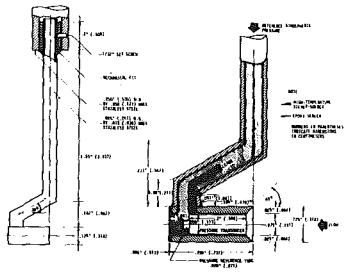

Fig. 3 Fast-response total-pressure probe details

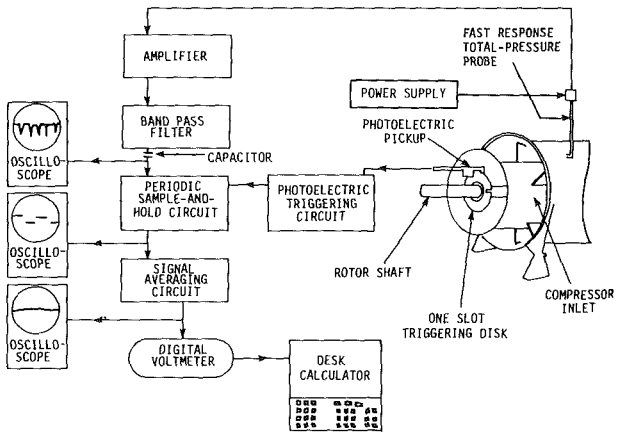

Fig. 4 Periodic-average total-pressure measurement system

Presentation and Discussion of Data

Data Uncertainty. The details of calibration of the cobra probe used to obtain time-average total-pressure data used in

[1] A note about the different kinds of average data discussed in this paper may be helpful. Time-average results represent the average value, over time, of a *continuously* measured quantity. Periodic-average results involve the average value of a *periodically* (e.g. once per rev) sampled quantity. Blade-to-blade-average results are the spatial average value of blade-to-blade profiles of either time-average or periodic-average quantities. Time-average results are independent of rotor sampling position while periodic-average results may vary.

Downloaded 01 Jun 2010 to 171.66.16.62. Redistribution subject to ASME license or copyright; see http://www.asme.org/terms/Terms_Use.cfm

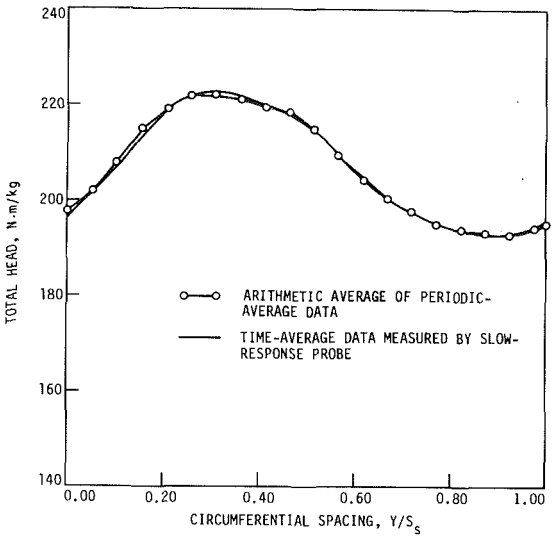

Fig. 5(*a*) Station 3

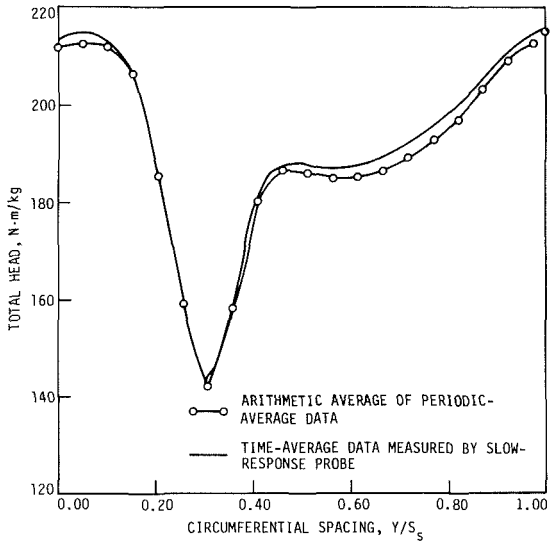

Fig. 5(*b*) Station 4

Fig. 5 Blade-to-blade distribution of time-average total head

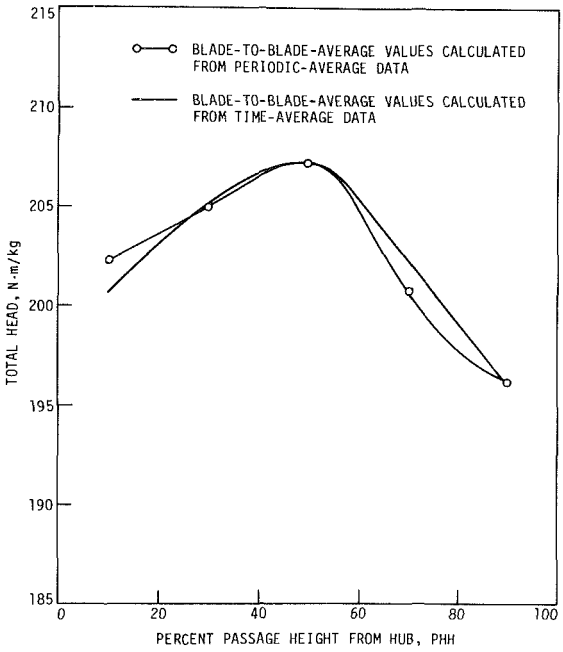

Fig. 6(*a*) Station 3

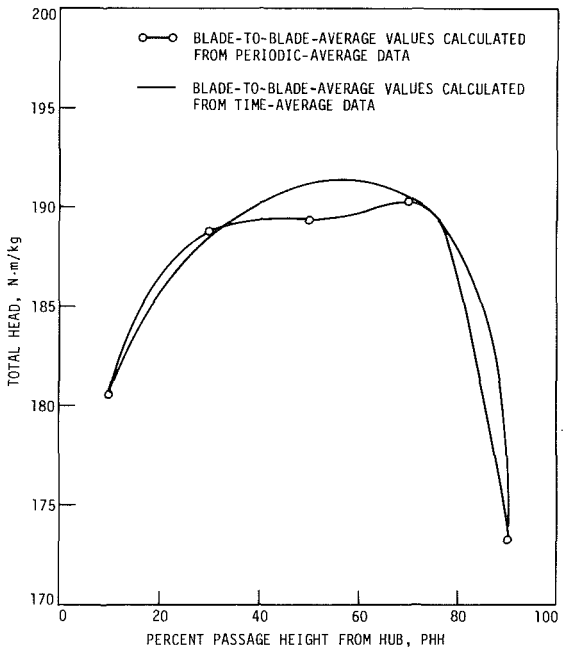

Fig. 6(*b*) Station 4

Fig. 6 Radial distribution of blade-to-blade-average total head

this paper are contained in reference [8]. By immersing the probe into the steady flow exiting from a calibrated converging nozzle, estimates of the effects of velocity level, yaw and pitch angles and time of measurement on total-pressure indication were obtained. To gain a better impression of how well the cobra probe would measure total pressure in the compressor, a comparison was made between cobra probe and Kiel probe results. Cobra probe blockage effects were small (0.3 percent at 90 percent immersion) compared to annulus cross-section area. Measurements were not made closer than 10 percent of blade span from an annulus wall or 20 percent of blade chord from a blade trailing edge. The total-pressure impact hole was from 2 to 2.5 percent of blade-to-blade distance. Based on these considerations, it was estimated that time-average total-head data measured with the cobra probe were reliable to within $\pm 0.5 N \cdot m/kg$ on the graphs used in this paper. This corresponds to about 0.3 percent of the total-head rise across the rotor.

The details of calibration of the fast-response total-pressure probe are contained in references [19] and [20]. Calibrated converging nozzle flow tests yielded impressions of probe sensitivity to velocity level, and yaw and pitch angles. Experience with the probe immersed in the compressor suggested that periodic-average yaw angle settings of the probe should be used instead of time-average ones. The relationship between change in total pressure and pressure transducer bridge output voltage change was found to be linear. The frequency response of the probe was approximated by passing a weak shock over the impact hole and observing the response of the probe to the sudden pressure change involved. Analysis of photos of the oscilloscope traces of probe response led to the conclusion that the fast-response probe had a natural frequency of 94 kHz and a damping ratio of 0.009. Fast-response probe blockage effects were small (0.19 percent at 90 percent span immersion) compared to annulus cross-section area. Measurements were not made closer than 10 percent of

Downloaded 01 Jun 2010 to 171.66.16.62. Redistribution subject to ASME license or copyright; see http://www.asme.org/terms/Terms_Use.cfm

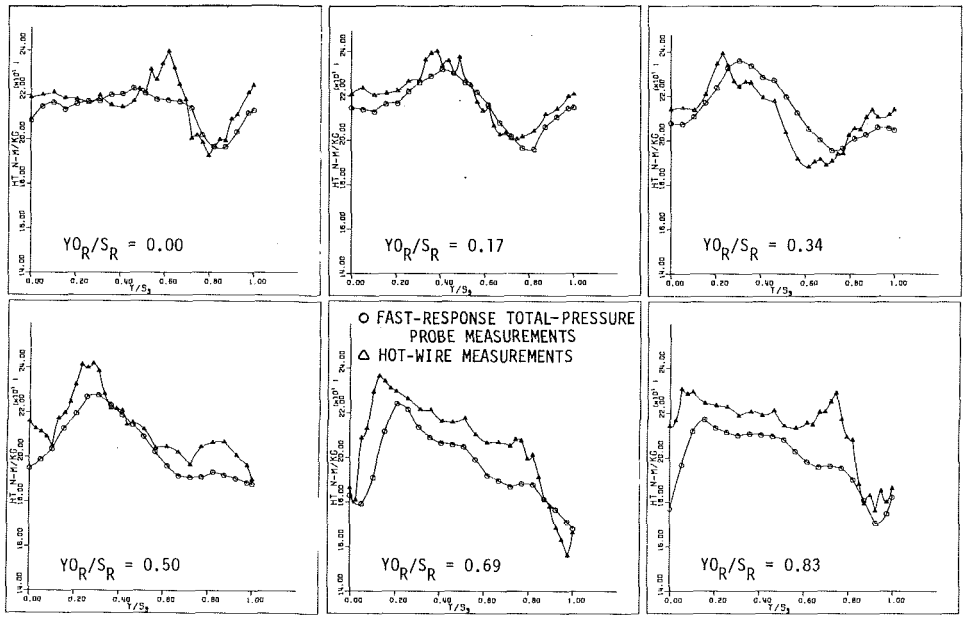

Fig. 7(*a*) Station 3

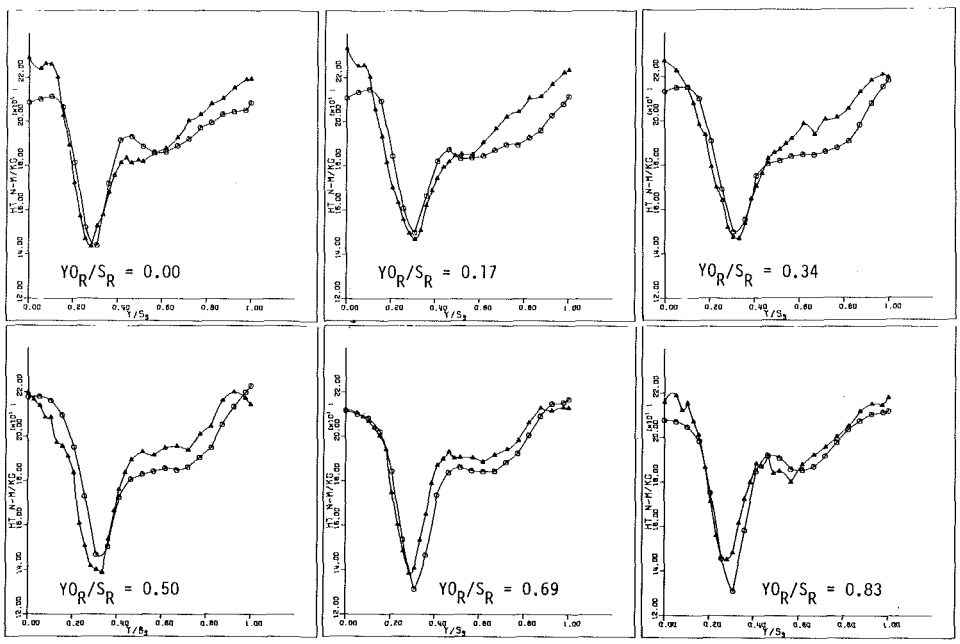

Fig. 7(*b*) Station 4

Fig. 7 Comparison of periodic-average total-head values measured by the fast-response total-pressure probe to those values calculated from hot-wire velocity data at 50 percent PHH

blade span from an annulus wall or 20 percent of blade chord from a blade trailing edge. The total-pressure measurement hole was from 10 to 13 percent of the blade-to-blade distance between blades.

To gain confidence in the periodic-average total-pressure data obtained with the fast-response and cobra probes, these data for the six rotor sampling positions were arithmetically averaged at selected blade-to-blade positions and compared with time-average total-pressure data obtained with the cobra probe at similar blade-to-blade locations. Sample comparisons are shown in Fig. 5 for rotor exit and stator exit flows at midspan. For an impression of how well these data compared at other span locations, blade-to-blade average values based on periodic-average and time-average data were compared from hub to tip as illustrated in Fig. 6. Finally, periodic-average total-head data obtained with the fast-response probe were compared with periodic-average total-head data calculated from periodic-average velocity data obtained with a hot-wire probe (see Schmidt, et al. [8]) assuming constant static pressure at each span location. Similar trends were indicated by both sets of data as illustrated by the sample comparison of Fig. 7. It should be noted that the hot-wire total-head values are reliable to within ± 15 N·m/kg only based on the hot-wire velocity measurement uncertainty reported in reference [8].

Based on the above mentioned considerations, it was estimated that the periodic-average total-head data were reliable to within ± 3 N·m/kg on the graphs used in this

Downloaded 01 Jun 2010 to 171.66.16.62. Redistribution subject to ASME license or copyright; see http://www.asme.org/terms/Terms_Use.cfm

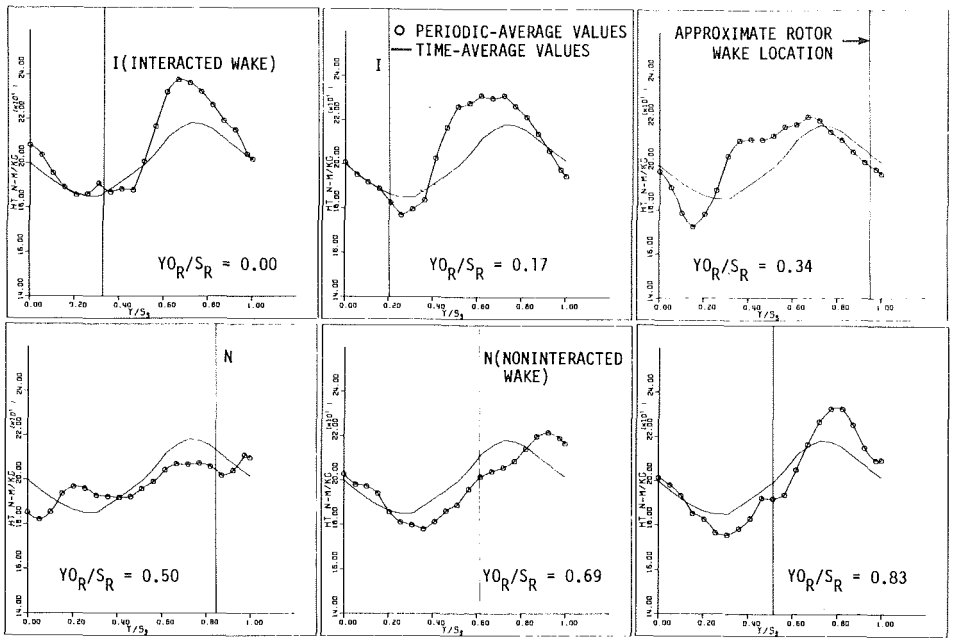

Fig. 8(*a*) Percent height from hub (PHH) = 10 percent

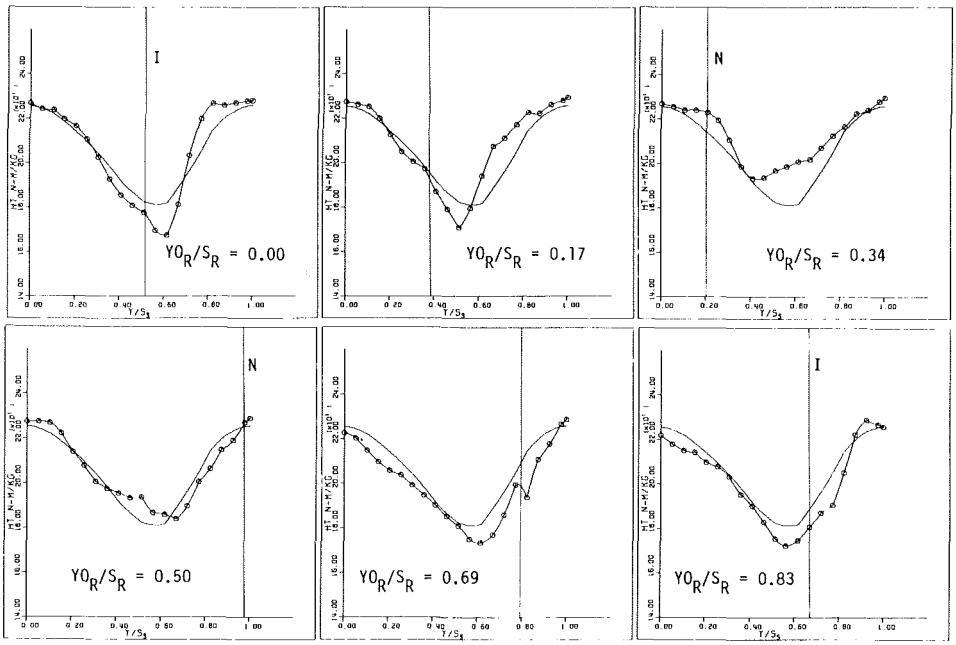

Fig. 8(*b*) PHH = 30 percent

paper. This corresponds to about 1.7 percent of the total-pressure rise across the rotor.

First Rotor Exit Flow Data.

Local Total-Head Data. First rotor exit time-average and periodic-average local total-head blade-to-blade profiles are compared in Fig. 8. The rotor sampling (YO_R/S_R) and data position (Y/S_S) parameters are explained in Fig. 9. The vertical line passing through each of the plots represents the approximate circumferential location of the rotor wakes as indicated by hot-wire data. An "*I*" label indicates an interacted wake while an "*N*" is used for a noninteracted wake. An interacted wake situation was defined by Wagner, et al. [13] as occurring when the rotor wake/IGV wake interaction was slightly upstream or at the measurement window (between +'*s* in Fig. 9). A noninteracted wake is characterized by rotor wake/IGV wake interaction occurring downstream of the measurement window. These conditions and their effects on periodic-average velocity data are illustrated in Figs. 10 and 11. The IGV wake avenues are characterized by lower time-average total-head values. Note that the periodic-average rotor wake local total-head values vary considerably with rotor sampling position. It was concluded that this unsteady behavior was related to the periodically varying spatial distribution and proportions of the different kinds of fluid particles (freestream, IGV wake, segment, noninteracted rotor wake, interacted rotor wake) present in the

Downloaded 01 Jun 2010 to 171.66.16.62. Redistribution subject to ASME license or copyright; see http://www.asme.org/terms/Terms_Use.cfm

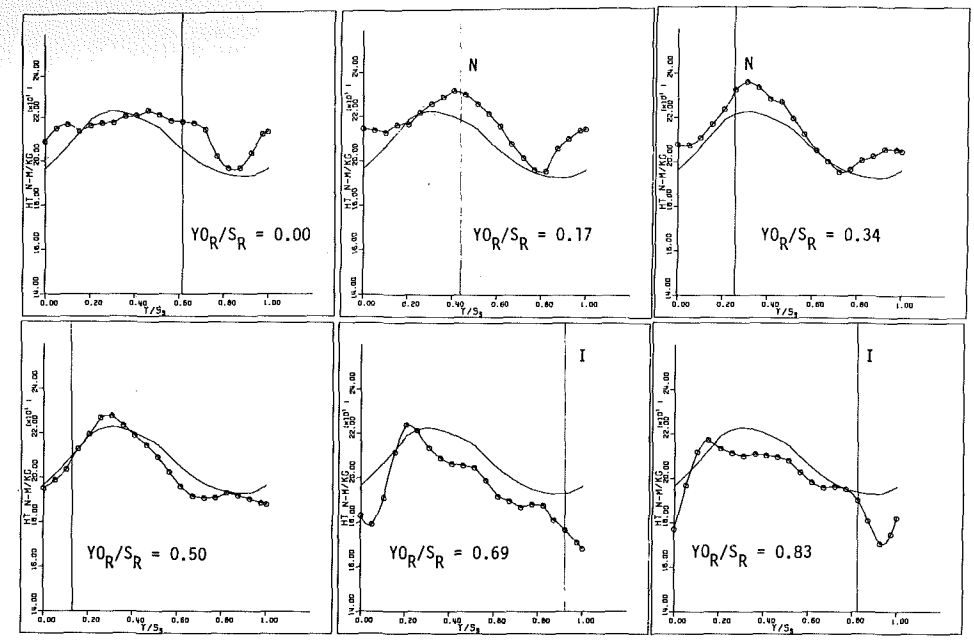

Fig. 8(c) PHH = 50 percent

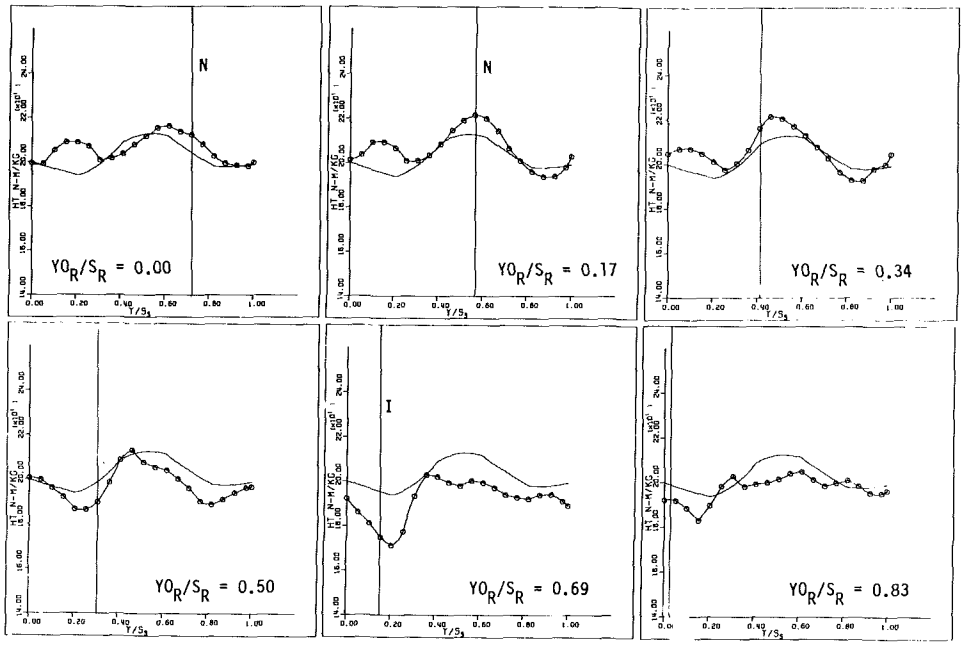

Fig. 8(d) PHH = 70 percent

measurement window for the different rotor positions. This reasoning was used earlier (Wagner, et al. [13]) to explain observed periodic variations in local velocities. The velocity polygons, shown in Fig. 12, in combination with the periodically varying cascade plots of Wagner and Okiishi [22], and the observed location of the rotor wakes relative to the IGV wakes avenues suggest, as might be expected, that interacted wakes generally involve lower total-head values than noninteracted wakes. This conclusion was made for data at midspan, but it also proved to be valid elsewhere in the passage. At all span locations, the interacted rotor wake total-head values are less than the chopped IGV wake segment total-head values and much less than the freestream total-head values. Further, the data indicates that except at 10 and 30 percent span from the hub, the noninteracting wake total-head values are larger than the total-head values measured at that circumferential location in the absence of any wake material (i.e. when freestream flow particles occupy that portion of the measurement window). For example, at 50 percent span (Fig. 8(*c*)), the total head at circumferential position $Y/S_s = 0.411$ is 231.78 N·m/kg for a noninteracting wake fluid particle ($YO_R/S_R = 0.17$) and 206.58 N·m/kg for a freestream fluid particle ($YO_R/S_R = 0.69$). At 10 percent span the opposite trend is true, the noninteracting total-head values are smaller than the total-head values measured at that circumferential location in the absence of any wake material. For example, at 10 percent span (Fig. 8(*a*)), the total head at circumferential position $Y/S_s = 0.617$ is 201.56 N·m/kg for a noninteracting wake fluid particle ($YO_R/S_R = 0.69$) and 232.06 N·m/kg for a freestream fluid particle

Downloaded 01 Jun 2010 to 171.66.16.62. Redistribution subject to ASME license or copyright; see http://www.asme.org/terms/Terms_Use.cfm

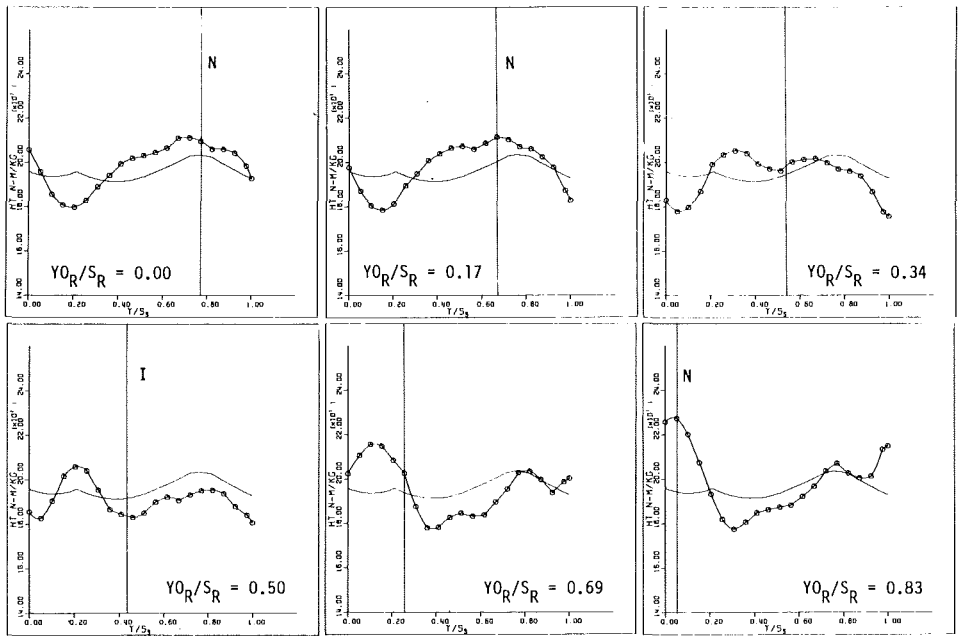

Fig. 8(e) PHH = 90 percent

Fig. 8 Blade-to-blade distribution of periodic-average total head and time-average total head at station 3

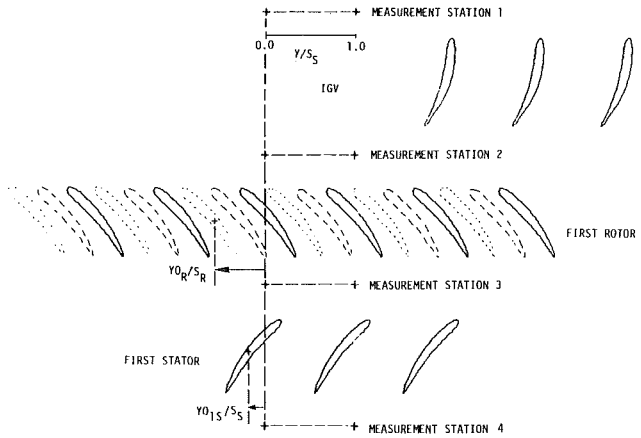

Fig. 9 Blade cascade showing relative positions of blades for several rotor sampling positions. (S_R is rotor blade spacing; S_S is stator spacing; Y is measurement circumferential location; YO_R is reference rotor blade circumferential location; YO_{1S} is reference first stator blade circumferential location.)

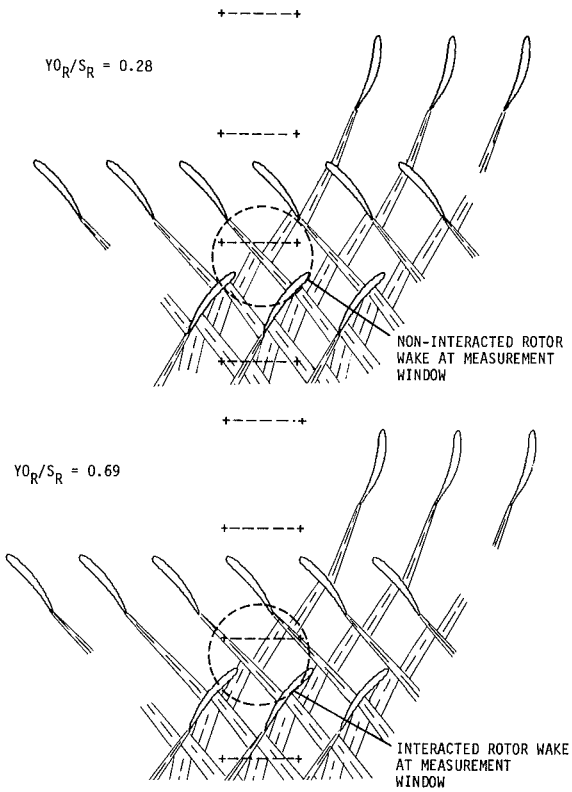

Fig. 10 Simplified drawings of blade-wake cutting, transport and interaction at two rotor sampling positions (Wagner and Okiishi [13])

($YO_R/S_R = 0.000$). At 30 percent span, both kinds of behavior are noted. These observations appear to be related to larger loss levels near the hub due to higher blade element loading and secondary flows there. As indicated by the data in Fig. 13, the blade-element loss levels (time-average and periodic-average amounts) near the hub are very high compared to elsewhere in the passage. The periodic-average velocity data in Fig. 14 show that the large loss near the hub is associated with a very deep wake. Elsewhere in the passage, the wakes are shallower. The larger loss observed near the tip is partly due to a tip clearance leakage effect.

All of these observations about the details of the local total-head variations prompted the organization of the information in Table 1. In summary form, the processes proposed in Table 1 suggests what local total-head levels will be observed at the measurement window when certain kinds of fluid flow particles are there. It is clear that the changing spatial distribution and proportions of the different kinds of particles present at the measurement station with rotor sampling position will lead to differing total-head profiles.

Blade-to-Blade-Average Data. The blade-to-blade periodic-average and time-average total-head profiles of Fig. 8

Downloaded 01 Jun 2010 to 171.66.16.62. Redistribution subject to ASME license or copyright; see http://www.asme.org/terms/Terms_Use.cfm

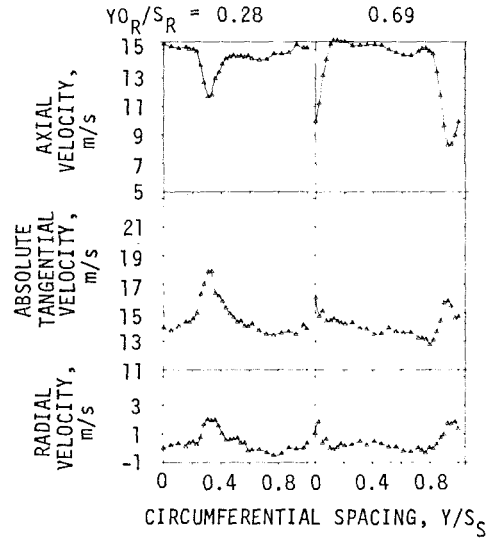

Fig. 11 Blade-to-blade distribution of periodic-average velocities at 50 percent PHH and station 3 for two rotor sampling positions (Wagner and Okiishi [13])

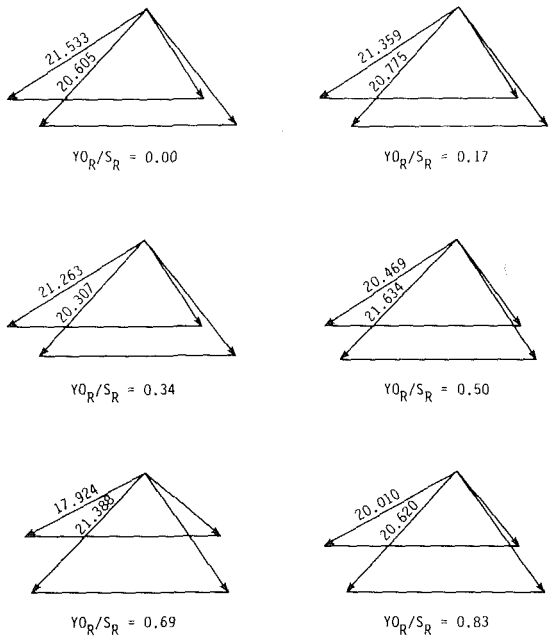

Fig. 12 Velocity triangles at station 3 and 50 percent PHH

were integrated and the blade-to-blade-average results are compared in Fig. 15. The periodic unsteadiness of the blade-to-blade-average total-head is large everywhere but appears to be greatest in the center portion of the blade span and less at either end. At 10 percent span from the hub, the interacting wake blade-to-blade-average total head is greater than the noninteracting wake value. Also, the interacting wake total-head value is greater than the time-average value while the noninteracting wake value is less than the time-average value. The opposite is true from 50 percent span on out to near the tip. The local effects mentioned and explained previously were influential enough to appreciably affect blade-to-blade-average results.

First Stator Exit Flow Data. Since energy was not added to the fluid flowing through the stator blade passage, and because the flow was approximately adiabatic, the total-head values in the stator wakes are indicative of the losses only, and the stator data are easier to interpret than the rotor data. Stator wake and chopped rotor and inlet guide vane wake fluid particles dominate the field at the measurement window downstream of the stator and result in mainly low levels of total pressure in the stator exit flow. The variation of the blade-to-blade-average total-head values with rotor sampling position is shown in Fig. 16. While the first rotor exit total-head values varied considerably with rotor sampling position due to energy transfer and wake interaction effects, the first stator exit total-head values varied little with rotor sampling position. The absence of energy addition in the stator row appears to be the main reason for the smaller variation of stator exit total pressure of the different kinds of fluid particles involved.

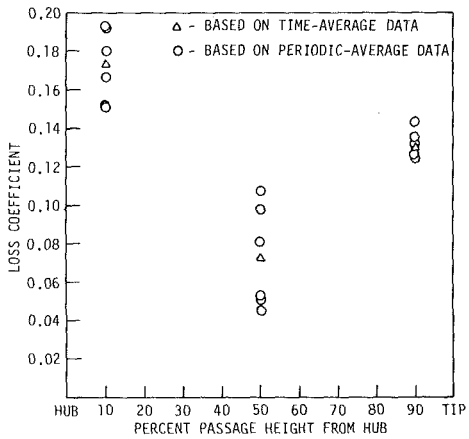

Fig. 13 Blade span distribution of time-average and periodic-average total-head loss coefficients for the first rotor row

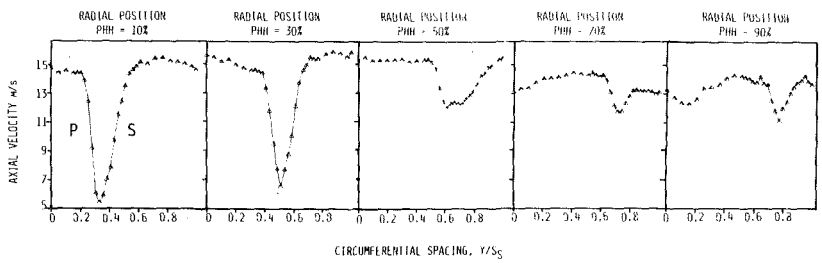

Fig. 14 Blade-to-blade distribution of first rotor exit periodic-average axial velocity component at different radial positions for $YO_R/S_R = 0.0$ (Schmidt and Okiishi [8])

Downloaded 01 Jun 2010 to 171.66.16.62. Redistribution subject to ASME license or copyright; see http://www.asme.org/terms/Terms_Use.cfm

Table 1 Behavior of fluid particles moving from the rotor inlet to the measurement station downstream of the rotor

Type of fluid particle	Total pressure at the rotor inlet	Energy added	Losses	Total pressure at the rotor exit measurement station
Freestream	A	B	C	D
Chopped IGV wake	$<A$	$>B$	$>C$	$<D$
Noninteracted rotor wake	A	$>>B$	$>C$(50 percent – 90 percent PHH)	$>D$
			$>>C$(30 percent)	D
			$>>>C$(10 percent)	$<D$
Interacted rotor wake	$<A$	$>>B$	$>>>C$	$<<D$

The freestream values are set arbitrarily at levels, A, B, C and D. Other values are estimated in terms of being less than, equal to, or greater than these reference values.

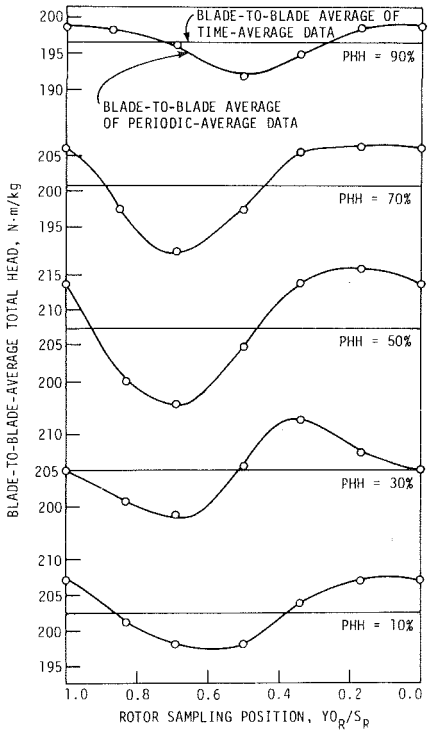

Fig. 15 Time varying blade-to-blade-average total-head values at station 3

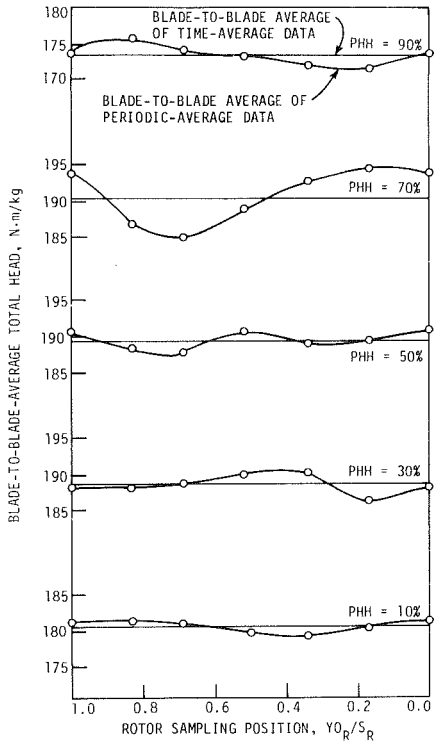

Fig. 16 Time varying blade-to-blade-average total-head values at station 4

Second Rotor Exit Flow Data. Data were taken at the exit of the second rotor at one radial position (PHH = 50 percent) to gain an impression of how much rotor exit total-pressure levels would vary with rotor sampling position in a downstream stage. As observed with the first rotor exit data, total-head values in the rotor wake regions were larger and smaller than freestream values depending on rotor sampling position. The larger rotor wake total heads occurred for noninteracted rotor wakes and the smaller total heads occurred for interacted rotor wakes. The variation in blade-to-blade-averages of rotor exit periodic-average total-head values with rotor sampling position is not as great for the second rotor (see Fig. 17) as it is for the first rotor. The second rotor exit flow data also show less difference in the shape of the total-head profiles from one rotor sampling position to another. Wake segments from more than one blade row are being transported through the second rotor row and thus through the measurement window at station 5. This would tend to smooth the variations with rotor sampling position of fluid properties such as total pressure and lead to smaller changes in that property.

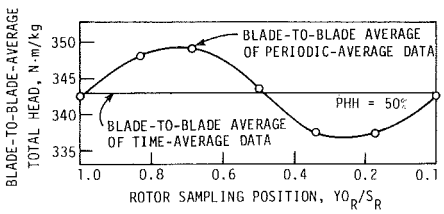

Fig. 17 Time varying blade-to-blade-average total-head values at station 5 and 50 percent PHH

Comparison of Results with Theory. The phenomena discussed in this paper are difficult to model mathematically. For this reason, we have concentrated on describing experimental results and proposing some physical reasons for the trends suggested by the data. Attempts to develop analytical models approximating some of the details of turbomachine blade row interaction have thus far been confined to applications of inviscid flow theory. It would be useful to check actual results as contained in this paper

Downloaded 01 Jun 2010 to 171.66.16.62. Redistribution subject to ASME license or copyright; see http://www.asme.org/terms/Terms_Use.cfm

against an appropriate inviscid flow model. The work of Horlock and Daneshyar [23] involving blade row interaction effects on time-average total pressures in a turbomachine stage offer some results that can be compared. They concluded that there would be point-to-point variations of time-average total pressure downstream of a row of moving blades undergoing fluctuations in circulation (lift) and suggested formulas for calculating the tangential and axial periods of these variations. The tangential period of variation of time-average total pressure they would predict for the rotor data contained in this paper calculates out to be the upstream blade row blade spacing. This seems to be followed by the experimental time-average total-pressure data. Horlock and Daneshyar [23] suggested that the order of magnitude of the variation of time-average total pressure with location downstream of the varying circulation rotor would be proportion to the fluctuating circulation. The present experiment did not result in enough independent data to verify this result.

Conclusions

Turbomachine flow total-pressure data are valuable because they are indicative of the amounts of energy gained and lost by the fluid particles involved. Rotor wake/stator or IGV wake interactions behind a rotor blade row have a strong effect on local total-pressure values. Rotor wakes which have interacted with stator or IGV wakes involve lower total pressures than rotor wakes which have not interacted with stator or IGV wakes. This effect is stronger in the first stage than in the later stages.

The extent of total-pressure variation with rotor sampling position behind the first stator row was appreciably less than the amount behind the first and second rotor rows. Periodic unsteadiness of total pressure between two adjacent blades is considerable downstream of a blade row that involves energy addition and loss and is minimal downstream of a blade row that involves energy loss only.

Acknowledgments

We acknowledge with gratitude the financial sponsorship received under Air Force Office of Scientific Research Contract F49620-79-C-0002. We are also grateful to the Engineering Research Institute and the Department of Mechanical Engineering of Iowa State University, Ames, Iowa for cost sharing participation and staff support. We thank our colleagues of the Turbomachinery Components Research Laboratory for their helpful comments and encouragement.

References

1 Meyer, R. X., "The Effect of Wakes on the Transient Pressure and Velocity Distributions in Turbomachines," *Trans. ASME*, Vol. 80, 1958, pp. 1547–1552.

2 Lefcort, M. D., "An Investigation into Unsteady Blade Forces in Turbomachines," ASME JOURNAL OF ENGINEERING FOR POWER, Vol. 87, 1965, pp. 345–354.

3 Smith, L. H., Jr., "Wake Dispersion in Turbomachines," ASME *Journal of Basic Engineering*, BBD, 1966, pp. 688–690.

4 Kerrebrock, J. L., and Mikolajczak, A. A., "Intra-Stator Transport of Rotor Wakes and Its Effect on Compressor Performance," ASME JOURNAL OF ENGINEERING FOR POWER, Vol. 92, 1970, pp. 359–368.

5 Brandone, B., and Bernard, P., "Visualisation par Analogie Hydraulique de L'Ecoulement dans une Grille D'Aubes Plane Mobile," *La Recherche Aerospatiale*, 141, 1971, pp. 125–128.

6 Walker, G. J., and Oliver, A. R., "The Effect of Interaction Between Wakes from Blade Rows in an Axial-Flow Compressor on the Noise Generated by Blade Interaction," ASME JOURNAL OF ENGINEERING FOR POWER, Vol. 94, 1972, pp. 241–248.

7 Lockhart, R. C., and Walker, G. J., "The Influence of Viscous Interactions on the Flow Downstream of an Axial Compressor Stage," In *Proceedings of the 2nd International Symposium on Air Breathing Engines*, University of Sheffield, Royal Aeronautical Society, London, 1974.

8 Schmidt, D. P., and Okiishi, T. O., "Multistage Axial-Flow Turbomachine Wake Production, Transport, and Interaction," Iowa State University Engineering Research Institute Interim Report TCRL-7, ISU-ERI-AMES-77130, 1976.

9 Schmidt, D. P., and Okiishi, T. H., "Multistage Axial-Flow Turbomachine Wake Production, Transport, and Interaction, *AIAA Journal*, Vol. 15, 1977, pp. 1138–1145.

10 Fleeter, S., Jay, R. L., and Bennett, W. A., "Rotor Wake Generated Unsteady Aerodynamic Response of a Compressor Stator," ASME JOURNAL OF ENGINEERING FOR POWER, Vol. 100, 1978, pp. 664–675.

11 Fleeter, S., Jay, R. L., and Bennett, W. A., "The Time-Variant Aerodynamic Response of a Stator Row Including the Effects of Airfoil Camber," ASME JOURNAL OF ENGINEERING FOR POWER, Vol. 102, 1980, pp. 334–343.

12 Adachi, T., and Murakami, Y., "Three-Dimensional Velocity Distribution Between Stator Blades and Unsteady Force on a Blade Due to Passing Wakes," *Bulletin of the JSME*, Vol. 22, 1979, pp. 1074–1082.

13 Wagner, J. H., Okiishi, T. H., and Holbrook, G. J., "Periodically Unsteady Flow in an Imbedded Stage of a Multistage, Axial-Flow Turbomachine," ASME JOURNAL OF ENGINEERING FOR POWER, Vol. 101, 1979, pp. 42–51.

14 Pfeil, H., and Herbst, R., "Transition Procedure of Instationary Boundary Layers," ASME Paper No. 79-GT-128, 1979.

15 Gallus, H. E., Lambertz, J., and Wallmann, Th., "Blade-Row Interaction in an Axial-Flow Subsonic Compressor Stage." ASME JOURNAL OF ENGINEERING FOR POWER, Vol. 102, 1980, pp. 169–177.

16 Larguier, R., "Experimental Analysis Methods for Unsteady Flows in Turbomachinery," In *Measurement Methods in Rotating Components of Turbomachinery*, B. Lakshminarayana and P. Rundstadler, Jr. Eds. ASME, New York, 1980.

17 Gallus, H. E., Kümmel, W., Lambertz, J., and Wallmann, Th., "Measurement of Rotor-Stator-Interaction in a Subsonic Axial-Flow Compressor Stage," In *Revue Francaise de Mécanique*, Symposium IUTAM sur L'Aéroelasticité dans les Turbomachines, Société Francaise des Mecaniciens Bulletin, 1976.

18 Franke, G. F., and Henderson, R. E., "Unsteady Stator Response to Upstream Rotor Wakes," *Journal of Aircraft*, Vol. 17, 1980, pp. 500–507.

19 Alarcon, G. A., Okiishi, T. H., and Junkhan, G. H. "Design and Application of a Fast Response Total-Pressure Probe for Turbomachinery Flow Measurement," Iowa State University Engineering Research Institute Technical Report TCRL-9, ISU-ERI-AMES-78205, Dec. 1977.

20 Zierke, W. C., and Okiishi, T. H., "Measurement and Analysis of the Periodic Variation of Total Pressure in an Axial-Flow Compressor Stage," Iowa State University Engineering Research Institute Technical Report TCRL-18, Dec. 1980.

21 Schmidt, D. P., Wagner, J. H., Holbrook, G. J., Zierke, W. C., and Okiishi, T. H. Iowa State University Department of Mechanical Engineering/Engineering Research Institute, Iowa Unpublished Tabulated Periodic-Average Hot-Wire Data, 1978.

22 Wagner, J. H., and Okiishi, T. H., "Analysis of Multistage, Axial-Flow Trubomachine Wake Production, Transport, and Interaction," Iowa State University Engineering Research Institute Technical Report TCRL-10, ISU-ERI-AMES-78173, 1977.

23 Horlock, J. H., and Daneshyar, H. "Stagnation Pressure Changes in Unsteady Flow," *The Aeronautical Quarterly* XXII, Pt. 3, 1971, pp. 207–224.

Downloaded 01 Jun 2010 to 171.66.16.62. Redistribution subject to ASME license or copyright; see http://www.asme.org/terms/Terms_Use.cfm

Nonequilibrium Streamline Curvature Throughflow Calculations in Wet Steam Turbines

C. C. Yeoh

J. B. Young

Whittle Laboratory,
University of Cambridge,
Cambridge, England

The paper describes a computer program which combines the streamline curvature throughflow calculation method with one-dimensional wet steam theory. Two subsonic applications are described in detail: (i) the nucleating flow in a convergent-straight annular duct and (ii) the flow in a 14-stage model high pressure turbine. Comparisons are made between the full nonequilibrium and conventional equilibrium solutions. Experimental results for the turbine show that the decrease in efficiency between dry and wet operation is underestimated by the theoretical calculation.

1 Introduction

Low efficiency and blade erosion are the two main problems associated with wetness in steam turbines employed in large scale electricity generation. With the trend towards large unit size and the increase in fuel cost, it has become particularly important to optimize the performance of these machines.

With regard to the wetness loss, it has been common design practice over the last 60 years to apply the simple Baumann rule [1]. This states that for each one percent of mean wetness the stage efficiency should be decremented by one percent. However, experimental results indicate that this model is unrealistic for both low pressure and nuclear high pressure turbines [2].

It has now been established that wetness loss is caused both by thermodynamic and mechanical effects. Gyarmathy [3] has suggested methods for the calculation of both phenomena and has shown that the magnitude of the various contributions depends strongly on the prevailing fog droplet size which is, in turn, a function of the degree of steam supercooling and rate of expansion at the Wilson Point. Subsequent theoretical approaches centred on the prediction of these effects by the application of one-dimensional wet steam theory to turbine geometry, e.g. [4].

The purpose of this paper is to extend the analysis a stage further and describe a method of combining a throughflow streamline curvature procedure with wet steam theory in order to predict nonequilibrium, axisymmetric turbine flows.

2 Theory

The streamline curvature technique for throughflow calculations involves the solution of the steady, adiabatic, inviscid flow equations in the meridional plane under the assumption of axial symmetry. Various authors, notably Smith [5], Novak [6] and Denton [7] have explored the different ways in which the flow equations can be integrated. The Denton method has the advantage that it can cope with transonic flow and the use of quasi-orthogonals allows a more realistic representation of the blade leading and trailing edges.

The two-phase radial equilibrium is described in Appendix 1 and it takes the form

$$\frac{d}{dq}\left(\frac{1}{2}Vm^2\right) = \frac{dH}{dq} - T_G\frac{dS}{dq} - \frac{1}{2r^2}\frac{d}{dq}(rV_\theta)^2 + \frac{Vm^2}{r_c}\sin(Q-\phi) + V_m\frac{dV_m}{d_m}\cos(Q-\phi) + \frac{dy}{dq}L(T_S-T_G)/T_S \quad (1)$$

All symbols are defined in the Nomenclature and the geometry is shown in Fig. 1. An additional assumption in the derivations has been that droplets and vapour move at the same velocity. Calculations of nucleating flows in nozzles indicate that this is an excellent approximation. Furthermore, the analysis is considerably simplified by the inclusion of this restraint.

Using a suitable finite difference scheme, equation (1) can be integrated numerically along the QO, the constant of integration being specified by the continuity requirement across AB (Fig. 1).

$$\dot{m} = \int_A^B 2\pi rb\rho Vm\sin(Q-\phi)\,dq \quad (2)$$

In the duct regions, the angular momentum of the fluid along each stream surface is conserved, that is,

Contributed by the Gas Turbine Division and presented at the International Symposium on Applications of Fluids Mechanics and Heat Transfer to Energy and Environmental Problems, University of Patras, Patras, Greece, June 29-July 3, 1981. Manuscript received at ASME Headquarters April 1, 1981. Paper No. 81-Gr/GT-3.

Copyright © 1982 by ASME

Downloaded 01 Jun 2010 to 171.66.16.62. Redistribution subject to ASME license or copyright; see http://www.asme.org/terms/Terms_Use.cfm

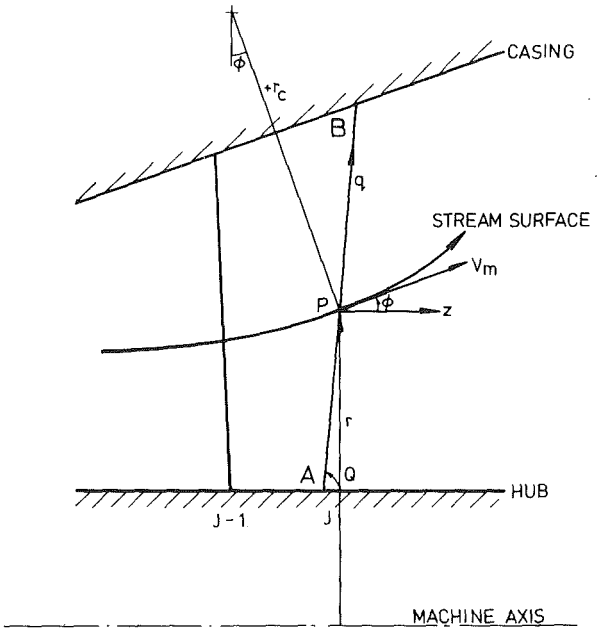

Fig. 1 Geometry of quasi-orthogonals and stream surfaces

$$\frac{d(rV_\theta)}{dm} = 0 \ . \tag{3}$$

For flow within the blade row, V_θ is determined from V_m and the imposed flow direction and blade speed.

The energy equation applied in the streamwise direction takes the form

$$\frac{dI}{dm} = 0 \ . \tag{4}$$

where

$$I = H - rwV_\theta \ . \tag{5}$$

In order to simulate the real flow, the entropy level is allowed to increase to account for both aerodynamic and thermodynamic losses. Hence

$$\frac{dS}{dm} = \frac{dS_A}{dm} + \frac{dS_T}{dm} \tag{6}$$

Steam properties are calculated using a truncated virial series [8,9]

$$P = \rho_G R T_G (1. + B\rho_G) \ . \tag{7}$$

where B is the second virial coefficient and is given by

$$B = 0.0020624 - \frac{2.61204}{T_G} .10\left(\frac{100800.}{T_G{}^2 + 34900}\right) \tag{8}$$

The nonequilibrium flow calculation is complicated by the estimation of the wetness fraction. It requires a knowledge of the nucleation and droplet growth characteristics of wet steam. Given the uncertainities in nucleation theory [10], the classical rate equation is adopted, which reads

$$J = \sqrt{\frac{2\sigma}{\pi m^3}} \cdot \frac{\rho_G}{\rho_L} .\exp\left(-\frac{4\pi r_*{}^2\sigma}{3kT_G}\right) \tag{9}$$

where

$$r_* = \frac{2\sigma}{\rho_L R T_G \ln(P/P_S)} \tag{10}$$

The droplet growth process is described by Gyarmathy's equation (3)

$$\frac{dr}{dt} = \frac{\lambda}{L\rho_L (r + 1.59\bar{\ell})}\left(1 - \frac{r_*}{r}\right)(T_S - T_G) \tag{11}$$

where λ is the thermal conductivity of the vapour and $\bar{\ell}$ is the mean free path of a vapor molecule and can be represented by the kinetic theory formula

$$\bar{\ell} = \frac{1.5\mu\sqrt{RT_G}}{P} \tag{12}$$

where μ is the dynamic viscosity of steam. For constant vapor conditions, the growth rate equation can be integrated to give the droplet radius as a function of time, the initial condition being

$$r = r_0 \quad \text{at} \quad t = t_0$$

The result is

$$\frac{1}{2}\left[\left(\frac{r}{r_*}\right)^2 - \left(\frac{r_0}{r_*}\right)^2\right] + \left(1 + \frac{1.59\bar{\ell}}{r_*}\right)\left[\left(\left(\frac{r}{r_*}\right) - \left(\frac{r_0}{r_*}\right)\right) + \ln\left(\frac{r/r_* - 1.}{r_0/r_* - 1.}\right)\right] = \frac{\lambda(T_S - T_G)}{L.\rho_L.r_*{}^2}(t - t_0) \tag{13}$$

Equation (13) must be solved iteratively for r and the Newton-Raphson method gives rapid convergence.

The thermodynamic loss is a consequence of the irreversible heat transfer between liquid and vapor phases caused by the

Nomenclature

A = area
B = second virial coefficient
b = blade blockage factor $\left(1 - \frac{\text{thickness}}{\text{pitch}}\right)$
F = blade force
H = stagnation enthalpy
h = specific enthalpy
I = rothalpy
J = QO number, nucleation rate
k = Boltzmann's constant
L = enthalpy of evaporation
$\dot{m}$ = mass flow rate
m = meridional direction, mass of a molecule
N = number of droplets per unit mass
P = static pressure
Q = angle between QO and machine axis
q = distance along a QO
R = specific gas constant
r = droplet radius, radius from machine axis
r_c = radius of curvature
S = specific entropy
T = absolute static temperature
t = time
ΔT = degree of supercooling
V = absolute velocity
W = relative velocity
y = wetness fraction
z = distance in the axial direction
α = loss factor
β = relative exit flow angle
ϕ = meridional pitch angle
λ = thermal conductivity of steam
μ = dynamic viscosity of steam
ρ = fluid density
σ = surface tension
ξ = energy loss coefficient
ω = rotational speed

Subscripts

A = Aerodynamic
E = equilibrium solution
G = gas phase
L = liquid phase
m = in meridional direction
N = nonequilibrium solution
q = in direction along Q0
S = saturation condition
T = thermodynamic
Z = in axial direction
θ = in circumferential direction

Downloaded 01 Jun 2010 to 171.66.16.62. Redistribution subject to ASME license or copyright; see http://www.asme.org/terms/Terms_Use.cfm

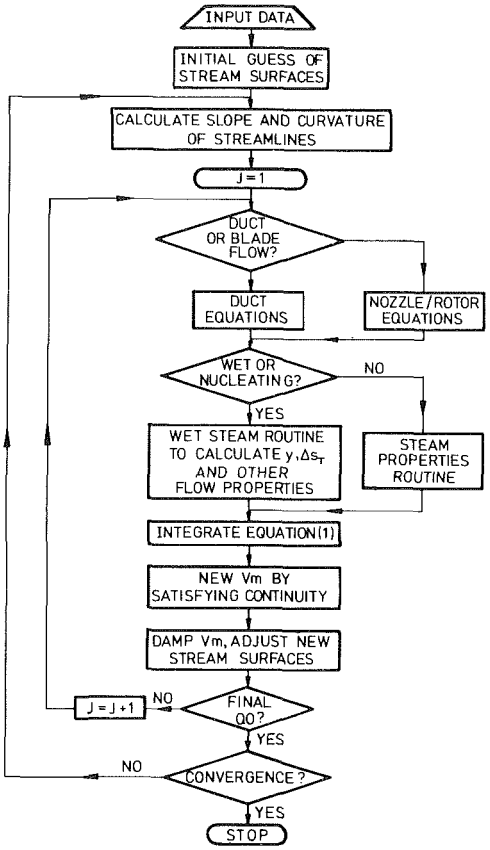

Fig. 2 Flowchart of the main numerical solution method

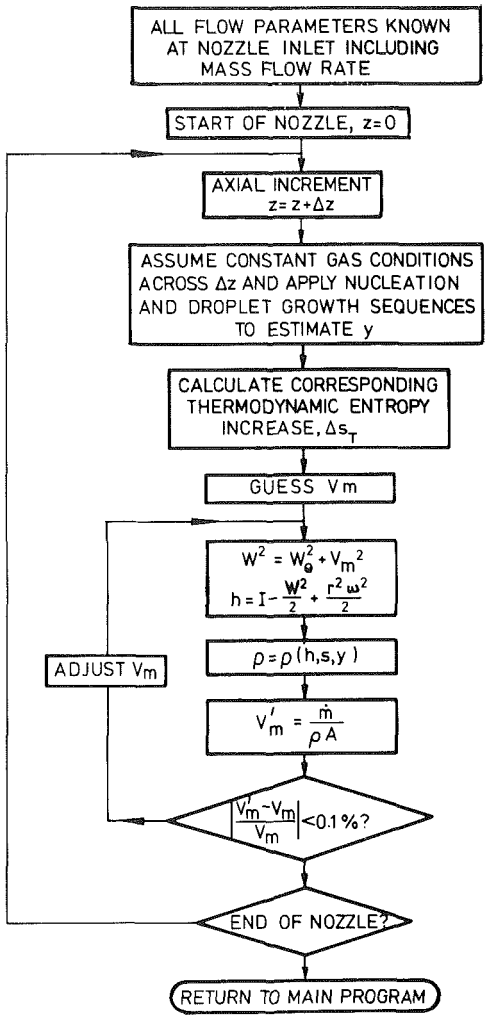

Fig. 3 Flowchart of nonequilibrium wet steam routines

interphase temperature difference and is derived by Young [11] to be

$$\frac{dS_T}{dm} = \frac{L}{T_S T_G}(T_S - T_G)\frac{dy}{dm} \tag{14}$$

3 Method of Solution

The basis of the numerical scheme for the simultaneous solution of the main conservation equations is similar to that described in [7] which is best illustrated by the flow chart depicted in Fig. 2.

The iterative procedure is initiated by making an initial guess of the stream surfaces. A simple three-point parabolic curve fit is used to estimate the slopes and curvatures necessary for solving equation (1).

The solution proceeds by marching downstream from one QO to the next. Depending on whether the current QO is in a duct region or a blade passage, one of the following sequences of calculation is performed along each stream surface.

(a) Duct Flow. Denoting the current QO by suffix J, it follows from equations (3,4) and (6) that

$$(rV_\theta)_J = (rV_\theta)_{J-1} \quad ,$$
$$H_J = H_{J-1} \quad ,$$

and

$$S_J = S_{J-1} + \Delta S_T \quad . \tag{15}$$

it being assumed that the aerodynamic losses are zero outside the blade rows.

(b) Blade Flow. Stators and rotors are treated in an identical fashion except that the angular speed, w, is set equal to zero within a stationary blade row.

$$(rV_\theta)_J = [r(V_m \sin(Q-\phi)\tan\beta + rw)]_J$$
$$H_J = H_{J-1} + w[(rV_\theta)_J - (rV_\theta)_{J-1}]$$

and

$$S_J = S_{J-1} + \left(\frac{\xi W^2}{2T_G}\right)_J + \Delta S_T \tag{16}$$

β is the relative flow angle and is specified data. It is measured from the axial direction and is positive in the direction of rotation. At blade exit

$$\beta = \cos^{-1}\left(\frac{\text{opening}}{\text{pitch}}\right) \tag{17}$$

if the flow relative velocity is subsonic. The energy loss coefficient ξ, is supplied as input data and allows the calculation of aerodynamic losses, which are imposed as sudden increases in entropy levels at the trailing edges of the blades. This gives a simple but effective method of including viscous effects.

An efficient routine based on equation (7) has been developed to calculate the pressure and temperature as functions of specific enthalpy and entropy. Comparison with data from [9] show that good accuracy is achieved for pressures below 10 bar.

With the updated property values, equation (1) is solved in conjunction with the continuity equation to give a new meridional velocity distribution along the quasi-orthogonal. The iterative process continues until the specified convergence

Downloaded 01 Jun 2010 to 171.66.16.62. Redistribution subject to ASME license or copyright; see http://www.asme.org/terms/Terms_Use.cfm

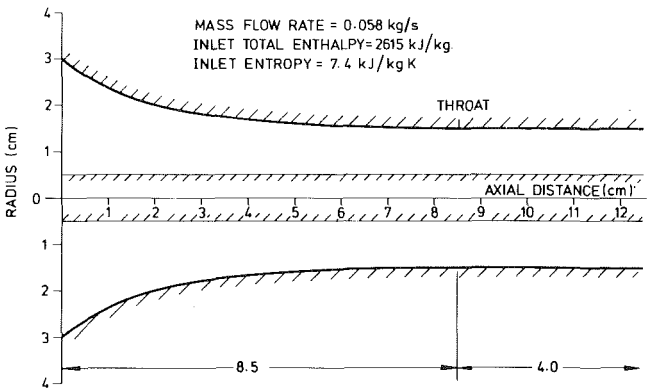

Fig. 4 Geometry of convergent-straight annular duct

criterion is satisfied. Damping is necessary to stabilize the numerical scheme.

The method of solution just described is applicable to both dry or equilibrium steam flow. In the case when the steam is wet or nucleating, it is necesary to consider the droplet growth along stream surfaces in order to calculate the change in wetness fraction between quasi-orthogonals. Due to the small characteristic times associated with relaxing wet steam flows it is not possible to apply the equations in finite difference form between adjacent QOs directly. Instead the stream surface must be treated as a pseudo one-dimensional nozzle which can be split into shorter sections purely for this part of the calculation.

The conventional methods for calculating one-dimensional wet steam flows, e.g. [13] involve a numerical integration of a set of first order differential flow equations by the Runge-Kutta method. This would be too time consuming in the present context and an alternative approach, as depicted in Fig. 3, has been developed.

The pseudo-nozzle geometry is specified by assuming a linear variation of streamline radius and meridional stream tube thickness between adjacent quasi-orthogonals. The blade blockage effect can be included if required.

Associated with this area in the radial-tangential plane is a relative flow angle, β. In duct regions β is defined by the conservation of angular momentum, but within blade passages β is the average flow angle of the three-dimensional flow between the blades. Often detailed blade geometry is not available, however, and in such cases the relative tangential velocity, W_θ, is assumed to vary in a parabolic fashion from leading to trailing edges with a condition of zero loading imposed at the leading edge.

The calculation thus proceeds step by step along the stream surface. At each station, the velocity level is achieved by satisfying energy and continuity. The wetness fraction is calculated as the sum of contributions from the freshly nucleated droplets (if the supercooling is high enough to promote strong nucleation) and the growth of established droplets by separate applications of equation (13). Thus

$$y = 4/3\pi r_{\text{NEW}}^3 \rho_L N_{\text{NEW}} + 4/3\pi r_{\text{OLD}}^3 \rho_L N_{\text{OLD}} \qquad (18)$$

N_{NEW}, the number of droplets per unit mass of steam nucleated in the increment Δ_Z is given by

$$N_{\text{NEW}} = J\frac{\Delta Z}{VZ} \quad , \qquad (19)$$

where J is the nucleation rate defined by equation (9). In order to economize on computational time, a surface average droplet radius,

$$r = \sqrt{\frac{N_{\text{NEW}} r_{\text{NEW}}^2 + N_{\text{OLD}} r_{\text{OLD}}^2}{N_{\text{NEW}} + N_{\text{OLD}}}} \qquad (20)$$

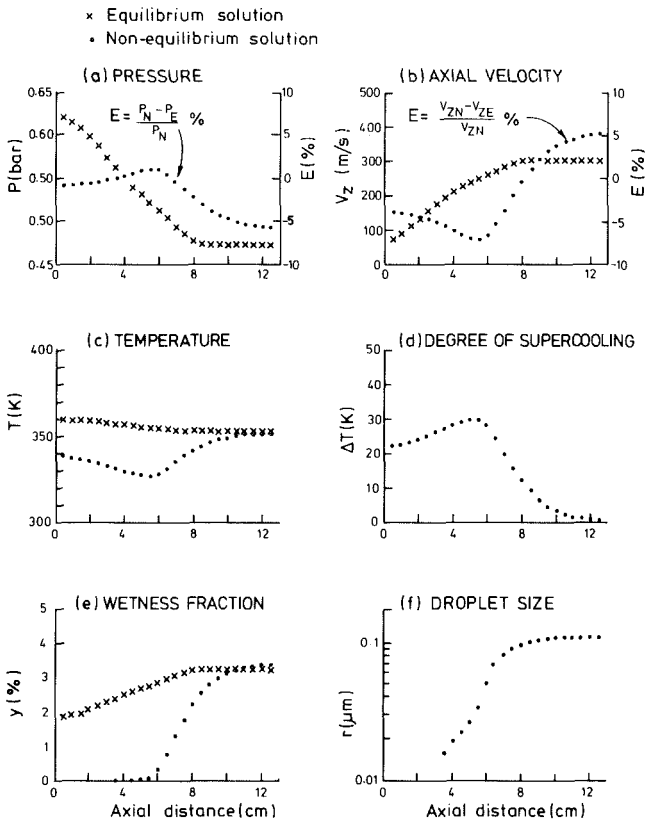

Fig. 5 Duct flow calculations (mean stream surface solution)

is adopted at the end of each step. In this way, a complete droplet spectrum need not be retained. Finally equation (14) can be applied for the estimation of the thermodynamic entropy rise.

4 Application to a Convergent-Straight Annular Duct

A small annular nozzle was designed for the initial development of the program. The converging profile is described by a quartic equation and the geometry is shown in Fig. 4.

A total of 26 quasi-othogonals and five streamlines were used in the calculations. The QOs were equally spaced and were all perpendicular to the nozzle axis.

The specified inlet steam conditions were the stagnation enthalpy, entropy and the mass flow rate. In order to induce nucleation in the converging section of the nozzle it was assumed that the steam at inlet was dry and this corresponded to a degree of supercooling of 22 K. For comparison purposes an isentropic equilibium solution was also obtained with the same inlet conditions (corresponding to a wetness of 1.85 percent).

The two solutions show little variation of flow properties across any section of the nozzle and, hence, only results for the mean stream surface are presented in Fig. 5. In the nonequilibrium solution the Wilson line, corresponding to the maximum degree of supercooling, is located at an axial position $z=0.055$m (Fig. 5(d)). Figure 5(a) shows that the exit pressure in the nonequilibrium solution is lower than that in the equilibrium calculation due to an entropy increase of 0.0104 kJ/kg K in the condensation zone.

The maximum difference of 7.2 percent in velocity levels at the Wilson Point is believed to have some practical significance. The inference is that turbine design calculations based on equilibrium steam properties would give an inac-

Downloaded 01 Jun 2010 to 171.66.16.62. Redistribution subject to ASME license or copyright; see http://www.asme.org/terms/Terms_Use.cfm

	MEASUREMENTS		THEORETICAL SOLUTIONS		
			DRY	DESIGN	
	DRY	DESIGN		EQUILIBRIUM	NON-EQUILIBRIUM
Mass Flow (kg/s)	1.906	2.041	1.925	2.041	2.080
H_{INLET} (kJ/kg)			2959.15	2783.31	2783.31
S_{INLET} (kJ/kg K)			7.0282	6.6654	6.6654
P_{INLET}(bar)	8.45	8.56	8.47	8.55	8.55
T_{INLET} (K)	528.0	451.7	528.8	451.2	451.2
LOSS FACTOR			1.400	1.725	1.640
P_{EXIT} (bar)	2.163	2.163	2.177	2.163	2.163
STAG. TEMP AT EXIT (K)	402.0		402.7		
TOTAL TO TOTAL EFFICIENCY (%)	86.2	82.4	86.3	82.7	82.4
POWER OUTPUT (kW)			456.5	410.2	416.10

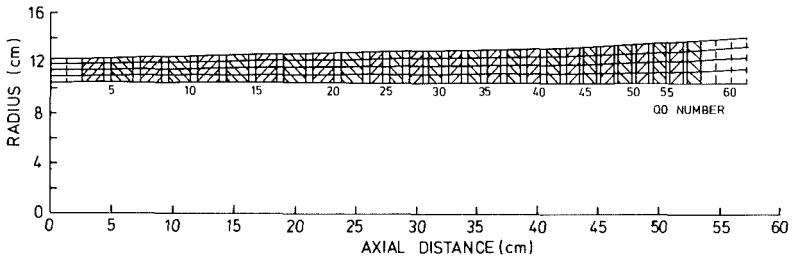

Fig. 6 14-Stage experimental HP turbine

curate prediction of flow incidence on the following blade row and would overestimate the stage work output.

The residual supercooling on entering the straight section of the duct is 9.1 K with the result that condensation and expansion continue to take place even though the flow area remains constant. However, by the end of the nozzle the steam is almost in equilibrium.

Typically, a converged solution for this type of geometry can be achieved in less than 15 complete passes through the flow field. The computational time for the nonequilibrium solution is about three times as long as for the equilibrium calculation.

5 Application to a 14-Stage Model HP Turbine

The turbine was built by a British steam turbine manufacturer for the study of wetness losses and the effectiveness of extraction belts. The blading had been designed to fulfil the specific functions described in [12] and the operating speed was 9000 rpm.

The available measurements (shown in Table 1) were those of the inlet steam conditions, exhaust pressure, mass flowrate and total-to-total efficiency. Two tests had been performed at nominally the same pressure ratio. The first, referred to as the dry test, was obtained by running the machine with the inlet temperature sufficiently high such that the steam remained superheated throughout the expansion. The second test was conducted under design conditions with an inlet superheat of 5 K and an exhaust wetness of about 5.8 percent.

All the 14 stages have straight blades and are of 50 percent reaction type. The 61 quasi-orthogonals forming the computational grid are shown in Fig. 6, together with the stream surfaces calculated in the nonequilibrium solution. It is evident that the flow in the machine is nearly two-dimensional with little radial shift of streamlines.

The estimation of the aerodynamic losses to predict the efficiency forms an important part of the analysis. Numerous loss correlations, the majority of which are based on cascade tests, can be found in the literature. Two well known examples are [14] and [15] which have been used in the present exercise for the estimation of profile and secondary losses of each blade row. A loss factor α was introduced to account for other sources of loss, such as tip leakage. The total loss coefficient was thus given by

$$\xi_{TOTAL} = \alpha(\xi_{PROFILE} + \xi_{SECONDARY}) \qquad (21)$$

Because of the low aspect ratio of the blading, it was decided to distribute the loss coefficients uniformly along each trailing edge. However, one obvious disadvantage of this method of loss inclusion is that the incidence loss cannot be determined independently.

It should be emphasized that the scheme adopted by the authors for the specification of losses is purely personal and is in no way governed by the structure of the computer prorgram. The choice of loss correlation is completely within the control of the designer and loss coefficients could be automatically calculated from the local flow conditions at run time if preferred.

An overall comparison between measurements and calculations is made in Table 1. For the dry test a loss factor of $\alpha = 1.4$ together with a mass flowrate 1 percent higher than measured gave good agreement with experiment in terms of exhaust pressure, stagnation temperature and efficiency. Similar agreement was achieved for an equilibrium solution

Downloaded 01 Jun 2010 to 171.66.16.62. Redistribution subject to ASME license or copyright; see http://www.asme.org/terms/Terms_Use.cfm

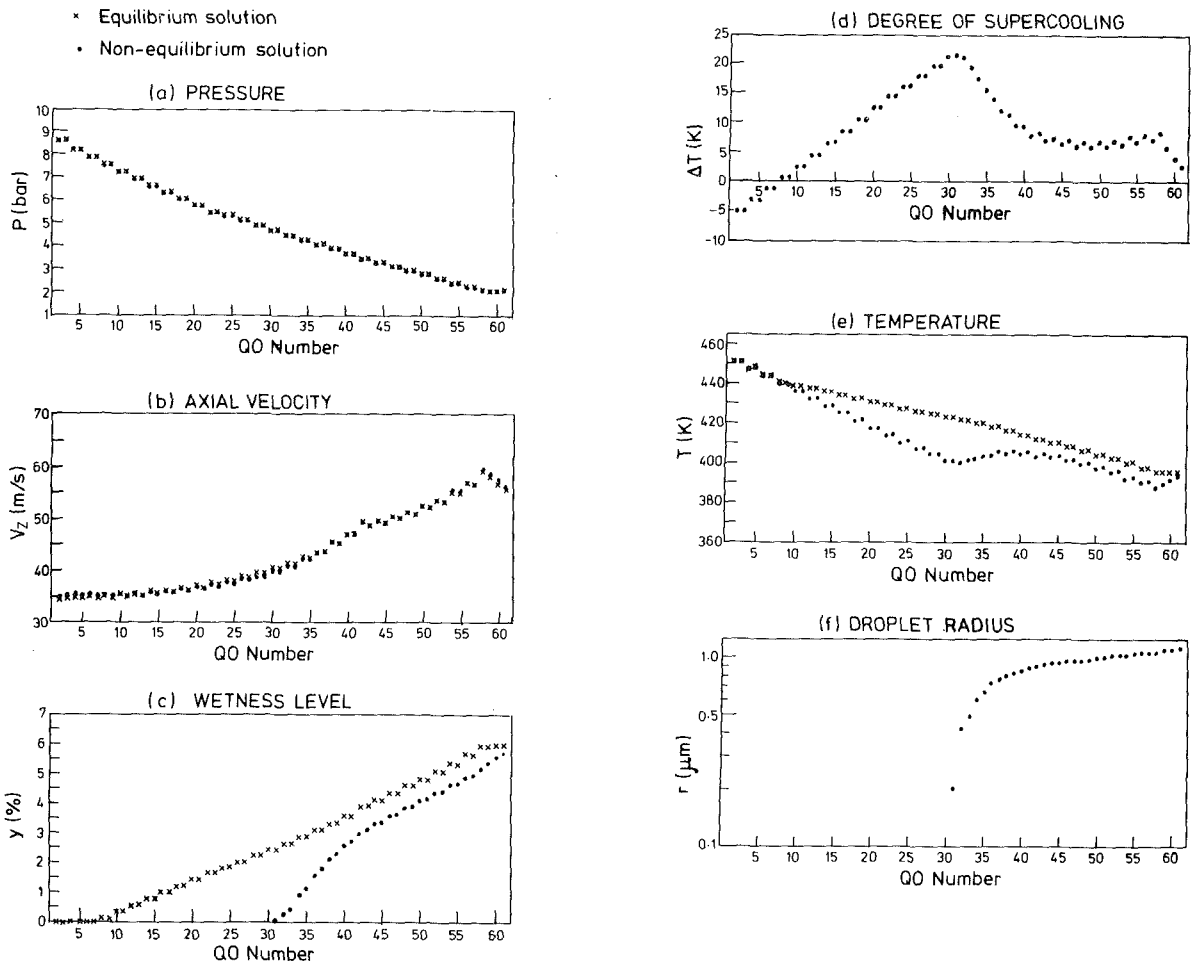

Fig. 7 Turbine calculations (mean stream surface solution)

of the design test using the measured mass flowrate and a loss factor of 1.725. With regard to the nonequilibrium solution it was necessary to increase the measured mass flowrate by 1.9 percent in order to predict the correct exhaust pressure. A loss factor of 1.64 (plus the calculated thermodynamic wetness loss) was required to obtain the measured efficiency.

It is tempting to ascribe the difference in loss factors used in the dry and nonequilibrium design solution completely to the mechanical effects of wetness. A closer examination of the solutions suggests that this may be misleading, because flow incidences do differ between the two solutions. No attempt was made to estimate the extra loss due to this effect, but it may well have a significant effect on the efficiency. It is therefore suggested that the customary procedure of performing dry and wet tests over the same pressure ratio to estimate the wetness loss may give erroneous results.

However, one positive result which does emerge from the analysis is that the thermodynamic wetness loss only accounts for 6.7 percent of the total loss of 44.5 kJ/kg. No estimate of the associated mechanical losses have yet been made, but the comparatively large mean droplet radius of 1.0 μm suggests that these could be appreciable.

A detailed comparison between equilibrium and nonequilibrium solutions is shown in Fig. 7. Only results along the mean stream surface are presented as radial variations are small. It will be noted that the pressure ratio across each stage is small and the relative Mach number never exceeds 0.5.

Figure 7(a) shows that the two solutions exhibit similar pressure distributions, but it can be seen from Figure 7(b) that the velocity level in the nonequilibrium solution is higher in the front part of the machine because of the slightly increased mass flowrate. As the steam becomes supercooled, this trend is reversed up to the nucleation zone. Once the reversion process is complete the velocity levels remain similar.

The saturation line is crossed in the nozzle row of the second stage and the Wilson line is predicted to be along the rotor trailing edge of the seventh stage. The average Wilson supercooling is 21.5 K. The subsequent reversion process is clearly shown in Figures 7(c,d) and (e) and the residual supercooling at the machine exit is 2.5 K. The wetness at this point is 5.68 percent and the corresponding value predicted by the equilibrium solution, 5.94 percent.

A converged nonequilibrium solution required under five minutes CPU time on an IBM 370/165 computer. Computational time required for the equilibrium solution was less than one minute. There is, however, considerable scope for reducing the run time of nonequilibrium solutions.

It is interesting to note that a one-dimensional, nonequilibrium study of the same turbine was undertaken by Bakhtar, et al. [4]. Their method was to represent the flow in each blade row by a one-dimensional nozzle flow and to ignore radial variations. Because of the high hub to tip ratio of the machine, similar results were obtained. However, it would be very difficult to extend their type of approach to highly three-dimensional turbine flows such as those in large LP cylinders.

The question remains as to whether the classical nozzle theory of spontaneous condensation can really be applied to

Downloaded 01 Jun 2010 to 171.66.16.62. Redistribution subject to ASME license or copyright; see http://www.asme.org/terms/Terms_Use.cfm

turbine flows. A number of recent publications have suggested that condensation in blade wakes, flow unsteadiness, temperature fluctuations and various other phenomena may promote strong nucleations at considerably lower values of mean stream supercoolings. At present these arguments have not been resolved. However, it is believed that the approach described above is sufficiently flexible that other models of the phenomena involved can be introduced into the analysis as more information becomes available.

6 Conclusions

A throughflow calculation procedure has been described which can predict the nonequilibrium effects in wet steam turbines. The method provides information on the spanwise variation of the Wilson Point, the average droplet radius nucleated, the thermodynamic wetness loss and the degree of supercooling throughout the flow field. Computational time is not excesive.

On applying the procedure to a model high pressure turbine it has been shown that the thermodynamic loss only accounts for 6.7 percent of the total loss. A comparison of the results with those from a conventional equilibrium design method demonstrate significant differences in flow parameters.

Further work is required to extend the method to the cases of supersonic and fully choked flows. At present progress is restricted by a lack of experimental data for comparison purposes. However, measurements of droplet size in turbines are now becoming available [16] and these should provide an impetus for future work.

Acknowledgments

The work was supported by a grant from C.A. Parsons & Co., Ltd., the General Electric Company and the Central Electricity Generating Board. The authors wish to thank Dr. J.D. Denton of the Whittle Laboratory, University of Cambridge for many invaluable suggestions and also for allowing them free access to his 'SLEQ' computer program which formed the basis of the work. They also wish to thank Mr. L. Cave of C.A. Parsons for making available the model HP turbine data.

References

1 Baumann, K., "Some Recent Developments in Large Steam Turbine practice," *Engineering*, Vol. III, 1921.

2 Troyanovskii, B.M., "Influence of Wetness on Efficiency of Steam Turbines," *Thermal Engineering*, Vol. 25 (10), 1978, pp. 32-37.

3 Gyarmathy, G., "Bases for a Theory for Wet Steam Turbines," Bull 6, Inst. for Thermal Turbo-Machines, Federal Technical University, Zurich, 1962.

4 Bakhtar, F., and Ghassemi, B., "A Study of Nucleating and Wet Steam Flows in High Pressure Steam Turbines," I. Mech. E. Conference, Steam Turbines for the 1980's, Paper C191/79, London 1979, pp. 327-336.

5 Novak, R.A., "Streamline Curvature Computing Procedures for Fluid Flow Problems," ASME JOURNAL OF ENGINEERING FOR POWER, Vol. 89, No. 4, 1967, pp. 478-490.

6 Smith, L.H. Jr., "The Radial-Equilibrium Equation of Turbomachinery," ASME JOURNAL OF ENGINEERING FOR POWER, Vol. 88, No. 1, 1966, pp. 1-12.

7 Denton, J.D., "Throughflow Calculations for Transonic Axial Flow Turbines," ASME JOURNAL OF ENGINEERING FOR POWER, Vol. 100, Apr. 1978, pp. 212-218.

8 Bakhtar, F., Ryley, D.J., Tubman, K.A. and Young, J.B., "Nucleation Studies in Flowing High Pressure Steam," *Proceedings of Institution of the Mechanical Engineers*, Vol. 189, 1975, pp. 427-436.

9 Keenan, J.H., Keyes, F.G., Hill, P.G., Moore, J.G., *Steam Tables*, John Wiley, New York, 1969.

10 Zettlemoyer, A.C., (ed) *Nucleation*, Marcel Dekker, 1969.

11 Young, J.B., "Spontaneous Condensation of Steam in Supersonic Nozzles," Cambridge University, Whittle Laboratory Report No. TR 97.

12 Smith, A., "Wilson Point Experiment in Turbines," Third Scientific Conference on Steam Turbines of Great Output, Gdansk, 1974, pp. 327-250.

13 Moore, M.J., Walters, P.T., Crane, R.I. and Davidson, B.J., "Predicting the Fog-Drop Size in Wet Steam Turbines," I. Mech E. Conference Publications 3, London 1973.

14 Ainley, D.G., and Mathieson, G.C.R, "A Method of Performance Estimation for Axial-Flow Turbines," A.R.C., R. & M., 2974, 1951.

15 Dunham, J., and Came, P.M., "Improvements to the Ainley-Mathieson Method of Turbine Performance Prediction," ASME Paper No. 70-GT-2.

16 Wyler, J.S., and Desai, K.H., "Moisture Measurement in a Low Pressure Steam Turbine using a Laser Light Scattering Probe," ASME JOURNAL OF ENGINEERING FOR POWER, Vol. 100, Oct. 1978, pp. 544-548.

APPENDIX 1

Derivation of Two-Phase Radial Momentum Equation

With the assumption of zero interphase velocity slip, the momentum equation in the direction of the quasi-orthogonal may be written as

$$-\frac{1}{\rho}\frac{dP}{dq} + F_q = \frac{dV_q}{dt} \tag{22}$$

where ρ is the mixture density and is given to a good approximation by

$$\rho = \frac{\rho_G}{1.-y} \tag{23}$$

Referring to Fig. 1, the acceleration of the fluid particle at the point P can be expressed as

$$\frac{dV_q}{dt} = -\frac{V_\theta^2}{r}\sin Q + \frac{V_m^2}{r_c}\sin(Q-\phi) + V_m\frac{dV_m}{dm}(Q-\phi) \tag{24}$$

The stagnation enthalpy and entropy of the mixture are defined by

$$H=(1-y)h_G + yh_L + V^2/2 \tag{25}$$

$$S = (1-y)S_G + yS_L \tag{26}$$

and these expressions are valid for both equilibrium and nonequilibrium flow.

The phases are assumed to be at equilibrium, although not with each other. Hence

$$\frac{1}{\rho_G}dP = dh_G - T_G dS_G \tag{27}$$

and

$$0 \doteqdot dh_L - T_L dS_L \tag{28}$$

where the term involving the liquid density has been neglected. Combining equations (25-28),

$$\frac{(1.-y)}{\rho_G}\cdot\frac{dP}{dq} = \frac{dH}{dq} - T_G\frac{dS}{dq} - V\frac{dV}{dq} + \frac{dy}{dq}[(h_G-h_L) - T_G(S_G-S_L)] - y\frac{dh_L}{dq}\left[1.-\frac{T_G}{T_L}\right] \tag{29}$$

Substituting equations (24) and (29) into (22) and rearranging gives

$$\frac{d}{dq}\left(\frac{1}{2}V_m^2\right) = \frac{dH}{dq} - T_G\frac{dS}{dq} - \frac{1}{2r^2}\frac{d}{dq}(rV_\theta)^2 + \frac{V_m^2}{r_c}\sin(Q-\phi) + V_m\frac{dV_m}{dm}\cos(Q-\phi) - F_q + \frac{dy}{dq}[(h_G-h_L) - T_G(S_G-S_L)] - y\frac{dh_L}{dq}\left(\frac{T_L-T_G}{T_L}\right) \tag{30}$$

The contribution from the blade force term, F_q, is zero for radial blades and has been ignored in the calculations. Note

Downloaded 01 Jun 2010 to 171.66.16.62. Redistribution subject to ASME license or copyright; see http://www.asme.org/terms/Terms_Use.cfm

that the final two terms involving the wetness fraction vanish when the flow is in equilibrium. In any case the final term is small and can be neglected. The magnitude of the penultimate term depends on the degree of nonequilibrium of the steam and may be written (to an accuracy greater than 3 percent)

$$\frac{dy}{dq}\left[(h_G - h_L) - T_G(S_G - S_L)\right] \simeq \frac{L(T_S - T_G)}{T_S}\frac{dy}{dq} \quad (31)$$

where L is the enthalpy of evaporation at saturation conditions. Hence the final form of the radial momentum equation is

$$\frac{d}{dq}\left(\frac{1}{2}V_m{}^2\right) + \frac{dH}{dq} - T_G\frac{dS}{dq} - \frac{1}{2r^2}\frac{d}{dq}(rV_\theta)^2 + \frac{V_m{}^2}{r_c}\sin(Q-\phi) + V_m\frac{dV_m}{dm}\cos(Q-\phi) + \frac{L}{T_s}(T_s - T_G)\frac{dy}{dq} \quad (32)$$

Downloaded 01 Jun 2010 to 171.66.16.62. Redistribution subject to ASME license or copyright; see http://www.asme.org/terms/Terms_Use.cfm

F. Bario
Doctor of Engineering,
Metraflu,
24 Bis Chemin des Mouilles,
69130 Ecully, France

F. Leboeuf
Doctor of Engineering,
Ecole Centrale de Lyon,
37 Avenue Guy de Collongue,
69130 Ecully, France

K.D. Papailiou
Professor,
National Technical University
of Athens,
Athens, Greece

Study of Secondary Flows in Blade Cascades of Turbomachines

Experiments have been performed with two cascades of turbomachines. The first cascade is composed of highly loaded turbine blades, and has been used in the low subsonic Mach number range. The second cascade consists of highly loaded compressor blades, of the DCA type. The Mach number was then in the high subsonic range. The experimental results are presented in the form of mean values in the pitch direction. Detailed local values are also described. The growth of a passage vortex and a corner effect are presented in the compressor case. Their interactions with the whole flow are analyzed. In the turbine case, the passage vortex is found to be a dominant effect. Results obtained with a theoretical method of calculation of the flow in the blade passage are used to complete the analysis.

Introduction

Detailed experiments have been realized at the Ecole Centrale de Lyon and under contract by the ONERA in order to get more information on secondary flow behavior inside the passage formed by two successive blades in an axial flow cascade configuration.

The objectives were to improve our knowledge about the physical aspects of the flow and to support theoretical calculation methods which have been and are currently under development in Lyon [1, 2, 3, 4, 9]. In this sense, no systematic tests have been realized in order to relate the general geometry of the cascade with the general flow behavior, but two cases have been experimentally investigated in detail. These two cases are the ones presented in this paper. The first cascade was composed of highly loaded turbine blades and was tested in the low subsonic Mach number range. The second cascade consisted of highly loaded compressor blades of the DCA type. The Mach number was kept in the high subsonic regime.

Before describing our results, it may be useful to discuss briefly the theoretical model we are using in order to calculate the secondary flow behavior. We shall analyze our experimental results more or less according to this model which is a two-zone model as it is generally accepted for the high Reynolds number regimes. Particular features of this model have been already used by different authors (see for instance : Anderson, et al. [13], Hosny [22]), other approaches have been used by Waterman and Tall [7], Patankar and Spalding [12]. Our model, which presents certain perculiarities, can be described as follows.

The real flow is subdivided into two parts:

a An inviscid external (or primary) flow part which disregards the wall shear layers but takes into account their displacement effects. This part, which may be rotational or irrotational, corresponds to the one which we assume not to be affected (directly or indirectly) by the effects of viscosity. We are talking about parts and not regions, because the two parts may coexist, in certain cases, everywhere in our flow field. The external flow part is extended up to the solid walls.

b A viscous flow part, which considers the wall shear layers with all their effects. The shear layers are considered along with the secondary vorticity they themselves create. In external flow problems, this situation is rather clear as generally both the viscous and vortical effects border on the same region. In internal flow problems, however, the secondary vorticity induced velocities are often not negligible inside the region traditionally occupied by the external flow alone. Consequently, as it is defined here and mentioned in the previous paragraph, the external flow does not necessarily coincide with the real flow outside of the viscous flow region. As before, however, by adding the viscous flow solution to the inviscid external flow, one may find the real flow field.

Considering the viscous flow problem, it is necessary to define a direction which is privileged in the sense that the shear flow properties are expressed according to existing similarity laws along this direction. As such, the external or primary flow direction is considered in our model. Of course, this privileged direction is generally changing with distance from the wall. In our particular case which is the two-dimensional cascade with uniform inlet conditions, this direction, which will be called longitudinal direction S, will be assumed constant along the spanwise direction Y.

In the transverse directions (denoted by N and B here, see Fig. 1), the corresponding velocity components are associated with the longitudinal vorticity component Ω_s, called the secondary vorticity component. A well known and well established first origin of this secondary vorticity development is associated with the streamline curvature and the existence of a transverse vorticity component Ω_n (see, for

Contributed by the Gas Turbine Division and presented at the International Symposium on Applications of Fluids Mechanics and Heat Transfer to Energy and Environmental Problems, University of Patras, Greece, June 29-July 3, 1981. Manuscript received at ASME Headquarters April 1, 1981. Paper No. 81-Gr/GT-4.

Copyright © 1982 by ASME
Downloaded 01 Jun 2010 to 171.66.16.62. Redistribution subject to ASME license or copyright; see http://www.asme.org/terms/Terms_Use.cfm

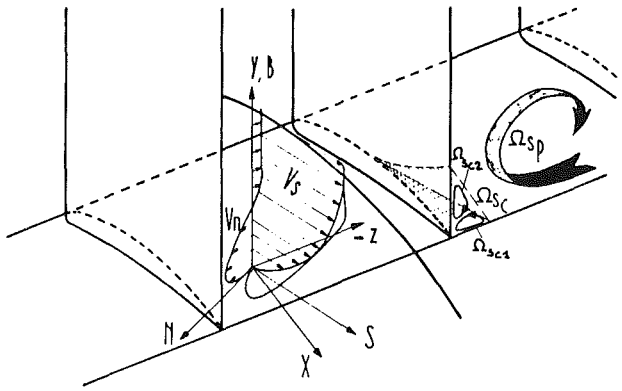

Fig. 1 Qualitative description of secondary flow in a cascade

instance, Lakshminarayana and Horlock [14]). A second origin, which is known but has been less studied than the first in the turbomachine case, is the one associated with the turbulent interaction of two Reynolds stress tensor components, as was described by Prandtl [18] and studied by Gessner [10] for the corner flow. For this second model, the normal velocity components V_n, V_b must be considered as being a direct consequence of viscosity and especially turbulence.

The calculation methods that have been developed up to now in Lyon (see cited references) consider the circumferentially averaged flow. In these methods, our model has been simplified even more, the viscosity effects are considered integrally only very near the wall, while, further away from it, viscous effects are associated only with the longitudinal velocity component V_s. Simplifying our problem, as it is usually done in shear flows, we shall further consider that momentum transport due to turbulence is taking place only along Y. This turbulent transport stops at the edge of the boundary layer δ, defined by the boundary layer thickness δ. In our model, in agreement with what has been said up to now, the boundary layer thickness is defined only in relation with the longitudinal velocity profile $V_s(y)$. Two-dimensional turbulent velocity profile families have been used to describe $V_s(y)$ in particular for the theoretical method of Comte, et al. [3].

Experimental evidences of the influence of the vortex motion and of the direct influence of viscosity on V_s can be found in numerous references [6–9,11,23].

The objective of this paper is to clarify some aspects of this model, namely the origins of the induced vortex Ω_s and its influence on the whole flow in compressor and turbine configurations. Also the validity of the boundary layer approach will be analyzed in the light of the measured details of the flow.

In can be seen that the external flow acceleration or deceleration will play a dominant role upon the evolution of secondary flow. In the case of decelerating external flows, the growth of the thicknesses of the viscous layers developing along the blades and along the adjacent walls may be sufficently important. Strong interaction between these viscous layers may be encountered in corner region. In the case of accelerating external flows, the results of this corner viscous interaction may be less important and it is expected that it will be masked by the secondary vorticity development related with the streamline curvature of the external flow field. This last effect tends to be amplified because of the vortex stretching induced by the external flow acceleration.

In the paper we will briefly describe the experimental means used to test the two cascades. We shall present and analyze the experimental results with the help of the model described previously. Then, some comparisons will be given between these experimental results and the prediction obtained by means of the theoretical method of computation as described in [3].

II Description of the Experimental Set-Up

The experiments on the compressor cascade have been

Nomenclature

B_e = fraction of the gap g free of solid boundaries
c = chord
C_p = pressure coefficient
D_{eq} = equivalent diffusion factor
D_2 = fluctuation term
g = gap (distance between two blades along the z direction)
h = blade height (full span)
M = Mach number
P_S = static pressure
P_T = stagnation pressure
R = radius of curvature of the inviscid streamline
R_{1e} = radius of curvature of the compressor leading edge
N,S,B = curvilinear coordinate system (Fig. 1)
t_m = maximum thickness for the compressor profile
X,Y,Z = cascade cartesian coordinate system
V = velocity
v = turbulent fluctuation for the velocity
$\beta = tg^{-1}(V_z/V_x)$
β' = angle between the tangent to the mean camber line of the blade profile and the axial direction
$\gamma = tg^{-1}(V_y/V_x)$
γ_c = stagger angle
Δ = absolute error
$\delta_s^* = \int_0^{h/2} (1 - \rho V_s/\rho_e V_{se})\, dy$
$\delta_x^* = \int_0^{h/2} (1 - \rho V_x/\rho_e V_{xe})\, dy$
$\theta_{ss} = \int_0^{h/2} (1 - V_s/V_{se})\rho V_s/\rho_e V_{se}\, dy$
$\theta_{xx} = \int_0^{h/2} (1 - V_x/V_{xe})\rho V_x/\rho_e V_{xe}\, dy$
$\theta_{zx} = \int_0^{h/2} \left(\frac{V_{ze} - V_z}{V_{xe}}\right)\rho V_x/\rho_e V_{xe}\, dy$
ρ = density
Ω = vorticity

Subscripts

e = inviscid flow
M_s = mid-span
n,b = along the transversal directions N and B
ref = reference value
S = static condition or along the longitudinal direction S
sp = passage vortex
sc = corner vortex
T = stagnation condition
x or ax = axial direction X
z,y = transversal Z, normal Y directions
w = wall condition
1 = upstream condition
2 = trailing edge condition
$'$ = fluctuation with respect to a mean (z-direction) value
$-$ = mean value in a z-direction as local value $q = q' + \bar{q}$

Downloaded 01 Jun 2010 to 171.66.16.62. Redistribution subject to ASME license or copyright; see http://www.asme.org/terms/Terms_Use.cfm

Table 1

	Compressor	Turbine
$c(10^{-3}m)$	79.	130.
g/c	.608	.765
γ_c(deg)	35.24	-53.30
β'_1(deg)	50.20	see figure 12
β'_2(deg)	20.30	
$h(10^{-3}m)$	100.	274.
t_m/c	.08	-

Table 2

β_1(deg)	51.	48.50
$\overline{\beta}_2$(deg)	27.	-76.50
$P_{t1}(N/m^2)$	79 873.	101 374.
$P_{s1}(N/m^2)$	51 098.	-
$\overline{P_{s2}}(N/m^2)$	-	99 948.
T_{t1}(deg K)	313.	300. $\pm$ 10.
$\delta^*_{s1}(10^{-3}m)$	2.10	4.20
$\theta_{ss1}(10^{-3}m)$	1.18	2.50
$\delta_{estimate}(10^{-3}m)$	26.	32.
D_{eq}	1.85	-

Table 3

ΔX, ΔY, ΔZ	$\pm$ .0005 m
$\Delta\beta$	$\pm$ .5 (deg)
$\Delta\gamma$	$\pm$ 1. (deg)
$\frac{\Delta P_t}{\frac{1}{2}\rho V^2}$, $\frac{\Delta P_s}{\frac{1}{2}\rho V^2}$	1 % (except in large gradient regions)

conducted under contract by ONERA (Chalais-Meudon, in the S5CH tunnel). The experiments on the turbine cascade were performed in the Fluid Mechanics Laboratory of the Ecole Centrale de Lyon (E.C.L.). We shall describe the experimental set-up for the two experiments and the general aerodynamic test conditions.

Description of the Experimental Set-Up for the Turbine Cascade. The experiments were performed in a cascade tunnel in the low subsonic Mach number range ($M < 0.20$). Processing from upstream to downstream, we find a honeycomb, a convergent section, and the cascade. A length of 5 m separates the cascade from the upstream grid. The top and bottom walls of the cascade are adjustable and porous in order to obtain the necessary uniformity of the upstream flow and periodicity downstream. Full details on the wind tunnel may be found in [15]. The main geometrical parameters of the cascade are given in Table 1. The geometry of the blade and the experimental stations used for measurements are given in Fig. 12.

A corba type pressure probe with five pressure taps has been used throughout the experiments. This probe was used to study the flow inside half of the passage, near one side wall on which the blades were fixed. Slots have been located in the opposite wall to allow probe displacements (see Fig. 12).

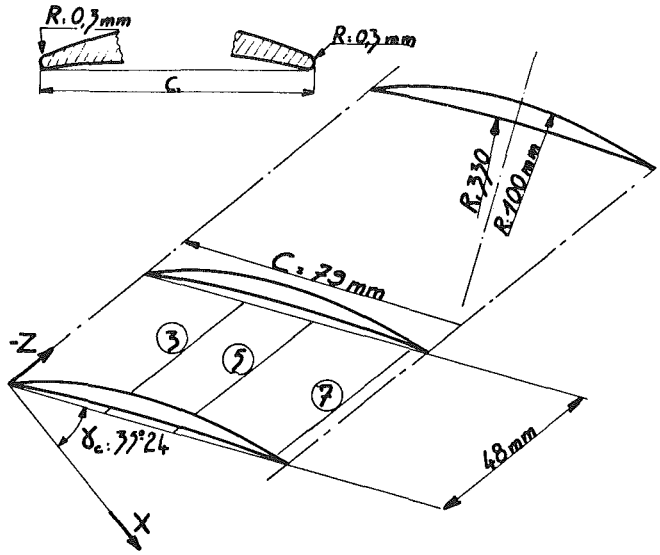

Fig. 2 Compressor cascade

Special attention has been paid to avoid fluid leakage through them. Three movements were used in order to fix the probe position, namely translations along Y and Z and a rotation around Y. Flow quantities are obtained in the following way: We first used a null method. The probe is rotated around the Y direction, equalizing the pressure readings obtained on two opposite taps in the (X,Z) plane. An approximative flow angle β in the (X,Z) plane is then obtained. Individual pressures are measured. Then, by means of prior calibration, the flow angle β is corrected by $d\beta$, and the flow angle γ is determined. Using the $d\beta$ and γ values, it is then possible to determine the stagnation and static pressures (P_T and P_S).

The accuracy of static pressure measurements have been often questioned when a cobra probe is used [19]. We have done many tests to validate the use of such a probe (see for instance [4, 5, 20, 21]). From the results obtained in transonic compressors, we have concluded [20] that the accuracy of a cobra probe is similar to the one of a cylindrical probe. The diameter of the head of the probe was 0.0015 m. A special instrumented blade was used to measure the static pressure along its surface by means of small taps drilled in it.

Differential pressure transducers of the VALIDYNE type were used. The experimental results were collected on paper tape and reduced on an HP 2108 computer. Boundary layer suction was applied on the opposite wall in the leading edge region to avoid strong interaction between the two opposite secondary flows.

Description of the Experimental Set-Up for the Compressor Cascade. The ONERA cascade was used in the high subsonic Mach number range. The main geometrical parameters of the cascade are given in Table 1 and Fig. 2. The profile was of the DCA type. No suction of the boundary layer was applied on the cascade opposite wall. A five hole probe has been introduced in the cascade from downstream. An instrumented blade was also used to measure static pressure.

Aerodynamic Testing Conditions. The upstream flow testing conditions can be found in Table 2 for the two test cases. In Table 2, the boundary layer integral quantities for the compressor and the turbine cases are given at $x/c_{ax} = -0.60$ and $x/c_{ax} = -0.46$ respectively, where the boundary layer may be considered collateral. The static pressure measurements on the blade profile at mid-span are presented in Figs. 3(*a*) and 3(*b*) for the compressor and the turbine case, respectively. The accuracy of the measurements is discussed

Downloaded 01 Jun 2010 to 171.66.16.62. Redistribution subject to ASME license or copyright; see http://www.asme.org/terms/Terms_Use.cfm

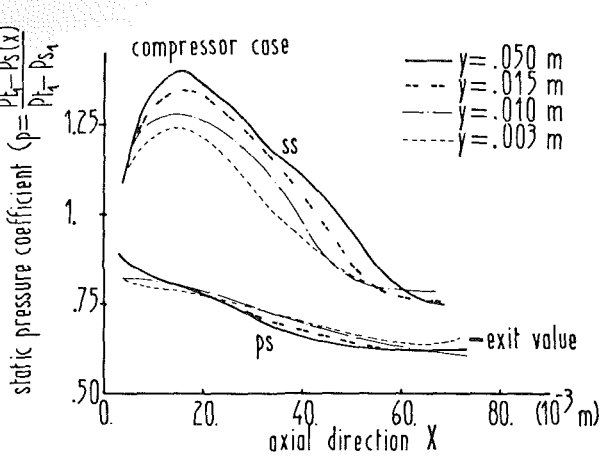

Fig. 3(*a*) Static pressure distribution on blade pressure (*PS*) and suction (*SS*) sides

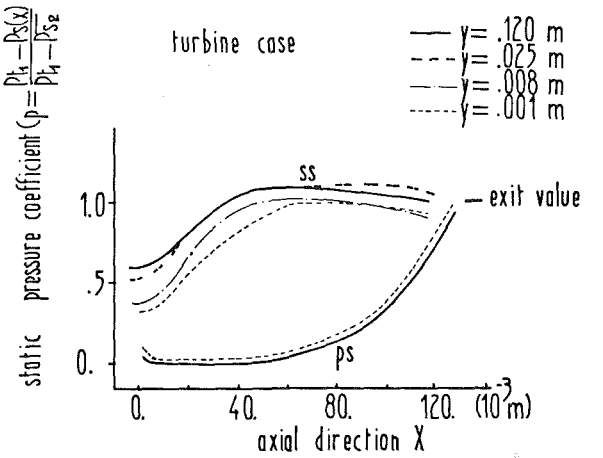

Fig. 3(*b*) Static pressure distribution on blade pressure (*PS*) and suction (*SS*) sides

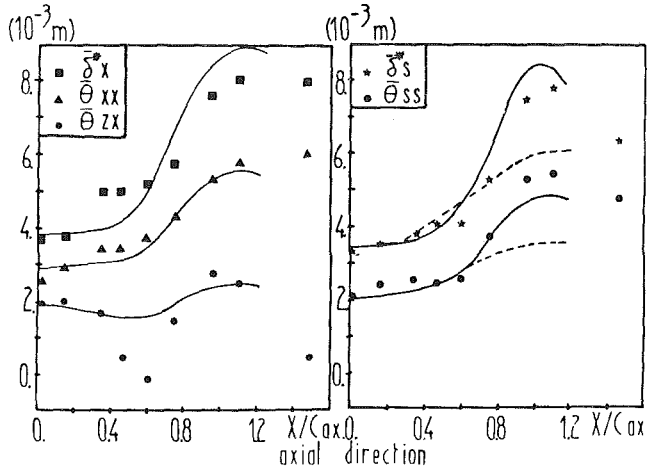

Fig. 4 Tangentially mean integral quantities for the compressor case (theory — with experimental fluctuation terms, · · · without these terms)

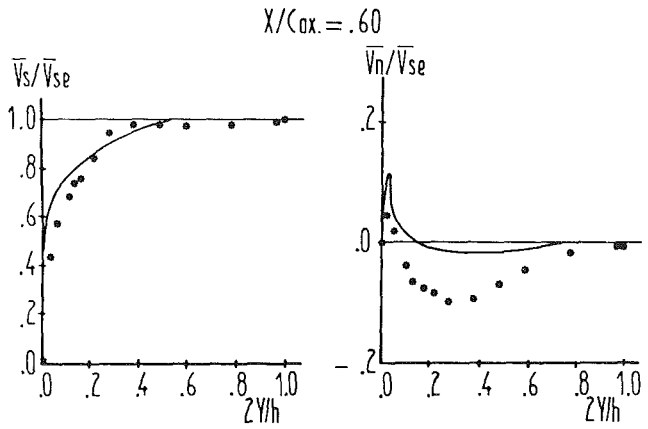

Fig. 5(*a*)

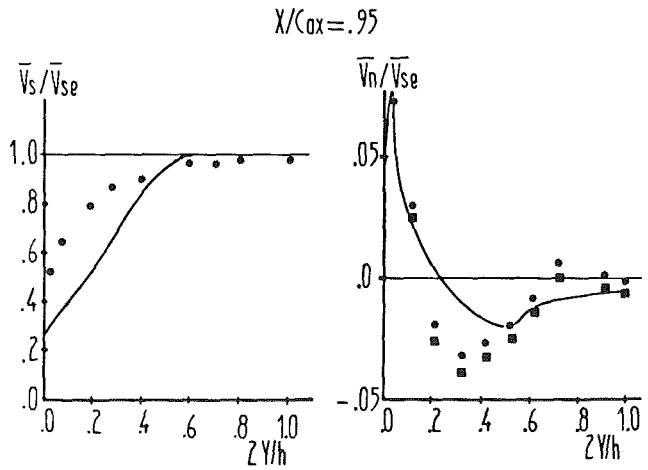

Fig. 5(*b*)

Fig. 5 Compressor case: Mean velocity profile $\bar{V}_S$ $\bar{V}_n$ in the azimutal direction Z along Y ($\bar{V}_{se}$ = 225.0 m/s at x/c_{ax} = 0.60, $\bar{V}_{se}$ = 205.2 m/s at x/c_{ac} = 0.95) (theory with experimental fluctuations terms) (*β_e = 29 deg, ■ β_e = 29 deg 3).

in Table 3. Note that the uncertainty estimates for P_S and P_T do not take into account the streamline displacement effects which occur when measuring in a strong pressure gradient. The uncertainty estimates for V_s, V_n, V_b depend on the values given in Table 3 for β, γ, and P_T, P_S. But they depend also strongly on the definition of the inviscid flow direction S. The influence of a slight variation of this direction ($\Delta\beta_e$ = 0.3 deg) on V_n is given in Fig. 5(*b*). For V_s, this effect is about ten times lower in the compressor case, and has not been given in Fig. 5(*a*).

A large number of measurements have been done in both cases. For example, more than 300 experimental points have been used to describe the flow at each station along the axial distance X.

III Presentation and Analysis of the Experimental Results-Compressor Cascade

Only a fraction of the obtained experimental results will be presented here. They are representative of the complete measurements. Their analysis will be discussed in relation with the already presented theoretical flow model.

The flow was computed at mid-span by Katsanis' blade-to-blade calculation [16]. The streamtube height distribution, along x, used in this blade-to-blade computation, takes into account of the mean (Z-direction) experimental displacement thickness δ_x^* (Fig. 4). It was supposed that the obtained solution was applicable at all distances from the wall, the blading being not twisted. The local direction of the inviscid flow solution indicated for us, according to our model, the longitudinal direction S at that position. The mean values that will be presented below for various flow quantities are tangential (Z-direction) arithmetic mean values.

Downloaded 01 Jun 2010 to 171.66.16.62. Redistribution subject to ASME license or copyright; see http://www.asme.org/terms/Terms_Use.cfm

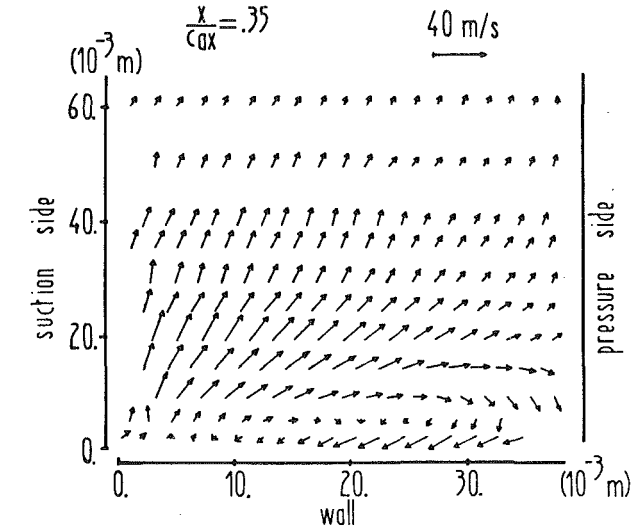

Fig. 6(a)

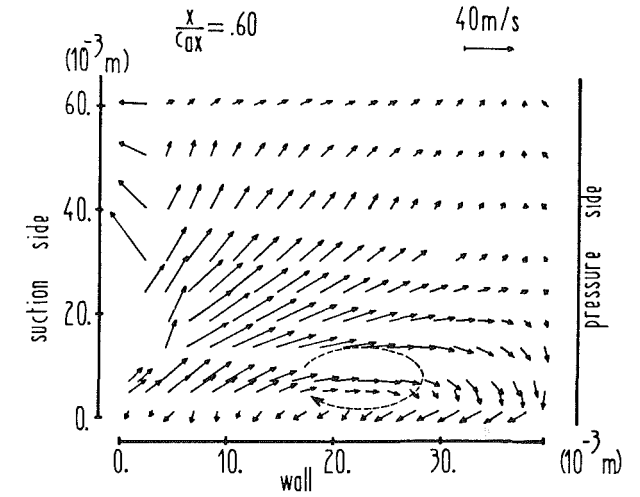

Fig. 6(b)

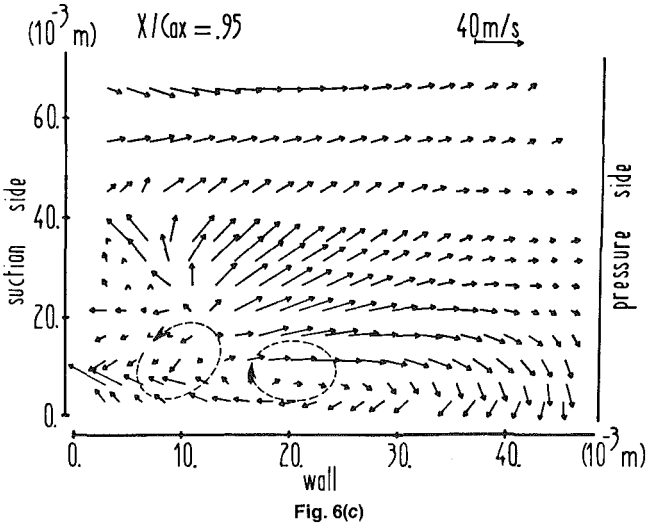

Fig. 6(c)

Fig. 6 Compressor case: Velocity vectors $V_n = V_y$ in the (Y,Z) plane at x/c_{ax} = 0.35, 0.60, 0.95 (velocity in m/s)

The Mean Values. Integral quantities of the tangential mean flow shear layers are presented in Fig. 4 as a function of the axial distance.

The corresponding mean velocity profiles $\bar{V}_s(y)$ and $\bar{V}_n(y)$ are presented in Fig. 5 for two axial stations (x/c_{ax} = 0.60 and 0.95). Note that the transverse velocity profiles and all quantities depending on them are relatively sensitive in respect to the direction of the external inviscid flow. This can be seen from the experimental results presented in Fig. 5.

The integral quantities present an abrupt increase after the axial distance x/c_{ax} = 0.60. The corresponding increase in δ, as it can be seen from the longitudinal velocity profile evolution is quite impressive. $\bar{\theta}_{zx}$ decreases first up to x/c_{ax} = 0.60. In the transverse direction, the secondary vorticity manifests itself in the S-shaped $\bar{V}_n(y)$ profiles.

The S-shaped $\bar{V}_n$ profiles becomes more pronounced from the leading edge to the axial distance x/c_{ax} = 0.60 (Fig. 5(*a*)). After this distance, the S-shaped $\bar{V}_n$ profiles are reduced (Fig. 5(*b*)).

In the following, we shall consider in more detail the structure, origin and development of the secondary vorticity in the passage of the cascade.

The Local Values. Static pressure distributions are given in Fig. 3(*a*) on the blade surface. We take notice of a strong variation of P_S in the shear layer near the suction side, while on the pressure side P_S varies only slightly. Also, before the axial distance x/c_{ax} = 0.60, P_S varies quickly in the Y direction, and at y = 0.015 m, it has almost reached the inviscid value. After x/c_{ax} = 0.60, we observe that the variation of P_S is more effective at some distance from the wall (y > 0.010 m).

Figures 6–9 present some detailed results concerning three axial stations (x/c_{ax} = 0.30, 0.60, 0.95), which may help us to describe the main features of the flow. From Figs. 6(*a*)–6(*c*), where we have plotted the secondary velocity vector $\mathbf{V}_n + \mathbf{V}_b$ (its modulus and its direction), we can study the evolution of the secondary vorticity (here $\mathbf{V}_b = \mathbf{V}_y$).

The velocity component V_y is not zero at mid-span (y = 0.05 m). This is presumably associated with a different evolution of the shear layer on the opposite side wall. In Fig. 6(*a*), we may isolate the influence of a vortex, centered halfway between the suction and pressure sides at y = 0.005 m, from the wall. The strength of this vortex is growing from the point where the external flow starts to turn under the influence of the cascade, that is a little upstream of the cascade. This vortex Ω_{sp} may be attributed to the curvature of the "inviscid streamline" S and to the transfer in the S direction of a part of an upstream transversal component Ω_n . This Ω_n component is associated with the upstream viscous velocity profile V_s. This vortex will be called the passage vortex, and its strength Ω_{sp} may be computed according to [14] as follows:

$$\frac{d}{ds}\left(\frac{\Omega_{sp}}{\rho V}\right) \sim \frac{2\Omega_n}{\rho V R} \tag{1}$$

In Figs. 6(*b*) and 6(*c*), it can be seen that this passage vortex moves from the pressure side to the suction side, and is centered approximately at the same y distance from the wall. At the axial position x/c_{ax} = 0.60, we start detecting the influence of the suction side shear layer on the generation of secondary velocities. This influence is growing downsteam at the axial position x/c_{ax} = 0.95, and hits mainly the corner region near the suction side. An assimilation of such a corner flow with those studied by Gessner [10], is far from obvious when Fig. 6(*c*) is considered. Usual turbulent corner flows are associated with two opposite vortex Ω_{sc}, as depicted in Fig. 1. In our case, this usual picture is only qualitatively the same. We take notice of some points (Fig. 6(*c*)) where the velocities are directed towards the corner edge as in usual turbulent corner flows. But four supplementary effects disturb this corner flow. Firstly, the passage vortex Ω_{sp} induces important velocities also in the corner region and this may mask near the

Downloaded 01 Jun 2010 to 171.66.16.62. Redistribution subject to ASME license or copyright; see http://www.asme.org/terms/Terms_Use.cfm

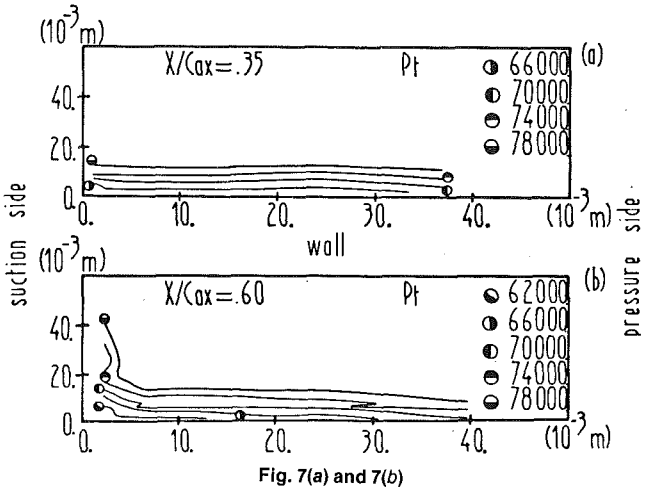

Fig. 7(a) and 7(b)

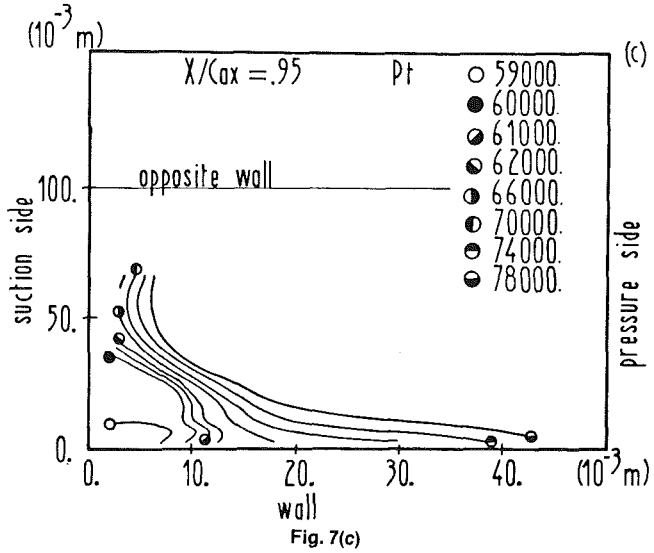

Fig. 7(c)

Fig. 7 Compressor case: isobaric curves for P_T in the (Y,Z) plane at x/c_{ax} = 0.35, 0.60, 0.95 (pressure in N/m^2)

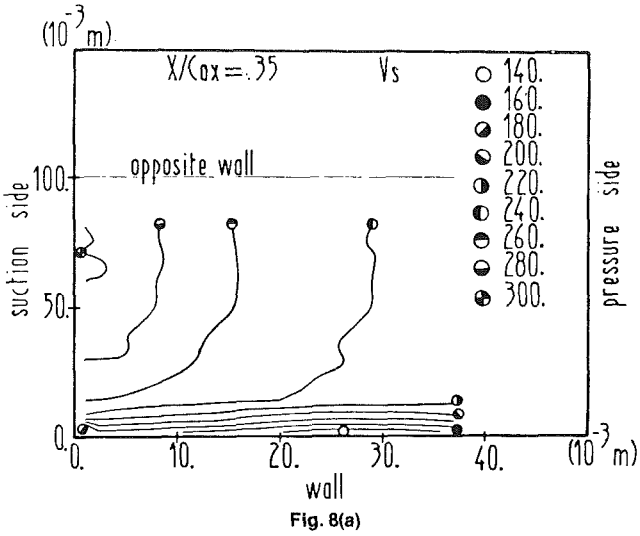

Fig. 8(a)

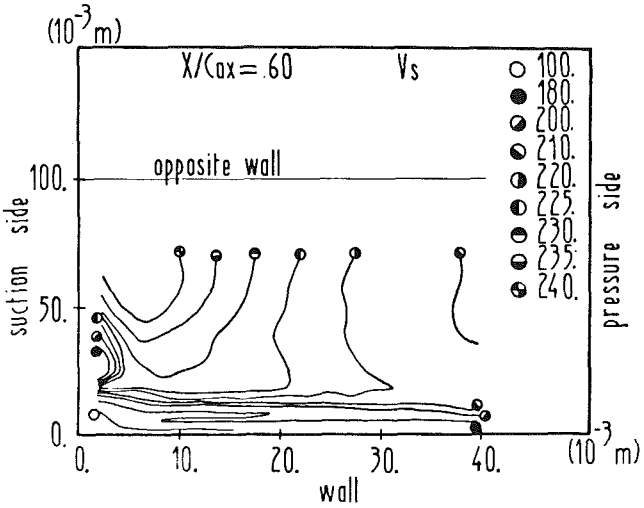

Fig. 8(b)

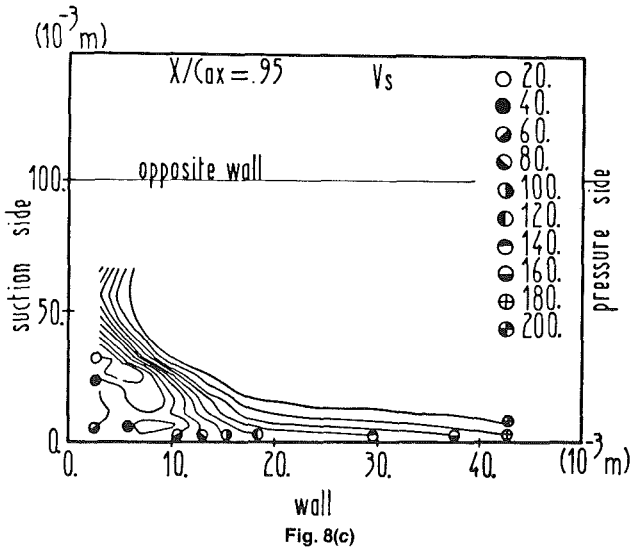

Fig. 8(c)

Fig. 8 Compressor case : iso-V_s curves in the (Y,Z) plane at x/c_{ax} = 0.35, 0.60, 0.95 (V_s in m/s)

wall the first opposite corner vortex Ω_{sc1} (Fig. 1). Secondly, as we shall see, Ω_{sp} induces a strong mass transport of low energy material towards the corner region. Thirdly, the two shear layers do not have the same thickness (Fig. 7), a fact which must reduce the "size" of the second corner vortex Ω_{sc2}. Fourthly, as will be shown, this corner flow is associated with a strong blockage effect. This fact must induce additional curvature of the inviscid flow along the Y-direction. The accuracy of the velocity components (V_n, V_b) is then lower in the corner region.

Take notice that a corner vortex Ω_{sc} must induce low velocities compare to Ω_{sp}, as Ω_{sc} is a second order effect of the viscous interaction in the corner (Gessner, [10]). First order effects must be detected like static pressure gradient as we shall see thereafter (Mojola [17]).

The isobaric curves of stagnation pressure P_T are presented in Figs. 7(*a*)–7(*c*) for the same stations. At x/c_{ax} = 0.35, the isobaric curves are parallel to the wall. This fact indicates that the boundary layer on the side wall has approximately the same evolution at all z position.

It must be noted that the assumptions, which form the basis of the calculation methods concerning the influence of the passage vortex, seem to be respected for this measuring

Downloaded 01 Jun 2010 to 171.66.16.62. Redistribution subject to ASME license or copyright; see http://www.asme.org/terms/Terms_Use.cfm

station. These assumptions are (*a*) inviscid nature of the induced velocity components (V_n, V_b) and (*b*) no rotation of the Bernoulli's surfaces.

The same remarks can be made for $x/c_{ax} = 0.60$ except near the suction side, where the growth of the blade boundary layer and the resulting interaction with the side wall shear layer occupy a small but appreciable region. At the last measuring station presented here ($x/c_{ax} = 0.95$), we can observe the rotation of Bernoulli's surfaces inside the wall shear layer, but, especially, the large region occupied by the corner flow and the importance of the corresponding losses in stagnation pressure. Comparing these station results with the previous results, we can see that the isobars at $x/c_{ax} = 0.95$ are found very near the side wall, indicating in this way the mass transport that is taking place from the pressure to the suction side of the cascade. This effect may be associated with the passage vortex Ω_{sp}. In fact, theoretical computations, taking into account Ω_{sp}, are able to predict such a mass transport, and corresponding inclinations of Bernoulli's surfaces (Anderson, et al. [22]).

Figures 8(*a*)–8(*c*) present the V_s = constant curves. Inside the viscous region, the iso-V_s curves are identical in form with the iso-P_T curves, while, outside they are quite different. This must be expected as, outside of the wall viscous layers, the value of the longitudinal velocity V_s is influenced essentially by the static pressure P_S. Inside the viscous layers, the value of the velocity V_s is essentially associated with the evolution of the stagnation pressure P_T. We note that the presented V_s values inside the corner layer (Fig. 8(*c*)) must be considered more qualitatively than quantitatively. In fact, in this region we have a low measuring accuracy due to high values of the V_y component in respect to V_s and due to high pressure gradients in both the Y and Z directions. Moreover, the inviscid solution we have computed at mid-span is not valid in the region near the wall, where it is perturbed locally by the three-dimensional distribution of the shear layers blockage effect.

Let us consider, now, in the isobaric curves P_S, Figs. 9(*a*)–9(*c*). Outside of the viscous layer, we have a static pressure gradient in the Z direction, negative from the pressure to the suction side which is associated with the curvature of the "inviscid" streamlines S in the (X,Z) plane (Fig. 9(*a*)). Approaching the cascade end wall, we should expect the isobaric curves P_S to be normal to it as the blades are not twisted ($\partial P_S/\partial_y \sim 0$). Nevertheless, the iso-P_S curves are inclined towards the suction side (Fig. 9(*a*)). Considering again the corresponding iso-P_T curves (Fig. 7(*a*)), it can be seen that these are practically parallel to the cascade end wall. On the other hand, the static pressure variation, corresponding to the induced secondary velocities V_n, V_b is of the order of 300 N/m^2. This, however, corresponds to the order of magnitude of the irregularities exhibited by each iso-P_S curves. Consequently, the only valid reason that may explain this additional static pressure gradient along the Y direction is the presence of an additional curvature of the external flow streamlines. This curvature is induced, presumably, by the blockage effect introduced downstream by the higher losses in the corner region, resulting from the interaction of the suction side and cascade end wall shear layers. In this sense, the corner layer blockage (see Fig. 7(*c*)) is felt far upstream.

Let us, now, consider the situation at $x/c_{ax} = 0.95$ (Fig. 9(*c*)). At mid-span, we have again a static pressure gradient in the direction Z but less strong than that upstream. The important fact is that the isobaric curves P_S exhibit a completly different trend as compared with the situation discussed for $x/c_{ax} = 0.35$.

These curves are now inclined towards the pressure side corner.

Let us consider first the iso-P_S curves near the pressure side. We take notice of a decrease of the boundary layer thickness in this region, and correspondly of the associated

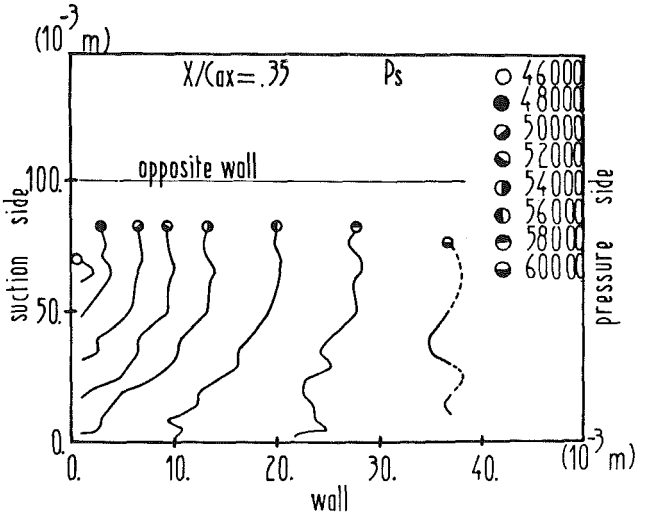

Fig. 9(*a*)

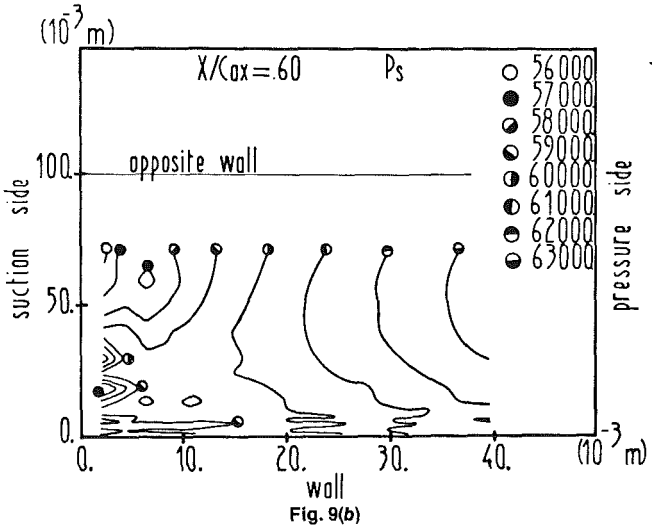

Fig. 9(*b*)

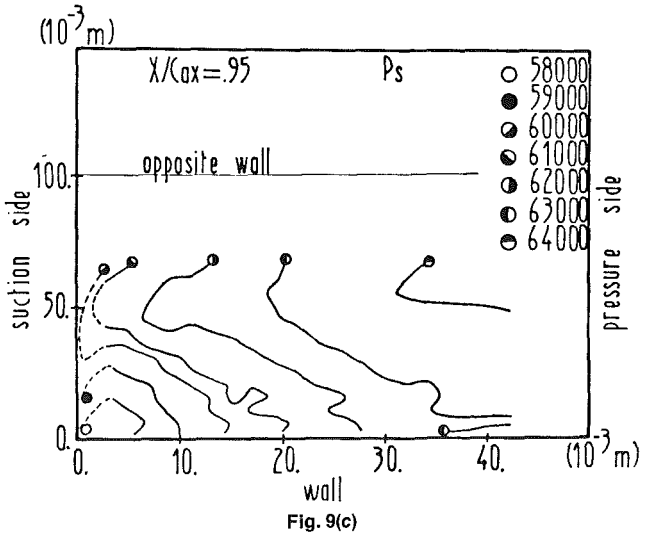

Fig. 9(*c*)

Fig. 9 Compressor case: isobaric curves for P_S in the (Y,Z) plane at $x/c_{ax} = 0.35, 0.60, 0.95$ (pressure in N/m^2)

Downloaded 01 Jun 2010 to 171.66.16.62. Redistribution subject to ASME license or copyright; see http://www.asme.org/terms/Terms_Use.cfm

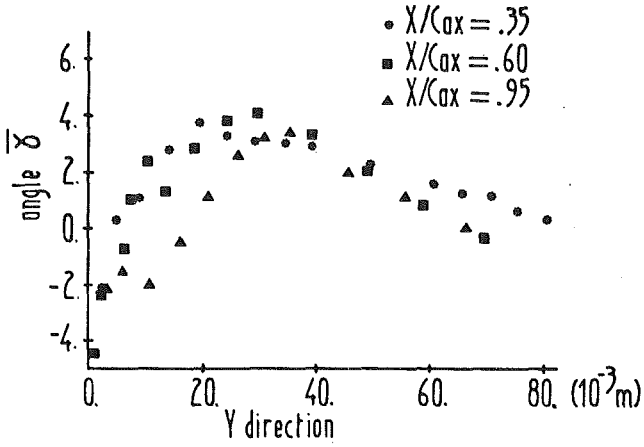

Fig. 10 Compressor case: Mean angle γ in the azimutal direction Z along Y at x/c_{ax} = 0.35, 0.60, 0.95

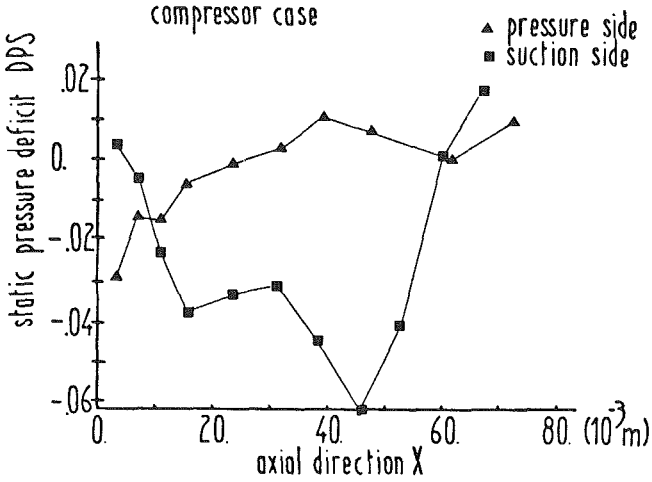

Fig. 11 Compressor case: Mean static pressure deficit along Y on the blade surface

blockage effect, as it may be seen from the inclinaison of the iso-P_T curves (Fig. 7(*c*)). Considering now Fig. 10 where we present the evolution along Y of the arithmetic mean values along Z of the angle $\bar{\gamma}$. These mean values result from the mean velocity components $\bar{V}_x$, $\bar{V}_y$, $\bar{V}_z$. At the axial station x/c_{ax} = 0.35, the angle $\bar{\gamma}$ is positive, which indicates a transfert of the flow outwards in the direction of the opposite wall. We observe also, that the flow is not symmetrical with respect to the mid-span, as was already noticed. At the axial stations x/c_{ax} = 0.60 and 0.95, we get increasing negative values of $\bar{\gamma}$ near the wall, which indicates that a growing part of the flow is going towards the wall. This fact may be observed in Fig. 6(*c*) near the pressure side of the blade. The observed inclination of the P_S curves are then a consequence of this movement of the flow along Y.

Let us consider now the iso-P_S curves near the suction side, in the so-called corner region. We cannot explain then the inclination of the iso-P_S curves either by the influence of the transverse velocity field or by an additional curvature of the external flow field as again this would correspond to a transport of fluid towards the wall. Note that the meaurements in this corner region may only be considered as qualitative ones. Looking for P_S on the suction side wall (Fig. 3(*a*)), we observe that P_S is approximately constant along Y in the corner region, but not in the Z-direction as may be seen Fig. 9(*c*). In fact, the origin of the particular shape of the iso-P_S curves may be searched in the strong viscous interaction between the side wall shear layer and the suction side boundary layer, leading to a corner effect (Gessner [10]). We may note that Mojola [17] has measured very similar iso-P_S curves in a corner formed by two straight walls. No turbulence meaurements have been realized for the present case, so that we cannot further discuss the origin of these static pressure gradients.

We present in Fig. 11 the mean static pressure deficit DP_S on the profile surface, which we define as

$$DP_S = \int_0^{h/2} \frac{(P_S(y=h/2) - P_S)\,dy}{h/2(P_{T1} - P_{S1})}$$

The difference between the values of DP_S on the pressure and suction surfaces is representative of the mean force deficit on the blade. We observe that the mean force deficit is maximum for x/c_{ax} = 0.60, at the beginning of the observed corner flow. Then, the force deficit decreases quickly, and reaches positive values near the trailing edge.

To summarize the above results, we may say that our measurements have put into evidence:

a The three-dimensional blockage effect of the corner flow on the upstream flow in the first part of the blade passage ($x/c_{ax} < 0.60$). As a consequence, the blade force decreases near the wall, as the static pressure increases on the suction side.

b A mass transport associated with the passage vortex Ω_{sp}, from the pressure side to the suction side when Ω_{sp} has grown sufficiently ($x/c_{ax} > 0.60$). The corresponding inclination of the Bernoulli's surfaces are associated with a decrease of the static pressure near the suction side wall, which reduces the blade force deficit in the second part of the blade passage ($x/c_{ax} > 0.60$).

c In the compressor case, the induced velocities V_n, V_b have not themselves sufficient energy to modify strongly the static pressure field. The level of Ω_{sp} is then a balance between an increase under the deflexion of the flow, and a decrease under the deceleration of the flow.

d The interaction of the suction side boundary layer with the cascade side wall shear layer seems to be at the origin of the stagnation pressure losses in the corner region. As in a classical turbulent corner layer, an increase of the dissipation results from the work of additional Reynolds stresses, with a corresponding inclination of the iso-P_S curves (Mojola [17]). But in our case, this corner flow is again complicated as it grows on a loaded surface, and under the influence of the mass transport associated with Ω_{sp}, towards the corner edge. The reader will take notice also that the corner flow appears mainly when the mass transport by Ω_{sp} is really effective. We shall describe now the main features of secondary flow in a turbine.

IV Presentation and Analysis of the Experimental Results in the Turbine Cascade

We shall present again the most significant results for three axial stations, labelled No. 7 (x/c_{ax} = 0.328), No. 10 (x/c_{ax} = 0.985 and No. 11 (x/c_{ax} = 1.203). The cascade is presented in Fig. 12, with the streamlines of the inviscid flow as computed using Katsanis's method [16]. The blades have been highly loaded so as to magnify the secondary flow and particularly the so-called passage vortex Ω_{sp} through the high turning of the inviscid flow.

The Mean Values. Mean (Z-direction) velocity profiles $\bar{V}_s$ and $\bar{V}_n$ are presented in Fig. 13 for measuring stations 7 (x/c_{ax} = 0.328) and 10 (x/c_{ax} = 0.985) (see Fig. 12). Near the trailing edge of the blade (station 10), we can observe the total disappearance of the viscous layer in the mean $\bar{S}$ direction. At station 7, we take notice of a striking increase of $\bar{V}_s$ over the external value $\bar{V}_{se}$ at mid-span.

The induced $\bar{V}_n$ velocities in the transverse plane are very

Downloaded 01 Jun 2010 to 171.66.16.62. Redistribution subject to ASME license or copyright; see http://www.asme.org/terms/Terms_Use.cfm

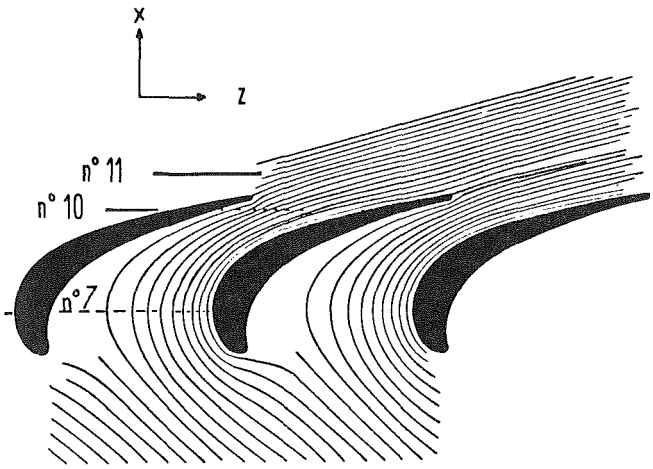

Fig. 12 Turbine case cascade arrangement and inviscid streamlines

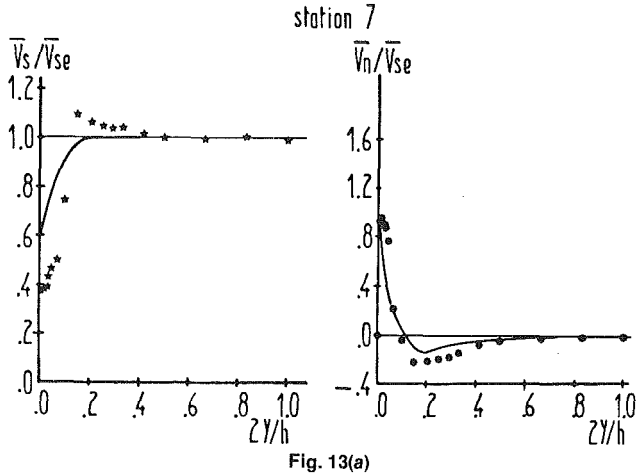

Fig. 13(a)

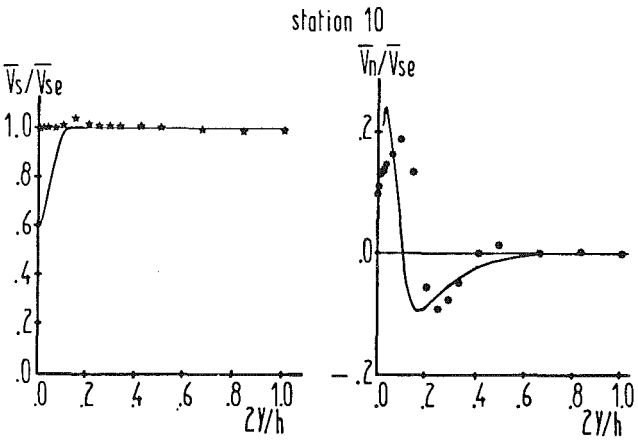

Fig. 13(b)

Fig. 13 Turbine case: Mean velocity $\bar{V}_s$, $\bar{V}_n$ in the azimutal direction Z along Y, ($\bar{V}_{se}$ = 13.0 m/s station No. 7, $\bar{V}_{se}$ = 49.0 m/s station No. 10)

important. Values of $\bar{V}_n / \bar{V}_{se}$ up to 0.9 are obtained at station 7, in the passage near the wall.

The Local Values. Local velocity vector ($\mathbf{V}_n + \mathbf{V}_b$) distributions are presented in Fig. 14(*a*) and 14(*b*). As we go downstream, a displacement of the passage vortex is observed towards the suction side of the blades and away from the cascade wall (see also Fig. 13). The high load imposed on the cascade blades has, as a consequence, the creation of a low kinetic energy zone near the pressure side in the leading edge region (see Fig. 17(*a*)). No kinetic energy losses are observed (Fig. 15(*a*)), so that, within the accuracy of the present measurements, the corresponding low kinetic energy zone takes the form of a stagnation region. Inside this region, the induced velocities V_n, V_b are also rather small.

Considering our measurements at station 7 (Figs. 14(*a*) and 15(*a*)), we may remark the absence of the two branches of the horseshoe vortex, which normally ought to occur at the blade leading edge (see, for instance, Langston [7,23], Marshal and Sieverding [24]).

Without claiming that this is the general case, we shall consider here that we have at station 7 only one streamwise vortex component which we shall name hereafter the passage vortex. At station 7, half of the flow turning has been realized, so that the streamline curvature contribution upon the passage vortex formation is rather important (equation (1)). On the other hand, the rather important acceleration of the external flow and its corresponding vortex stretching tend to amplify this first effect. As a result, as can be seen from Fig. 15(*a*), (note that for this and all subsequent figures, $P_{\text{ref}} = P_{T1}$), the two-dimensional character of the upstream boundary layer has completely disappeared and the iso-P_T curves are on longer parallel to the cascade side wall. We may remark, as a consequence, that the vortex, which stands in the middle of the passage, is not brought into light only by the velocity field (V_n, V_b) but also by the total pressure field. The low energy material existing inside the vortex occupying the passage at station 7, may have come either from the low energy shear layer near the wall, or from a merging of the passage vortex with one of the branches of the leading edge horseshoe vortex or finally, from a combination of the two effects.

Looking at Figs. 14(*b*) and 15(*b*) at station 10, we may say that the remarks, we have done above, concerning station 7 are valid also here. The effects are, however, more pronounced, the passage vortex more organized and the losses more important.

We have added here the iso-P_T curves for station 11 (x/c_{ax} = 1.203), (Fig. 15(*c*)). With this figure, we would like to indicate the good flow periodicity obtained during our experiment. One may note that the passage vortex has been moved further towards the blade suction side and, also, that a low energy core is present inside the wake regoin at a distance of 0.1 m from the wall. This form of trailing edge loss concentration is rather common in external aerodynamics.

The isobaric curves of $P_{T1} = P_S$ are presented in Figs. 16(*a*) and 16(*b*). Apart from the static pressure gradient associated with the inviscid curvature of the flow at mid-span, we may observe a strong gradient in P_S inside the vortex region. This gradient in P_S is twice the gradient in P_T (Fig. 16(*b*)). In Fig. 3(*b*) we give the evolution of P_S on the blade surface near the wall. We observe an important decrease of the blade force very near the wall. From the preceding discussion, the relation of this force deficit with the passage vortex is clearly evident.

The iso-V_s curves are given in Figs. 17(*a*) and 17(*b*). The stagnation region near the pressure side (Fig. 17(*a*)) has already been observed in a preceding paragraph. We can take notice that the striking increase of $\bar{V}_s$ and $\bar{V}_{se}$ on the mean $\bar{V}_s$ profile (Fig. 13(*a*), 13(*b*)) is in fact a consequence of the strong decrease of P_S in the vortex center. A similar observation can be made in Fig. 17(*b*).

Summarizing our results, we may describe the secondary flow development inside the passage of the test turbine cascade as follows: A strong passage vortex is formed inside the blade passage, already near the cascade leading edge region. This passage vortex is certainly the result of the

Downloaded 01 Jun 2010 to 171.66.16.62. Redistribution subject to ASME license or copyright; see http://www.asme.org/terms/Terms_Use.cfm

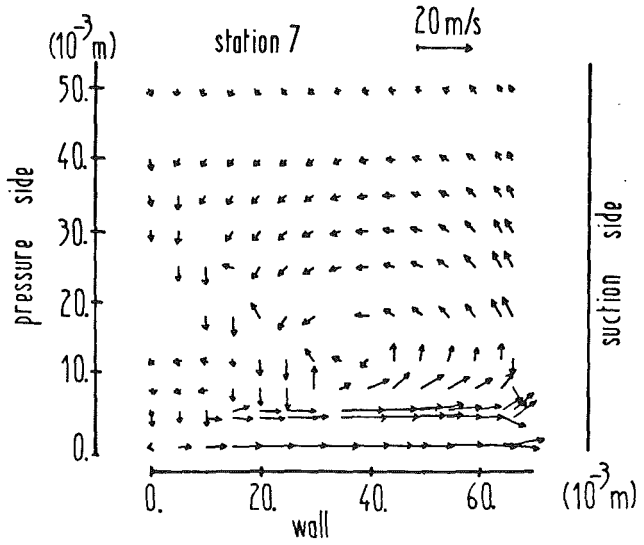

Fig. 14(a)

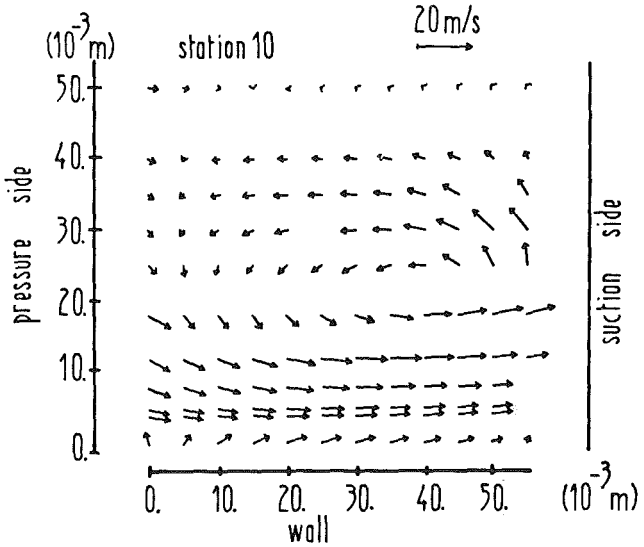

Fig. 14(b)

Fig. 14 Turbine case: Velocity vectors $V_n + V_b$ in the (Y,Z) plane, stations No. 7, No. 10 (velocity in m/s)

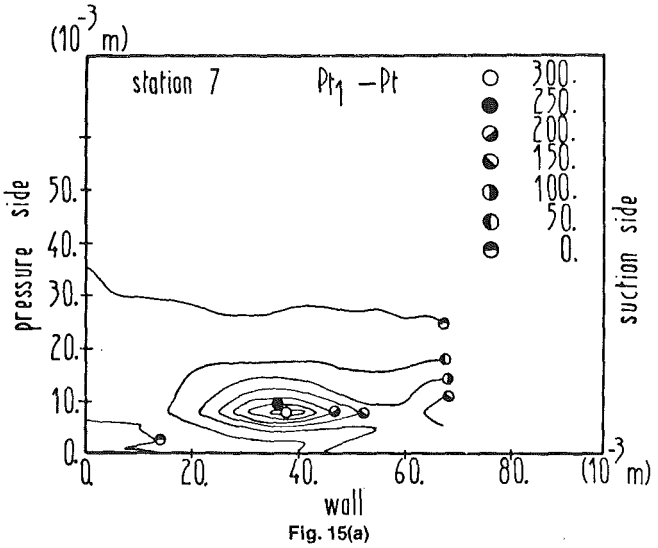

Fig. 15(a)

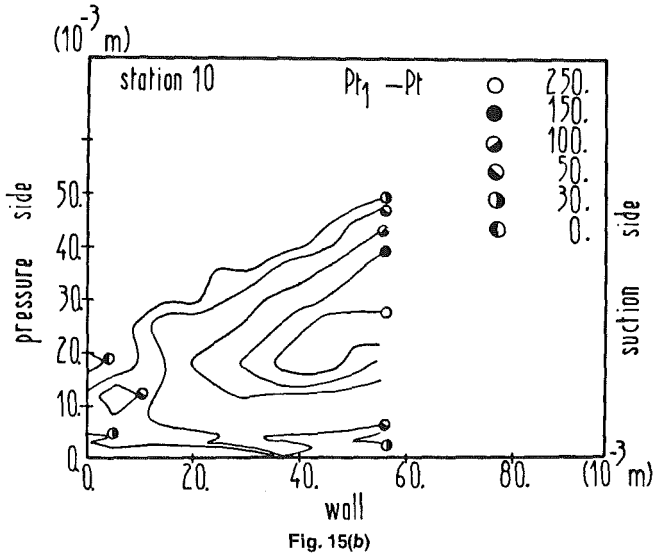

Fig. 15(b)

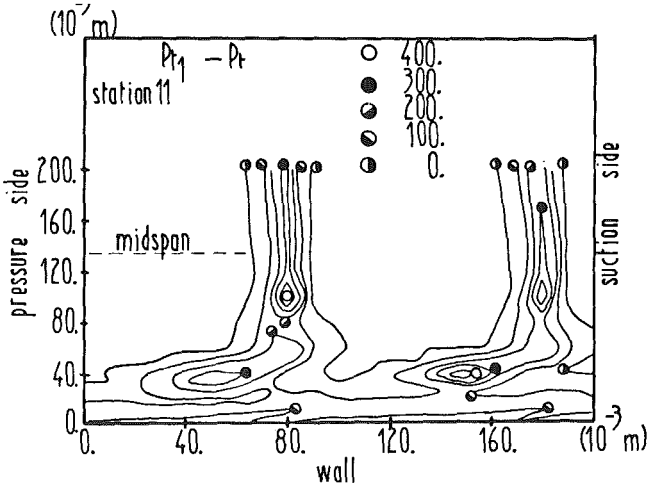

Fig. 15(c)

Fig. 15 Turbine case: Isobaric curves for ($P_{T1} - P_T$) in the (Y,Z) plane, stations No. 7, No. 10, No. 11 (pressure in N/m²)

combination of a streamline curvature effect (equation (1)) with a vortex stretching effect imposed by the strong acceleration of the freestream flow. However, the accumulation of low energy material in and around the vortex center suggests (*a*) either a low energy material transport from regions near the cascade side wall by the vortex, (see for instance the computations of Anderson [13], Hosny [22]), or (*b*) the merging of the suction side branch of the horseshoe leading-edge vortex (the pressure side branch being rather weak) with the passage vortex or (*c*) the combination of both effects.

As one travels downstream, the passage vortex moves toward the suction side and the cascade side wall. Low energy transport toward the passage vortex center is so effective that at the cascade exit plane practically all low energy material is engaged inside the passage vortex motion. At the same time, the vortex strength is increased considerably as can be seen from the static pressure gradients, which become twice as high as those of the total pressure. This can be seen also from the secondary velocities which attain values of the order of the freestream velocity.

Some more comments will be made about secondary flow behavior in both compressor and turbine cases in the

Downloaded 01 Jun 2010 to 171.66.16.62. Redistribution subject to ASME license or copyright; see http://www.asme.org/terms/Terms_Use.cfm

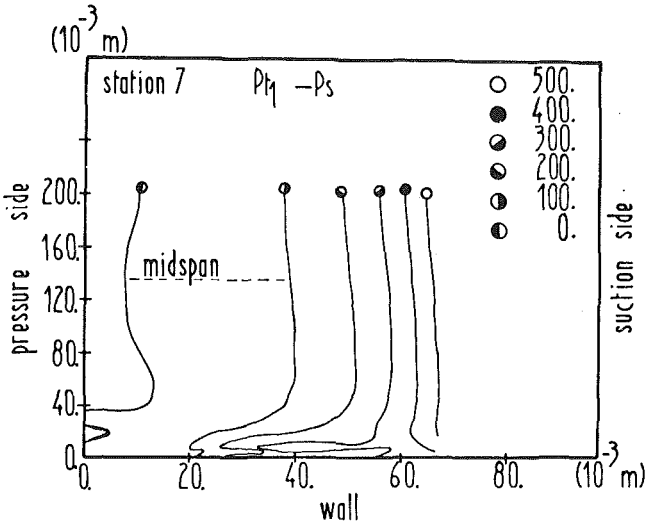

Fig. 16(a)

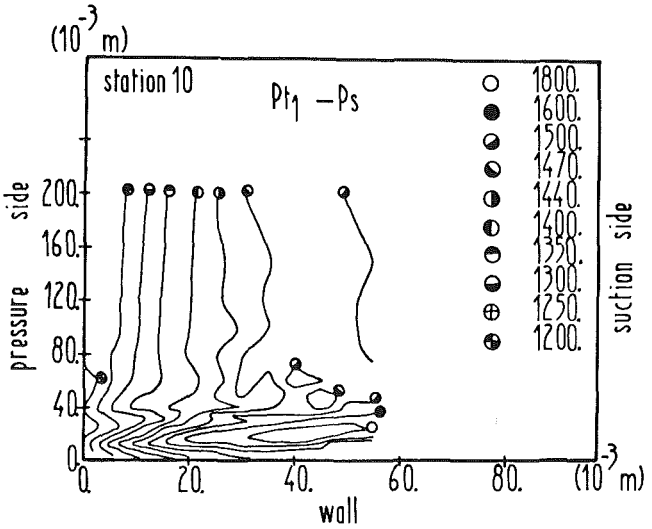

Fig. 16(b)

Fig. 16 Turbine case: Isobaric curves for ($P_{T1} - P_s$) in the (Y,Z) plane, stations No. 7, No. 10, No. 11 (pressure in N/m^2)

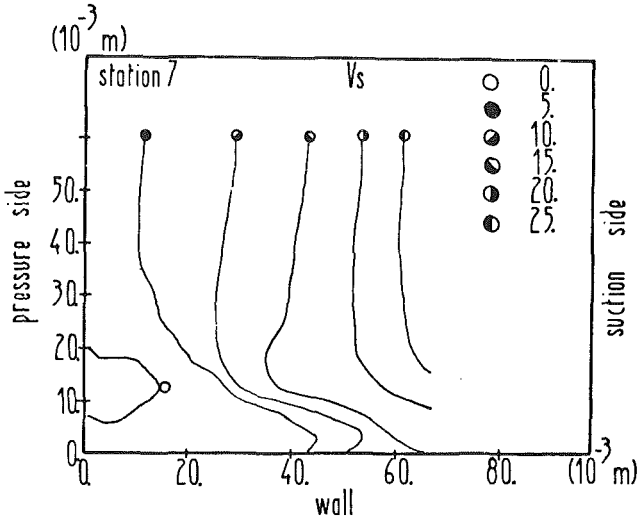

Fig. 17(a)

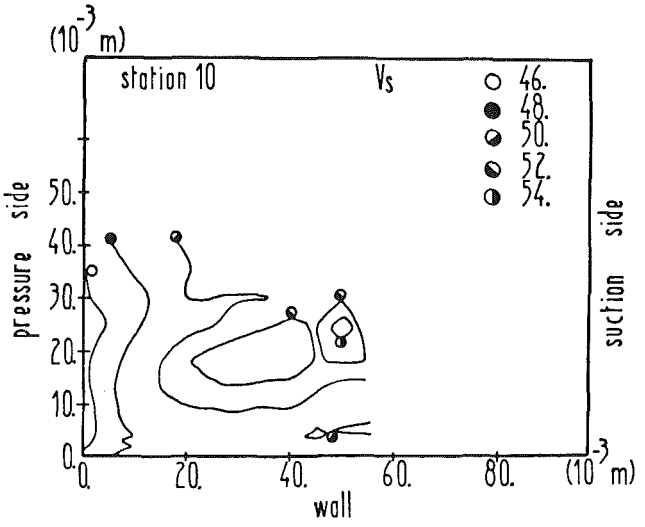

Fig. 17(b)

Fig. 17 Turbine case: iso-V_s curves in the (Y,Z) plane, stations No. 7, No. 10 (velocity in m/s)

following section where the experimental results are compared with a secondary flow calculation method.

V Comparison of Calculation Results with our Experiments

In the following, we will compare our tangentially mean experimental results with those obtained with a theoretical computational method of secondary flow behavior inside the passage of a plane cascade. This method has been initiated by Papailiou [3, 9] and is fully described by Comte [1] and Ohayon [2].

We will only present the most important assumptions of this method, as full details can be found in the aforementioned references.

- The method has been developed on the basis of the tangentially mean Navier-Stokes equations.
- The boundary layer approximation is used for the longitudinal velocity component $\bar{V}_s$ of the resulting flow.
- The secondary vorticity equation is used for the tangentially mean secondary vorticity component calculation. The tangentially mean transverse velocity component $\bar{V}_n$ is computed on the basis of the tangentially mean secondary vorticity component $\bar{\Omega}_{sp}$.
- This same calculation provides the basis for the calculation of the force deficit terms appearing in the momentum conservation equations. An additional assumption is used concerning the direction of the force deficit vector. This direction is taken to be constant throughout the side wall shear layer.
- Tangential variations of the various velocity components are present in the equations by means of the so called "fluctuation" terms. These fluctuation terms are defined in [1] as:

$$B_e D_2 = \int_0^{h/2} \frac{\partial}{\partial x} \left(B_e \left(\overline{V_x'^2}(y=h/2) - \overline{V_x'^2} \right) \right) dy$$

$$+ tg\beta' \int_0^{h/2} \frac{\partial}{\partial x} \left(B_e \left(\overline{V_x'(y=h/2) V_z'(y=h/2)} - \overline{V_x' V_z'} \right) \right) dy$$

- Compressibiltiy effects have been incorporated in the method since its first publication [1, 2].
- Tip clearance effects can also be taken into account [2].

No allowance has been made in the method, either for the

Downloaded 01 Jun 2010 to 171.66.16.62. Redistribution subject to ASME license or copyright; see http://www.asme.org/terms/Terms_Use.cfm

effects resulting from the presence of the corner effect or for a low energy mass transfer effect associated with the vortex motion.

For the compressor case, two computations have been realized. One without and the other with the experimental values of the "fluctuation" terms. In Fig. 4, we have compared the theoretical results with the measured distributions of $\overline{\delta_s^*}$, $\overline{\theta_{ss}}$, $\overline{\delta_x^*}$, $\overline{\theta_{xx}}$, $\overline{\theta_{zx}}$. Note that the introduction of the measured fluctuation terms in the equations demands a differentiation, which, in view of the experimental uncertainties, may introduce a considerable error.

This comparison shows that the theoretical and experimental results agree up to $x/c_{ax} = 0.70$. Beyond this station, the discrepancy between theory and experiment is evident even when the experimental value of the fluctuation terms has been introduced into the equations.

The experimental tangential thickness $\overline{\theta_{zx}}$ presents a strong variation around the station $x/c_{ax} = 0.60$, that the theory is not able to reproduce. In view of the rather good estimates of $\overline{\delta_s^*}$ and $\overline{\theta_{ss}}$, this discrepancy must be attributed to the transversal mean velocity $\overline{V_n}$.

Figure 5 shows the comparison between calculated and measured mean longitudinal and transverse velocity profiles. The agreement is fair for the longitudinal velocity profile for the two stations, but good for the transverse velocity profile at $x/c_{ax} = 0.95$.

The disagreement for $\overline{V_n}$ at $x/c_{ax} = 0.60$ is rather important. Owing to the good prediction of $\overline{V_n}$ at $x/c_{ax} = 0.95$, one possible explanation of this fact may be attributed to an error in the definition of the inviscid longitudinal S direction. In view of the downstream blockage effect introduced in the flow by the corner effect, we may suppose that the real inviscid angle β_e is greater than expected near the wall ($2y/h \sim 0.3$). This error will introduce more negative experimental value for $\overline{V_n}$, with a comparitive small influence on the theoretical prediction $\overline{V_n}$.

It is felt that the general disagreement between theory and experiment for the compressor cascade must be searched in the fact that in our computational model, the influence of the corner effect has not been incorporated properly. For the turbine, a comparison is given for the tangentially mean velocity profiles $\overline{V_n}$, $\overline{V_s}$ in Fig. 13. As the boundary layer character disappears completely from the station 7, the prediction of $\overline{V_s}$ is only fair. The computed level of the mean $\overline{V_n}$ velocity is correct, a fact which is quite surprising. It has been repeatly said in the literature (see the references of [5]) that the inviscid mean secondary flow calculations could only qualitatively represent what happens inside the passage of a high deflexion turbine blading. In addition, our experimental results have demonstrated the strong mass transport of low energy material towards the center of the passage vortex. This fact is not taken into account in our calculation method as we consider that Bernoulli's surfaces are not rotating. This mass transfer seems to influence mainly the longitudinal mean velocity profile $\overline{V_s}$, and probably also the position of the vortex center along Y, which is computed nearer to the wall than measured.

VI Conclusions

Results of two experiments have been presented concerning secondary flow effects in plane cascades of highly loaded compressor and turbine bladings.

We have been able to isolate main features of the secondary flow behavior in the two test cases. These are:

- For the compressor cascade blading, besides the passage vortex, a corner effect is generated through the interaction of the blade suction side boundary layer with the mass transport associated with the passage vortex. This corner effect becomes important essentially in the last third of the axial chord of the cascade. Its blockage effects, however, are felt upstream and modifications that are caused to the static pressure field because of its presence, are, very probably, influencing the blade force distribution (particularly near the suction side) and, consequently, the blade force deficit.

A last aspect, but one which may be the most important of the two shear layers interaction, and which is associated with the corner flow generation, is the development of turbulent shearing stresses not only in the longitudinal direction but also in the transverse one. The comparison between theory and experiment that has been presented in the previous section, seems to point out that, besides the fluctuation terms influence, a direct dissipation effect is missing in the equations which have been used for the calculation. This dissipation effect would come from the transverse turbulent shearing stresses, which have been neglected in the calculation procedure.

In discussing the compressor case, we have not talked extensively about the passage vortex. This was done because its origin and effects are well known and have been discussed extensively in the literature. We may simply add that our theoretical model seems to predict through external flow streamline curvature effects the final strength of the secondary vorticity. (See the comparison of the calculated and measured mean transverse velocity profile, presented in Fig. 5.) This may mean that the vorticity component Ω_{sc} is negligible or that the simplified calculation is predicting the net secondary vorticity correctly. At this stage, we cannot decide which of the two possibilities is the correct one.

In the turbine case, high deflection of the inviscid flow in the (X,Z) plane and the external flow acceleration both produce a passage vortex with a high energy of rotation. This vortex modifies completely the static and total pressure fields. Low kinetic energy material is transported towards the center of the vortex under the influence of high transverse static pressure gradients.

It is not quite evident whether at least one of the two branches of the horseshoe vortex generated at the leading edge merges with the passage vortex. The total pressure field, as we have already pointed out, suggests as one of the possibilities the merging of the two secondary vorticities.

The low energy material transport is a factor which determines the whole structure of the flow. In the first place, it contributes in invalidating any attempt to model the flow in the longitudinal direction as a boundary layer problem. In the second place, it contributes to the formation of the secondary vorticity structure, which is present at station 10.

Certainly, moderately loaded turbine cascade, such as the one tested by Marchal and Sieverding [24], may exhibit a different behavior. Finally, the comparison of theoretical and experimental results presented in Fig. 13, has shown that the strength of the experimental secondary vorticity (although not its position near the trailing edge) can be calculated through the usual simple secondary vorticity computation procedures with a good approximation.

Acknowledgments

This work has been sponsored by the Ministère de la Défense, Délégation Générale pour l'Armement, Direction des Recherches, Etudes et Techniques (DRET) under contracts 75-317 and 77-430. The authors wish to express their thanks to DRET as well as to SNECMA (Société Nationale d'Etudes et de Constructions de Moteurs d'Avions) for their interest and encouragement, which contributed to the accomplishment of the present work. Their sincere thanks must also be expressed to Mr. G. Halter for his help in accomplishing the experimental work and to Mrs. J. Caro for her help in reducing the experimental data.

Downloaded 01 Jun 2010 to 171.66.16.62. Redistribution subject to ASME license or copyright; see http://www.asme.org/terms/Terms_Use.cfm

References

1 Comte, A., "Calcul des Ecoulements Secondares à l'Intérieur du Canal d'une Grille d'Aubes," Doctorial Thesis, Universite de Lyon I, July 1978.

2 Ohayon, G., "Contribution a l'Etude des Ecoulements Secondares dans les Compresseurs Axiaux avec Effets du Jeu radial," Doctorial Thesis, Universite de Lyon I, July 1979.

3 Comte, A., Ohayon, G., and Papailious, K.D., "A Method for the Calculation of the Wall Layers inside the Passage of a Compressor Cascade with and without Tip Clearance," to be presented at the Gas Turbine Conference, Houston, 1981.

4 Vouillarmet, A., "Contribution a l'Etude et a la Comprehension de l'Ecoulement Visqueux dans un Compresseur Centrifuge," Doctoral thesis, Universite de Lyon I, Oct. 1979.

5 "Secondary Flows in Turbomachines," Agard conferences CP 214, The Hague, Mar. 1977.

6 Langston, L.S., "Crossflows in a Turbine Cascade Passage," ASME Paper No. 80-GT-5, New Orleans, Mar. 10-13, 1980.

7 Waterman, W.F., and Tall, W.A., "Measurement and Prediction of 3.D. Viscous Flow in Low Aspect Ratio Turbine Nozzle," ASME Paper No. 76-GT-73, 1976.

8 Flot, R., "Contribution a l'Etude des Ecoulements Secondaries dans les Compresseurs Axiaux," Doctorial Thesis, Universite de Lyon I, 1975.

9 Papailiou, K. D., Flot, R., and Mathieu, J., "Secondary Flow in Compressor Bladings," ASME paper No. 76-GT-57, 1976.

10 Gessner, F.B., "The Origin of Secondary Flow in a Turbulent Flow along a Corner," *Journal of Fluid Mechanics,* 1973, Vol. 58, part 1, pp. 1-25.

11 Sieverding, C.H., and Wilputte, Ph., "Influence of Mach Number and Wall Coooling on Secondary Flows in a Straight Nozzle Cascades," ASME Paper No. 80-GT-52, New-Orleans, Mar. 10-13, 1980.

12 Patankar, S.V., Spalding, D.B., "A Calculation Procedure for Heat , Mass and Momentum Transfer in Three-Dimensional Parabolic Flows," *International Journal Heat Mass Transfer,* Vol. 15, 1972. pp. 1787-1806.

13 Anderson O.C., Briley, W.R., and McDonald, H., "Derivation and Evaluation of an Approximate Analysis for Three-Dimensional Viscous Subsonic Flow with Large Secondary Velocities," NASA-CR-159430, Oct. 1978.

14 Lakshminarayana, B., Horlock, J.H., "Generalized Expressions for Secondary Vorticity Using Intrinsic Coordinates," Vol. 59, part 1, 1973, pp. 97-115.

15 Bario, F., "Mesures en Soufflerie de Grille," report of D.E.A., Laboratoire de Mécanique des Fluides de l'ECL, Lyon, 1973.

16 Katsanis, T., "Computer Program for Calculating Velocities and Streamlines on a Blade-to-Blade Stream Surface of a Turbo-Machine," NACA TND 4525, 1968.

17 Mojola, O.O., "Turbulent Boundary Layer along a Streamwise Corner," Thesis, Faculty of Engineering, London, Mar. 1972.

18 Prandtl, L., *Essential of Fluid Dynamics.* London, ed. B. Lackle, 1952.

19 Armentrout, E.C., Kicks, J.C., "Pressure Instrumentation for Gas Turbine Engines- A Review of Measurement Technology." ASME JOURNAL OF ENGINEERING FOR POWER, Vol. 101, July 1979, pp. 373-383.

20 Bois, G., Leboeuf, F., Comte, A., Papailiou, K.D., "Measurements of Secondary Flows in Transonic Axial Compressor," *Symposium on Measuring Techniques in Transonic and Supersonic Cascade Flow,* Lausanne, Nov. 1976.

21 Leboeuf, F., "Etude Expérimentale et Théorique de l'Ecoulement dans une Turbomachine Axiale Transsonique," Doctorial Thesis, Lyon I, 1978.

22 Hosny, W.M., "A Solution to the Three-Dimensional Secondary Flow Problem," Thesis, University of Cincinnati, 1976.

23 Langston, L.S., Nice, M.L., Hooper, R.M., "Three-Dimensional Flow within a Turbine Cascade Passage," ASME JOURNAL OF ENGINEERING FOR POWER, Jan. 1977, pp. 21-28.

24 Marchal, Ph., Sieverding, C.M., "Secondary Flow within Turbine Bladings," AGARD CP-214, on "Secondary Flow in Turbomachines", Mar. 1977.

25 Bailey, D.A., "Study of Mean-and Turbulent Velocity Fields in a Large - Scale Turbine-Vane Passage," ASME JOURNAL OF ENGINEERING FOR POWER, Vol. 102, Jan. 1980, pp. 88-95.

Downloaded 01 Jun 2010 to 171.66.16.62. Redistribution subject to ASME license or copyright; see http://www.asme.org/terms/Terms_Use.cfm

A Computation and Comparison With Measurements of Transonic Flow in an Axial Compressor Stage With Shock and Boundary Layer Interaction

U. K. Singh
Mechanical Engineering Laboratory,
GEC Power Engineering Ltd.,
Whetstone, Leicester, England.

The flow field within a transonic axial flow compressor stage has been computed using a three-dimensional time-marching technique. Limited viscous effects are considered by including a calculation of the blade surface boundary layers. The boundary layer calculation forms an integral part of the whole computation scheme, which consists of, respectively: (i) inviscid Mach number calculations, (ii) blade surface boundary layer displacement thickness calculations, (iii) inviscid Mach number calculations with mass flow adjustment (based on the calculated displacement thicknesses) on the blade surfaces. The boundary layer computation is done by using integral calculation methods and has specifically been developed to account for a shock and boundary layer interaction (should one exist). Comparisons are made with measured results obtained with an advanced laser velocimeter. The calculated Mach number contours are in extremely good agreement with the experimental results. It is concluded that the calculation technique is a useful tool in the design of transonic axial flow turbomachines.

Introduction

In the past decade considerable progress has been made in the calculation of inviscid turbomachine flows. This progress is exemplified by the recent widespread adoption of the time marching [1-4] method for calculation of inviscid transonic turbomachine flow, including the prediction of shock waves. However, relevant viscous effects, and in particular the effects of shock and boundary layer interactions, are important in the prediction of such flows. It has been demonstrated by the author [5,6] that considerable enhancement in the quality of flow computations in transonic cascades can be achieved by the inclusion of an integral blade surface boundary layer method in an inviscid time marching calculation for cascade flows. The boundary layer method used in the earlier cascade flow work included a comparatively simple treatment of shock and boundary layer interaction effects. This boundary layer method has now been applied in the three-dimensional time marching technique [1] for the computation of flow in a full turbomachine stage.

Essentially the time marching technique serves as a tool for determining the inviscid surface Mach number distributions at specified radial positions from hub to tip for each blade row of the stage. These Mach numbers are then used for the blade surface boundary layer computations, which are an integral part of the iterative scheme. Having computed the boundary layer development at a number of spanwise locations the time marching technique is then reused to solve the flow in the turbomachine stage, with the exception that sources of strength $v \rho d (\delta^*)/ds$ are placed along the blade surfaces.

The method outlined above has been applied to determine the flow through a transonic axial flow compressor stage for which detailed laser anemometer experimental results are available [7]. Good agreement is obtained between the calculated Mach number contours and the experimental results.

Computational Method. The details of the finite volume time maching inviscid flow calculation used in this work have been published previously by Denton and Singh [1]. The type of grid used is shown in Fig. 1. To date, the grid spacing in the pitchwise and the spanwise directions has been kept constant although uneven spacing has been used in the axial direction.

When solving the equations for a rotating blade row absolute flow quantities are used for convenience and the conservation equations are applied to a fixed grid that instantaneously coincides with the rotating grid on which the solution is required. The rate of change of property P at a point in the rotating grid is then related to the rate of change of the same property at the corresponding point in the fixed grid by

Contributed by the Gas Turbine Division and presented at the International Symposium on Application of Fluids Mechanics ahd Heat Transfer to Energy and Environmental Problems, University of Patras, Patras, Greece, June 29—July 3, 1981. Manuscript received at ASME Headquarters April 1, 1981. Paper No. 81-Gr/GT-5.

Copyright © 1982 by ASME

Downloaded 01 Jun 2010 to 171.66.16.62. Redistribution subject to ASME license or copyright; see http://www.asme.org/terms/Terms_Use.cfm

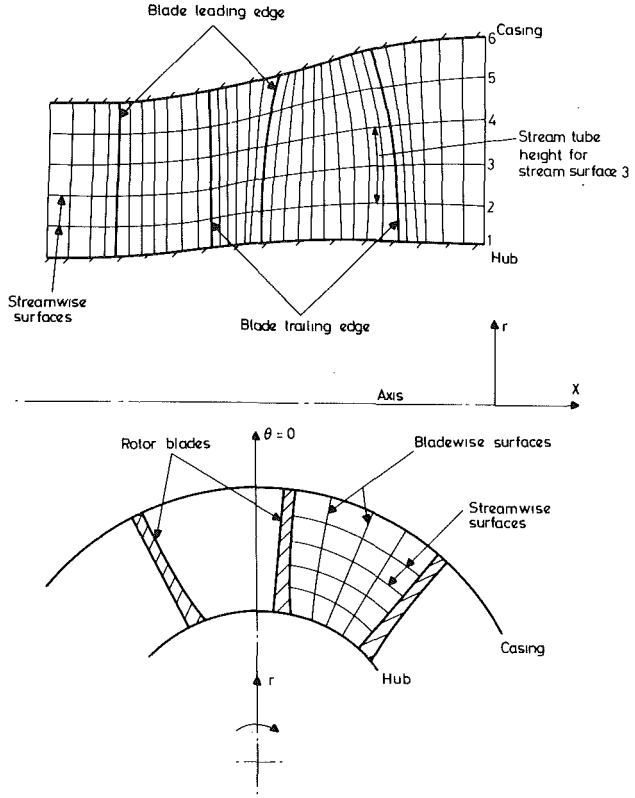

Fig. 1 Calculation grid

$$\left(\frac{\partial P}{\partial t}\right)_R = \left(\frac{\partial P}{\partial t}\right)_F + \Omega \left(\frac{\partial P}{\partial \Theta}\right)_F \tag{1}$$

The conservation equations used are:

$$\text{VOL}\ \Delta\rho = \Delta t \sum \rho \mathbf{V}\cdot\mathbf{A} + \Omega \frac{\partial \rho}{\partial \Theta} \Delta t\ \text{VOL} \tag{2}$$

$$\text{VOL}\ \Delta(\rho V_x) = \Delta t \sum (p i_x \cdot \mathbf{A} + \rho V_x \mathbf{V}\cdot\mathbf{A}) + \Omega \frac{\partial(\rho V_x)}{\partial \Theta} \Delta t\ \text{VOL} \tag{3}$$

$$\text{VOL}\ \Delta(\rho r V_\theta) = \Delta t \sum (p r\ i_\theta \cdot \mathbf{A} + \rho r\ V_\theta \mathbf{V}\cdot\mathbf{A}) + \Omega \frac{\partial(\rho r V_\Theta)}{\partial \Theta} \Delta t\ \text{VOL} \tag{4}$$

$$\text{VOL}\ \Delta(\rho V_r) = \Delta t \sum (p i_r \cdot \mathbf{A} + \rho V_r \mathbf{V}\cdot\mathbf{A}) + \Omega \frac{\partial(\rho V_r)}{\partial \Theta} \Delta t\ \text{VOL} \tag{5}$$

$$\text{VOL}\ \Delta(\rho E) = \Delta t \sum (\rho H \mathbf{V}\cdot\mathbf{A}) + \Omega \frac{\partial(\rho E)}{\partial \Theta} \Delta t\ \text{VOL} \tag{6}$$

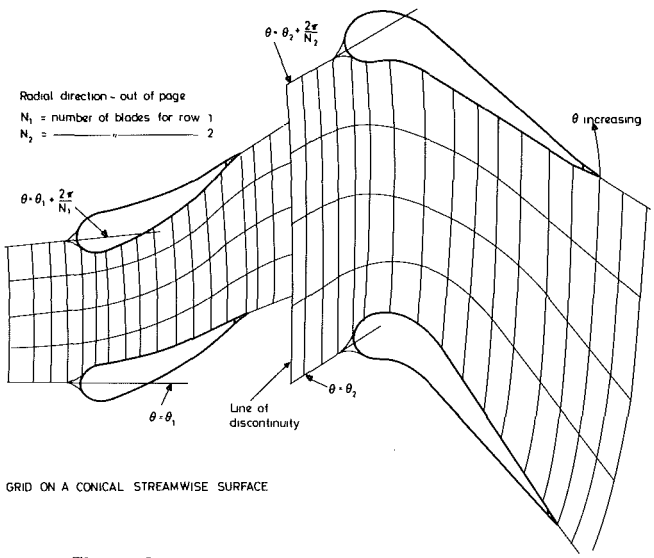

Fig. 2 Calculation grid on a conical streamwise surface

At the upstream boundary the stagnation pressure and temperature are specified separately on each streamwise surface (see Fig. 1). This enables the calculation of rotational flows with nonuniform stagnation pressures and/or temperatures. Also at the upstream boundary, either the absolute flow direction, the relative flow direction, or the absolute tangential velocity, may be held constant on each streamwise surface. The first condition cannot be used when the absolute Mach number exceeds unity nor the second condition when the relative Mach number exceeds unity.

At the downstream boundary the static pressure on the hub is specified. For the other streamwise surfaces at different span locations the static pressure is calculated, as the calculation proceeds, by assuming radial equilibrium.

To obtain a time averaged solution for the turbomachine stage the flow properties are averaged over one blade pitch at some axial location between the two rows (see Fig. 2). The downstream boundary conditions to the first blade row and the upstream boundary conditions to the second blade row are therefore circumferentially (but not radially) uniform.

On the periodic boundaries in the blade to blade plane, after each time step, the properties at corresponding points are equalized by averaging.

The hub and casing are treated as solid boundaries such that no mass may flow across them.

The blade surface boundaries are treated as if sources of

Nomenclature

$\mathbf{A}$ = surface area vector
c_a = axial chord
C_p = specific heat at constant pressure
c_v = specific heat at constant volume
E = internal energy = $c_v T + 1/2\ v^2$
H = total enthalpy = $c_p T + 1/2\ v^2$
$\mathbf{i}$ = unit vector
p = static pressure
P = a fluid property
r = radius
s = surface length
t = time
T = static temperature
$\mathbf{V}$ = absolute velocity vector
VOL = volume of element
x,r,Θ = cylindrical co-ordinates
ρ = fluid density
δ^* = boundary layer displacement thickness
Ω = rotational speed

Subscripts

F = in fixed co-ordinate system
R = in rotating co-ordinate system
x,r,Θ = in co-ordinate direction

Downloaded 01 Jun 2010 to 171.66.16.62. Redistribution subject to ASME license or copyright; see http://www.asme.org/terms/Terms_Use.cfm

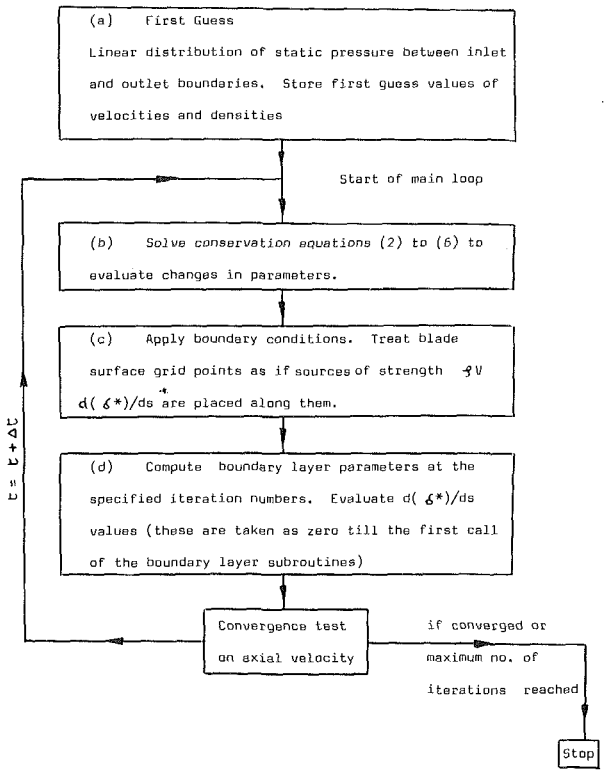

Fig. 3 Outline of the iterative scheme

strength $v\,\rho\,d\,(\delta^*)/ds$ are placed along them. This means that mass flow is assumed to occur across the blade boundaries. Hence the velocities normal to the blade surfaces are no longer zero but are equal to $v\,d\,(\delta^*)/ds$. However, in the early stages of the calculation when no displacement thicknesses, δ^*, have been calculated, the blade surface boundaries are treated as solid boundaries. The boundary layer calculation is performed at specified iteration numbers such that the values of the displacement thicknesses are updated at appropriately spaced intervals.

At the trailing edge, where the blade surface boundary layer transforms into the wake, a sharp discontinuity arises in the displacement thickness distribution. To avoid this discontinuity, the value of $d\,(\delta^*)/ds$ has been set equal to zero at the trailing edge. The justification for the selection of this value is that, in general, $d\,(\delta^*)/ds$ changes sign at the trailing edge from a positive to a negative value.

The blade surface boundary layer calculations are achieved using a two-dimensional integral method which is applied along each streamwise surface as defined by the calculation grid (see Fig. 1). The method can account for streamtube height variation along the blade surfaces, which in the present application is given by the height variation of adjacent streamwise grid surfaces (see Fig. 1). Clearly, this type of application of the boundary layer method will incur errors where the flow streamlines depart markedly from the calculation grid surfaces. The boundary layer method also includes a simple procedure for calculating shock and boundary layer interaction effects. A full description of the boundary layer calculation can be found in references [5] and [6].

The method is programmed in FORTRAN IV. For the results presented in the next section a $8 \times 50 \times 8$ grid was used giving a total of about 3200 nodes and requiring 500K bytes of storage on a CDC 7600. Run time per point per time step was 2.5×10^{-4} s. The number of time steps required for convergence was 1350. Figure 3 gives details of the iterative scheme.

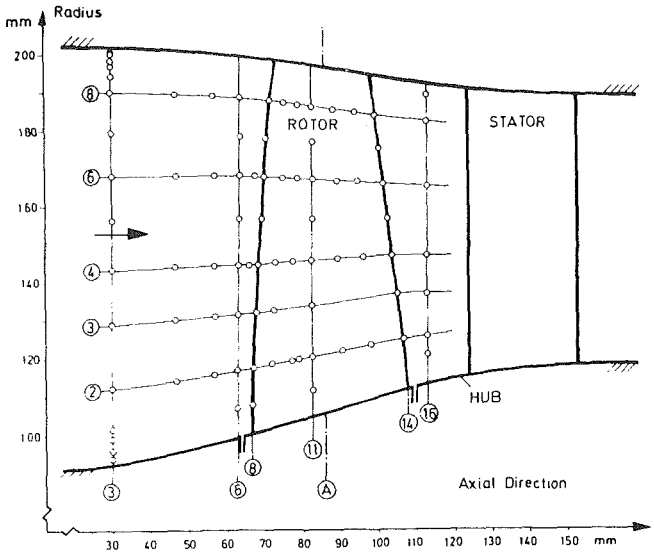

Fig. 4 Flowpath with Laser measuring locii

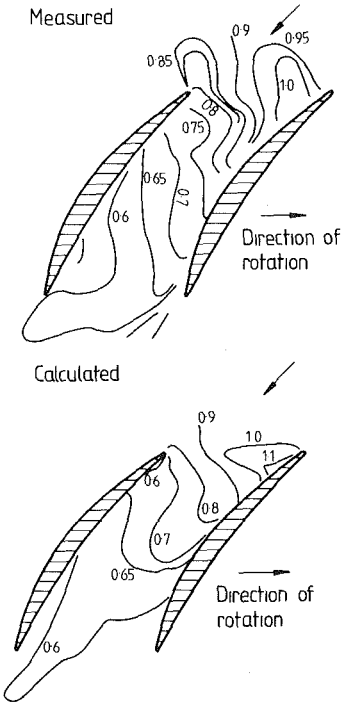

Fig. 5 Mach number contours within rotor - 18 percent blade height - peak efficiency - 100 percent speed

Comparison between Experimental and Computational Results. The method developed has been used to determine the flow field within a transonic axial single-stage compressor for which detailed experimental results are available [7]. The compressor design total pressure ratio is 1.51 with a mass flow of 17.3 Kg/s at 20260 rpm. The rotor has 28 blades with an inlet tip diameter of 399 mm and a radius ratio of 0.5. The rotor tip solidity is 1.34. The blades are composed of multiple - circular - arc profiles, having the shape of a DCA profile near the hub and of a wedge type profile in the supersonic position near the tip. The stator consists of 60 blades having NACA-65-profiles with a circular arc camber line.

The flowpath of this stage, with the experimental measuring stations, is shown in Fig. 4. The measurements of the velocity vectors ahead, within, and downstream of the fast

Downloaded 01 Jun 2010 to 171.66.16.62. Redistribution subject to ASME license or copyright; see http://www.asme.org/terms/Terms_Use.cfm

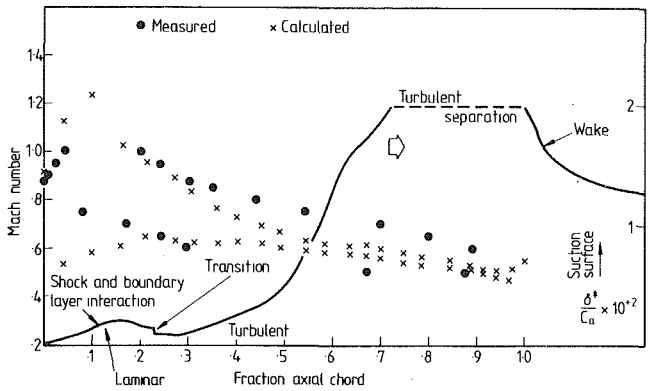

Fig. 6 Transonic compressor rotor - 18 percent blade height

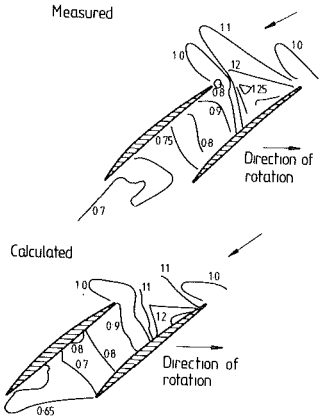

Fig. 7 Mach number contours within rotor - 45 percent blade height - peak efficiency - 100 percent speed

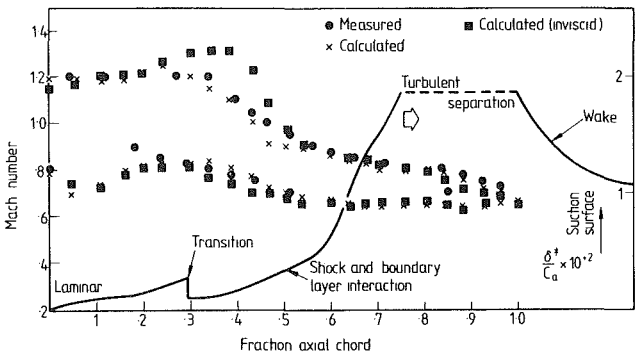

Fig. 8 Transonic compressor rotor - 45 percent blade height

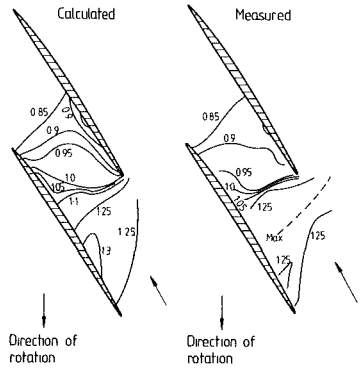

Fig. 9 Mach number contours within rotor - 68 percent blade height - peak efficiency - 100 percent speed

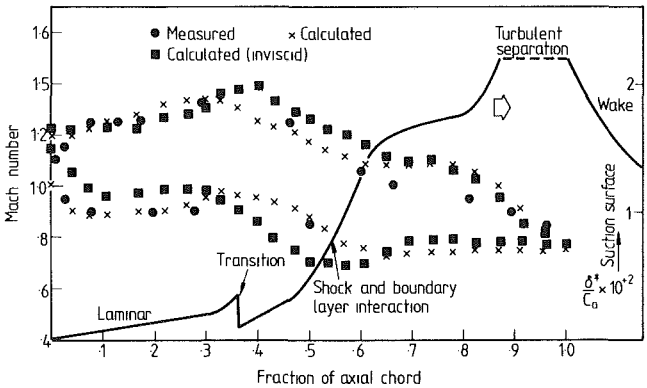

Fig. 10 Transonic compressor rotor - 68 percent blade height

moving rotor blade channel were obtained with an advanced laser (L2F) velocimeter.

The flow field for this stage has been computed by the method outlined above for the peak efficiency condition, at 100 percent speed.

Figure 5 shows the comparison of the measured flow field with the calculated results for the rotor at 18 percent blade height. Both the calculation and the experiment show a supersonic region behind the leading edge, although the method computes a higher subsonic diffusion for the suction surface. This could be due to the poor modelling of the growth of the boundary layer displacement thickness after turbulent separation, see Fig. 6, before the trailing edge of the blade is reached. Separation is also predicted on the pressure surface, although this result is not shown in Fig. 6. Figure 6 also compares the local Mach numbers around the blade surface. The calculated results near the leading edge (especially the dip in the plot near the leading edge on the pressure surface) suggests the calculation of slightly higher inlet flow angle than the experimental value.

Figure 7 compares the calculated and measured contours of constant relative Mach number through the rotor blade passage at 45 percent blade height. The relative inlet Mach number is slightly supersonic due to the increased blade speed. Both the calculation and the experiment show the presence of detached shock waves at the blade channel entrance. The experiments show a subsonic bubble region ahead of the leading edge, but the calculation method does not predict this phenomenon to the same degree. The method predicts acceleration of the flow on the suction surface to a local Mach number level in excess of 1.2 before reducing to subsonic values through a normal shock. This acceleration and deceleration of the flow is in excellent agreement with the experimental results. The method calculates a higher diffusion in the rear part of the blade channel. This again is probably due to the prediction of separated flows on both the surfaces at the rear end of the blades, see Fig. 8, where boundary layer results are shown for the suction surface only. Figure 8 also compares the local Mach numbers around the blade surface. The calculated distribution is in excellent agreement with the experimental distribution, although the calculated incidence angle appears slightly higher than the experimental value. Figure 8 also shows surface Mach number distributions due to the method described in this paper, but with the boundary layer calculation by-passed i.e. no boundary layer effects taken into account. The inviscid result shows an over prediction of the shock wave on the suction surface.

Figure 9 gives the comparison of the measured flow field with the calculated results for the rotor at 68 percent blade height. The relative inlet Mach number is about 1.2. Both the

Downloaded 01 Jun 2010 to 171.66.16.62. Redistribution subject to ASME license or copyright; see http://www.asme.org/terms/Terms_Use.cfm

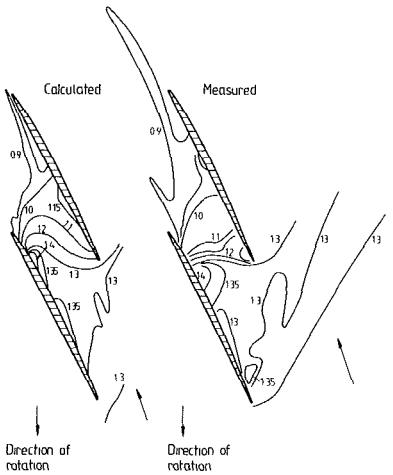

Fig. 11 Mach number contours within rotor - 89 percent blade height - peak efficiency - 100 percent speed

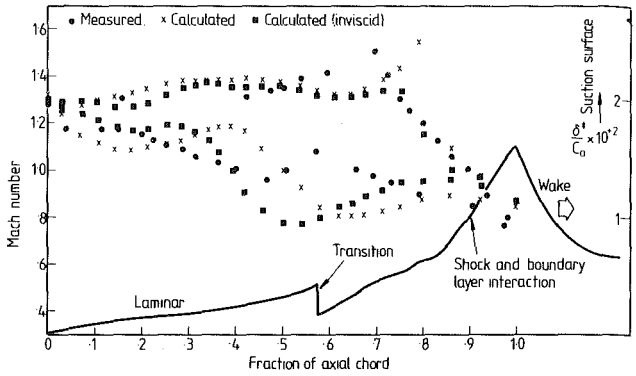

Fig. 12 Transonic compressor rotor - 89 percent blade height

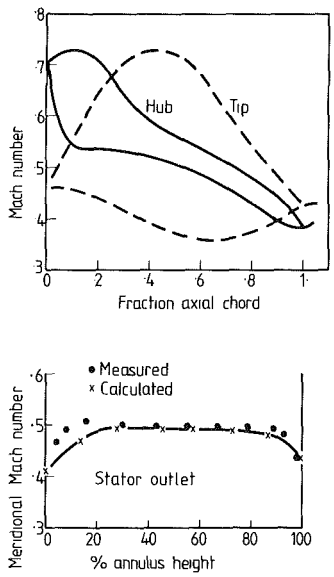

Fig. 13 Transonic compressor stator

calculation and the experiment show the presence of a bow shock wave ahead of each blade. Within the blade passage the experimental results show the presence of a normal shock wave impinging on the suction side of the adjacent blade at nearly 50 percent chord. The calculation, however, predicts an oblique shock wave, with a strong shock and boundary layer interaction. This boundary layer undergoes turbulent separation at about 90 percent chord, see Fig. 10. However, the boundary layer on the pressure surface, (not shown) is fully attached. Figure 10 also shows the local Mach numbers around the blade surfaces. The calculated (with boundary layer) and experimental distributions are in excellent agreement except at the rear end of the suction surface, where the calculated results indicate flow separation and reattachment. Results due to the without boundary layer calculation are also shown. This gives an, overprediction of the suction surface shock strength and also a generally less well predicted pressure surface result.

Figure 11 compares the calculated and measured contours of constant relative Mach number through the rotor blade passage at 89 percent blade height. The relative inlet Mach number is increased to 1.3. Both the experimental and calculated results show the presence of an attached shock wave at the blade leading edge. This shock wave has an oblique branch within the blade channel which impinges on the adjacent blade (experiment at 80 percent chord, calculation at 85 percent chord). Figure 12 shows the local Mach numbers around the blade surfaces. On the suction surface agreement between calculated and experimental results is extremely good. However, the calculated shock wave is located slightly downstream compared with the experimental shock wave. On the pressure surface the experimental diffusion through the Mach 1.0 level is more gradual than the computed flow field, which appears to pass through a mild shock of inlet strength 1.18. The Mach number distribution calculated without the inclusion of boundary layer effects is also shown in Fig. 12. This predicts a lower shock strength on the suction surface, than the experimental value. Also, the diffusion through the Mach 1.0 level on the pressure surface is predicted to occur earlier than in the with boundary layer calculation. This worsens the comparison of this result with experiment. Again, the plot of displacement thickness for the suction surface only is shown on the Mach number distribution plot (see Fig. 12). The boundary layers on both the surfaces are fully attached.

Figure 13 gives the calculated Mach number distribution around the blade surfaces for the stator at the hub and the tip sections. Both sections experience strong diffusion in the blade passages. This figure also gives a plot of calculated and measured meridional Mach numbers at the stator exit against the percentage annulus height. The agreement between the two is extremely good.

Conclusion

Considerable enhancement in the quality of flow computations in a transonic axial turbomachine stage has been achieved by the inclusion of blade surface boundary layer blockage effects in a time marching calculation method for turbomachine flows. The integral boundary layer method used in this work is strictly two-dimensional and includes a comparatively simple treatment of shock and boundary layer interaction effects. Nevertheless, results obtained are extremely encouraging, and it is believed that further improvements will follow from improvements in the boundary layer method and inclusion of boundary layer blockage effects on the hub and the casing of the turbomachine stage.

Acknowledgments

The work described in this paper was sponsored jointly by GEC Gas Turbines Ltd., Whetstone, and Ruston Gas Turbines Ltd., Lincoln. The author is grateful to the managements of both these companies for their permission to publish the work and Mr. A. R. Eves for his valuable suggestions.

Downloaded 01 Jun 2010 to 171.66.16.62. Redistribution subject to ASME license or copyright; see http://www.asme.org/terms/Terms_Use.cfm

References

1 Denton, J.D., and Singh, U.K., "Time Marching Methods for Turbomachine Flow Calculation," Von Karman Institute, Brussels, lecture series "Application of Numerical Methods to Flow Calculations in Turbomachines," Apr. 1979.

2 Thompkins, W.T., and Oliver, D.A., "Three-Dimensional Flow Calculation for a Transonic Compressor Rotor," AGARD Conference Proceedings No. 195, "Through-Flow Calculations in Axial Turbomachinery," May 1976.

3 Haymann-Haber, G., and Thompkins, W.T., "Comparison of Experimental and Computational Shock Structure in a Transonic Compressor Rotor," ASME Paper No. 80-GT-81, 1980.

4 McDonald, P.W., Bolt, C.R., Dunker, R.J., and Weyer, H.B., "A Comparison Between Measured and Computed Flow Fields in a Transonic Compressor Rotor," ASME Paper No. 80-GT-7, 1980.

5 Singh, U.K., "Computation of Transonic Flow in Cascade with Shock and Boundary Layer Interaction," *Proceedings of the 1st International Conference on Numerical Methods in Laminar and Turbulent Flow*, Swansea, July 1978.

6 Singh, U.K., "Computation of Transonic Flows in Cascade with Shock and Boundary Layer Interaction," Von Karman Institute, Brussels, lecture series "Shock-Boundary Layer Interaction in Turbomachines," June 1980.

7 Dunker, R.J., Strunning, P.E., and Weyer, H.B., "Experimental Study of the Flow Field Within a Transonic Axial Compressor Rotor by Laser Velocimetry and Comparison with Through Flow Calculations," ASME Paper No. 77-GT-28, 1977.

Downloaded 01 Jun 2010 to 171.66.16.62. Redistribution subject to ASME license or copyright; see http://www.asme.org/terms/Terms_Use.cfm

Development of Screening Criteria for Selecting Long-Distance Heat Transmission Fluids

S. Szepe
Department of Energy Engineering,
University of Illinois at
Chicago Circle,
Chicago, Ill. 60680

J. M. Calm
Energy Management and
Utilization Division,
Electric Power Research Institute,
Palo Alto, Calif. 94303

Selection criteria are developed for screening liquids for long-distance thermal energy transport. The model used in developing these criteria employs power function approximations for physical and economical relations. Its simplified version provides analytical insights into the optimal allocation of major cost components, as well as a solution for the total transmission cost. The resulting hierarchy of selection criteria can be used for fast screening and ranking of a large number of fluids, thereby eliminating the need for detailed engineering, economic, environmental, and safety studies on fluids which would ultimately prove undesirable. Representative fluids are discussed and compared with transmission by hot water. It is found that most thermal fluids can be rejected, because of less desirable physical properties compared with those of hot water, with the simplest of the criteria presented.

Introduction

Alternatives to conventional energy systems are presently being developed and evaluated in order to make more efficient use of energy resources and to avoid depletion of those which are scarce. Beyond conservation goals, these alternative technologies are being considered for economic, social, and environmental reasons as well. Among available options are use of natural energy sources, such as solar and geothermal power. Also included are coal, refuse, and biomass firing of boilers, as well as nuclear reactor produced power. For physical, safety, economic, and environmental reasons, such sources may be remotely located from the points of energy use.

Conventional approaches to transport of energy over long distances are generally limited to its chemical (fossil and synthetic fuels), electrical, and nuclear (fissile materials) forms. Electrical transmission is the most commonly practiced. However, the use of this high thermodynamic availability (theoretical maximum available work) energy form for end-uses such as resistance heating is inefficient due to the mismatch between the quality and requirement of available energy used. Furthermore, lower quality energy forms, such as hot water, can be produced more efficiently on a thermodynamic first law basis than electricity.

Energy transport in thermal form is generally restricted to short distances not exceeding 12 mi/(20 km) with liquids (e.g., district heating distribution) and very much shorter distances with gases (e.g., air in building heating systems).

Approximately 75 percent of residential and 55 percent of commercial end-use energy consumption, measured at the point-of-entry to the power plants for electricity and to the buildings for other fuels, is used for space and water heating in the U. S. [1]. Based on 1978 domestic energy consumption, this amounts to about 19.1 quads (20.2 EJ), quadrillion Btu, of energy, of which approximately 83 percent, or 15.8 quads (16.7 EJ), is supplied by direct combustion of natural gas and petroleum distillates.

District heating, and particularly district heating involving cogeneration often referred to as combined heat and power, offers significant conservation potential in meeting these large demands. For the aforementioned reasons, it may be desirable to produce thermal energy remotely from its use. In this case, long distance transmission of thermal energy is necessary.

Thermal Fluids

Various studies have explored thermal transmission in hot water, steam, and oil form [2–5], as well as by chemical heat pipes [6]. Investigations of alternative concepts indicate that it may be desirable to transmit thermal energy at very high temperatures to allow split system cogeneration [7] or reduced transport [8].

The present study focuses on an analytical method of selecting thermal fluids for long distance heat transmission. *This study has been limited to liquids which do not, for thermal transmission, involve either phase changes or chemical reactions.* Such heat transfer fluids may include water, oils, or other organic fluids, or any other fluid conforming to the assumptions hereafter explained. Since alternatives to water, taken as the reference fluid, are considerably more expensive and since piping networks are capital-intensive subsystems [5], the basic model which follows is an economic one based on consideration of relevant physical and engineering factors. Because the number of parameters involved is large, a number of approximations, explained were made.

Model for Hot Water

The basic components of a heat transmission system are its

Contributed by the Advanced Energy Systems Division for publication in the JOURNAL OF ENGINEERING FOR POWER. Manuscript received at ASME Headquarters July 14, 1980.

Copyright © 1982 by ASME
Downloaded 01 Jun 2010 to 171.66.16.62. Redistribution subject to ASME license or copyright; see http://www.asme.org/terms/Terms_Use.cfm

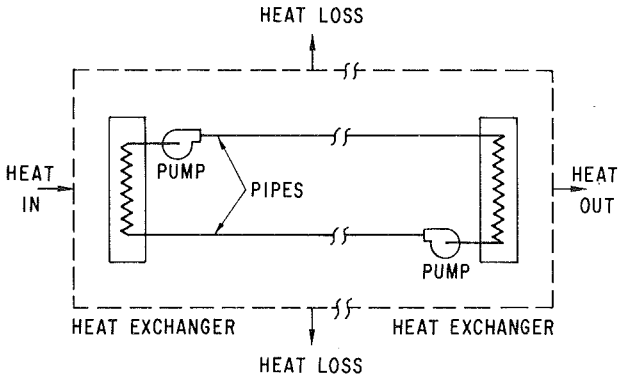

Fig. 1 Transmission system schematic

pipes, pumps, and heat exchangers. For a given heat transmission rate, the cost of pipes and pumps varies approximately linearly with the transmission distance, while the cost of heat exchangers is independent of this distance. Consequently, for long-distance heat transmission, pipeline (including rights-of-way, trenching, and related costs), and pumping costs dominate the total cost equation. A lower bound to the total cost, which closely approximates it, can be determined from these two cost components alone.

Using only these dominant terms, a simple model for long-distance heat transmission in a closed hot water system has been developed. To further simplify the model, the effects of vertical gradients of the piping network on pumping power, heat losses in transmission, and the cost of water were disregarded, and the pipes were assumed to be round. These assumptions affect the costs obtained by the model, but they do not influence the general conclusions reached regarding thermal fluid selection. A schematic of the simplified system depicting the thermal exchanges is shown in Fig. 1. In an actual system, booster and secondary pumping may also be utilized.

These simplifying assumptions allow concentration on the important cost parameters and result in a simple analytical solution for system optimization; this optimum is very close to the optimum obtained with a more rigorous model. The simplified model can be easily used to closely approximate transmission system costs and also as a learning tool to gain understanding of the significance of various design parameters.

The cost of a thermal transport system is based on both physical and economical relationships, some of which are rather complex. To obtain an analytically tractable formulation, both types of relationships can be approximated either by linear or power functions (see Appendices I and II). Since the physical and economic relations involved are all monotonic, linear and power function approximations are satisfactory for modeling thermal transport economics.

The primary physical relations involved are those describing flow rate, pressure drop, and pumping power requirements. Neglecting the variation of C_p with temperature, which is very small, the effect of the mass flow rate can be calculated for a specified thermal transmission requirement with a temperature differential between the supplied and returned fluid as:

$$\dot{m} = \frac{\dot{Q}}{C_p \Delta T} \tag{1}$$

The pressure drop for turbulent flow, can be approximated by the Moody relation [9] as:

$$\Delta p = a\left[1 + \left(\frac{2 \cdot 10^4 \epsilon}{D} + \frac{10^6}{N_{\mathrm{Re}}}\right)^{1/3}\right]\frac{\rho V^2 L}{D} \tag{2}$$

where the Reynolds number is given by:

$$N_{\mathrm{Re}} = \frac{V \rho D}{\mu} \tag{3}$$

Nomenclature

a = constant in equation (2)
A = constant in the approximate power requirement, equation (6)
A_j = constants in investment cost, equation (7)
b = constant in equation (5)
B_j = constants in investment cost, equation (7)
c = constant in equation (18)
C_f = price of thermal fluid (money/volume)
C_{fb} = break-even price of thermal fluid (money/volume)
C_p = heat capacity of fluid (energy/(mass × temperature difference))
D = inside pipe diameter (length)
$\dot{E}$ = power requirement for pumping (energy/time)
F = term defined by equation (17)
g = unit price of energy for pumping (money/energy)
I_j = capital investment costs (money)
k_i = fixed charge rates (1/time)
K_j = economic constants defined by equations (10, 11) and (18)
L = transmission distance (length)
$\dot{m}$ = mass flow rate (mass/time)
M = term defined by equation (35)
n_i = exponents in the power function approximation for pumping power requirements
n_{ij} = exponents in investment cost equations
N_{Re} = Reynolds number
ΔP = pressure drop in pipeline (force/area)
P = property term as defined by equation (27)
q = volumetric flow rate (volume/time)
$\dot{Q}$ = energy transmission rate (energy/time)
R = term defined by equation (28)
S = total cost per unit of operating time (money/time)
S_{fl} = lower bound for minimum total cost with thermal fluid (money/time)
S_{fu} = upper bound for minimum total cost with thermal fluid (money/time)
ΔT = temperature difference between the supplied and returned fluid (temperature)
v = velocity (length/time)
x_i = independent variable in equation (6)
y_{ij} = independent variable in investment costs, equation (7)
Z = dimensionless number of merit for thermal fluids defined in equation (34)
ϵ = pipe roughness
η = pumping efficiency
μ = viscosity (mass/(length × time))
ρ = density (mass/volume)

Subscripts

f = thermal fluid
i = identifies variables
j = identifies cost components
min = minimum

Superscripts

$*$ = optimal

Downloaded 01 Jun 2010 to 171.66.16.62. Redistribution subject to ASME license or copyright; see http://www.asme.org/terms/Terms_Use.cfm

The pumping power requirement is:

$$\dot{E} = \frac{\Delta p q}{\eta} \tag{4}$$

After appropriate substitutions, the pumping power can be expressed for a round pipe as:

$$\dot{E} = b\left[1 + \left(\frac{2 \cdot 10^4 \epsilon}{D} + \frac{10^6 \pi}{4}\frac{\mu D}{\dot{m}}\right)^{1/3}\right]\frac{\dot{m}^3 L}{D^5 \rho^2} \tag{5}$$

which can be approximated as:

$$\dot{E} = A\prod_{all\ i} x_i^{n_i} \tag{6}$$

The variables of equation (6) are listed in Table 1, where the lower and upper bounds of the exponents are also shown.

Investment costs are:

$$I_j = A_j + B_j \prod_{all\ i} y_{ij}^{n_{ij}} \tag{7}$$

The total cost includes operating costs which are proportional to the power requirements, as well as costs proportional to the capital investment requirements:

$$S = g\dot{E} + \sum_{all\ j} k_j I_j \tag{8}$$

where the fixed charge rates are determined by depreciation, interest rates, property and income taxes, and other financial factors.

As an illustration, the optimal design and corresponding minimum operating cost will now be determined for a representative case which involves common "first-cut" assumptions, namely:

- All exponents in the power requirement equation are considered at the mean values of the respective ranges indicated in Table 1.
- The pump investment cost is taken as proportional to the power requirement.
- The pipeline investment cost is taken as proportional to the pipeline diameter and to the pipeline length.

For these conditions, the total cost function has the following form:

$$S = K_1 \frac{(\epsilon\mu)^{1/6}}{\rho^2}\left(\frac{\dot{Q}}{C_p \Delta T}\right)^{17/6}\frac{L}{D^5} + K_2 D L \tag{9}$$

where

$$K_1 = A[g + k_1 B_1] \tag{10}$$

and

$$K_2 = k_2 B_2 \tag{11}$$

For a specified transmission rate and temperature differential, an expression for the optimum pipe diameter can be obtained by differentiating the total cost with respect to the diameter and setting the derivative equal to zero:

Table 1 Power function approximation of pumping power requirements based on equation (6)

i	x	n
1	D	$-16/3 < n < -14/3$
2	L	1
3	$\dot{m}$	$8/3 < n < 3$
4	ϵ	$0 < n < 1/3$
5	μ	$0 < n < 1/3$
6	ρ	-2

$$D^* = \left(5\frac{K_1}{K_2}\right)^{1/6}\frac{(\epsilon\mu)^{1/36}}{\rho^{1/3}}\left(\frac{\dot{Q}}{C_p \Delta T}\right)^{17/36} \tag{12}$$

Substituting the optimum diameter into equation (9), the minimum total cost can be found as:

$$S_{\min} = \left(\frac{K_1 K_2^{\,5}}{5^5}\right)^{1/6}\frac{(\epsilon\mu)^{1/36}}{\rho^{1/3}}\left(\frac{\dot{Q}}{C_p \Delta T}\right)^{17/36} L + (5K_1 K_2^{\,5})^{1/6}\frac{(\epsilon\mu)^{1/36}}{\rho^{1/3}}\left(\frac{\dot{Q}}{C_p \Delta T}\right)^{17/36} L \tag{13}$$

Note that the first term of the preceding equation represents expenses associated with the pump, while the second term includes costs due to the pipeline. The ratio of these terms is:

$$(S_2/S_1)^* = 5 \tag{14}$$

indicating that the dominant cost term in the minimum cost equation corresponding to the optimal design is that of the pipeline. At the optimum, 5/6 of the operating expenses should be due to actual pipeline cost components, and only 1/6 due to pump components. This important conclusion, arrived at analytically, is confirmed by detailed case studies of other investigators [2].

The simplicity of this conclusion, as expressed by equation (14), is a direct consequence of the fact that the minimization of equation (9) constitutes a geometric programming problem of zero degree difficulty [10].

The foregoing result provides valuable guidance for more accurate economic studies and for research priorities related to thermal transport. Clearly, in developing a more rigorous model of thermal transmission economics, accurate cost data for the pipeline is much more important than for the pumps or pumping. Similarly, any research efforts aimed at reducing the operating cost of thermal transport should concentrate on reducing pipeline material and installation costs since these provide much higher savings in the overall cost than do reduction in capital and operating costs for the pumps.

Further important conclusions regarding the effects of physical properties on the total operating costs can be reached by studying the results provided by equation (13), which can be rewritten as:

$$S_{\min} = 6\left(\frac{K_1 K_2^{\,5}}{5^5}\right)^{1/6}\frac{(\epsilon\mu)^{1/36}}{\rho^{1/3}}\left(\frac{\dot{Q}}{C_p \Delta T}\right)^{17/36} L \tag{15}$$

As indicated by equation (15), heat capacity and density are the most significant properties affecting the minimum cost, with exponents of $-17/36$ and $-1/3$, respectively. The strong sensitivity of costs to transport fluid density, observed analytically in this study, confirms findings of other studies in which steam was, in most cases, found to be a less economical thermal transport fluid than hot water for long-distance transmission [2].

Viscosity has an extremely small effect, entering the minimum cost equation with a power of only 1/36. This indicates that it is not important to have very accurate values for viscosity or for its variation with temperature, even for more detailed numerical studies of thermal transport economics, and the reduction of viscosity by drag reducing agents, or other means, would have little effect on the total cost.

Model for Other Thermal Fluids

In the foregoing case, the cost of the water inventory of the pipeline was assumed to be negligible compared to other capital costs. Such an assumption, of course, cannot be made when using thermal fluids other than hot water and steam.

Downloaded 01 Jun 2010 to 171.66.16.62. Redistribution subject to ASME license or copyright; see http://www.asme.org/terms/Terms_Use.cfm

Here the capital costs of the fluid inventory, which are proportional to the total volume of the transport system, must also be considered.

In this case, the total operating cost equation becomes:

$$S_f = \left(\frac{K_{1f}F_f}{D^5} + K_{2f}D + K_{3f}D^2\right)L \tag{16}$$

where

$$F_f = \frac{(\epsilon\mu_f)^{1/6}}{\rho_f{}^2}\left(\frac{\dot{Q}}{C_{pf}\Delta T}\right)^{17/6} \tag{17}$$

and

$$K_{3f} = K_{3f}\frac{\pi}{4}\,c\,C_f \tag{18}$$

The number c, here, is 2 if only the inventory in the transmission and return pipes is considered, and higher if standby inventory is also included.

The economic constants of the first two terms of equation (16) may be significantly different from the respective constants for hot water because of environmental, safety and other considerations.

The minimization of equation (16) constitutes, in geometric programming terms, a problem of first degree difficulty. This problem can be easily solved for any given values of the four constants. Moreover, simple analytical expressions, applicable for all values of these constants, may be found for the upper and lower bounds on the minimum total cost, described as follows.

The following observations can now be made. First, the exponent for D in the power function approximation for the sum of the second and third terms of equation (16) is between 1 and 2 (see Appendix II). Second, this exponent is much closer to 1 than to 2 since the thermal fluid investment costs must be much smaller than the pipeline investment costs in order to be economically feasible compared to a hot water system.

Consequently, if one solves for the optimum diameter for the truncated equation (i.e., without the third term), instead of the actual optimal diameter, D^*, of equation (16):

$$D_T{}^* = \left(\frac{5K_{1f}F_f}{K_{2f}}\right)^{1/6} \tag{19}$$

a lower and an upper bound for the minimum total cost are obtained:

$$S_{f1} \le S_{f\min} \le S_{fu} \tag{20}$$

The lower bound is arrived at by substituting the preceding value into the first two terms only:

$$S_{f1} = 6\left(\frac{K_{1f}F_fK_{2f}{}^5}{5^5}\right)^{1/6} L \tag{21}$$

and the upper bound by repeating this step with all three terms:

$$S_{fu} = \left[6\left(\frac{K_{1f}F_fK_{2f}{}^5}{5^5}\right)^{1/6} + \left(\frac{5K_{1f}F_f}{K_{2f}}\right)^{1/3} K_{3f}\right]L \tag{22}$$

As follows from the aforesaid second observation, the exact minimum will be much closer to the upper bound than to the lower one.

Comparison of Thermal Fluids with Hot Water

The minimum cost when using a thermal fluid may now be compared to that of using hot water. A thermal fluid surely cannot be economically feasible if the lower bound of its minimum cost exceeds the minimum cost with hot water:

$$S_{f1} \ge S_{\min} \tag{23}$$

On the other hand, a fluid can be expected to be economically feasible if the upper bound to its minimum cost is lower than the minimum cost with hot water:

$$S_{fu} \le S_{\min} \tag{24}$$

Substitution of equations (15) and (22) into (24) leads, after rearrangement, to the following criterion for likely economic feasibility:

$$\frac{(K_{1f}F_f)^{1/6}}{K_{2f}{}^{7/6}} K_{3f} \le \frac{6}{5^{7/6}}\left[\left(\frac{K_1f}{K_{1f}F_f}\right)^{1/6}\left(\frac{K_2}{K_{2f}}\right)^{5/6} - 1\right] \tag{25}$$

The physical properties now can be separated from the other terms in F as follows:

$$F = \frac{R}{P} \tag{26}$$

where P denotes a physical property term:

$$P = \frac{\rho^2 C_p{}^{17/6}}{\mu^{1/6}} \tag{27}$$

and R denotes a term based primarily on design requirements:

$$R = \epsilon^{1/6}\left(\frac{\dot{Q}}{\Delta T}\right)^{17/6} \tag{28}$$

Similar terms can be defined for the thermal fluid.

The criterion for likely economic feasibility, inequality (25), can be rewritten, after recognizing that:

$$R_f \simeq R \tag{29}$$

even for pipes of differing smoothness, as:

$$P_f{}^{1/6}\left[\left(\frac{K_1}{K_{1f}}\right)^{1/6}\left(\frac{K_2}{K_{2f}}\right)^{5/6}\left(\frac{P_f}{P}\right)^{1/6}\right] - 1 \le \frac{5^{7/6}}{6}\left(\frac{K_{1f}F_f}{K_{2f}}\right)^{1/6} K_{3f} \tag{30}$$

where the physical property term is a measure of merit of the thermal fluid for heat transmission.

Inequality (30) can be used to identify thermal fluids likely to be desirable. A similar criterion can be developed from inequality (23) for rejection of candidate fluids which are surely undesirable:

$$\left(\frac{K_1}{K_{1f}}\right)^{1/6}\left(\frac{K_2}{K_{2f}}\right)^{5/6}\left(\frac{P_f}{P}\right)^{1/6} \le 1 \tag{31}$$

It should be noted that the cost of the thermal fluid is not required for this criterion, indicating that fluids which cannot satisfy inequality (31) are not economically feasible at any price. This implies, in turn, that some fluids can be rejected even without knowledge of their prices, provided that the prices are equal to or greater than that of water.

Values for the economic parameters of thermal fluids are dependent on environmental, safety, and other factors which may not be precisely known at the time of candidate fluid selection. These costs will invariably be higher than those for hot water or steam where the latter are not eliminated from consideration by physical or other requirements (e.g., temperatures at which water would freeze or temperatures where extremely high pressures would result). Consequently,

$$\left(\frac{K_1}{K_{1f}}\right)^{1/6}\left(\frac{K_2}{K_{2f}}\right)^{5/6} < 1 \tag{32}$$

from which it follows that if the physical property term for the fluid is lower than that of water:

$$P_f < P \tag{33}$$

Downloaded 01 Jun 2010 to 171.66.16.62. Redistribution subject to ASME license or copyright; see http://www.asme.org/terms/Terms_Use.cfm

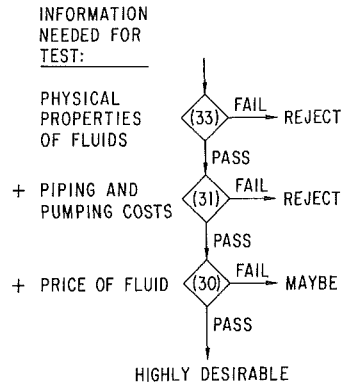

Fig. 2 Hierarchy of screening tests

then the fluid can be rejected based on physical properties alone, without consideration of any economic factors.

For fluids which neither satisfy inequality (30) nor fail inequality (31), no definite conclusions can be made on the basis of these simple criteria alone.

Based on these results, a hierarchy of screening tests, shown in Fig. 2, may be employed before performing detailed studies of candidate fluids for thermal transport. Many fluids can be rejected on the basis of the *first test*, inequality (*33*), alone. Fluids passing this physical property criterion may be subjected to a *second test*, inequality (*31*), and then a *third test*, inequality (*30*). Thermal fluids satisfying all three tests are probably desirable. Those passing only the first two are candidates for further examination. Fluids which fail either the first or second tests are to be rejected.

The findings in Fig. 2 may be summarized by defining a dimensionless number which may be used to rank various fluids:

$$Z = \frac{6}{5^{7/6}} \frac{K_{2f}^{7/6}}{K_{3f}} \left(\frac{P_f}{K_{1f} R_f}\right)^{1/6} (M-1) \tag{34}$$

where the term M is defined by

$$M = \left(\frac{K_1}{K_{1f}}\right)^{1/6} \left(\frac{K_2}{K_{2f}}\right)^{5/6} \left(\frac{P_f}{P}\right)^{1/6} \tag{35}$$

Fluids for which Z is negative are definitely not economically viable. Those with Z values between 0 and 1 are possible, but not promising, candidates. Those with Z values greater than 1 warrant detailed study of suitability and their use is probably economically more attractive than use of water.

Finally, an alternate expression for inequality (30) may be developed in terms of a "break-even price." In order to be economically feasible, the actual price of the thermal fluid must be less than this break-even price for its physical properties:

$$C_f \leq C_{fb} \tag{36}$$

where

$$C_{fb} = \frac{24}{5^{7/6}} \frac{K_{2f}^{7/6}}{\pi G C} \left(\frac{P_f}{K_{1f} R_f}\right)^{1/6} (M-1) \tag{37}$$

Application of Testing Criteria

Application of the methodology previously described may result in significant savings by eliminating detailed studies and related experimental work on the environmental and safety aspects of candidate fluids which would ultimately prove uneconomical.

The simple model presented is not expected to result in completely accurate values for the total cost of energy transmission, but only to provide a reliable and fast method for comparing various candidate fluids with each other and with hot water. These tests have been applied to a number of commonly used thermal fluids shown in Table 2, based on physical data from Fried [11]. No liquid examined to date has favorably met the first condition, primarily because the heat capacity of most organic liquids is much less than that of water [12]. This finding is confirmed by recent detailed case studies of several commercially available thermal fluids [4].

The search for a fluid for thermal transmission which is more economical than hot water or steam, on a life-cycle cost basis, is continuing. However, it seems unlikely that such a liquid will be found, at least not for the temperature ranges of present concern.

Table 2 Physical properties of selected thermal fluids at 400°F

	C_{pf} Btu/lb°F	ρ_f lb/ft³	μ_f lb/ft hr	$P_f = \frac{\rho_f^2 C_{pf}^{17/6}}{\mu_f^{1/6}}$ (see note 1)	$\frac{P_f}{P}$	$\left(\frac{P_f}{P}\right)^{1/6}$
Dowtherm[2] A	.45	60	1.0	375	.085	.66
Dowtherm[2] E	.35	55	0.7	165	.037	.58
Dowtherm[2] G	.45	60	2.0	335	.076	.65
Dowtherm[2] H	.50	55	2.5	365	.083	.66
Dowtherm[2] J	.55	45	0.3	455	.104	.69
Humbletherm[3] 500	.60	45	3.0	395	.090	.67
Hitec[4] salt	.35	120	20.0	445	.101	.68
Mobiltherm[5] 500	.50	55	3.0	355	.080	.66
Therminol[6] 55	.60	50	2.5	505	.115	.70
Therminol[6] 66	.50	55	2.0	375	.086	.66
Therminol[6] 88	.45	60	2.5	320	.073	.65
Ucon[7] 50-HB-280X	.55	60	8.0	470	.106	.69
Water	1.00	60	0.3	4400	1.000	1.00

[1] $(Btu)^{17/6}(hr)^{1/6}/(°F)^{17/6}(lb)(ft)^{35/6}$.

[2] Trademark of the Dow Chemical Company.

[3] Trademark of Exxon Corporation.

[4] Trademark of E.I. DuPont Company.

[5] Trademark of Mobil Oil Company.

[6] Trademark of Monsanto Industrial Chemicals Company.

[7] Trademark of Union Carbide Company.

Summary

A model for thermal fluid selection for long-distance heat transmission has been described, and screening tests for thermal fluids have been analytically derived from this model. Application of these criteria may save considerable effort by eliminating the need for detailed engineering, economic, environmental, and safety studies on those fluids which would ultimately prove physically or economically undesirable. Of the liquids examined to date, none has been found which is more attractive than hot water and it is doubtful that any will be. The findings of the present study are in agreement with studies by others based on detailed examination of candidate thermal fluids for specific case studies.

Acknowledgment

This paper is a summary of work at Argonne National Laboratory (ANL) sponsored by the former Office of Buildings and Community Systems, U.S. Department of Energy (DOE). Dr. Stephen Szepe's participation was on a appointment to ANL's faculty research program. Mr. Calm, now at EPRI, was a Mechanical Engineer and Project Manager in ANL's Energy and Environmental Systems Division. An abridged report of parts of this work has been previously published by the authors [13]. A draft of this paper was reviewed by Mr. Kon Lee, Dr. Ishai Oliker, and Mr. Gary Phetteplace; their recommendations are appreciated.

References

1 Federal Energy Administration, "Project Independence Blueprint Task

Downloaded 01 Jun 2010 to 171.66.16.62. Redistribution subject to ASME license or copyright; see http://www.asme.org/terms/Terms_Use.cfm

Force Report — Residential and Commercial Energy Use Patterns 1970-1990," NTIS Report PB-248 508, Nov. 1974, pp. 6-12.

2 Aamot, H. W. C., and Phetteplace, G. E., "Heat Transmission with Steam and Hot Water," *Congeneration District Heating Applications,* ASME Book No. H00128, July 1978, pp. 17-23.

3 Aamot, H. W. C., and Phetteplace, G. E., "Long Distance Heat Transmission with Steam and Hot Water," Cold Regions Research and Engineering Laboratory Technical Note presented at the International Total Energy Congress, Copenhagen, Denmark, Oct. 1976.

4 Hydroscience, Inc., "Assessment of Long-Distance Thermal Energy Transport: A Comparison Between Water, Steam, and Hot Oils," Oak Ridge National Laboratory Report ORNL/SUB-79/14274-1, Mar. 1979.

5 Karkheck, J., "Long-Distance Transmission of Hot Water for District Heating," *Proceedings of the 13th Intersociety Energy Conversion Engineering Conference,* Paper No. 789514, Aug. 1978, pp. 1022-1028.

6 Institute of Gas Technology, "Transmission of Energy by Open-Loop Chemical Energy Pipelines," prepared for Sandia Laboratories under Project 8990, June 1978.

7 Calm, J. M., and Rabl, V. A., "Bottoming Cycle Split System Cogeneration," *Proceedings of the Third National Conference on Technology for Energy Conservation,* Jan. 1979, pp. 100-107.

8 Taube, M., "Duplex Chemical System for the Storage and Container Transport of Heat for District Heating," *Nuclear Technology,* Vol. 38, No. 1, Apr. 1978, pp. 62-68.

9 Moody, L. F., "An Approximate Formula for Pipe Friction Factors," *Mechanical Engineering,* Vol. 69, 1947, pp. 1005-1006.

10 Duffin, R. J., Peterson, E. L., and Zener, C., *Geometric Programming,* Wiley, New York, 1967.

11 Fried, J. R., "Heat Transfer Agents for High-Temperature Systems," *Chemical Engineering,* Vol. 80, No. 12, May 28, 1973, pp. 89-98.

12 National Research Council of the United States, E. W. Washburn, Editor-in-Chief, *International Critical Tables of Numerical Data, Physics, Chemistry, and Technology,* McGraw-Hill, New York, Vol. 5, 1929, pp. 106-117.

13 Szepe, S., and Calm, J., "Thermal Fluid Selection for Long-Distance Heat Transmission," *Proceedings of the 14th Intersociety Energy Conversion Engineering Conference,* Boston, Paper No. 799428, Vol. 2, Aug. 1979, pp. 1985-1990.

APPENDIX I

Power Function Approximation

Consider a positive function $f(x)$ around a positive point x_0 and its power function approximation:

$$g(x) = A\,x^n \tag{38}$$

The Taylor-series approximation of $ln\ f(x)$ in the coordinate $n\,x$ around $ln\ x_0$ will be:

$$ln\,f(x) = ln\,f(x_0) + \left.\frac{d\,ln\,f(x)}{d\,ln\,x}\right|_{x_0} (ln\,x - ln\,x_0) \tag{39}$$
$$+ \text{higher order terms}$$

Neglecting the higher order terms of equation (39), and rewriting equation (38) as:

$$ln\,g(x) = ln\,A + n\,ln\,x, \tag{40}$$

it is clear that

$$n = \left.\frac{d\,ln\,f(x)}{d\,ln\,x}\right|_{x_0} \tag{41}$$

and

$$ln\,A = ln\,f(x_0) - n\,ln\,x_0, \tag{42}$$

thus

$$A = \frac{f(x_0)}{{x_0}^n} \tag{43}$$

Note that by using the chain rule, equation (41) can be put into a simpler form:

$$n = \left.\frac{d\,ln\,f(x)}{d\,f(x)}\right|_{x_0} \cdot \left.\frac{d\,f(x)}{dx}\right|_{x_0} \cdot \left.\frac{dx}{d\,ln\,x}\right|_{x_0}$$

$$= \left.\frac{d\,f(x)}{dx}\right|_{x_0} \cdot \frac{x_0}{f(x_0)} \tag{44}$$

The extension of the foregoing results for the case of more than one independent variable is straightforward, given as follows.

The Taylor-series expansion of a multidimensional function $F(\mathbf{x})$ in the space of $ln\ x_i - s -$ around the point $ln\ \mathbf{x}_0$ is:

$$ln\,F(\mathbf{x}) = ln\,F(\mathbf{x}_0)$$

$$+ \sum_{all\ i} \left.\frac{\partial\,ln\,F(\mathbf{x})}{\partial\,ln\,x_i}\right|_{\mathbf{x}_0} (ln\,x_i - ln\,x_{i0}) \tag{45}$$

$$+ \text{higher order terms}$$

Following the same method as used for the case of one independent variable, the power function approximation of $F(x)$,

$$G(\mathbf{x}) = A \sum_{all\ i} {x_i}^{n_i} \tag{46}$$

is shown to have the following coefficients:

$$n_i = \left.\frac{\partial\,ln\,F(x)}{\partial\,ln\,x_i}\right|_{\mathbf{x}_0} = \left.\frac{\partial\,F(\mathbf{x})}{\partial\,x_i}\right|_{\mathbf{x}_0} \frac{x_{io}}{F(\mathbf{x}_0)} \text{ for all } i \tag{47}$$

and

$$A = \frac{ln\,F(\mathbf{x}_0)}{\prod_{all\ i} {x_{io}}^{n_i}} \tag{48}$$

Note that the goodness of the power function approximation can be well judged by considering the second order term in the expansion, equation (39). Clearly, the approximation is especially well suited for monotonic functions.

APPENDIX II

Single Power Function Approximation of Sums of Power Functions

Consider the sum of positive function:

$$f(x) = A_1 x^{n_1} + A_2 x^{n_2} \tag{49}$$

This function may be approximated around a positive point x_0 by a single power function:

$$g(x) = A\,x^n, \tag{50}$$

where, following the definitions given in Appendix I,

$$n = \frac{n_1 A_1 {x_0}^{n_1} + n_2 A_2 {x_0}^{n_2}}{A_1 {x_0}^{n_1} + A_2 {x_0}^{n_2}} \tag{51}$$

and

$$A = \frac{A_1 {x_0}^{n_1} + A_2 {x_0}^{n_2}}{{x_0}^n} \tag{52}$$

As indicated by equation (51), the exponent of the single power function, equation (50) will be always within the bounds of n_1 and n_2:

$$n_1 \le n \le n_2 \text{ if } n_1 < n_2,$$

and

$$n_2 \le n \le n_1 \text{ if } n_2 < n_1 \tag{53}$$

Note the special case of:

$$n = \frac{n_1 + n_2}{2} \text{ if } A_1 {x_0}^{n_1} = A_2 {x_0}^{n_2} \tag{54}$$

Similar results can be easily obtained for the sum of more than two power functions, as well as for the sum of the sum of power functions of more than one independent variable.

Note that in case of the sum of more than two power functions:

$$n_{\min} \le n \le n_{\max} \tag{55}$$

Downloaded 01 Jun 2010 to 171.66.16.62. Redistribution subject to ASME license or copyright; see http://www.asme.org/terms/Terms_Use.cfm

Journal of Engineering for Power

Discussion

Rotor Tip Leakage: Part II - Design Optimization Through Viscous Analysis and Experiment[1]

U. Okapuu[2] and S. H. Moustapha.[3] The authors should be congratulated on their timely and interesting paper. The effects of overtip leakage on unshrouded axial turbine blades indeed contribute a substantial portion of pressure losses in the turbine stage. Aerodynamic means to minimize these losses exist, but their relative merits and applicability must be established for each unique combination of velocity triangles, blade loading, and blade surface velocity distribution. The analysis described in the paper appears to be a very significant step in that direction.

The generally good agreement between analysis and water-table experiments indicates that the analytical approach taken is a sound one. Since the water rig simulated the pressure-side velocity only, on the blade tip section under study, analysis must have similarly assumed a constant back pressure to the leakage flow. Would the authors confirm this, and elaborate somewhat on how the integration was carried out in the analysis, from one chordwise station to the next, so that the total leakage flow could be calculated in a manner analogous to the water-table experiments.

Also, would it not be more appropriate for the computation domain at each chordwise station to be parallel to the leakage paths rather than perpendicular to the camberline? The directions of leakage paths, which can differ significantly from the camberline perpendicular, can be quite accurately predicted by relatively simple calculations based on estimated pressure distributions on both surfaces of the blade. The adequacy of such calculations has been established on the Pratt & Whitney, Canada, water flow analogy rig, and appears to be confirmed in part I of this paper.

Figures 6–10 show sections of the blade tip, normal to the chord line. What chordwise station (percent chord) do these sections represent? Is the blade analysed the same as that shown in Fig. 6 of part I of this paper?

The paper substantiates the analysis by a comparison of calculated C_D with that measured on the single-sided water table. The relative performance of the various tip treatments examined therefore pertains to blade sections having a constant suction surface pressure. These tip treatments may exhibit a different behaviour with more conventional suction surface pressure distributions, and the turbine designer should therefore be cautioned not to take the given C_D values as absolute and universally applicable. Similarly, the slotted and cut tip geometries tested appear to extend to a spanwise depth equal to the tip clearance. A deeper pressure side cut, for example, would very likely have caused that configuration to seal more effectively.

The primary benefit of this analysis lies in its potential for specifying the tip treatment giving the lowest leakage discharge coefficient for any given rotor blade tip section. However, the ultimate performance of the tip will also depend, to some degree, on the interaction between leakage and primary flows. Rotating rig tests would therefore seem a necessary final proof of the merits of any tip treatment scheme.

[1] By A. R. Wadia and T. C. Booth, published in January 1982 issue of the JOURNAL OF ENGINEERING FOR POWER, pp. 162–169.

[2] Chief, Turbine Aerodynamics, Pratt & Whitney Aircraft of Canada Ltd., Longueuil, Quebec, Canada.

[3] Staff Aerodynamicist, Pratt & Whitney Aircraft of Canada Ltd.

Improved Particle Trajectory Calculations Through Turbomachinery Affected by Coal Ash Particles[1]

A. El-Sayed.[2] The authors are to be congratulated for their interesting paper. The three-dimensional network represents another expression for the well-known $S_{1,2,3}$ surfaces [1]. The x-θ plane is merely Wu's blade-to-blade (S_1) surface. Lines of constant percent of θ distance between surfaces represent the intersections of the meridional (S_2) surfaces with the (S_1) surface. Similarly, the lines of constant percent of axial chord length represent the intersections of the passage cross-sectional (or orthogonal) S_3 surfaces with the (S_1) surface.

Neither the governing equations nor the solution procedure are described in the paper. Therefore, it is not clear what viscous effects were incorporated in the model. In the paper a new vectorial relationship for pre- and post-impact velocities of the particle was introduced. However, the equation $(\bar{n} \times \bar{V}_1) \cdot \bar{V}_2 = 0$ is incorrect for the three-dimensional case and correct only for the two-dimensional one. An alternative for this equation in the three-dimensional case would be $\bar{n} \cdot \bar{V}_1 = \cos\theta_1$.

Additional References

1 Wu, Chung-Hua, "A General Theory of Three-Dimensional Flow in Subsonic and Supersonic Turbomachines in Axial, Radial and Mixed Flow Types," NACA TN 2604, 1952.

[1] By B. Beacher, W. Tabakoff and A. Hamed, published in the January 1982 issue of the JOURNAL OF ENGINEERING FOR POWER, pp. 64–68.

[2] Post-Doctoral Research Fellow, Department of Mechanical Engineering, Carnegie-Mellon University, Pittsburgh, Pa. 15213.

Copyright © 1982 by ASME

Downloaded 01 Jun 2010 to 171.66.16.62. Redistribution subject to ASME license or copyright; see http://www.asme.org/terms/Terms_Use.cfm